EDITED and PUBLISHED quarterly at the offices of The American Society of Mechanical Engineers, United Engineering Center, 345 E. 47th St., New York, N. Y. 10017. Cable address, "Mechaneer," New York. Second-class postage paid at New York, N. Y., and at additional mailing offices.
CHANGES OF ADDRESS must be received at Society headquarters seven weeks before they are to be effective. Please send old label and new address.
PRICES: To members, $25.00, annually; to nonmembers, $50.00. Single copies, $15.00 each. Add $1.50 for postage to countries outside the United States and Canada.
STATEMENT from By-Laws. The Society shall not be responsible for statements or opinions advanced in papers or . . . printed in its publications (B 13, Par. 4).

INDEXED by the Engineering Index, Inc.

transactions of the ASME

Published Quarterly by
The American Society of
Mechanical Engineers
Volume 100 • Number 3
AUGUST 1978

journal of heat transfer

(Contents continued on page 415)

TECHNICAL NOTES

DISCUSSION

ANNOUNCEMENTS

S. B. Thomason
Graduate Research Assistant.

J. C. Mulligan
Professor.
Mem. ASME

J. Everhart
Graduate Research Assistant.

Department of Mechanical and Aerospace Engineering,
North Carolina State University,
Raleigh, N. C. 27650

The Effect of Internal Solidification on Turbulent Flow Heat Transfer and Pressure Drop in a Horizontal Tube

A simple analysis of the steady-state heat transfer and pressure drop in turbulent flow in a tube is presented for the case involving a "thin," steady-state frozen deposit on the inside tube wall. Sparrow-Hallman-Siegel type internal flow convective heat transfer expressions and Blasius type pressure drop expressions are employed while neglecting second order interface curvature effects. Experimental heat transfer and pressure drop data are presented for comparison. It is shown that simple analyses of the type developed can be used to predict heat transfer and pressure drop in tube flow under freezing conditions and that, for the experimental conditions tested, basic agreement between theory and experiment was obtained. It is also shown experimentally that small nonuniformities in wall temperature can produce wide variations in pressure drop when a frozen layer exists within a tube.

Introduction

Melting and freezing problems commonly occur in a wide variety of processes and situations which involve fluid flow and heat transfer. Fundamentally, these phase change problems have in common a characteristic nonlinearity which complicates their analysis and which renders each problem somewhat unique. In addition, sometimes complicated and oftentimes perplexing physical phenomena occur in the melting-freezing process which invalidate conventional analyses. A variety of studies dealing with the analytical as well as experimental aspects of particular problems have appeared in the literature over the past decade. Good summaries of these have been published by Muehlbauer and Sunderland [1], Boley [2], Bankoff [3], and Gilpin [4]. A survey of some of the more recent literature was carried out by Shamsunder and Sparrow [5].

Those melting-freezing problems involving internal flow often present unusually troublesome modeling and analytical difficulties, especially when natural convection and supercooling are significant superimposed mechanisms. In some cases of supercooling, it has been shown [4] that an annular phase differentiation does not even exist but, instead, a dendritic matrix occludes the flow area. The importance of these internal problems was recognized as early as 1916 when Brush [6] pointed out some general freezing characteristics of water mains. It has only been in recent years, however, that they have received substantial development. In cases of relatively large flow rate and liquid phase superheat, wherein an annular growth might be expected for most liquids, most of the work has been directed to the laminar flow case. Some early one-dimensional analyses applicable to annular freezing in laminar tube flow were presented by London and Seban [7], Poots [8], and Hirshburg [9]/ In 1968 Zerkle and Sunderland [10] published an important analytical and experimental investigation of thermal entrance region annular freezing in laminar tube flow, wherein the steady-state problem was reduced to the classical Graetz problem. Experimental studies of freezing in thermal entrance region laminar flow were also recently carried out by Depew and Zenter [11] and Mulligan and Jones [12]. DesRuisseaux and Zerkle [13] used the results of [10] to show how one can predict the overall system conditions which will lead to the blockage of a laminar flow in a tube with a simple entrance and entrance length and with a prescribed static pressure at the exit. They also considered the procedures which would be involved in the prediction of blockage conditions for other upstream flow systems. The transient flow characteristics preceding the blockage, however, were not considered.

As indicated, most of the work on internal flow with annular freezing has addressed the freezing process in laminar flow. However, many internal flow problems involve fluid flow which is turbulent in nature and, specifically, little exists in the literature to indicate the

Contributed by the Heat Transfer Division for publication in the JOURNAL OF HEAT TRANSFER. Manuscript received by the Heat Transfer Division July 22, 1977.

effects of turbulent flow on freezing in tubes. The material presented here represents the results of a study of the internal annular freezing in the thermal entrance region of a cooled horizontal tube when the flow is steady, hydrodynamically fully developed and turbulent. The development of an approximate analysis which is relatively simple and direct is outlined, along with the results of its use in predicting the steady-state heat transfer and pressure drop. Experimental heat transfer and pressure drop data are presented for comparison.

Analysis

The inlet flow is assumed to be of uniform temperature, greater than the freezing temperature, and to be hydrodynamically fully developed at the entrance where the cooling begins. The tube wall temperature is taken to be uniform, constant, and lower than the freezing temperature of the liquid. The bulk temperature of the liquid decreases as it flows down the tube, promoting solidification and thus causing the thickness of the frozen shell to increase with distance down the tube. This change in flow area results in an acceleration of the fluid and produces a two-dimensional velocity distribution. The steady-state interface profile exists primarily as a result of the liquid phase superheat at the entrance. Without this superheat, the tube would freeze solid. A sketch of the process is shown in Fig. 1.

For purposes of the theoretical analysis, the following initial assumptions are made:

1 The flow is steady, axisymmetric, fully developed hydrodynamically, turbulent, and of uniform temperature at the entrance to the cooling section of the tube.

2 The fluid is incompressible and Newtonian, the properties of both phases are constant, and their densities assumed equal and evaluated at saturated liquid conditions. The fluid Prandtl number is assumed to be in the intermediate range and evaluated at the tube inlet conditions.

3 Radiation, free convection, viscous dissipation, and body forces are negligible. Also, it is assumed that the fluid acceleration is not sufficiently strong to influence the structure of the turbulent flow.

4 The temperature at the liquid-solid interface is equal to the freezing temperature.

5 The wall temperature is uniform, constant, and below the freezing temperature of the liquid.

6 The tube wall has negligible thermal resistance.

With these assumptions, the standard equations governing conservation of mass (continuity) and linear momentum for the liquid phase, the heat conduction in the solid phase, and the convective heat transfer in the interior liquid phase can be formulated and applied in the usual way. The interfacial radial heat transfer coupling can be expressed as

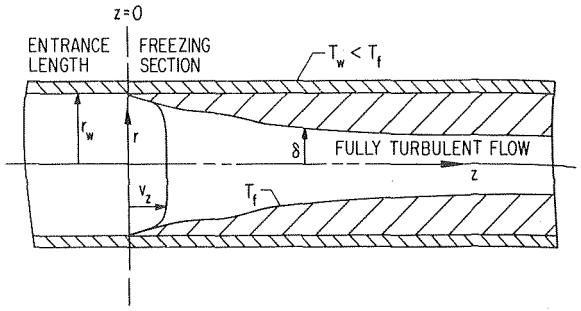

Fig. 1 Illustration of freezing section entrance and steady-state frozen shell profile

$$-k_s \left.\frac{\partial T_s}{\partial r}\right|_{r=\delta} - q_\ell \Big|_{r=\delta} = 0 \tag{1}$$

The boundary conditions at $r = 0$ for $z \geq 0$ are

$$\frac{\partial v_z}{\partial r} = v_r = 0, \frac{\partial T_\ell}{\partial r} = 0 \tag{2}$$

and at $r = \delta(z)$ and $z \geq 0$

$$v_z = v_r = 0, \quad T_\ell = T_s = T_f \tag{3}$$

At the tube wall, $r = r_w$ and $z > 0$

$$T_s = T_w < T_f \tag{4}$$

and at the entrance, $z = 0$ and $0 \leq r \leq r_w$

$$T_\ell = T_0 = \text{constant}, \quad v_r = 0 \tag{5a}$$

$$v_z = \text{Fully developed turbulent flow velocity profile} \tag{5b}$$

It was shown by Zerkle and Sunderland [10] that the growth of an

Nomenclature

c = specific heat of the liquid
D = inside diameter of tube
g = acceleration of gravity
Gz = Graetz number, Re·Pr·D/L
h = mean heat transfer coefficient based on arithmetic mean of inlet and exit bulk temperatures, $Q/\pi DL[(T_{b0} + T_{be})/2 - T_f]$
h_z = local convective heat transfer coefficient, $q_{if}/(T_b - T_f)$
h_p = total pressure head, $P/\rho + v_z{}^2/2$
$\bar{h}_p$ = radially averaged total pressure head
h^* = nondimensional radially averaged total pressure drop in test section, $(\bar{h}_{p0} - \bar{h}_p)\cdot z^*/P_B$
Δh = difference in upstream and downstream reservoir liquid levels
k = thermal conductivity
L = length of test section
$\dot{m}$ = mass flow rate
Nu = mean Nusselt number based on tube diameter, hD/k_ℓ
Nu_z = local Nusselt number, $h_z(2\delta)/k_\ell$
Nu_∞ = fully developed asymptotic Nusselt number
P = static pressure
P_B = pressure drop based on mean inlet velocity and diameter and calculated using Blasius friction relationship
Pr = Prandtl number, ν/α
P^* = nondimensional test section static pressure drop, $(P_0 - P_e)/(\rho V^2/2)$
q = heat flux
q_{if} = interface heat flux
q^* = nondimensional rate of heat transfer, $(T_{b0} - T_{be})/(T_{b0} - T_f)$
Q = total rate of heat transfer
r = radial coordinate
Re_D = inlet Reynolds number based on tube diameter, VD/ν
$Re_{2\delta}$ = local Reynolds number based on the diameter of the ice interface, $\bar{v}_z(2\delta)/\nu$
T = temperature
T_b = bulk liquid temperature
$\bar{T}_b$ = mean bulk temperature, $(T_{b0} + T_{be})/2$
T_f = freezing temperature
$T_w{}^*$ = nondimensional wall temperature parameter, $k_s(T_f - T_w)/k_\ell(T_{b0} - T_f)$
v = velocity
$\bar{v}_z$ = radial mean of axial velocity component
V = mean inlet velocity at $z \leq 0$
z = axial position coordinate
z^* = nondimensional axial position, $4z/(D\cdot Re_D\cdot Pr)$
α = thermal diffusivity of the liquid
δ = radius of the solid phase interface
δ^* = nondimensional solid phase interface radius, δ/r_w
ν = kinematic viscosity
θ^* = nondimensional liquid phase temperature, defined in equation (14a)
ρ = fluid density
τ_{rz} = axial component of liquid shear stress
τ_{if} = fluid shear stress at solid-liquid interface

Subscripts

e = evaluated at tube exit conditions
ℓ = refers to the liquid phase
0 = refers to conditions at the freezing section inlet
r = component in the radial direction
s = refers to the solid phase
w = evaluated at the tube wall
z = refers to axial component as well as designating axial position dependence

ice shell initiated in a flowing liquid in a tube is smooth and gradual. Since the L/D of a tube is relatively large, the change in the thickness of the shell with respect to change in axial position is small, that is $\partial\delta/\partial z$ is of a small magnitude. It can also be shown by expansion and use of the chain rule on the governing conservation equations that the second derivatives with respect to axial position are of the order of $\partial^2\delta/\partial z^2$ and $(\partial\delta/\partial z)^2$. If $\partial\delta/\partial z$ is small, then these axial derivatves are quite small and can be taken to be negligible in a first order approximation of the process. These higher order effects are neglected in the present analysis, and the solid phase assumed to be thin in comparison to axial distance. The pressure thus becomes a function of axial position alone.

By utilizing the above assumptions and neglecting terms of order $(\partial\delta/\partial z)^2$, the axial momentum equation for axisymmetric flow in a tube becomes

$$\rho\left(v_r\frac{\partial v_z}{\partial r}+v_z\frac{\partial v_z}{\partial z}\right)=-\frac{\partial P}{\partial z}-\frac{1}{r}\frac{\partial}{\partial r}(r\tau_{rz}) \tag{6}$$

Radial averaging results in

$$\frac{d\bar{h}_p}{dz}=-\frac{2\tau_{if}}{\rho g\delta} \tag{7}$$

which relates the gradient of the mean pressure head in the axial direction to the interface shear stress and the interface radius, δ. Using the Blasius friction formula, this change in pressure may be expressed to a first order approximation in $(\partial\delta/\partial z)$ as

$$\frac{d\bar{h}_p}{dz}=\frac{-0.079\ (\delta/r_w)^{-15/4}V^2}{g\delta \mathrm{Re}_D{}^{1/4}} \tag{8}$$

The solid phase energy equation, neglecting axial conduction, becomes the conduction equation in a shell and may be integrated directly giving

$$T_s=T_f-\frac{(T_f-T_w)\ln(\delta/r)}{\ln(\delta/r_w)} \tag{9}$$

after imposing the boundary conditions (3) and (4).

Using the definition of the local heat transfer coefficient, h_z, the interface heat transfer coupling relation becomes

$$\frac{k_s}{\delta}\frac{(T_f-T_w)}{\ln(\delta/r_w)}=-h_z(T_b-T_f) \tag{10}$$

The liquid phase energy equation, also approximated by dropping terms of order $(\partial\delta/\partial z)^2$, may be written as

$$\rho c\left(v_r\frac{\partial T_\ell}{\partial r}+v_z\frac{\partial T_\ell}{\partial z}\right)=-\frac{1}{r}\frac{\partial}{\partial r}(rq_r) \tag{11}$$

When radially averaged this equation becomes

$$\frac{\partial T_b}{\partial z}=-\frac{2\delta}{\rho c V(r_w)^2}h_z(T_b-T_f) \tag{12}$$

Integration of equation (12) from T_{b0} to T_b and from 0 to z yields

$$\ln\left(\frac{T_b-T_f}{T_{b0}-T_f}\right)=-\frac{2}{\rho c V(r_w)^2}\int_0^z \delta h_z dz \tag{13}$$

An appropriate nondimensional form of the governing equations can now be obtained by introducing the dimensionless variables

$$\theta^*=\frac{T_b-T_f}{T_{b0}-T_f},\ z^*=\frac{4z}{\mathrm{Re}_D P_r(2r_w)},\ \delta^*=\frac{\delta}{r_w} \tag{14a}$$

$$h^*=\frac{\bar{h}_{p0}-\bar{h}_p}{\lambda},\ T_w{}^*=\frac{k_s}{k_\ell}\frac{T_f-T_w}{T_{b0}-T_f} \tag{14b}$$

where

$$\lambda=0.079(V^2/2g)\mathrm{Re}_D{}^{3/4}\mathrm{Pr} \tag{15}$$

The equations become

$$\theta^*=-\frac{2T_w{}^*}{\mathrm{Nu}_z\ln\delta^*} \tag{16}$$

$$\ln\theta^*=-\int_0^{z^*}\mathrm{Nu}_z dz^* \tag{17}$$

and

$$\frac{dh^*}{dz^*}=(\delta^*)^{-19/4} \tag{18}$$

with boundary conditions

$$\delta^*(z^*=0)=\theta^*(z^*=0)=1 \tag{19a}$$

$$h^*(z^*=0)=0 \tag{19b}$$

To close the above system of equations, an independent expression for the Nusselt number is required. This is obtained by adapting the Sparrow, Hallman, and Siegel [14] solution for the Nusselt number in the thermal entrance region of a circular tube to the present problem. Thus, results developed here depend totally upon the applicability of this solution to the present problem. The expression for the Nusselt number localized to actual internal conditions is

$$\mathrm{Nu}_z=\left[\frac{1}{\mathrm{Nu}_\infty}-\frac{1}{2}\sum\frac{\exp(-\gamma_m{}^2 z/(\bar{v}_z(2\delta)/\nu)(\nu/\alpha)\delta)}{A_m\gamma_m{}^4}\right]^{-1} \tag{20}$$

Since $2\pi_w{}^2V=2\pi\delta^2\bar{v}_z$ under steady-state conditions, the expression becomes

$$\mathrm{Nu}_z=\left[\frac{1}{\mathrm{Nu}_\infty}-\frac{1}{2}\sum\frac{\exp(-\gamma_m{}^2 z/\mathrm{Re}_D\mathrm{Pr}r_w)}{A_m\gamma_m{}^4}\right]^{-1} \tag{21}$$

where A_m and γ_m are the eigenconstants and eigenvalues of the solution, both of which are functions of Reynolds number and Prandtl number for turbulent flow.

Values of A_m and γ_m which should be appropriate for this formulation are those presented in Kays [15], for a constant heat flux with a Reynolds number of 50,000 and a Prandtl number of 10. Though the problem considered in this investigation is one of constant wall temperature, the difference between this case and the case of constant heat flux is insignificant for the range of Prandtl numbers being considered. It has also been shown that the Reynolds number effects are increasingly insignificant with increasing Prandtl number and are of little importance for Prandtl numbers of 10 or greater. Thus, there should be little error in the results obtained using the eigenvalues from Kays [15].

Values of the Nusselt number for very small values of z/D are difficult to calculate from the entrance region solution because of the truncation error of the series of eigenvalues and eigenconstants. Instead, a Nusselt number expression of the form

$$\mathrm{Nu}_z=A+\frac{B}{(z^*)^C} \tag{22}$$

is assumed, and the values of the constants A and B are determined by matching equations (21) and (22) at the lowest value of z^* for which equation (21) is applicable. The values of A and B are peculiar to each set of flow conditions, that is, A and B are functions of Re_D, Pr, and $T_w{}^*$. The exponent C is taken as 0.2 so as to approximate the turbulent thermal boundary-layer like flow which would be expected at the entrance.

For the asymptotic Nusselt number, the localized empirical correlation from Kays [15]

$$\mathrm{Nu}_\infty=h_\infty(2\delta)/k=0.0155(\bar{v}_z(2\delta)/\nu)^{0.83}(\mathrm{Pr})^{0.5} \tag{23}$$

or

$$\mathrm{Nu}=0.0155\ \mathrm{Re}_D{}^{0.83}\mathrm{Pr}^{0.5}/(\delta^*)^{0.83} \tag{24}$$

is assumed.

Thus, the system of equations to be solved is composed of equations (16) through (24), excluding equations (20) and (23). Essentially, these equations describe one-dimensional heat transfer and pressure drop. The unknowns in this system of equations are δ^*, $\theta^*=H^*$, Nu_z, Nu_∞, A, and B. The seventh equation needed for the solution is obtained by matching the values of the derivative $\partial\mathrm{Nu}_z/\partial z^*$ as taken from equations (21) and (22). Numerical solution of this approximate system of equations yields the solid-liquid interface profile and the turbulent flow pressure drop.

In terms of nondimensional variables, the expression for the heat transfer rate becomes

$$q^* = -2 \int_0^{z^*} \frac{dz^*}{\ln (\delta^*)^{1/T_w^*}} \tag{25}$$

Thus, once the profile of the ice shell (δ^* versus z^*) is determined, the heat transfer rate is evaluated directly from equation (25) by numerical integration.

Analytical Results

The system of governing equations, with approximations, was solved using a digital computer and the results are presented in Figs. 2, 3, 4, and 5 for selected values of the various independent parameters. The analytical results showed only slight dependence on Prandtl number over the intermediate range considered (Pr = 8, 10, 12) and thus, data are presented for only one value of Pr, chosen equal to 10.0 so that comparisons between theory and the experiments utilizing water would be meaningful.

The theoretical dimensionless heat transfer rate, q^*, and the quantity $(\delta^*)^{1/T_w^*}$ are plotted versus dimensionless axial position z^* in Fig. 2 for various turbulent flow cases (differing only in Reynolds number) as well as for the laminar flow case as taken from Zerkle and Sunderland [10]. It can be seen that for a given value of z^* the turbulent flow dimensionless heat transfer rate q^* is very sensitive to changes in Reynolds number over the range of values considered, this sensitivity diminishing somewhat at the higher Reynolds numbers. An increase in Reynolds number while holding z^* constant results in an increase in q^*, and for all cases plotted the turbulent flow dimensionless heat transfer rates are seen to be significantly higher than those for the laminar flow case for comparable values of z^*. If one considers flows of the same Reynolds number in tubes with varying L/D, bearing in mind that z^* varies directly with L/D, it can be seen from Fig. 2 that q^* increases with an increase in L/D. Thus a longer tube yields greater heat transfer, as one might expect, than does a shorter tube with flow of the same inlet Reynolds number.

Another useful comparison may be made by examining flows of different Reynolds numbers in tubes of the same L/D. For this case, remembering that z^* varies inversely with changes in Re_D, Fig. 2 shows that an increase in inlet Reynolds number yields a lower value of q^* for a given tube. This of course does not indicate a decrease in actual heat transfer, but simply that the ratio of actual heat transfer to maximum possible heat transfer has decreased. The actual heat transfer from the fluid is increased due to the higher values of the heat transfer coefficient resulting from higher inlet, and thus local, Reynolds numbers. However, due to the increase in flow area resulting

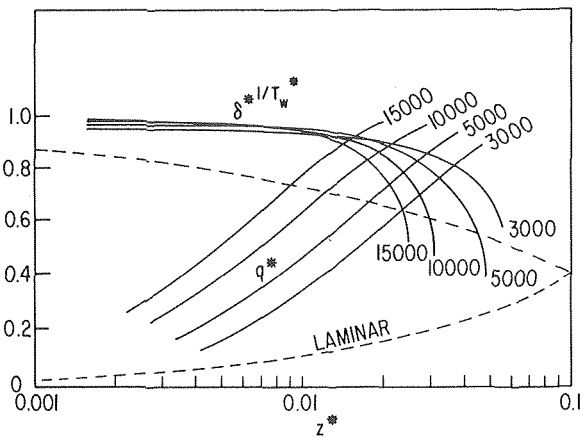

Fig. 2 Variation of the dimensionless heat transfer and solid phase interface radius with axial position for Pr = 10, T_w^* = 3, and various Reynolds numbers

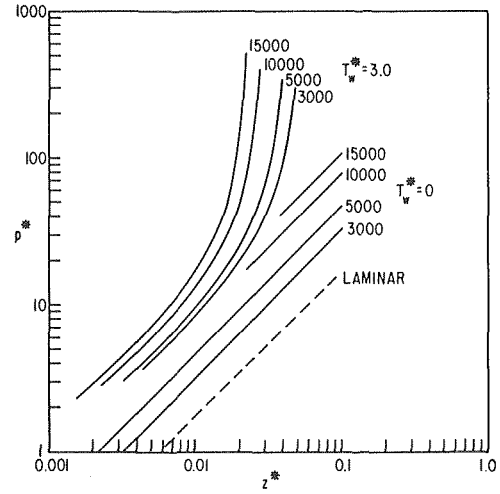

Fig. 4 Variation of dimensionless pressure drop with axial position for Pr = 10 and various Reynolds numbers and wall temperatures

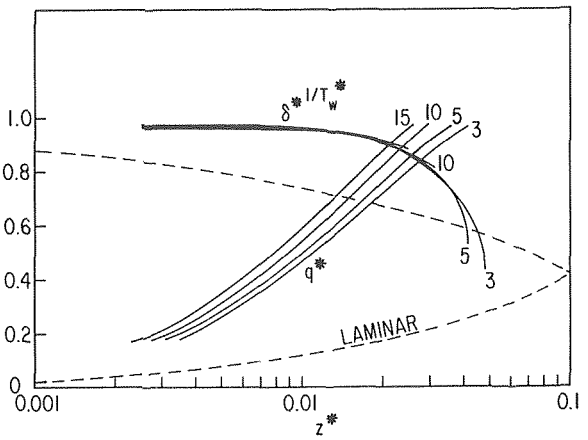

Fig. 3 Variation of the dimensionless heat transfer and solid phase interface radius with axial position for Pr = 10, Re_D = 5000, and various wall temperatures.

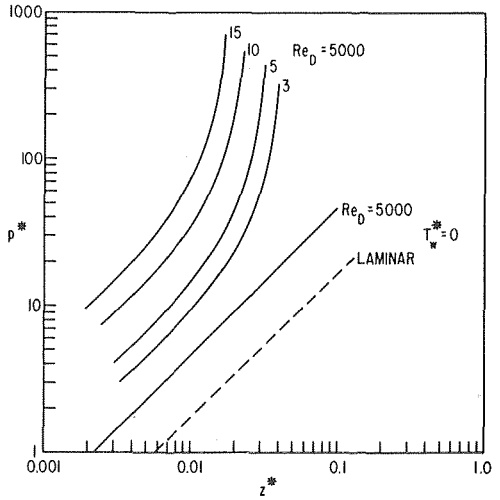

Fig. 5 Variation of dimensionless pressure drop with axial position for Pr = 10, Re_D = 5000, and various wall temperatures.

from thinning of the ice shell, the local Reynolds numbers and thus the heat transfer rates do not increase in proportion with increases in inlet Reynolds number. Thus, the ratio defining q^* decreases wth increasing flow rate.

Fig. 2 also shows $(\delta^*)^{1/T_w^*}$ for the turbulent flow case to be sensitive to Reynolds number over the range of z^* values where the degree of tube closure is significant. In this range the effect of increasing Re_D, for the case of a constant L/D, is that of increasing $(\delta^*)^{1/T_w^*}$ and thus the radius of the solid-liquid interface. That is, for a given tube with a greatly reduced flow area due to freezing, increasing the inlet Reynolds number increases the heat transfer and thus causes the thickness of the frozen shell to be reduced, thus opening the tube. In tubes with flow over the range of z^* values where closure is minimal, the effects of changing Re_D are also minimal. Fig. 2 also shows $(\delta^*)^{1/T_w^*}$ to be greater for the turbulent flow cases than for the laminar case with a comparable value of L/D, indicating a reduction in the ice thickness in going from the laminar flow case to the turbulent case.

Fig. 3 is a plot of q^* and $(\delta^*)^{1/T_w^*}$ versus z^*, but for cases involving variations of the dimensionless wall temperature parameter T_w^*. It may be seen from this figure that, for a given value of z^*, the turbulent flow dimensionless heat transfer rate q^* is only moderately sensitive to changes in T_w^* and thus wall temperature, with increases in T_w^* resulting in higher values of q^* as expected. The increase in heat transfer, however, is not nearly in proportion to the increase in T_w^*. This reduced sensitivity to wall temperature can be explained by noting that a reduction in wall temperature (an increase in T_w^*) results in thickening the internal frozen shell which subsequently increases the overall resistance to heat transfer. Comparing tubes with different L/D values but the same T_w^* and Re_D shows that the longer tubes transfer more heat than the shorter ones, as expected, and once again the turbulent flow heat transfer is significantly greater than the comparable laminar flow case.

Fig. 3 also shows the $(\delta^*)^{1/T_w^*}$ curves to be almost identical over most of the range of z^* values considered, the only significant deviation occurring when z^* nears complete blockage. This similarity of results for different values of T_w^* is explained in the same manner as was the lack of sensitivity of $q+$ to T_w^*. That is, increases in T_w^* are accompanied by increases in ice thickness such that the resulting changes in the value of $(\delta^*)^{1/T_w^*}$ are not significant. It is also noted from Fig. 3 that the values of $(\delta^*)^{1/T_w^*}$ are higher for the turbulent cases than for the laminar case (with the same L/D) which is an indication that the higher heat transfer rates associated with the turbulent flow again cause a thinner ice shell than is found in the comparable laminar flow case.

A particularly interesting result regarding the streamwise curvature of the ice interface can be seen in both Figs. 2 and 3. For very small values of z^* (less than 0.005) and for very large values of z^* at the higher T^* values (for example $z^* > 0.015$ and $T_w^* \simeq 10$, $z^* > 0.03$ and $T_w^* \simeq 3$), the curvature is convex as expected. However, in the intervening region the interface is concave, a characteristic shape suggested in Fig. 1. Such a result has not heretofore been shown to exist, even though a similar pattern can be deduced from the analyses presented by Shibani and Ozisik [16]. The phenomenon cannot be found to exist, however, in the results of analyses of freezing in channel flows, also studied by Shibani and Ozisik [17], nor in the results regarding freezing in laminar tube flow. It is believed that this phenomenon occurs with freezing in turbulent tube flow because the entrance effects decay very rapidly, allowing the classical balance between a logarithmic conductive resistance and the internal linear convective resistance. Thus, the crossover point occurs at a critical ice thickness. When freezing occurs in laminar flow, the entrance effects dominate beyond the location of this critical thickness.

In carrying out the numerical computations, particularly those involving pressure drop, care was exercised to insure that the assumption $(\partial\delta/\partial z)^2 \ll$ unity was not violated, particularly in plotting the nondimensional results. Thus $(\partial\delta^*/\partial z^*)$ was never allowed to become greater than approximately 250, which corresponds to a $(\partial\delta/\partial z)$ of 0.01 for a Peclet number of 50,000. Therefore even though $p^*(z^*)$ plots appear very steep for large z^*, the basic assumptions of the analysis remain valid. Dimensionless pressure drop P^* is plotted versus z^* in Fig. 4 for several different turbulent flow Reynolds numbers and two values of the dimensionless wall temperature T_w^*. In addition to the curves representing flow with a frozen shell in the tube, the case of flow in the absence of a frozen shell ($T_w^* = 0$) is also presented for both laminar as well as turbulent flow. Laminar flow with freezing could not be included because of the absence of analytical data in [10] for comparable values of T_w^*. It is apparent that the freezing section dimensionless pressure drop is dependent on Reynolds number for the turbulent flow case, and that increases in Re_D yield higher values of P^* for a given value of z^*. As in the case of q^*, this dependence on Re_D for a given z^* is seen to diminish as Reynolds number increases. The laminar flow dimensionless pressure drop P^* was shown in [10] to be, unlike the turbulent flow case, independent of Re_D when z^* was held constant.

If one considers turbulent flows of the same Reynolds number in tubes with different values of L/D, again remembering that z^* varies directly with L/D, it may be seen from Fig. 4 that P^* increases with an increase in L/D, indicating greater pressure drop across a longer tube, as one might expect. Comparing tubes with the same L/D but containing turbulent flows of different inlet Reynolds number, and noting that z^* varies inversely with Re_D, one can see that P^* decreases with an increase in Reynolds number. However, even though this dimensionless pressure drop P^* decreases, the actual pressure drop increases as Reynolds number is increased, although not at the same rate as expected for turbulent flow in a tube with no frozen shell. The increased flow rate and resulting higher heat transfer rates cause thinning of the frozen shell, thus increasing the flow area. This larger flow area partially offsets the increase in pressure drop caused by the greater frictional losses resulting from the higher velocities, with the net effect being an increase in pressure drop but not as great an increase as would be found in a tube with no frozen shell.

Fig. 5 is a plot of dimensionless pressure drop P^* versus z^* for flows of the same Reynolds number but having different values of T_w^*. Again the case of laminar flow with freezing could not be included because of lack of comparable analytical data in [10]. This figure shows P^* to be sensitive to changes in dimensionless wall temperature T_w^* with increases in T_w^* being accompanied by increases in P^* for a fixed value of z^*. As was shown in Fig. 3, increases in T_w^* cause increased tube blockage which then results in the greater pressure drop shown in Fig. 5. Increasing the tube L/D and thus z^* shows pressure drop to increase accordingly as might be expected for a longer tube with the same T_w^*.

Experiments

Experiments were made with an apparatus in which water was used as the freezing medium. It consisted of a closed water circulation and temperature control system and a test section cooling system, with instrumentation for the measurement and recording of temperatures, pressures and flow rate. A schematic of the apparatus is shown in Fig. 6.

The water circulation system utilized inlet and exit constant head reservoirs, an entrance section of length 171.1 cm, a test section 116.0 cmin length, a constant temperature bath, and a circulating pump.

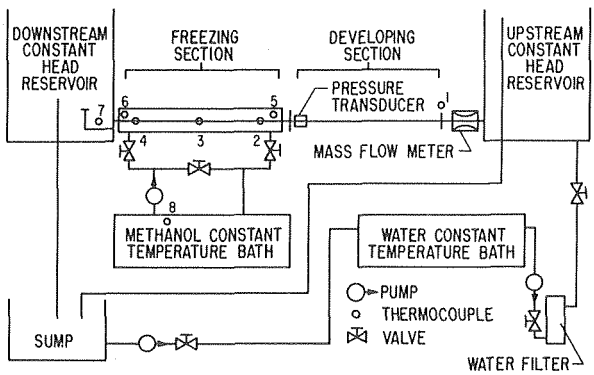

Fig. 6 Schematic of experimental apparatus.

The entrance and test section were made continuous and were constructed of thin wall copper tubing, 1.45 cm in inside diameter. The constant temperature bath and inlet reservoir provided sufficient capacity and control to allow the setting of inlet temperature with no noticeable fluctuation. The entrance section of the tube as well as the external side of the test section were well insulated and the circulating water was filtered to eliminate algae and particulates. The L/D for the entrance and the test section were 118 and 80.1, respectively.

A counterflow, forced circulation cooling system using methanol as coolant was employed to control the tube wall temperature by circulating the methanol in the cooling jacket of the test section. A constant temperature bath was used to control and maintain the coolant temperature, and this was done with no noticeable fluctuation. Methanol was used as a coolant because of its low viscosity at low temperatures, and a ½ hp pump was used to circulate the methanol at a flow rate sufficient to insure a negligible temperature difference (usually on the order of 0.2°C) between methanol entering and leaving the test section. Great care was taken in the design of the test section and in the conduct of the experiments to insure that the nonuniformity in tube wall temperature was minimized. In most of the experimentation this variation was less than 0.8°C.

A thermocouple at location 1 insured no variation in inlet water temperature. Thermocouples were installed in grooves in the tube wall at each end and the middle of the test section (at locations 2, 3, and 4 in Fig. 6) to accurately measure the wall temperature. The exit mean temperature was measured by a thermocouple located in a small mixing cup at the exit of the tube (location 7 in Fig. 6). The mixing cup was designed to trap and mix fluid issuing from the tube yet allow the exit reservoir to impose the prescribed exit static pressure. The test section inlet pressure was measured using a diaphragm-type strain gauge transducer that was calibrated to 0.03 cm of water. The system was leveled with a surveying transit so that all points along the axis of the entrance and test section were at the same elevation within 0.04 cm. The head height of the constant head reservoirs at inlet and exit was measured to within 0.03 cm with a cathetometer. All thermocouples were calibrated with NBS certified thermometers.

The inlet water temperature was held constant at 5.6°C and the exit static pressure at 7.9 cm of water in all the experiments reported here. The water level in the upstream reservoir and the coolant temperature were varied to produce different steady-state conditions. Once the desired upstream water level and coolant temperature were attained, coolant circulation through the test section was begun, thus lowering the tube wall temperature below 0°C. If the coolant temperature was sufficiently low, the water started freezing spontaneously. However, there were certain combinations of coolant temperature and upstream water level at which freezing did not begin when the coolant flow was started. For these cases, it was necessary to temporarily block the tube at the exit of the test section, thus stopping the water flow and initiating the freezing process. Once freezing started, the tube exit was unblocked and flow allowed to resume. Solidification then continued until the steady-state condition corresponding to the chosen coolant temperature and upstream reservoir level was attained. To insure that a true steady state had been reached, most experiments were allowed to run for at least one hour after equilibrium conditions were initially attained. The steady-state mass flow rate was then determined from water samples timed and weighed to within approximately two percent.

The dimensionless heat transfer rate q^* was evaluated directly as a temperature ratio, and the dimensionless axial position ($z^* = 4/\mathrm{Gz}$) was evaluated from the inlet Reynolds number Re_D, Prandtl number Pr, and test section L/D. All fluid properties were evaluated at the arithmetic average of the inlet and exit bulk temperatures. The Nusselt number, based on the arithmetic mean of inlet and exit temperatures instead of the more usual logarithmic mean, was computed from

$$\mathrm{Nu} = 2q^*/(2 - q^*)z^* \tag{26}$$

The arithmetic mean was used to facilitate a comparison with the results of [10]–[13]. In computing the Nusselt number the effective wall temperature was taken as 0°C.

Experimental Results

The complete set of experimental results is shown in Table 1 along with some pertinent quantities which were computed from the data. Comparisons of the theoretical and experimental data are presented in Figs. 7 and 8 as plots of dimensionless turbulent flow heat transfer q^* and dimensionless freezing section pressure drop P^* versus dimensionless axial position z^*.

Examination of Fig. 7 shows the experimental values of q^* to be approximately 20 percent lower than those predicted by the analysis for the same value of z^*. Whether this is a result of the analytical approximations or experimental error is not clear. The major source of experimental error probably lies in accurately determining the mean exit temperature to which the value of q^* is highly sensitive. The discrepancy between experimental and analytical results in this case, for instance, could be accounted for by an error in the exit bulk temperature measurement of only 0.4°C. With this degree of sensitivity and the inherent difficulty in accurately determining a bulk temperature of this nature, it is very likely that error in the experimentally determined q^* values does exist. It is also likely and indeed expected that some analytical error will occur because of the simplified nature of the analytical formulation. Deviation between the experimental and analytical results of the magnitude encountered in the present study are often encountered in investigations of this type, and in the present case this agreement is considered satisfactory when all factors are considered.

In addition to the analytical solutions for constant Reynolds

Table 1 Steady-state experimental data and computed results

RUN	$\dot{m}$ (kg/min)	T_{b0} (°C)	T_{be} (°C)	$\overline{T}_b$ (°C)	T_w (°C)	Re_D	$z^* \times 10^3$	T_w^*	q^*	Nu	P^*	Δh (cm)
1	4.94	5.6	4.1	4.8	−4.3	4742	6.09	3.12	.26	49.1	5.34	45.0
2	4.79	5.6	4.2	4.9	−4.6	4593	6.29	3.33	.25	45.4	7.53	45.0
3	4.62	5.6	4.2	4.9	−4.7	4439	6.51	3.41	.24	41.9	10.04	45.0
4	4.56	5.6	4.2	4.9	−4.3	4378	6.60	3.10	.25	43.3	7.37	41.0
5	4.49	5.6	4.2	4.9	−4.3	4305	6.71	3.09	.25	42.6	8.58	41.0
6	4.69	5.6	4.2	4.9	−4.0	4508	6.41	2.89	.25	44.6	5.39	41.0
7	4.81	5.6	4.1	4.8	−4.3	4617	6.25	3.08	.26	47.8	5.46	43.0
8	4.63	5.6	4.2	4.9	−4.5	4446	6.50	3.24	.24	41.9	8.14	43.0
9	4.55	5.6	4.2	4.9	−4.5	4374	6.61	3.26	.24	41.3	9.33	43.0
10	4.70	5.6	4.1	4.8	−4.3	4512	6.40	3.11	.26	46.7	6.15	42.0
11	4.80	5.6	4.1	4.8	−3.9	4603	6.27	2.85	.26	47.6	4.83	42.0
12	4.48	5.6	4.2	4.9	−4.4	4300	6.72	3.23	.24	40.6	9.66	42.0
13	4.61	5.6	4.2	4.9	−4.1	4421	6.53	2.93	.25	43.7	5.79	40.0
14	4.42	5.6	4.2	4.9	−4.2	4248	6.80	3.05	.24	40.1	8.62	40.0
15	4.48	5.6	4.2	4.9	−4.1	4297	6.72	2.91	.25	42.5	6.79	39.0
16	4.70	5.6	4.1	4.8	−4.5	4512	6.40	3.26	.26	46.7	7.88	44.0
17	4.89	5.6	4.1	4.8	−4.3	4687	6.16	3.11	.26	48.5	5.30	44.0

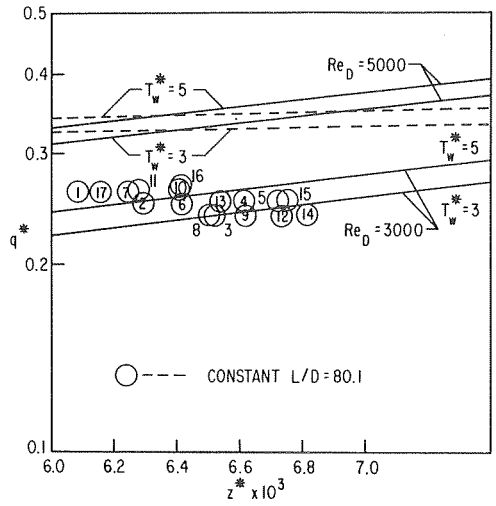

Fig. 7 Comparison of experimental and analytical heat transfer data.

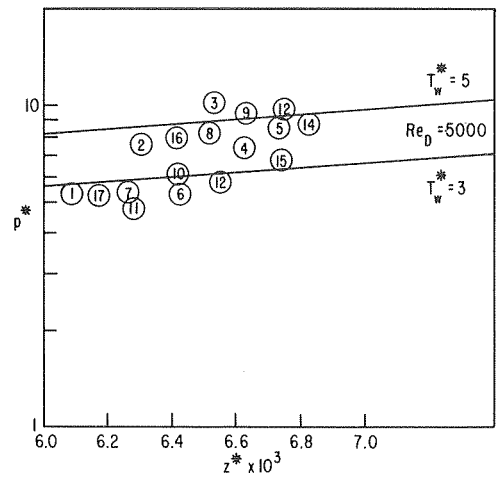

Fig. 8 Comparison of experimental and analytical pressure drop data.

number, the theoretical results are also plotted in Fig. 7 for the case of flow in a tube with constant L/D, that value of L/D being chosen the same as that of the actual tube used in the experimental investigation. While the magnitude of the experimental values differ somewhat from the analytical data, it should be noted that the slopes of the analytical constant L/D lines agree with the slope of the experimental results within the statistical significance of the data.

Experimental and analytical dimensionless pressure drop data are plotted versus dimensionless position in Fig. 8. This figure shows a scattering of the experimental P^* data in the near neighborhood of values predicted by the analysis. The experimental data were obtained for T_w^* values of approximately 3.1 with a deviation of approximately ± 0.25 for Reynolds numbers in the range of 4000 to 5000. It can be seen in Fig. 8 that in general the mean of the scattered experimental P^* values exceeds the analytical predictions by approximately 20 percent. Freezing in a tube with a nonuniform wall temperature distribution would likely cause greater pressure drop than would freezing in a tube with a uniform wall temperature equal to the mean. Examination of the tabulated data shows that, in general, the experimental P^* data with the greatest deviation from the analytical results are those having T_w^* values near the high end of the range considered, and it was observed during the conduct of the experiments that runs with higher T_w^* values (lower actual wall temperatures) displayed wall temperature distributions with the greatest degree of nonuniformity. Thus, the scatter and positive shift of the experimental P^* data is believed to be due primarily to the non-uniformities in wall temperature which experimentally result from increases in T_w^*.

The experiments were designed to provide data in an intermediate range of z^*. During the conduct of the experiments, the z^* range was limited on the low side (0.006) by troublesome supercooling effects and by intolerable wall temperature variations on the high side (0.007). Although this appears to be a rather narrow and arbitrary range, it does represent a realistic situation with a δ^* of approximately 0.85. Moreover, if the data confirm the analysis at these arbitrary conditions within reason, then it seems likely that the analysis will be satisfactory at other conditions which do not obviously violate the assumptions of the analysis. The actual applicability of the theory, however, at much larger and smaller values of z^* remains to be tested.

During the experiments every attempt was made to observe the ice inside the tube. All that could be determined was that the ice shell was well formed with a distinct interface. In view of the appreciable liquid phase superheat and the high Reynolds numbers, it seems reasonable to assume the ice interface was smooth.

Conclusions

The analysis was found to be simple, direct, and acceptably accurate in representing steady-state conditions. Heat transfer predictions within 20% of the data measured experimentally were obtained for all conditions of tube wall temperature and Reynolds number. In fact, it is believed that the source of this deviation, albeit nominal, was primarily error in the measurement of the liquid exit bulk temperature. An inconsistency of 0.4°C in this measurement is all that would be required to produce the 20% deviation under the conditions of the experiments. Thus, it is believed that the analysis predicts actual conditions much more accurately than indicated by this comparison.

Analytical predictions of the pressure drop across the tube agreed very well with the experimental data for comparable conditions when the imposed wall temperature was uniform. However, conditions of high Reynolds number and/or very low wall temperature tended to produce actual pressure drops in excess of the prediction, a result believed to be caused by the more severe nonuniformity of wall temperature characteristic of these conditions. In fact, it was found experimentally that the actual pressure drop was extremely sensitive to this nonuniformity, while only moderately dependent upon the actual wall temperature as predicted by the analysis. Conclusions pertaining to the sensitivity of pressure drop to wall temperature for freezing in tube flow have been reported previously [10, 11, 12], although it has not been demonstrated previously that this is actually a sensitivity to the nonuniformity in the wall temperature rather than to its mean value.

One very important conclusion of the analytical work is that a very peculiar crust profile occurs during freezing in turbulent flow in tubes. A concave curvature was found to occur in the z^* midrange, although this result could not be verified experimentally and must await corroboration in experiments designed specifically to accomplish this.

Acknowledgment

The authors wish to acknowledge the financial support of this research by the National Science Foundation through NSF Grant GK 38131.

References

1 Muehlbauer, J. C. and Sunderland, J. E., "Heat Conduction with Freezing and Melting," *Applied Mechanics Reviews*, Vol. 18, 1965, pp. 951–959.

2 Boley, B. A., "The Analysis of Problems of Heat Conduction and Melting, High Temperature Structures and Materials," *Proceedings of 3rd Symposium on Naval Structural Mechanics*, Pergamon Press, Oxford, 1963, pp. 200–315.

3 Bankoff, S. B., "Heat Conduction or Diffusion with Change of Phase," *Advances in Chemical Engineering*, Vol. 5, Academic Press, New York, 1964.

4 Gilpin, R. R., "The Effects of Dendritic Ice Formation in Water Pipes," *International Journal of Heat Mass Transfer*, Vol. 20, 1977.

5 Shamsundar, N. and Sparrow, E. M., "Analysis of Multidimensional

Conduction Phase Change Via the Enthalpy Model," ASME JOURNAL OF HEAT TRANSFER, Vol. 97, Aug. 1975, p. 333.

6 Brush, W. W., "Freezing of Water in Subaqueous Mains Laid in Salt Water and in Mains and Services Laid on Land," *Journal of American Water Works*, Vol. 3, 1916, pp. 962–980.

7 London, A. L. and Seban, R. A., "Rate of Ice Formation," *Trans. ASME*, Vol. 65, 1943, pp. 771–779.

8 Poots, G., G., "On the Application of Integral Methods to the Solution of Problems Involving the Solidification of Liquids Initially at the Fusion Temperature," *International Journal of Heat Mass Transfer*, Vol. 5, 1962, pp. 525–531.

9 Hirschburg, H. G., "Freezing of Piping Systems," *Kaltetechnik*, Vol. 14, 1962, pp. 314–321.

10 Zerkle, R. D. and Sunderland, J. E., "The Effect of Liquid Solidification in a Tube Upon the Laminar-Flow Heat Transfer and Pressure Drop, ASME JOURNAL OF HEAT TRANSFER, Vol. 90, 1968, pp. 183–190.

11 Depew, C. A. and Zenter, R. C., "Laminar Flow Heat Transfer and Pressure Drop with Freezing at the Wall," *International Journal of Heat Mass Transfer*, Vol. 12, 1969, pp. 1710–1714.

12 Mulligan, J. C. and Jones, D. D., "Experiments on Heat Transfer and Pressure Drop in a Horizontal Tube with Internal Solidification," *International Journal of Heat Mass Transfer*, Vol. 19, 1976, pp. 213–219.

13 DesRuisseaux, N. and Zerkle, R. D., "Freezing in Hydraulic Systems," ASME Paper No. 68-HT-24, 1968.

14 Sparrow, E. M., Hallman, T. M., and Siegel, R., "Turbulent Heat Transfer in the Thermal Entrance Region of a Pipe with a Uniform Heat Flux," *Applied Science Reviews*, Vol. 7, 1959, pp. 37–52.

15 Kays, W. M., "Heat Transfer: Turbulent Flow Inside Smooth Tubes," *Convective Heat and Mass Transfer*, McGraw-Hill, New York, 1966, pp. 173, 187.

16 Shibani, Ali A. and Ozisik, M. N., "Freezing of Liquids in Turbulent Flow Inside Tubes," to appear in *Canadian Journal of Chemical Engineering*, (Now in press).

17 Shibani, Ali A. and Ozisik, M. N., "A Solution of Freezing of Liquids of Low Prandtl Number in Turbulent Flow Between Parallel Plates," ASME JOURNAL OF HEAT TRANSFER, Vol. 99, 1977, pp. 20–24.

E. M. Sparrow
S. Ramadhyani
S. V. Patankar

Department of Mechanical Engineering,
University of Minnesota,
Minneapolis, Minn.

Effect of Subcooling on Cylindrical Melting

An analysis is made of the melting of a subcooled solid surrounding a heated circular cylinder. The solution is facilitated by coordinate transformations which immobilized both the moving interface between the melt region and the solid and the moving temperature wave that diffuses into the solid. The actual solutions were carried out numerically via a finite-difference procedure which circumvents the nonlinearity associated with the moving interface. Results were obtained for a wide range of a subcooling parameter and of the Stefan number. It was found that the subcooling can have a marked effect on the melting characteristics. Depending on the degree of subcooling, the surface heat transfer can be several times greater than that for no subcooling. Furthermore, at high levels of subcooling and at long melting times, the liquid layer thickness may be only a small fraction of that without subcooling. Subcooling also sharpens the differences between cylindrical and plane melting. The ratio of the heat flux for cylindrical melting to that for plane melting increases substantially due to subcooling, while the thickness of the cylindrical melt layer is only a fraction of that of a corresponding plane melt layer.

Introduction

Heat conduction problems involving solid-liquid phase change have generated an extensive analytical literature. In the main, these analyses have been concerned with transients in which, initially, the phase change medium is at its melting temperature. It appears that only in the case of the melting (or freezing) of a plane layer has the problem of an initially subcooled (superheated) medium been examined. This is the well-known Neumann problem which is described in various heat conduction texts.

The preoccupation of the literature with situations without initial subcooling (superheating) is remarkable in that such a condition is difficult to achieve in practice, especially when the dimensions of the phase change medium are large. For instance, in melting experiments performed in our laboratory, painstaking control and long waiting periods (~ one week) were required to attain temperature uniformity just below the melting point in a 0.3 m (1 ft) cubical solid before the actual phase change studies could be initiated. Various degrees of subcooling (superheating) can be expected in practice, for other geometrical configurations as well as for the plane layer.

The present paper is concerned with phase change in a subcooled (superheated) medium surrounding a circular cylinder. For concreteness, the analysis and the presentation of results will be couched in terms of melting, but the same analysis and results apply to freezing with only slight rephrasing. Specific consideration is given to a cylinder situated in a solid phase-change material whose initial temperature T_∞ is lower than the melting temperature T^*. At time equals zero, the temperature of the cylinder surface is raised to a value T_w and maintained constant thereafter.

An annular melt layer forms around the cylinder, and the outer radius of the melt region grows with time. In addition, since the temperature of the liquid-solid interface (i.e., the melting temperature T^*) exceeds that of the solid, a temperature wave emanating from the interface moves into the solid. Thus, there are, in effect, two moving boundaries in the present problem—the liquid-solid interface and the forward edge of the temperature wave.

Even without subcooling, the cylindrical melting problem does not yield an analytical solution, and this same state of affairs prevails with subcooling. A finite difference technique was employed here in conjunction with a formulation in which both the liquid-solid interface and the forward edge of the temperature wave were immobilized (i.e., are rendered stationary in a transformed coordinate system). The energy equations for the liquid and the solid which result from the dual immobilization are discretized by an implicit difference scheme, while an explicit representation is used for the interfacial energy balance. This treatment enables the solution to march steadily forward in time, without iterations being required at each time step.

The problem involves two prescribable parameters. One of these is the Stefan number (based on $(T_w - T^*)$), to which numerical values of 0.1, 0.5, and 1.0 are assigned. The second parameter is the subcooling ratio $(T^* - T_\infty)/(T_w - T^*)$ which ranged between zero and four.

The presentation and discussion of results will be focused on three quantities: the instantaneous rate of surface heat transfer, the time-integrated surface heat transfer, and the instantaneous position of the liquid-solid interface. These results will be examined from two viewpoints. In one, the subcooling-affected results are compared with

Contributed by the Heat Transfer Division for publication in the JOURNAL OF HEAT TRANSFER. Manuscript received by the Heat Transfer Division December 9, 1977.

those without subcooling. In the other, the cylinder and plane layer results are compared at a given degree of subcooling.

A search of the literature failed to reveal any prior work on the effects of subcooling in a cylindrical melting arrangement. For phase change without subcooling in this geometry, Stephan and Holzknecht [1][1] have reported results for the timewise movement of the liquid-solid interface, but do not report heat transfer results. Various investigators (e.g., [2, 3] and those cited in [4]) have used coordinate transformations to immobilize a moving phase-change boundary, but the present dual immobilization appears not to have been previously employed. Furthermore, the prior use of phase boundary immobilization appears to have been numerically implemented with either an implicit or an explicit difference scheme. As already noted, the present scheme involves the selective use of implicit and explicit differencing and is free of the iterations that are typically encountered in the implicit scheme and of the highly restrictive time step limitations of the explicit scheme.

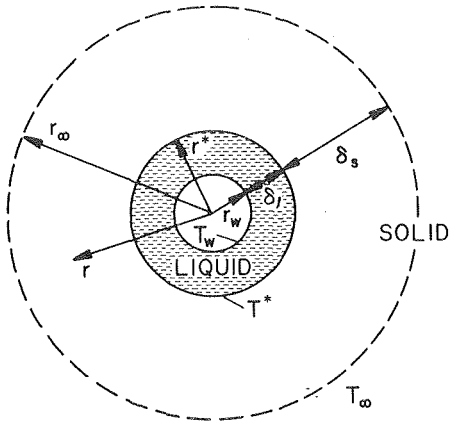

Fig. 1 Schematic diagram of the subcooled melting problem

Analysis

A schematic diagram of the subcooled melting problem is presented in Fig. 1. The diagram shows dimensional and coordinate designations and the participating temperatures T_w, T^*, and T_∞. The instantaneous radii of the liquid-solid interface and the forward edge of the solid-phase temperature wave are r^* and r_∞, respectively. As will be elaborated later, r_∞ is chosen large enough so as not to affect the surface heat transfer or the interface position. Subcooled solid (temperature T_∞) occupies the region $r > r_\infty$. The thermal properties of the liquid and solid phases are assumed to be equal in order to keep the number of prescribable parameters within reason.

Governing Equations. The heat transfer processes in the liquid and solid regions are governed by the heat equation written in cylindrical coordinates

$$\frac{\partial T_i}{\partial t} = \frac{\alpha}{r}\frac{\partial}{\partial r}\left(r\frac{\partial T_i}{\partial r}\right), \quad i = \ell, s \tag{1}$$

The other key equation is the energy balance at the liquid-solid interface, in which the heat conducted to the interface from the liquid is equated to the latent heat required by the phase change plus the conduction into the solid.

$$-k(\partial T_\ell/\partial r) = \rho\lambda(d\delta_\ell/dt) - k(\partial T_s/\partial r) \quad \text{at } r = r^*(t) \tag{2}$$

The other thermal boundary conditions to be satisfied by the solution are that

$$T = T_w \text{ at } r_w, \quad T = T^* \text{ at } r^*(t), \quad T = T_\infty \text{ at } r_\infty(t) \tag{3}$$

In addition, prior to the onset of melting, the temperature of the phase-change material is uniform and equal to T_∞ ($<T^*$).

Since the problem does not permit an exact analytical solution, numerical techniques were adopted because they can provide results of assured accuracy (in contradistinction to approximate methods such as the Heat Balance Integral). To facilitate solutions via finite differences, it appears advantageous to work in a domain of unchanging size in which the grid can be fixed once and for all. This requires that the moving boundaries be immobilized and, to this end, a transformation of variables is carried out. The transformation also serves to introduce dimensionless variables and parameters.

First, new space coordinates η and ξ, respectively for the liquid and the solid regions, are defined as

$$\eta = (r - r_w)/\delta_\ell, \quad \xi = (r - r^*)/\delta_s \tag{4}$$

Since $r_w \le r < r^*$ in the liquid and $r^* < r \le r_\infty$ in the solid and, furthermore, $\delta_\ell = (r^* - r_w)$ and $\delta_s = (r_\infty - r^*)$, it follows that

$$0 \le \eta < 1, \quad 0 < \xi \le 1 \tag{5}$$

for all time. Thus, in the new coordinates, both the liquid and solid domains are of unit dimension, unchanging with time. This simplification is, however, purchased at the price of greater complexity in the governing equations, as will be demonstrated shortly.

Next, a dimensionless time variable τ is defined by

$$\tau = (\alpha t/r_w{}^2)[c(T_w - T^*)/\lambda] = (\text{Fo})(\text{Ste}) \tag{6}$$

The inclusion of the Stefan number in the definition of τ is prompted by experience with melting problems without subcooling. In those problems, with τ defined as in equation (6), the results show only a modest dependence on the Stefan number.

[1] Numbers in brackets designate References at end of paper.

Nomenclature

c = specific heat
Fo = Fourier number, $\alpha t/r_w{}^2$
k = thermal conductivity
Q = time-integrated surface heat transfer, equation (23)
q = instantaneous surface heat flux
r = radial coordinate
r_w = radius of heated cylinder
r^* = coordinate of liquid-solid interface
r_∞ = radial position in solid beyond which $T = T_\infty$
Ste = Stefan number, $c(T_w - T^*)/\lambda$
T = temperature
T_w = temperature of cylinder surface
T^* = melting temperature
T_∞ = temperature of subcooled solid
t = time
α = thermal diffusivity
Δ = dimensionless layer thickness, δ/r_w
δ_ℓ = liquid layer thickness
δ_s = conduction layer thickness in solid
η, ξ = transformed coordinates, equation (4)
θ = dimensionless temperature, equation (7)
λ = latent heat of melting
ρ = density
τ = dimensionless time, equation (6)
ϕ = subcooling parameter, equation (8)
ψ = constant in plane layer solution

Subscripts

c = cylindrical melting
ℓ = liquid
o = without subcooling
p = plane melting
s = solid

Finally, dimensionless temperature variables for the liquid and solid regions are introduced as

$$\theta_\ell = (T_\ell - T^*)/(T_w - T^*), \quad \theta_s = (T^* - T_s)/(T_w - T^*) \tag{7}$$

along with the subcooling ratio

$$\phi = (T^* - T_\infty)/(T_w - T^*) \tag{8}$$

The transformation of the governing equations is faciliated by the relations, respectively, for the liquid region

$$\frac{\partial}{\partial r} = \frac{1}{\delta_\ell}\frac{\partial}{\partial \eta}, \quad \frac{\partial}{\partial t} = \frac{\alpha\,\mathrm{Ste}}{r_w{}^2}\frac{\partial}{\partial \tau} - \frac{\eta}{\delta_\ell}\frac{d\delta_\ell}{dt}\frac{\partial}{\partial \eta} \tag{9}$$

$$\frac{\partial}{\partial r} = \frac{1}{\delta_s}\frac{\partial}{\partial \xi}, \quad \frac{\partial}{\partial t} = \frac{\alpha\,\mathrm{Ste}}{r_w{}^2}\frac{\partial}{\partial \tau} - \left[\frac{\xi}{\delta_s}\frac{d\delta_s}{dt} + \frac{1}{\delta_s}\frac{d\delta_\ell}{dt}\right]\frac{\partial}{\partial \xi} \tag{10}$$

and the solid region. The "extra" terms in the transformation of $\partial/\partial t$, i.e., the $\partial/\partial\eta$ and $\partial/\partial\xi$ terms in (9) and (10) respectively, have an interesting physical interpretation. They represent convection associated with the immobilization of a moving boundary. An observer positioned on an immobilized moving boundary sees mass moving toward (or away) from him, and this is the mass responsible for the convection. The $\partial/\partial t$ transformation of equation (10) contains two such convective terms because both boundaries of the solid are being immobilized.

The transformation of the conservation equations (1) can then be carried out, with the result

$$\mathrm{Ste}\left[\frac{\partial\theta_\ell}{\partial\tau} - \frac{\eta}{\Delta_\ell}\frac{d\Delta_\ell}{d\tau}\frac{\partial\theta_\ell}{\partial\eta}\right] = \frac{1}{\Delta_\ell{}^2}\frac{\partial^2\theta_\ell}{\partial\eta^2} + \frac{1}{1+\eta\Delta_\ell{}^2}\frac{\partial\theta_\ell}{\partial\eta} \tag{11}$$

$$\mathrm{Ste}\left[\frac{\partial\theta_s}{\partial\tau} - \left(\frac{\xi}{\Delta_s}\frac{d\Delta_s}{d\tau} + \frac{1}{\Delta_s}\frac{d\Delta_\ell}{d\tau}\right)\frac{\partial\theta_s}{\partial\xi}\right] = \frac{1}{\Delta_s{}^2}\frac{\partial^2\theta_s}{\partial\xi^2} + \frac{1}{1+\Delta_\ell+\xi\Delta_s}\frac{\partial\theta_s}{\partial\xi} \tag{12}$$

where

$$\Delta_\ell = \delta_\ell/r_w, \quad \Delta_s = \delta_s/r_w \tag{13}$$

The interface energy balance (2), after transformation, becomes

$$-\frac{1}{\Delta_\ell}\frac{\partial\theta_\ell}{\partial\eta} = \frac{d\Delta_\ell}{d\tau} + \frac{1}{\Delta_s}\frac{\partial\theta_s}{\partial\xi}, \quad \text{at } \eta = 1 \text{ and } \xi = 0 \tag{14}$$

and in the new variables the boundary conditions are

$$\theta_\ell = 1 \text{ at } \eta = 0, \quad \theta_\ell = 0 \text{ at } \eta = 1 \tag{15a}$$

$$\theta_s = 0 \text{ at } \xi = 0, \quad \theta_s = (T^* - T_\infty)/(T_w - T^*) = \phi \text{ at } \xi = 1 \tag{15b}$$

while the initial condition is $\theta_s = \phi$ for $\xi > 0$.

Solution Methodology. As has been noted earlier, solutions will be obtained via numerical techniques. A key feature in the implementation of the solution method is the selection of Δ_s, which represents a position in the solid that lies beyond the region affected by the temperature wave emanating from the interface. One approach would be to take Δ_s as a constant that is large enough to insure that the temperature wave never reaches Δ_s during the entire range of τ values to be used in the computations. Although attractive because of its simplicity, this approach leads to an inefficient use of the finite-difference grid. This is because, in the solid, the grid spans the entire space between the interface and Δ_s at all times, while at relatively short times only the region adjacent to the interface is thermally active. Thus, the grid points lying outside the thermally active zone do not contribute to the progress of the solution even though they are involved in the computations.

A more effective and equally simple approach is to let

$$\Delta_s = C\Delta_\ell \tag{16}$$

where C is a constant for each case. With this model, Δ_s increases along with the timewise increase of the melt layer thickness Δ_ℓ. Thus, the portion of the solid which is spanned by the finite-difference grid grows larger with time. Inasmuch as the thermally active zone also enlarges with time, this model enables relatively efficient use of the entire grid. It should be noted, however, that Δ_s/Δ_ℓ is not strictly a constant in cylindrical systems and so, to make the method work, C is chosen to accommodate the largest value of Δ_s/Δ_ℓ occurring during the computation period.

The C values varied from case to case, with a typical magnitude being about 100. Verification runs were made with other values of C to insure that the results for the surface heat transfer and the interface position were insensitive to the selected C values to within 0.1 percent.

The transformed conservation equations (11) and (12) were recast as implicit finite-difference equations. To solve the resulting difference equations for the temperature distributions θ_ℓ and θ_s at time $\tau = \tau^{(m)}$, the interface and external boundary positions, Δ_ℓ and Δ_s, and their derivatives, $d\Delta_\ell/d\tau$ and $d\Delta_s/d\tau$, are needed as input. These quantities are obtained with the aid of the interface energy balance (14) and the Δ_s, Δ_ℓ relation (16).

First, $d\Delta_\ell/d\tau$ is evaluated from (14) by introducing the values of $\partial\theta_\ell/\partial\eta$, $\partial\theta_s/\partial\xi$, Δ_ℓ, and Δ_s which are known at time $\tau = \tau^{(m-1)}$; then $d\Delta_s/d\tau = C(d\Delta_\ell/d\tau)$. These values of $d\Delta_\ell/d\tau$ and $d\Delta_s/d\tau$ are used as input to the discretized forms of equations (11) and (12). In addition, if, in equation (14), $\partial\theta_\ell/\partial\eta$ and $\partial\theta_s/\partial\xi$ are regarded as constants during the interval $\tau = \tau^{(m-1)}$ to $\tau = \tau^{(m)}$ and equal to their values at $\tau^{(m-1)}$, then this equation can be written as

$$\Delta_\ell d\Delta_\ell = Kd\tau \tag{17}$$

which gives

$$\Delta_\ell{}^{(m)} = [(\Delta_\ell{}^{(m-1)})^2 + 2K(\tau^{(m)} - \tau^{(m-1)})]^{1/2} \tag{18}$$

from which Δ_ℓ at $\tau = \tau^{(m)}$ can be computed, and $\Delta_s{}^{(m)} = C\Delta_\ell{}^{(m)}$. These Δ_ℓ and Δ_s are the input values to the finite-difference counterparts of (11) and (12).

The aforementioned treatment of equation (14) has a philosophical kinship to an explicit difference formulation in that certain terms are evaluated at time $\tau = \tau^{(m-1)}$, which is at the beginning of the time interval. The advantage of this approach is that it enables the solution to march steadily forward in time, without having to mark time (i.e., iterate) while the position of the interface is being updated. Thus, in effect, the nonlinearity associated with the moving interface is eliminated.

The implicit difference equations were solved noniteratively at each time step by using the tridiagonal matrix algorithm. 80 grid points were deployed uniformly throughout the liquid region. In the solid, between 300 to 500 points were used, depending on the case. These points were deployed nonuniformly according to the relation

$$\xi_i = \left[\frac{i-1}{N-1}\right]^{1.7} \tag{19}$$

where N is the total number of points. Equation (19) places a greater density of points near the liquid-solid interface than in more remote parts of the solid. The time steps were selected so that the melt layer thickness increased by about two percent at each step. If a negative value of $d\Delta_\ell/d\tau$ was obtained from the evaluation of equation (14), the size of the increment in the melt layer thickness was diminished.

Starting difficulties were avoided by beginning the solution at a time when the thickness of the melt layer is $0.01r_w$. It was assumed that the Neumann solution for the plane layer is applicable up to that time.

As a verification of the solution methodology, the computer program encompassing the aforementioned time step and space step patterns was employed to solve the Neumann problem for a large range of times. Agreement to within 0.1 percent or better was attained.

Results and Discussion

The presentation of results will be focused on the instantaneous and time-integrated heat transfer at the cylinder surface and on the thickness of the liquid-solid interface. These results will be presented

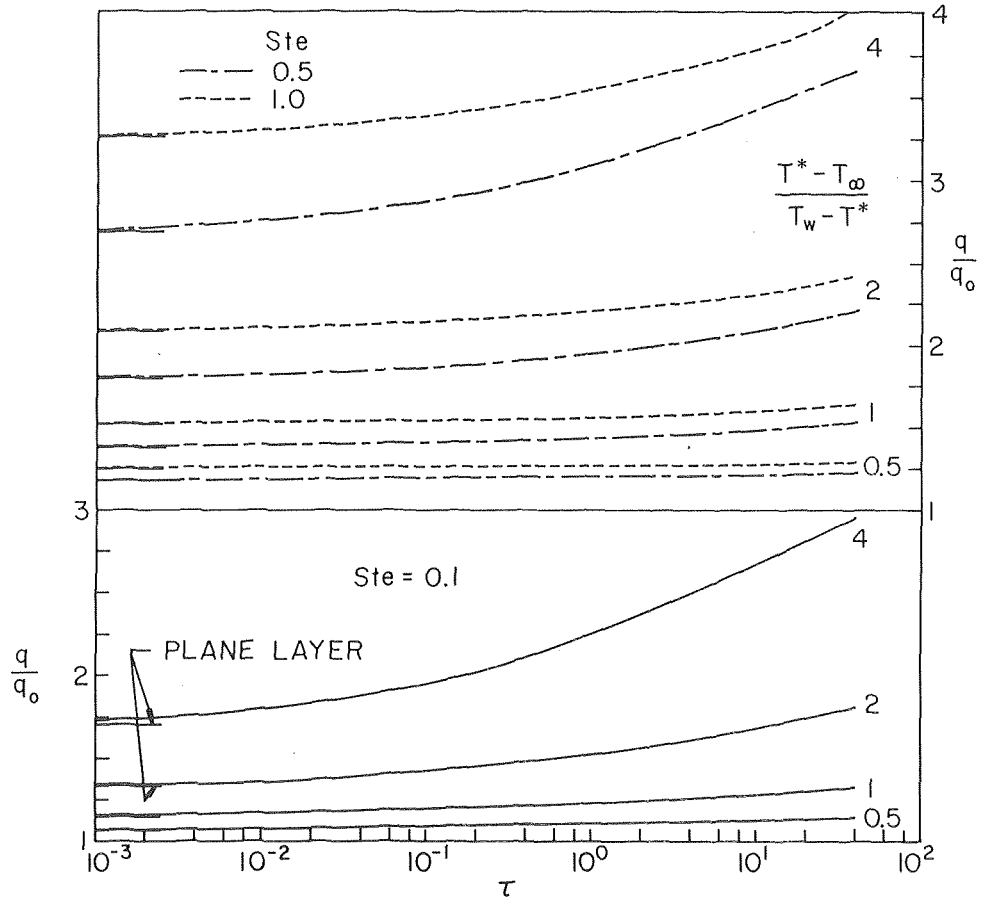

Fig. 2 Comparison of the instantaneous surface heat fluxes with and without subcooling

from two viewpoints. In the first, the subcooling-affected results are compared with those without subcooling. In the second, the results for cylindrical melting are compared with those for plane melting at the same degree of subcooling.

Subcooling/No-subcooling Comparison. The comparison of results with and without subcooling is made in Figs. 2, 3, and 4, for the instantaneous surface heat flux, the time-integrated surface heat transfer, and the interface position respectively. These figures will be discussed successively.

The ratio of the instantaneous surface heat fluxes with and without subcooling, q and q_0 respectively, are plotted in Fig. 2 as a function of the dimensionless time variable τ. Results for Ste = 0.1 are presented in the lower graph, while the upper graph is for Ste = 0.5 and 1.0. The curves are parameterized by the temperature ratio $(T^* - T_\infty)/(T_w - T^*)$, which is a measure of the degree of subcooling.

The curves appearing in these graphs are for cylindrical melting. In addition, short horizontal segments have been inserted along the left-hand margin of the figure to denote the q/q_0 results for melting of a plane layer. Since, as will be demonstrated shortly, both q and q_0 for a plane layer vary as $\tau^{-1/2}$, then q/q_0 is independent of τ. Therefore, the horizontal line segments could have been extended across the entire graph but were not so drawn in order to avoid confusion.

The deviations of the curves of Fig. 2 from an ordinate value of 1.0 give an immediate indication of the effect of subcooling on the instantaneous heat flux. As expected, subcooling increases the surface heat flux (i.e., $q/q_0 \geq 1$), and the extent of the increase is more marked at higher degrees of subcooling. In this regard, it may be noted that for subcooling ratios up to about 0.5, the heat flux is not very much affected by the subcooling (i.e., $q/q_0 \sim 1.1$ to 1.25, depending on Ste). On the other hand, for subcooling ratios on the order of four, the subcooling becomes a major factor in establishing the level of the heat flux.

It may further be observed that at small subcooling, q/q_0 does not vary appreciably with time. In contrast, at large subcooling, there is a substantial timewise increase in q/q_0.

The Stefan number has only a small effect on the results at small subcooling ratios, but becomes a significant parameter when the subcooling is large. In general, higher values of q/q_0 occur at larger Stefan numbers.

At small values of the time τ, the heat flux ratios for cylindrical melting approach those for the plane layer. When the subcooling is small, the q/q_0 values for the cylindrical case do not deviate significantly from those for the plane layer for the entire range of times that was investigated. On the other hand, at large subcooling, the timewise increase of q/q_0 for cylindrical melting gives rise to significant deviations from that of the plane layer. In general, the instantaneous heat flux for cylindrical melting is more affected by subcooling than is that for plane-layer melting, with the plane case serving as the lower bound for the q/q_0 of the corresponding cylindrical case.

The increase in the surface heat flux due to subcooling results from the involvement of the mass of the solid as a heat sink that is additional to the latent heat required by the melting process. The relative capacity of this sensible heat sink is greater at large Stefan numbers, with a corresponding increase in the surface heat flux. In the case of cylindrical melting, the fanning out of the radial heat flow lines in the solid gives rise to a thermal resistance that is lower than that for a plane layer. In addition, the fanning out enables more mass to become involved with the energy storage function. Both these factors contribute to the greater increase in surface heat flux encountered in cylindrical melting than in plane melting. These factors are especially effective when the subcooling is large and when the cylindrical geometry asserts itself, i.e., for thicker melt layers.

Before leaving Fig. 2, it is appropriate, for completeness, to state the equation for the instantaneous surface heat flux for a plane layer. From [5], Chapter 5,

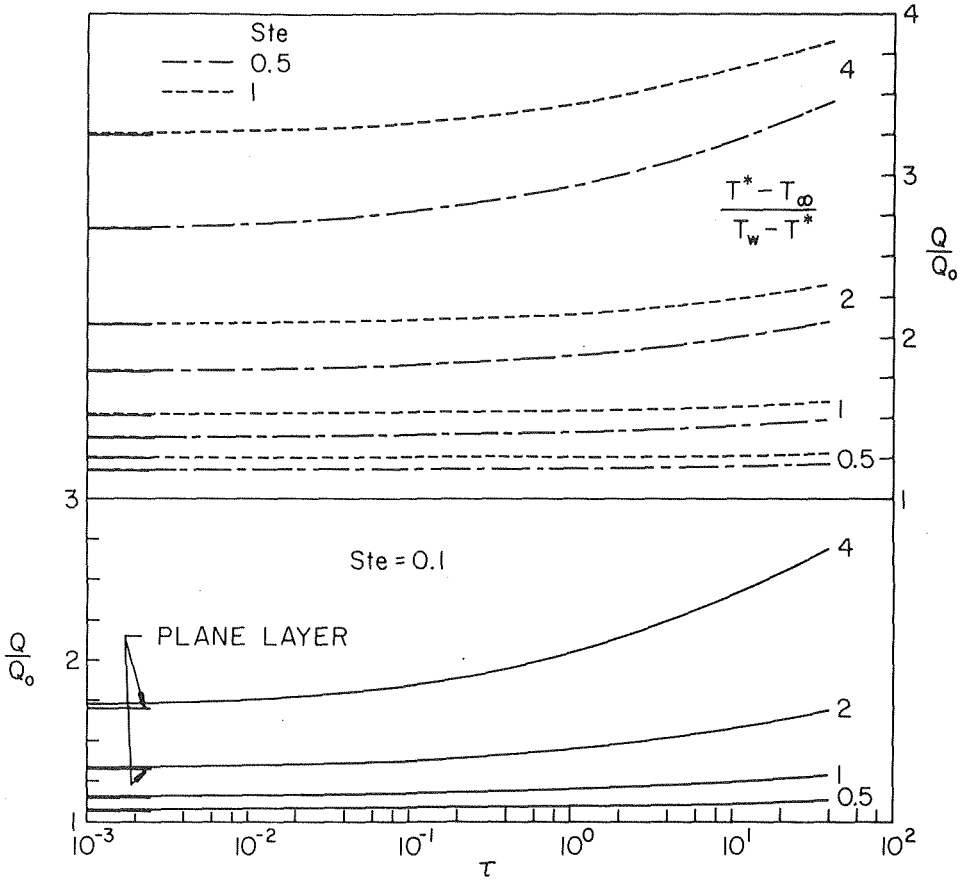

Fig. 3 Comparison of the time-integrated surface heat transfers with and without subcooling

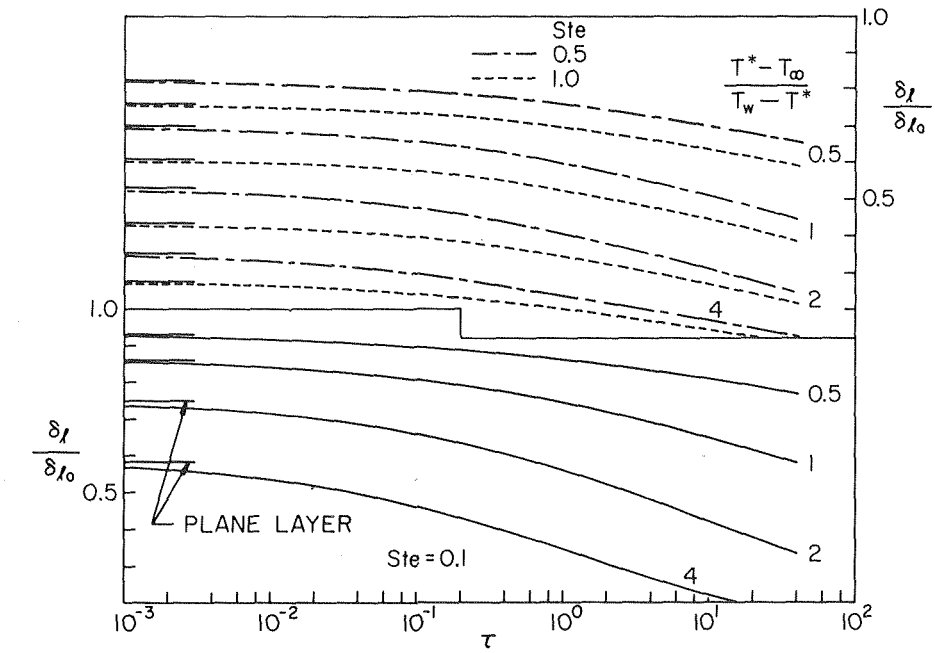

Fig. 4 Comparison of the instantaneous liquid layer thicknesses with and without subcooling

$$q_p = k(T_w - T^*)/(\pi\alpha t)^{1/2}\, erf\psi \qquad (20)$$

where ψ is a constant whose value is obtained by solving the following transcendental equation

$$\frac{\sqrt{\pi}}{\mathrm{Ste}}\psi e^{\psi^2} erf\psi - \frac{\phi\, erf\psi}{1 - erf\psi} = 1 \qquad (21)$$

If ψ_0 denotes the solution of equation (21) for $(T^* - T_\infty) = 0$ (no subcooling), then

$$q_p/q_{p0} = erf\psi_0/erf\psi \tag{22}$$

Numerical values of ψ are listed in Table 1 for the cases for which results are presented in Fig. 2.

In certain applications (e.g., thermal storage), the amount of heat transferred from the surface during a time interval $\tau = 0$ to $\tau = \tau$ is of importance. The time-integrated heat transfer is denoted here by Q and was evaluated from

$$Q = \int_0^t q dt \tag{23}$$

The results for the surface-integrated heat transfer in the presence and in the absence of subcooling, Q and Q_0, respectively, are presented in ratio form in Fig. 3. The structure of the figure is identical to that of Fig. 2. Furthermore, all of the trends that were enumerated in connection with Fig. 2 also apply to Fig. 3.

It can be verified by comparing the two figures that each Q/Q_0 curve for cylindrical melting lies below its q/q_0 counterparts, with the deviations being greater at higher subcooling. In physical terms, this finding reflects the fact that the Q value corresponding to a time τ includes contributions from earlier times when the cylindrical geometry had asserted itself less strongly with respect to heat conduction in the solid. It is also consistent with the fact that q/q_0 is an increasing function of τ.

For plane melting, the application of equations (20) and (23) to the subcooled and nonsubcooled cases shows that $Q_p/Q_{p0} = q_p/q_{p0}$. Therefore, the segments representing the plane layer results in Figs. 2 and 3 are identical.

The results for the instantaneous thickness of the liquid layer are presented in Fig. 4. The figure gives the ratio of the layer thickness in the presence of subcooling to that without subcooling, δ_ℓ and $\delta_{\ell 0}$, respectively, both evaluated at the same instant of time. This ratio is plotted as a function of the dimensionless time τ. The general layout of the figure is similar to that used in the preceding figures.

The departure of $\delta_\ell/\delta_{\ell 0}$ from a value of 1.0 is a direct measure of the effect of subcooling on the liquid layer thickness. Inspection of Fig. 4 shows that in the presence of subcooling, the melt layer is thinner than it would be if there were no subcooling (at a given time and Stefan number), that is, $\delta_\ell/\delta_{\ell 0} < 1$ at all times. This effect is accentuated at higher degrees of subcooling and at larger Stefan numbers. Furthermore, for cylindrical melting, the timewise growth of δ_ℓ is slower than than of $\delta_{\ell 0}$, so that $\delta_\ell/\delta_{\ell 0}$ decreases with time.

The respective curves for cylindrical melting are asymptotic at small times to, but otherwise lie below, the horizontal line segments which represent the results for plane melting. Thus, the liquid layer thickness for cylindrical melting is more affected by subcooling than is that for plane melting.

The aforementioned findings relevant to the layer thickness can be viewed as resulting from the competition between two heat sinks, namely, the latent heat for the melting process and the storage inherent in the solid. Both a high degree of subcooling and a large Stefan number favor the storage sink and thereby diminish the rate of melting. In addition, when the cylindrical geometry asserts itself, i.e., at larger melt layer thicknesses (larger time), the storage becomes even more competitive and further diminishes the rate of melting.

Table 1 Numerical values of the constant ψ

Ste	$(T^* - T_\infty)/(T_w - T^*)$	ψ
0.1	0	0.22002
	0.5	0.20372
	1	0.18913
	2	0.16431
	4	0.12780
0.5	0	0.46479
	0.5	0.38341
	1	0.32462
	2	0.24606
	4	0.16300
1.0	0	0.62006
	0.5	0.46985
	1	0.37776
	2	0.27005
	4	0.17039

To complete the discussion of Fig. 4, it remains to give the expression for the liquid layer thickness, which is [5]

$$\delta_{\ell p} = 2\psi\sqrt{\tau/\mathrm{Ste}} \tag{24}$$

where ψ is determined from (21). It is readily verified that $\delta_\ell/\delta_{\ell 0}$ is independent of time for plane melting.

Cylindrical/Plane Comparison. The results will now be presented in terms of a direct comparison between the cylindrical and plane melting cases. In Fig. 5, the ratio of instantaneous heat fluxes q_c/q_p is plotted as a function of time. The figure contains a full set of results (i.e., subcooling ratios from 0 to 4) for Ste = 0.1 and 1.0. To minimize overlap, the ordinate scales for the two cases have been slightly displaced. With a view to avoiding further congestion, the results for Ste = 0.5 are not presented here except for the zero subcooling case, the particular use of which will be described shortly.

The figure shows that for all cases the instantaneous heat flux for cylindrical melting exceeds that for plane melting, and the deviation between the two cases grows rapidly with time. This trend reflects the fact that the decrease of the heat flux with time, which is a natural consequence of the thickening of the thermally active layers, is substantially slower for the cylindrical case than for the plane case. Within the range of melting times for which computations were performed, cylinder surface heat fluxes are encountered that are on the order of five times as large as the fluxes on a surface bounding a plane melting layer.

As the degree of subcooling increases at a fixed Stefan number, the deviation between the cylindrical and plane heat fluxes increases. This is because the cylindrical solid surrounding the melt layer offers less resistance to heat inflow and larger storage capacity than does the plane solid, and these attributes are activated with subcooling. The results also display an effect of Stefan number, but it is difficult to relate this effect to physical occurrences since Ste appears both as a curve parameter and as a factor in the abscissa variable τ.

The results presented in Figs. 2 and 5, when used in conjunction with equation (20), enable the heat flux at the cylindrical surface to be evaluated. Thus,

$$q_c = (q/q_0)_c (q_c/q_p)_0 q_{p0} \tag{25}$$

where the first and second factors are respectively read from Figs. 2 and 5, and q_{p0} is computed from equation (20). The inclusion of the $(q_c/q_p)_0$ curve for Ste = 0.5 in Fig. 5 enables evaluation of q_c for that Stefan number.

The time-integrated heat transfer results for cylindrical and plane melting, Q_c and Q_p, respectively, are defined by equation (23) and are presented in ratio form in Fig. 6. The structure of the figure and the qualitative trends in evidence therein are identical to those of Fig. 5. The main message of Fig. 6 is that the time-integrated heat transfer is less sensitive to geometry (i.e., cylindrical versus plane) than is the instantaneous heat transfer rate. This is because the time-integrated heat transfer includes substantial contributions from early times, when q_c and q_p do not differ appreciably and when both are large.

The determination of Q_c can be made from an equation identical to (25) in which q is replaced by Q. The quantities $(Q/Q_0)_c$ and $(Q_c/Q_p)_0$ are read respectively from Figs. 3 and 6, and Q_{p0} is obtained from an equation derived by integrating q_p from equation (20) in accordance with (23).

The final graph, Fig. 7, compares the liquid layer thicknesses for cylindrical and plane melting. The curves in the lower and upper parts of the figure span the range of subcooling ratios from 0 to 4 and pertain respectively to Ste = 0.1 and 1.0; the zero subcooling case for Ste = 0.5 is also included. It is seen from the figure that for the same set of operating parameters, the cylindrical melt layer is always thinner than the plane melt layer. Furthermore, the deviation increases with time, reflecting the fact that the thickness of a cylindrical layer grows more

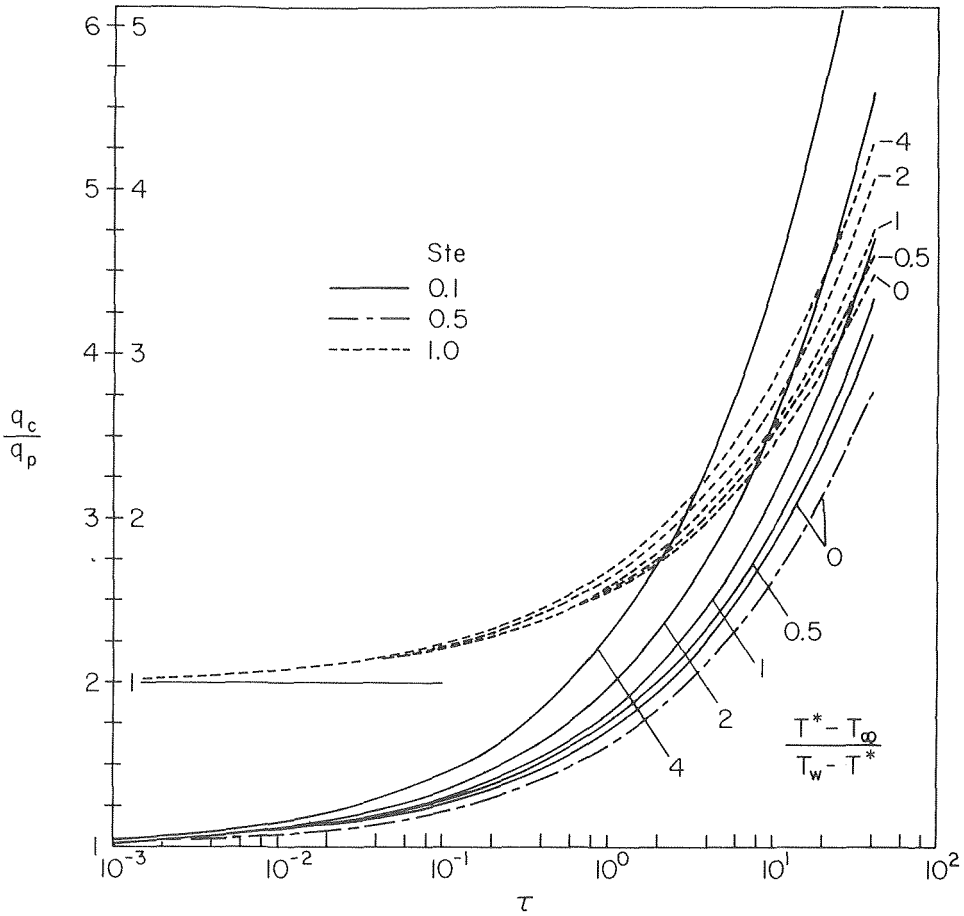

Fig. 5 Comparison of the instantaneous surface heat fluxes for cylindrical and plane melting

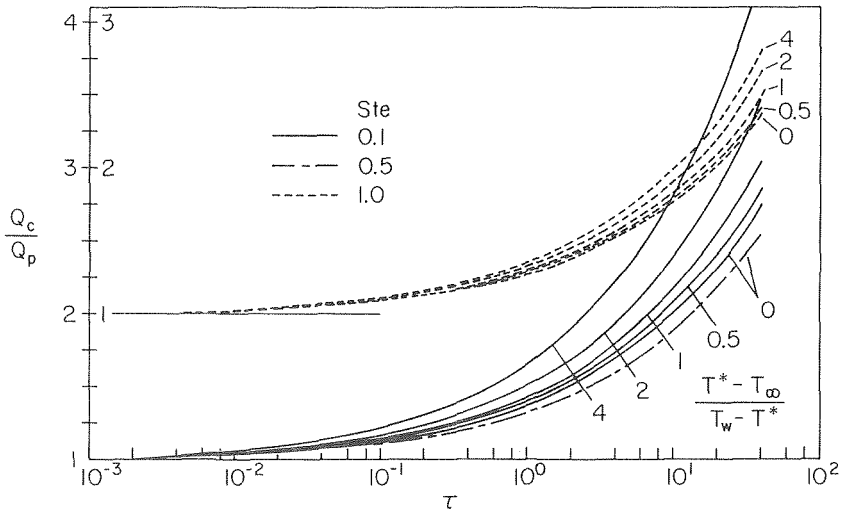

Fig. 6 Comparison of the time-integrated surface heat transfers for cylindrical and plane melting

slowly than the thickness of a plane layer.

Of particular note is the marked effect of subcooling on the thickness ratio. At a high degree of subcooling and at long melting times, the thickness of a cylindrical melt layer may be only a third of that of a plane melt layer.

Numerical values of $\delta_{\ell c}$ can be obtained from an equation such as (25), with q replaced by δ_ℓ. Figs. 4 and 7 are used for $(\delta_\ell/\delta_{\ell 0})_c$ and $(\delta_{\ell c}/\delta_{\ell p})_0$, and $\delta_{\ell p 0}$ is from (24).

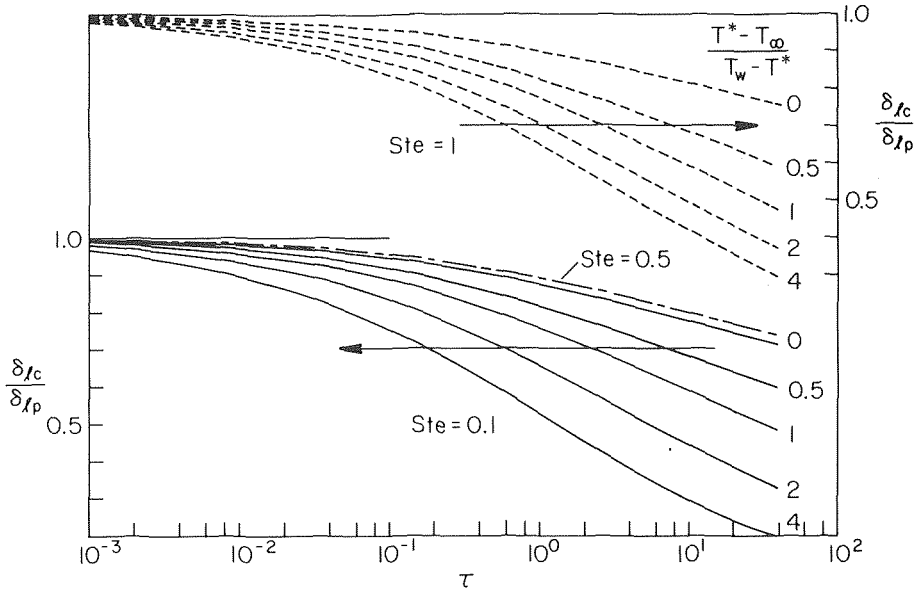

Fig. 7 Comparison of the instantaneous liquid layer thicknesses for cylindrical and plane melting

Concluding Remarks

The results of this analysis have shown that subcooling of the solid can have a marked effect on melting due to an embedded cylindrical heat source. Both the instantaneous and time-integrated surface heat transfer are substantially augmented (relative to the nonsubcooling case) when the subcooling ratio exceeds two. The extent of the augmentation is greater at larger times as the cylindrical geometry asserts itself. In the presence of subcooling, the melt layer is thinner than it would be without subcooling, and this effect is accentuated as the melting proceeds. At high levels of subcooling and at long melting times, the layer thickness may be only about a fifth of that for no subcooling.

Subcooling also sharpens the differences between cylindrical and plane melting. The ratio of the surface heat fluxes for cylindrical and plane melting, which always exceeds unity, increases substantially due to subcooling. Similarly, in the presence of subcooling, the thickness of a cylindrical melt layer is only a fraction of the thickness of a corresponding plane melt layer.

In the absence of other published results for cylindrical melting of a subcooled solid, the only possible comparisons between the present results and the literature are for subcooled plane melting and for cylindrical melting without subcooling. Verification runs comparing the present numerical solution with the classical Neumann (analytical) solution for subcooling of a plane melt layer yielded agreement to within 0.1 percent or better. For cylindrical melting without subcooling, the only information published in the literature is for the melt layer thickness (i.e., surface heat transfer results are not given), with the most accurate available results being those obtained numerically by Stephan and Holzknecht [1]. The graphical presentation of the information in [1] does not enable a very precise reading but, within this limitation, good agreement with the present results appears to prevail.

References

1 Stephan, K., and Holzknecht, B., "Heat Conduction in Solidification of Geometrically Simple Bodies," Wärme-und Stoffübertragung, Vol. 7, 1974, pp. 200–207.

2 Saitoh, T., "Numerical Method for Multi-Dimensional Freezing Problems in Arbitrary Domains," ASME JOURNAL OF HEAT TRANSFER, Vol. 100, No. 2, 1978, pp. 249–299.

3 Duda, J. L., Malone, M. F., Notter, R. H., and Vrentas, J. S., "Analysis of Two-Dimensional Diffusion-Controlled Moving Boundary Problems," *International Journal of Heat and Mass Transfer*, Vol. 18, 1975, pp. 901–910.

4 Bankoff, S. G., "Heat Conduction or Diffusion with Change of Phase," in *Advances in Chemical Engineering*, Vol. 5, pp. 75–150, Academic Press, New York, 1964.

5 Eckert, E. R. G., and Drake, R. M., *Analysis of Heat and Mass Transfer*, McGraw-Hill, New York, 1972.

R. R. Schmidt
E. M. Sparrow

Department of Mechanical Engineering,
University of Minnesota,
Minneapolis, Minnesota

Turbulent Flow of Water in a Tube with Circumferentially Nonuniform Heating, with or without Buoyancy

Experiments have been performed to study the effect of circumferentially nonuniform heating on the fully developed turbulent heat transfer characteristics for water flow in a horizontal circular tube. The use of a specially fabricated tube enabled heat to be supplied to the fluid over half its circumference, while the other half was unheated. Separate sets of experiments were conducted with the heated portion at the top and at the bottom. By varying the temperature level, the Prandtl number was varied from 3.5 to 11.5. The Reynolds number ranged from 3,000 to 70,000. The measurements enabled circumferential distributions of the Nusselt number, wall temperature, and heat flux to be determined, and circumferential average Nusselt numbers were also evaluated. Both the circumferential average and circumferential local results demonstrate that significant buoyancy effects are present for bottom heating at low Reynolds numbers and high Rayleigh numbers, and a criterion is deduced for the onset of these effects. The top heating experiments were not affected by buoyancy. The buoyancy-unaffected circumferential average Nusselt numbers increase smoothly over the entire range of Reynolds numbers, and the Prandtl number dependence is correlated as $Pr^{0.47}$. These Nusselt numbers are within about ten percent of literature correlations (applicable for $Re \geq 10{,}000$) for circumferentially uniform thermal conditions. The circumferential distributions of the Nusselt number and temperature on the heated wall tend toward uniformity when the turbulence is well developed (i.e., higher Reynolds numbers) or when buoyancy is present. The temperatures on the unheated wall are generally lower than the bulk temperature in the absence of buoyancy, but, when buoyancy is active, they are above the bulk temperature.

Introduction

Turbulent heat transfer in circular tubes has been the subject of extensive investigation for many years. In the main, the work has been concerned with the case where the wall heat flux and wall temperature are uniform around the circumference of the tube. Although circumferential uniformity is an attractive simplification in both analysis and experiment, it does not reflect reality in many established applications (e.g., boiler, condenser, and heat exchanger tubes) as well as in newer technologies.

With regard to the latter, the receiver tubes of solar collectors are a case in point. The solar flux arriving at a tubular receiver will, in general, vary around the circumference of the tube. The extent of the variation depends on whether the solar collector is concentrating or nonconcentrating and, if concentrating, on the degree of concentration and the sharpness of the focus. In addition, for horizontal or inclined tubes, another issue that may be relevant is whether the upper portion of the circumference is more or less strongly heated than the lower portion. The orientation of the heating may be a factor in the creation or suppression of buoyancy-induced secondary motions superposed on the forced convection mainflow.

The foregoing considerations provided motivation and direction for the present research. Experiments were performed for turbulent flow in a horizontal circular tube which was uniformly heated over half of its circumference and was unheated over the other half. To permit examination of possible buoyancy effects, Reynolds numbers as low as 3,000 were investigated. Furthermore, two orientations of the heated section were examined: (i) heating above and adiabatic below (top heating), (ii) heating below and adiabatic above (bottom heating). To investigate the buoyancy-unaffected regime, the range of the Reynolds number was extended to about 70,000. Although a single working fluid, water, was employed in the experiments, its bulk Prandtl number was systematically varied to cover a relatively wide range, 3.5 to 11.5. Wall-to-bulk temperature differences were kept sufficiently small so that variable property effects were minimized.

The measurements were focused on the determination of fully developed heat transfer results. Both the heated and unheated portions of the tube were heavily instrumented, which enabled both circumferentially local and average heat transfer resulted to be obtained. An appraisal of the circumferential average results yielded

Contributed by the Heat Transfer Division for publication in the JOURNAL OF HEAT TRANSFER. Manuscript received by the Heat Transfer Division September 23, 1977.

a criterion for the onset of buoyancy effects. The buoyancy-unaffected average Nusselt numbers have been correlated as a function of the Reynolds and Prandtl numbers and are, in addition, compared to analytical predictions for nonuniform heating and to empirical correlations for uniform heating. Circumferential distributions are presented for the Nusselt number, wall temperature, and heat flux on the heated portion of the tube and for the wall temperature on the unheated portion of the tube. Comparisons are made between the measured circumferential variations of the Nusselt number and heat flux and those predicted by analysis.

A review of the literature revealed that only a few experiments have been performed on turbulent tube flow with circumferentially nonuniform thermal boundary conditions [1–3].[1] Those experiments were generally of a more limited scope than the present in that neither buoyancy effects nor the influence of heating orientation were investigated, the Prandtl number was restricted to a single value, and low Reynolds numbers were not studied. Furthermore, the extent of the nonuniformity in heat flux was not as great as that of the present experiments. Heat transfer coefficients were not reported in [2], and the length of the heated portion of the tube was only three diameters. In [3], sparse instrumentation led to some uncertainties in the results.

The effect of circumferentially nonuniform thermal boundary conditions on turbulent forced convection heat transfer in tubes has been analyzed in [4–7] for various turbulence models. The present experimental results will be compared with the predictions from the most recent and encompassing model [7], which takes account of differences in the tangential and radial eddy diffusivities near the wall.

Buoyancy effects on turbulent forced convection heat transfer in horizontal tubes have, apparently, not been previously investigated in the presence of circumferentially nonuniform thermal conditions. For circumferentially uniform conditions, available flow regime maps [8–10] indicate that there are combinations of the Reynolds and Rayleigh numbers where buoyancy effects are significant.

The Experiments

The experimental apparatus is an open-loop flow circuit. The flow is delivered to the system by an elevated constant head tank which is, in turn, fed by both hot and cold water lines whose adjustment enables control of the tank temperature (and, thereby, the Prandtl number). From the tank, the water passes downward into an insulated inlet chamber which serves as a vertical/horizontal transition while avoiding the secondary flows associated with an elbow or a bend. The water then is ducted through an 80-diameter long hydrodynamic development section and into the electrically heated test section. From the test section, it passes through an exit section which is slightly elevated to ensure that the test section and hydrodynamic development length are always filled with water. The discharge from the exit section is directed into a weigh tank situated on a balance—thereby enabling direct metering of the flow. The system is equipped with cut-off, by-pass, and control valves.

The test section, the hydrodynamic development length, and the exit section are all heavily insulated. In particular, the test section insulation consists of a core of free-pouring silica aerogel powder (which envelops the tube) contained within walls made of polyurethane sheet. Both the aerogel and the urethane have thermal conductivities less than that of air. Heat losses were further combated by the use of conical-tipped plastic supports for the test section.

The heart of the apparatus is the test section tube, which was especially designed and fabricated so that the fluid could be uniformly heated over half of its circumference and be unheated over the other half. Since this heating condition has, apparently, not been previously investigated in the research literature, there were no precedents to follow in designing the test section for the present experiments. Therefore, a substantial amount of development work had to be undertaken and new fabrication procedures devised. These procedures are described in detail in Appendix A of [11], and only a brief description will be given here.

In simplest terms, the test section was fabricated by first taking longitudinal cuts along a thin-walled stainless steel tube, thereby dividing it into two portions. The circumference of one portion subtended an arc of 180 deg, whereas the circumference of the other portion subtended a 150 deg arc (30 deg of circumference was removed by the machining). Then, the tube was re-formed about a circular rod, with a special epoxy being used to fill the two 15 deg gaps between the respective edges of the two portions of the tube. The re-formed tube had an internal diameter of 3.07 cm (1.21 in.) and was 30 diameters in length.

The tube had been internally honed prior to the longitudinal cutting operation. After re-forming, it was lightly honed again to remove any epoxy that was not flush with the stainless steel wall. The end result was such that no discontinuity could be sensed when a finger, inserted through the end of the tube, was moved over the epoxy joint.

The successful fabrication of the test section tube involved a myriad of factors encompassing design and fabrication of auxiliary parts, numerous machining operations, rational selection of an epoxy and its proper curing, etc. Special attention had to be given to minimizing and compensating for possible warpage and twisting of the tube due to residual stress unlocked by the longitudinal cutting operation. Also, during the re-forming operation, the epoxy had to be maintained at its curing temperature (~120°C), necessitating the heating of the rod about which the tube was re-formed.

Once the test section tube had been fabricated, the internal diameters of the hydrodynamic development length and the exit section were machined to conform to that of the re-formed tube. In this way,

[1] Numbers in brackets designate References at end of paper.

Nomenclature

A = convective area at heated surface
c_p = specific heat at constant pressure
D = inside diameter of tube, $2r_i$
g = acceleration of gravity
k = thermal conductivity of water at T_{bz}
k_w = thermal conductivity of tube wall
$\dot{m}$ = mass flow rate
Nu = circumferential local Nusselt number, equation (4)
$\overline{\text{Nu}}$ = circumferential average Nusselt number, equation (5)
Pr = Prandtl number at T_{bz}
Q = rate of heat transfer over $-80° \le \theta \le 80°$
q = local heat flux at θ
$\bar{q}$ = average heat flux over $-80° \le \theta \le 80°$
$\bar{\bar{q}}$ = average heat flux for heated arc
Ra = Rayleigh number, $(g\beta\bar{\bar{q}}r_i^4/k\nu^2)\text{Pr}$
Re = Reynolds number, $2\dot{m}/\mu\pi r_i$
r = radial coordinate
r_i = inside radius
r_m = mean radius, $(r_i + r_o)/2$
r_o = outside radius
S = volume heat source due to ohmic heating
T = temperature
T_{bz} = local bulk temperature
T_i = inside wall temperature at θ
$\bar{T}_i$ = average value of T_i over $-80° \le \theta \le 80°$
T_o = outside wall temperature at θ
t = local wall thickness
$\bar{t}$ = average thickness of heated wall
z = axial coordinate
β = thermal expansion coefficient at T_{bz}
θ = angular coordinate
μ = viscosity at T_{bz}
ν = kinematic viscosity at T_{bz}

continuity of the flow cross section was assured. The starting length and the exit section were fabricated from pvc piping.

The heating of the test section was accomplished by passing a-c electric current longitudinally through the tube wall. The current flowed in only one of the longitudinal halves of the test section, specifically, that whose circumference encompasses 180 deg of arc. This was achieved because the current carrying leads were attached only to that half and because the nonconducting epoxy prevented the current from entering the other half.

In view of the low resistance of the test section (~0.016 ohms), the currents were typically on the order of hundreds of amperes. Precautions were taken to minimize potential thermal distortions at the ends of the test sections caused by attachment of leads suitable to carry such high currents. In particular, the bus bars attached to the respective ends of the tube contained radial slits to minimize circumferential heat conduction. Furthermore, the temperature of the leads which carry current to the bus bars was controlled and matched to that at the end of the tube.

Measurement of the electric power input (power factor = 0.996) to the test section served as the basis for the determination of the convective heat transfer rate. The power measurement was supplemented by measurements of the local wall thickness distribution that had been made subsequent to the longitudinal sectioning of the test section tube and prior to its re-forming. The knowledge of the local thickness enabled the local ohmic dissipation in the tube wall to be evaluated. The mean thickness of the heated wall is 0.0831 cm (0.0327 in.).

Calibrated 30-gage copper-constantan thermocouples were spot welded to the test section tube to measure its outside surface temperature. At the two axial stations of specific interest in this study, 20 and 25 diameters downstream of the onset of heating, there were 18 and 14 thermocouples, respectively, affixed to the tube. Four thermocouples were situated in the hydrodynamic development section to measure the inlet bulk temperature. The thermocouples were read by a printing digital millivoltmeter.

All electronic and electrical instruments used in connection with the experiments were specifically calibrated, as was the beam balance for the flow metering.

Prior to each data run, the bore of the test section tube was cleaned and thoroughly flushed. The high Prandtl number runs were made during the winter season when the temperature of the cold water supply was in the range of 5°C. The runs at the lower Prandtl numbers were carried out in warmer seasons.

The experiments were performed for nominal values of the Prandtl number equal to 3.5, 5.5, 7.5, 9.5, and 11.5. The Reynolds numbers of the data runs encompassed (in thousands) 3, 5, 10, 20, 40, and 70—again nominal values. For a large number of these cases, separate runs were made for top heating and bottom heating. All told, 47 final data runs were made, the specific characteristics of which are listed in Table 5.1 of [11].

Data Reduction

For the evaluation of the heat transfer coefficients, it is necessary to translate the measured power input and outside wall temperatures into inside wall temperatures and heat fluxes. For this purpose, the heat conduction equation for the heated portion of the tube wall can be employed. The analysis is simplified because (a) the heat loss from the outer surface of the tube is negligible, (b) the net axial conduction is also negligible, (c) the temperature dependence of the tube-wall thermal conductivity can be neglected, and (d) the electric current density is uniform. Items (a)–(c) were verified by calculation, whereas item (d) was affirmed by measurements.

The heat conduction equation which serves as the starting point of the data reduction is

$$\frac{1}{r}\frac{\partial}{\partial r}\left(r\frac{\partial T}{\partial r}\right)+\frac{1}{r^2}\frac{\partial^2 T}{\partial \theta^2}+\frac{S}{k_w}=0 \tag{1}$$

where S is the rate of ohmic heat generation per unit volume and k_w is the thermal conductivity of the stainless steel wall. Based on iterative calculations that will be described shortly, $\partial^2 T/\partial\theta^2$ was typically found to vary by one or two percent across the thickness of the wall. In those few cases which were exceptions, the net circumferential conduction was less than ½ percent of the heat generation term.

In view of these facts, it is reasonable to regard $\partial^2 T/\partial\theta^2$ as a constant across the wall thickness, with the constant being denoted as $\overline{(\partial^2 T/\partial\theta^2)}$ and evaluated as the average of the values at the inner and outer radii. In general, $\overline{(\partial^2 T/\partial\theta^2)}$ varies with the angular coordinate θ.

Then, at any fixed angular position, equation (1) may be integrated in r. With the application of the boundary conditions $\partial T/\partial r = 0$ and $T = T_o(\theta)$ at $r = r_o$ (the outer radius), the temperature distribution along the inner radius ($r = r_i$) is

$$T_i(\theta) = T_o(\theta) + (Sr_o^2/4k_w)\,(1 + 2\,\ell n(r_i/r_o) - r_i^2/r_o^2) - \tfrac{1}{2}\overline{(\partial^2 T/\partial\theta^2)}\,(\ell n(r_i/r_o))^2 \tag{2}$$

The use of equation (2) in the data reduction procedure will now be described. The outside wall temperatures $T_o(\theta)$ were available from measurements at discrete angular positions on the heated portion of the tube. If $\theta = 0$ deg corresponds to the circumferential mid-point of the heated arc, then the available values of T_o were at 0 deg, ±20 deg, ±40 deg, ±60 deg, and ±80 deg, for both $z/D = 20$ and 25 (z = streamwise coordinate).[2] Correspondingly, the inside wall temperatures were evaluated at these θ values. The $T_o(\theta)$ not only served as direct inputs to equation (2), but were also employed to compute $(\partial^2 T/\partial\theta^2)_o$ for use as first-round approximations to $\overline{(\partial^2 T/\partial\theta^2)}$ in an iterative procedure.

The volume heat generation rate was evaluated as the product $j^2\rho$, where j is the current density in the cross section of interest (z/D = 20 or 25), and ρ is the specific resistivity. Both of these quantities were determined from the measurements of current, voltage drop, and tube wall thickness as described in Appendix F of [11]. The radius ratio r_i/r_o that appears in equation (2) was written as $(r_o - t)/r_o$ and then evaluated using the local (θ-dependent) wall thickness.

A first approximation to the inside wall temperature variation $T_i(\theta)$ was obtained using $(\partial^2 T/\partial\theta^2)_o$ as input in lieu of $\overline{(\partial^2 T/\partial\theta^2)}$. With these $T_i(\theta)$, values of $(\partial^2 T/\partial\theta^2)_i$ were computed at $\theta = 0$ deg, ±20 deg, . . . , ±80 deg. At each angular position, $(\partial^2 T/\partial\theta^2)_i$ and $(\partial^2 T/\partial\theta^2)_o$ were averaged, and the average was introduced into equation (2) to enable a new value of $T_i(\theta)$ to be calculated. The new $T_i(\theta)$ was so close to the first-round values that the iterative process was not carried further.

With the inside wall temperatures thus determined, attention may be turned to the local heat flux q at discrete angular positions on the inside wall. Whereas equation (1) is integrated twice in r to get $T_i(\theta)$, it is integrated only once to get $q(\theta)$, with the result

$$q(\theta) = (r_m t/r_i)S + (k_w/r_i)\overline{(\partial^2 T/\partial\theta^2)}\ell n(r_o/r_i) \tag{3}$$

where $r_m = (r_i + r_o)/2$ is the mean radius.

A circumferential local heat transfer coefficient h and local Nusselt number Nu were then evaluated from

$$h = q/(T_i - T_{bz}),\ \mathrm{Nu} = hD/k \tag{4}$$

in which both q and T_i correspond to a specific angular position. T_{bz}, which represents the bulk temperature at the axial station of interest, was obtained by adding the bulk rise to the measured inlet temperature.

The circumferential average heat transfer coefficient and Nusselt number were defined as

$$\overline{h} = Q/A(\overline{T}_i - T_{bz}),\ \overline{\mathrm{Nu}} = \overline{h}D/k \tag{5}$$

where both Q and A are per unit axial length. Ideally, Q should be evaluated as the convective heat transfer to the fluid along the entire

[2] In addition, at $z/D = 20$, thermocouples were positioned at $\theta = \pm 88$ deg, but these thermocouples were surrounded by epoxy that overlay the tube surface to strengthen the bond between the two halves of the tube. Because of this, the temperatures sensed by these thermocouples were difficult to interpret, and they were not used in the data reduction

heated arc, i.e., -90 deg $\leq \theta \leq 90$ deg, with $\overline{T}_i$ being the circumferential average inner wall temperature over that same arc and $A = \pi r_i$. However, as mentioned earlier, the temperature measurements in the neighborhood of $\theta = \pm 90$ deg were of uncertain accuracy, and their use would have given rise to an uncertainty in both Q and $\overline{T}_i$. Therefore, to assure reliable results, Q, $\overline{T}_i$, and A were evaluated over the arc -80 deg $\leq \theta \leq 80$ deg and, correspondingly, the $\overline{\text{Nu}}$ values correspond to that arc.

In addition to the Nusselt number, the other dimensionless groups that are to be employed in the presentation of the results are the Reynolds, Prandtl, and Rayleigh numbers

$$\text{Re} = 2\dot{m}/\mu\pi r_i, \quad \text{Pr} = c_p\mu/k, \quad \text{Ra} = (g\beta\bar{q}r_i^4/k\nu^2)\text{Pr} \qquad (6)$$

In these groups, as well as in the Nusselt number, all fluid properties are evaluated at the bulk temperature T_{bz}. It may be noted that in the Rayleigh number, the grouping contained in the parentheses is the so-called modified Grashof number which involves the surface heat flux. The quantity $\bar{q}$ is an average heat flux defined as $(\pi r_m t S)/(\pi r_i)$, where the numerator is the heat input to the fluid at a given axial station and the denominator is the surface area of the heated arc, both per unit axial length. The use of a Rayleigh number based on heat flux is motivated by the fact that the heat flux is nearly uniform on the heated arc.

Results and Discussion

Circumferential average results; buoyancy effects. The presentation that follows will deal successively with the circumferential average results and the circumferential local results. With regard to the average results, the first task is to identify the operating conditions at which significant buoyancy effects were encountered. In this connection, there is persuasive evidence that none of the top-heated runs were affected by buoyancy. This evidence has two facets. First, for those conditions where the likelihood of buoyancy is greatest (i.e., the lowest Prandtl number and the lowest Reynolds numbers), runs at different Rayleigh numbers did not show any variation in $\overline{\text{Nu}}$ beyond typical data scatter [11]. Second, as will soon be demonstrated, the $\overline{\text{Nu}}$ values for the low Reynolds number runs fall directly on $\overline{\text{Nu}}$, Re curves that are logical extensions of results at higher Reynolds numbers.

In contrast to the foregoing, there are operating conditions where the bottom-heated runs were affected by buoyancy. This is demonstrated in Fig. 1. In this figure, the ratio of the Nusselt numbers for top and bottom heating ($\overline{\text{Nu}}_t$ and $\overline{\text{Nu}}_b$) at the same Reynolds and Prandtl numbers is plotted as a function of the Rayleigh number. Inasmuch as the Nusselt numbers at $z/D = 20$ and 25 typically agreed to within one percent, they were averaged and then plotted in the figure. The Reynolds number is the curve parameter. The Prandtl number is not shown explicitly because mixed convection is believed to depend on Re and Ra, but not Pr. Since $\overline{\text{Nu}}_t$ is not affected by buoyancy, the figure shows that $\overline{\text{Nu}}_b$ is buoyancy affected at low Reynolds numbers, with the effect being enhanced with increasing Rayleigh number.

A Reynolds-Rayleigh criterion for the onset of buoyancy effects for bottom heating was deduced from Fig. 1 and from a crossplot thereof [11]. The criterion was based on $\overline{\text{Nu}}_b/\overline{\text{Nu}}_t = 1.05$. Fig. 2 contains a Re, Ra diagram which is subdivided into mixed convection and forced convection portions. As is physically reasonable, the threshold Rayleigh number for the onset of buoyancy effects increases with the Reynolds number.

Attempts to compare the results of Fig. 2 with literature information for circumferentially uniform thermal conditions did not prove fruitful. Neither [8] nor [9] provide mixed convection threshold criteria which overlap the Re, Ra range of the present experiments and are based on circumferential average heat transfer results. The threshold criteria of [10] are based on ten percent deviations (rather than five percent) and are reported in terms of a Rayleigh number which involves the wall-to-bulk temperature difference (rather than the wall heat flux).

Attention may now be turned to the buoyancy-unaffected circumferential average Nusselt number results, which are plotted as

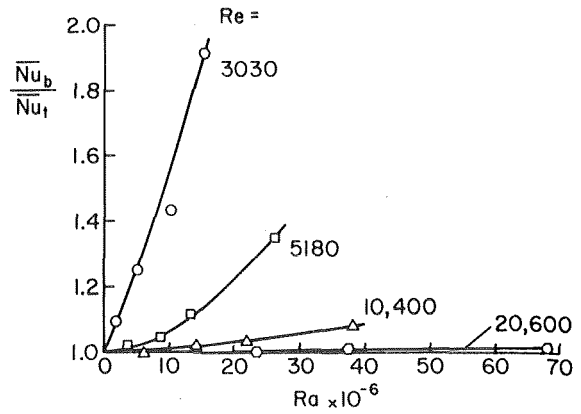

Fig. 1 Ratio of circumferential average Nusselt numbers for bottom and top heating at low Reynolds numbers

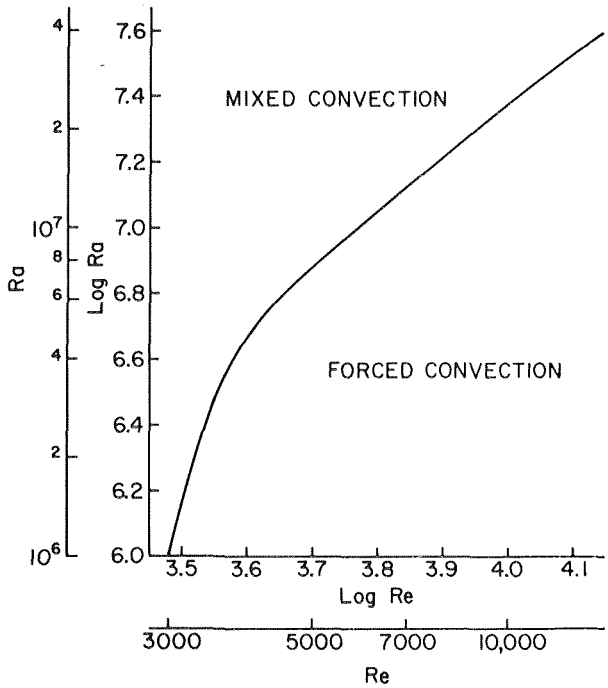

Fig. 2 Criterion for the onset of buoyancy effects for bottom heating based on five percent change in $\overline{\text{Nu}}$

a function of the Reynolds number in the upper part of Fig. 3 with the Prandtl number as curve parameter. Separate data points are shown for top and bottom heating, although the differences are very small. The plotted points represent the data at both $z/D = 20$ and 25, which were typically within one percent of each other.

The Nusselt numbers are seen to increase smoothly with the Reynolds number over the entire range, but do not fall along a straight line. This is consistent with the newer correlations for turbulent pipe flows (e.g., [12]), which no longer force a power-law relation between the Nusselt and Reynolds numbers. The Nu, Re curves for all Prandtl numbers have the same shape, which permits them to be brought together as shown in the lower part of Fig. 3 in terms of the grouping $\overline{\text{Nu}}/\text{Pr}^{0.47}$.

The circumferential average Nusselt numbers will now be compared with literature information. These comparisons will include the recent correlations of [12] and [13] as well as the venerable Dittus-Boelter (DB) equation, all of which pertain to circumferentially uniform thermal boundary conditions. Also, the prediction procedure of [7]

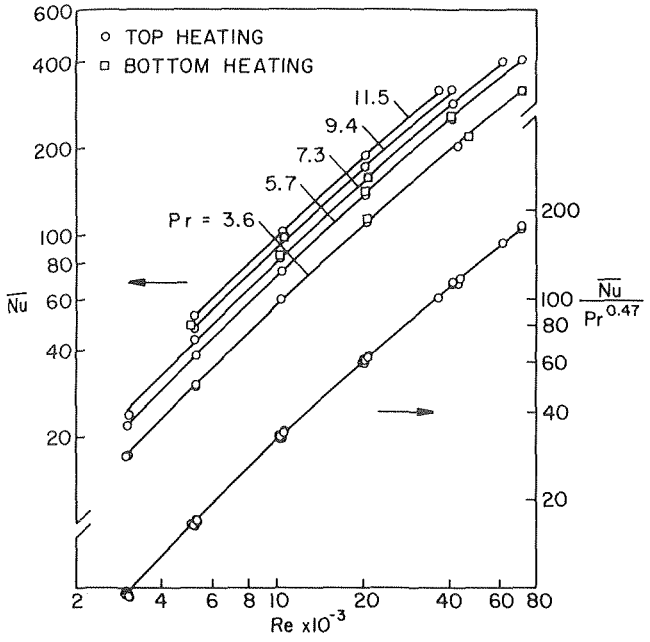

Fig. 3 Circumferential average Nusselt numbers for buoyancy-unaffected turbulent flow

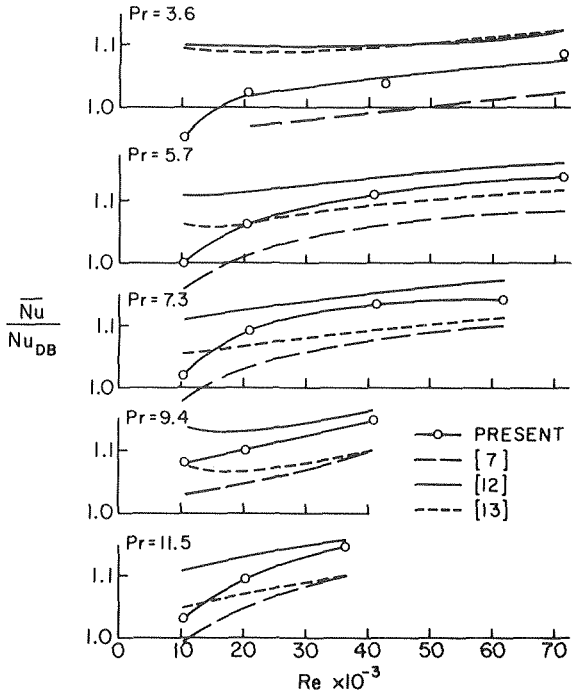

Fig. 4 Comparison of present $\overline{Nu}$ results with literature information

for circumferentially nonuniform boundary conditions was employed by the present authors to compute $\overline{Nu}$ for the range of θ between $-80°$ and 80°, which is the same range for which the experimental $\overline{Nu}$ values were evaluated.

The comparisons are shown in Fig. 4. To mute the variation of the results with Reynolds number and to achieve ordinate values on the order of one, the Nusselt numbers have been normalized by those computed from the Dittus-Boelter equation. Since the literature information is not intended to be applied for Re below 10,000, the curves have been terminated at that point.

From an overall appraisal of the figure, it is seen that none of the predictions from the literature, including those based on circumferentially uniform conditions, are very far from the present data. This is still another affirmation of the forgiving nature of turbulent flow. The general level of agreement is on the order of ten percent. The predictions of [7], which take account of circumferential nonuniformities, lie parallel to the present data and are displaced below them by about five percent. It is also interesting to note the general consensus in evidence in the figure that the Dittus-Boelter equation gives Nusselt numbers that are too low at the higher Reynolds number.

Circumferential local results. The results that will now be presented include circumferential distributions of the local Nusselt number, temperature, and heat flux on the heated arc and the distribution of temperature on the adiabatic wall. A comparison of these quantities with those computed using the prediction procedure of [7] will also be presented. Owing to space limitations, only representative results will be given here, but a complete presentation is available in [11].

Local Nusselt number results for both top heating and bottom heating are plotted in Fig. 5 as a function of angular position between $-80°$ and 80°. For top heating, $\theta = 0°$ corresponds to the topmost position on the circumference, whereas for bottom heating $\theta = 0°$ is the bottom-most position. The figure is subdivided into three parts, respectively, for Pr = 3.6, 5.7, and 9.4. Each part contains a stack of graphs corresponding to successively increasing values of Reynolds number. Data points are shown only in a few graphs for illustration, but are otherwise omitted to preserve clarity.

Attention will be focused on the results for Pr = 3.6, which portray a sequence of events that is also in evidence for the other Prandtl numbers, but to a lesser extent. At the lowest Reynolds number, the bottom-heated Nusselt number distribution is nearly uniform owing to the circumferential transport provided by the buoyancy-induced secondary flow. On the other hand, the distribution for top heating

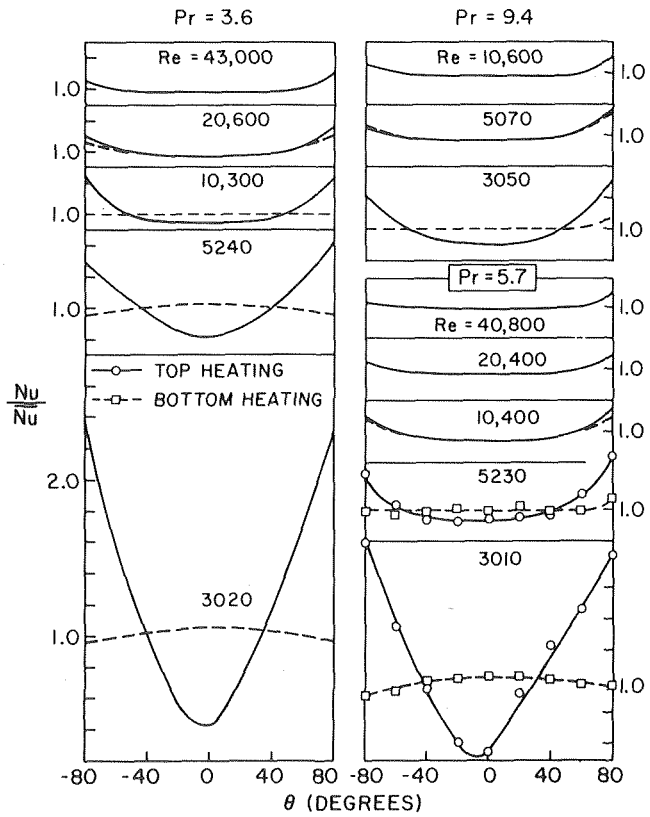

Fig. 5 Circumferential distributions of the local Nusselt number

is distinctly nonuniform[3] inasmuch as buoyancy is absent and the circumferential turbulent transport is weak. As the Reynolds number increases, the buoyancy is rendered ineffectual and the circumferential turbulent transport grows stronger. These factors cause the top-heating and bottom-heating results to come together and merge.

Representative distributions of inside wall temperature and heat flux on the heated arc are presented in Fig. 6, respectively for Pr = 3.6 (left-hand portion) and Pr = 9.4 (right-hand portion). For each Prandtl number, results are shown for Re ~5,000 and 40,000. The wall temperature and heat flux distributions are respectively expressed as $(T_i - T_{bz})/(\overline{T}_i - T_{bz})$ and $q/\overline{q}$, where both T_i and q are functions of θ, and $\overline{T}_i$ and $\overline{q}$ are averages over -80 deg $\leq \theta \leq 80$ deg. The data for top heating are portrayed by circles, whereas those for bottom heating are portrayed by squares. The actual data points are plotted for all cases in preference to showing faired curves since, in many cases, the faired curve would be a horizontal line at an ordinate of 1.0.

Inspection of Fig. 6 shows that the heat flux is very nearly circumferentially uniform for all of the cases. On the other hand, the wall temperatures exhibit various degrees of nonuniformity. At Pr = 3.6 and Re ~ 5,000, the top-heated (buoyancy-unaffected) distribution is distinctly nonuniform, whereas the bottom-heated (buoyancy-affected) distribution is uniform. With increasing Reynolds number, the distinction between top and bottom heating disappears, and the shape of the distribution for Re ~ 40,000 is typical of that for all of the buoyancy-unaffected, fully turbulent cases.

For Pr = 9.4 and Re ~ 5,000, the distributions for top heating and bottom heating are coincident, thereby reflecting the absence of buoyancy effects. At Re ~ 40,000, the temperature distribution possesses the aforementioned universal shape.

Circumferential distributions of the temperature on the unheated wall are plotted in Fig. 7 for the same cases and with the same format as was used in Fig. 5 for the Nusselt numbers on the heated arc. The angular coordinate $\theta = \pm 180$ deg marks the circumferential mid-point of the unheated wall and is also the mid-point of the abscissa of Fig. 7. The ordinate compares the wall-to-bulk temperature difference at a point on the unheated wall with the average wall-to-bulk temperature difference on the heated arc. A negative value of the ordinate indicates that the local wall temperature is lower than the bulk temperature, and vice-versa. As before, the results for Pr = 3.6 are the most demonstrative and are, therefore, singled out for discussion.

If attention is turned to the lowest Reynolds number (~3,000), it is seen that for top heating (solid line) the adiabatic wall temperature is lower than the bulk, whereas the opposite relation is in evidence for bottom heating (dashed line). This is another clear affirmation of the presence of buoyancy for the bottom heating case and of its absence for top heating. The buoyancy, when present, gives rise to a secondary flow which carries hot fluid into the upper portion of the tube. The shape of the dashed curve suggests a secondary flow pattern whereby hot fluid moves upward along the walls of the two vertical halves of the tube and descends along the vertical diameter. As the Reynolds number increases, the buoyancy-induced secondary flow diminishes. The distribution curves for top and bottom heating draw together and are characterized by adiabatic wall temperatures that are lower than the bulk.

As a final matter, attention will be turned to the application of the procedure of [7] for predicting the circumferential variations in the absence of buoyancy. To use that method, the inside wall temperature distributions (over the entire 360 deg arc) were fit with a Fourier series. The Fourier coefficients were then employed, along with tabulated influence coefficients, to compute $q/\overline{q}$ and $\mathrm{Nu}/\overline{\mathrm{Nu}}$. One limitation of the method is that only six influence coefficients are available in [7] for each Re and Pr, thereby requiring that the Fourier series be truncated after six terms. This truncation introduces a degree of waviness in the results.

A representative comparison, taken from [11], between the predictions of [7] (solid lines) and the present data for both top and bottom heating is presented in Fig. 8. Aside from the waviness, generally good agreement is seen to prevail.

Concluding Remarks

The experiments described in this paper have encompassed both buoyancy-affected and buoyancy-unaffected turbulent flow in a

[3] Note that from their definitions, $\overline{\mathrm{Nu}}$ is not the circumferential average of Nu.

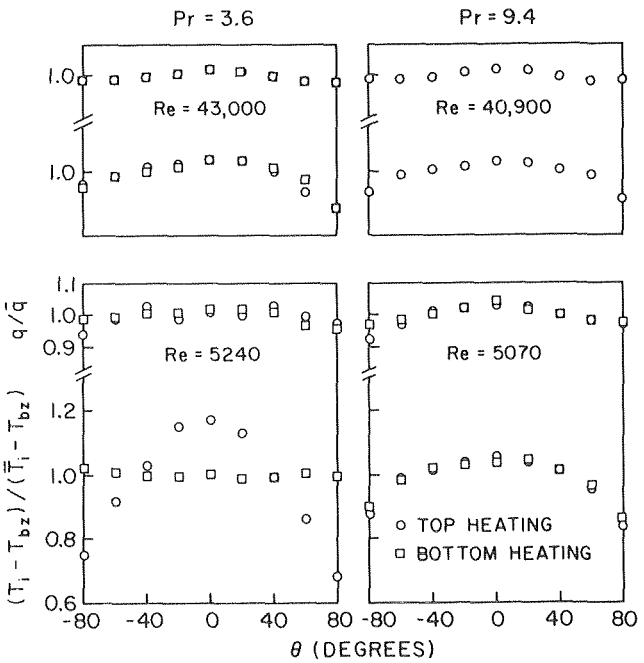

Fig. 6 Representative circumferential distributions of inside wall temperature and heat flux on the heated arc

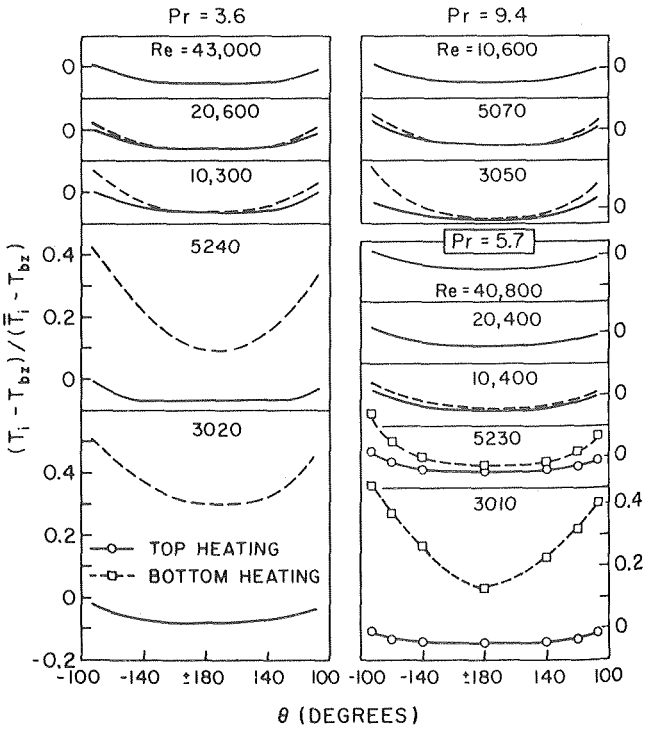

Fig. 7 Circumferential distributions of the temperature on the unheated wall

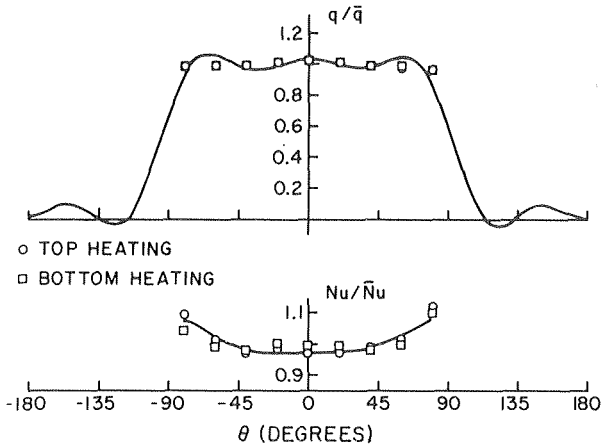

Fig. 8 Representative comparison of the present data for $q/\bar{q}$ and $Nu/\overline{Nu}$ with predictions based on the method of [7], Re = 20,600, Pr = 3.6

horizontal tube which is nonuniformly heated around its circumference. By employing a specially fabricated tube, it was possible to heat the fluid uniformly over a 180 deg circumferential arc, while the other half of the circumference was unheated. Experiments were carried out both with the heated portion at the top and at the bottom. Water was the working fluid, and its Prandtl number was varied from 3.5 to 11.5 by controlling the temperature level. Results were obtained for the thermally developed regime.

There was an array of evidence showing that significant buoyancy effects were present for bottom heating at the lower Reynolds numbers and higher Rayleigh numbers (i.e., lower Prandtl numbers in the present experiments). This evidence included augmented values of the circumferential average Nusselt number, uniform local Nusselt numbers and temperatures on the heated arc, and relatively high temperatures on the adiabatic wall. On the other hand, the top-heated experiments were not affected by buoyancy. A Reynolds number-Rayleigh number criterion for the threshold of significant buoyancy effects for bottom heating was deduced from the experimental results.

The buoyancy-unaffected circumferential average Nusselt numbers increased smoothly with the Reynolds number over the entire range from 3,000 to 70,000. The Prandtl number dependence was correlated as $Pr^{0.47}$. The present results for circumferentially nonuniform heating are within ten percent of the Nusselt numbers predicted by current literature correlations for circumferentially uniform thermal conditions. The prediction procedure of [7] for nonuniform heating yielded Nusselt-Reynolds curves that parallel the experimental data, with a deviation of about five percent.

Circumferential distributions of the Nusselt number, wall temperature, and wall heat flux on the heated arc were presented. Substantial circumferential variations of the Nusselt number and the wall temperature are in evidence for low Reynolds number, buoyancy-unaffected turbulent flow, whereas buoyancy-affected flows exhibited circumferential uniformity. Relatively uniform distributions also occur for buoyancy-unaffected fully turbulent flow (i.e., at higher Reynolds numbers).

The temperatures on the unheated wall are generally lower than the bulk temperature in the absence of buoyancy, whereas the opposite relationship applies when buoyancy is present.

Acknowledgment

Scholarship support accorded to Roger R. Schmidt by the Northern Natural Gas Company is gratefully acknowledged.

References

1 Black, A. W., and Sparrow, E. M., "Experiments on Turbulent Heat Transfer in a Tube with Circumferentially Varying Thermal Boundary Conditions," ASME JOURNAL OF HEAT TRANSFER, Vol. 89, 1967, pp. 258–268.

2 Quarmby, A., and Quirk, R., "Measurements of the Radial and Tangential Eddy Diffusivities of Heat and Mass in Turbulent Flow in a Plain Tube," *International Journal of Heat and Mass Transfer*, Vol. 15, 1972, pp 2309–2327.

3 Chan, A. L., Baughn, J. W., and Hoffman, M. A., "Nonuniform Circumferential Heat Flux Experiments in a Circular Tube," ASME Paper No. 75-WA/HT-52, presented at Winter Annual Meeting, Houston, 1975.

4 Reynolds, W. C., "Turbulent Heat Transfer in a Circular Tube with Variable Circumferential Heat Flux," *International Journal of Heat and Mass Transfer*, Vol. 6, 1963, pp. 445–454.

5 Sparrow, E. M., and Lin, S. H., "Turbulent Heat Transfer in a Tube with Circumferentially Varying Temperature or Heat Flux," *International Journal of Heat and Mass Transfer*, Vol. 6, 1963, pp. 866–867.

6 Rapier, A. C., "Forced Convection Heat Transfer in a Circular Tube with Non-Uniform Heat Flux Around the Circumference," *International Journal of Heat and Mass Transfer*, Vol. 15, 1972, pp. 527–538.

7 Gärtner, D., Johannsen, K., and Ramm, H., "Turbulent Heat Transfer in a Circular Tube with Circumferentially Varying Thermal Boundary Conditions," *International Journal of Heat and Mass Transfer*, Vol. 17, 1974, pp. 1003–1018.

8 Petukhov, B. S., and Polyakov, A. F., "Flow and Heat Transfer in Horizontal Tubes under Combined Effect of Forced and Free Convection," Heat Transfer, 1970, *Proceedings of the Fourth International Heat Transfer Conference*, Versailles, France, Vol. 4, Paper No. NC 3.7, 1970.

9 Nagendra, H. R., "Interaction of Free and Forced Convection in Horizontal Tubes in the Transition Regime," *Journal of Fluid Mechanics*, Vol. 57, 1973, pp. 269–288.

10 Metais, B., and Eckert, E. R. G., "Forced, Mixed and Free Convection Regimes," ASME JOURNAL OF HEAT TRANSFER, Vol. 86, 1964, pp. 295–296.

11 Schmidt, R. R., "Experiments on Buoyancy-Affected and Buoyancy-Unaffected Turbulent Heat Transfer for Water in a Tube with Circumferentially Nonuniform Heating," Ph.D. Thesis, Department of Mechanical Engineering, University of Minnesota, Minneapolis, Minnesota, 1977.

12 Petukhov, B. S., "Heat Transfer and Friction in Turbulent Pipe Flow with Variable Physical Properties," *Advances in Heat Transfer*, Vol. 6, Academic Press, 1972, pp. 503–564.

13 Sleicher, C. A., and Rouse, M. W., "A Convenient Correlation for Heat Transfer to Constant and Variable Property Fluids in Turbulent Pipe Flow," *International Journal of Heat and Mass Transfer*, Vol. 18, 1975, pp. 677–683.

S. M. ElSherbiny
Research Assistant.

K. G. T. Hollands
Professor.

G. D. Raithby
Professor.

Department of Mechanical Engineering,
University of Waterloo,
Waterloo, Ontario, Canada N2L 3G1
Assoc. Membs. ASME

Free Convection across Inclined Air Layers with One Surface V-Corrugated

Experimental measurements are presented for free convective heat transfer across inclined air layers, heated from below, and bounded by one V-corrugated plate and one flat plate. The measurements covered three values for the ratio, A, (average plate spacing to V-height), namely, A = 1, 2.5 and 4. It also covered angles of inclination with respect to the horizontal, θ, of 0, 30, 45 and 60 deg, and a range in Rayleigh number of 10 < Ra < 4 × 10⁶. The study proves, both theoretically and experimentally, that the free convective heat transfer is essentially the same, regardless of whether the V-corrugated plate is above or below. It was found that for the same average plate spacing, L, the convective heat losses across air layers bounded by one V-corrugated and one flat plate are greater than those for two parallel flat plates by up to 50 percent for the range studied. Experimental results are given as plots of Nusselt number versus Rayleigh number. A correlation equation is given for Nusselt number, Nu, as a function of A, θ and Ra.

1 Introduction

The heat transfer processes occurring in the conventional flat plate solar collector are of particular importance to solar engineers. Not the least important of these processes is the free convective heat transfer from the absorber plate to the adjacent flat glass cover. Ordinarily the absorber plate is made flat; however, a number of studies have pointed out the advantageous effects of V-corrugating the absorber plate, especially in air heaters [1–3]. Although a considerable number of studies [4–18] have investigated free convection across air layers bounded by two flat plates, there is a lack of information in the case where one of the plates is V-corrugated. In the only previous study, Chinnappa [19] reported measurements for the horizontal case only, and for a rather narrow range in Rayleigh number (7×10^3 to 7×10^5).

In the present study, the free convective heat transfer across an air layer bounded by a V-corrugated plate and a flat plate was measured (see Fig. 1). The opening angle of the V-corrugations was 60 deg. Three aspect ratios, A, equal to the ratio of the mean plate spacing (L) to the height of the V's (H), were covered; these were: $A = 1$, 2.5 and 4. Measurements were taken at four angles of tilt with respect to the horizontal: $\theta = 0$, 30, 45 and 60 deg. The ratio of W/L was kept at values equal to 12 or greater. For these values it is assumed that the heat transfer in the central region of the plates is independent of W/L; the heat transfer was measured in this region. Measurements were performed over a wide range of Rayleigh number, $10 < \mathrm{Ra} < 4 \times 10^6$, where Ra is based on the mean plate spacing, L. The experiments covered the two possible configurations shown in Fig. 1. In the first, Fig. 1(a), the lower plate is V-corrugated and heated, and the upper is flat and cooled (this situation corresponds to that in a solar collector having a V-corrugated absorber plate). In the second, Fig. 1(b), the upper plate is V-corrugated and cooled and the lower plate is flat and heated. In fact, as will be discussed later, the free convective heat transfer is essentially the same for both configurations.

Previous studies of free convection in plane air layers are highly relevant to the present work and hence the results of these are briefly discussed here. For the case of the *horizontal* air layer heated from below, the layer remains stagnant, and therefore heat transfer is by conduction alone, until the Rayleigh number exceeds a critical value, $\mathrm{Ra}_c = 1708$. The cellular fluid motion accompanying this instability results in an abrupt rise in the Nusselt number with increasing Rayleigh number. A further increase in Ra produces more complex flows. For $\mathrm{Ra} > 10^6$, the flow is often considered to be fully turbulent. Measurements of the temperature profile at high Ra [15–17] show that conductive layers develop close to the surface and the resistance to heat transfer appears to be localized in these layers; away from these, the mean local temperature was approximately constant. For the case of *inclined* air layers bounded by plane surfaces, and for low Ra, a unicellular base flow circulates up the heated surface and down the cooled one, for any finite value of Ra. Except at the ends of the layer, the base flow does not contribute to the heat transfer, and the local

Contributed by the Heat Transfer Division for publication in the JOURNAL OF HEAT TRANSFER. Manuscript received by the Heat Transfer Division September 14, 1977.

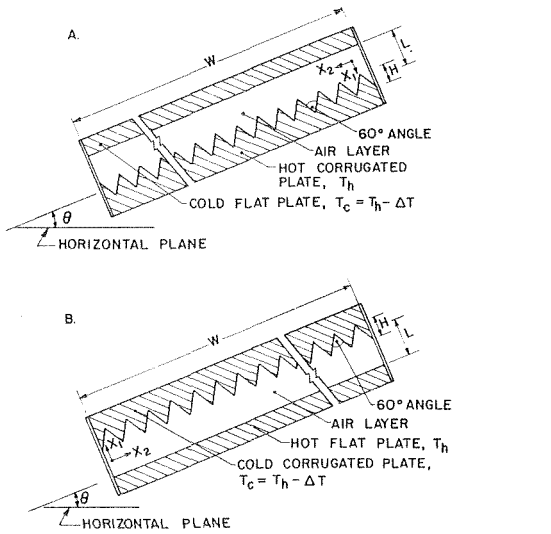

Fig. 1 Schematic of inclined air layers bounded by one V-corrugated plate and one flat plate. The Nusselt number for both configurations is the same (for practical purposes) for the same value of A and Ra for a given fluid

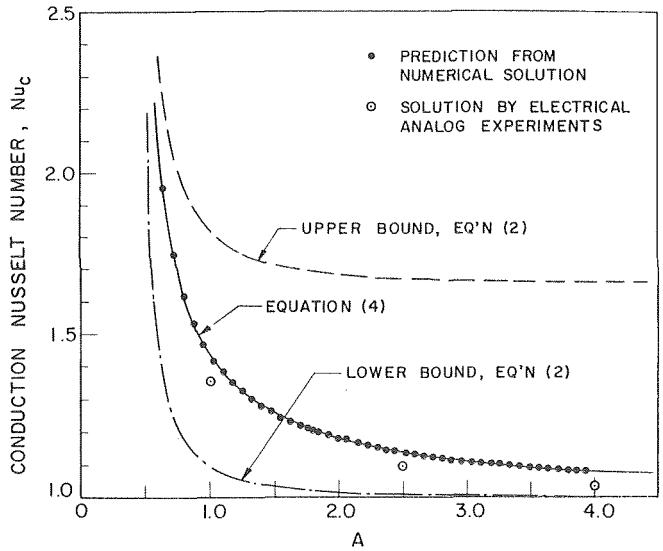

Fig. 2 Conduction Nusselt number for the V-corrugated problem

Nusselt number in the central region is unity for Rayleigh numbers less than a critical value Ra_c. For $\theta \leq 60$ deg, the critical value is $Ra_c = 1708/\cos\theta$ [10, 18]. The immediate post-critical flow consists of steady longitudinal rolls with their axes along the up-slope [18]. For very high Ra, the flow is expected to take up the boundary layer structure. Reference [9] gives a recommended correlation equation for $Nu = Nu(Ra, \theta)$ for $0 \leq \theta \leq 60$ deg.

2 Theoretical Considerations

Reciprocity. If the heat transfer across the fluid layer in Fig. 1(a) is identical to that in Fig. 1(b) for the same aspect ratio, angle of tilt and Rayleigh number, then by our present definition, "reciprocity" holds. Starting from the fundamental equations of motion, the Appendix shows that reciprocity does hold provided terms in the energy equation associated with the Eckert number (viscous heating and DP_d/Dt) are negligible. In the present experiments, and in solar collectors, these terms are of order 10^{-7} relative to retained terms, so that reciprocity holds to a high level of approximation. Reciprocity was also demonstrated experimentally where virtually the same results were obtained for both orientations. These results will be discussed later.

The same analyses showed that, for a given fluid, the Nusselt number is primarily a function of the following dimensionless groups:

$$Nu = Nu(Ra, A, \theta) \tag{1}$$

Conduction Solution. At very small Rayleigh number, the heat transfer across the air layer is purely by conduction (aside from the radiation), and the corresponding Nusselt number is denoted by Nu_c. Due to the corrugations, Nu_c is not unity in the present problem, as is the case for two flat plates. Since a closed form solution does not seem possible, it is helpful to establish upper and lower bounds on Nu_c using the method of Elrod [21]. For this problem (see [20] for details) two bounds are:

$$A \ln\left(\frac{2A+1}{2A-1}\right) \leq Nu_c \leq \frac{3\sqrt{3}}{\pi} A \ln\left(\frac{2A+1}{2A-1}\right) \tag{2}$$

These are plotted in Fig. 2. It will be seen that the form of the equation for both bounds is the same, suggesting that the exact values of Nu_c could be correlated by an equation of the form:

$$Nu_c = f(A) \cdot A \ln\left(\frac{2A+1}{2A-1}\right) \tag{3}$$

where $f(A)$ is a bounded function of the aspect ratio. The following equation of this form closely fits the result obtained in a recent numerical study of this problem [26]:

$$Nu_c = \left(\frac{1}{1 - 0.3025/A + 0.06825/A^2}\right) \cdot A \ln\left(\frac{2A+1}{2A-1}\right) \tag{4}$$

This equation is also plotted in Fig. 2.

Nomenclature

A = aspect ratio = L/H
B = correlation function of θ given by equation (9)
C_p = specific heat at constant pressure of air
Ec = Eckert number = $k^2/\rho^2 C_p{}^3 L^2 \Delta T$
g = gravitational acceleration; g_k is component of g in x_k direction
H = the height of the V's (Fig. 1)
h = coefficient of heat transfer across the air layer by convection and conduction, based on the *flat* plate area
k = thermal conductivity of air
K = correlation function of A given by equation (8)
L = mean plate spacing (Fig. 1)
Nu = Nusselt number in central region of plates = hL/k
Nu_c = Nusselt number applying when the air is effectively stagnant, and consequently due only to conduction
P_d = pressure departure from hydrostatic pressure
Pr = Prandtl number, $C_p\mu/k$
Ra = Rayleigh number = $L^3\rho^2\beta g C_p(T_h - T_c)/\mu k$
Ra_c = critical Rayleigh number, or Rayleigh number below which air is effectively stagnant
Ra_t = correlation function of θ given by equation (10)
t = time
T = temperature of air
T_c = temperature of cold plate
T_h = temperature of hot plate
$\Delta T = T_h - T_c$
u_1, u_2, u_3 = velocity components in directions x_1, x_2, x_3
W = the width of the air layer (Fig. 1)
x_1, x_2, x_3 = spatial coordinates (see Fig. 1)
α = thermal diffusivity of air
β = coefficient of thermal expansion of air
θ = angle of inclination of air layer measured from horizontal (Fig. 1)
$\Theta = (T_h - T)/\Delta T$ for Fig. 1(a) orientation; $(T - T_c)/\Delta T$ for Fig. 1(b) orientation
μ = dynamic viscosity of air
ν = kinematic viscosity of air
ρ = density of air
Φ = dimensionless dissipation function, see [25] for full expression

An electric analog experiment using Teledeltos paper was undertaken to measure the conduction Nusselt number (see [22] for description of method) as an additional check on the numerical results. These were carried out at the three aspect ratios at which convective heat transfer was to be measured. These measurements fell consistently lower than the predicted values but differences were less than or equal to about five percent. The anisotropic conductivity of the Teledeltos paper could have caused most of this discrepancy.

Turbulent Boundary Layer Limit. At very high Rayleigh numbers, the flow is considered to be fully turbulent and the thermal resistance lies totally in the conduction layers developed close to each surface [15–17]. A method for obtaining an approximate asymptotic relation between Nu and Ra at high Ra from an expression for the turbulent conduction layer thickness is given in [23]. Applying this to each of the two boundary layers, and equating the free convective heat transfer for each surface, gives the following asymptotic relation in the turbulent regime for $\theta = 0$ deg:

$$\mathrm{Nu} = \left(\frac{\mathrm{Ra}}{3377}\right)^{1/3} \qquad \mathrm{Ra} \to \infty, \quad \theta = 0 \text{ deg} \tag{5}$$

Full details of this derivation are given in [20].

3 Description of Experiment

The University of Waterloo Natural Convection Apparatus was used in this experiment. It has been fully described in [9, 10, 24]. For the present problem, the upper plate was replaced with a corrugated copper plate which was constructed by folding a 0.813 mm (0.032 in.) thick copper sheet into a V-corrugated shape. The opening angle of the V's was 60 deg and the height (H) was 12.7 mm (0.5 in.). The corrugated plate was maintained at a constant uniform temperature of ~27°C (~80°F) by passing water through many copper tubes, that were soldered to the back of the corrugated plate. The lower flat plate was heated to a constant temperature of 35°C (95°F). To reach the upper limit in Rayleigh number, a second V-corrugated plate with large corrugations was also used, having a sheet thickness of 1.626 mm (0.064 in.), and the height (H) was 31.75 mm (1.25 in.). Full details of the experimental procedure and data processing are given in [9, 10, 20].

In order to calculate the Nusselt number, the radiative component of the measured heat transfer must be subtracted away. For a temperature difference between the plates that closely matched those in the experiments (the value of Ra was changed experimentally by altering the pressure holding ΔT fixed), a radiative heat transfer coefficient was determined by measuring the total heat transfer across the layer at pressures which were sufficiently low (<0.07 atm) to insure effectively no convective heat transfer, but sufficiently high to avoid rarified effects on the thermal conductivity. The radiative heat transfer coefficient was calculated by subtracting the conductive heat transfer (calculated from equation (4)) away from the total measured value and dividing by the temperature difference between the plates. At higher Ra values where heat transfer by convection plus conduction was desired, the total heat transfer was measured and the radiative component subtracted away using the same radiative heat transfer coefficient. The absolute uncertainty in the Nusselt number introduced by this method of radiative correction can be shown to be equal to the absolute uncertainty in estimating Nu_c; this error is not expected to exceed .05 and is most probably considerably less.

The thermal properties of air were calculated at the arithmetic mean of the plate temperatures. An error analysis indicated that the maximum error in measuring Rayleigh number was 5.6 percent, and in Nusselt number, four percent.

In order to investigate the effect of the various parameters on the free convective heat transfer, a wide range in these parameters was used ($A = 1$, 2.5 and 4; for θ, $\theta = 0$, 30, 45 and 60 deg; and for Ra, $10 < \mathrm{Ra} < 4 \times 10^6$). The plate with small corrugations, $H = 12.7$ mm (0.5 in.), was used for all aspect ratios. For $A = 1$, the mean plate spacing (L) was too small to obtain the upper limit of Ra, so the plate with large corrugations, $H = 31.75$ mm (1.25 in.), was used as well, allowing the upper limit of Rayleigh number ($\mathrm{Ra} \approx 4 \times 10^6$) to be obtained.

Most experimental runs were made with the configuration shown in Fig. 1(b), using the guarded heater plate imbedded in the flat lower plate to measure the heat flux. Some measurements were also made on the situation shown in Fig. 1(a), in which case the plate containing the guarded heater plate was used as the upper plate. In this situation, cooling rather than heating would have to be applied to the heater plate to keep it at the same temperature as the rest of the upper plate. Since such cooling was not possible, the heater plate could deviate from the upper plate by up to 1.5°F (or ten percent of the total temperature difference) for these runs, depending on the Nusselt number. Since the deviation represents an experimental uncertainty, experiments using the situation shown in Fig. 1(b) were preferred.

4 Experimental Results

Fig. 3 shows the experimental results for both cases, A and B (Fig. 1), for aspect ratio $A = 4$ and $\theta = 45$ deg. Nearly identical results were obtained for both cases for the same Rayleigh number. This plot gives an experimental proof that reciprocity is valid within experimental uncertainty. The above experiment was repeated with $\theta = 0$ deg. In this case, some significant differences were observed (≈15 percent) between cases A and B, but these were shown to be due to the nonisothermality of the upper plate in Case A. Details are given in [20]. All further experiments were performed using the configuration shown in Fig. 1(b).

The experimental measurements of Nusselt number, Nu, and Rayleigh number, Ra, are plotted in Figs. 4, 5 and 6, for aspect ratios, A, of 1, 2.5 and 4, respectively. The plots are given in the form of Nu versus Ra cos θ.

For $A = 1$, the data points from the V-corrugated plate with small corrugations agreed with those from the second plate with larger corrugations. This substantiates that the Nusselt number is only dependent on the aspect ratio, A (and not separately on H), as was indicated by the dimensional analysis. For $\theta = 0$, the Nusselt number was constant and equal to Nu_c, indicating absence of convection up to a critical Rayleigh number, Ra_c, after which convection started and a sudden increase in Nu was observed with the increase in Ra. The concept of a critical Rayleigh number governing the start of convection motion, one that has been developed in many studies for plane air layers, therefore appears equally relevant for V-corrugated air-layers. For $\theta > 0$ and $A = 1$, the absence of the distinct break in the Nu-Ra curve suggests that a cellular base flow exists within the trough of each V-groove that contributes significantly to the heat transfer through the Ra-range in which the abrupt increase in Nu would be otherwise expected. At the larger aspect ratios, this effect appears to be lost, presumably because base flow circulation cells in the troughs have either vanished or are sufficiently weak to be unable to contribute to the heat transfer across the larger gap between the plates.

A dashed line representing the correlation equation given by Hollands, et al [9] for *plane* air layers, and using the *average* plate spacing, is plotted on each figure for comparison with the present problem. It is seen from the figures that the conduction Nusselt number is higher by 43, 14 and 8 percent for $A = 1$, 2.5 and 4, respectively. The Rayleigh number at which convection starts ($\theta = 0$ deg) or begins to play a significant role (for $\theta > 0$ deg) is slightly higher for the V-corrugated case, indicating some suppression of convection by the V's.

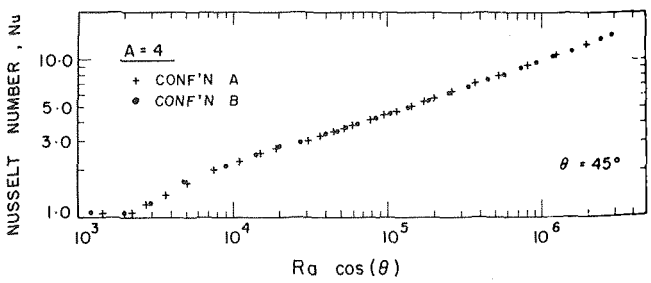

Fig. 3 Measured Nusselt numbers for both configurations in Fig. 1, proving that reciprocity holds

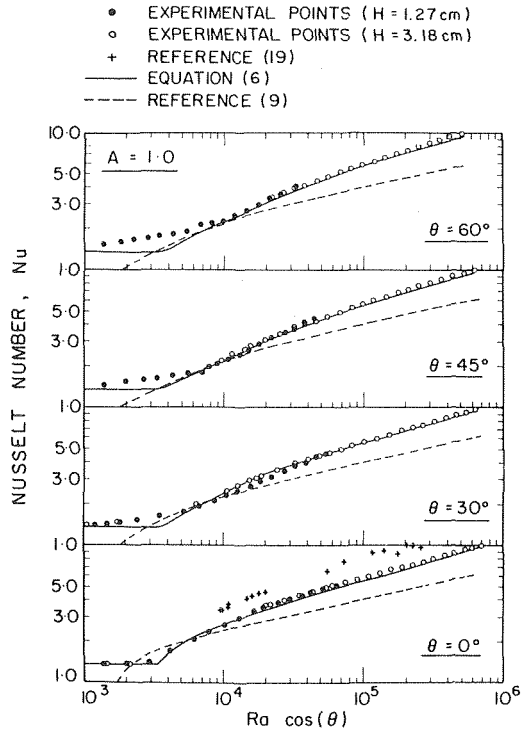

Fig. 4 Measurements of Nu as a function of Ra cos θ for $A = 1$

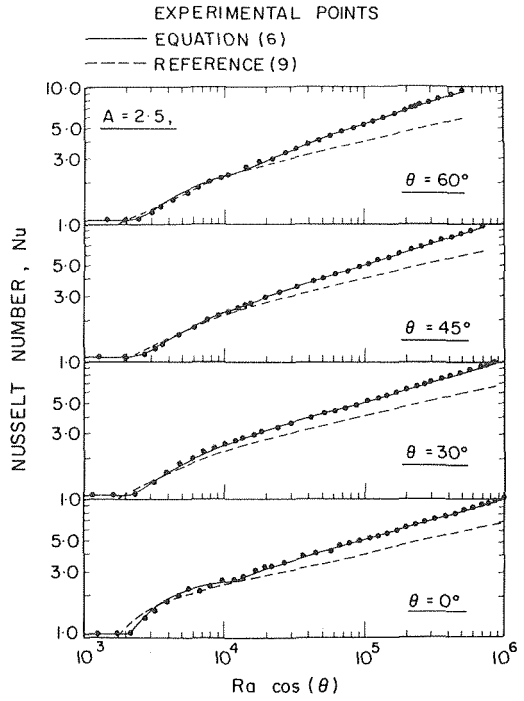

Fig. 5 Measurements of Nu as a function of Ra cos θ for $A = 2.5$

There is reasonable agreement between the plane and V-corrugated air layers for $3 \times 10^3 < \text{Ra} < 3 \times 10^4$ for $A = 2.5$ and 4, and in a very narrow band about 8×10^3 for $A = 1$. At still higher Ra, the data fall progressively higher than the corresponding flat plate data. It is speculated that this is caused by cold jets of air departing from the tips of the grooves that penetrate the boundary layer in the opposite flat wall. If this is the mechanism, then it would be expected that the Nusselt number at much higher Rayleigh numbers would not continue to depart from the dashed lines, but rather approach from above asymptotes parallel to those for the plane layer.

For $A = 1$ and $\theta = 0$ deg, the data points from the previous study given by Chinnappa [19] are plotted for air layers bounded by a lower heated corrugated plate and an upper cooled flat plate. He used aspect ratio $A = 0.968$ with $H = 16.256$ mm (0.64 in.) in the range $8.9 \times 10^3 < \text{Ra} < 2 \times 10^4$, and $A = 0.931$ with $H = 44.196$ mm (1.74 in.) in the range $5.3 \times 10^4 < \text{Ra} < 4 \times 10^5$. The results from the present study are seen to be somewhat lower than those given by Chinnappa, but the reason for this difference is not clear. However, it may be of interest to note that the apparatus used in the present study has been subjected to a number of checks, such as measurements of the critical Rayleigh number [10], and measurement of the thermal conductivity of air [24], and no such checks were reported for Chinnappa's apparatus. Chinnappa evaluated the radiative component of heat transfer through calculations, while in the present study, this component was evaluated through measurements made at a very low pressure and perhaps, therefore, the difference could be related to the radiative correction.

5 Correlation Equation

It would be useful, for practical applications of these measurements, to have a single equation correlating Nu with Ra, A and θ, valid for the entire experimental range of values. Guided by the form of the equation for inclined plane layers (Hollands, et al [9]), the following equation was found to be suitable over most of the range of interest:

$$\text{Nu} = \text{Nu}_c + K\left[1 - \frac{\text{Ra}_c}{\text{Ra}\cos\theta}\right]^* \left(1 - \frac{\text{Ra}_c(\sin 1.8\theta)^{1.6}}{\text{Ra}\cos\theta}\right) + B\left[\left(\frac{\text{Ra}\cos\theta}{\text{Ra}_t}\right)^{1/3} - 1\right]^* \quad (6)$$

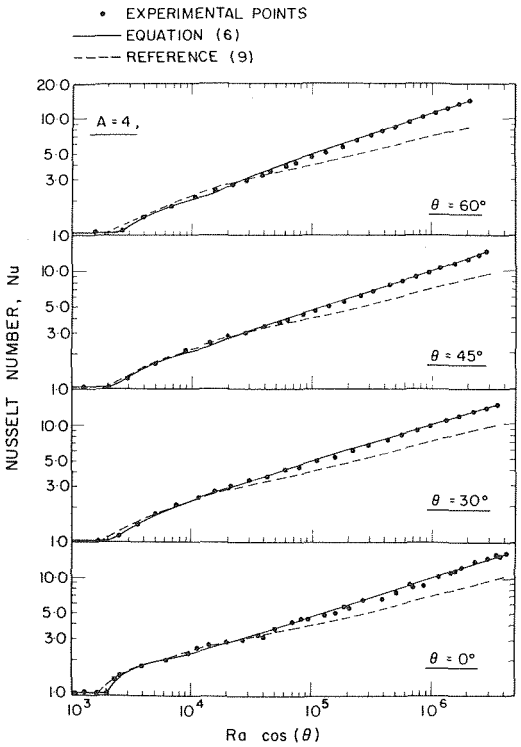

Fig. 6 Measurements of Nu as a function of Ra cos θ for $A = 4$

where Nu_c is given by equation (4), and

$$\text{Ra}_c = 1708\left[1 + \frac{0.036}{A} + \frac{2.69}{A^2} - \frac{1.70}{A^3}\right] \quad (7)$$

$$K = \frac{2460}{\text{Ra}_c}\left[1 - \frac{0.195}{A} + \frac{5.97}{A^2} - \frac{4.16}{A^3}\right] \quad (8)$$

$$B = 2.23 - 0.0123\theta + 0.34 \times 10^{-3}\theta^2 \quad (9)$$

$$Ra_l = 11{,}300[1 + 0.204 \sin [4.50(\theta - 37.8 \text{ deg})]] \quad (10)$$

In these equations, θ must be expressed in degrees. The operator $[\ ]^*$ denotes that the value of the quantity is to be taken as zero if the argument inside the brackets is negative but otherwise takes on the value of the argument; that is, if x represents any quantity,

$$[x]^* = (|x| + x)/2$$

Equation (6) has been plotted in Figs. 4, 5 and 6 as a solid line. Agreement is seen to be good (within eight percent) except for the narrow range $10^3 < Ra < 10^4$ for $A = 1$ where errors of up to 30 percent are observed.

A few brief comments about the correlation equation may prove helpful. The first term, pure conduction, is the only term which remains in the equation for $Ra < Ra_c$. For $Ra > Ra_c$, the next term represents the abrupt rise in heat transfer which accompanies the onset of convective motion for $Ra > Ra_c$. The value of Ra_c was found experimentally to depend on an inverse fashion on the aspect ratio, A; equation (7) represents an empirical fit to the three measured Ra_c's, using data from the three aspect ratios for $\theta = 0$ deg, and using 1708 (for plane layers) as the asymptote for $A \to \infty$. The rise in Nu with Ra at the onset of convection is governed by the parameter K. The equation for K is an empirical fit to the three separate values obtained for K (using the methods described in [10]) at $\theta = 0$ deg for the three aspect ratios, and using again the plane-layer value for the $A \to \infty$ asymptote.

In the correlation equation for plane layers [9], the counterpart of the third term in equation (6) arose from the conduction-layer analysis for fully turbulent heat transfer, and represented the limiting expression for Nu for asymptotically high Ra. The analogous procedure for the V-corrugated layer leads to equation (5), for $\theta = 0$ deg, and therefore to the form of the third term in equation (6). However, the asymptotic value of Nu from equation (6) are higher than those predicted by equation (5) by about 33 percent. If the predicted asymptotes are correct, one would conclude that the experimental Ra values are not sufficiently high to have reached the asymptotic fully turbulent state; for the present geometry, it is possible that extremely high Ra is required to destroy the cold jets departing from the tips of the V's, and prevent them from penetrating the boundary layer on the opposing flat surface.

6 Conclusions

1 Free convective heat transfer across inclined air layers with one surface V-corrugated is greater than that for plane air layers with the same average spacing by up to 50 percent over the range studied.

2 Heat transfer by free convection between a lower heated V-corrugated plate and an upper cooled flat plate is essentially unchanged if the two plates are interchanged, provided the lower plate is heated in both cases.

3 A semi-empirical equation for the conductive Nusselt number, Nu_c, for the V-corrugated problem was determined. It is given by equation (4).

4 The concept of a critical Rayleigh number, Ra_c, governing the first appearance of convective motion, appears to be as valid for the V-corrugated layer as for a flat layer, at least for $\theta = 0$. The value of Ra_c for a V-corrugated layer is generally slightly higher, indicating convection suppression by the V's (equation (7)). For $\theta > 0$ and small aspect ratio, base flow may contribute substantially to the heat transfer at Rayleigh numbers below critical.

5 A single correlation equation (equation (6)) was found to agree within ~8 percent with measurements covering the range of variables, $1 \le A \le 4$, $0 \text{ deg} \le \theta \le 60$ deg, and $10 \le Ra \le 4 \times 10^6$, except for $A = 1$, and $10^3 < Ra < 10^4$ where differences were up to 30 percent.

Acknowledgments

The authors greatly appreciate the financial support provided through the Energy Research and Development Administration (ERDA) (Solar Heating and Cooling Branch) of the U.S. Government, under grant number EY-76-C-02-2597.

We also thank the National Research Council of Canada for providing the original funds for building up the apparatus.

References

1 Hollands, K. G. T., "Directional Selectivity: Emittance and Absorptance Properties of Vee-Corrugated Specular Surfaces," *Solar Energy*, Vol. 7, No. 3, 1963, pp. 108–116.

2 Close, D. J., "Solar Air Heaters for Low and Moderate Temperature Applications," *Solar Energy*, Vol. 7, No. 3, 1963, pp. 117–124.

3 Close, D. J., Dunkle, R. V., and Robeson, K. D., "Design and Performance of a Thermal Storage Air Conditioning System," *Mech. Chem. Eng. Trans. Inst. Engrs. Aust.*, Vol. 4, No. 1, 1968, p. 45.

4 Globe, S., and Dropkin, D., "Natural Convection Heat Transfer in Liquids Confined by Two Horizontal Plates and Heated from Below," ASME JOURNAL OF HEAT TRANSFER, Vol. 81, 1959, pp. 24–28.

5 O'Toole, J. L., and Silveston, P. L., "Correlations of Convective Heat Transfer in Confined Horizontal Layers," *A.I.ChE. Chem. Engng. Progr. Symp. Ser.* 57 32, 1961, pp. 81–86.

6 Hollands, K. G. T., Raithby, D. G., and Konicek, L., "Correlation Equations for Free Convection Heat Transfer in Horizontal Layers of Air and Water," *Int. J. Heat and Mass Transfer*, Vol. 18, 1975, pp. 879–884.

7 Schmidt, E., and Silveston, P. L., "Natural Convection in Horizontal Liquid Layers," *Chem. Engng. Progr. Symp.* Ser. 29, Vol. 55, 1959, pp. 163–169.

8 Buchberg, H., Catton, I., and Edwards, D. K., "Natural Convection in Enclosed Spaces—A Review of Application to Solar Energy Collection," ASME JOURNAL OF HEAT TRANSFER, Vol. 98, No. 2, 1976, pp. 182–188.

9 Hollands, K. G. T., Unny, T. E., Raithby, G. D., and Konicek, L., "Free Convective Heat Transfer Across Inclined Air Layers," ASME JOURNAL OF HEAT TRANSFER, Vol. 98, No. 2, 1976, pp. 189–193.

10 Hollands, K. G. T., and Konicek, L., "Experimental Study of the Stability of Differentially Heated Inclined Air Layers," *Int. J. Heat Mass Transfer*, Vol. 16, 1973, pp. 1467–1476.

11 Dropkin, D., and Somerscales, E., "Heat Transfer by Natural Convection in Liquids Confined by Two Parallel Plates which are Inclined at Various Angles with respect to the Horizontal," ASME JOURNAL OF HEAT TRANSFER, Vol. 87, 1965, pp. 77–84.

12 Arnold, J. N., Catton, I., and Edwards, D. K., "Experimental Investigation of Natural Convection in Inclined Rectangular Regions of Differing Aspect Regions," ASME JOURNAL OF HEAT TRANSFER, Vol. 98, No. 2, 1976, pp. 67–71.

13 Hollands, K. G. T., "Convectional Heat Transport Between Rigid Horizontal Boundaries after Instability," *Physics Fluids*, Vol. 8, 1965, pp. 389–390.

14 Koschmieder, E. L., and Pallas, S. G., "Heat Transfer through a Shallow Horizontal Convecting Fluid Layer," *Int. J. Heat Mass Transfer*, Vol. 17, 1974, pp. 991–1002.

15 Somerscales, E. F. C., and Dropkin, D., "Experimental Investigation of the Temperature Distribution in a Horizontal Layer of Fluid Heated from Below," *Int. J. Heat Mass Transfer*, Vol. 9, 1966, pp. 1189–1204.

16 De Graaf, J. G. A., and Van der Held, E. F. M., "The Relation Between the Heat Transfer and the Convection Phenomena in Enclosed Plane Air Layers," *Appl. Sci. Res. A*, Vol. 3, 1953, pp. 393–409.

17 Difederico, I., and Foraboschi, F. P., "A Contribution to the Study of Free Convection in a Fluid Layer Heated from Below," *Int. J. Heat Mass Transfer*, Vol. 9, 1966, pp. 1351–1360.

18 Hart, J., "Stability of the Flow in a Differentially Heated Inclined Box," *J. Fluid Mech.*, Vol. 47, 1971, pp. 547–576.

19 Chinnappa, J. C. V., "Free Convection in Air Between a 60° Vee-Corrugated Plate and a Flat Plate," *Int. J. Heat Mass Transfer*, Vol. 13, 1970, pp. 117–123.

20 ElSherbiny, S. M., "Free Convection in an Inclined Air Layer Contained Between V-Corrugated and Flat Plates," M.A.Sc. Thesis, Univerity of Waterloo, Waterloo, Canada, 1977.

21 Elrod, H. G., "Two Simple Theorems for Establishing Bounds on the Total Heat Flow in Steady-State Heat Conduction Problems with Convective Boundary Conditions," ASME JOURNAL OF HEAT TRANSFER, Vol. 96, 1974, pp. 65–70.

22 Kreith, F., *Principles of Heat Transfer*, 3rd Edition, McGraw-Hill, pp. 95–97.

23 Raithby, G. D., and Hollands, K. G. T., "A General Method of Obtaining Approximate Solutions to Laminar and Turbulent Free Convection Problems," *Advances in Heat Transfer*, Vol. 11, Academic Press, 1975, pp. 265–315.

24 Hollands, K. G. T., "Natural Convection in a Horizontal Layer of Air with Internal Constraints," Ph.D. Thesis, McGill University, Montreal, Canada, 1967.

25 Bird, R. B., Stewart, W. E., and Lightfoot, E. N., *Transport Phenomena*, John Wiley and Sons, Inc., 1960, p. 91.

26 Van Doormaal, J., Personal Communication, Dept. of Mechanical Eng., University of Waterloo.

APPENDIX

In order to prove reciprocity, the full equations of motion and energy [25] for a Newtonian fluid are used with the assumption that all fluid properties are constant, except for density in the buoyancy

terms; here a linear dependence on temperature is assumed (Boussinesq's approximation). The equations, including boundary conditions, are written twice, once for each of the two geometries and coordinate systems shown in Figs. 1(a) and 1(b). These equations are then nondimensionalized using the scale L for length, $k/\rho LC_p$ for velocity, $\rho C_p L^2/k$ for time, and $k^2/\rho C_p{}^2 L^2$ for pressure. The other symbols are contained in the Nomenclature. The average Nusselt number for both problems is given by identical equations in terms of the nondimensional temperature Θ. This quantity is in turn governed by identical equations and boundary conditions (in terms of nondimensional quantities) except for the signs of two terms in the energy equations. These equations are now presented; where two signs appear before a given term, the upper sign refers to the geometry in Fig. 1(b) and the lower to Fig. 1(a).

$$\partial u_i/\partial x_i = 0$$

$$\frac{Du_i}{Dt} = -\frac{\partial P_d}{\partial x_i} + \mathrm{Pr}\frac{\partial^2 u_i}{\partial x_k \partial x_k} + \mathrm{RaPr}\,\Theta\left(\frac{g_i}{g}\right)$$

$$\frac{D\Theta}{Dt} = \pm(\beta T)\mathrm{Ec}\frac{DP_d}{Dt} - \frac{(\beta T)L(g_k u_k)}{C_p(T_h - T_c)} + \frac{\partial^2\Theta}{\partial x_k \partial x_k} \pm \mathrm{EcPr}\,\Phi$$

It is clear that viscous dissipation effects (the last term in the energy equation) will not permit reciprocity to hold exactly because it creates an upward buoyancy force for both geometries. Both the terms that have sign changes have the Eckert number, Ec, as a coefficient, which is of order 5×10^{-13} to 8×10^{-8} in the present experiments. Dropping these terms, the equations and boundary conditions become identical for both problems. The parameters on which the Nusselt number depends are Ra, Pr, $(\beta T)Lg/C_p(T_h - T_c)$ and A (from the boundary conditions). The third term can be dropped from the list of relevant parameters because the adiabatic lapse rate, $(\beta T)g/C_p$, is much smaller than the temperature gradient across the layer $(T_h - T_c)/L$ in the present problem $(\beta TgL/C_p(T_h - T_c) \approx 10^{-5})$.

F. B. Cheung

Reactor Analysis & Safety Division,
Argonne National Laboratory,
9700 South Cass Avenue,
Argonne, Ill. 60439

Correlation Equations for Turbulent Thermal Convection in a Horizontal Fluid Layer Heated Internally and from Below

High Rayleigh number thermal convection in a horizontal fluid layer with uniform volumetric energy sources and a constant rate of bottom heating is studied analytically by a simple boundary layer approach. Heat transfer characteristics of the layer are defined in terms of local boundary-layer variables. Correlation equations are derived for the upper and the lower surface Nusselt numbers as functions of two independent Rayleigh numbers, based respectively on the surface to surface temperature difference and the volumetric heating rate. Variation of the turbulent core temperature, which so far has not been determined successfully by existing analytical methods, is obtained. This is found to depend on a single dimensionless parameter which measures the relative rates of internal and external heating. Results of this study are presented with available experimental data.

Introduction

This communication presents some heat transfer properties of a horizontal fluid layer undergoing turbulent thermal convection. The fluid motion of the layer is considered to be induced by buoyancy due to a temperature-caused density variation. There are three different mechanisms of heating which can result in an unstable buoyancy force distribution of the layer. These are: (a) heating from below (external mode), (b) heating from within (internal mode), and (c) simultaneous internal and external heating. In case (a), corresponding to Rayleigh-Benard convection, the unknown heat transfer quantity is usually the surface heat flux. This is correlated to an "external" Rayleigh number based on the surface to surface temperature difference. On the other hand, the unknown quantity in case (b) is the maximum temperature difference of the layer, which customarily is correlated to an "internal" Rayleigh number based on the rate of volumetric heat generation. In both cases, heat transfer is governed principally by a single parameter. The physical situation of interest in the present study is represented by case (c). Here, not only the surfaceheat flux (both the upper and lower ones) but also the fluid temperature are unknown. These unknown quantities are, in general, functions of two independent parameters which are characterized by the internal and external Rayleigh numbers. So far, there is no existing correlation in the literature which displays the combined effects of these parameters. The purpose of this study is to seek such a correlation.

Turbulent thermal convection in horizontal fluid layers has recently played an important role in nuclear reactor safety analysis. In one failure mode, the processes of natural convection occurring in an internally heated layer of molten fuel and in an externally heated layer of molten steel or liquid sodium have been considered, among others, as the major mechanisms of decay heat removal. Following a postulated core meltdown event, the molten steel layer with some dissolved fission products in it is likely to rest on the top of the heat-generating layer of fuel. While the molten steel layer is heated from below by the fuel, it is also heated internally by the dissolved fission products (at a much lower power level than that of the fuel). The capability of upward heat removal from the fuel-steel system relies on the thermal convection process occurring in the molten steel phase. Heat transfer coefficients as functions of the internal and external Rayleigh numbers of the steel layer are needed to provide realistic estimates of the thermostructural requirements of molten core retention devices. A similar class of natural convection problems can be encountered in many geophysical processes such as the buoyancy-induced motions in the earth's mantle [1, 2].[1] Because of radioactive heat generation within the continental crust, energy source driven thermal convection is considered to play an important role in the mantle convective processes [3, 4].

Without volumetric heating, the classical Rayleigh-Benard con-

Contributed by the Heat Transfer Division for publication in the JOURNAL OF HEAT TRANSFER. Manuscript received by the Heat Transfer Division

[1] Numbers in brackets designate References at end of paper.

vection has been studied quite extensively, as reviewed by Brindley [5] and Spiegel [6]. Current experiments by Threlfall [7], Chu and Goldstein [8], and Garon and Goldstein [9] have yielded excellent data on the Nusselt number-Rayleigh number relationship. The asymptotic behavior of the Nusselt number as the Rayleigh number approaches infinity has recently been re-examined by Long [10] and Hollands, Raithby, and Konicek [11]. The behavior was clearly shown to obey the 1/3 power law. For nature convection driven by internal energy sources, there are many studies known [12–15]. Consistent measurements on the surface heat transfer coefficient have currently been obtained by Kulacki and Goldstein [16], Kulacki and Nagle [17], and Kulacki and Emara [18]. A recent general review of the subject has been given by Tritton [19]. For this type of buoyancy-driven motions, the asymptotic behavior of the Nusselt number is less understood. A simple dimensional reasoning seems to suggest a 1/4 power-law dependence at high Rayleigh numbers [20] Thus far, the heat transfer correlations for this kind of flow appear to bear no simple relationship to those for Rayleigh-Benard convection.

It is now generally accepted that for high Rayleigh number free convection between two smooth horizontal surfaces the fluid temperature varies markedly only in thin diffusion layers near each surface. This boundary layer-dominant aspect of turbulent flows is to be employed in the present study. Heat transfer characteristics of an unstably stratified horizontal fluid layer are analyzed in terms of local parameters for the individual thermal boundary layer. A simple boundary layer equation, common to both heat source-driven and Rayleigh-Benard convection, is obtained. This equation, when applied to a horizontal fluid layer heated volumetrically and from below, reduces the number of independent controlling parameters of the layer to one. Correlation expressions are derived accordingly for the upper and lower surface heat transfer as functions of the internal and external Rayleigh numbers.

Simple Boundary Layer Analysis

Consider a steady heat transfer process in a horizontal fluid layer with uniform volumetric energy sources q and bottom heating rate Q_d. In the absence of convection, the conductive temperature profile of the layer is

$$T = T_1 + \frac{q}{2k}(L^2 - z^2) + \frac{Q_d}{k}(L - z) \tag{1}$$

where both q and Q_d are positive constants. With equation (1), the upper and lower surface heat transfer can be expressed by

$$Q_u = \frac{k\Delta T}{L} + \frac{qL}{2} \text{ and } Q_d = \frac{k\Delta T}{L} - \frac{qL}{2} \tag{2}$$

where $\Delta T = T_0 - T_1$ is the surface-to-surface temperature difference. From conservation of energy, we have $Q_u = Q_d + qL$. This relation holds even though convection is present in the layer. Thus, Q_u always differs from Q_d by a constant value of qL. In terms of the average value of Q_d and Q_u, the conventional definition of Rayleigh number becomes

$$\mathrm{Ra} = \frac{g\beta(Q_d + Q_u)L^4}{2k\alpha\nu} \tag{3}$$

At the limit when the heat flux is entirely from below, i.e., $q = 0$, we have, from equations (2) and (3),

$$\mathrm{Ra}_E = \frac{g\beta\Delta TL^3}{\alpha\nu} \tag{4}$$

This is the definition of the external Rayleigh number. On the other hand, when all the heat is generated within the layer and the lower boundary is thermally insulated, i.e., $Q_d = 0$, we have,

$$\mathrm{Ra}_I = \frac{g\beta qL^5}{2k\alpha\nu} \tag{5}$$

This is the definition of the internal Rayleigh number. In general, Ra_E and Ra_I are independent heat transfer parameters of the layer.

At large values of Ra_E, the fluid of the layer is in turbulent convection. Because of strong turbulent mixing in the central core region, the bulk of the fluid is nearly isothermal. For the case in which there are no distributed energy sources, i.e., $\mathrm{Ra}_I = 0$, the total heat flux is constant throughout the layer. The flow is practically symmetrical with respect to the center, with thermals rising from the bottom and cold plumes falling from the top [8, 9]. The isothermal core region, which is at a temperature approximately midway between T_0 and T_1, is contained between two thin thermal boundary layers of the same thickness δ (see Fig. 1 (a)). As Ra_E is increased, δ diminishes, resulting in a larger boundary layer temperature gradient. When there is internal heating of the layer, i.e., $\mathrm{Ra}_I \neq 0$, the situation is quite different. The total heat flux increases linearly with distance from the lower surface. Because heat is being generated everywhere within the layer, the flow must bring all parts of the fluid close to the upper surface to permit them to lose heat by conduction. Therefore, the rising plume is less important than the sinking one.[2] As a result of this lack of symmetry in the convection, the two thermal boundary layers are of different thicknesses, with larger temperature drop in the upper layer than in the lower one (Fig. 1(b)). As Ra_I is increased, this state of

[2] From conservation of energy, it is not difficult to realize that the sinking plume is responsible for higher rate of heat transfer at the upper surface.

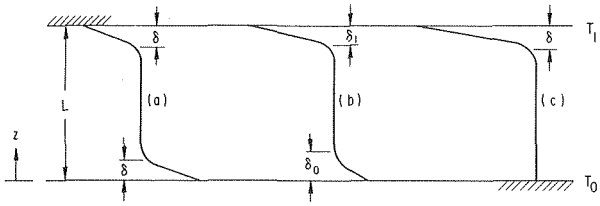

Fig. 1 Schematic of the horizontal fluid layer: (a) heating from below (b) simultaneous internal and external heating (c) heating from within

Nomenclature

g = acceleration due to gravity
Θ_{core} = dimensionless core temperature, $(T_{\mathrm{core}} - T_1)/(T_0 - T_1)$
k = thermal conductivity
L = layer thickness
Nu = Nusselt number
q = volumetric energy sources
Q = surface heat flux
Q_d = conductive heat flux at the lower surface
Q_u = conductive heat flux at the upper surface
Ra_δ = boundary layer Rayleigh number, $g\beta\Delta T_\delta\delta^3/\alpha\nu$
Ra_I = internal Rayleigh number, $g\beta qL^5/2k\alpha\nu$
Ra_E = external Rayleigh number, $g\beta\Delta TL^3/\alpha\nu$
T = mean temperature at any z
T_1 = upper surface temperature
T_0 = lower surface temperature
T_{core} = turbulent core temperature
ΔT = surface-to-surface temperature difference, $T_0 - T_1$
ΔT_δ = temperature drop across the individual boundary layer
z = vertical coordinate, $0 \le z \le L$
β = isobaric coefficient of thermal expansion
δ = boundary layer thickness
ν = kinematic viscosity
α = thermal diffusivity
Φ = nonlinear ratio of the Rayleigh numbers, equation (25)

Subscripts

1 = upper surface
0 = lower surface
E = external
I = internal
δ = boundary layer

asymmetry in the temperature and flow field becomes more pronounced. The difference in temperature between the bulk fluid and the lower surface is much less significant. At sufficiently high Ra_I (depending on the corresponding value of Ra_E), an extreme situation can be reached such that bottom heating (with lower surface temperature fixed) is completely suppressed, i.e., $Q_d = 0$. There is virtually no thermal boundary layer at the bottom of the layer (Fig. 1 (c)). The relation between Ra_I and Ra_E for the existence of this situation is to be determined in the subsequent analysis. If Ra_I is increased still further, Q_d can become negative, so that the layer is being cooled from below. In that case, however, the downward heat flux is largely controlled by conduction through a relatively stagnant fluid sublayer near the lower surface. One cannot appeal to the present boundary layer model, which applies only to turbulent flows. In the remainder of this work, we shall restrict our attention to cases in which $Q_d \geq 0$.

The boundary layer-dominant aspect of turbulent convection suggests that the surface heat transfer coefficients be governed principally by local heat transfer parameters. From dimensional considerations, a boundary-layer Rayleigh number can be defined as

$$\mathrm{Ra}_\delta = \frac{g\beta\Delta T_\delta \delta^3}{\alpha\nu} \tag{6}$$

where ΔT_δ is the temperature difference across the thermal boundary layer and δ is the nominal boundary layer thickness. The latter is defined as the thickness such as to offer the same "local" resistance by conduction as the actual boundary layer. With this definition, the surface heat flux Q can be related directly to the boundary layer heat transfer characteristics ΔT_δ and δ. The two extreme cases represented respectively by Fig. 1 (a) and (c) are to be considered first. For a bottom-heated layer with no internal heat source, the above definition of δ leads to $\delta \sim k\Delta T_\delta/Q$. To evaluate δ and Ra_δ, the following transformations are used:

$$\frac{\delta}{L} = \left(\frac{k\Delta T/L}{Q}\right)\left(\frac{\Delta T_\delta}{\Delta T}\right) \text{ and } \mathrm{Ra}_\delta = \left(\frac{g\beta\Delta T L^3}{\alpha\nu}\right)\left(\frac{\Delta T_\delta}{\Delta T}\right)\left(\frac{\delta}{L}\right)^3 \tag{7}$$

Following the conventional definition of Nusselt number, we have $\mathrm{Nu} \sim Q/(k\Delta T/L)$. With $\Delta T_\delta \sim \Delta T/2$ for high Rayleigh number flows, equation (7) can be written as

$$\frac{\delta}{L} = \frac{1}{2\mathrm{Nu}} \tag{8}$$

Substituting equations (4) and (8) into (7), we obtain

$$\mathrm{Ra}_\delta = \frac{\mathrm{Ra}_E}{16\mathrm{Nu}^3} \tag{9}$$

The above expressions for δ and Ra_δ enable us to determine the boundary layer characteristics directly from the existing heat transfer data. For a volumetrically heated horizontal fluid layer with an adiabatic lower boundary (Fig. 1 (c)), the following relation can be derived for the upper surface heat transfer [20]:

$$qL = [2k\Delta T_\delta q + q^2(L-\delta)^2]^{1/2} \tag{10}$$

At high Rayleigh numbers, the conduction layer should be very thin compared to the fluid layer as a whole, i.e., $\delta/L \ll 1$. Also, we should have $\Delta T_\delta \sim \Delta T$ in this situation. Equation (10) thus reduces to $\delta \sim k\Delta T/qL$. The Nusselt number in this case is defined by[3]

$$\mathrm{Nu} = \frac{qL}{2k\Delta T/L} \tag{11}$$

where qL is virtually equal to the upper surface heat flux. From the above equation, we obtain $\delta/L \sim 1/2\mathrm{Nu}$, which is exactly the same as equation (8). Therefore, in terms of δ/L, the definition of Nusselt number is common to both types of thermal convection. To express Ra_δ in terms of Nu and Ra_I, the following transformation is used

$$\mathrm{Ra}_\delta = \left(\frac{g\beta q L^5}{2k\alpha\nu}\right)\left(\frac{2k\Delta T}{qL^2}\right)\left(\frac{\Delta T_\delta}{\Delta T}\right)\left(\frac{\delta}{L}\right)^3 \quad \text{or} \quad \mathrm{Ra}_\delta = \frac{\mathrm{Ra}_I}{8\mathrm{Nu}^4} \tag{12}$$

where $\Delta T_\delta \sim \Delta T$ has been used in the above derivation. As in the case of bottom-heated layers, equations (8) and (12) enable us to evaluate δ and Ra_δ directly from the existing heat transfer data for internally heated layers.

Let us at this stage examine briefly equation (9). Without volumetric heating, the Nusselt number is related to the Rayleigh number by

$$\mathrm{Nu} \sim (\mathrm{Ra}_E/\mathrm{Ra}_\delta)^{1/3} \tag{13}$$

According to the boundary layer instability model of Howard [21], Ra_δ is approximately constant at large Ra_E. Therefore, Nu should be proportional to $Ra_E^{1/3}$ at high Rayleigh numbers, indicating that the buoyancy flux Q should be independent of the layer depth. However, recent experiments [7–9] clearly show a relationship $\mathrm{Nu} \sim \mathrm{Ra}_E{}^m$, where m is unmistakably less than 1/3. Instead, estimates of m range from 0.278 to 0.293. This result may be interpreted as an indication of the fact that the Rayleigh numbers so far explored are still too small for the boundary layer model to be strictly valid. A recent analysis by Long [10] suggests that Ra_E has to be larger than 3×10^{21} for Nu to approach $Ra_E^{1/3}$ with an error less than one percent in the Nusselt number. For turbulent thermal convection at a Rayleigh number far below this value, Ra_δ is expected to be a function of δ/L. Similar arguments can be made in regard to equation (12).

As previously discussed, the surface heat transfer in the turbulent convective regime depends primarily upon the boundary layer parameters. Since $\delta/L \ll 1$, the total heat generated within the thin thermal boundary layer (for the case with volumetric heating) is negligible compared to the surface heat flux. Therefore, the relationship between Ra_δ and δ should be independent of the mechanisms of heating (Fig. 1). To examine the validity of this hypothesis, the published heat transfer data from references [7–9] and [17, 18] are employed. The experimental results of Kulacki and Nagle [17], and Kulacki and Emara [18] for internally heated water layers having an adiabatic lower boundary are compared with three sets of data for Rayleigh-Benard convection, those of Threlfall [7], Chu and Goldstein [8], and Garon and Goldstein [9]. The results are shown in Fig. 2.[4] The data set (a)–(b) represents the internally heated layer while (c)–(d)–(e) represents the Rayleigh-Benard layer. The scatter[5] of each data set is believed to be caused by experimental uncertainties. For $\delta/L > 0.03$, corresponding approximately to $Ra_I < 1 \times 10^6$, the boundary layer approach becomes a very crude approximation. The present analysis is thus restricted to $\delta/L < 0.03$ (see Fig. 2). For the bottom-heated case, the Ra_δ and δ/L relationship can be represented by a correlation of the form

$$\mathrm{Ra}_\delta = 53.1\,(\delta/L)^{-0.391} \tag{14}$$

Similarly, for the internally heated case, the Ra_δ and δ/L relationship can be represented by

$$\mathrm{Ra}_\delta = 106.2\,(\delta/L)^{-0.391} \tag{15}$$

Thus, the two cases differ from each other only by a constant factor of ~2,[6] indicating that the boundary layer behaviors of the two

[3] From equation (2), the conductive heat flux at the upper surface is given by $2k\Delta T/L$. With $\mathrm{Nu} \sim Q_{\text{actual}}/Q_{\text{conductive}}$, equation (11) follows.

[4] The theoretical prediction by Cheung [20], based on calculated heat transfer results for an internally heated layer with an adiabatic lower boundary, is also shown in the figure.

[5] The plot of Ra_δ versus δ/L tends to amplify the differences among various measured data. The experimental results represented by (c), (d), and (e), for example, show considerably better agreement when presented in the conventional $\mathrm{Nu} - \mathrm{Ra}_E$ space.

[6] From equations (8) and (12), it can be shown that this is equivalent to a factor of $2^{1/4.391}$ or 1.17 in the $\mathrm{Nu} - \mathrm{Ra}_I$ space. As a result, a small difference in the coefficients of equations (14) or (15) would lead to a negligible error in the calculated Nusselt number.

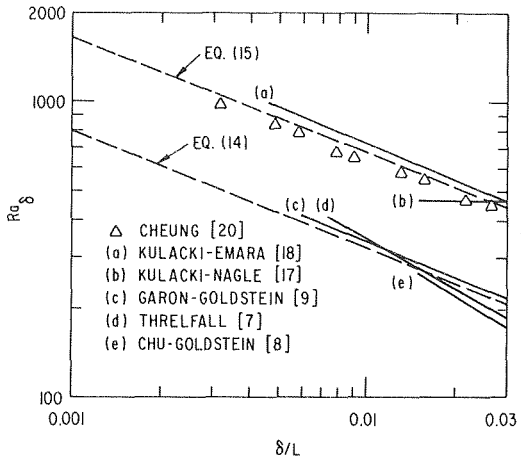

Fig. 2 Generalized heat transfer correlation for high Rayleigh number thermal convection

transport processes are qualitatively similar yet quantitatively different. The similarity part is likely to be a result of the boundary layer-dominant nature of the two processes. The nonsimilarity part, on the other hand, may be caused by the difference in turbulence structures outside the thermal boundary layers in the two different cases. Unlike the bottom-heated layer, the flow in the internally heated layer has to bring all parts of the fluid close to the upper surface to permit them to lose heat by conduction. This implies different transport mechanisms in the turbulent core regions of the two layers. Note that there are no data reported in the literature beyond $\delta/L \sim 0.0045$.[7] The validity of the boundary layer equation at very small values of δ/L is, therefore, uncertain and must be determined by future experiments. As δ/L approaches zero, Ra_δ is expected to approach a constant value, independent of δ/L.

Derivation of the Correlation Expressions

With the boundary layer equation, we are now able to determine the combined effects of the internal and external Rayleigh numbes on turbulent thermal convection in a horizontal fluid layer heated simultaneously from within and from below. Consider again the physical process represented by Fig. 1(b). In a region close to the lower surface, the effect of internal heat generation is negligible. The thermal boundary layer there can be expected to behave in the same way as that in the Rayleigh-Benard case. Applying equation (14) to the lower boundary layer, we have

$$\frac{g\beta\Delta T_{\delta_0}\delta_0^3}{\alpha\nu} = 53.1\left(\frac{\delta_0}{L}\right)^{-0.391} \tag{16}$$

Similar arguments cannot be applied to the region near the upper surface. There, the internal heat generation effect is not negligible, except in the case when the external Rayleigh number is considerably greater than the internal one. At other times, the effect is quite significant, being more and more pronounced as the internal heating rate is increased. For a given value of Ra_E, the dimensionless turbulent core temperature, Θ_{core}, is a monotonically increasing function of Ra_I (see Fig. 1). The value of Θ_{core} varies gradually from one-half to unity as we go from case (a) to case (c). Thus, the effect of internal heat generation on Ra_{δ_1} can be measured conveniently in terms of the dimensionless core temperature. Applying this idea to the upper thermal boundary layer, we have, from equations (14) and (15),

$$\frac{g\beta\Delta T_{\delta_1}\delta_1^3}{\alpha\nu} = f(\Theta_{\mathrm{core}})\left(\frac{\delta_1}{L}\right)^{-0.391} \tag{17}$$

where $f(1/2) = 53.1$ and $f(1) = 106.2$. The exact dependence of f on Θ_{core} is unknown and must be determined experimentally. In the subsequent analysis a simple functional form is assumed for f as follows:

$$f = 53.1\,[1 + (2\Theta_{\mathrm{core}} - 1)^m] \tag{18}$$

With the above expression, the boundary conditions at $\Theta_{\mathrm{core}} = 1/2$ and $\Theta_{\mathrm{core}} = 1$ are satisfied automatically. The variation of f can be adjusted systematically by assuming different values for m. In particular, f is a constant for $m = 0$, and is a linear function of Θ_{core} for $m = 1$, etc. It will be shown later that the choice of m does not affect substantially the calculated surface heat transfer of the layer,[8] indicating that equation (18) is not a crucial element of the present analysis. Thus, more accurate expressions for f are not needed, although the physics behind them may be of interest to explore.

Equations (16) to (18) indicate that the surface heat transfer is determined completely by the local temperature drops. At high Rayleigh numbers, the temperature difference between the upper and the lower surfaces must be equal to the sum of those across the individual boundary layers, i.e., $\Delta T = \Delta T_{\delta_1} + \Delta T_{\delta_0}$. In terms of the dimensionless core temperature, which is practically constant throughout the central region, we obtain

$$\begin{cases} \Delta T_{\delta_1} = \Theta_{\mathrm{core}}\Delta T \\ \Delta T_{\delta_0} = (1 - \Theta_{\mathrm{core}})\Delta T \end{cases} \tag{19}$$

As a result, there is only one controlling variable of the layer, i.e., Θ_{core}. To close the above system of equations, an independent expression for the surface heat transfer is required. This is obtained from conservation of energy:

$$Q_1 - Q_0 = qL \tag{20}$$

where the upper and the lower surface heat fluxes can be approximated, respectively, by

$$Q_1 = \frac{k\Delta T_{\delta_1}}{\delta_1} \text{ and } Q_0 = \frac{k\Delta T_{\delta_0}}{\delta_0} \tag{21}$$

In the above equation, the effects of heat generation within the thin thermal boundary layers have been neglected. The validity of this approximation will be discussed later. Substituting equations (19) and (21) into (20), we obtain, after rearrangement,

$$\frac{2\mathrm{Ra}_I}{\mathrm{Ra}_E} = \frac{\Theta_{\mathrm{core}}}{\delta_1/L} - \frac{1 - \Theta_{\mathrm{core}}}{\delta_0/L} \tag{22}$$

where the relation $\mathrm{Ra}_I/\mathrm{Ra}_E = qL^2/2k\Delta T$ has been used. From equations (16) and (18), δ_1 and δ_0 can be related to Θ_{core} by

$$\begin{cases} \dfrac{\delta_0}{L} = \dfrac{(53.1)^{0.295}}{\mathrm{Ra}_E{}^{0.295}(1 - \Theta_{\mathrm{core}})^{0.295}} \\ \dfrac{\delta_1}{L} = \dfrac{\{(53.1)[1 + (2\Theta_{\mathrm{core}} - 1)^m]\}^{0.295}}{\mathrm{Ra}_E{}^{0.295}\Theta_{\mathrm{core}}{}^{0.295}} \end{cases} \tag{23}$$

Combining equations (22) and (23), an implicit expression for Θ_{core} can be derived. This is

$$1 - \left[\frac{1 + (2\Theta_{\mathrm{core}} - 1)^m}{2}\right]^{0.295}\left(\frac{\Phi}{\Theta_{\mathrm{core}}}\right)^{1.295} = [1 + (2\Theta_{\mathrm{core}} - 1)^m]^{0.295}\left(\frac{1}{\Theta_{\mathrm{core}}} - 1\right)^{1.295} \tag{24}$$

where

$$\Phi = \frac{\mathrm{Ra}_I{}^{0.772}}{0.202\,\mathrm{Ra}_E} \tag{25}$$

[7] The highest Rayleigh number data so far reported is that given by Kulacki and Emara [18].

[8] As pointed out earlier, the conventional Nu – Ra relationship is amplified when presented in the $\mathrm{Ra}_\delta - \delta/L$ space. A small difference in the $\mathrm{Ra}_\delta - \delta/L$ expression would, therefore, result in negligible error in the corresponding Nu – Ra expression. This explains why the calculated results are not too sensitive to the assumed values of m.

Thus, the dimensionless core temperature is a function of the nonlinear ratio, Φ, of the Rayleigh numbers alone. This result indicates that the factor, Φ, which is a measure of the combined effects of Ra_E and Ra_I on the process of heat transfer, is the only independent controlling parameter of the layer.

In the absence of convection, the conductive heat fluxes are given by equation (2). Following the conventional definition of Nusselt number, i.e., $Nu \sim Q_{actual}/Q_{conductive}$, the surface heat transfer can be written as

$$Nu_1 = \frac{k\Delta T_{\delta_1}/\delta_1}{k\Delta T/L + qL/2} \text{ and } Nu_0 = \frac{k\Delta T_{\delta_0}/\delta_0}{k\Delta T/L - qL/2}$$

or, in dimensionless variables,

$$Nu_1 = \frac{\Theta_{core}}{\delta_1/L}\left(1 + \frac{Ra_I}{Ra_E}\right)^{-1}$$

$$\text{and } Nu_0 = \frac{1 - \Theta_{core}}{\delta_0/L}\left(1 - \frac{Ra_I}{Ra_E}\right)^{-1} \quad (26)$$

Combination of equations (23) to (26) yields, after some manipulation, the heat transfer correlations at the upper and the lower surfaces:

$$Nu_1 = \frac{2}{1 + Ra_E/Ra_I}\left\{1 - [1 + (2\Theta_{core} - 1)^m]^{0.295}\left(\frac{1}{\Theta_{core}} - 1\right)^{1.295}\right\}^{-1} \quad (27)$$

$$Nu_0 = \frac{-2}{1 - Ra_E/Ra_I}\left\{[1 + (2\Theta_{core} - 1)^m]^{-0.295}\left(\frac{1}{\Theta_{core}} - 1\right)^{-1.295} - 1\right\}^{-1} \quad (28)$$

The negative sign for Nu_0 denotes that the lower surface heat flux is directed upward (i.e., the layer is heated from below). With equation (24), the upper and the lower surface heat fluxes can be evaluated directly as functions of Φ.[9]

The relationship between Ra_E and Ra_I corresponding to the situation in which there is no heat transfer at the lower surface of the layer (Fig. 1 (c)) can be determined by the use of equations (24), (25), and (28). Setting $Nu_0 = 0$ in equation (28), we obtain $\Theta_{core} = 1$, with which equation (24) gives $\Phi = 1$. It follows from equation (25) that the condition of an adiabatic lower boundary is given by

$$Ra_I = 0.126\, Ra_E^{1.295} \quad (29)$$

The result is show graphically in Fig. 3. Note that equation (29) holds for all values of m, indicating that the role played by the function f_δ (equation (18)) is relatively minor in the overall heat transfer process. For values of Ra_I (Ra_E) located above the "thermally insulated" line, the layer in question is being cooled from below instead of being heated. Thus, the domain of interest of the present study is represented by the shaded region in Fig. 3. It can be shown from equation (25) that this region is bounded by $0 \le \Phi \le 1$.

The calculated turbulent core temperature and surface heat transfer are presented in Figs. 4 and 5, respectively, as functions of Φ within the domain (0, 1). Different values of m are used in the calculation. As expected, the predicted results are only weakly affected by the choice of m. The experimental data of Suo-Anttila and Catton [22] are also shown in the figures. The study reported in reference [22] appears to be the only existing experimental work on the turbulent thermal convection problem in a horizontal fluid layer with simultaneous internal and external heating.[10] They employed an electrolytically heated water layer to study the effects of Ra_E and Ra_I. In their experimental set-up, the bottom of the layer was intended to be cooled. Consequently, most of their measurements were performed in the region $\Phi > 1$. Only a few data points were obtained for $0 < \Phi < 1$. The portion of their results which is applicable to the present study is listed in Table 1 for the purpose of comparison[11] In view of the experimental uncertainties and the approximation of the present approach, the agreement between the predicted and the measured values is considered to be satisfactory.

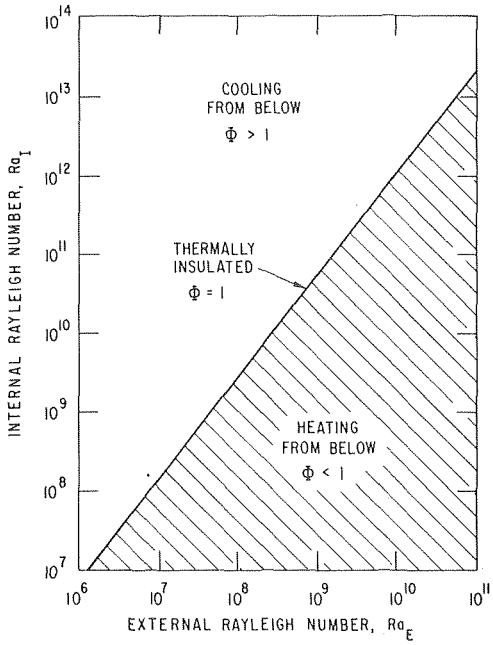

Fig. 3 Domain of interest: the $Ra_I - Ra_E$ space

For $0 \le \Phi \le 1$, the turbulent core temperature is a monotonically increasing function of Φ (see Fig. 4). As the volumetric heating rate of the layer is increased (with fixed values of L and ΔT), Θ_{core} rises. Physically, this results in a larger temperature difference across the thin sheet of vertical plumes at the upper surface compared to that at the lower one. Therefore, more heat is being carried through the upper boundary as Θ_{core} is raised. Up to the present time, there has been no analytical method able to successfully correlate the turbulent core temperature for given values of the internal and external Rayleigh numbers. The power integral method, for example, which is able to predict the surface heat transfer with accuracy, fails to predict the mean core temperature [22]. The implicit correlation given by equation (24) is, therefore, of particular value to analysts. Nevertheless, further experimental evidences are needed to confirm the validity of the correlation.

Superficially, there are two independent parameters governing the state of the fluid. These are the external Rayleigh number, Ra_E and the internal Rayleigh number, Ra_I. The upper and the lower surface Nusselt numbers are at first sight very difficult to correlate, since these dependent variables represent the "surfaces" in the $Ra_E - Ra_I$ space. With equations (27) and (28), however, the heat transfer correlations can be presented in a simple Φ domain, as illustrated in Fig. 5. In this way, the "surfaces" are reduced to "curves." This convenient approach can be quite useful in many practical applications.

The conditions for equation (21) to be valid need to be clarified. At high Rayleigh numbers, the boundary layer at the upper surface is always very thin compared to the fluid layer as a whole, i.e., $\delta_1/L \ll 1$. With $Q_1 = Q_0 + qL$, we have $Q_1 \gg q\delta_1$ for all values of $Q_0 (\ge 0)$. Thus, the expression for Q_1 given by equation (21) is a valid approx-

[9] As a result of the conventional definition of Nusselt number, Nu_0 and Nu_1 are functions of Ra_E and Ra_I. But the convective surface heat fluxes (Q_0 and Q_1) depend actually on Φ alone.

[10] The purpose of their work is to investigate the effect of unequal surface temperatures on a volumetrically heated fluid layer "cooled" from below.

[11] The calculated results presented in Table 1 are based on $m = i$. As can be seen from Figs. 4 and 5, this value of m seems to fit the data best.

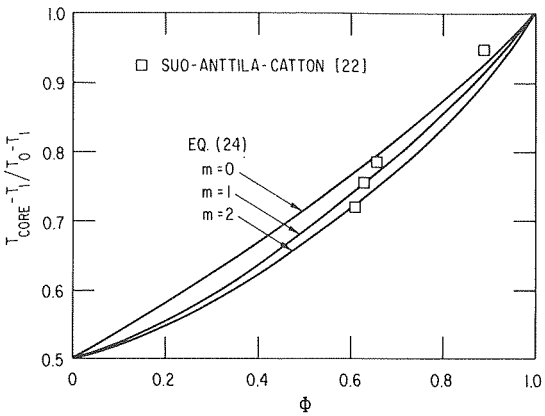

Fig. 4 Variation of the turbulent core temperature under different heating conditions

imation in the domain $0 \leq \Phi \leq 1$. Similar arguments, however, cannot be applied to the boundary layer at the lower surface, since the situation is quite different there. For $\delta_0/L \ll 1$[12], the heat flux relation is given by

$$Q_0 + q\delta_0 = [2k\Delta T_{\delta_0} q + Q_0^2]^{1/2}$$

$$\text{or } Q_0\left[1 + \frac{q\delta_0}{2Q_0}\right] = \frac{k\Delta T_{\delta_0}}{\delta_0} \quad (30)$$

Clearly, the expression for Q_0 given by equation (21) is a valid approximation only if $Q_0 \gg q\delta_0$. As the lower surface heat flux becomes very small, i.e., when Φ approaches unity, equation (21) is invalid. Fortunately, this equation is no longer needed as Φ approaches unity, since both δ_0 and ΔT_{δ_0} are of negligible importance to the heat transfer. To illustrate this point, consider the overall energy balance of the layer as given by equation (20). Substituting the expression for Q_0 in equation (30) and that for Q_1 in equation (21) into equation (20), we obtain

$$qL + \left[\frac{k\Delta T_{\delta_0}}{\delta_0} - \frac{q\delta_0}{2}\right] = \frac{k\Delta T_{\delta_1}}{\delta_1}$$

or

$$\frac{2\mathrm{Ra}_I}{\mathrm{Ra}_E}\left[1 - \frac{1}{2}\frac{\delta_0}{L}\right] = \frac{\Theta_{\text{core}}}{\delta_1/L} - \frac{1-\Theta_{\text{core}}}{\delta_0/L} \quad (31)$$

Thus, equation (22) is a valid approximation provided that $\delta_0/L \ll 1$.[13] Since $1/2 \leq \Theta_{\text{core}} \leq 1$, it can be seen from equation (23) that this is also a sufficient condition for $\delta_1/L \ll 1$. In the case when there is no internal heat generation in the layer, i.e., $\Theta_{\text{core}} = 1/2$, equation (23) gives $\mathrm{Ra}_E \geq 6 \times 10^8$ for $\delta_0/L \leq 0.01$. As Ra_I is increased (with Ra_E fixed), Θ_{core} increases, resulting in a larger value of δ_0/L. For $\Theta_{\text{core}} < 0.99$ (and $\mathrm{Ra}_E \geq 6 \times 10^8$), we have $\delta_0/L < 0.03$, which is still much less than one. Therefore, equations (22) and (23) are valid approximations in the region $0.5 \leq \Theta_{\text{core}} < 0.99$. The major difficulty arises when Θ_{core} approaches unity. However, for $\Theta_{\text{core}} > 0.95$, equation (23) indicates that

$$\frac{\Theta_{\text{core}}}{\delta_1/L} \gg \frac{1-\Theta_{\text{core}}}{\delta_0/L} \quad (32)$$

With the above inequality, equation (22) reduces to

$$\frac{2\mathrm{Ra}_I}{\mathrm{Ra}_E} = \frac{\Theta_{\text{core}}}{\delta_1/L} \quad (33)$$

Hence, the expressions for Q_0 and δ_0/L are no longer needed for Θ_{core}

[12] The conditions for $\delta_0/L \ll 1$ can be derived from equation (23), as will be examined later in this section.

[13] This, in turn, imposes certain restrictions upon the values of Q_0, and is equivalent to the condition that $Q_0 \gg q\delta_0$.

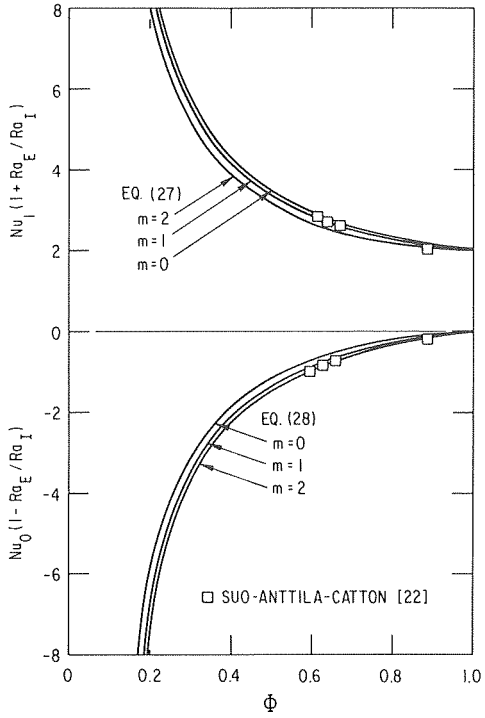

Fig. 5 Comparison of the calculated and measured surface Nusselt numbers

Table 1 High Rayleigh number thermal convection: horizontal layers with combined internal and external heating

External Rayleigh Number Ra_E	Internal Rayleigh Number Ra_I	Ratio Φ	Turbulent Core Temperature Θ_{core}		Upper-surface Nusselt Number Nu_1		Lower-surface Nusselt Number Nu_0	
			Exp.*	Calc.	Exp.*	Calc.	Exp.*	Calc.
1.01×10^8	2.525×10^9	0.89	0.95	0.91	1.930	2.039	-0.137	-0.126
5.35×10^9	2.79×10^{11}	0.63	0.75	0.75	2.512	2.675	-0.738	-0.741
5.66×10^9	2.88×10^{11}	0.61	0.72	0.74	2.687	2.754	-0.898	-0.825
6.03×10^9	3.45×10^{11}	0.66	0.78	0.77	2.516	2.584	-0.642	-0.639

*Based on measurements reported in Ref. [22].

> 0.95, although these expressions remain valid for $\Theta_{\text{core}} < 0.99$. This justifies the present approach.[14] Note that equation (33) is exact when $\Theta_{\text{core}} = 1$.[15] Substituting the expression for δ_1/L (equation (23)) into this equation and rearranging, we obtain

$$\Phi^{1.295} = \left\{\frac{1 + [2\Theta_{\text{core}} - 1]^m}{2}\right\}^{-0.295} \Theta_{\text{core}}^{1.295} \quad (34)$$

Hence, we have $\Phi = 1$ at $\Theta_{\text{core}} = 1$ (or $Q_0 = 0$). This result shows that there is a unique condition for which the heat flux to the bottom surface approaches zero. This condition is given by equation (29).[16]

4. Concluding Remarks

The correlations of the surface Nusselt numbers and the mean core temperature derived primarily from the boundary layer concept. The ranges of applicability of these correlations must be confirmed by

[14] As can be seen in Figs. 4 and 5, there is no singularity at $\Phi = 1$.

[15] For $\Theta_{\text{core}} = 1$, we have $Q_0 = 0$. The overall energy balance becomes $qL = Q_1$, which is equivalent to equation (33).

[16] For $\mathrm{Ra}_E < 6 \times 10^8$, the foregoing arguments are less rigorous. The lower bond of Ra_E (Fig. 3) for the validity of the present analysis must, therefore, be determined by experiments.

experiments. On the other hand, the functional forms of the correlations that resulted from this study may be used as to provide a general guideline for correlating future experimental data. In the absence of sufficient information on the flow, equations (24–28) constitute a useful model for engineering calculations in many analogous problems.

Acknowledgments

The author wishes to thank Ms. Marilyn Goldman for typing and manuscript preparation. This work was performed under the auspices of the U. S. Department of Energy.

References

1 Allan, D. W., Thompson, W. B., and Weiss, N. O., "Convection in the Earth's Mantle," *Mantles of the Earth and Terrestrial Planets* (Ed. S. K. Runcorn), Wiley, New York, 1967, pp. 507–512.

2 Turcotte, D. L. and Oxburgh, E. R., "Mantle Convection and the New Global Tectonic," *Annual Reviews of Fluid Mechanics*, Vol. 4, 1972, pp. 33–68.

3 Howard, L. N., Malkus, W. V. R., and Whitehead, J. A., "Self-convection of Floating Heat Sources: A Model for Continental Drift," *Geophysical Fluid Dynamics*, Vol. 1, 1970, pp. 123–142.

4 McKensie, D. P., Roberts, J. M., and Weiss, N. O., "Convection in the Earth's Mantle: Towards a Numerical Simulation," *Journal of Fluid Mechanics*, Vol. 62, 1974, pp. 465–538.

5 Brindley, J., "Thermal Convection in Horizontal Fluid Layers," *Journal of Inst. Maths. Applics.*, Vol 3, 1967, pp. 313–343.

6 Spiegel, E. A., "Convection in Stars, I. Basic Boussinesq Convection," *Annual Review of Astronomy and Astrophysics*, Vol. 9, 1971, pp. 323–352.

7 Threlfall, D. C., "Free Convection in Low-temperature Gaseous Helium," *Journal of Fluid Mechanics*, Vol. 67, 1975, pp. 17–28.

8 Chu, T. Y. and Goldstein, R. J., "Turbulent Convection in a Horizontal Layer of Water," *Journal of Fluid Mechanics*, Vol. 60, 1973, pp. 141–159.

9 Garon, A. M. and Goldstein, R. J., "Velocity and Heat Transfer Measurements in Thermal Convection," *The Physics of Fluids*, Vol. 16, 1973, pp. 1818–1825.

10 Long, R. R., "Relation between Nusselt Number and Rayleigh Number in Turbulent Thermal Convection," *Journal of Fluid Mechanics*, Vol. 73(3), 1976, pp. 445–451.

11 Hollands, K. G. T., Raithby, G. D., and Konicek, L., "Correlation Equations for Free Convection Heat Transfer in Horizontal Layers of Air and Water," *Int. Journal of Heat and Mass Transfer*, Vol. 18, 1975, pp. 879–884.

12 Tritton, D. J. and Zarraga, M. N., "Convection in Horizontal Fluid Layers with Heat Generation Experiments," *Journal of Fluid Mechanics*, Vol. 30, 1967, pp. 21–32.

13 Thirlby, R., "Convection in an Internally Heated Fluid Layer," *Journal of Fluid Mechanics*, Vol. 44, 1970, pp. 673–693.

14 Fielder, H. E. and Wille, R., "Turbulante Freie Konvektion in Einer Horizontalea Flussigkeitsschicht mit Volumen-Warmequelle," *Proc. 4th Int. Heat Transfer Conf.*, NC 4.5, Paris, 1970.

15 Schwiderski, E. W. and Schwab, H. J. A., "Convection Experiments with Electrolytically Heated Fluid Layers," *Journal of Fluid Mechanics*, Vol. 48, 1971, pp. 703–719.

16 Kulacki, F. A. and Goldstein, R. J., "Therman Convection in a Horizontal Fluid Layer with Uniform Volumetric Energy Sources," *Journal of Fluid Mechanics*, Vol. 55, 1972, pp. 271–287.

17 Kulacki, F. A. and Nagle, M. Z., "Natural Convection in a Horizontal Fluid Layer with Volumetric Energy Sources," ASME JOURNAL OF HEAT TRANSFER, Vol. 97, 1975, pp. 204–211.

18 Kulacki, F. A. and Emara, A. A., "High Rayleigh Number Convection in Enclosed Fluid Layers with Internal Heat Sources," U. S. Nuclear Regulatory Commission, NUREG-75/065, 1975.

19 Tritton, D. J., "Convection in Horizontal Layers," *Physical Fluid Dynamics*, Van Nostrand Reinhold, New York, 1977, pp. 30–41, ibid. pp. 201–212.

20 Cheung, F. B., "Natural Convection in a Volumetrically Heated Fluid Layer at High Rayleigh Numbers," *Int. Journal of Heat and Mass Transfer*, Vol. 20, 1977, pp. 499–506.

21 Howard, L. N., "Convection at High Rayleigh Number," *Proc. 11th Int. Cong. Appl. Mech.*, Springer, Berlin, 1966, pp. 1109–1115.

22 Suo-Anttila, A. J. and Catton, I., "An Experimental Study of a Horizontal Layer of Fluid with Volumetric Heating and Unequal Surface Temperatures," Paper No. AIChE-5, 16th National Heat Transfer Conference, St. Louis, 1976.

J. R. Parsons, Jr.
Graduate Research Assistant.

J. C. Mulligan
Professor.
Mem. ASME

Department of Mechanical and Aerospace Engineering
North Carolina State University
Raleigh, North Carolina 27607

Transient Free Convection from a Suddenly Heated Horizontal Wire

Experimental data are presented for the transient free convective heat transfer from a horizontal wire in air subjected to a step change in heat rate. An unbalanced Wheatstone bridge is described which allows simultaneous observation of wire temperature and heat rate, under transient as well as steady-state conditions. An "overshoot" of the steady state is shown to occur in the transient decay of the Nusselt number, and the occurrence, magnitude, and duration of this phenomenon is shown to depend upon the Rayleigh number. Simple stability theory is shown to explain the delay in the convective process which is associated with the overshoot in heat transfer. Steady-state data are also presented and are shown to agree well with proposed low Rayleigh number correlations.

Introduction

The great majority of transient free convection studies reported in the literature are concerned with geometries such as vertical cylinders and plates. Indeed, these problems have been shown to possess certain very characteristic mathematical difficulties and, at the same time, to display a very characteristic transient heat transfer behavior. Typically, an initial pure conduction regime is followed by a convective transition regime in which leading edge effects become dominant. Finally, a transient approach to the steady state occurs where the heat transfer coefficient approaches its steady-state value either from above or below. The limit of pure conduction and the overshoot which sometimes occurs in the heat transfer coefficient are well known characteristics of these transient problems and have been clearly related to the existence of a sharp leading edge.

Few studies, however, have been carried out which attempt to define the typical characteristics of the transient free convection from horizontal cylinders, spheres, and other bluff geometries characterized by streamwise body curvature. Only two investigations, for example, have been carried out which deal directly with the transient free convection from a horizontal cylinder or wire, the topic of the present paper. The first was the experimental study of Ostroumov [1]. In this classical work, an optical technique was used to observe the transient pattern of the temperature field around a fine wire, and a resistance bridge was used to measure the actual temperature response of the wire. Overshoots were rather casually observed in some of the wire temperature response data, while a delay in the convective motion was observed optically. Ostroumov attempted to generally associate the overshoot in heat transfer with the convective delay, although with little success. Neither the mechanism of the delay nor the reason only some of his data indicated an overshoot seems to have been clearly understood. More recently Vest and Lawson [2] carried out interferometer experiments using a small diameter horizontal wire in an effort to prove the hypothesis that the governing mechanism in the process is that of thermal stability. They formulated a simple theory for the delay time based on an established critical Rayleigh number, and found excellent agreement with their optically observed delays. No temperature response data, however, were obtained in their experiments. The evidence to date, therefore, indicates that an overshoot in heat transfer similar to that which occurs for vertical elements also occurs under certain conditions for the horizontal cylinder or wire and that, in contrast to the mechanisms which have been identified for the vertical geometries, this overshoot is related to thermal stability.

The transient experiments of Vest and Lawson, and Ostroumov, were both primarily optical in nature. No temperature versus time information is available from Vest and Lawson and only limited and somewhat inconsistent data are given by Ostroumov. Moreover, steady-state data in the Rayleigh number range of pertinence in many applications involving fine wires are rather scanty and not entirely definitive. The steady-state results for horizontal cylinders and fine wires that are of primary pertinence to the present study are those of Churchill and Chu [3], Nakai and Okazaki [4], and Collis and Williams [5]. The first is essentially applicable in the higher Rayleigh number range and the latter two studies primarily present results for very small Rayleigh numbers.

Characteristics of both the transient and the steady-state convective heat transfer from the horizontal cylinder and wire are obviously important in numerous applications. In the present paper, an experimental study is described in which data were obtained describing both the transient and the steady-state free convection from a horizontal wire which is subjected to sudden and constant heating. The purpose of the experiments was first to provide more quantitative

Contributed by the Heat Transfer Division for publication in the JOURNAL OF HEAT TRANSFER, Manuscript received by the Heat Transfer Division September 9, 1977.

information on the transient decay of the Nusselt number, the convective delay formulated by Vest and Lawson, and the general pattern of the overshoot phenomenon and, secondly, to develop additional steady-state data applicable in the Rayleigh number range of 10^{-3} to 10^{-6}.

Experiments

The principal components of the experimental apparatus are shown in Fig. 1. A fine platinum wire was mounted in a test chamber constructed of fiberglass coated plywood and covered with styrofoam sheet for insulation. Wires of 0.127 ± .003 mm and 0.030 ± .003 mm dia were used in the experiments. The diameter of the larger test wire was determined by multiple measurements with a precision micrometer while the smaller wire was photographed under an electron microscope against a reference background. The test wire was secured between brass terminal posts 29.2 cm apart. One side of the wire was attached to a pulley and weight system that maintained the wire in tension during the experiments. The test wire constituted one arm of a standard Wheatstone bridge. The power supply was a 12 volt wet cell storage battery. Bridge unbalance was monitored on a high speed oscillograph, and voltage drop across the test wire was measured with a storage oscilloscope. Input power control and bridge balancing were accomplished using various rheostats and the temperature of the air within the test chamber was measured with an NBS calibrated thermometer. The resistance resolution of the Wheatstone bridge circuit used was estimated to be ±0.15 percent. As no lead wire resistance compensation scheme was utilized, the resistance of the lead wires was minimized by using large (No. 8) diameter copper wire. Total lead wire resistance was calculated to be 0.007 Ω compared to the room temperature resistance of the platinum test wires of 2.62 Ω for the 0.127 mm dia wire and 65.10 Ω for the 0.030 mm dia wire.

Each test wire was calibrated by accurately determining its temperature versus electrical resistance characteristic. This was done by applying heat within the insulated test chamber and allowing several hours for the air to come to an equilibrium temperature. The bridge circuit was then energized with a 1½ volt dry cell battery to produce a trickle current of approximately four milliamperes in the wire. This was sufficient to allow measurement of the resistance of the wire with the bridge circuit but insufficient to significantly heat the wire (this heating effect was calculated to be approximately 0.005°C). The temperature and wire resistance were repeatedly recorded as the test chamber was allowed to slowly cool. This calibration procedure was then repeated on successive days, with a minimum of three runs required to determine a calibration for a wire. During calibration and all subsequent test runs the test chamber thermometer was located far enough away from the test wire to avoid the thermal plume of the heated wire. Calibration tests performed with the thermometer in other locations in the chamber confirmed that the air temperature was indeed uniform during calibration.

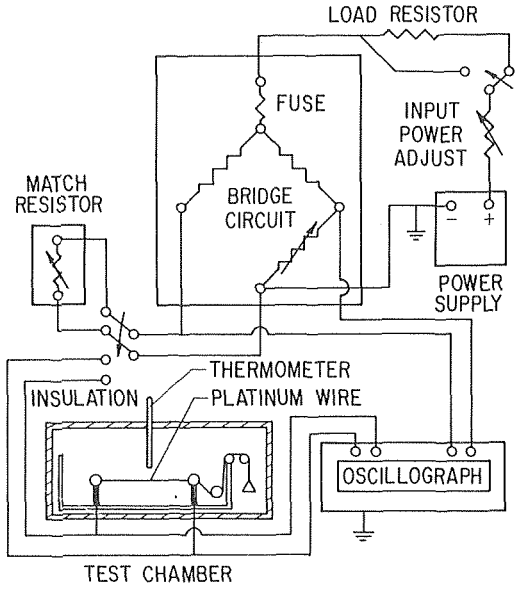

Fig. 1 Schematic diagram of apparatus

Wire temperature versus time transients were measured during test chamber heating as well as cooling cycles using the principal of the unbalanced bridge. Before each run, the bridge was balanced with a large load resistor in series with the test wire, representing a zero power condition. This resistor was then suddenly removed from the circuit to create the transient, allowing the wire to heat up. After a steady-state condition was reached, the resistor was suddenly reinserted into the circuit and the cooldown of the wire measured. During each transient, both wire voltage drop and degree of bridge unbalance were monitored. These two variables provide wire heat rate and temperature versus time data, respectively. It was noted that the wire heat rate remained essentially constant throughout the transient (the change in heat rate is on the order of the percent change in wire resistance or a maximum of 3.5 percent). The rheostat in series with the power supply was adjusted between runs to affect changes in wire current and thus, heat rate. Before and after each test run the chamber temperature, wire resistance, battery voltage (under load), power rheostat resistance, and wire voltage drop (with and without load resistor) were recorded.

A series of preliminary experiments were conducted to specifically determine if the transient heating of the other bridge resistors would significantly affect the observed wire transient. A resistor decade box

Nomenclature

c = specific heat of fluid at constant pressure
d = diameter of test wire
g = gravitational acceleration
Gr = Grashof number, $g\beta(T_w - T_\infty)\rho^2 d^3/\mu^2$
h = convective heat transfer coefficient, $q'/\pi d(T_w - T_\infty)$
k = thermal conductivity of fluid
Nu = Nusselt number, hd/k
Nu_{ss} = Nusselt number at steady-state conditions, $\mathrm{Nu}(\tau \to \tau_\infty)$
Pr = Prandtl number, $c\mu/k$
q' = wire linear heat rate
Ra = Rayleigh number, Gr·Pr
Ra* = modified Rayleigh number based on heat rate, Ra·Nu
Ra_0* = modified Rayleigh number above which no overshoot occurs, referred to as "overshoot" Rayleigh number
t = time
T_w = wire temperature
T_∞ = bulk fluid temperature
α = thermal diffusivity of fluid, $k/\rho c$
α_1 = heat capacity parameter with subscript 1 denoting properties of the wire, $2\rho c/\rho_1 c_1$
β = coefficient of thermal expansion of fluid
$\Delta\tau_1$ = duration of overshoot, $\tau_\infty - \tau(\mathrm{Nu} = \mathrm{Nu}_{ss})$
$\Delta\tau_2$ = duration of transient, $\tau_\infty - \tau_0$
μ = dynamic viscosity of fluid
ρ = density of fluid
τ = Fourier number, $4\alpha t/d^2$
τ_∞ = estimate of Fourier number at instant steady state occurs
τ_D = Fourier number at the onset of significant convection, referred to as "delay time" or "limit of pure conduction"
τ_0 = limit of pure conduction corresponding to "overshoot" Rayleigh number, $\tau_D(\mathrm{Ra}^* = \mathrm{Ra}_0^*)$

was placed in parallel with the test wire so that either resistance could be placed in the unknown bridge arm by positioning a toggle switch. A transient run was conducted with the test wire and decade box resistances matched. After the load resistor was removed from the circuit, the bridge was preheated to its steady state using the decade box as a dummy arm. Then the test wire was switched into the circuit replacing the decade box and the transient observed. It was concluded from these tests that no measurable bridge resistor heating effects were present.

Accurate measurement of the temperature of the wire and the bulk fluid was critical because of the small temperature differences involved. The bulk fluid temperature was measured using a calibrated thermometer accurate to ±0.05°C, while resolution of wire resistance to ±0.001 Ω introduced an error in wire temperature of ±0.1°C. These accuracies were sufficient for the interpretation of most of the transient and steady-state results where temperature differences ranged from 3 to 15°C, but some care had to be exercised in evaluating results at the onset of heating. Repetition of transient runs at the same input heat rate served to minimize this effect. Radiation losses were calculated for the appropriate test wire conditions and found to be no more than 0.7 percent. This was considered to be negligible.

Results and Discussion

Transient Response. Immediately after power is applied to a wire, the temperature of the wire increases and heat is transferred externally to the surrounding medium initially by pure conduction. This initial conductive heat transfer is characterized by isotherms in the axial plane being concentric circles, a result which has been observed experimentally in [1] and [2]. This pure conduction from a small cylinder subjected to constant heating at $t = 0$ and dissipating heat to an infinite medium has been described analytically by Blackwell [6] and presented in Carslaw and Jaeger [7] for the case of infinite cylinder thermal conductivity and finite cylinder heat capacity. The initial temperature response, therefore, to be expected of a small wire in which internal thermal conductivity effects are negligible is given by

$$T_w - T_\infty = \frac{2\alpha_1^2 q'}{\pi^3 k} \int_0^\infty \frac{[1 - \exp(-\tau\mu^2)]d\mu}{\mu^3 \Delta(\mu)} \tag{1}$$

where

$$\Delta(\mu) = [\mu J_0(\mu) - \alpha_1 J_1(\mu)]^2 + [\mu Y_0(\mu) - \alpha_1 Y_1(\mu)]^2 \tag{2}$$

The parameter α_1 is twice the ratio of the heat capacity of an equivalent volume of the medium to that of the wire. A numerical integration of this expression was carried out with the results displayed in Fig. 2, along with the data from selected experimental runs which most clearly illustrate the transient behavior encountered in the experiments. The analytical solution for negligible wire heat capacity ($\alpha_1 \to \infty$) as well as for a platinum wire in air ($\alpha_1 = 0.00082$) is shown. The ordinate in this figure is defined on the basis of the input heating rate and the wire temperature, $q'/\pi k(T_w - T_\infty)$, and should be viewed as an inverse dimensionless surface temperature for a prescribed constant heating rate. When the thermal capacitance of the wire is depleted in the transient, this quantity becomes a true convective Nusselt number, Nu.

It can be seen that during the initial pure conductive heat transfer the inverse dimensionless temperature decreased rapidly from infinity, with the pure conduction theory and the experimental data agreeing very well initially. However, at some point during the transient the data are seen to deviate abruptly from the pure conduction trend, indicating a distinct limit of pure conduction followed by the subsequent transition region where convective effects become important. A convective delay is therefore seen to occur wherein the convection process is delayed, allowing pure conductive transfer to dominate for a distinct period of time. In some of the cases, the Nusselt number even decreased below its steady state value, a phenomenon referred to as "overshoot." In those cases displaying an overshoot, the delay time or limit of pure conduction can be identified with the minimum of the Nusselt number. As the heating rate was decreased in the experiments, the overshoot first appeared sharp and pronounced and, finally, longer in duration and somewhat greater in magnitude. The actual value of the delay time was therefore more difficult to quantify in these latter runs. The magnitude of the Nusselt number overshoot ranged from 0 to 7.5 percent of the steady-state value. A complete tabulation of the more important computed data for all the experiments is included in Table 1.

As the heating rate was increased, an upper bound was reached beyond which no overshoot occurred. In these high heat rate runs, $Ra^* > 0.5 \times 10^{-3}$, the transient was typically a monotonically decreasing phenomenon but not smooth since a distinct departure from pure conduction occurred at specific times for each heating rate. Hence, convective delays still occurred at high heat rates, only their termination was sufficiently early to preclude an overshoot in heat transfer. This behavior, along with the general pattern of the occurrence of the delay, is illustrated in Fig. 3. Ostroumov concluded that neither an overshoot nor a delay occur in air. It appears the heating rates in his air experiments were too high ($Ra^* \sim 10^{-1}$) to show the overshoot and

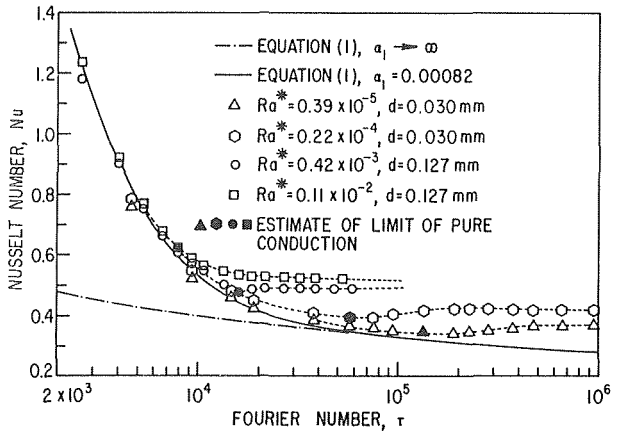

Fig. 2 Selected data describing the transient decay of the Nusselt number typically encountered in the experiments

Run No.[1]	Wire Heat Rate, q' (w/m)	Modified Rayleigh No., Ra^* ($\times 10^{-6}$)	Steady-State Nusselt No., Nu_{ss} ($\times 10^{-2}$)	Delay Time, τ_D ($\times 10^3$)	Overshoot, % of Nu_{ss}	Duration of Overshoot, $\Delta\tau_1$ ($\times 10^3$)	Time to Steady State, τ_{ss} ($\times 10^3$)
1	0.073	2.41	36.9	208	7.5	1800	1800
2	0.085	2.79	34.8	178	5.2	1800	1800
3	0.100	3.30	36.6	208	4.1	1800	1800
4	0.120	3.94	35.9	189	5.6	320	378
5	0.148	4.89	37.1	160	1.9	300	378
6	0.184	6.05	37.2	133	5.6	220	378
7	0.238	7.86	38.2	133	3.9	300	473
8	0.315	10.4	38.0	91.5	4.5	150	378
9	0.445	14.7	40.0	85.4	4.5	170	283
10	0.670	22.0	41.1	66.2	4.4	87	132
11	0.107	264	47.4	21.5	1.3	9	32.2
12	0.107	265	47.9	21.5	1.5	15	32.2
13	0.133	329	47.9	21.5	2.0	17	32.2
14	0.161	393	48.2	20.2	0.8	11	27.0
15	0.164	409	48.3	20.1	0.6	16	26.8
16	0.167	417	49.1	16.1	2.4	5	18.8
17	0.185	457	49.7	20.1	0.6	16	26.9
18	0.207	506	50.0	9.2	-	-	18.9
19	0.205	510	49.4	10.7	-	-	37.5
20	0.237	591	50.5	9.2	-	-	32.2
21	0.257	634	50.0	9.2	-	-	43.4
22	0.268	656	50.1	9.0	-	-	32.3
23	0.268	668	51.1	9.0	-	-	37.5
24	0.305	761	51.3	9.4	-	-	37.5
25	0.352	865	51.9	8.0	-	-	26.9
26	0.358	892	51.4	9.2	-	-	37.5
27	0.372	910	51.7	8.0	-	-	32.3
28	0.427	1065	51.5	8.0	-	-	37.5
29	0.441	1085	52.5	8.0	-	-	37.7

[1]Runs 1-10, d=0.030 mm; Runs 11-29, d=0.127 mm; τ_0 for all runs=12700.

Table 1 Computed results obtained from continuous data recordings

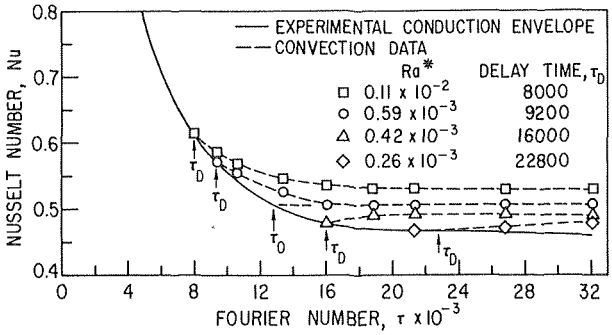

Fig. 3 Selected data illustrating the typical pattern of convection delay observed in the experiments, showing limits of pure conduction for monotonically decreasing as well as overshoot transients

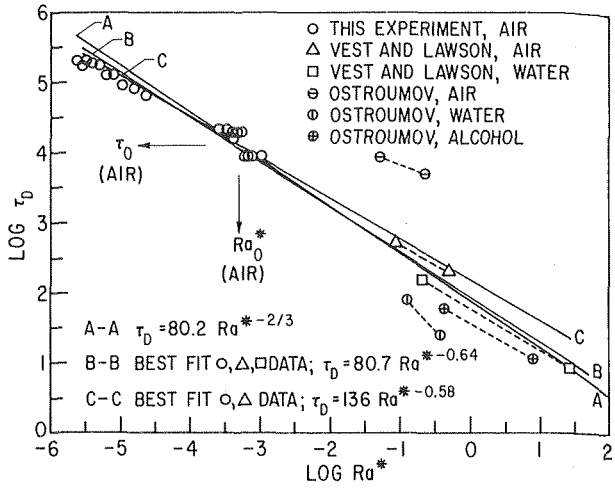

Fig. 4 Correlation of the limit of pure conduction (convective delay) with Rayleigh number on the basis of thermal stability criteria

his understanding of the mechanism not sufficiently clear to anticipate this.

Vest and Lawson determined that thermal stability was the underlying physical mechanism governing the duration of the conductive heat transfer (the limit of pure conduction). That is, an unstable equilibrium occurs in the fluid at the upper point on the surface of a heated cylinder, viscosity stabilized, thus producing a delay of global convective motion. Conduction was presumed to break down when the Rayleigh number, defined on the basis of the penetration depth of the temperature field around the wire, reached a critical value of 1100. Using an approximate temperature profile, the delay time was expressed as

$$\tau_D = 80.2\,(\mathrm{Ra}^*)^{-2/3} \tag{3}$$

As noted by Vest and Lawson, the results of Ostroumov suggest the similar form

$$\tau_D \sim (q')^{-0.6} \tag{4}$$

Equation (3) is shown in Fig. 4 along with the delay time data of the present study for conditions associated with the overshoot as well as those associated with the monotonically decreasing transient. Data from Vest and Lawson's and Ostroumov's experiments are also shown, along with some significant regression lines. The agreement between this experiment and Vest and Lawson's correlation is seen to be good while Ostroumov's data are only in general agreement. Significantly, the best fit regression line for the current data and Vest and Lawson's data is very close to equation (3). The deviation of the data about either of these two lines is approximately ±30 percent. The use of the −2/3 exponent which occurs exactly under the assumption of a very small diameter wire, sufficiently small that thermal conductivity and wire heat capacity effects are negligible, seems adequate to this degree of accuracy. In air, however, these effects can become important and the air data, taken alone, does show some influence of wire diameter. That is, the exponent in the regression line for the air data significantly differs from −2/3 and the accuracy of the line is better than for the overall regression line, ±20 percent. In fact, the ±30 percent deviation in the overall regression line is believed due to the wire diameter effects which occur to differing degrees in the various test fluids. Thus, the concept and application of the simple stability theory of Vest and Lawson certainly appears valid, even though an extension of the theory to include wire thermal conductivity and heat capacity effects would probably increase its accuracy.

Steady-State Results. When the convective delay is overcome, the limit of pure conduction exceeded, a dominant convection transient is established as the Nusselt number approaches its steady state for either above or below. Many empirical correlations have been established for predicting the steady-state natural convection Nusselt number on a horizontal cylinder. Fig. 5 compares the steady-state results of this experiment with several existing correlations. The correlation of McAdams [8] is of the classical form $\mathrm{Nu} = A(\mathrm{GrPr})^B$

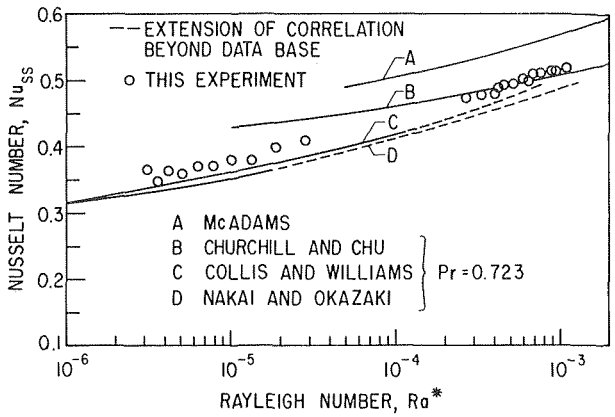

Fig. 5 Correlation of the steady-state Nusselt number data and comparison with existing high and low Rayleigh number correlations

where A and B are functions of the Rayleigh number range of interest. The recent correlation due to Churchill and Chu [3] contains a more complicated function of Prandtl number that is of utility in extending the range of applicability of the correlation. Their equation is

$$\mathrm{Nu}_{ss}{}^{1/2} = 0.60 + 0.387\left\{\frac{\mathrm{Ra}}{[1.0 + (0.559/\mathrm{Pr})^{9/16}]^{16/9}}\right\}^{1/6} \tag{5}$$

and is recommended for both isothermal and constant heat flux boundary conditions. The data from this experiment for the 0.127 mm wire ($\mathrm{Ra}^* \sim 10^{-3}$) is in excellent agreement with Churchill and Chu's correlation although the data for the smaller wire ($\mathrm{Ra}^* \sim 10^{-5}$) deviate significantly, a result which confirms that the lower limit of applicability of this correlation is $\mathrm{Ra}^* \sim 10^{-4}$.

The correlations of Nakai and Okazaki [4]

$$\mathrm{Nu}_{ss} = 6/[\ln E - \ln(\mathrm{Nu\,Gr}/16)] \tag{6}$$

where $E = f(\mathrm{Pr}) = 18.87$ for $\mathrm{Pr} = 0.723$, and Collis and Williams [5] for air

$$\mathrm{Nu}_{ss} = 1/[0.88 - 0.43 \log \mathrm{Gr}] \tag{7}$$

specifically address the small Rayleigh number problem, the upper limit of their applicability being $\mathrm{Ra}^* \sim 10^{-4}$. As can be seen in Fig. 5, both of these correlations agree well with the data from the present experiments, the agreement being slightly better with Collis and Williams' expression.

Occurrence of Overshoot and Transient Duration. An important and indeed essential aspect of the transient processes gov-

erning the free convective heat transfer from a small wire is seen to be the occurrence of an overshoot in the heat transfer coefficient. In the experiments it was observed that a critical overshoot Rayleigh number, Ra_0^*, exists above which no overshoot occurs. As already noted, the overshoot only occurs if the Nusselt number has decayed to a value below the steady-state value at the limit of pure conduction. Using the equality of the transient and steady-state Nusselt numbers ($Nu = Nu_{ss}$) as a criterion, and equations (1), (3), and the appropriate steady-state correlation (equation (5) or (7), depending on the Grashof number), all the information is available to allow prediction of this overshoot Rayleigh number, Ra_0^*, as a function of α_1 and Pr. The Prandtl number dependence introduced by the steady-state Nusselt number correlation, however, is not a strong function and can be ignored when an intermediate range of Prandtl numbers is being considered. The equations were solved iteratively for a Prandtl number of 0.723, and the results plotted in Fig. 6. Note that for $\alpha_1 > 1.0$, the overshoot Rayleigh number is constant at a value of approximately 20. This behavior is not unexpected since the pure conduction solution, equation (1), is sensitive to α_1 only for $\alpha_1 < 1$ in the range of dimensionless time necessary for decay to steady state. The data of Ostroumov are also shown to be in overall agreement, although not sufficient to accurately confirm the value of the overshoot criterion, Ra_0^*.

In reducing the data an attempt was made to judge the overall duration of the transient, τ_∞. In doing so, it was noted that the duration of the transient, $\Delta\tau_2$, cast as $(\tau_\infty - \tau_0)$, was always approximately a constant multiple of the quantity $|\tau_D - \tau_0|$. Here τ_D is the delay time and τ_0 the value of τ_D when $Ra^* = Ra_0^*$ (approximately 12,700 for all runs). For a given wire, medium, and heating rate, the dimensionless delay time is easily predictable from equation (3), with τ_0 also readily determined from equation (3) assuming Ra_0^* has already been computed (perhaps from Fig. 6). Thus, the difference $|\tau_D - \tau_0|$ forms a readily predictable implicit function of α_1, Ra^*, and Pr. It also forms an experimental measurement when these dimensionless time measures are deduced from continuous recordings and, therefore, was thought to be an appropriate function against which to correlate the observed transient duration, $(\tau_\infty - \tau_0)$. Such an $X - Y$ plot of the present data as well as that of Ostroumov is shown in Fig. 7. The solid line represents a regression line which includes both the present overshoot data and Ostroumov's overshoot data. The dashed line is simply a nominal (exponent of unity) best fit line through the present overshoot data, shown here primarily because a regression line through this same data is not significantly different. Because some difficulty was encountered in accurately determining τ_D for those runs which do not overshoot (the monotonically decreasing transient), these data have been included in Fig. 7 to confirm the trend and the validity of the correlation although excluded from the correlating lines themselves due to some loss in confidence as to their accuracy. The spread in this latter data is primarily due to the sensitivity of the difference $|\tau_D - \tau_0|$ to τ_D.

The correlation shown in Fig. 7, in essence, determines a configuration or shape factor for the transient response profile which ultimately allows the estimation of the transient time τ_∞. Although the magnitude of the data scatter is relatively large, most of the large deviations can be attributed directly to difficulties in determining τ_D or τ_∞ from individual data recordings. The latter measure was made difficult to determine in some of the very low heat rate runs because of a slight oscillating approach to steady state, a phenomenon which could not be identified as experimentally significant yet complicated the evaluations of τ_∞. If, indeed, the oscillations are significant, a possible explanation is suggested by the linear stability theory for a plane plume. This is discussed by Pera and Gebhart [9] and Mollendorf and Gebhart [10]. Statistically, when one considers the range of the data and the type of measurements represented, the confirmation of the profile expression $(\tau_\infty - \tau_0) = 2.5(|\tau_D - \tau_0|)$ was thought striking. Note that the correlations presented in Figs. 6 and 7 also utilize "fine" wire theory (negligible internal thermal conductivity effects) and appropriate care should be used when applying the results to larger, less conducting wire.

Conclusions

1 Transient heat transfer from a fine wire subjected to a step change in applied heat rate has been clearly shown to occur in three well defined stages, as suggested in previously published studies. An initial pure conduction stage, followed by a convective transition and, finally, to the state of steady free convection. Each of these stages of heat transfer were found to be predictable by theoretical or empirical considerations.

2 For a fine wire, the initial conductive regime is well described by established theory. The limit of the pure conduction, however, was shown to be governed by thermal stability and well represented by the simple theory of Vest and Lawson, even though some improvement in the theory to include wire heat capacity and thermal conductivity effects was suggested by the data.

3 The convective transition from pure conduction to steady free convection which begins at the limit of pure conduction occurs either as a monotonically decreasing transient or an overshoot, depending upon the value of Ra^*. In the former case, $Ra^* > Ra_0^*$, the steady state is approached from above while in the latter case, $Ra^* < Ra_0^*$, the steady state is approached from below.

4 As a simple criterion for overshoot, the critical overshoot Ray-

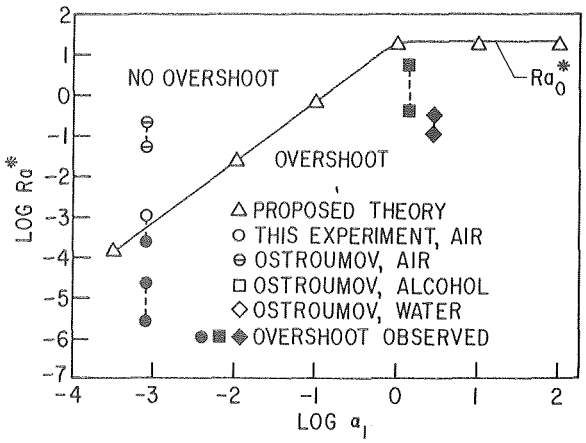

Fig. 6 Critical overshoot Rayleigh number, Ra_0^*, as a criterion for the occurrence of an overshoot transient

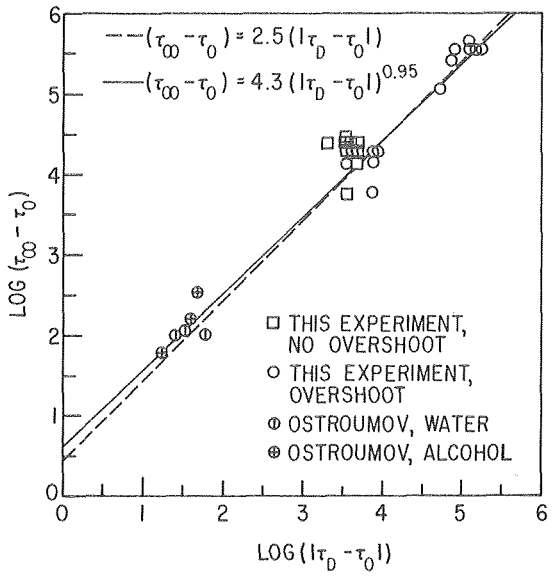

Fig. 7 Duration of the observed transients correlated as a transient profile shape factor

leigh number $Ra_0^*(\alpha_1, Pr)$ is easily developed and applicable for a variety of wire materials and fluid media. For air, the criterion was found to be relatively accurate and, in addition, to give the proper indication for the conditions of the water and alcohol experiments of Ostroumov.

5 The time required for the transient free convective Nusselt number to reach steady state can be estimated from a shape factor characterization of the transient profile, i.e., $(\tau_\infty - \tau_0)/(|\tau_D - \tau_0|) = 2.5$. Such an expression was found to correlate relatively well the present air data as well as the data of Ostroumov.

6 The steady-state data confirmed that the correlation of Churchill and Chu is correctly valid down to $Ra^* \sim 10^{-4}$, as recommended, and that the low Rayleigh number correlations of Collis and Williams, and Nakai and Okazaki, are satisfactory even up to $Ra^* \sim 10^{-3}$. The data suggest that the transition from the former to the latter type of correlation occurs at approximately 5×10^{-4}, even though in the intermediate range of $10^{-4} - 10^{-3}$ the correlations do not differ appreciably.

Acknowledgment

This work was supported by the National Science Foundation through grant number ENG 75-14616.

References

1 Ostroumov, G. A., "Unsteady Heat Convection Near A Horizontal Cylinder," *Soviet Technical Physics*, Vol. 1, 1956, pp. 2627–2641.

2 Vest, C. M., and Lawson, M. L., "Onset of Convection Near a Suddenly Heated Horizontal Wire," *International Journal of Heat and Mass Transfer*, Vol. 15, 1972, pp. 1281–1283.

3 Churchill, S. W., and Chu, H. H. S., "Correlating Equations for Laminar and Turbulent Free Convection From a Horizontal Cylinder," *International Journal of Heat and Mass Transfer*, Vol. 18, 1975, pp. 1049–1053.

4 Nakai, S., and Okazaki, T., "Heat Transfer from a Horizontal Circular Wire at Small Reynolds and Grashof Numbers, parts I and II," *International Journal of Heat and Mass Transfer*, Vol. 18, 1975, pp. 387–413.

5 Collis, D. C., and Williams, M. J., "Free Convection of Heat From Fine Wires," A. R. L. Aero. Note 140, 1954.

6 Blackwell, J. H., "A Transient-Flow Method for Determination of Thermal Constants of Insulating Materials in Bulk," *Journal of Applied Physics*, Vol. 25, No. 2, 1954, pp. 137–144.

7 Carslaw, H. S., and Jaeger, J. C., *Conduction of Heat in Solids*, 2nd ed., Oxford University Press, London, 1959, pp. 342–345.

8 McAdams, W. H., *Heat Transmission*, 3rd ed., McGraw-Hill Book Company, New York, 1954, pp. 175–176.

9 Pera, L., and Gebhart, B., "On the Stability of Laminar Plumes: Some Numerical Solutions and Experiments," *International Journal of Heat and Mass Transfer*, Vol. 14, 1971, pp. 975–984.

10 Mollendorf, J. C., and Gerhart, B., "An Experimental Study of Vigorous Transient Natural Convection," ASME JOURNAL OF HEAT TRANSFER, Vol. 92, 1970, pp. 628–634.

H. Imura[1]
R. R. Gilpin
K. C. Cheng

Department of Mechanical Engineering,
University of Alberta,
Edmonton, Alberta, Canada

An Experimental Investigation of Heat Transfer and Buoyancy Induced Transition from Laminar Forced Convection to Turbulent Free Convection over a Horizontal Isothermally Heated Plate

The flow over a horizontal isothermally heated plate at Reynolds numbers below that at which hydrodynamic instabilities exist, is characterized by a region of laminar forced convection near the leading edge, followed by the onset of longitudinal vortices and their growth to a finite amplitude and finally a transition to a turbulent flow regime. Results are presented for the temperature profiles, the thermal boundary layer thickness, and the local Nusselt number. They are used to identify the various flow regimes. It was found that the transition from laminar forced convection to turbulent convection was characterized by the parameter $Gr_x/Re_x^{1.5}$ falling in the range 100 to 300. For values of this parameter greater than 300 the heat transfer rates were independent of Reynolds number and typical of those for turbulent free convection from a horizontal surface.

1 Introduction

When a laminar boundary layer (Blasius flow) on a horizontal flat plate is heated isothermally from below, longitudinal (streamwise) vortices will appear for Grashof numbers exceeding some critical value. These vortices are produced by the top-heavy, unstable density variation that exists through the boundary layer when it is heated from below. The conditions for the onset of this instability have recently been studied theoretically by Wu and Cheng [1] and experimentally using water by Gilpin, Imura and Cheng [2]. The flow visualization studies in [2] revealed that a succession of flow regimes actually occurs. These include the familiar steady two-dimensional laminar flow near the plate leading edge, the onset of instability and the growth of longitudinal vortices, and finally the breakup of these vortices into a turbulent flow. A number of similarities were observed between this problem and that of the Görtler instability on a concave wall [3–7] even though the source of the instability in the case of Görtler vortices is centrifugal force in contrast to the buoyancy force for the thermal instability problem.

It was observed qualitatively in [2] that after the onset of longitudinal vortices, the flow field assumes a three-dimensional character and the heat transfer rates at the wall deviate from those predicted by the Pohlhausen's solution [8] for laminar forced convection.

In the past, theoretical attempts to predict the effects of buoyancy on heat transfer in a horizontal boundary layer have employed a two-dimensional combined free and force convection formulation [9–12] where the vertical buoyancy force acts primarily to produce a stream-wise pressure gradient in the fluid adjacent to the plate. In light of the vortex rolls observed in [2] the range of applicability of the two-dimensional formulation may, however, be somewhat limited.

[1] On leave from the Department of Mechanical Engineering, Kumamoto University, Japan.

Contributed by the Heat Transfer Division for publication in the JOURNAL OF HEAT TRANSFER. Manuscript received by the Heat Transfer Division January 12, 1978.

Previously, experimental investigations of the combined free and forced convection heat transfer have been made for the case of horizontal plane Poiseuille flow heated from below. For this flow finite amplitude convection in the fully developed region has been studied experimentally by Mori and Uchida [13] and Ostrach and Kamotani [14]. Kamotani and Ostrach [15] have also studied the thermal entrance region for this problem.

Also the related problem of the effect of Görtler vortices on heat transfer through a boundary layer on a concave wall was studied by McCormack, Welker and Kelleher [16]. Wortmann [6] has also reported an experimental study of the stability of the Görtler vortices. For the case of a hydrodynamically turbulent boundary layer over a flat plate the familiar von Karman [17] or Prandtl [18] analogies are normally used. The Nusselt number expression derived from these analogies applies only in the case of pure forced convection when the effects of temperature differences on the flow are negligible. Extensive studies have, of course, been made on the hydrodynamic stability of a boundary layer flow with respect to the onset of Tollmien-Schlichting waves and their subsequent effects on heat transfer rates. However, very little information is available for the equally important thermal instability of a horizontal Blasius flow where longitudinal vortex-type disturbances can produce substantial changes in the post-critical heat transfer rates.

The purpose of the present experimental investigation was primarily to study the heat transfer rates occurring on a flat plate in the post-critical regime after the onset of longitudinal vortices. Also of importance to this study was the determination of the conditions for the transition from longitudinal vortex flow to turbulent convection.

2 Experimental Apparatus and Procedure

The present work was carried out in a closed-circuit water tunnel having a test section with dimensions 25.4 × 45.7 × 213.4 cm, width by height by length. An isothermal plate fabricated of 6.35 mm thick copper, 24.1 cm wide and 152.4 cm long was installed in the test section with its leading edge immediately downstream from a converging section in the tunnel. This arrangement produced a flow of uniform temperature and velocity with a depth of 25 cm over the plate. The isothermal temperature of the plate was maintained by circulating fluid from a controlled temperature bath at high velocity under the plate. Schematic diagrams of the water tunnel and the heating plate assembly are shown in Fig. 1 and 2 of [2].

Most of the results presented in this study are derived from temperature measurements in the boundary layer. These measurements were made using 51 μm diameter copper-constantan thermocouple wire that was formed in a loop [2]. The plane of the loop was aligned perpendicular to the main flow and could be positioned with a traversing mechanism with a resolution of 0.2 μm. Heat transfer coefficients at the isothermal plate were calculated from the temperature gradient in the water adjacent to the wall.

During the tests three velocities, nominally 4, 7 and 12 cm/s, and three temperature differences, nominally 4, 7.5 and 11°C, were combined to produce the nine test conditions shown in Table 1. Note that the symbols used to depict results for each of these test conditions are also indicated in the table. The total range of parameters covered by these test conditions is $Re_x = 3 \times 10^3$ to 2×10^5 and $Gr_x = 4 \times 10^6$ to 9×10^{10}.

Table 1 Range of parametric values for experiments

Symbols	ΔT, °C	T_∞, °C	U_∞, cm/s	Re_x	Gr_x	Pr
×	10.8-11.5	23.6-25.1	4.0-4.4	4.72×10^3-6.67×10^4	3.07×10^7-8.67×10^{10}	6.1-6.5
▽	7.1-7.8	23.4-24.8	3.5-4.0	3.21×10^3-5.86×10^4	8.38×10^6-5.28×10^{10}	6.2-6.5
△	3.5-4.1	22.4-25.3	3.9-4.4	3.46×10^3-6.70×10^4	3.98×10^6-3.32×10^{10}	6.1-6.6
▩	9.8-11.7	24.2-25.6	6.8-7.4	1.22×10^4-1.13×10^5	1.21×10^8-8.27×10^{10}	6.0-6.5
+	6.8-8.3	22.8-25.0	6.7-7.4	8.02×10^3-1.11×10^5	2.28×10^7-6.14×10^{10}	6.1-6.5
◉	3.6-4.1	23.5-25.2	7.2-7.7	1.23×10^4-1.17×10^5	3.86×10^7-3.24×10^{10}	6.1-6.5
○	10.0-11.7	24.1-24.8	12.1-12.5	2.03×10^4-1.91×10^5	1.14×10^8-7.55×10^{10}	6.2-6.5
□	6.6-7.8	23.4-24.8	11.6-12.4	1.94×10^4-1.82×10^5	7.00×10^7-5.03×10^{10}	6.2-6.5
◇	3.4-4.2	24.3-25.6	11.8-12.6	2.02×10^4-1.99×10^5	3.86×10^7-3.20×10^{10}	6.0-6.3

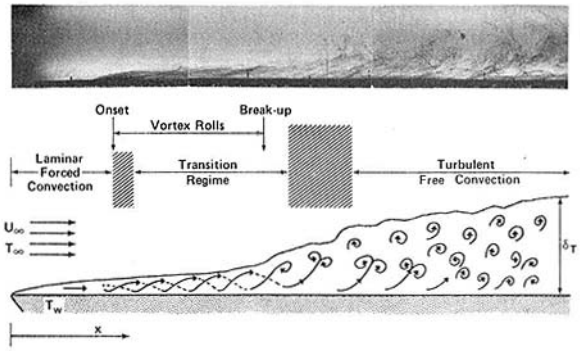

Fig. 1 A schematic interpretation of the flow regimes in the boundary layer over a horizontal, heated plate

3 General Description of the Flow Regimes Over a Heated Flat Plate at Low Reynolds Number

Fig. 1 shows photographs and a schematic interpretation of the side view of a thermal boundary layer developing over a heated flat plate. The behavior shown would be characteristic of flows at a Reynolds number based on the length of the plate of 10^5 or less, that is, at values below the range at which hydrodynamic generation of turbulence would be expected.

The laminar forced convection regime exists from the leading edge of the plate to the onset point of the longitudinal vortices. In the electrochemical flow visualization technique [2] that was used for the photograph at the top of Fig. 1 the dye which is generated at the plate surface is not observed until the onset of longitudinal vortices spreads it throughout the boundary layer. The longitudinal vortices generate a finite amplitude secondary flow which exists in the form of relatively regular vortex rolls for some distance down the plate. These rolls then begin to break up into a more turbulent flow pattern. This breakup appears to occur by the separation and rise of plumes from the plate surface. In this region a rapid increase in the thermal boundary layer thickness is observed. Downstream of the breakup of the longitudinal vortices a turbulent "free" convection regime is indicated. This region was so named because as will be seen later the heat transfer coefficients in this regime were typical of those encountered in free con-

Nomenclature

Gr_x = local Grashof number, $g\beta(\Delta T)x^2/\nu^2$
g = gravitational acceleration
h_x = local heat transfer coefficient, $-k(\partial T/\partial y)_{y=0}/\Delta T$
k = thermal conductivity
$Nu_x, (Nu_x)_0$ = local Nusselt numbers, $h_x x/k$, with and without buoyancy effect
Pr = Prandtl number
Re_x = local Reynolds number, $U_\infty x/\nu$
T, T_w, T_∞ = fluid, wall and free stream temperatures
U_∞ = free stream velocity
x, y = distance from leading edge and normal distance from plate surface
β = coefficient of thermal expansion
δ_T = thermal boundary layer thickness
ζ = correlation variable, $-\partial\theta/\partial y|_{y=0} y = h_x y/k$
η = similarity variable, $y(U_\infty/\nu x)^{1/2}$
θ = dimensionless temperature difference, $(T - T_\infty)/\Delta T$
ν = kinematic viscosity
ΔT = temperature difference, $(T_w - T_\infty)$

vection. In the "transition" regime, which is defined as the zone between the laminar forced convection zone and the turbulent free convection regime, heat transfer occurs by a combined free and forced convection mode.

4 Results

4.1 **Temperature Profiles.** Temperature profiles representative of the three regimes, laminar forced convection, transition, and turbulent free convection, are shown in Fig. 2. In this figure the nondimensional height above the plate is $\zeta = -\partial\theta/\partial y|_{y=0}\, y = h_x y/k$. By choosing this variable [19] the part of each boundary layer near the wall that is dominated by conduction will follow the linear equation $\theta = 1 - \zeta$, the solid curve in Fig. 2. The ordinate θ is the temperature $(T - T_\infty)/(T_w - T_\infty)$. The mean temperatures in the boundary layer will be noted to lie near the conduction line for values of ζ out to about 0.6 to 0.8 for all three temperature profiles. This, of course, does not mean that the heat transfer rate is the same for each profile because, as will be seen later, h_x varies dramatically from one regime to the next.

Outside the conduction layer the profile in the laminar regime declines to zero at about $\zeta = 1.5$, the approximate thickness of the thermal boundary layer in Blasius flow. In the flow regime dominated by vortices the mean temperature profile generally exhibited an approximately constant temperature region from $\zeta = 0.8$ to 2.0. This would be the expected result of strong vortex roll convection in the boundary layer. The temperature profile in this regime drops fairly abruptly to zero at $\zeta \approx 3$. The temperature profile in the turbulent free convective zone is dramatically thicker. The mean temperatures in this regime decline slowly to zero for ζ out to about 30.

As noted in [2] the vortices in the Blasius flow constantly shifted from side to side across the flow direction. This behavior contrasts with that of the vortex rolls in the plane Poiseuille flow [13, 14] where the vortices are in relatively fixed positions on the plate. As a result of the motion of the vortices on the plate a good measure of the mean temperature and its variation across the vortex rolls was obtained in the present experiment by recording the temperature at a fixed position above the plate for a period of 1 or 2 min. Measurements of the temperature profiles were normally made along the center line of the plate. Some measurements made at positions either side of the center line showed that the mean and fluctuating components of the temperatures in the boundary layer were constant over at least the center 15 cm of the heating plate. The approximate peak-to-peak amplitude of the temperature fluctuation observed at various points in the boundary layer is indicated on Fig. 2 by the vertical bars—the solid bars pertain to points in the vortex flow regime and the dashed bars to the turbulent regime. It can be seen that for both the vortex rolls and the turbulent flow a very substantial temperature fluctuation exists for $\zeta > 0.2$. No significant temperature fluctuations were observed in the laminar flow regime.

4.2 **Thermal Boundary Layer Thickness.** Further insight into the effect of the instability on the thermal boundary layer was obtained by measuring the change of the boundary layer thickness along the plate for various conditions, Figs. 3 and 4. The thickness indicated in these figures is the height above the plate at which there was a detectable change in the water temperature from its free stream value, approximately one percent of the temperature difference, ΔT. Fig. 3 shows the effect of varying the temperature difference at a constant

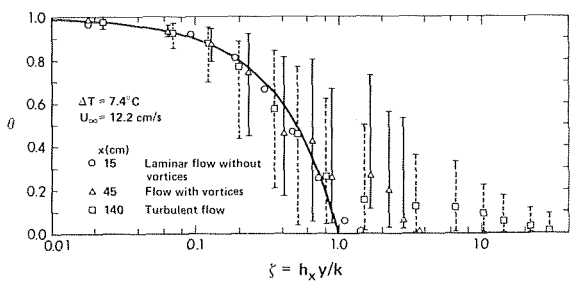

Fig. 2 Temperature profiles in the three flow regimes

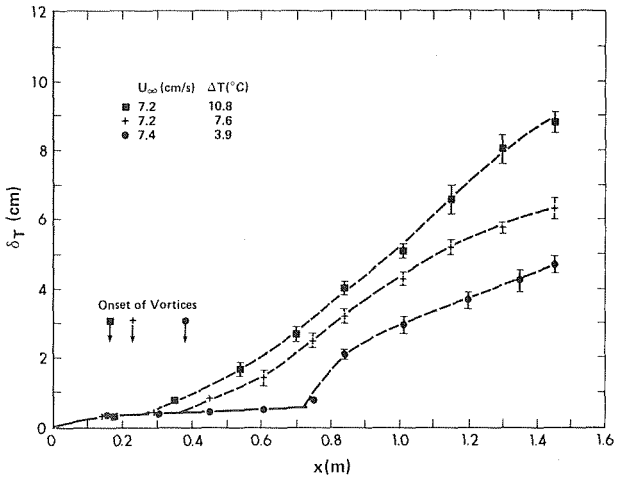

Fig. 3 The effect of temperature difference on thermal boundary layer growth

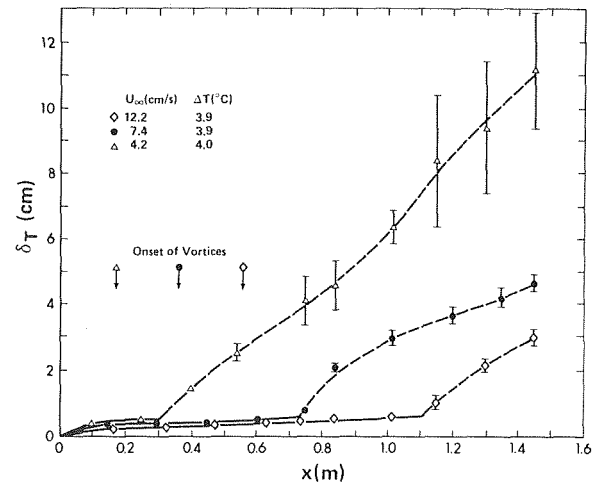

Fig. 4 The effect of free stream velocity on thermal boundary layer growth

free stream velocity and Fig. 4 shows the effect of varying free stream velocity at a constant temperature difference. In each figure the approximate position for the onset of longitudinal vortices as determined in [2] is also indicated. It will be noted that the onset of vortices in the boundary layer is not associated with any immediate increase in the rate of boundary layer growth. However, downstream from the onset point a rather sharp increase in the rate of growth of the boundary layer is observed. The photograph at the top of Fig. 1 shows that this increased rate of boundary layer growth is associated with the development of turbulence in the boundary layer. The measurement of the boundary layer growth therefore provides a measure of the "second transition" in the boundary layer, the transition from longitudinal vortices to turbulent flow. For the higher velocities the transition flow regime between the onset of vortices and the development of a turbulent boundary layer can be quite lengthy. For example, in Fig. 4 at a velocity of 12.2 cm/s the onset of vortices is observed at 56 cm from the leading edge of the plate but the development of turbulent boundary layer growth does not occur until about 110 cm. The error bars on the boundary layer thickness shown in Figs. 3 and 4 give a measure of the uncertainty in the thickness that results from the unsteady nature of the plumes rising in the turbulent regime. The observations of the position of the transition to turbulence in the boundary layer will be used primarily to interpret the measured heat transfer coefficients to follow.

4.3 **Heat Transfer Coefficients.** Figs. 5 and 6 show the heat transfer coefficients calculated from the temperature gradient at the wall for the same conditions as used in Figs. 3 and 4, respectively. It can be seen that the heat transfer coefficients measured near the plate's leading edge ($x = 0$) initially fall along the expected curve for laminar forced convection (solid curves in the figures). At some point slightly downstream of the onset of vortices the heat transfer coefficient undergoes a sudden rise. This is interpreted as being the result of finite amplitude secondary flow in the boundary layer. After this sudden rise, the heat transfer coefficients in most cases settle down to a value which is constant to within the accuracy of the measurement technique (about ±15 percent). In the case of $U_\infty = 12.2$ cm/s and $\Delta T = 3.9°C$ (Fig. 6) the heat transfer coefficient is still increasing with x at $x = 1.45$ m. Perhaps with a longer test surface the data for this case would also have shown a leveling out.

A comparison of the figures shows that the sudden rise in heat transfer coefficients in Figs. 5 and 6 occurs before the onset of turbulent growth of the boundary layer thickness observed in Figs. 3 and 4. This latter phenomenon correlates most closely with the establishment of a heat transfer coefficient that is constant along the plate.

4.4 **Heat Transfer Correlations.** The heat transfer coefficients measured on the plate were written in the form of a Nusselt number, $h_x x/k$, and are plotted in Fig. 7 against Reynolds number. These are, of course, the normal correlation parameters for forced convection. For the case of pure forced convection the transition from laminar to turbulent convection occurs at around $Re_x = 10^5$, the exact value depending on the magnitude of the free stream turbulence [20]. After transition has occurred the heat transfer coefficients have normally been found to be as predicted by the von Karman analogy [17].

For the present case where strong buoyancy effects are present, deviation from the laminar forced convection correlation can occur at much lower Reynolds numbers. Also it is apparent in Fig. 7 that, although the Nusselt numbers in the turbulent flow regime are of the same order of magnitude as those predicted for turbulent forced convection, they are not correlated by the forced convection parameters Nu_x and Re_x in the Reynolds number range which was investigated, $Re_x < 2 \times 10^5$.

For combined free and forced laminar convection in a two-dimensional boundary layer [9, 12] the relative importance of free convection over forced convection is represented by the correlation parameter $Gr_x/Re_x^{2.5}$. These theories show that for $Pr = 10$ a maximum of a 5 percent increase in Nusselt number could be expected when $Gr_x/Re_x^{2.5} = 0.14$ for a two-dimensional boundary layer (solid line in Fig. 8). The ratio of the measured Nusselt number to the pure laminar forced convection value, $(Nu_x)_0$, has been plotted in this figure. The sharp divergence of the measured results from the theoretical curve is the result of the onset of secondary flow vortices in the boundary layer. It can be seen that the range of applicability of the two-dimensional theory is restricted to rather small values of the parameter $Gr_x/Re_x^{2.5}$. Also it is apparent that this parameter is not adequate to correlate the heat transfer results after the onset of the vortices.

Thermal instability theory [1] suggests that the onset of longitudinal vortices in a Blasius flow occurs at a critical value of the Grashof

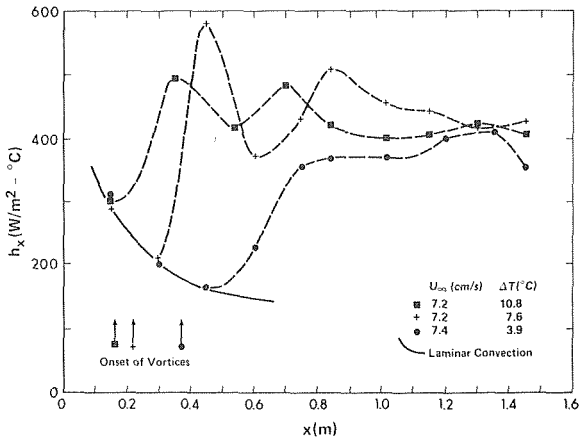

Fig. 5 The effect of temperature difference on plate heat transfer coefficients

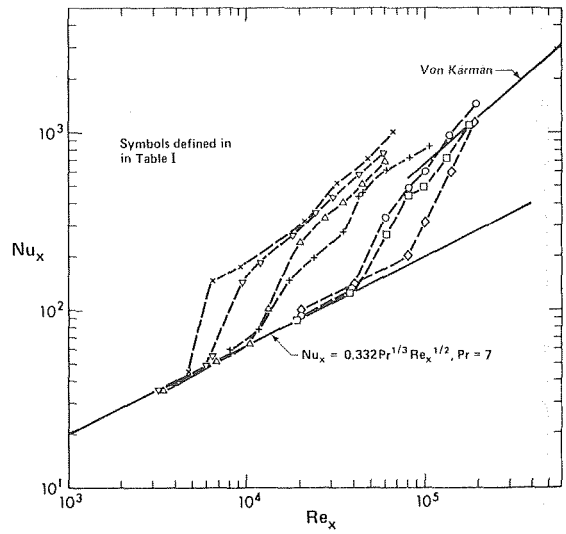

Fig. 7 Relationship between Nu_x and Re_x

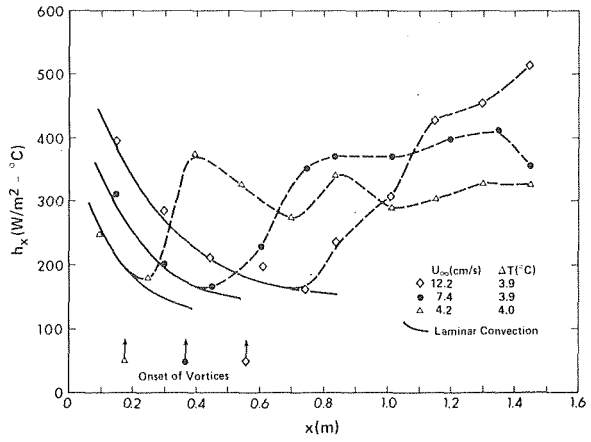

Fig. 6 The effect of free stream velocity on plate heat transfer coefficients

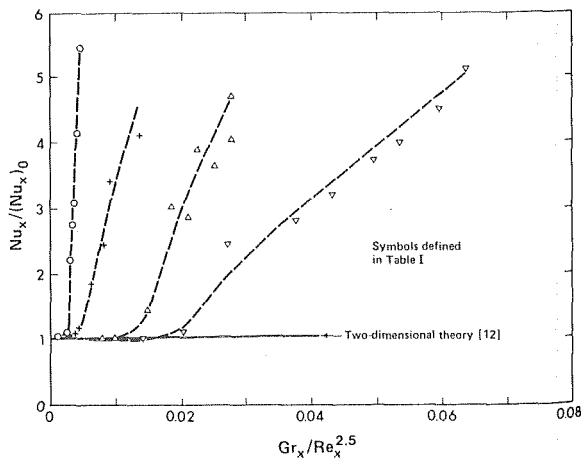

Fig. 8 Heat transfer results plotted against the parameter $Gr_x/Re_x^{2.5}$

number based on the characteristic thickness of the boundary layer. In terms of the distance x from the leading edge of the plate this parameter is $Gr_x/Re_x^{1.5}$. Experiments [2] confirmed that the critical value for a boundary layer developing in water over an isothermally heated, horizontal plate was approximately 100. It was therefore anticipated that this parameter may also be useful in correlating the heat transfer results in the post-critical regime. In Fig. 9, $Nu_x/Re_x^{0.5}$ is plotted as a function of the parameter $Gr_x/Re_x^{1.5}$ using all the experimental data from the nine test conditions in Table 1. In this figure the three flow regimes, laminar forced convection, transition and turbulent free convection, can clearly be identified. For values of $Gr_x/Re_x^{1.5} < 100$, that is before the onset of vortices, the heat transfer is given by the well-known Pohlhausen relationship, $Nu_x = 0.332\ Pr^{1/3}Re_x^{1/2}$, for a laminar forced convection boundary layer.

The transition regime corresponds to values of $Gr_x/Re_x^{1.5}$ between 100 and approximately 300. In this regime the sharp rise in heat transfer coefficients observed in Figs. 5 and 6 occurs and the turbulent growth of the boundary layers as seen in Figs. 3 and 4 begins.

For $Gr_x/Re_x^{1.5} > 300$ the data in Fig. 9 follow a line with approximately a one-third slope. Such a line on this figure represents a Nusselt number which is Reynolds number independent and is characteristic of turbulent free convection over a heated horizontal surface in the absence of a main flow. For such a surface Fishenden and Saunders [21] have recommended a correlation

$$Nu_\ell = 0.14\ (Gr_\ell Pr)^{1/3} \tag{1}$$

for free convection in the turbulent domain where ℓ is a characteristic length of the heating surface. More recently Fujii and Imura [22] have suggested a similar correlation with a constant of 0.13 instead of 0.14. The expression

$$Nu_x = 0.13\ (Gr_x Pr)^{1/3} \tag{2}$$

is plotted in Fig. 9 and can be seen to correlate the data satisfactorily.

In Fig. 9 the range in the local Nusselt number is indicated for some of the data points by a vertical bar. This range was obtained from measurements of the fluctuation of temperature gradient recorded at the plate surface. In the transition regime this Nusselt number range is associated with the variation in heat transfer coefficients across the vortex rolls. In the turbulent regime it is associated with the basic unsteady nature of the flow. The very substantial magnitude of the local fluctuation of the heat transfer coefficient is apparent from this data.

5 Concluding Remarks

At Reynolds numbers below that at which hydrodynamic instabilities are important it was found that buoyancy induced instabilities can dominate the flow behavior. In the present investigation the effects of buoyancy were studied on the growth of a thermal boundary layer over a horizontal isothermally heated plate. The flow pattern in this case could be characterized by three flow regimes, the boundaries between these regimes being defined by critical values of the instability parameter $Gr_x/Re_x^{1.5}$.

For values of $Gr_x/Re_x^{1.5} < 100$ the effects of buoyancy are negligible for all practical purposes. In this regime the heat transfer coefficients can be obtained form the Pohlhausen or similar solution for a laminar boundary layer. Alternatively for $Gr_x/Re_x^{1.5} > 300$ turbulent free convection dominates. In this turbulent regime the local Nusselt number increases with the Rayleigh number ($Gr_x Pr$) in a manner similar to that for a horizontal plate with no main flow in the high Rayleigh number range. This means that the forced convection effects are negligible in this regime.

The range $100 < Gr_x/Re_x^{1.5} < 300$ is a complex transition regime where combined effects of free and forced convection influence the flow. The details of this flow regime have not been studied; however, the basic phenomena occurring in the regime can be outlined. As studied in [2], the onset of the thermal instability in the boundary layer occurs at a value of $Gr_x/Re_x^{1.5}$ approximately equal to 100 and manifests itself in the form of longitudinal vortices. The longitudinal vortices produce finite amplitude secondary flows which give rise to a substantial increase in the wall heat transfer rates. As the boundary layer grows thicker the vortices do not remain as the stable flow pattern but begin to break up into a more turbulent-like flow. The mechanism of the breakup was not studied but one may suspect that the secondary and tertiary instabilities observed by Wortmann [6] for longitudinal vortices on a concave wall may be involved. At the onset of turbulence, thermal plumes were seen to separate and rise from the plate. This results in the rapid increase in the boundary layer growth rate observed at transition to turbulence. After the transition the heat transfer coefficient becomes constant along the plate, indicative of the turbulent free convection regime.

In the theoretical treatment of the problem of combined free and forced convection above a horizontal plate the buoyancy effects are introduced into a two-dimensional boundary layer model [11]. This results in the forced and free convection regimes being defined in terms of the parameter $Gr_x/Re_x^{2.5}$. The present investigation has shown that the buoyancy effects produce finite amplitude secondary flows which make the two-dimensional formulation and the parameter $Gr_x/Re_x^{2.5}$ inadequate to describe the flow after the onset of instability. The range of applicability of this theory is therefore rather limited. These results would suggest that for a theory adequately to predict the heat transfer behavior in the combined free and forced convection regime it must be able to account for the non-linear effects of finite amplitude vortex rolls.

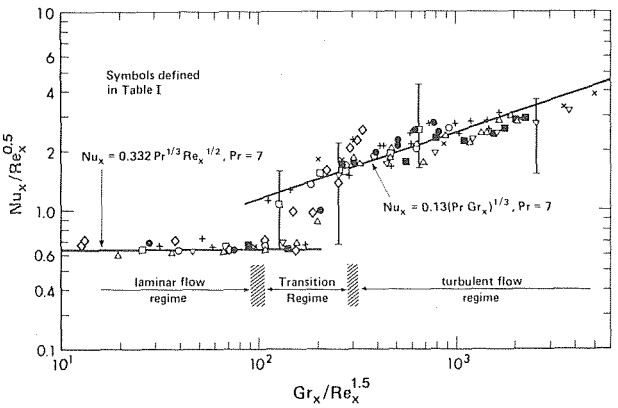

Fig. 9 Heat transfer results correlated with the parameters $Nu_x/Re_x^{0.5}$ and $Gr_x/Re_x^{1.5}$

Acknowledgment

This work was supported by the National Research Council of Canada.

References

1 Wu, R. S. and Cheng, K. C., "Thermal Instability of Blasius Flow along Horizontal Plates," *International Journal of Heat and Mass Transfer*, Vol. 19, 1976, pp. 907–913.

2 Gilpin, R. R., Imura, H. and Cheng, K. C., "Experiments on the Onset of Longitudinal Vortices in Horizontal Blasius Flow Heated from Below," ASME JOURNAL OF HEAT TRANSFER, Vol. 100, 1978, pp. 71–77.

3 Görtler, H., "Über eine Analogie zwischen den Instabilitäten laminarer Grenzschichtströmungen an konkaven Wänden und an erwärmsten Wänden," *Ingenieur-Archiv*, Vol. 28, 1959, pp. 71–78.

4 Tani, I., "Production of Longitudinal Vortices in the Boundary Layer along a Concave Wall," *J. Geophys. Res.*, Vol. 67, 1962, pp. 3075–3080.

5 Smith, A. M. O., "On the Growth of Taylor-Goertler Vortices along Highly Concave Wall," *Quarterly of Applied Mathematics*, Vol. 8, 1955, pp. 233–262.

6 Wortmann, F. X., "Visualization of Transition," *J. Fluid Mech.*, Vol. 38, 1969, pp. 473–480.

7 Bippes, H. and Görtler, H., "Dreidimensionale Störungen in der Grenzschicht an einer konkaven Wand," *Acta Mechanica*, Vol. 14, 1972, pp. 251–267.

8 Pohlhausen, E., "Der Wärmeaustausch zwischen festen Körpern und Flüssigkeiten mit kleiner Reibung and kleiner Wärmeleitung," *Zeitschrift für angewandte Mathematik und Mechanik*, Vol. 1, 1921, pp. 115–120.

9 Mori, Y., "Buoyancy Effects in Forced Laminar Convection Flow over a Horizontal Flat Plate," ASME JOURNAL OF HEAT TRANSFER, Vol. 83, 1961, pp. 479–482.

10 Sparrow, E. M. and Minkowycz, W. J., "Buoyancy Effects on Horizontal Boundary Layer Flow and Heat Transfer," *International Journal of Heat and Mass Transfer*, Vol. 5, 1962, pp. 505–511.

11 Hieber, C. A., "Mixed Convection Above a Heated Horizontal Surface," *International Journal of Heat and Mass Transfer*, Vol. 16, pp. 769–785.

12 Chen, T. S., Sparrow, E. M. and Mucoglu, A., "Mixed Convection in Boundary Layer Flow on a Horizontal Plate," ASME JOURNAL OF HEAT TRANSFER, Vol. 99, 1977, pp. 66–71.

13 Mori, Y. and Uchida, Y., "Forced Convective Heat Transfer Between Horizontal Plates," *International Journal of Heat and Mass Transfer*, Vol. 9, 1966, pp. 803–817.

14 Ostrach, S. and Kamotani, Y., "Heat Transfer Augmentation in Laminar Fully Developed Channel Flow by Means of Heating form Below," ASME JOURNAL OF HEAT TRANSFER, Vol. 97, 1975, pp. 220–225.

15 Kamotani, Y. and Ostrach, S., "Effect of Thermal Instability on Thermally Developing Laminar Channel Flow," ASME JOURNAL OF HEAT TRANSFER, Vol. 98, 1976, pp. 62–66.

16 McCormack, P. D., Welker, H. and Kelleher, M., "Taylor-Goertler Vortices and Their Effect on Heat Transfer," ASME JOURNAL OF HEAT TRANSFER, Vol. 92, 1970, pp. 101–112.

17 von Kármán, T., "The Analgoy Between Fluid Friction and Heat Transfer," *Trans. ASME*, Vol. 61, 1939, pp. 705–710.

18 Prandtl, L., "Eine Beziehung zwischen Wärmeaustausch und Strömungswiderstand der Flüssigkeiten," *Physik. Zeitschr.*, Vol. 11, 1910, pp. 1072–1078.

19 Fujii, T., Takeuchi, M., Fujii, M., Suzaki, K. and Uehara, H., "Experiments on Natural-Convection Heat Transfer from the Outer Surface of a Vertical Cylinder to Liquids," *International Journal of Heat and Mass Transfer*, Vol. 13, 1970, pp. 753–787.

20 Kestin, J., Meader, P. F. and Wang, H. E., "Influence of Turbulence on the Transfer of Heat from Plates with and without a Pressure Gradient," *International Journal of Heat and Mass Transfer*, Vol. 3, 1961, pp. 133–154.

21 Fishenden, M. and Saunders, O. A., *An Introduction to Heat Transfer*, Oxford University Press, 1957, p. 97.

22 Fujii, T. and Imura, H., "Natural-Convection Heat Transfer from a Plate with Arbitrary Inclination," *Int. J. Heat Mass Transfer*, Vol. 15, 1972, pp. 755–767.

E. J. Shaughnessy
Assistant Professor,
Mem. ASME

J. Custer
Graduate Student,
Assoc. Mem. ASME

Department of Mechanical Engineering
and Materials Science,
Duke University,
Durham, N. C. 27706

R. W. Douglass
Assistant Professor,
Department of Mechanical Engineering,
University of Nebraska,
Lincoln, Neb. 68588
Assoc. Mem. ASME

Partial Spectral Expansions for Problems in Thermal Convection

The use of spectral expansions for solving nonlinear partial differential equations is explained, and two examples drawn from convective heat transfer are presented. For both problems the results agree well with regular perturbation solutions at parameter values for which the latter remain valid. Evidence is given to indicate that the spectral solutions are valid for considerably larger parameter values than can be reached with the perturbation methods.

1 Introduction

Spectral methods have undergone an interesting development since they were first described by Galerkin [1] for a problem in elasticity. Meteorologists in particular have long favored these methods for modeling the behavior of the earth's atmosphere despite rather severe computer time and storage problems encountered in nonlinear problems. Because of these difficulties, spectral methods have not been extensively used in problems of fluid mechanics and heat transfer, but the situation is changing rapidly. In a recent series of papers, Orszag [2–5] has demonstrated that, in three-dimensional flows, properly implemented spectral methods require about an order of magnitude less computer time and storage than finite difference methods of comparable accuracy. This economy is achieved through the use of transform techniques for the efficient evaluation of the spectral equations. One of the early applications of the method was made by Munson [6], who investigated the axisymmetric flow between rotating spheres. Though not using transforms, Munson was successful in generating solutions for Reynolds numbers up to transition. Orszag and his associates (Orszag [7], Israeli [8], Metcalfe [9], Orszag and Israeli [10, 11], Orszag and Pao [12]) have since used the spectral method in a variety of problems in fluid mechanics. Douglass [13], Custer [14], and Custer and Shaughnessy [15] have employed the technique in problems of thermal convection.

This paper relates the experience of the authors in applying partial spectral expansions to thermal convection problems in spheres and cylinders. We consider steady, two-dimensional motion with periodic angular dependence. The flow variables are expanded in basis functions of the angle with coefficients which are functions of the radial coordinate. Galerkin's procedure is used to produce a coupled set of nonlinear ordinary differential equations for the coefficient functions. The system of differential equations with associated boundary values constitutes a two-point boundary value problem which is solved numerically. Since the transform methods offer no real advantage in economy for the series employed here, we have evaluated the spectral equations directly. In calculations involving larger spectral series, the complicated programming required for the transform techniques is more than offset by the resulting efficiency.

In Section 2 the spectral solution method is outlined and used in Section 3 to calculate the natural convection of a liquid metal in a horizontal cylindrical annulus. Solutions are obtained for the case in which the walls of the annulus are maintained at different temperatures. The results are shown to agree well with a perturbation solution. Section 4 considers the more complex convection problem in a rotating spherical annulus. In this case the velocity of the fluid must match the angular velocity of the rotating boundaries. This difficult boundary condition is easily handled by the partial spectral method. Where appropriate, the solutions are compared to a perturbation solution at low rotation rates and with the results of Munson [6] and Pearson [16].

2 The Method of Partial Spectral Expansions

To illustrate the basic theory and problem preparation of the spectral method, we consider the boundary value problem

$$L_1\psi(x_1, x_2) + G(\psi, T, x_1, x_2) = 0$$
$$L_2T(x_1, x_2) + H(\psi, T, x_1 x_2) = 0 \qquad (1)$$

where L_1, L_2 are linear partial differential operators and G, H are nonlinear functions of the dependent variables ψ, T, as well as x_1, x_2. The solution is sought in some domain D subject to separable boundary conditions for ψ and T. We seek an approximate solution to this problem in the form

Contributed by the Heat Transfer Division for publication in the JOURNAL OF HEAT TRANSFER. Manuscript received by the Heat Transfer Division November 15, 1977.

$$\psi(x_1, x_2) = \sum_{i=0}^{N} g_i(x_1)\phi_i(x_2)$$

$$T(x_1, x_2) = \sum_{j=0}^{N} h_j(x_1)\phi_j(x_2) \tag{2}$$

where the basis functions $\phi_i(x_2)$ form a complete set in the space spanned by x_2 and allow satisfaction of the boundary conditions for ψ and T. The functions $g_i(x_1)$ and $h_j(x_1)$ are unknown functions, to be determined.

The first question facing a potential user of this method is how to choose the basis functions $\phi_i(x_2)$. Orszag [4] suggests that Chebyshev or Legendre polynomials are the best choice for spatial variables, while trigonometric functions are superior for angular variables. The reason for selecting these functions rather than the eigenfunctions of the operators L_1 and L_2 is that the error incurred in retaining N terms in the recommended expansions decreases faster than any power of $1/N$ as N increases. Orszag terms this "infinite order" accuracy. Other choices for the basis functions lead to finite order accuracy. For example, if the error decreases as $1/N^2$, then the expansion has second order accuracy.

Inserting the expansions for ψ, T into the governing equations leads to equations of the form

$$\sum_{i=0}^{N} (L_1\{g_i(x_1)\phi_i(x_2)\} + G(g_i, h_j, \phi_i, \phi_j, x_1, x_2)) = 0$$

$$\sum_{j=0}^{N} (L_2\{h_j(x_1)\phi_j(x_2)\} + H(g_i, h_j, \phi_i, \phi_j, x_1, x_2)) = 0$$

The boundary conditions are similarly treated. The final step in the method is to project the above equations into the space spanned by the basis functions. In the Galerkin method, the projection is accomplished by taking the inner product of the equations with each of the ϕ_i. The result is a set of $2N$ ordinary differential equations describing the behavior of the $2N$ unknown functions $g_i(x_1)$, $h_j(x_1)$. The boundary conditions are treated similarly, leading to $2N$ boundary values for the g_i, h_j.

To complete the solution, the set of $2N$ coupled, nonlinear equations must be solved numerically. In convection problems this two-point boundary value problem will often be so sensitive that simple shooting methods will not work. The authors have had some success in such cases with the method of quasi-linearization (Roberts and Shipman [17]), and expect that finite difference methods would work equally well. Once the functions g_i, h_j are obtained, approximate solutions for ψ and T are easily constructed. It is worth noting that there are many variations on the above procedure. For example, a three-dimensional problem might be solved by expanding in one independent variable, followed by a finite difference solution to the resulting set of two-dimensional problems. This approach is particularly attractive for problems in cylindrical coordinates. In the next two sections the partial spectral method is applied to two problems in thermal convection.

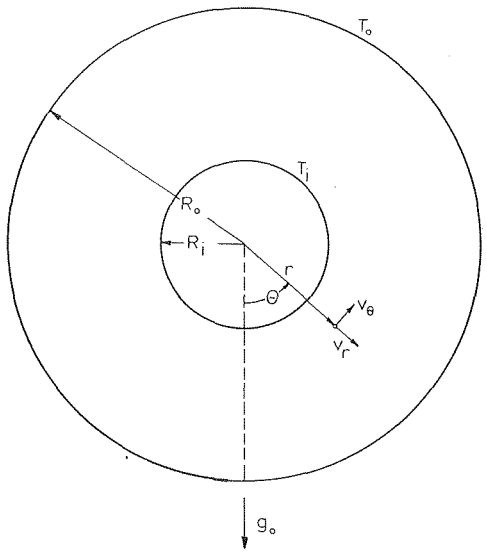

Fig. 1 Cylindrical flow geometry

3 Convection in a Cylindrical Annulus

The problem of natural convection in a horizontal cylindrical annulus has attracted the attention of numerous investigators because of the relative simplicity of the geometry, the practical applications, and the surprising complexity of flow phenomena which appear. A considerable amount of experimental data have been taken since the first efforts by Beckman [18], and a number of analytical studies have also been made. The interested reader may consult the bibliography of Kuehn and Goldstein [19] for further details. In this section we apply the Galerkin method to the problem of natural convection in liquid metals contained in a horizontal cylindrical annulus. The problem has application to the use of liquid metals as heat transfer agents in power plants under conditions of loss of pumping. Due to experimental difficulties associated with liquid metals, few observations of this flow are available. Thus analytical results are of great value.

The geometry for this flow is shown in Fig. 1. The gap between the cylinders is filled with a viscous fluid which is set in motion by the temperature difference across the annulus. The inner and outer cylinders are maintained at the uniform temperatures T_i and T_0, and gravity is assumed to act vertically as shown. The flow is assumed to be steady, laminar and two-dimensional. Experiments have shown

Nomenclature

C_p = specific heat at constant pressure of the fluid
$\tilde{D}^2$, $\tilde{D}^4$ = operators in spherical coordinates
f_n, g_n, h_n = radial functions in the spectral series
G, H = generalized nonlinear functions
g_0 = gravitational constant
Gr = Grashof number
k = thermal conductivity of the fluid
L_1, L_2 = generalized linear operators
N = number of terms in the spectral series
$P_n(\theta)$ = Legendre polynomial of the first kind
Pr = Prandtl number
r = radial coordinate
Re = Reynolds number
R_1, R_2 = spherical radii
R_i, R_0 = cylindrical radii
T = temperature function
T_1, T_2 = temperatures of the spheres
T_i, T_0 = temperatures of the cylinders
v_r, v_θ = velocity components in cylindrical coordinates
v_r, v_θ, v_ϕ = velocity components in spherical coordinates
x_1, x_2 = generalized coordinates
α = thermal diffusivity of the fluid
β = coefficient of thermal expansion of the fluid
ζ = nondimensional temperature function
η = radius ratio
θ = angular coordinate
μ = absolute viscosity of the fluid
$\tilde{\mu}$ = angular velocity ratio
ν = kinematic viscosity of the fluid
ρ = density of the fluid
ϕ = angular coordinate
ϕ_i = spectral basis function
ψ = streamfunction
ω_0 = reference angular velocity
ω_1, ω_2 = angular velocity of the spheres
Ω = nondimensional angular velocity function
∇^2, ∇^4 = Laplacian and biharmonic operators

that for fluids with Prandtl numbers of order one or larger, there is a range of gap widths and temperature differences for which a steady, laminar, two-dimensional flow exists. In the absence of experimental data for liquid metals, we assume that this is true for these fluids as well. In formulating the equations of motion viscous dissipation is neglected, all fluid properties except the density are assumed constant, and density variations are modeled with the Boussinesq approximation (Chandrasekhar, [20]).

The motion is measured in cylindrical coordinates (r, θ) with (v_r, v_θ) the corresponding velocity components. The equations of motion are written in terms of the stream function $\psi(r, \theta)$ defined by the relations

$$v_\theta = -\frac{\partial \psi}{\partial r},$$

and

$$v_r = \frac{1}{r}\frac{\partial \psi}{\partial \theta}. \tag{4}$$

The equations are nondimensionalized using R_0 and $T_0 - T_i$ as the characteristic length and temperature scales. The stream function is nondimensionalized by ν, the kinematic viscosity of the fluid. This scaling leads to the following nondimensional equations of motion:

$$\nabla^4\psi = \frac{1}{r}\left[\frac{\partial\psi}{\partial\theta}\frac{\partial(\nabla^2\psi)}{\partial r} - \frac{\partial\psi}{\partial r}\frac{\partial(\nabla^2\psi)}{\partial\theta}\right] + \mathrm{Gr}\left[\frac{\cos\theta}{r}\frac{\partial T}{\partial\theta} + \sin\theta\frac{\partial T}{\partial r}\right],$$

and

$$\nabla^2 T = \frac{\mathrm{Pr}}{r}\left[\frac{\partial\psi}{\partial\theta}\frac{\partial T}{\partial r} - \frac{\partial\psi}{\partial r}\frac{\partial T}{\partial\theta}\right]. \tag{5}$$

The dimensionless parameters here are the Grashof number $\mathrm{Gr} = g_0\beta(T_0 - T_i)R_0^3/\nu^2$ and the Prandtl number $\mathrm{Pr} = \nu/\alpha$, where β is the coefficient of thermal expansion, ν the kinematic viscosity, and α is the thermal diffusivity of the fluid. The operators ∇^2 and ∇^4 are the harmonic and biharmonic operators expressed in cylindrical coordinates.

The boundary conditions on the problem are that the fluid velocity be zero on the cylindrical boundaries, and that the fluid temperature equal the appropriate wall temperature. In addition the flow is assumed to be symmetrical about the vertical plane through the axis of rotation. In terms of the nondimensional variables these conditions are

$$\psi(\eta, \theta) = \psi(1, \theta) = 0,$$

$$\frac{\partial\psi}{\partial r}(\eta, \theta) = \frac{\partial\psi}{\partial r}(1, \theta) = \frac{\partial\psi}{\partial\theta}(\eta, \theta) = \frac{\partial\psi}{\partial\theta}(1, \theta) = 0,$$

and

$$T(\eta, \theta) = 1, \quad T(1, \theta) = 0. \tag{6}$$

The domain of the independent variables is $\eta \le r \le 1$, and $0 \le \theta \le 2\pi$. The parameter $\eta = R_i/R_0$ is the radius ratio of the cylinders.

The solution to this problem was obtained by assuming expansions for $\psi(r, \theta)$ and $T(r, \theta)$ of the form

$$\psi(r, \theta) = \sum_{n=1}^{\infty} f_n(r)\sin(n\theta),$$

and

$$T(r, \theta) = \sum_{p=0}^{\infty} g_p(r)\cos(p\theta). \tag{7}$$

As discussed earlier, the choice of a trigonometric expansion of the angular dependence is recommended by Orszag [4] for best accuracy. These expansions also have the desired property of reflection about the vertical plane.

Since one can only retain a finite number of terms in the spectral expansion (7), these series are truncated after N terms. The number of functions kept is determined by various factors including prior knowledge of the flow, accuracy requirements, and the cost of numerical solutions. Here the choice was made to truncate the series after three terms. Thus the representations actually used are

$$\psi(r, \theta) = f_1(r)\sin\theta + f_2(r)\sin 2\theta + f_3(r)\sin 3\theta,$$

and

$$T(r, \theta) = g_0(r) + g_1(r)\cos\theta + g_2(r)\cos 2\theta + g_3(r)\cos 3\theta \tag{8}$$

This choice is partially motivated by the knowledge [19, 21] that in air and water the streamlines at moderate Grashof numbers take the form shown in Fig. 2. These crescent shaped flows can be described mathematically by the first term $f_1(r)\sin\theta$. The three terms together then allow solutions for moderately large Grashof numbers to be obtained at a reasonable cost in computer time and storage. Equations for the unknown functions $f_n(r)$ and $g_p(r)$ are obtained by substituting the expansions (8) into the equations of motion (5). The result is

$$\sum_{n=1}^{3}\left[f_n'''' + \frac{2}{r}f_n''' - \frac{2n^2+1}{r^2}f_n'' + \frac{2n^2+1}{r^3}f_n' + \frac{n^4-4n^2}{r^4}f_n\right]\sin n\theta = \frac{1}{r}\left\{\sum_{n=1}^{3}\sum_{m=1}^{3}\left[mf_m\left(f_n''' + \frac{1}{r}f_n'' - \frac{n^2+1}{r^2}f_n' + \frac{2n^2}{r^3}f_n\right)\cos m\theta\sin n\theta\right] - \sum_{j=1}^{3}\sum_{k=1}^{3}\left[jf_k'\left(f_j'' + \frac{1}{r}f_j' - \frac{j^2}{r^2}f_j\right)\cos j\theta\sin k\theta\right]\right\} + \mathrm{Gr}\left\{\sum_{p=0}^{3}\left[g_p'\cos p\theta\sin\theta\right] - \sum_{\ell=1}^{3}\left[\frac{\ell}{r}g_\ell\sin\ell\theta\cos\theta\right]\right\}, \tag{9a}$$

and

$$\sum_{n=0}^{3}\left[g_n'' + \frac{1}{r}g_n' - \frac{n^2}{r^2}g_n\right]\cos n\theta = \frac{\mathrm{Pr}}{r}\left\{\sum_{n=0}^{3}\sum_{m=1}^{3}\left[mg_n'f_m\cos n\theta\cos m\theta\right] + \sum_{j=0}^{3}\sum_{k=1}^{3}\left[jf_k'g_j\sin j\theta\sin k\theta\right]\right\} \tag{9b}$$

where the primes signify derivatives with respect to r.

The equations (9a,b) are projected into the spaces spanned by $\sin(n\theta)$ and $\cos(p\theta)$ using Galerkin's method. The equations for the $f_n(r)$ are obtained by multiplying equation (9,a) by $(1/\pi)\sin(n\theta)$ and integrating over the interval $(0, 2\pi)$. The equations for the $g_n(r)$ are obtained by multiplying (9,b) by $(1/\pi)\cos(p\theta)$ and integrating.

The boundary conditions for this system of equations are obtained by substituting the expansions (8) into the boundary conditions (6), and using the projection technique just described. The results are

$$f_n(\eta) = f_n(1) = 0,$$

$$f_n'(\eta) = f_n'(1) = 0 \quad n = 1, 2, 3$$

$$g_0(\eta) = 1 \quad g_0(1) = 0,$$

and

$$g_n(\eta) = g_n(1) = 0 \quad n = 1, 2, 3. \tag{10}$$

Solutions to this system of equations were obtained using the method of quasi-linearization. This method generates linear differential equations by expanding the original nonlinear equations in a Taylor series about a nominal solution. These series are truncated after the first order terms. The resulting set of linear differential equations was solved with the method of adjoints. The quasi-linearization scheme proceeds iteratively using the solutions from one step as the nominal solution used to evaluate the derivatives in the next step. Conditons under which the solutions of the linear problems converge to the solution of the original nonlinear problem have been stated in the work by Roberts and Shipman [17].

Typical results obtained from the calculations are shown in Fig. 2.

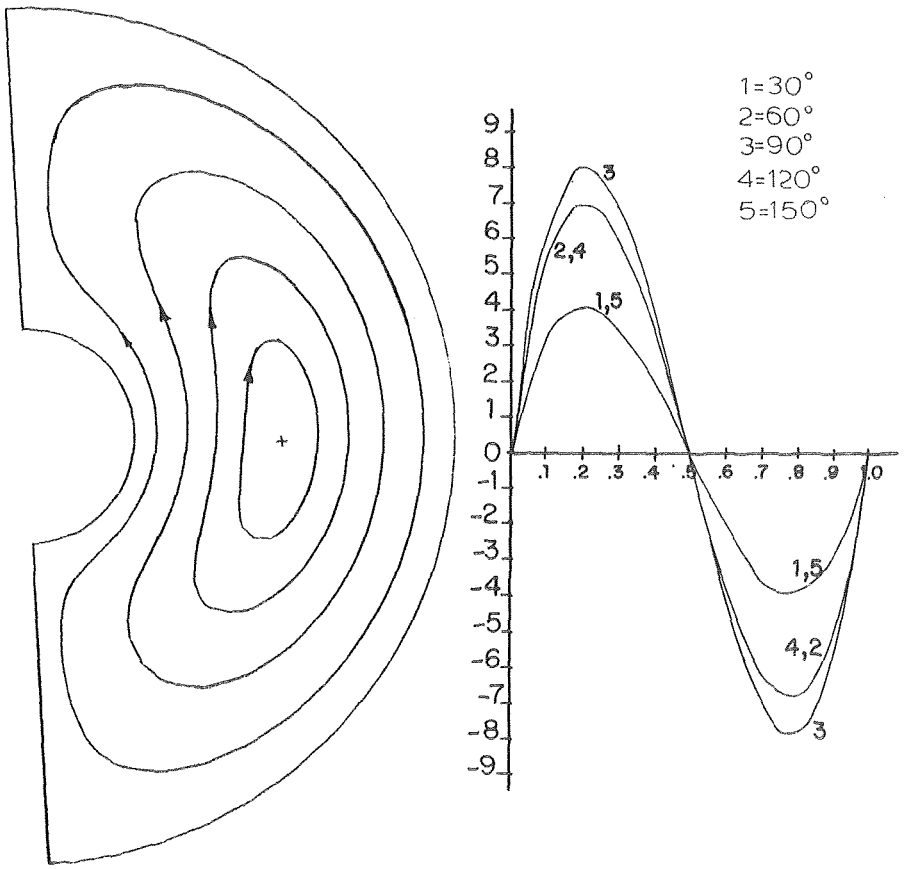

Fig. 2 Streamlines and circumferential velocity profiles in the cylindrical annulus for $\eta = 0.25$, Pr = 0.01, and Gr = 100

The streamline plots all show a characteristic single eddy pattern which occurred for all Grashof numbers for which numerical solutions could be obtained. This is a striking contrast to results obtained by Mack and Bishop [22] using a perturbation method. For $\eta = 0.5$, Pr = 0.02 and Gr = 15000 they found a multicellular flow composed of one large eddy and two smaller and weaker counter-rotating eddies. The large eddy rotates clockwise and occupies the region of the annulus between $\theta = 25$ deg and $\theta = 140$ deg. The two smaller eddies occupy the top and bottom of the annulus. The conditions necessary for the formation of these multiple eddies were determined. It was found that for a Prandtl number of 0.02 both eddies form when the radius ratio is greater than or equal to 1.55. Fluids with Prandtl number 0.07 and 0.3 behave similarly. In an effort to investigate these interesting flows computations were carried out with Pr = 0.1. With this Prandtl number successful calculations could be made at Grashof numbers which yield Rayleigh numbers in the range appropriate to multicellular flows. In all cases the single crescent eddy was the only flow pattern found.

Careful examinations of the reasons for this discrepancy were carried out by Custer [14] and Custer and Shaughnessy [15, 23]. Using the premise that the $(n + 1)$th term of a perturbation expansion should be a small correction to the solution represented by the first n terms, they tested the multiple eddy flows predicted by the perturbation methods. In each case the highest order term in the perturbation expansion was of the same order as the sum of the previous terms, indicating that more terms should be included in the expansions. This test is not conclusive, however, as indicated in Custer and Shaughnessy [23], and work is now in progress using a spectral expansion containing additional terms in an attempt to determine what causes the multicellular flow. For small Grashof numbers, the streamlines calculated with the three term spectral expansions agree with those obtained using Mack and Bishop's perturbation method. Thus the occurrence of steady multicellular flow may be a feature of the linearized equations at large Grashof numbers which is not present in the truncated nonlinear equations. A second interesting possibility is the presence of a transition mechanism which depends on the Prandtl number. It is hoped that further work will answer this question.

4 Convection in a Rotating Spherical Annulus

In this section the steady laminar motion of an incompressible viscous fluid contained between two concentric spheres which rotate about a common axis with fixed but different angular velocities is discussed. Each sphere is maintained at a uniform but different temperature. Spherical annulus flows of this type are of interest in both engineering and geophysics, as well as being a comparatively simple example of the interaction of buoyancy and centrifugal forces. An extensive bibliography on this type of flow appears in Douglass [13].

The geometry for this flow is shown in Fig. 3. A viscous fluid fills the gap between the inner and outer spheres which are of radii R_1 and R_2, have uniform temperatures T_1 and T_2, and rotate about a common axis with constant angular velocities ω_1 and ω_2. A positive angular velocity denotes clockwise rotation looking in the direction indicated on the polar axis. Both the magnitude and sign of each angular velocity are arbitrary; if ω_1 and ω_2 differ in sign, the spheres are counter-rotating. A uniform gravitational field of magnitude g_0 is assumed to act towards the center of the spheres. In formulating the equations of motion, viscous dissipation is neglected, all fluid properties except the density are assumed constant, and density variations are modeled with the Boussinesq approximation (Chandrasekhar, [20]).

The motion is measured in spherical coordinates (r, θ, ϕ) fixed in space, with (v_r, v_θ, v_ϕ) the corresponding velocity components. The angular coordinate θ is measured from the polar axis, while ϕ is the azimuthal angle. Solutions are sought which are steady, independent of ϕ, and symmetric about the equator $\theta = \pi/2$. Because of these symmetries the results are presented in the upper portion of a meridian plane only.

The dimensionless equations of motion are conveniently formulated in terms of a stream function ψ, an angular velocity function Ω, and a temperature function ζ (Douglass, [13]):

$$\frac{1}{\mathrm{Re}}\tilde{D}^2\Omega = \frac{1}{r^2\sin\theta}\left(\frac{\partial\Omega}{\partial r}\frac{\partial\psi}{\partial\theta} - \frac{\partial\Omega}{\partial\theta}\frac{\partial\psi}{\partial r}\right), \tag{11}$$

$$\begin{aligned}\frac{1}{\mathrm{Re}}\tilde{D}^4\psi = &-(\mathrm{Gr}/\mathrm{Re}^2)\sin\theta\frac{\partial\zeta}{\partial\theta} \\ &+\frac{1}{r^2\sin\theta}\left\{\frac{2}{r\sin\theta}\left[\Omega\left(\cos\theta r\frac{\partial\Omega}{\partial r} - \sin\theta\frac{\partial\Omega}{\partial\theta}\right)\right.\right. \\ &\left.+\tilde{D}^2\psi\left(\cos\theta r\frac{\partial\psi}{\partial r} - \sin\theta\frac{\partial\Psi}{\partial\theta}\right)\right] \\ &\left.+\frac{\partial\psi}{\partial\theta}\frac{\partial}{\partial r}(\tilde{D}^2\psi) - \frac{\partial\psi}{\partial r}\frac{\partial}{\partial\theta}(\tilde{D}^2\psi)\right\}\end{aligned} \tag{12}$$

and

$$\nabla^2\zeta = \frac{\mathrm{RePr}}{r^2\sin\theta}\left(\frac{\partial\zeta}{\partial r}\frac{\partial\psi}{\partial\theta} - \frac{\partial\zeta}{\partial\theta}\frac{\partial\psi}{\partial r}\right) \tag{13}$$

Here $\mathrm{Re} = R_2^2\omega_0/\nu$ is the Reynolds number, $\mathrm{Gr} = g_0\beta(T_2 - T_1)R_2^3/\nu^2$ is the Grashof number, and $\mathrm{Pr} = \mu C_p/k$ is the Prandtl number. The fluid properties are the kinematic viscosity ν, the absolute viscosity μ, the coefficient of thermal conductivity k, the specific heat at constant pressure C_p, and the coefficient of thermal expansion β. The nondimensionalization employs R_2, ω_0^{-1}, and $(T_2 - T_1)$ as the characteristic length, time, and temperature scales. The characteristic angular velocity ω_0 is taken to be either ω_1 or ω_2 depending on the type of flow considered. For example, if the outer sphere is stationary, $\omega_0 = \omega_1$; if the inner sphere is stationary, $\omega_0 = \omega_2$. The various operators are:

$$\begin{aligned}\tilde{D}^2 &= \frac{\partial^2}{\partial r^2} + \frac{1}{r^2}\left(\frac{\partial^2}{\partial\theta^2} - \cot\theta\frac{\partial}{\partial\theta}\right) \\ \tilde{D}^4 &= \tilde{D}^2(\tilde{D}^2)\end{aligned} \tag{14}$$

and

$$\nabla^2 = \frac{1}{r^2}\left[\frac{\partial}{\partial r}\left(r^2\frac{\partial}{\partial r}\right) + \csc\theta\frac{\partial}{\partial\theta}\left(\sin\theta\frac{\partial}{\partial\theta}\right)\right].$$

The dimensional flow variables are defined by the relations

$$\begin{aligned}v_r &= \frac{R_2\omega_0\dfrac{\partial\psi}{\partial\theta}}{r^2\sin\theta} \\ v_\theta &= -\frac{R_2\omega_0\dfrac{\partial\psi}{\partial r}}{r\sin\theta} \\ v_\phi &= \frac{R_2\omega_0\Omega}{r\sin\theta}\end{aligned} \tag{15}$$

and

$$T = T_1 + (T_2 - T_1)\zeta$$

The boundary conditions on the flow are that the fluid temperature equal the wall temperature at the spherical boundaries, and that the fluid velocity at the boundaries equal the velocity of the boundaries. In terms of the dimensionless variables, these conditions are

$$\zeta(\eta, \theta) = 0 \quad \zeta(1, \theta) = 1$$

$$\psi(\eta, \theta) = \psi(1, \theta) = \frac{\partial\psi}{\partial r}(\eta, \theta) = \frac{\partial\psi}{\partial r}(1, \theta) = 0$$

and either

$$\Omega(\eta, \theta) = \eta^2\sin^2\theta, \quad \Omega(1, \theta) = \tilde{\mu}\sin^2\theta \tag{16}$$

for $\omega_0 = \omega_1$, or

$$\Omega(\eta, \theta) = (\eta^2/\tilde{\mu})\sin^2\theta, \quad \Omega(1, \theta) = \sin^2\theta$$

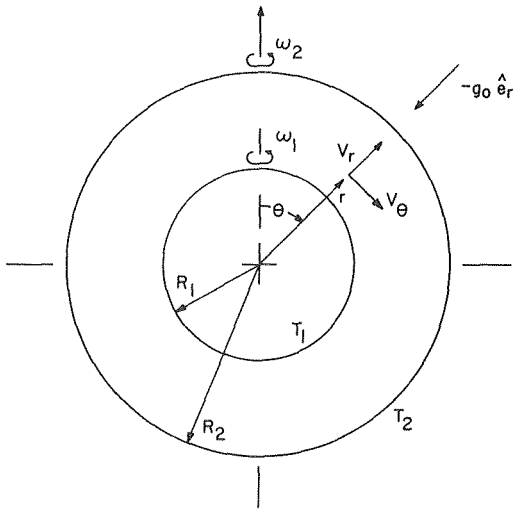

Fig. 3 Spherical flow geometry

for $\omega_0 = \omega_2$. The parameters η and $\tilde{\mu}$ in these boundary conditions are the radius ratio of the spheres $\eta = R_1/R_2$, and the angular velocity ratio $\tilde{\mu} = \omega_2/\omega_1$. The occurrence of these parameters in the boundary conditions would require that some sort of transformation be performed in order to use a full spectral method. In the partial spectral method, however, these boundary conditions are applied numerically and thus require no additional problem preparation.

The solution to this problem was obtained by expanding the dependent variables in the following series:

$$\begin{aligned}\psi(r, \theta) &= \sin^2\theta\sum_{n=0}^{N}P_n(\theta)g_n(r), \\ \Omega(r, \theta) &= \sin^2\theta\sum_{n=0}^{N}P_n(\theta)f_n(r),\end{aligned} \tag{17}$$

and

$$\zeta(r, \theta) = \sum_{n=0}^{N}P_n(\theta)h_n(r),$$

The expansion functions $P_n(\theta)$ are Legendre polynomials of the first kind of order n. The $\sin^2\theta$ factor in the expansions is chosen to simplify the boundary conditions stated in (16). Although Gegenbauer polynomials are the eigenfunctions for the $\tilde{D}^2$ and $\tilde{D}^4$ operators, Orszag [5] has shown that using Legendre polynomials in the expansion produces better accuracy. Munson [6] and Douglass [13] have demonstrated that because of the symmetries of the problem, only even n need to be considered for Ω and ζ. For ψ, only odd n need be included. For the calculations presented here the expansions were truncated at $N = 4$. The nonlinear ordinary differential equations governing the spectral coefficient functions $f_n(r)$, $g_n(r)$, and $h_n(r)$ were obtained in the same manner as described in Section 2 using the appropriate orthogonality relations for Legendre polynomials. Details may be found in Douglass [13].

The boundary conditions for this system are

$$g_n(\eta) = g_n(1) = g_n'(\eta) = g_n'(1) = 0$$

$$h_n(\eta) = 0 \quad h_0(1) = 1 \quad h_n(1) = 0 \quad n \geq 0,$$

and either

$$\begin{aligned}&f_0(\eta) = \eta^2, \quad f_0(1) = \tilde{\mu} \\ &f_n(\eta) = f_n(1) = 0 \quad n \geq 1 \quad \text{for } \omega_0 = \omega_1,\end{aligned} \tag{18}$$

or

$$\begin{aligned}&f_0(\eta) = \eta^2/\tilde{\mu}, \quad f_0(1) = 1 \\ &f_n(\eta) = f_n(1) = 0 \quad n \geq 1 \quad \text{for } \omega_0 = \omega_2.\end{aligned}$$

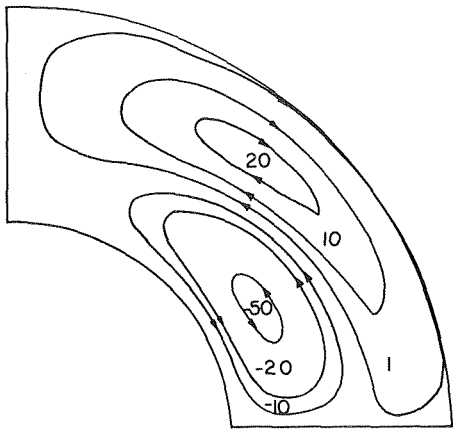

Fig. 4 Streamlines in the spherical annulus for $\tilde{\mu} = -1/3$, $\eta = 0.5$, Re = 100, Pr = 1, and Gr = −10,000

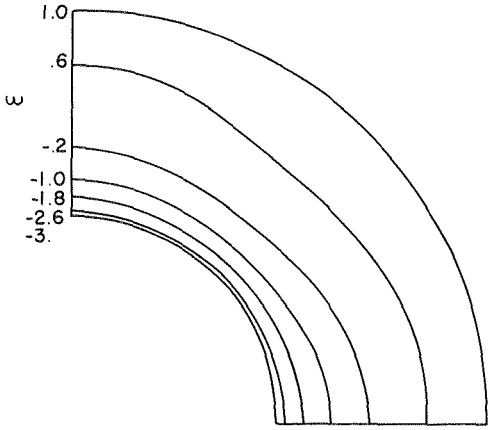

Fig. 5 Angular velocity contours in the spherical annulus for $\tilde{\mu} = -1/3$, $\eta = 0.5$, Re = 100, Pr = 1, and Gr = −10,000

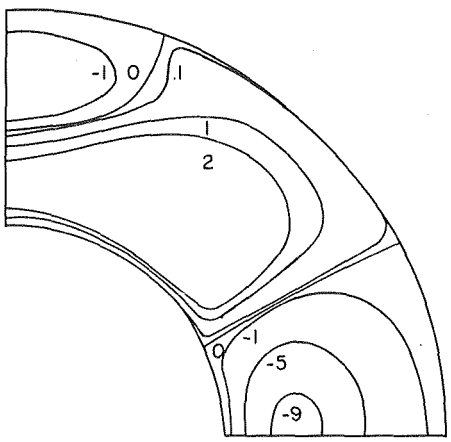

Fig. 6 Differential isotherms $\zeta - \zeta_c$ showing the departure from the conduction solution; $\tilde{\mu} = -1/3$, $\eta = 0.5$, Re = 100, Pr = 1, and Gr = −10,000

Solutions to this system of equations were obtained numerically using the method of quasi-linearization.

Because it is not possible to conduct experiments with a radial gravity field, the convection solutions obtained with the Galerkin method can only be compared with other numerical results. The perturbation results of Douglass [13] are useful for comparisons at small values of the rotational Reynolds number. The flow shown in Figs. 4, 5, and 6 corresponds to combined convection in a moderately deep annulus ($\eta = 0.5$) between counter-rotating spheres. The angular velocity ratio is $\tilde{\mu} = -1/3$, corresponding to the inner sphere rotating at three times the speed of the outer sphere and in the opposite direction. The figures show the streamlines, angular velocity contours, and isotherms at a Reynolds number of 100 and a Grashof number $Gr = -10^4$. The angular velocity contours indicate that the primary motion is precisely as expected: fluid near each sphere is dragged along in the direction of rotation. The secondary flow consists of a pair of counter-rotating eddies of about the same strength and size. These eddies are responsible for the convective heat transfer which this flow exhibits.

This flow and several others at lower Reynolds numbers are compared with perturbation solutions given by Douglass [13] in Table 1. In each case the ratio Gr/Re^2 is fixed at −1, which implies that the buoyancy forces are the same order of magnitude as the centrifugal forces. The negative value indicates that the inner sphere is hotter than the outer sphere. The Reynolds number here is a measure of the ratio of centrifugal forces to viscous forces. The flow produced by the partial spectral method was compared with the perturbation solution by computing the average fractional difference in the values of ψ, Ω, and ζ over the entire flowfield. The numerical solution is known on a mesh of 51 radial locations and 91 angular locations, but only interior points were considered in the comparison since the boundary values are applied numerically.

The table shows that at a Reynolds number of 30, which is the largest value for which the perturbation solution is considered valid by Douglass, the flows agree to within 6 percent for ψ and better than 0.1 percent for Ω and ζ. As expected, at larger Reynolds numbers the differences increase. At a Reynolds number of 100 the spectral solution satisfies two tests of consistency and appears physically valid. The consistency checks are based on the fact that in steady flow the torque and heat transfer acting at the inner sphere must equal those at the outer sphere.

It is difficult to discuss the accuracy of the spectral calculations because there are apparently no other results available in the literature on this convection problem. The situation is quite different for the isothermal flow case however, and it is worthwhile to ask how the present calculations with Gr = 0 compare to results from Pearson [16] and Munson [6]. Pearson's investigation of the time dependent flow between rotating spheres provides a number of steady-state solutions for Reynolds numbers between 10 and 1000 with which the spectral calculation can be compared. Fig. 7 shows our calculation of the flow between a fixed inner sphere and rotating outer sphere at Re = 100. These streamlines are virtually identical to those given by Pearson in Fig. 3 of his paper. Fig. 8 shows further that our four term expansions agree to within six percent with Munson's five term expansions for Reynolds numbers less than 200. The angular velocity contours are essentially identical while the streamfunction is slightly underestimated. Thus for a Reynolds number of 100 there is little to be gained from using more than four terms in the spectral expansions. In fact, Munson concluded that this flow required fewer than ten

Table 1 Average fractional difference between the spectral calculation and perturbation solution

Re	$\Delta\psi/\psi$	$\Delta\Omega/\Omega$	$\Delta\zeta/\zeta$
10	8.90×10^{-3}	3.94×10^{-6}	3.00×10^{-4}
30	5.85×10^{-2}	1.07×10^{-3}	2.48×10^{-6}
50	2.36×10^{-1}	2.32×10^{-2}	2.52×10^{-3}
80	1.58	6.27×10^{-1}	2.56×10^{-2}
100	1.98	1.76	7.76×10^{-2}

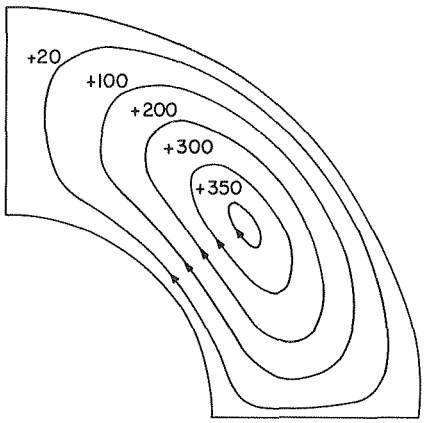

Fig. 7 Calculated streamlines for Pearson's flow; $\eta = 0.5$, Re = 100, $\tilde{\mu} = \infty$

terms for all Reynolds numbers up to transition. For the low order expansions employed here we used direct evaluation of the spectral equations. The work required by the spectral method compared favorably with that necessary for the perturbation method, but the range of Reynolds numbers for which the spectral solution was accurate was considerably larger.

5 Conclusion

Partial spectral expansions are an effective tool in solving the nonlinear partial differential equations of applied mechanics. The authors' experience with two problems in thermal convection has shown that these techniques can provide useful results for a greater range of parameter values than perturbation methods. The time and cost in both cases appear similar, but the spectral method preserves the nonlinearities in the problem. For problems requiring a large number of terms in the spectral series, transform methods can improve the calculational efficiency at some cost in programming effort.

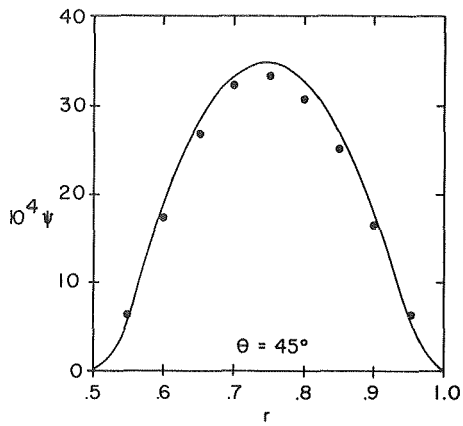

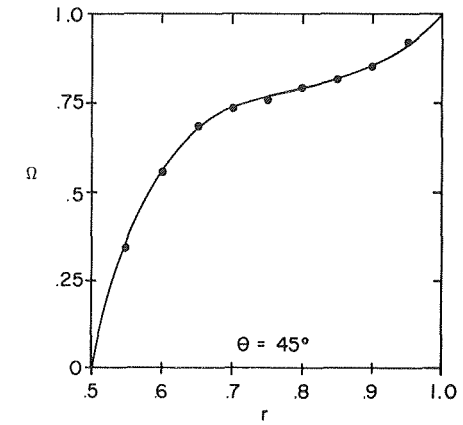

Fig. 8 Spectral solutions for $\tilde{\mu} = \infty$, $\eta = 0.5$, Re = 200, Pr = 1, and Gr = 0. Solid curves for $N = 5$ from Munson [6]. Present calculations (points) for $N = 4$

Acknowledgment

The support of the National Science Foundation through grant ENG-7518398 is gratefully acknowledged.

References

1 Galerkin, B., "Rods and Plates: Series Occurring in Various Questions Concerning the Elastic Equilibrium of Rods and Plates," *Eng. Bull.,* (Vest. inzh.) Vol. 19, 1915, pp. 897–908.

2 Orszag, S., "Transform Method for Calculation of Vector Coupled Sums: Application to the Spectral Form of the Vorticity Equation," *Journal of Atmos. Sci.,* Vol. 27, 1970, pp. 890–895.

3 Orszag, S., "Numerical Simulation of Incompressible Flows Within Simple Boundaries," I. Galerkin (spectral) representations, *In Studies in Applied Mathematics,* Vol. L, No. 4, 1971, pp. 293–327.

4 Orszag, S., "Galerkin Approximations to Flows Within Slabs, Spheres, and Cylinders," *Physical Review Letters,* Vol. 26, 1971, pp. 1100–1103.

5 Orszag, S., "Numerical Simulation of Incompressible Flows Within Simple Boundaries: Accuracy," *Journal of Fluid Mech.,* Vol. 49, 1971, pp. 75–112.

6 Munson, B., "Hydrodynamic Stability of Flow Between Rotating Spheres and Rotating Sliding Cylinders," Ph.D. Dissertation, University of Minnesota, Minneapolis, Minn., 1970.

7 Orszag, S., "Accurate Solution of the Orr-Sommerfeld Stability Equation," *Journal of Fluid Mech.,* Vol. 50, 1971, pp. 689–703.

8 Israeli, M., "Time Dependent Motions of Confined Rotating Fluids," Ph.D. Dissertation, MIT, Cambridge, Ma., 1971.

9 Metcalfe, R. W., "Spectral Methods for Boundary-Value Problems in Fluid Dynamics," Ph.D. Dissertation, MIT, Cambridge, Ma., 1973.

10 Orszag, S., and Israeli, M., "Numerical Flow Simulation by Spectral Methods," *Proceedings of the Symposium on Numerical Models of Ocean Circulations,* National Academy of Science, Washington, D.C., 1973, pp. 284–300.

11 Orszag, S. and Israeli, M., "Numerical Simulation of Viscous Incompressible Flows," *Annual Review of Fluid Mechanics,* Vol. 6, 1974, pp. 281–318.

12 Orszag, S., and Pao, Y. H., "Numerical Simulation of Turbulent Shear Flow," *Proc. Second IUTAM-IUGG Symp. on Turbulent Diffusion in Environmental Pollution,* 1973.

13 Douglass, R. W., "Combined Natural and Forced Thermal Convection in a Rotating Spherical Annulus," Ph.D. Dissertation, Duke University, Durham, N.C., 1975.

14 Custer, J., "Natural Convection in Low Prandtl Number Fluids Within a Horizontal Cylindrical Annulus," M.S. Thesis, Duke University, Durham, N.C., 1976.

15 Custer, J., and Shaughnessy, E., "Natural Convection in Liquid Metals in an Enclosure," ASME JOURNAL OF HEAT TRANSFER, Vol. 99, 1977, pp. 675–676.

16 Pearson, C., "A Numerical Study of the Time-Dependent Viscous Flows Between Two Rotating Spheres," *Journal of Fluid Mech.,* Vol. 28, 1967, pp. 323–336.

17 Roberts, S. M., and Shipman, J. S., *Two-Point Boundary Value Problems: Shooting Methods,* American Elsevier Publishing Co., N.Y., 1972.

18 Beckmann, W., "Die Wärmeübertragung in Zylindrischen Gasschichten bei naturlicher Konvektion," *Forsch. Geb. d. Ingenieurwesen,* Vol. 2 (5), 1931, pp. 165–178.

19 Kuehn, T. H., and Goldstein, R. J., "An Experimental and Theoretical Study of Natural Convection in the Annulus between Horizontal Concentric Cylinders," *Journal of Fluid Mech.,* Vol. 74, 1976, pp. 695–719.

20 Chandrasekhar, S., *Hydrodynamic and Hydromagnetic Stability,* Oxford University Press, 1961.

21 Powe, R. E., Carley, C. T., and Bishop, E. H., "Free Convective Flow Patterns in Cylindrical Annuli," ASME JOURNAL OF HEAT TRANSFER, Vol. 91, 1969, pp. 310–314.

22 Mack, L. R., and Bishop, E. H. "Natural Convection Between Horizontal Concentric Cylinders for Low Rayleigh Numbers," *Quart. Journal of Mech. Appl. Math.,* Vol. 21, 1968, pp. 223–241.

23 Custer, J., and Shaughnessy, E., "Thermoconvective Motion of Low Prandtl Number Fluids Within a Horizontal Cylindrical Annulus," ASME JOURNAL OF HEAT TRANSFER, Vol. 99, 1977, pp. 596–602.

L. R. Davis[1]
Research Mechanical Engineer
Mem. ASME

M. A. Shirazi
Chief, Ecosystems Modeling & Analysis Branch
Mem. ASME

D. L. Siegel[2]
Research Mechanical Engineer

Corvallis Environmental Research Laboratory,
U.S. Environmental Protection Agency,
Corvallis, Oregon

Measurement of Buoyant Jet Entrainment from Single and Multiple Sources

An experimental investigation was conducted to determine the dilution characteristics of single and multiple port buoyant discharges typical of modern natural and mechanical draft cooling towers. Simultaneous measurements of velocity and tracer concentration profiles were taken at various downstream locations in the three-dimensional plumes discharged into a stagnant ambient using a hot film anemometer and conductivity probe. The number of discharge ports was varied from one to seven. Discharge densimetric Froude numbers were varied from 1.5 to infinity. Numerical integration of the profiles gave dilution, tracer conservation, and momentum fluxes. The effect of reducing Froude number was to increase entrainment considerably. Increasing the number of discharge ports reduced the rate of entrainment. In multiple port discharges the shape of the plume changed from an elongated configuration to nearly axisymmetric within the first 20–30 diameters of discharge.

Introduction

With the changing emphasis of waste heat disposal to large cooling towers instead of once through cooling systems, an increased interest has developed into the dilution characteristics of a finite number of neighboring jets discharging at relatively low densimetric Froude numbers, F_0, such as are found in mechanical draft cooling towers. This system produces a three-dimensional plume whose dilution depends on combined turbulent heat and mass transfer with the environmental ambient fluid.

Once-through cooling systems consist mainly of surface discharge or submerged discharge from a large single port or from a multiple port diffuser that may be several hundred feet long with many discharge ports. However, mechanical draft cooling towers usually have fewer than ten discharge ports. Thus, end effects cannot be neglected and, because of the initial merging process, they cannot be considered as single axisymmetric jets.

Buoyant jets have been investigated extensively in the past. Excellent reviews can be found in Hirst [1], Baumgartner and Trent [2], Briggs [3], and Silberman and Stefan [4]. Therefore, only those references directly related to this work will be discussed. Most of the reports in the above reviews deal with single jets with dilution expressed as excess temperature decay $\Delta T_c/\Delta T_0$. However, true dilution is defined in terms of the ratio of local mass flow rate of fluid in the plume to the discharge mass flow rate, m/m_0. The latter definition is related exclusively to excess temperature only in the fully developed region of the plume where similarity of profiles exists and in non-stratified ambients. Since multiport discharges of finite number have nonaxisymmetric, nonsimilar velocity and temperature profiles, both must be measured in order to determine dilution and its relation to excess temperature decay.

One of the classic papers on single port buoyant plumes in which both temperature and velocity were measured was presented by Schmidt [5]. He created a purely buoyant or thermal plume by placing a heating coil in a hole in a horizontal board inducing flow through it. No measurements were reported at the hole so neither a discharge flow rate nor a Froude number could be determined. The rate of dilution determined from his data, however, indicates his Froude number was less than 1.5 when compared to the data of this study. Integrating his published values of velocity and temperature at different cross sections in the plume shows a variation in the conservation of energy by as much as a factor of 2.0. This indicates the difficulty in obtaining accurate simultaneous readings of temperature and velocity, especially in stagnant ambients where the tail of the profiles goes to zero. Similar problems occurred in the present study.

Rouse, et al. [6] also investigated buoyancy induced flows from a point heat source. Although interesting to look at, an idealized point source is difficult to relate to results of a finite discharge with initial turbulence, momentum and development length. The inability to determine an initial mass flux and Froude number further complicates the problem. However, such studies are useful in determining trends in plume dynamics in the far field. The authors were able to do this very successfully. Jirka and Harleman [7] investigated multiport discharges into shallow water from submerged outfall diffusers. Both two and three-dimensional configurations were examined. They de-

[1] Also Professor of Mechanical Engineering at Oregon State University.
[2] Presently at EG&G, Idaho Falls. Id.

Contributed by the Heat Transfer Division and presented at the AIChE-ASME Heat Transfer Conference, Salt Lake City, Utah, August 15–17, 1977.
Revised manuscript received at ASME Headquarters August 6, 1977. Paper No. 77–HT-43.

veloped stability criteria useful in analyzing plume spreading at the water surface but due to the shallowness of the water and the long length of the diffusers, their data do not apply directly to this study. Kannberg and Davis [8] experimentally investigated temperatures in deep submerged multiport discharges and developed models primarily applicable to two-dimensional diffusers with no end effects. Sforza, et al. [9] investigated velocities in the isothermal discharge of air into air from a variety of discharge shapes including rectangular slots. Their findings will be compared with the results of this investigation.

Kotsovinos [10] studied the entrainment of plane (two-dimensional) turbulent buoyant slot jets. As in the present study, he conducted simultaneous measurements of temperature and velocity within the plumes for a variety of Froude numbers and was able to determine both dilution and excess temperature decay directly. His is an excellent study but it does not include end effects or mixing and merging of plumes.

The emphasis in the present investigation was to obtain simultaneous measurements of velocity and tracer across the plume in a variety of single and three-dimensional multiple jets discharging into stagnant ambients. The objective was to obtain direct entrainment data to facilitate modeling of a three-dimensional plume from cooling towers with one or more neighboring cells.

Apparatus and Procedure

Water was chosen as the working fluid with the buoyant jets being created by discharging salt water downward into fresh water. Using this technique, a wide range of Froude numbers could be obtained by adjusting the salinity of the discharge water while maintaining Reynolds numbers high enough to insure turbulent flow. This technique is not able to model latent heat effects due to moisture condensation or evaporation within the plume on plume characteristics. In addition, laboratory turbulence scales will be different from atmosphere turbulence. However, since the main objective of this study was to determine merging and end effects on dilution in the near and intermediate fields where jet induced turbulence is dominant and since moisture effects are expected to be minor in this region [11], the use of water in the laboratory as a working fluid was felt to be justified.

Fig. 1 is a sketch of the test apparatus used in this study. The main tank was a towing channel 12.1 m long, 0.61 m wide, and 0.91 m high located at EPA's Corvallis Environmental Research Laboratory. Both sides of the tank were of plexiglass so visual measurements could be made. The discharge tank containing salt water was located on rails above the receiving tank. It was airtight except for breather tubes which maintained a constant velocity head regardless of the water level in the discharge tank. This system is described in detail in Kannberg and Davis [8]. From this tank, the salt water passed through a control valve into a plenum chamber with baffle and discharge tubes as shown in Fig. 2. Also shown in this figure is the coordinate system used. The number of discharge tubes used were 1, 2, 3, 5 and 7. The tubes, 9.53 mm inside diameter and 12.7 mm outside diameter, were

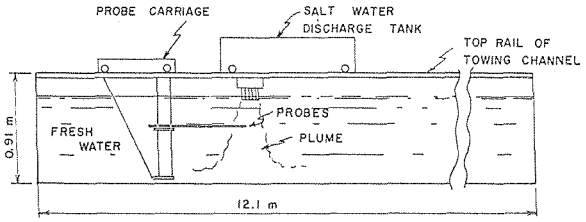

Fig. 1 Sketch of overall test arrangement

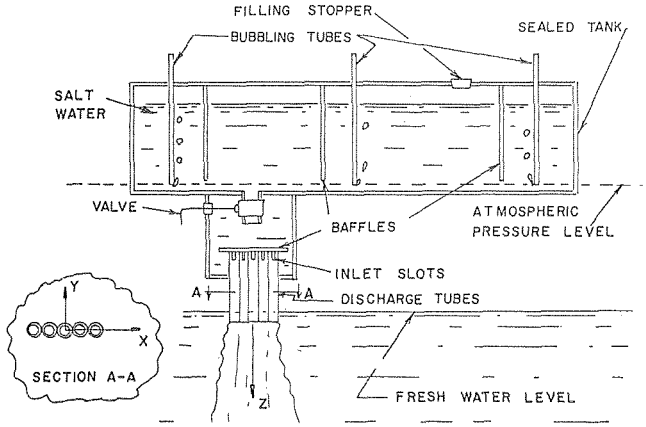

Fig. 2 Sketch of discharge system

placed as close together as possible with centerlines in one plane. This gave a port spacing to discharge diameter, L/D, of 1.33, approximating that of multiple cell mechanical draft cooling towers. Since the ports were right against each other, the number of ports approximately represented the discharge aspect ratio, A. The length of the tubes was such as to give fully developed turbulent flow at discharge.

In addition, several runs were conducted with single discharge ports of 11.2 mm, 13.5 mm, 23.3 mm, and 38.1 mm inside diameter to give the range in Froude and Reynolds numbers desired. The Froude numbers tested ranged from 1.5 to infinity (a momentum jet). The Reynolds numbers were all greater than 2100 which was sufficient to maintain turbulent discharge. This was easily detected by observing the density waves created by the discharge of salt water into fresh water.

Salinity within the plumes was measured with a conductivity probe and carrier amplifier similar to those described by Keeler [12] and McQuivey, et al. [13]. Velocities were measured with a Thermal Systems, Inc. (TSI) constant temperature hot film anemometer system.

Nomenclature

A = aspect ratio ~ number of discharge ports
b = local characteristic width of jet = $\sqrt{2}\sigma$
$b_{0.5}$ = local characteristic width of jet where $U/U_c = 0.5$
D = port discharge diameter
F = densimetric Froude number at outlet, $U_0/\sqrt{g_0'D}$
F_L = local densimetric Froude number $U_c/\sqrt{g_c'b}$
g = acceleration due to gravity
g' = reduced gravitational acceleration, $g\Delta\rho/\rho_a$
J = mass flux of salt $-\int \rho USdA$
m = mass flux $-\int \rho UdA$
M = momentum flux $-\int U^2dA$
Q = volumetric flow rate $-\int UdA$
r = radial coordinate perpendicular to jet centerline
S = salinity—mass fraction
ΔT_c = excess water temperature on jet centerline
ΔT_0 = discharge excess water temperature
U = jet velocity—variable in all directions
U_0 = discharge velocity from outlet
X = rectilinear horizontal coordinate parallel to port connecting line
Y = rectilinear horizontal coordinate perpendicular to X
Z = coordinate in vertical direction
$\Delta\rho$ = difference between jet centerline and ambient water densities
ρ = fluid density
σ = standard deviation of Gaussian profile

Subscripts

a = ambient conditions
c = centerline value
o = discharge conditions

The two probes were mounted side-by-side on a remotely controlled sting. The tips of the two probes were about 2.0 mm apart. The discharge system, traversing mechanism and probes were attached to a carriage on rails above the receiving tank and could be towed at desired velocities ranging from 0.5 to 50.0 cm/s along the length of the receiving tank. This feature was only used for probe calibration since tests were conducted in stagnant water.

Calibration of the conductivity probe was fairly stable as long as it was kept clean of dirt and oxidation. Considerable care was taken before each test to clean the probe and to make slight adjustments required in the gain of the carrier amplifier to bring the signal output in agreement with a predetermined calibration curve. This procedure was found to cause the response of the probe to agree with the calibration curve over the full range of salinities of interest.

The overheat ratio for the hot film anemometer probe could not be set as high as recommended by the manufacturer without causing vapor bubbles to form on the probe, thus causing the signal to drift. Operation at a reduced overheat caused the response to be sensitive to the water temperature. To resolve this problem, a calibration curve was obtained at a desired nominal reduced overheat by towing the probe through the tank for a full range of speeds. Then before each run, the probe was towed at one known speed and a minor adjustment in the overheat was made until the signal response agreed with the previously determined calibration curve. This brought the probe back into calibration as the tank temperature changed from day to day.

After selecting the desired discharge configuration, the discharge velocity and salinity were adjusted to give the desired Froude and Reynolds numbers. Most runs were with sea water at a salinity of 32 ppt. For runs with F = 1.5 and 3.0, the salinity was increased so the discharge Reynolds number could be maintained above the critical value.

With the system properly adjusted, runs were made while traversing the plume horizontally at desired locations. The probes were left at each point long enough to obtain a good time average reading. The velocity signal was squared and averaged with several time constants using a true RMS meter. It was found that a record length of up to one minute was required to provide sufficient information for a stable variance. For single port discharges where the plume can be assumed symmetrical, a single horizontal traverse was made through the center of the plume at each downstream location, Z/D. For multiport discharges, however, several horizontal traverses were made through the plume at each Z/D location in order to provide sufficient readings for a three-dimensional picture of the plume cross section. The usual spacing for these readings was on 1.0 cm centers in both the X and Y directions. In high shear areas, 0.5 cm spacings were used.

Downstream locations, Z/D, ranging from 5–40 diameters were investigated with the bulk of the data taken at 10, 20, and 30 diameters. Readings near the discharge ports were not taken due to the inaccuracies of the probes in high gradient regions caused by their size relation to the shear layer thickness. In the far field, the hot film probe could not give accurate readings in the low velocity tail of the expanding plumes. Since this region grew more important in determining dilutions as Z/D increased and because bottom effects began to appear, far field readings were not taken. The tank was drained after each series of runs and refilled with fresh water to prevent salt build up in the ambient receiving water.

Several multiport runs were made with dye in the discharge water. This was done with the line of ports both perpendicular and in line with the tank side walls. Photographs were taken to determine plume spreading in both the X and Y directions visually to support the data taken with the two sensors.

Results

Table 1 presents the basic results of this study both for single and multiport discharges. Given on this table are: number of ports, discharge densimeteric Froude number, the plume half widths in the X and Y directions, and terms relating local mass, momentum and salinity fluxes to discharge conditions. Dilution is defined as the local mass flow rate as compared to the discharge flow rate or m/m_0. Mathematically this is given as $\int \rho U dA/\rho_0 Q_0$. Since the density across the plume changes less than 1.0 percent from the ambient, the dilution can be determined approximately by considering volume fluxes only. In this study, the dilution was calculated numerically for the three-dimensional plumes by

$$Q/Q_0 = \Sigma U_{ij} \Delta A/Q_0 \tag{1}$$

where U_{ij} were the velocities at each grid point and ΔA was the grid size. For the single plumes, dilution was determined by using a best fit Guassian curve to the data expressed is

$$Q/Q_0 = 2\pi U_c \int \exp[-(r/b)^2] r dr/Q_0 \tag{2}$$

where U_c was the maximum cross section velocity and b was the characteristic width determined from the data.

An indication of the accuracy of the data was obtained from the

Table 1 Summary of results

Ports (A)	Froude No.	Z/D	Q/Q_0	M/M_0	J/J_0	$b_{0.5x}/D$	$b_{0.5y}/D$	S_c/S_0	U_c/U_0
1	∞	5	2.6	0.97	—	0.8	—	—	0.81
1	∞	10	3.4	0.83	—	0.95	—	—	0.56
1	∞	20	5.7	0.92	—	1.2	—	—	0.37
1	∞	30	10.2	1.15	—	2.8	—	—	0.24
1	∞	40	11.4	0.8	—	3.2	—	—	0.17
1	36	25	10.7	1.3	0.95	2.1	—	0.16	0.29
1	36	37	16.3	1.5	0.96	2.9	—	0.11	0.22
1	8	10	5.5	1.6	1.0	1.1	—	0.33	0.64
1	8	20	12.2	2.4	1.0	2.2	—	0.18	0.40
1	3	10	8.7	3.4	*N/A**	1.3	—	*N/A*	0.84
1	3	20	11.6	3.6	*N/A*	1.6	—	*N/A*	0.69
1	3	25	30.7	10.2	*N/A*	3.9	—	*N/A*	0.54
1	1.5	10	9.5	4.6	*N/A*	1.4	—	*N/A*	1.0
1	1.5	20	30.7	17.1	*N/A*	2.3	—	*N/A*	1.0
1	1.5	30	61.0	33.0	*N/A*	3.5	—	*N/A*	0.95
2	6	10	4.8	1.4	0.5	2.0	1.6	0.26	0.58
2	6	20	10.2	3.0	0.7	3.4	2.3	0.17	0.46
2	6	30	15.2	4.5	0.7	4.0	3.7	0.11	0.49
3	6	10	4.0	1.6	0.8	2.4	1.7	0.26	0.6
3	6	20	7.4	2.8	0.8	3.0	3.1	0.21	0.57
3	6	30	8.5	2.4	0.6	3.5	3.9	0.14	0.49
5	6	10	2.8	1.0	0.7	3.4	1.2	0.30	0.62
5	6	20	7.3	2.5	0.9	3.6	3.3	0.21	0.69
5	6	30	10.0	3.9	0.8	3.8	4.0	0.14	0.63
7	6	10	2.8	1.6	0.9	4.6	1.3	0.34	0.64
7	6	20	5.5	2.3	0.8	6.0	2.6	0.22	0.58

* *N/A* Not available due to equipment failure.

expression

$$J/J_0 = \int USdA/(Q_0S_0) \tag{3}$$

where S is the salinity. Since the receiving water was fresh, the mass flux of salt in the plume should be constant or $J/J_0 = 1.0$ at all Z/D along the plume. The value of this ratio was determined in the same manner as dilution.

The momentum flux ratio, M/M_0

$$M/M_0 = \int U^2dA/U_0^2 \tag{4}$$

is also helpful in evaluating plume dynamics. For momentum jets the value of this ratio should be unity at all times due to the lack of external forces on the plume. For buoyant jets, however, this ratio should increase under the influence of buoyant forces. The values of M/M_0 for each Z/D were calculated by numerically integrating the velocity squared over each plume cross section.

Single Plume Results. Fig. 3 is a plot of Q/Q_0 versus Z/D for the single port discharges at various Froude numbers. Lines have been drawn through the data to indicated approximate trends. Even though the data are scattered, it can be seen that the effects of Froude number are considerable. It can also be seen that the trends are not necessarily linear, reflecting partly the influence of the development zone. For the momentum jet, F = ∞, the rate of dilution is linear with distance and agrees well with published data [14, 15 and 16]. Most buoyant discharge experiments have been interested in temperature or concentration decay. Dilution as such was usually not measured. Ricou and Spalding [16] measured dilution for hydrogen discharged into air. The trend in their data agrees with Fig. 3, however, they suggest that $m/m_0 = 0.32(x/d)(\rho_1/\rho_2)^{1/2}$ where ρ_1/ρ_2 is the ratio of the heavier fluid density to the lighter fluid density. This expression considerably underpredicts the observed dilutions in this study.

The entrainment of ambient fluid causing dilution, $E = dQ/dz$, has been expressed as a function of an entrainment coefficient and local plume properties [17 and 18] such that $E = \alpha U_c b$. In this expression α is the entrainment coefficient. For momentum jets $\alpha = 0.057$ has proven to be a good value. Abraham [19] suggested a value of $\alpha = 0.085$ for low Froude number discharges. Using the slope of the mean curves on Fig. 3 for dQ/dz, U_c and b from Table 1 for individual points, the entrainment coefficients in this study were found to vary from 0.06 for momentum jets to 0.14 for very low Froude numbers. The expression

$$\alpha = 0.057 + 0.083\ F_0^{-0.3} \tag{5}$$

was found to fit the general trend in data for the single port discharges without ambient current.

An alternate expression, derived by Fox [20] using a combination of the mechanical energy, momentum and continuity equations is $E = (\alpha_1 + \alpha_2/F_L^2)U_c b$ where F_L is the local Froude number given by $F_L = U_c/[\Delta\rho_c g b/\rho]^{1/2}$. The value of the first coefficient is the momentum jet value of 0.057. Hirst [1] suggested a value of 0.97 for the second. This expression does not agree with the data from this study. For example it was 40 percent low for $F_0 = 36$ and $Z/D = 30$ and 30 percent low for F = 6 and $Z/D = 10$.

Fig. 4 is a plot of plume half width, $b_{0.5}$, versus distance for the single port discharges investigated. These widths were based on the location where $U/U_c = 0.5$ at each cross section. Because of the scatter in these data, it was difficult to make any profound conclusions regarding plume growth except possibly that low Froude numbers of the order of 1.5 produce slightly larger plumes than momentum jets and that the general trend in plume growth agrees with Albertson's [14] data for a momentum jet. Fig. 5 is a plot of the plume centerline velocities versus distance for Froude numbers ranging from 1.5 to infinity. Lines indicating approximate trends have been drawn through the data. It is seen that at very low Froude numbers the buoyant forces maintain high centerline velocities relative to discharge which cause higher dilution rates when compared to the higher Froude number discharges.

Multiple Plume Performance. Fig. 6 is a plot of dilution versus distance for several multiport discharges at a nominal Froude number $F_0 = 6$. The single port discharge values for this Froude number are also included for reference. Although the data are scattered, the effect of aspect ratio A (number of ports) is evident. The greater the number of ports, the lower the rate of dilution. This is explained by the interference of the merging plumes on the entrainment mechanism. Not only is the surface area available to entrain ambient fluid decreased upon merging, but neighboring plumes also compete for the same ambient fluid thus decreasing the entrainment of each. Also included

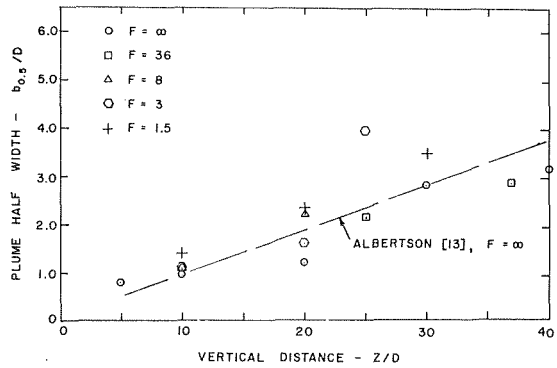

Fig. 4 Plot of plume half width versus distance for single port discharge

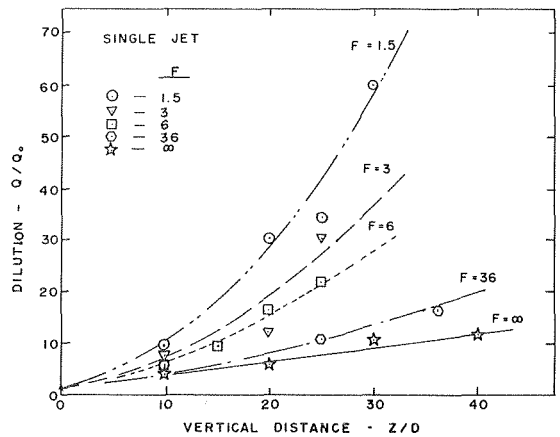

Fig. 3 Plot of dilution versus distance for single port discharge

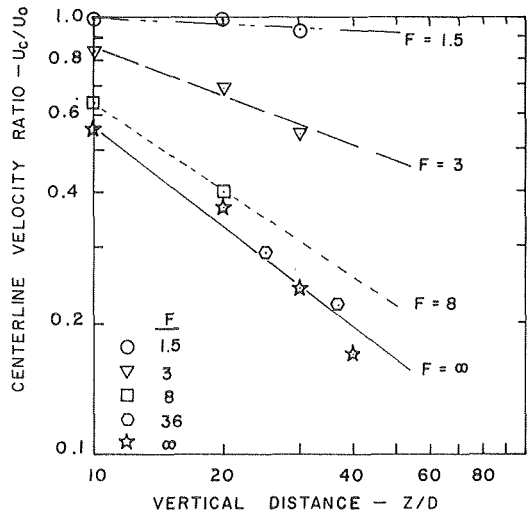

Fig. 5 Plot of centerline velocity ratio versus distance for single port discharge

in this figure are data points taken from Kotsovinos [10] for an infinite slot ($A = \infty$) at Froude numbers of 8.4 and 5.5. Within the experimental limits of this study the dilution was found to approximately fit the expression,

$$Q/Q_0 = 1.0 + 0.46\,(Z/D)^{1.1}(A)^{-0.52} \tag{6}$$

One of the more interesting characteristics of the multiple port discharges was the change in plume shape along its trajectory. Near discharge the jets from each port maintained their individual character but soon merged into a single elongated plume with the major axes in line with the line of discharge ports. As the plume grew, spreading perpendicular to this line was greater than along the line. Thus, this elongated character soon disappeared and the plume became essentially round. Fig. 7 shows four different cross-sectional shapes for $A = 5$. These are full widths as observed by dye studies. Half widths in the X and Y directions are given in Table 1. This same phenomenon was observed by Sforza, et al. [9] for rectangular slot jets of air. They divided the flow into three regions as follows: 1) The potential core or development zone where ambient mixing had not penetrated into the center of the jet. 2) The characteristic decay region where major and minor axes of the plume depended on discharge conditions but spreading in the minor axis direction was faster than in the major axis direction. Velocity profiles in the plane of the minor axis are similar; in the planes of the major axis they are nonsimilar. 3) Axisymmetric decay region where the plume behaves as one axisymmetric plume. These same regions were observed in this study.

Since the widths of the multple port plumes within the characteristic decay region are different in the X and Y directions, it is not correct to express the entrainment in terms of either one alone. In addition, since the profiles in the plane of the major axis are not similar, it is probably not correct to express the entrainment in the classic manner at all. As a result this was not done.

The decay in maximum salt concentration S_c/S_0 along the plume centerline is of interest since this represents the decay of excess temperature in a thermal plume. Fig. 8 is a plot of centerline concentration ratio versus distance for the multiple port discharges. Again the effect of aspect ratio is evident with a more rapid decrease in concentration as the number of ports is decreased.

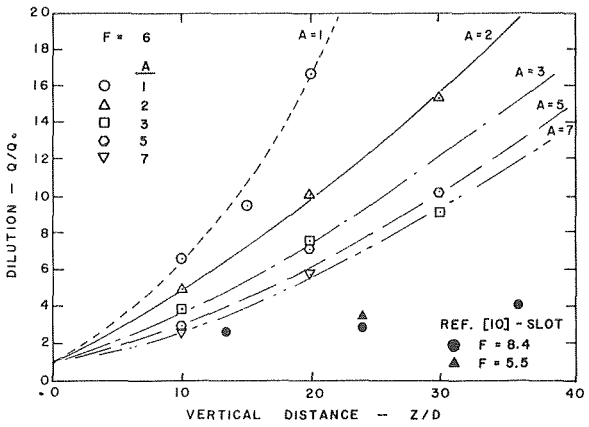

Fig. 6 Plot of dilution versus distance for multiple port discharge

Conclusions

The measurement of dilution from single and multiple port buoyant jets with no ambient current has been made along with the decay in centerline salt concentration by simultaneously measuring velocities and salinity within the plumes. The effect of Froude number on dilution was considerable with greater dilution at lower Froude numbers. The approximate expression showing this effect was given in terms of the entrainment coefficient,

$$\alpha = 0.057 + 0.083\,F^{-0.3}$$

For multiple port discharge the effect of aspect ratio (number of discharge ports) was to decrease dilution with increasing aspect ratio. The approximate expression showing this effect was found to be

$$Q/Q_0 = 1.0 + 0.46(Z/D)^{1.1}(A)^{-0.52}$$

It was found that the shape of multiple port plumes changed from an elongated configuration to nearly axisymmetric within the first 20–30 diameters of discharge.

The experimental scatter in the results and the inability to accurately measure the low velocities in the "tail" of the velocity profiles using a hot film anemometer precludes the drawing of firm conclu-

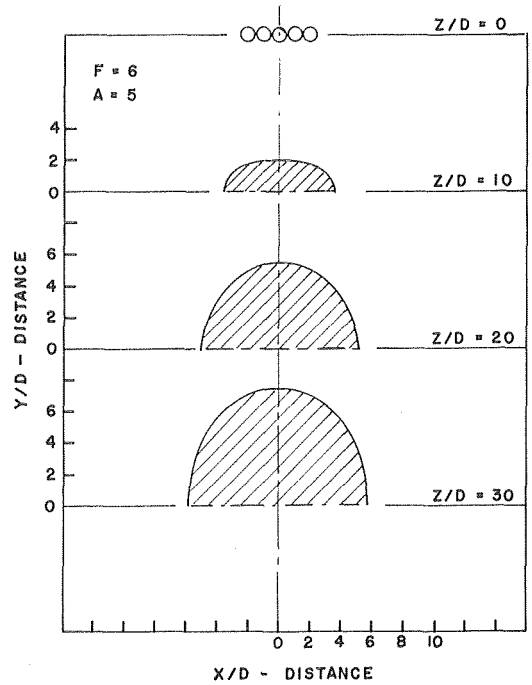

Fig. 7 Cross section of multiple port discharge plumes at four different values of Z/D for $A = 5$

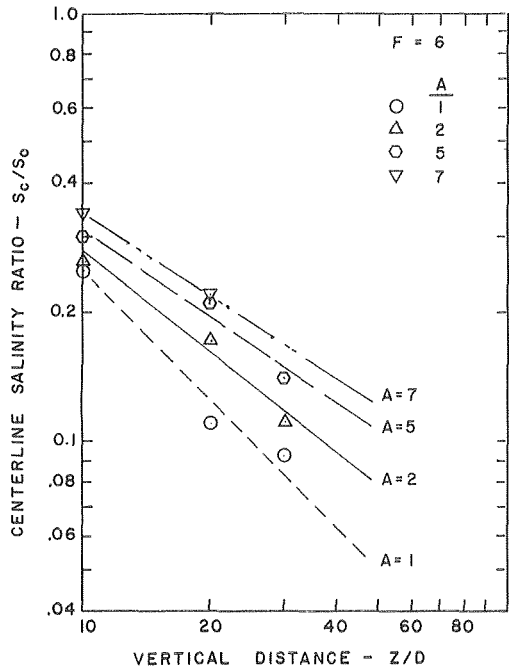

Fig. 8 Centerline salinity ratio versus distance for multiple port discharge

sions at present. It is recommended that the results of this study be checked with a different anemometer such as a Laser Doppler system with a "Bragg" cell so the lower velocities will be more accurate. It is also recommended that the work be extended to include ambient velocity effects and discharge line orientation relative to the ambient current.

References

1 Hirst, E. A., "Analysis of Round Turbulent, Buoyant Jets Discharged to Flowing Stratified Ambients," Oak Ridge National Laboratory No. ORNL-4685, 1971.

2 Baumgartner, D. J. and Trent, D. S., "Ocean Outfall Design Part I: Literature Review and Theoretical Development," U.S. Dept. of Interior, Federal Water Quality Administration, 1970.

3 Briggs, G. A., "Plume Rise," AEC Critical Review Series Report, No. TID-25075, 1969.

4 Silberman, E. and Stefan, H., "Physical (Hydraulic) Modeling of Heat Dispersion in Large Lakes, a Review of the State of the Art," University of Minn., St. Anthony Falls Hydraulic Lab., Project Report No. 115, 1970.

5 Schmidt, W., "Turbulente Ausbreitung eines Stromes erhitzter Luft," *Zeitschr, Angew. Math. und Mech.*, Vol 21, 1941.

6 Rouse, H., Yih, C. S., and Humphreys, H. W., "Gravitational Convection from a Boundary Source," *Tellus*, Vol 4, 1952.

7 Jirka, G. and Harleman, D. R. F., "The Mechanics of Submerged Multiport Diffusers for Buoyant Discharges in Shallow Water," MIT Ralph M. Parsons Laboratory for Water Resources and Hydrodynamics, Report No. 169, 1974.

8 Kannberg, L. D. and Davis, L. R., "An Experimental/Analytical Investigation of Deep Submerged Multiple Buoyant Jets," EPA-600/3-76-101, U.S. Environmental Protection Agency, Corvallis, Oregon, Sept. 1976.

9 Sforza, P. M., Steiger, M. H., and Trentacoste, N., "Studies on Three-Dimensional Viscous Jets," *AIAA Journal*, Vol. 4, No. 5, May 1966.

10 Kotsovinos, N. E., "A Study of the Entrainment and Turbulence in a Plane Buoyant Jet," W. M. Keck Laboratory, California Institute of Technology, Report No. KH-R-32, Aug. 1975.

11 Wigley, T. M. L., and Slawson, P. R., "On the Condensation of Buoyant Moist, Bent-Over Plumes," *Journal of Applied Meteorology* Vol. 10, 1971, pp. 253–259.

12 Keeler, R. M., "Mixing and Chemical Reaction to Turbulent Flow Reactors," California University, Livermore, Report No. UCRL-7852, June 1964.

13 McQuivey, R. S., Keefer, T. N., and Shirazi, M. A., "Basic Data Report on the Turbulent Spread of Heat and Matter," U.S. Department of Interior, Geological Survey and the U.S. Environmental Protection Agency, Open file Report, Fort Collins, Colorado, Aug. 1971.

14 Albertson, M. L., Dai, Y. B., Jensen, R. A., and Rouse, H., "Diffusion of Submerged Jets," *ASCE Transactions*, 115, No. 150, 1950.

15 Becker, H. A., Hottel, H. C., and Williams, G. C., "The Nozzle-Fluid Concentration Field of the Round, Turbulent, Free Jet," *Journal of Fluid Mechanics*, Vol. 32(2), 1967, pp. 231–252.

16 Ricou, F. P. and Spalding, D. B., "Measurements of Entrainment by Axisymmetrical Turbulent Jets," *Journal of Fluid Mechanics*, Vol. 11(1), Aug. 1961, pp. 21–32.

17 Morton, B. R., Taylor, A. G., and Turner, J. S., "Turbulent Gravitational Convection from Maintained and Instantaneous Sources," *Proceedings of the Royal Society of London*, Vol. A234, 1956, pp. 1–23.

18 Fan, L-N., "Turbulent Buoyant Jets into Stratified or Flowing Ambient Fluids," W. M. Keck Laboratory, California Institute of Technology, Report No. KH-R-15, June 1967.

19 Abraham, R., "Entrainment Principle and its Restrictions to Solve Problems of Jets," *Journal of Hydraulic Research*, Vol. 3(2), 1965, pp. 1–23.

20 Fox, D. G., "Forced Plume in a Stratified Fluid," *Journal of Geophys. Res.*, Vol. 75(33), 1970, pp. 6818–6835.

R. N. Horne
Department of Petroleum Engineering,
Stanford University,
Stanford, Calif. 94305

M. J. O'Sullivan
Department of Theoretical and Applied Mechanics,
University of Auckland,
New Zealand

Convection in a Porous Medium Heated from Below: The Effect of Temperature Dependent Viscosity and Thermal Expansion Coefficient

The natural convection of water through permeable formations is an important phenomenon governing the behavior of geothermal aquifers. In such situations the temperature of the fluid can vary by amounts of the order of 250 K, over which range the viscosity of the water may decrease by as much as a factor of 10, and the coefficient of thermal expansion may increase by an even greater factor. Although previous studies have examined the effect of this behavior on the onset conditions at which natural convective flow in the medium first occurs, the actual flow patterns that will result from the convection of a fluid with such widely varying properties has not been reported. To this end, numerical methods of solution are applied to this problem and a visualization of the flows obtained. By solving in terms of both pressure and stream function instead of stream function alone, it was possible to maintain semiconservative properties of the numerical scheme. The convective motion is unstable (in two dimensions) at even moderate values of the Rayleigh number and exhibits a fluctuating convective state analogous to the case of a fluid with constant viscosity and coefficient of thermal expansion. In some cases the acceleration of the flow in certain areas due to the decrease in viscosity causes localized thermal instabilities.

Introduction

The convective flow of fluid through porous media heated from below is of considerable interest in the study of the behavior of geothermal systems and has been investigated extensively in the past, from early studies by Horton and Rogers [1] and Lapwood [2] into the onset of natural convection, through numerical studies by Wooding [3], Donaldson [4], Elder [5, 6], Horne and O'Sullivan [7–9], and Caltagirone [10, 11], and analytical studies by Palm, Weber, and Kvernvold [12], Busse and Joseph [13], and Straus [14]. There have also been experimental studies by Combarnous and LeFur [15] and Caltagirone, Cloupeau and Combarnous [16]. However, with the exception of the experimental investigation which worked with real fluids, all of the studies listed above assumed that fluid properties such as thermal expansivity α, viscosity ν, and specific heat C_p remain constant. In addition, each of them also invoked the Boussinesq approximation that the fluid density ρ is constant except insofar as it affects the buoyancy forces. This approximation causes a misrepresentation of the transient terms in the continuity equation—Horne [17].

Other investigations have avoided making the approximation of constant fluid properties. Rogers and Morrison [18] considered a viscosity exponentially dependent on temperature and its effect on the conditions for the onset of convection of infinitesimal order, and Kassoy and Zebib [19] performed a similar study using an empirical viscosity dependence for water. Wooding [3] and Horne [17] in numerical investigations of finite amplitude convection of a Boussinesq fluid used both temperature dependent viscosity and thermal expansivity. The latter study considered a cubic variation of viscosity that matched the behavior of water to within 5 percent in the range of temperatures 15–250°C.

Sorey [20] and Straus and Schubert [21] have also considered the convection of water as a non-Boussinesq fluid with viscosity and thermal expansivity dependence. Sorey [20] studied finite amplitude convection assuming variation with temperature only, whereas Straus and Schubert [21] considered the onset of convection of infinitesimal amplitude assuming dependence on pressure as well (although they showed that the pressure dependence of the onset conditions did not become significant until the temperature difference across the me-

Contributed by the Heat Transfer Division of THE AMERICAN SOCIETY OF MECHANICAL ENGINEERS and presented at the AIChE-ASME Heat Transfer Conference, Salt Lake City, Utah, August 15–17, 1977. Manuscript received by the Heat Transfer Division March 22, 1978. Paper No. 77-HT-56

dium exceeded 250 K, provided the overall mean temperature gradient was not less than 50 K/km).

In a physical example of a geophysical convective system, such as the geothermal reservoir, the convecting fluid is frequently water (it may also be brine, steam, or a two-phase mixture), and the temperatures at depth may reach 250°C (and in a few cases even higher). The kinematic viscosity ν of water over such a temperature range decreases by a factor of approximately 10, and the thermal expansivity α increases by an even larger factor. Clearly the temperature dependence of ν and α are significant effects in geothermal applications. The onset of convection is dependent on the value of the Rayleigh number (see section 2) which is a parameter linearly dependent on α, and inversely dependent on ν. Thus if ν decreases with temperature and α increases, then the actual Rayleigh number in the system will be higher than the apparent Rayleigh number defined in terms of "cold water" quantities. Thus, not unexpectedly, Kassoy and Zebib [19] and Straus and Schubert [21] both noted a considerable decrease in the critical Rayleigh number (defined in terms of cold water properties) at which convection begins to occur, as compared to the value $4\pi^2$ calculated by Lapwood [2] who assumed constant properties. However, Rayleigh numbers in geothermal reservoirs are frequently very much higher than this. For example, the Wairakei geothermal reservoir is estimated to have a (cold water) Rayleigh number of at least 1500 (Horne and O'Sullivan [22]) which with a temperature differential of 250 K and a variable viscosity would correspond to a value of about 150. Thus the current investigation considers the influence of temperature dependent properties on finite amplitude convection in geothermal applications. Bearing in mind the results of Straus and Schubert [21], the less significant pressure dependence is not considered, and apart from the temperature dependence of thermal expansivity, the fluid is considered to be Boussinesq.

Governing Equations

The governing equations for convective flow through porous media for the nondimensional velocity U_i, pressure P and temperature θ, are

$$\frac{\partial U_i}{\partial X_i} = 0 \tag{1}$$

$$\frac{\partial P}{\partial X_i} = \frac{\mathrm{R}}{\lambda}(\theta + \alpha\theta^2) - \frac{U_i}{\beta(\theta)}, \tag{2}$$

and

$$\frac{\partial \theta}{\partial \tau} + \lambda U_i \frac{\partial \theta}{\partial X_i} = \nabla^2\theta, \tag{3}$$

where the viscosity ν varies as

$$\nu = \frac{\nu_0}{\beta(\theta)}, \tag{4}$$

and

$$\beta(\theta) = 1 + \beta_1\theta + \beta_2\theta^2 + \beta_3\theta^3, \tag{5}$$

and the density ρ varies as

$$\rho = \rho_0\,[1 - \alpha^*(\theta\Delta T) - \alpha'(\theta \cdot \Delta T)^2], \tag{6}$$

and

$$\alpha = \frac{\alpha'}{\alpha^*}\Delta T. \tag{7}$$

Here R the Rayleigh number is defined as

$$\mathrm{R} = \frac{gak\Delta T\alpha^*}{\kappa\nu_0}. \tag{8}$$

These equations may be simplified in two dimensions by formulation in terms of a stream function such that

$$U = \frac{\mathrm{R}}{\lambda}\frac{\partial \psi}{\partial Y}, \tag{9}$$

$$V = -\frac{\mathrm{R}}{\lambda}\frac{\partial \psi}{\partial X}, \tag{10}$$

where $U = U_1$, $V = U_2$, $X = X_1$, $Y = X_2$, after which

$$\nabla^2\psi = -(1 + 2\alpha\theta)\frac{\partial \theta}{\partial X}\beta(\theta) + \left(\frac{\partial \psi}{\partial X}\frac{\partial \theta}{\partial X} + \frac{\partial \psi}{\partial Y}\frac{\partial \theta}{\partial Y}\right)\frac{\beta'(\theta)}{\beta(\theta)}, \tag{11}$$

and

$$\frac{\partial \theta}{\partial \tau} = \nabla^2\theta - \mathrm{R}\left(\frac{\partial \psi}{\partial Y}\frac{\partial \theta}{\partial X} - \frac{\partial \psi}{\partial X}\frac{\partial \theta}{\partial Y}\right). \tag{12}$$

In this form the two equations (11) and (12) are a suitable pair of governing equations for the flow; however, difficulties arise in the numerical representation of the nonlinear terms in Equation (11),

$$\frac{\partial \psi}{\partial X}\frac{\partial \theta}{\partial X} \tag{13}$$

In order to satisfactorily represent physical instabilities in this flow it is desirable (see [7]) to use a numerical method which semiconserves the kinetic energy of the flow—such a method is the Arakawa scheme [23]. This scheme may be used directly when the nonlinear terms are in the form of a Jacobian, as they are in equation (12). However, it has proved impossible to derive a similarly conservative scheme for nonlinear terms like (13) which are not in the form of a Jacobian. Therefore equation (11) is reformulated, substituting pressure for the stream function in the nonlinear terms and scaling the pressure to simplify the equation, after which

$$\nabla^2\psi = -\frac{\partial \theta}{\partial X}[(1 + 2\alpha\theta)\beta(\theta) + \theta(1 + \alpha\theta)\beta'(\theta)] - \delta(P, \theta)\beta(\theta), \tag{14}$$

where $\delta(P, \theta)$ is the Jacobian

$$\delta(P, \theta) \equiv \frac{\partial P}{\partial X}\frac{\partial \theta}{\partial Y} - \frac{\partial P}{\partial Y}\frac{\partial \theta}{\partial X}. \tag{15}$$

The scaled pressure may be evaluated from equations (2) and (3), so

$$\nabla^2 P = (1 + 2\alpha\theta)\frac{\partial \theta}{\partial Y} + \delta(\psi, \theta)\frac{\beta'(\theta)}{[\beta(\theta)]^2}. \tag{16}$$

Nomenclature

- a = depth of porous layer
- C_p = specific heat of saturating fluid
- g = acceleration due to gravity
- k = permeability of permeable material
- Nu = Nusselt number
- P = pressure (nondimensional)
- R = Rayleigh number (see equation 8)
- T_1, T_0 = maximum and minimum temperatures
- V_i = fluid velocities (nondimensional)
- X_i = space coordinates (nondimensional)
- α^* = linear coefficient of thermal expansion of fluid
- α' = quadratic coefficient of thermal expansion of fluid
- α = thermal expansion parameter (see equation 7)
- $\beta(\theta)$ = temperature dependence of viscosity (see equation 4)
- $\beta_1, \beta_2, \beta_3$ = coefficients of $\beta(\theta)$ (see equation 5)
- ΔT = temperature differential ($T_1 - T_0$)
- λ = ratio of volumetric heat capacities, fluid to saturated formation
- κ = thermal diffusivity of saturated medium
- θ = temperature (nondimensional)
- ψ = stream function
- ν, ν_0 = kinematic viscosity of fluid (and base value)
- ρ, ρ_0 = fluid density (and base value)
- τ = time (nondimensional)
- τ_p = fluctuation time period

The heat transport equation (12) completes the set of governing equations, and using Jacobian notation,

$$\frac{\partial \theta}{\partial \tau} = \nabla^2 \theta + R\delta(\psi, \theta). \tag{17}$$

Thus, everywhere that a product of first derivatives appears in the equations the expression may be evaluated using Arakawa's scheme, since these products are all in Jacobian form.

Physical Parameters

From empirical tables given by Engineering Sciences Data [24], a least squares fit is obtained to determine the coefficients of the variation of the viscosity and density of water with temperature. Using the method of orthogonal polynomials, the number of coefficients may be increased until the desired accuracy is obtained. Over a range of temperatures 15–250°C a cubic variation in ν and a quadratic variation in ρ gives accuracy of within 5 per cent. These values are

$$\alpha = 0.9229\ (\Delta T)$$

$$\beta_1 = 2.606\ (\Delta T)$$

$$\beta_2 = 1.335\ (\Delta T)^2$$

$$\beta_3 = -0.4762\ (\Delta T)^3, \tag{18}$$

where ΔT is in units of 100 K.

This variation is illustrated in Fig. 1.

It is seen that in this case the only parameters governing the problem are the Rayleigh number R and the temperature differential ΔT. A value of ΔT of 150 K is chosen as a conservative minimum value for geothermal reservoirs of physical interest, and a range of Rayleigh numbers from 50 to 160 is considered. It should be noted that the variation of viscosity between 150 K and 250 K is very much less significant than the variation at lower temperatures.

The boundary configurations used are the same as those described in Horne and O'Sullivan [7, 8], namely, a two-dimensional region with a line of vertical symmetry, enclosed on both sides by impermeable, insulating sidewalls, and heated along half of the base. This configuration is chosen because, in the constant viscosity case, it demonstrates a regular oscillatory convective behavior (see [7]) whereas a uniformly heated configuration shows an irregularly fluctuating convective state (see [16]). The half heated case therefore has less degrees of freedom and is thus better able to illustrate the effects of variable viscosity.

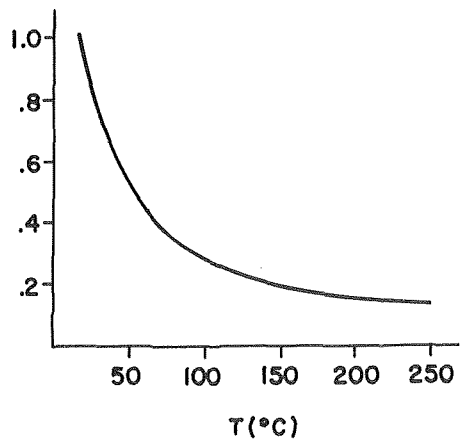

Fig. 1 Normalized cubic approximation to the variation of kinematic viscosity with temperature T in pure water

The top boundary of the region may be either impermeable as in Horne and O'Sullivan [7] or infinitely permeable (i.e., at constant pressure) as in Horne and O'Sullivan [8, 9]. These two cases represent the extremes of geothermal systems that are either totally capped or totally recharged.

The solutions are generated on a 33 × 33 finite difference mesh and require about ⅔ s/time step on an IBM 370/168 computer when direct Poisson equation solving routines (Busbee, Golub, and Nielson [24]) are used for the solution of equations (14) and (16). Convective patterns at least as vigorous as those in the constant viscosity solutions occur at considerably lower Rayleigh numbers (based on the cold water conditions). Choice of the grid size was made as in Horne and O'Sullivan [7], with fourth-order accurate spatial differences used throughout. In [7] a similar numerical scheme showed excellent agreement with both analytical and experimental results.

Results

The results for the series of solutions are collated in Table 1 for the closed and open boundary configurations. In all but one case the flow regimes are fluctuating convective, and the Nusselt numbers vary between Nu_{min} and Nu_{max}. τ_p is a time period characteristic of the fluctuation—in the case of the regular oscillatory flows this is strictly the time period of the oscillation, and in the case of fluctuating flows it is the minimum time between successive local temperature maxima at a reference point in the rising plane of the flow. (See Table 1 on following page.)

These flows demonstrate some interesting differences from and similarities to the constant viscosity solutions. Fig. 2 (impermeable top boundary) and Fig. 3 (permeable top boundary) may be compared to Figs. 1 and 2 in Horne and O'Sullivan [9].

The closed region flows at lower Rayleigh numbers (as in Fig. 2, for example) are distinctive in that the viscosity effects are emphasized. The rising plume follows a less viscous "channel" bringing hot fluid so close to the surface that the thermal boundary layer at the top of the plume becomes unstable, and a smaller reverse circulation is set up. However, apart from this additional instability the flows are not dissimilar to the regular oscillatory flows observed in the constant viscosity case, although it should be noted that the Nusselt number variation is not as large at higher values of the Rayleigh number.

At the highest Rayleigh number value 160 in the open boundary case, the flow exhibits an almost triperiodic behavior, generating three evenly spaced thermals at irregular intervals. The time interval reported in Table 1 is the interval between these disturbances, but the sets of three occur at intervals up to six times this value. At lower values of the Rayleigh number the open boundary case also is similar to its constant viscosity counterpart, except that velocities in the plume are much higher. Fig. 4 shows a comparison of the streamlines at comparable effective Rayleigh numbers. The fluid accelerates rapidly as it loses viscosity in crossing the heater.

Having used the numerical procedure to generate solutions of practical interest, it is also possible to produce more commonly observed flows such as those in the uniformly heated configuration normally used in experiments. At a Rayleigh number of 50 the flow closely resembles the fluctuating convective state reported by Cal-

Table 1

Top Boundary	R	Nu_{min}	Nu_{max}	ψ_{max}	τ_p	Flow Regime
Impermeable	50	3.60	5.10	0.259	0.0248	Regular Oscillatory
	80	5 59	5.71	0.281	0.0024	Regular Oscillatory
	160	8.13	8.23	0.312	0.0013	Regular Oscillatory
Permeable	50	13.29	3.29	0.342	—	Steady
	80	2.80	3.55	0.265	0.0031	Approximately Regular Oscillatory
	160	2.75	3.80	0.295	~0.00025	Irregular Fluctuations

tagirone, et al. [16] (see Fig. 5) with the exception of the small reverse circulation in one of the rising plumes due to the decreasing viscosity effects (the temperature differential 150 K used here is higher than that in experiments at atmospheric pressure). This reverse cell does not appear with smaller temperature differentials. In this case the flow is fluctuating with a characteristic period of order 0.0045, with a Nusselt number varying approximately within the range 6–10.

Discussion

Interactions between thermal disturbances in the flow are less prominent if the effects of increasing α and decreasing ν are included. The fluid becomes buoyant faster as it reaches high temperature and since it also loses viscosity the net effect is a rapid acceleration of the flow passing over and leaving the heater. The evolution of the thermal boundary layer over the heater is then an accumulation both of thermal energy and of low viscosity fluid, and the flight of a thermal disturbance depletes the layer in a less regular manner than would be the case in constant viscosity fluid. Also the velocities of the flows across the heater and the effective local Rayleigh numbers are both higher, so even though disturbances are generated more rapidly, they are also easily swept away. So, the magnitude of their anomalous temperature is less than that in the constant viscosity/constant expansivity case. The Nusselt number variation is correspondingly lower.

Thus it is seen that the effect of inclusion of real fluid behavior in considerations of natural convective motion in porous media is to weaken the mechanism of the production of fluctuating flows and to introduce a degree of randomness into their occurrence. It is also interesting to note that the flow patterns may appear as if they are following physical channels in the region even though the medium is in fact homogeneous and isotropic and the channels are merely produced by the physical characteristics of the flow. The implications of these results in studies of goethermal convection are twofold. First, regions of high thermal gradient may be distinctly delineated and, secondly, oscillatory fluid flow instabilities may not be as prominent as might be expected using only a constant viscosity analysis.

Acknowledgments

The support of Stanford University Departments of Chemical Engineering and Petroleum Engineering and the Stanford Institute for Energy Studies for one of the authors R. N. Horne during the preparation of this paper is gratefully acknowledged.

References

1 Horton, C. W., and Rogers, F. T., "Convection Currents in a Porous Medium," *Journal of Applied Physics,* Vol. 16, 1945, p. 367.

2 Lapwood, E. R., "Convection of a Fluid in a Porous Medium," *Proceedings of the Cambridge Philosophical Society,* Vol. 44, 1948, p. 508.

3 Wooding, R. A., "Steady State Free Convection of a Liquid in a Saturated Permeable Medium," *Journal of Fluid Mechanics,* Vol. 2, 1957, p. 273.

4 Donaldson, I. G., "Temperature Gradients in the Upper Layers of the Earth's Crust Due to Convective Water Flows," *Journal of Geophysical Research,* Vol. 67, 1962, p. 3449.

5 Elder, J. W., "Steady Free Convection in a Porous Medium Heated from Below," *Journal of Fluid Mechanics,* Vol. 27, 1967, p. 29.

6 Elder, J. W., "Transient Convection in a Porous Medium," *Journal of Fluid Mechanics,* Vol. 27, 1967, p. 609.

7 Horne, R. N., and O'Sullivan, M. J., "Oscillatory Convection in a Porous Medium Heated from Below," *Journal of Fluid Mechanics,* Vol. 66, 1974, p. 339.

8 Horne, R. N., and O'Sullivan, M. J., "Oscillatory Convection in a Porous Medium: The Effect of Throughflow," *Proceedings of the 5th Australian Conference on Hydraulics and Fluid Mechanics,* University of Canterbury, New Zealand, Vol. 2, 1974, p. 231.

9 Horne, R. N., and O'Sullivan, M. J., "The Origin of Oscillatory Convection in a Porous Medium Heated from Below," to appear in *The Physics of Fluids,* 1978.

10 Caltagirone, J. P., "Convection Naturelle Fluctuante en Milieu Poreux," *Comptes Rendus Academie Sciences Paris,* t. 278, série B, 1974, p. 259.

11 Caltagirone, J. P., "Thermoconvective Instabilities in a Horizontal Porous Layer," *Journal of Fluid Mechanics,* Vol. 72, 1975, p. 269.

12 Palm, E., Weber, J. E., and Kvernvold, O., "On Steady Convection in a Porous Medium," *Journal of Fluid Mechanics,* Vol. 54, 1972, p. 153.

13 Busse, F. H., and Joseph, D. D., "Heat Transport in a Porous Layer," *Journal of Fluid Mechanics,* Vol. 54, 1972, p. 521.

14 Straus, J. M., "Large Amplitude Convection in Porous Media," *Journal of Fluid Mechanics,* Vol. 64, 1974, p. 51.

15 Combarnous, M. A., and LeFur, B., "Transfert de Chaleur par Convection Naturelle dans une Couche Poreuse Horizontale," *Comptes Rendus Academie Sciences Paris,* t. 269, Série B, 1969, p. 1009.

16 Caltagirone, J. P., Cloupeau, M., and Combarnous, M. A., "Convection

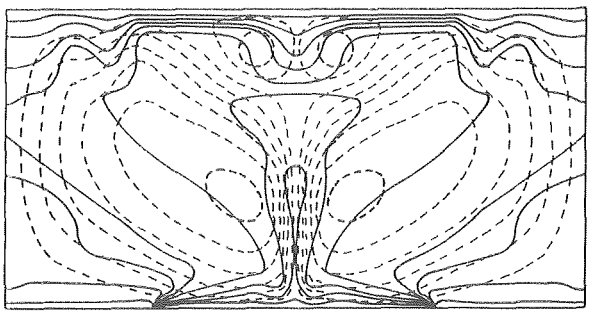

Fig. 2 Flow patterns (broken lines) and isotherms (full lines) for closed region at R = 80. The flow is unsteady so this diagram represents only the pattern at a particular instant.

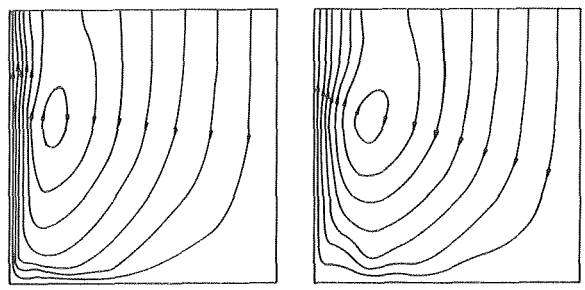

Fig. 4 Comparison of streamlines between variable and constant viscosity flows at comparable Rayleigh numbers. Left: variable viscosity at R = 80. Right: constant viscosity at R = 500. The region is open.

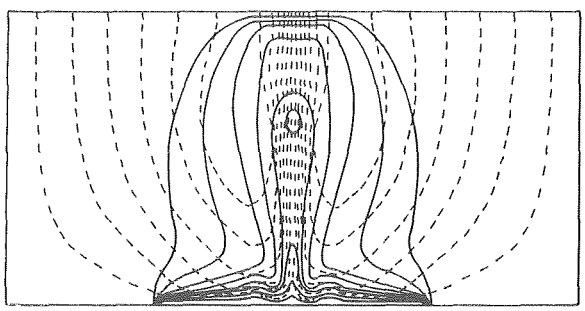

Fig. 3 Flow lines and isotherms for open region at R = 80

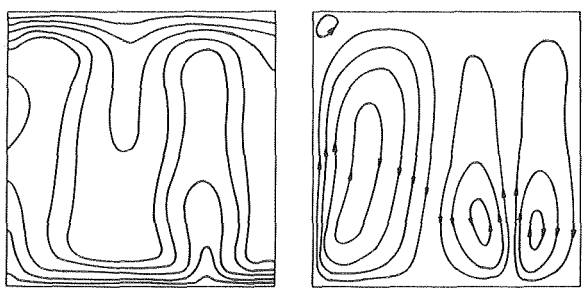

Fig. 5 Flow lines and isotherms for closed region at R = 50 with uniform heat source. Left: isotherms, Right: streamlines

Naturelle Fluctuante dans une Couche Poreuse Horizontale," *Comptes Rendus Academie Sciences Paris*, t. 273, Série B, 1971, p. 833.

17 Horne, R. N., "Transient Effects in Geothermal Convective Systems," unpublished Ph.D. thesis, University of Auckland, New Zealand, 1975.

18 Rogers, F. T., and Morrison, H. L., "Convection Currents in Porous Media. III. Extended Theory of the Critical Gradient," *Journal of Applied Physics*, Vol. 21, 1950, p. 1177.

19 Kassoy, D. R., and Zebib, A., "Variable Viscosity Effects on the Onset of Convection in a Porous Media," *The Physics of Fluids*, Vol. 18, 1975, p. 1649.

20 Sorey, M. L., "Numerical Modeling of Liquid Geothermal Systems," USGS Open File Report 75-613, Menlo Park, California, 1976.

21 Straus, J. M., and Schubert, G., "Thermal Convection of Water in a Porous Medium: Effects of Temperature and Pressure Dependent Thermodynamic and Transport Properties," *Journal of Geophysical Research*, Vol. 82, 1977, p. 325.

22 Horne, R. N., and O'Sullivan, M. J., "Numerical Modeling of a Desaturating Geothermal Reservoir," to appear in *Numerical Heat Transfer*, 1978.

23 Arakawa, A., "Computational Design for Long-Term Numerical Integration of the Equations of Fluid Motion: Two-Dimensional Incompressible Flow. Part 1," *Journal of Computational Physics*, Vol. 1, 1966, p. 119.

24 Engineering Sciences Data, Item nos. 68009, 68010, Engineering Sciences Data, London.

25 Busbee, B. L., Golub, G. H., and Nielson, C. W., "On Direct Methods for Solving Poisson's Equations," *Society of Industrial and Applied Mathematics Journal of Numerical Analysis*, Vol. 7, 1970, p. 627.

O. C. Jones, Jr.

Head, Thermal Hydraulic Development Division,
Department of Nuclear Energy,
Brookhaven National Laboratory,
Upton, N. Y.
Mem. ASME

N. Zuber

Senior Reactor Analyst,
Division of Water Reactor Safety Research,
U. S. Nuclear Regulatory Commission,
Washington, D. C.
Mem. ASME

Bubble Growth in Variable Pressure Fields[1]

The case of a spherical vapor bubble growing in an infinite, uniformly heated liquid, has been analyzed under the thin boundary layer approximation for the effects of a variable pressure field, including density variation. It has been shown that, in addition to the usually accepted effects of initial superheat, variable pressure effects can be quite important and dominate the rate of growth. For the case where pressure changes cause the vapor temperature to behave as t^n, (t being time), the bubble radius will grow as $t^{n+1/2}$, significantly faster than the $\sqrt{t}$ behavior usually expected. The analysis has been shown to compare favorably with existing data.

Introduction

In problems involving boiling heat transfer, especially in calculations of nonequilibrium vapor generation, the growth rate of bubbles has been shown to be of fundamental importance. Numerous studies have been undertaken beginning with the hydrodynamic formulations of Besant [1] and Rayleigh [2] and continuing with the thermal interactions considered by Bosnjakovic, [3] Fritz and Ende, [4] Forster and Zuber, [5] Plesset and Zwick, [6] Scriven, [7] and more recently by Theofanous, et al. [8] among others. With the exception of the work of Theofanous, et al. [8] which involved a numerical solution to the nonequilibrium phase change problem, most modern results, which apply to the constant pressure case, agree that during the thermally dominated growth period after the first few or tens of microseconds, bubble growth in a uniformly superheated liquid with constant properties may be expressed as

$$R = R_0 + \frac{2K_s}{\sqrt{\pi}} \mathrm{Ja}_T \sqrt{\alpha_\ell t} \tag{1}$$

The Jakob number, Ja_T, is based on the initial superheat, and the vapor density is assumed constant. The factor K_s is a sphericity correction factor determined by Forster and Zuber [5] to be $\pi/2$, and by Plesset and Zwick [6] to be $\sqrt{3}$. It is interesting to note that, while it is well known that (1) applies only to the case of a constant pressure field, it has been applied in recent work to the case of varable pressure fields, [9, 10] even though the results of Hooper, et al. [17] indicate that variable pressure effects result in significant deviations between (1) and experimental results.

With the increasing importance of flashing-induced vapor production such as found in critical, two-phase flows during a hypothetical Loss-of-Coolant Accident (LOCA) transient in a Pressurized Water Reactor (PRW), the description of the thermal nonequilibrium vapor production process due to decompression assumes a fundamental place in a phenomenological description of the process. This problem was treated numerically by Theofanous, et al. [8], including the effects of thermodynamic nonequilibrium at the interface. For nitrogen systems, where thermodynamic nonequilibrium effects were small, the agreement between the theory and the data was good.

Hooper, et al. [17] devised an explicit, semi-empirical method based on the results of Plesset and Zwick [6] where the dimensionless bubble size was analytically bounded by

$$1 \leq \frac{R(t) - R_0}{\dfrac{k_\ell}{\sqrt{\pi \alpha_l} \rho_v \Delta i_{fg}} \displaystyle\int_0^{\tau_b} \frac{[T_\ell - T_s(\xi)]}{\sqrt{\tau_b - \xi}} d\xi} \leq 3 \tag{2}$$

Here R and R_0 are the current and initial bubble sizes, k_ℓ and α_ℓ are the liquid conductivity and diffusivity, ρ_v is the vapor density, and Δi_{fg} is the latent heat. τ_b is the time measured with respect to the time when the pressure has decreased to the saturation value according to the initial liquid temperature T_ℓ, and T_s is the time varying saturation temperature. If we call the denominator in (2) Ψ, then Hooper, et al. plotted the values of $R(t) - R_0$ obtained from photographic measurements against values of Ψ where $T_s(\tau)$ was determined from pressure measurements. The relevant data were indeed bounded as in (2), and an apparent relationship $R(\tau) - R_0 = N\Psi$ was found, where $N = 2.2$ was obtained as an average from the data. The authors did not account for the variable vapor density with pressure, nor is there any a priori reason to expect N to remain universally constant.

Niino [11] recently analyzed the problem by assuming a parabolic temperature profile across the thermal boundary layer in the liquid which was given by $[T(r, t) - T_s(t)] = [T_\ell - T_s(t)][2(r - R)/\delta - (r - R)^2/\delta^2]$. The boundary layer thickness δ was the thickness required to obtain a vanishing temperature gradient and the uniform temperature T_ℓ. His saturation temperature $T_s(t) = T_s[p(t)]$ varied with the pressure p. He correctly accounted for vapor density variations in his differential equation, but the approximate solution obtained contained some errors in accounting for the effects of variable vapor

Contributed by the Heat Transfer Division for publication in the JOURNAL OF HEAT TRANSFER. Manuscript received by the Heat Transfer Division July 30, 1976.

density, the property most affected by the decompression process. For small R_0 with $\rho_{v0}/\rho_v \sim 1$, his result becomes

$$R(t) = \frac{2k_\ell}{\Delta i_{fg}\sqrt{\alpha_\ell}} \sqrt{\int_0^t \frac{[T_\ell - T_s(\eta)]^2}{\rho_v{}^2} d\eta} \tag{3}$$

Since a parabolic profile can only account for monotonically decreasing pressure and not the case where recompression causes vapor temperature turn-around, the result cannot be of general utility.

In the work which follows, a reasonably exact formulation, without any free parameters, for the thermally-dominated, thin boundary layer, decompressive growth problem shall be formulated for the case where variations in vapor density cannot be neglected. It will be shown that the $\sqrt{t}$ growth behavior is a special case of a more general problem and cannot adequately predict decompressive growth. In general, it will be shown that if the saturation temperature changes as t^n, then bubble growth occurs as $t^{n+1/2}$. In particular, for a linear saturation temperature decay it is shown that the dominant growth is $R \sim t^{3/2}$ rather than the square root behavior commonly accepted.

Formulation

General Bubble Growth. In the present problem, inertial effects shall be neglected. For the constant superheat case Forster and Zuber [18] have shown that this assumption results in errors of order $0(\Delta T/T)$. While a detailed evaluation of this approximation is well beyond the scope of this paper, it seems reasonable to expect similar errors where ΔT is taken as the instantaneous, variable-pressure-induced superheat and thus to be of similar order as other factors neglected in this work as described below. The accommodation coefficient for evaporation shall be taken to be unity. That is, the liquid temperature at the liquid-vapor interface shall be taken to be the vapor temperature which is assumed to be the saturation temperature according to the system pressure, neglecting surface tension effects. The energy and continuity equations then combine to yield

$$\frac{dm_b}{dt} = \frac{4\pi R^2 \phi}{\Delta i_{fg}}, \tag{4}$$

m_b being the mass of the bubble, R its radius, ϕ the interfacial heat flux, and Δi_{fg} the latent heat. Substituting for the bubble mass in terms of the vapor density and its radius, and then expanding yields

$$\frac{1}{3\rho_v R^2}\frac{d\rho_v R^3}{dt} = \frac{\phi(t)}{\Delta i_{fg}\rho_v(t)} \tag{5}$$

The point of view is taken that the pressure and thus the density of saturated vapor may be specified in time. Equation (5) may be solved using standard techniques yielding

$$R(t) = \left(\frac{\rho_{v0}}{\rho_v}\right)^{1/3}\left\{R_0 + \frac{1}{\rho_{v0}\Delta i_{fg}}\int_0^t \left(\frac{\rho_{v0}}{\rho_v}\right)^{2/3}\phi(\eta)d\eta\right\} \tag{6}$$

Note that the constant R_0 is the radius of the bubble at its initial appearance before heat exchange has begun; i.e., at the start of the growth process where no boundary layer has developed and the liquid temperature is constant throughout. It is not an artificial radius but the "critical radius" of a metastable bubble having been instantaneously nucleated to a size just large enough to begin to grow spontaneously.

In order to proceed further, an expression must be obtained for the interfacial heat flux to the vapor, $\phi(t)$. This will be accomplished in the next section.

Interfacial Heat Flux. We wish to determine the instantaneous value for the heat flux through the liquid which goes to evaporation at the interface. It has been commonplace to treat the liquid as a semi-infinite medium undergoing transient conduction of heat to or from the interface. If the present problem is considered, the overall behavior being sought is a description of the growth of a nucleation site from its critical or initial radius due to decompression. We thus visualize the following steps in the process:

(1) Pressure begins to decrease in an initially subcooled liquid.
(2) The pressure decreases below the saturation pressure according to the liquid temperature, thus superheating the liquid.
(3) As the pressure continues to decrease, a vapor nucleus is formed with the vapor temperature, (and hence the initial interfacial liquid temperature), at saturation temperature according to the internal bubble pressure, $p(t_0) + 2\sigma/R_0$. Since at this point the liquid is superheated the effect is to produce a step change to the temperature of the liquid at the interface giving it initial superheat ΔT_s.
(4) The pressure continues to change causing the vapor temperature, (and thus the interfacial liquid temperature), to continue to change, resulting in continued variation in boundary

Nomenclature

A = Jakob number ratio $\mathrm{Ja}_T/(\mathrm{Ja}_T + \mathrm{Ja}_p)$
b = slope of linear temperature-time decay curve
C_ℓ = specific heat of the liquid
$D(u)$ = Dawson's integral
$F(t)$ = generalized time behavior of the vapor temperature
F_0 = initial difference between the vapor and uniform liquid temperature
Δi_{fg} = latent heat of vaporization
Ja_T = Jakob number based on initial superheat: $\rho_\ell C_\ell \Delta T/\rho_{v0}\Delta i_{fg}$
Ja_p = Jakob number for pressure effects: $\rho_\ell C_\ell b R_0{}^2/\rho_{v0}\Delta i_{fg}\alpha_\ell$ for linear temperature decay; $\rho_\ell C_\ell \Delta T_{0\infty}/\rho_{v0}\Delta i_{fg}$ for exponential pressure decay.
k_ℓ = thermal conductivity of the liquid
K_s = sphericity correction: $\pi/2$ for Forster-Zuber [5]; $\sqrt{3}$ for Plesset-Zwick [6]
$L = T_0\Delta P_{0\infty}/\rho_{v0}\Delta i_{fg}$
m_b = mass of vapor in the bubble
M = error ratio – equation (13)
n = exponent for temperature-time decay
p = pressure
P_0 = pressure at start of bubble growth
P_r = reduced pressure (based on critical pressure)
P_∞ = final pressure following exponential decay
$\Delta P_{0\infty} = (P_0 - P_\infty)$
R = bubble radius – function of time
R_0 = initial bubble radius
$\mathcal{R}$ = gas constant – $p/\rho T$
t = time
$t^+ = \Omega t$ – dimensionless time
$t^* = \alpha t/R_0{}^2$ – dimensionless time
T = temperature
T_ℓ = initial uniform liquid temperature
T_0 = vapor temperature at start of bubble growth
T_s = saturation temperature
T_∞ = vapor temperature at end of exponential decay
ΔT_s = initial superheat $(-F_0)$
$\Delta T_{0\infty} = (T_0 - T_\infty)$
x = distance into liquid from interface
α_ℓ = thermal diffusivity of the liquid
ϕ = heat flux; ϕ_ℓ – into the liquid; ϕ_v – into the vapor
Ω = pressure decay frequency (inverse time constant)
ρ = density
ρ_ℓ = liquid density
ρ_v = vapor density
ρ_{v0} = initial vapor density
θ = transformed bubble radius – $\rho_v{}^{1/3}R$
τ = generalized time
τ_b = time at start of bubble growth

temperature for thermal conduction to the bubble, and resulting in variation of the growth rate of the bubble from that caused by the initial superheat.

Since it is well known [5, 6] that the sphericity effects are well accounted for by a constant multiplier, K_s, a Cartesian reference frame will be utilized in Lagrangian coordinates for an observer positioned on the interface. To the first order approximation, the moving boundary effects are thus neglected. We therefore choose the semi-infinite solid bounded on the left by $x = 0$ as representing the liquid surrounding the bubble and wish a solution to the transient conduction problem with the following conditions:

at $x = 0$, $T(0, t) = T_\ell + F(t)$;
as $x \to \infty$, $T(x, t)$ is finite:
at $t = 0$, $T(x, 0) = T_\ell$

Thus T_ℓ is the initial liquid temperature, the initial superheat is $\Delta T_s = F(0) = -F_0$, and the time behavior of the interface is represented by $F(t)$.

The solution has been given by Carslaw and Jaeger [12] among others resulting in

$$\phi_\ell(t) = \frac{k_\ell F_0}{\sqrt{\pi\alpha_\ell t}} + \frac{k_\ell}{\sqrt{\pi\alpha_\ell}} \int_0^t \frac{F'(\eta)}{(t-\eta)^{1/2}} d\eta \tag{7}$$

where $F'(t) \equiv dT(0, t)/dt$ is the time rate of change of saturation temperature according to the vapor pressure, within our previous assumptions.

Bubble Growth Solution. Having specified the heat flux at the liquid surface in (7) as the solution to the transient conduction problem, the spherical correction, K_s, may be included with (7) into (6) while realizing that the heat flux to the vapor is the opposite of that into the liquid, $\phi_v(t) = -\phi_\ell(t)$. The result becomes

$$R(t) = \left(\frac{\rho_{v0}}{\rho_v}\right)^{1/3} \left\{ R_0 + \frac{K_s k_\ell \Delta T_s}{\rho_{v0} \Delta i_{fg} \sqrt{\pi\alpha_\ell}} \int_0^t \left(\frac{\rho_{v0}}{\rho_v}\right)^{2/3} \eta^{-1/2} d\eta - \frac{K_s k_\ell}{\rho_{v0} \Delta i_{fg} \sqrt{\pi\alpha_\ell}} \int_0^t \left(\frac{\rho_{v0}}{\rho_v}\right)^{2/3} \int_0^\eta \frac{F'(\xi)}{(\eta-\xi)^{1/2}} d\xi d\eta \right\} \tag{8}$$

Equation (8) is quite general insofar as the previously specified assumptions can be maintained as reasonable. It properly describes the thermally limited growth of a spherical vapor cavity due to changes in vapor temperature caused by decompression and initial superheat, as well as short periods of compression-induced collapse where the thermal boundary layer is still relatively thin.

For constant vapor density, the first integral within the brackets of (8) would immediately yield the recognized growth given by equation (1). On the other hand, the second integral yields an additional effect not previously recognized—an effect which may be predominant in the behavior during decompression. In fact, since bubbles could conceivably be formed at zero superheat, $\Delta T_s = 0$, equation (1) would predict zero growth due to the variable pressure effects.

At this point several cases may be discussed according to the various simplifications or special circumstances which may arise. The balance of this paper shall be devoted to examining the application of (8) to various special cases, comparisons with existing data, and discussing the implications of the results. But first, an approximation allowing the density ratio within the integral terms to be expressed in terms of temperature will be developed.

Vapor Density Approximation. In this case, the ideal gas law may be combined with the Clausius-Clapeyron equation to express the density in terms of the temperature along the saturation line at low reduced pressures. The result is

$$\left(\frac{\rho_{v0}}{\rho_v}\right)^{2/3} = \left(\frac{T_0}{T}\right)^{-2/3} \exp\left\{\frac{2\Delta i_{fg}}{3\mathcal{R}T_0}\left(\frac{T_0}{T} - 1\right)\right\} \tag{9}$$

Now if we take $T_0/T = 1 + \epsilon$ and expand $(1 + \epsilon)^{-2/3}$ in a binomial expansion, it may then be combined with the standard exponential expansion to yield for (9),

$$\left(\frac{\rho_{v0}}{\rho_v}\right)^{2/3} \sim + \frac{2}{3}\left(\frac{\Delta i_{fg}}{\mathcal{R}T_0} - 1\right)\left(\frac{T_0}{T} - 1\right) + 0\left[\left(\frac{T_0}{T} - 1\right)^2\right] \text{ as } T \to T_0 \tag{10}$$

Using (10) with (8) yields an approximation for small vapor temperature variations given by

$$R(t) = \left(\frac{\rho_{v0}}{\rho_v}\right)^{1/3} \left\{ R_0 + \frac{K_s k_\ell \Delta T_s}{\rho_{v0} \Delta i_{fg} \sqrt{\pi\alpha_\ell}} \times \left[2\sqrt{t} + \frac{2}{3}\left(\frac{\Delta i_{fg}}{\mathcal{R}T_0} - 1\right) \int_0^t \times \left(\frac{T_0}{T} - 1\right) \eta^{-1/2} d\eta \right] - \frac{K_s k_\ell}{\rho_{v0} \Delta i_{fg} \sqrt{\pi\alpha_\ell}} \times \left[\int_0^t \int_0^\eta \frac{F'(\xi)}{(\eta-\xi)^{1/2}} d\xi d\eta + \frac{2}{3}\left(\frac{\Delta i_{fg}}{\mathcal{R}T_0} - 1\right) \times \int_0^t \left(\frac{T_0}{T} - 1\right) \int_0^\eta \frac{F'(\xi)}{(\eta-\xi)^{1/2}} d\xi d\eta \right] \right\} \tag{11}$$

In order to determine the importance of the density correction terms, we are interested in examining the ratio

$$M = \frac{2}{3}\left(\frac{\Delta i_{fg}}{\mathcal{R}T_0} - 1\right) \frac{\int_0^t \phi(\eta)\left(\frac{T_0}{T} - 1\right) d\eta}{\int_0^t \phi(\eta) d\eta} \tag{12}$$

By using the mean value theorem, expanding T to first order, and taking an average first derivative, the expected error over time t may be expressed as

$$|M_E| \sim \frac{1}{3}\left(\frac{\Delta i_{fg}}{\mathcal{R}T_0} - 1\right) \frac{\Delta T}{T_0} + 0\left(\frac{\Delta T^2}{3T_0^2}\right) \quad \text{as} \quad \Delta T/T_0 = [T_0 - T(t)]/T_0 \to 0 \tag{13}$$

Typical values of this expected correction term are shown in Table 1 where the temperature change was taken to be 5.5°C. Of course the actual importance of the correction can only be determined if the actual expressions in (12) are evaluated. Since the temperatures to be evaluated are on the absolute scale, a constant temperature change will have a larger effect on cryogens at low pressure than on water or most fluoro-carbons. This fact is demonstrated in the table. For most practical purposes, the case of small temperature change may thus be approximated by

$$R(t) = \left(\frac{\rho_{v0}}{\rho_v}\right)^{1/3} \left\{ R_0 + \frac{2K_s}{\sqrt{\pi}} \mathrm{Ja}_T \sqrt{\alpha_\ell t} - \frac{K_s k_\ell}{\rho_{v0} \Delta i_{fg} \sqrt{\pi\alpha_\ell}} \int_0^t \int_0^\eta \frac{F'(\xi)}{(\eta-\xi)^{1/2}} d\xi d\eta \right\} \tag{14}$$

where the Jakob number for initial superheat, Ja_T, is given by

$$\mathrm{Ja}_T = \frac{\rho_\ell C_\ell \Delta T_s}{\rho_{v0} \Delta i_{fg}} \tag{15}$$

If the time rate of change of system pressure is small so that $F'\Delta t \ll \Delta T_s$, equation (14) becomes

$$R(t) \sim \left(\frac{\rho_{v0}}{\rho_v}\right)^{1/3} (R_0 + \mathrm{Ja}_T \sqrt{\pi\alpha_\ell t}) \quad \text{as} \quad F'\Delta t \to 0 \tag{16}$$

which we call the modified Forster-Zuber relationship in view of the

Table 1 Expected contribution of the integral effect of variable density on bubble growth for the case of a 5.5°C decrease in temperature

Pressure Bar	M_E – Water %	M_E – Nitrogen %
1	0.6	11
10	4	5
34	3	1.5
100	2	—

density correction term, where the spherical corrector was taken as $K_s = \pi/2$.

Results and Discussion

It would be desirable to obtain exact, nonintegral expressions for $R(t)$ directly from (8) or at least from (11). This is quite difficult to do, and the mathematics involved would unnecessarily obfuscate the results. The goal here is to confirm the theory by comparison with existing data as simply as possible. As a result, we shall concentrate on equation (14) where the integral effects of the vapor density correction are neglected with expected errors similar to those shown in Table 1.

Case 1: Generalized Polonomial Decay. In this case the temperature of the vapor shall be taken to be

$$T = T_0 - \sum_{n=1}^{\infty} b_n t^n \tag{17}$$

If all $b_n > 0$ this curve is generally concave downward in time, similar to the Lagrangian behavior observed with flashing in a uniform pipe (cf. Reocreux [21]). Since from (17) we find $F_n'(t) = -nbt^{n-1}$, (14) becomes immediately integrable for $n > -1/2$ assuming uniform convergence so that

$$R(t) = \left(\frac{\rho_{v0}}{\rho_v}\right)^{1/3} R_0 \left\{1 + \frac{2K_s}{\sqrt{\pi}}\left[\mathrm{Ja}_T\, t^{*\,1/2} + \sum \frac{n\beta(n, 1/2)}{(2n+1)} \mathrm{Ja}_{pn} t^{*\,n+1/2}\right]\right\} \tag{18}$$

where

$$t^* = \frac{\alpha_\ell t}{R_0^2}; \quad \mathrm{Ja}_T = \frac{\rho_\ell C_\ell \Delta T_s}{\rho_{v0} \Delta i_{fg}}; \quad \mathrm{Ja}_{pn} = \frac{b_n \rho_\ell C_\ell R_0^{2n}}{\rho_{v0} \Delta i_{fg} \alpha_\ell{}^n} \tag{19}$$

Note that there is no ready reference for the pressure-change-induced superheat, so that the transient Jakob number terms have reference temperatures chosen equivalent to $\Delta T_{rn} = b_n R_0^{2n}/\alpha_\ell{}^n$. Note also that if all effective n's are greater than unity, the bubble growth goes faster than $t^{3/2}$ so that the void volumes grow faster than $t^{9/2}$, almost explosive growth. This explains the strong autocatalytic effects in flashing-induced void growth in pipes [21] and indicates a very strong importance on the determination of initial void location (point of net vapor generation) in such systems.

Finally, note that if $b_n < 0$, (18) describes bubble collapse. If the thin boundary layer approximation is to hold in this case, the ratio δ/R must be much less than unity. This ratio is of order $0(\mathrm{Ja}^{-1})$ which implies that $1/(\mathrm{Ja}_T + \Sigma \mathrm{Ja}_{pn} t^n) \ll 1$. Since Ja_p has the coefficient "b" included, this ratio either increases or decreases in time and would be expected to give reasonable indications of validity, especially where linear superposition describes polynomial behavior. Note also as a result that in the case of pure decompression, the thin boundary layer approximation should even be better than for the case of uniform initial superheat.

Case 2: Linear Temperature Decay. As a special case of equation (18) we take $b_1 = b$ and $b_n = 0$, so that the result becomes

$$R(t) = \left(\frac{\rho_{v0}}{\rho_v}\right)^{1/3} R_0 \left\{1 + \frac{2K_s}{\sqrt{\pi}}\left[\mathrm{Ja}_T t^{*1/2} + \frac{2}{3}\mathrm{Ja}_p t^{*3/2}\right]\right\} \tag{20}$$

consistent with previous definitions.

Equation (20) may be put into dimensionless form involving only functions of the dimensionless time on the right hand-side. The result is

$$\frac{1}{K_s}\left\{\frac{1}{\mathrm{Ja}_T + \mathrm{Ja}_p}\right\}\left\{\frac{R}{R_0}\left(\frac{\rho_v}{\rho_{v0}}\right)^{1/3} - 1\right\} = \frac{2}{\sqrt{\pi}}\left(\frac{\mathrm{Ja}_T}{\mathrm{Ja}_T + \mathrm{Ja}_p}\right)\left(\sqrt{t^*} + \frac{2}{3}\frac{\mathrm{Ja}_p}{\mathrm{Ja}_T} t^{*3/2}\right) \tag{21}$$

where we have chosen to include the sphericity factor, K_s, on the left. Since these are known functions of the dimensionless time t^*, equation (21) may immediately be plotted with the Jakob fraction $A = \mathrm{Ja}_T/(\mathrm{Ja}_T + \mathrm{Ja}_p)$ as a parameter. This has been done in Fig. 1. It is seen that except where the initial superheat Jakob number, Ja_T, is much larger than the flashing Jakob number, the growth is dominated by the $t^{*3/2}$ term for $t^* \gg 1$. This is in substantive agreement with the results of Lipkis, Liu, and Zuber, [19] and Zwick [20] who analyzed the specific case of linear heating.

The only data the authors are aware of which would provide a comparison for the present theory are those of Niino [11]. In these experiments, he provided a uniformly heated pool of water, slightly subcooled with respect to the initial pressure, and then suddenly let the pressure begin to decay, almost exponentially. During the pressure decay period, and after the liquid had become superheated with respect to the instantaneous pressure, he caused a bubble to nucleate by pulsing a laser beam into the pool through a window, and took photographs by means of a high speed motion picture camera. The pressure transients were quite rapid, occurring over 6–20 ms, and his bubble growth data were recorded only for times less than ~2.5 ms, during which period the bubbles grew from the order of 1–10 μm to sizes of 150–300 μm.

The results of the comparison are shown in Figs. 2, 3, and 4. In these figures, the measured pressure variations are plotted, along with the corresponding values of saturation temperature and density. The solid lines in each of these three figures are the results of equations (20), which show a remarkably good agreement with the data. Note that while the temperature-time curve in Fig. 2 is quite linear, there is increasing curvature in the other two cases. In all three cases, the values for the best fit temperature-time slope, b, are included, as are the experimental values for the superheat and flashing Jakob numbers. For comparison purposes, the modified Forster-Zuber equation (16) is also plotted confirming the previously specified inapplicability of that theory to the present problem

Case 3: Exponential Pressure Decay. In this instance, we shall assume that the pressure decays exponentially such that

$$\frac{p - P_\infty}{P_0 - P_\infty} = e^{-\Omega t} \tag{22}$$

The integral in (14) with the Clausius-Clapeyron equation may be written as

$$I = -\frac{L}{\sqrt{\Omega}} \int_0^{t^+} \int_0^u (u - y)^{-1/2} e^{-y} dy du \tag{23}$$

where $L = T_0 \Delta P_{0\infty}/\rho_{v0} \Delta i_{fg}$ and the dimensionless time is $t^+ = \Omega t$. It is easily shown that similar order errors occur through neglect of the variable density terms here as were neglected earlier. A series of elementary steps including one integration by parts yields

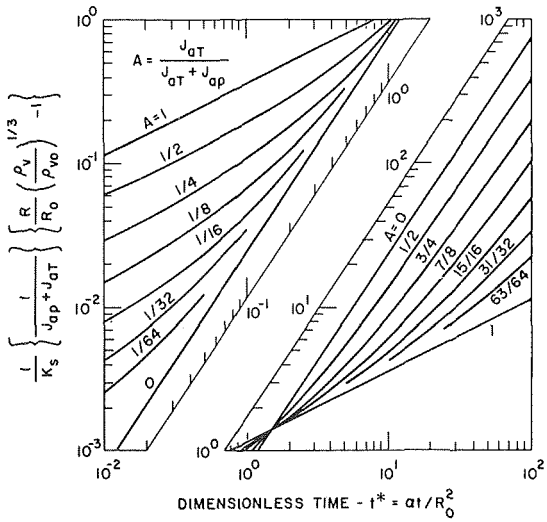

Fig. 1 Bubble growth function for the case of a linear temperature decay

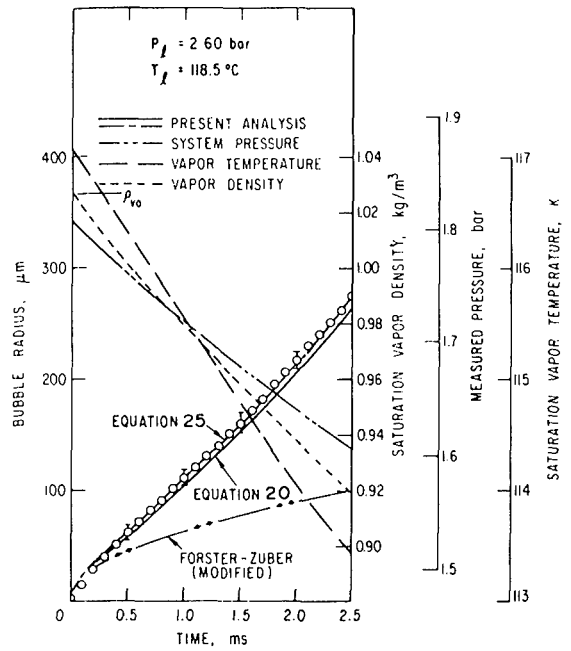

Fig. 2 Comparison of Niino's Fig. 67 data (reference [11]) with the present theory for cases of linear temperature decay and exponential pressure decay. For equation (26): $Ja_T = 2.57$, $Ja_p = 0.094$, $b = 1.462$°C/ms. For equation (40): $Ja_T = 2.57$, $Ja_p = 21.8$, $\Omega = 0.095$ ms^{-1}

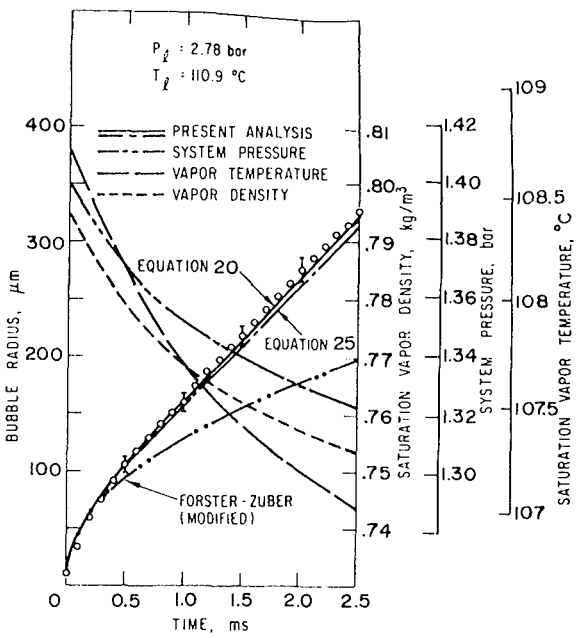

Fig. 4 Comparison of Niino's Fig. 68 data (reference [11]) with the present theory for cases of linear temperature decay and exponential pressure decay. For equation (26): $Ja_T = 5.04$, $Ja_p = 1.43$, $b = 0.89$°C/ms. For equation (40): $Ja_T = 5.04$, $Ja_p = 19.2$, $\Omega = 0.105$ ms^{-1}

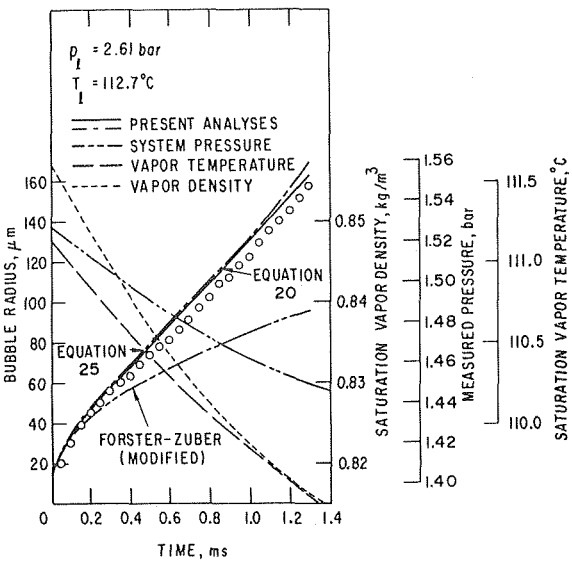

Fig. 3 Comparison of Niino's Fig. 66 data (reference [11]) with the present theory for cases of linear temperature decay and exponential pressure decay. For equation (26): $Ja_T = 3.29$, $Ja_p = 1.09$, $b = 1.367$°C/ms. For equation (40): $Ja_T = 3.29$, $Ja_p = 27.9$, $\Omega = 0.122$ ms^{-1}

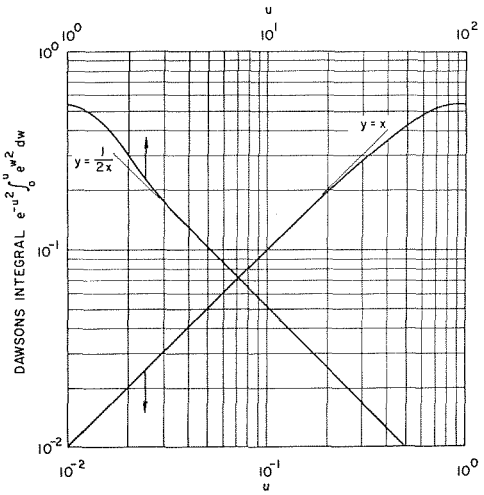

Fig. 5 Dawson's integral (reference [15])

$$I = 2\sqrt{t^+} - 2e^{-t^+}\int_0^{\sqrt{t^+}} e^{u^2}du \tag{24}$$

The integral expression in (24) is a form of Dawson's integral so that the bubble size is given by

$$R(t) = \left(\frac{\rho_{v0}}{\rho_v}\right)^{1/3}\left\{R_0 + \frac{2K_s}{\sqrt{\pi}}\mathrm{Ja}_T\sqrt{\alpha_\ell t} + \frac{2K_s}{\sqrt{\pi}}\mathrm{Ja}_p\sqrt{\frac{\alpha_\ell}{\Omega}}\left[\sqrt{\Omega t} - D(\sqrt{\Omega t})\right]\right\} \tag{25}$$

where the reference temperature in Ja_p is taken as $\Delta T_{0\infty}$. Dawson's integral is expressed as

$$D(u) = e^{-u^2}\int_0^u e^{z^2}dz \tag{26}$$

This integral has been tabulated by Lohmender and Riggsten, [14] and has been included herein as Fig. 5. Note that Dawson's integral has asymptotic behavior such that $D(u) \sim u$ as $u \to 0$, and $D(u) \sim \frac{1}{2}u$ as $u \to \infty$. It may be noted that (25) may be rewritten as

$$\frac{1}{K_s}\left\{\frac{1}{\mathrm{Ja}_T + \mathrm{Ja}_p}\right\}\left\{\frac{R}{R_0}\left(\frac{\rho_v}{\rho_{v0}}\right)^{1/3} - 1\right\} = \frac{2}{\sqrt{\pi}}\left\{\sqrt{t^*} - \frac{\mathrm{Ja}_p}{\mathrm{Ja}_T + \mathrm{Ja}_p}\sqrt{\frac{\alpha_\ell}{R_0^2\Omega}}D\left(\sqrt{\frac{\Omega R_0^2}{\alpha_\ell}}t^*\right)\right\} \tag{27}$$

from which several interesting features can be noticed. First, if there is no initial superheat, equation (27) for $t^* \to 0$ shows that the initial growth rate is zero rather than being unbounded. This is because there has been no driving force developed for energy transfer. Secondly, for large Ωt, the behavior approaches that for the uniform superheat case

where the combined Jakob number is important. That is

$$R(t) \sim \left(\frac{\rho_{v0}}{\rho_v}\right)^{1/3}\left\{R_0 + \frac{2K_s}{\sqrt{\pi}}\,\mathrm{Ja}\sqrt{\alpha_\ell t}\right\} \quad \text{as } \Omega t \to \infty \qquad (28)$$

where the reference temperature in Ja is now $(\Delta T_s + \Delta T_{0^\infty})$. In other words, far out in the exponential, the bubble loses the identity of the pressure behavior and experiences growth as if the entire temperature difference were an initial step change in superheat.

Equation (25) was used to calculate Niino's data with the results shown also in Figs. 2, 3, and 4. The Jakob numbers are given along with the value of Ω in each curve. Note that the values of Ja_T, Ja_p, and Ω were obtained by best fit of Niino's temperature and pressure-time behavior as required by (22), and not as a free parameter simply to obtain good results with (25). The agreement is again seen to be excellent, thus confirming the exponential pressure decay analysis.

A second set of data is available which give bubble growth during approximately exponential pressure decays. These are the data of Hewitt and Parker [16], who examined both the growth and collapse of large ($R > 250$ μm) nitrogen bubbles in a pool of liquid nitrogen under steady and transient pressure conditions for long times. Their decompression data were obtained from existing bubbles, it appears, where pressure decay followed a bubble collapse or equilibrium stage with zero initial superheat. Pressure decay frequencies of $0.03 \le \Omega \le 0.042$ ms^{-1} were obtained directly from Hewitt and Parkers pressure-time data using (22), and may be compared with the data of Niino [11] where $0.095 \le \Omega \le 0.122$ ms^{-1}. Comparisons of equation (25) with these data are shown in Figs. 6, 7, and 8.

Note that the observation times in these cases are almost two orders of magnitude longer than those of Niino [11]. While the agreement is reasonable, it is not as pleasing as that obtained in Figs. 2, 3, and 4. It is impossible to say, however, for bubbles with a previous growth or collapse history, what the thermal boundary layer looks like and how it actually affects the subsequent behavior.

The data of Hewitt and Parker [16] have also been analyzed by Theofanous, et al. [8], who completed a detailed numerical study on bubble growth in constant and time-dependent pressure fields including nonequilibrium vaporization effects. They, like Niino [11], assumed a quadratic temperature distribution in the liquid thermal boundary layer adjacent to the interface in order to solve the energy equation in the liquid, but included the integral effects of variable properties. Their single predictive curve has also been included in Figs. 6, 7, and 8, adjusted by as much as 50 μm to account for deviations between their average curve and the actual data for initial radius at $t = 0$. Since their analysis included the total effects of variable vapor properties, deviations between their theory and the present theory (which incidentally showed no noticeable effect on accommodation coefficient in this case), might be expected to indicate the importance of variable properties which for low pressure nitrogen are expected to be appreciable (Table 1). It is seen that the maximum deviations noted are of the same order as that given in the table.

It appears that the data in [16] behave somewhat differently than predicted. First, the data indicate oscillations in the bubble radius, not unexpected in view of the large sizes and times observed. These

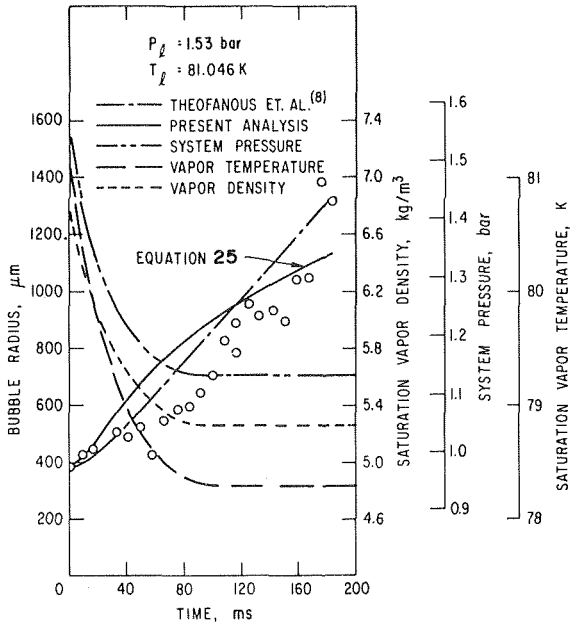

Fig. 7 Comparison of data of Hewitt and Parker (reference [16]) (their Fig. 10) for the case of exponential pressure decay. For equation (40): $\mathrm{Ja}_T = 0$, $\mathrm{Ja}_p = 3.32$, $\Omega = 0.414$ ms^{-1}

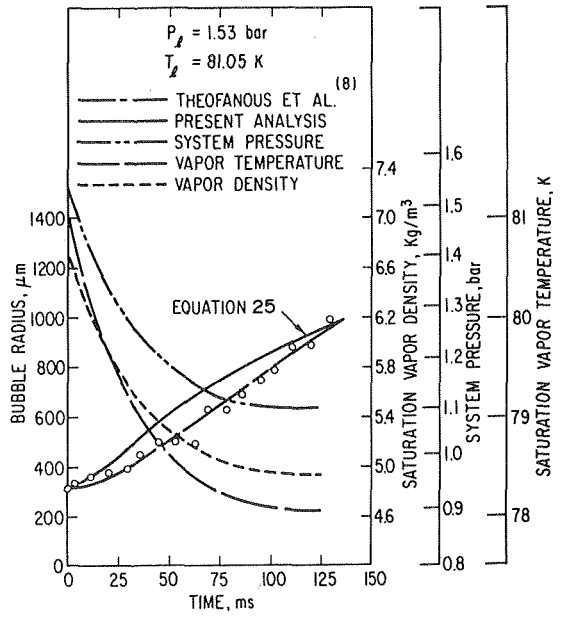

Fig. 6 Comparison of data of Hewitt and Parker (Reference [16]) (their Fig. 9) for the case of exponential pressure decay. For equation (40): $\mathrm{Ja}_T = 0$, $\mathrm{Ja}_p = 3.71$, $\Omega = 0.0299$ ms^{-1}

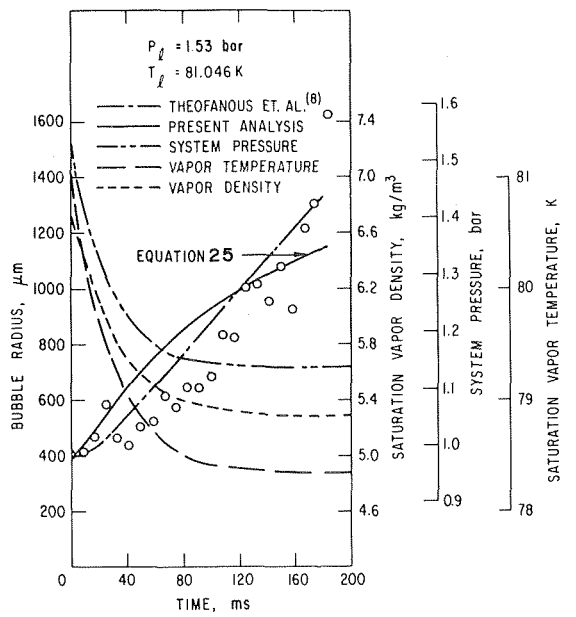

Fig. 8 Comparison of data of Hewitt and Parker (reference [16]) (their Fig. 11) for the case of exponential pressure decay. For equation (40): $\mathrm{Ja}_T = 0$, $\mathrm{Ja}_p = 3.383$, $\Omega = 0.0371$ ms^{-1}

data are also fit extremely well by a $t^{3/2}$ curve in each case, indicating a possible extraneous effect. If, for instance, there happened to be a thermal gradient in the apparatus, the long growth times could have allowed the bubble to rise through layers of successively hotter fluid, giving a power law behavior in the growth. It appears that more data will have to be obtained to resolve these questions.

Conclusion

The thermal growth of vapor bubbles in a uniformly heated liquid with an arbitrary, variable pressure has been analyzed using the thin boundary layer approximation including the effects of variable vapor density. The result, containing no free parameters, shown in equation (8), indicates that the effects of variable density are both expansive due to the $(\rho_{v0}/\rho_v)^{1/3}$ multiplier on the total solution, and integral accounting for the variable volume a unit mass of liquid will occupy on vaporization. It was shown that except for large temperature differences, the integral effects can be ignored resulting in equation (14). This solution contains the standard $\sqrt{t}$ behavior with Ja_T being the standard Jakob number based on initial superheat, and an additional effect due to the changing vapor temperature with time, $F'(t)$, due to variations in external pressure, and should be valid for general decompressive growth and short compressive collapse behavior.

Several cases have been examined and found to agree quite well with existing data, confirming the theory. For an exponential pressure decay it has been found that the additional form in (14) yields a time behavior of $\sqrt{\Omega t} - D(\sqrt{\Omega t})$ as shown in equation (25), where $D(u)$ is Dawson's integral. Thus, for short times, ($\Omega t \ll 1$), $D(u) \to u$ and the additional term adds little to the initial superheat effects, to build up. At long times $D(u) \to \frac{1}{2}u$ and the effect becomes identical to an initial superheat which includes that due to the decompression. On the other hand, for a pressure-time behavior which causes the vapor temperature to change as t^n, the analysis (equation 14) shows the growth rate to behave as $t^{(n+1/2)}$. In particular, for a linear temperature-time decay, the bubble grows as $t^{3/2}$, indicating much more rapid growth than the initial superheat would produce. These results can be expected to be quite important in nonequilibrium flashing flows where the vapor volume might then be expected to increase (in the Lagrangian sense) as $t^{3(n+1/2)}$, extremely rapid in comparison with $t^{3/2}$ for the initial superheat case alone.

Acknowledgment

The authors are indebted to Ms. A. L. Swoboda, who aided in the calculations. This work was performed under the auspices of the U. S. Nuclear Regulatory Commission.

References

1 Besant, W. H., *Hydrostatics and Hydrodynamics*, Cambridge, 1958. Lamb, H., *Hydrodynamics*, Dover, 1945.

2 Rayleigh, L., "Pressure Due to Collapse of Bubbles", Phil. Mag., XXXIV, 9498, 1917, Papers, vi. 504. (Lamb, H., *Hydrodynamics*, Dover, 1945.)

3 Bosnjakovic, F., "Verdampfung und Flussigkeitsuberhitzung," *Techn. Mech. und Thermo.*, Vol. 1, 1930, pp. 358–362.

4 Fritz, W., and Ende, W., "Verdampfungsvorgangnach Kinematographischen Aufnahmen an Dampfblasen," *Phys. Zeitsh.*, Vol. 37, 1936, pp. 391–401.

5 Forster, H. K., and Zuber, N., "Growth of a Vapor Bubble in a Superheated Liquid," *J. Appl. Phys.*, Vol. 25, 1954, pp. 474–478.

6 Plesset, M. S., and Zwick, S. A., "The Growth of Bubbles in Superheated Liquids," *J. Appl. Phys.* Vol. 25, 1954, pp. 493–500.

7 Scriven, L. E., "On the Dynamics of Phase Growth," *Chem. Eng. Sci.*, Vol. 10, 1959, pp. 113.

8 Theofanous, T., Biasi, H. S. Isbin, and H. K. Fauske, "Theoretical Study on Bubble Growth in Constant and Time-Dependent Pressure Fields," *Chem. Eng. Sci.*, Vol. 24, 1969, pp. 885–897.

9 Malnes, D., "Critical Two-Phase Flow Based on Non-Equilibrium Effects," in *Non-Equilibrium Two-Phase Flows*, Lahey, R.T., and Wallis, G.B., Ed., ASME 1975, pp. 11–17.

10 Rohatgi, U. S., and E. Reshotko, "Non-Equilibrium One-Dimensional Two-Phase Flow in Variable Area Channels," in *Non-Equilibrium Two-Phase Flows*, Lahey, R. T., and Wallis, G. B., Ed., ASME, 1975, pp. 47–54.

11 Niino, M., "Study of Single Bubble Generation and Growth by Laser Beam," Ph.D. Thesis, University of Tohoku, Japan, 1975. (in Japanese)

12 Carslaw, H. S., and J. C. Jaeger, *Conduction of Heat in Solids*, Oxford, 1959.

13 Kaplan, W., *Advanced Calculus*, Addison-Wesley, 1952, pp. 346.

14 Lohmender, B., and Riggsten, S., "Table of the Function $y = e^{-x^2}\int_0^x e^{t^2}dt$," *Kungl. Fysiogr. Sällsk. i Lund Föhr.*, Vol. 28, 1958, pp. 45–52.

15 Abromowitz, M., and I. A. Stegun, "Handbook of Mathematical Functions," NBS *Applied Math.* Series 55, Nov. 1964.

16 Hewitt, H. C., and J. D. Parker, "Bubble Growth and Collapse in Liquid Nitrogen," ASME JOURNAL OF HEAT TRANSFER, Vol. 90, 1968, pp. 22–26.

17 Hooper, F. C., G. Faucher, and A. Eidlitz, "Pressure Effects on Bubble Growth in the Flashing of Superheated Water," *Proc. Int. Heat Trans. Conf.*, V, Paper B2.3, 1970.

18 Forster, H. K., and Zuber, N., "Dynamics of Vapor Bubbles and Boiling Heat Transfer," *AIChE Journal*, Vol. 1, 1955, pp. 531.

19 Lipkis, R. P., Liu, C., and Zuber, N., "Measurement and Prediction of Density Transients in a Volume Heated Boiling System," *AIChE Chem. Eng. Prog. Sym. Ser.*, No. 18, Vol. 52, 1956, pp. 105–113.

20 Zwick, S. A., "Growth of Vapor Bubbles in a Rapidly Heated Liquid," *Phys. Fluids*, Vol. 3, 1960, pp. 685–692.

21 Reocreux, M., "Contribution a l'Etude des Debits Critiques en Ecoulement Diphasique Eau-Vapeur," Ph.D. Thesis, Universite Scientifique et Medicale de Grenoble, France, 1974.

K. Hijikata
Associate Researcher.

Y. Mori
Professor.

T. Nagatani
Graduate Student.

Department of Physical Engineering,
Tokyo Institute of Technology,
Meguro, Tokyo, Japan

Experimental Study on Bubble Nucleation in the Oscillating Pressure Field

In bubble nucleation under the oscillating pressure field, when the oscillation period τ is of the same order of magnitude as the characteristic time τ_n of bubble nucleation, it is expected that the distribution of radius of bubble embryo in liquid will be largely affected by the pressure oscillation and the degree of superheat limit may change. In order to clarify this point, superheat limits of homogeneous nucleation under the oscillating pressure field generated by ultrasonic oscillators are measured for propane with and without dissolved carbon dioxide by the floating droplet method. From the experimental results it is found that when $\tau > \tau_n$ the measured superheat limit agrees with that calculated by the conventional theory where the quasi-steady state is assumed, but the bubble nucleation occurs at temperature lower than that predicted by the theory when τ nearly equals τ_n. It is also found that the characteristic time of bubble nucleation is changed by the amount of dissolved carbon dioxide.

Introduction

Homogeneous nucleation of bubbles is a fundamental and essential phenomenon to be investigated in connection with boiling heat transfer and has been investigated theoretically by Döring [1] and Moore [2] and experimentally by Skripov [3], Clark [4] and others [5]. Heterogeneous nucleation caused by bubble nucleus such as gas bubble in a wall cavity, small solid particle, ion, radiation, etc. has also been studied by many researchers [6, 7]. In the heterogeneous nucleation, the degree of superheat is much lower than that predicted by the homogeneous nucleation theory. In experimental studies of homogeneous nucleation with carbon dioxide gas dissolved in liquid, the authors [8] have proved that nucleation of bubbles may occur at pressures greater than the saturation pressure of pure liquid at the same temperature. It is expected from homogeneous nucleation theory that, when disturbances, such as of pressure or temperature, are imposed, the degree of superheat for homogeneous nucleation will decrease. This effect of the unsteady field on homogeneous nucleation is very important in the actual phenomenon where disturbances are generated by the growth or motion of other bubbles. Theoretical predictions [9, 10] have been reported on this subject, but relatively few experimental studies have been reported so far. From this standpoint, the purpose of this paper is to make an experimental study on homogeneous bubble nucleation in a liquid with or without dissolved gas under the effect of an oscillating pressure field as part of a systematic research of bubble nucleation phenomena.

Contributed by the Heat Transfer Division of THE AMERICAN SOCIETY OF MECHANICAL ENGINEERS and presented at the AIChE-ASME Heat Transfer Conference, Salt Lake City, Utah, August 15–17, 1977. Revised manuscript received by the Heat Transfer Division February 6, 1978. Paper No. 77-HT-22.

In bubble nucleation under the oscillating pressure field, when the oscillation period is of the same order of magnitude as the characteristic time of bubble nucleation, the distribution of radius of bubble embryo in the liquid will be largely affected by the pressure oscillation and the degree of superheat limit may change. On the other hand, when the oscillation period is sufficiently long compared with the characteristic time of nucleation, nucleation can follow the pressure oscillation, and the superheat limit is expected to be predicted by the conventional theory of bubble nucleation. In the present report, an experimental study on homogeneous nucleation was made by changing the frequency and the amplitude of the oscillating pressure by ultrasonic generators. The superheat limits of propane with and without dissolved carbon dioxide gas were measured by the floating droplet method.

Theoretical Prediction

It is considered that the superheat limit under the oscillating pressure field would largely depend on the relative relation between the oscillation period of pressure and the characteristic time of the bubble nucleation. Therefore, first the order of magnitude of the characteristic times of bubble nucleation of a liquid with and without a dissolved gas should be investigated. The bubble nucleation phenomenon is expressed by a stochastic partial differencial equation for an existent probability $P(n)$ of an embryo composed of n molecules, so called the Fokker-Planck equation. The time variation of $P(n)$ balances with a convection term due to the mean growth of the embryo and a diffusion term due to the thermal fluctuation. Therefore, the characteristic time of homogeneous nucleation is given by the ratio of the unsteady term and the diffusion term of the Fokker-Planck equation, and is expressed by $n_c{}^2q^2/4\pi\lambda T_0{}^2R_c$ where R_c is the critical bubble radius, n_c is the number of molecules at a critical point, q is

the latent heat per molecule, λ is the thermal conductivity, k is the Boltzmann constant and T_0 is the temperature, because the process is rate-controlled by heat transfer for phase change. For pure propane under the normal pressure, the order of magnitude of the characteristic time obtained from the above relation is about 10^{-6} s. The derivation of the characteristic time is given in the Appendix.

On the other hand, when a gas is dissolved in a liquid, the characteristic time of bubble nucleation is rate-controlled by diffusion process of the dissolved gas. Therefore, the characteristic time is regarded as $n_c^2/4\pi DN_{g0}R_c$, where D and N_{g0} are the diffusivity in the liquid and the number of molecule per unit volume of the dissolved gas, respectively. For carbon dioxide dissolved in propane the characteristic time is about 10^{-5} s, or about 10 times that for pure propane.

From the consideration described above, ultrasonic waves of 450 kHz and 25 kHz were adopted to generate the pressure oscillation, where the period of the 450 kHz oscillation is of the same order as the characteristic time of homogeneous nucleation and the period of the 25 kHz oscillation is considerably longer.

Experimental Apparatus and Method

The experimental apparatus is composed of a mixing section, a bubble generation section, a droplet formation section and a test section as shown in Fig. 1. Excluding the test section, other sections are almost the same as those used in the previous paper [8]. The test section placed in a pressure vessel is of 20 mm ID and 200 mm length. The droplet formation section and the bubble generation section are incorporated with a pyrex-glass pipe of 4 mm ID and 400 mm length. At the top of the pressure vessel, an ultrasonic generator is placed to generate the oscillating pressure field. From the consideration of the characteristic time of the bubble nucleation stated in the preceding section, the ultrasonic waves of 450 kHz and 25 kHz were selected. A disk type piezo oscillator of 50 mm OD and 5 mm thickness was used for 450 kHz and a cylindrical type of 20 mm OD and 14 mm ID was adopted for 25 kHz wave.

The wave length of 450 kHz was 4 mm and the plane wave was supposed to be formed in the test section. In the case of 25 kHz the standing pressure of 76 mm wave length was formed. The detail structures of test section provided with the generators of 450 kHz and 25 kHz are shown in Fig. 2(a) and 2(b), respectively. The generator of 450 kHz was cooled with water and an aluminum plate reflector of 0.5 mm thickness and an air layer between the generator and the reflector worked to reduce the power loss of the generator.

At the mixing section, the noncondensable gas (CO_2) was added to the test vapor (propane) to make a mixture gas which was sent as a bubble to the lower part of the droplet formation section. The droplet formation section was cooled down to between $-20 \sim -30$°C with liquid nitrogen, making a droplet containing a dissolved gas bubble. It was also possible to make a droplet of a pure material. These sections and the pressure vessel containing the test section were filled with glycerine. An electric heater set at the upper part of the pressure vessel was used to make a given linear temperature gradient in the test section. Before the droplet came into the pressure vessel, the

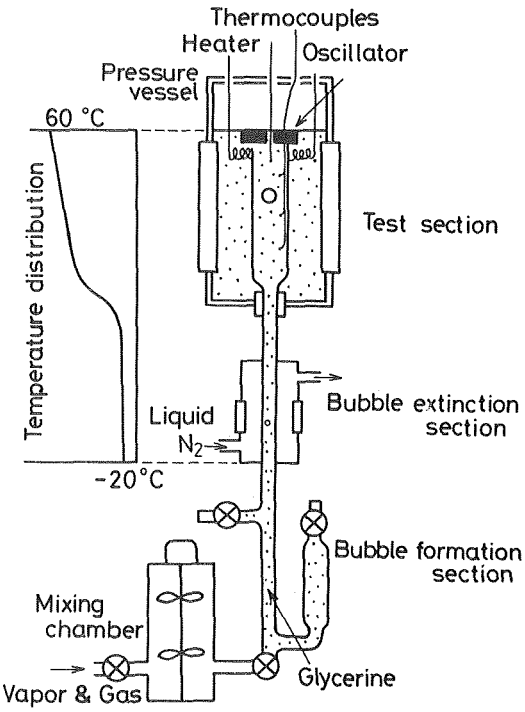

Fig. 1 Experimental apparatus

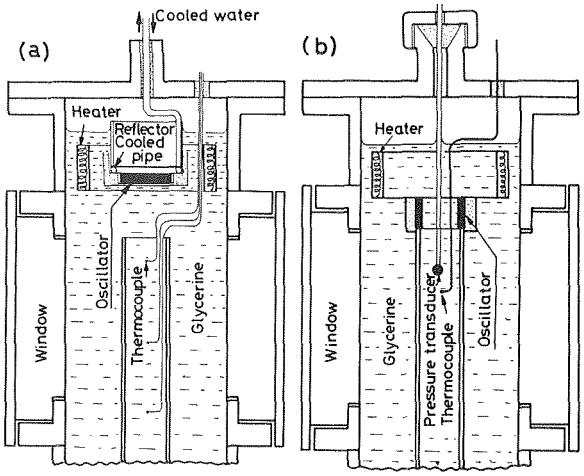

Fig. 2 Generators of pressure oscillation

Nomenclature

A = constant
C = acoustic velocity (m/s)
D = diffusivity in liquid (m^2/s)
F = radiation pressure (Pa)
g = gravitational acceleration (m/s^2)
J = nucleation rate ($1/m^3s$)
K = wave number (1/m)
k = Boltzmann constant (J/K)
N = number of molecules per unit volume ($1/m^3$)
n = number of molecules
m = mass of molecule (kg)
P = probability
p = pressure, acoustic pressure (Pa)
q = latent heat per molecule (J)
R = bubble radius (m)
T = temperature (K)
λ = thermal conductivity of liquid (W/mK)
ρ = density (kg/m^3)
σ = surface tension (N/m)
ω = angular velocity (rad/s)
τ = characteristic time (s)

Subscripts

c = critical point
g = dissolved gas
max = maximum value
min = minimum value
0 = mean value
s = saturation

pressure of the system was increased as for the gas to be completely dissolved in the liquid phase. Then, the droplet formed was slowly raised by buoyancy and entered the test section. The droplet was gradually heated up by the surrounding glycerine when rising in the test section. In the case of 450 kHz the ultrasonic wave came to a standstill at the point where the buoyancy force was balanced with the radiation pressure. During the nonradiation period, the droplet rose by about 5 mm and was heated.

In the repetition of these processes the bubble formation is considered to occur when the droplet temperature equals the superheat limit of bubble nucleation in the oscillating pressure field. The temperature difference between the droplet and the surrounding liquid caused by vertical temperature gradient along the test section was about 1.0°C. As the ultrasonic wave was radiated at every 5 mm rise of the droplet, the inaccuracy due to this discontinuous radiation was about 1.0°C, and the total accuracy of the measurement of superheat limit in an experiment was about 2.0°C.

In the case of 25 kHz, the droplet was at a stanstill at a point below the ultrasonic oscillator, and the accuracy of the measured superheat limit was about 1.0°C.

The acoustic pressure of ultrasonic waves of 450 kHz and 25 kHz was measured as follows. In the case of high frequency ultrasonic wave, the direct measurement of acoustic pressure is difficult, but is calculated by the following relation from the radiation pressure measurement:

$$p = \sqrt{2\rho C^2 F}, \tag{1}$$

where p is the acoustic pressure, F is the radiation pressure and ρ and C are the density and the acoustic velocity in glycerine, respectively. An apparatus which was acoustically equivalent to the section and as shown in Fig. 3 was used to measure the characteristics of the ultrasonic oscillator. When the ultrasonic wave was generated, the sphere was moved by the radiation pressure acting on the sphere and balanced with the horizontal component of the tension of the string suspending the sphere. Thus the radiation pressure was obtained from the displacement of an alumina sphere of 15 mm D. The radiation pressure measured by the displacement of the sphere was found to be proportional to the square of the supplied voltage to the oscillator. Using this proportional constant, the radiation pressure in the test section was calculated from the supplied voltage. As the attenuation of the radiation pressure along the test section was very small, the ultrasonic wave strength in the test section was assumed to be constant.

When a droplet diameter is small enough compared with the wave length, the ultrasonic wave is not diffracted by the droplet and the phase and amplitude of the wave along the surface of the droplet always coincide with those of the surrounding liquid. For the droplet of 0.4 mm OD and the ultrasonic wave of 450 kHz, the diffraction coefficients are 1.1, 0.95 and 1.02 at 0 deg, 90 deg and 180 deg, respectively, and they can be regarded as unity. Therefore, the amplitude of the pressure wave in the droplet varies to a small extent according to that in the surrounding liquid, but it can be considered that the nucleation occurs at the maximum amplitude point in the droplet.

According to Apfel [11], the trapping pressure on the droplet is given as follows.

$$\Delta p \left(\frac{\partial \Delta p}{\partial x}\right) \approx 2\rho_d C_d^2 (\rho - \rho_d) g \tag{2}$$

where Δp is the amplitude of the pressure, x is the distance, g is the gravitational acceleration, ρ is the density of surrounding liquid, and ρ_d and C_d are the density and the acoustic velocity of the droplet material, respectively. For the standing wave, Δp is given by $\Delta p_{\max} \times \sin Kx$ where K is the wave number and $\Delta p_{\max}$ is the amplitude of the wave. The left hand side term of equation (2) is rewritten by $(K\Delta p_{\max}/2) \sin 2Kx$ and by using this relation, the point where the droplet is come to a standstill is calculated. The value of $\sin 2Kx$ is smaller than 0.2 for the experimental condition, the droplet is considered to be trapped at the loop or the node of the wave. The instantaneous degree of superheat and the possibility of nucleation at the loop are larger compared with that at the node, therefore, the homogeneous nucleation of the droplet is expected to occur at the loop of the wave, being affected by the wave of the radiation pressure calculated from the supplied voltage of the oscillator.

For the low frequency ultrasonic wave of 25 kHz, the wave length in glycerine was very long and a small acoustic pressure detector as shown in Fig. 4 was newly developed to measure a local value. The detector was small enough and the diffraction coefficient of the detector was nearly equal to unity, therefore, the detector was assumed to accurately measure the local acoustic pressure. The main part of the detector was made by an ultrasonic oscillator of PZT of 5 mm D, and 1 mm thickness whose natural frequency was 2 MHz, which was supported and electrically shielded by a stainless steel pipe of 2 mm

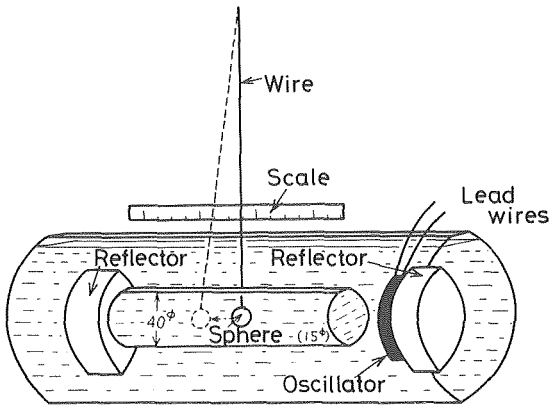

Fig. 3 Apparatus for measuring radiation pressure

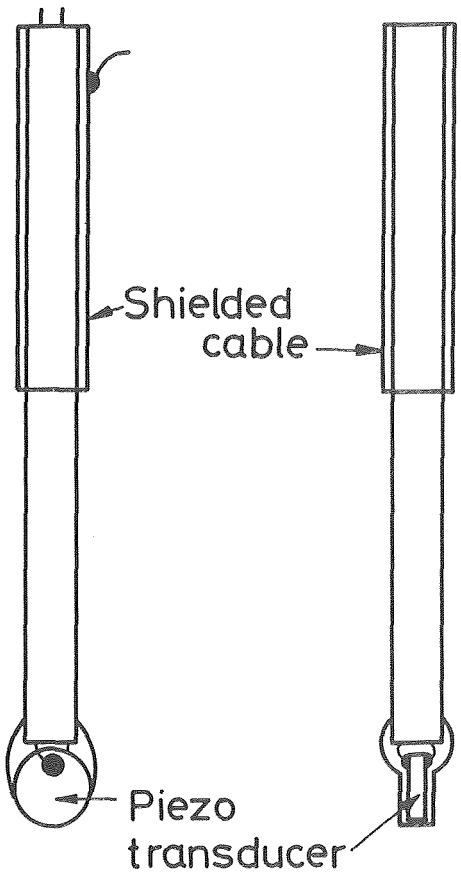

Fig. 4 Acoustic pressure detector

ID. The sensitivity of the detector was calibrated in a glycerine bath of 60°C by a semi-conductor pressure transducer whose natural frequency was about 100 kHz. The typical acoustic pressure distribution in the test section measured by the detector is shown in Fig. 5. At the lower oscillating surface of the cylindrical oscillator there was the loop of the wave and, there was a node at 4 cm under it. The amplitude distribution inside the cylindrical oscillator is different from that outside as shown by the broken and solid lines in the figure. Therefore, the half wave length was determined from the distribution outside the oscillator and was given as about 4 cm and it coincided with the calculated value from the acoustic velocity of glycerine.

As the natural frequency of the droplet is about 1 kHz and lower than the frequency of pressure oscillation used in the experiment, the resonance oscillation of the droplet was not observed. In this experiment, the pressure wave was confirmed and it can be assumed that the plane wave is formed in the core region of the test section.

Experimental Result and Discussion

Experiments were carried out on bubble nucleation, in pure propane and in propane with dissolved carbon dioxide in it, under the influence of an oscillating pressure field generated by the ultrasonic oscillator. Experimental results of superheat limit of pure propane at the mean pressure of 4 atm are shown in Fig. 6. The horizontal and vertical axes are the amplitude of oscillating pressure and the difference between the superheat limits with and without the oscillating pressure field. The positive temperature difference shows the decrease of superheat limit under the oscillating pressure field. Black and white circles show the experimental results of 25 kHz and 450 kHz, respectively. When a period of the pressure oscillation is sufficiently longer than the characteristic time of the bubble nucleation, it is considered that the size distribution of embryo and the bubble nucleation rate may be calculated by the quasisteady approximation. When the bubble nucleation rate under the oscillating pressure field is assumed to be given by the conventional homogeneous nucleation theory, it is given as follows:

$$J_s = A(t) \exp\left[-\frac{4\pi\sigma R_c(t)^2}{3kT_0}\right]$$

$$A(t) = N_0 \exp\left(-\frac{q}{kT_0}\right)\left\{\frac{6\sigma p}{(4p - p_s)\pi m}\right\}^{1/2}$$

$$R_c(t) = 2\sigma/\{p_s(T_0) - p_0 - \Delta p \sin\omega t\}, \tag{3}$$

where J_s is the nucleation rate, σ is the surface tension, m is the mass of a molecule, N_0 is the number of molecules per unit volume, R_c is the critical radius, k is the Boltzmann constant, T_0 is the temperature, p_0 is the mean pressure, p_s is the saturation pressure, Δp is the amplitude of pressure wave and q is the latent heat per molecule. The maximum nucleation rate $J_{s\max}$ is obtained when $R_c(t)$ has a minimum value, and we have

$$J_{s\max} = A_{\max} \exp\left[-\frac{4\pi\sigma R_{c\min}^2}{3kT_0}\right]$$

$$R_{c\min} = 2\sigma/(p_s(T_0) - p_0 + \Delta p). \tag{4}$$

The superheat limit is not very dependent on a value of J_s and it has been considered so far that the homogeneous nucleation could occur when J_s becomes 1 $cm^{-3}\,s^{-1}$, and in this work the theoretical value of the superheat limit is calculated by putting J_s equal to 1 $cm^{-3}\,s^{-1}$ and this value is henceforth referred to as that of the equilibrium model. This relation is shown by the single dotted chain line in Fig. 6 and it can be seen that the results obtained with the 25 kHz low frequency pressure oscillation are in good agreement with the superheat limit by the equilibrium model. On the other hand, the results indicated by white circles show that the superheat limit for high frequency oscillation of 450 kHz differs from that predicted by the equilibrium model and the bubble nucleation occurs at the lower superheat condition.

From these results, it is concluded that when the period of the pressure oscillation is sufficiently long compared with the characteristic time of bubble nucleation, the quasi-steady state is established and the superheat limit is predicted for the minimum instant pressure by the equilibrium model, but when the period of oscillation is of the same order of the characteristic time of homogeneous nucleation, the quasi-steady state distribution of embryo cannot be expected and the diffusion process caused by the temperature fluctuation becomes predominant (see Appendix) and the possibility of nucleation increases remarkably. It is considered that the decrease of the superheat limit is caused by these reasons. At higher frequencies it is supposed that the nucleation process cannot follow the pressure field.

The superheat limits of pure propane under the oscillating pressure field are shown in Fig. 7 with the mean pressure as parameter. The vertical and the horizontal axes are mean pressure and temperature, respectively. Experimental results are shown by black and white squares for 25 kHz and by black and white triangles for 450 kHz. The solid line of the left hand side in the figure is the saturation curve of pure propane, and the solid line of the right hand side is the superheat limit of a propane with no pressure oscillation. The two dotted chain line and the three dotted chain line show the superheat limits calculated by the equilibrium model under the pressure oscillation whose amplitudes are 3 atm and 4 atm, respectively. The results for 25 kHz are also in good agreement with the equilibrium model, while the experimental results for 450 kHz shown by the broken lines differ considerably from the equilibrium theory. It is worth stressing from

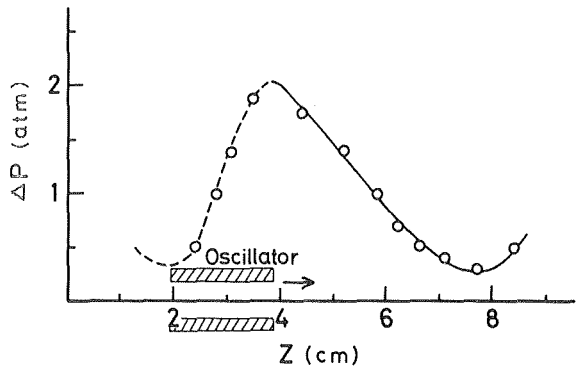

Fig. 5 Acoustic pressure distribution for 25 kHz

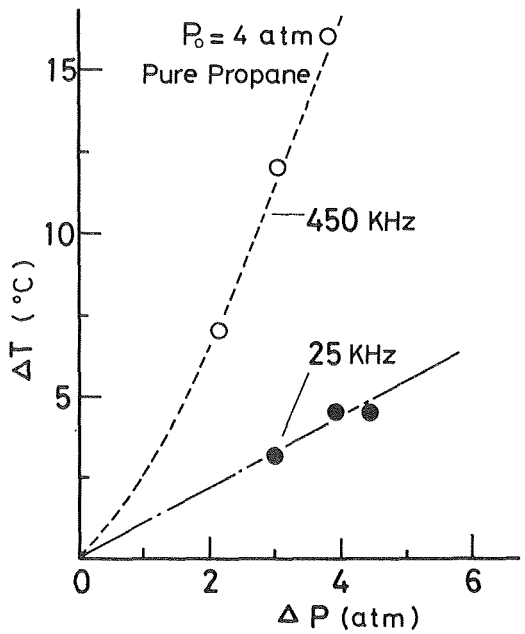

Fig. 6 Difference between superheat limits with and without oscillating pressure field

Fig. 7 that the homogeneous nucleation occurs under the negative pressure as seen in the mean pressure region lower than 3 atm, namely, when the mean pressure is 1 atm and the amplitude of pressure oscillation is 3 atm or 4 atm, the negative pressure acts on the droplet at an instant and the superheat limit is given by the conventional theory for the steady or quasi-steady cases.

It is considered that the characteristic time of bubble nucleation of the droplet containing the dissolved gas differs from that for the single component, because the gas diffusion in liquid controls the rate of the phenomenon. Therefore, it is expected that the frequency dependence of the superheat limit would be changed by the gas dissolved in liquid. The superheat limits of the droplet of propane containing dissolved CO_2 under the oscillating field of 450 kHz are shown in Fig. 8. The results for pure propane shown in Fig. 7 are also indicated for reference. White circles show the superheat limit without pressure oscillation, and the solid line for dissolved CO_2 without the pressure oscillation is obtained from the theory reported by Ward [12]. The mole fraction of CO_2 is about 21 percent and black circles, black triangles and white triangles show the experimental results for the pressure oscillation whose amplitudes are 2.0, 3.0 and 4.0 atm, respectively. The difference of the superheat limit under the oscillating pressure field from that without the oscillation field for propane containing djssolved CO_2 is smaller than that for pure propane.

In the case of propane with dissolved CO_2, the period of the 450 kHz oscillation is short compared with the characteristic time of bubble nucleation as stated already. Therefore, the fluctuation of dissolved gas concentration at the interface between embryo and liquid cannot follow the pressure oscillation and is smaller than that calculated from the pressure oscillation by using the quasisteady assumption. This is why the decrease of superheat limit of propane with dissolved CO_2 is smaller than that of pure propane under the oscillating field of 450 kHz. On the other hand, without pressure oscillation the experimental result is in good agreement with that predicted by Ward's theory [12], where the equilibrium between the gas in embryo and the dissolved gas in liquid is assumed. This means that when the pressure oscillation period is long compared with the characteristic time of nucleation, the superheat limit of liquid containing dissolved gas under the pressure oscillation field is calculated by the equilibrium model. Therefore, the maximum decrease of superheat limit under the pressure oscillating field is considered to be realized when its period is of the same order of magnitude as the characteristic time for liquid with or without dissolved gas. To clarify this point quantitatively, it might be required to carry out an experiment under an adequate oscillation frequency. However, an investigation of experimental setup was made to find a serious difficulty to measure the amplitude of the pressure oscillation with such the frequency.

The solubility of materials such as N_2, O_2 and air other than CO_2 is one or two order of magnitude smaller than that of CO_2 as stated in the previous report [8], the difference between superheat limits of liquid with and without such dissolved gas as air under the oscillating field is considered to be so small to be measured by our experimental apparatus. Therefore, the experiment was carried out only by using CO_2 as a dissolved gas.

Conclusion

Superheat limits of homogeneous nucleation under the oscillating pressure field generated by the ultrasonic oscillators are obtained experimentally for the droplets of propane with and without dissolved CO_2. Comparing these results and the conventional theory of homogeneous nucleation, the following conclusions have been obtained.

1 When a liquid does not include any dissolved gas and when the period of pressure oscillation is sufficiently longer than the characteristic time of bubble nucleation, the superheat limit can be estimated by the conventional theory under the assumption of the quasi-steady state.

2 When the period of pressure oscillation is nearly equal to the characteristic time of nucleation, the superheat limit of liquid without dissolved gas is considerably decreased with increase of the amplitude of pressure oscillation, and the bubble nucleation under the oscillating pressure field can occur at temperatures lower than that predicted by the conventional nucleation theory.

3 The difference of the performance of homogeneous nucleation for pure propane and propane with dissolved CO_2 shows that the bubble nucleation of the material with a dissolved gas is rate-controlled by the diffusion of dissolved gas.

APPENDIX

The Fokker Planck equation of the distribution function $P(n, t)$ of the embryo for homogeneous nucleation is written as follows:

$$\frac{\partial P(n,t)}{\partial t} + \frac{\partial}{\partial n}[\overline{V}(n)P(n,t)] = \frac{\partial}{\partial n}\left[D_n \frac{\partial}{\partial n} P(n,t)\right] \quad \text{(A-1)}$$

where n is the number of molecule in the embryo, t is the time, and D_n is the diffusivity in the space of molecule number. In equation

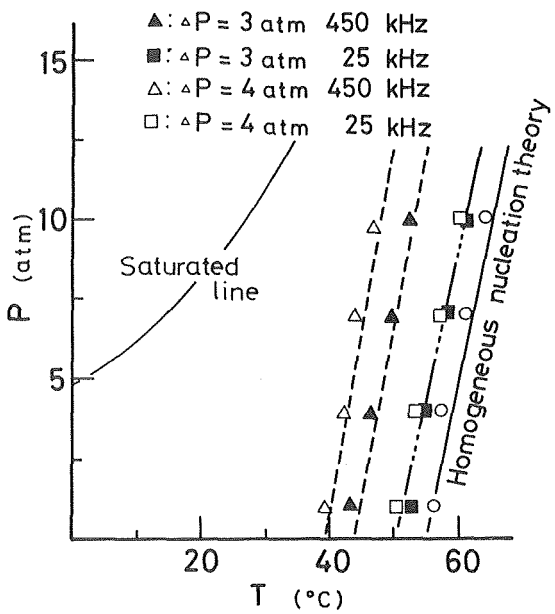

Fig. 7 Superheat limit of propane under oscillating pressure field

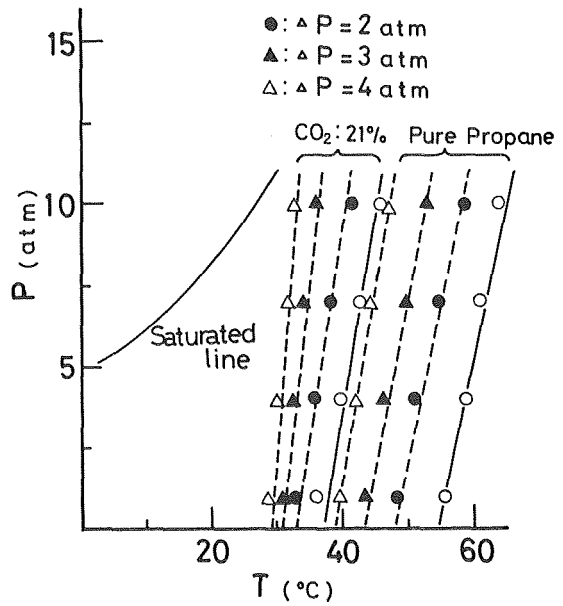

Fig. 8 Superheat limit of propane with dissolved CO_2 gas under oscillating pressure field

(A-1), the second term in the left side means the convection term and the right side means the diffusion term. $V(n, t)$ in equation (A-1) is the time derivative of molecule number of the embryo which is composed of n molecules, and is expressed by its mean term $\overline{V}(n)$ and the fluctuation term $V'(n, t)$.

$$V(n, t) = \overline{V}(n) + V'(n, t). \tag{A-2}$$

If the fluctuation V' is assumed to be a white noise, the diffusivity D_n can be written as follows.

$$2D_n\delta(\tau) = \overline{V'(n, t)V'(n, t + \tau)}, \tag{A-3}$$

where δ means the delta function and the overline means the time smoothed value.

In the bubble nucleation without dissolved gas, it is considered that the fluctuation of V is caused by the heat flux fluctuation $\vec{Q}'$ to the embryo.

$$V'(n, t) = \frac{1}{q}\int_R \vec{Q}'(n, t, \vec{r}) \cdot d\vec{s} \tag{A-4}$$

where q is the latent heat per molecule, $\vec{r}$ is the position vector and $\vec{s}$ is the surface vector of the embryo surface R. The correlation of the heat flux fluctuation $\vec{Q}'$ was given by Landau [13] as follows:

$$\overline{\dot{Q}_i'(\vec{r}_1, t_1)\dot{Q}_j'(\vec{r}_2, t_2)} = 2\lambda kT^2\delta_{ij}\delta(t_1 - t_2)\delta(\vec{r}_1 - \vec{r}_2), \tag{A-5}$$

where $\dot{Q}i'$ means the component of $\vec{Q}'$ to i direction, λ is the thermal conductivity and δ_{ij} is Kronecker delta. Substituting equations (A-4) and (A-5) for equation (A-3), we can get D_n as follows:

$$D_n = \frac{4\pi\lambda kT_0^2}{q^2}R. \tag{A-6}$$

Therefore the characteristic time τ of nucleation at the critical point is given as follows by comparing between the unsteady term and the diffusion term in equation (A-1) and using equation (A-6).

$$\tau = \frac{n_c{}^2q^2}{4\pi\lambda kT_0{}^2R_c}. \tag{A-7}$$

On the other hand, when the droplet contains dissolved gas, the mass transport of the dissolved gas in the liquid rate-controls the nucleation process, therefore the fluctuation V' is derived from the moler flux fluctuation of the dissolved gas $\vec{m}'$ to the embryo.

$$V'(n, t) = N_0\int_R \vec{m}'(n, t, \vec{r}) \cdot d\vec{s}, \tag{A-8}$$

where N_0 is the Avogadro number.

The correlation of $\vec{m}'$ is given by Foch [14] corresponding to equation (A-5).

$$\overline{\dot{m}_i'(\vec{r}_1, t_1)\dot{m}_j'(\vec{r}_2, t_2)} = \frac{2cD}{N_0}\delta_{ij}\delta(\vec{r}_1 - \vec{r}_2)\delta(t_1 - t_2), \tag{A-9}$$

where c and D are the moler concentration and the diffusivity of the dissolved gas, respectively. Therefore D_n and the characteristic time τ are given from equations (A-3), (A-8) and (A-9) as follows:

$$D_n = 4\pi N_0cDR = 4\pi N_{g0}DR, \tag{A-10}$$

$$\tau = \frac{n_c{}^2}{4\pi N_{g0}DR_c}, \tag{A-11}$$

where N_{g0} is the number of molecule of the dissolved gas per unit volume.

References

1 Döring, W., "Die Uberhitzungsgrenze and Zerreissfestigkeit von Flussigkeiten," *Z. Phys. Chem.*, Vol. 36, 1937, pp. 371–386.

2 Moore, G. R., "Vaporization of Superheated Drops in Liquids," *AIchE J.*, Vol. 5, 1959, pp. 458–466.

3 Sinitsyn, E. N. and Skripov, V. P., "Kinetics of Nucleation in Superheated Liquids," *Russ. J. Phys. Chem.*, Vol. 42, 1968, pp. 440–443.

4 Clark, H. B., Strenge, P. S. and Westwater, J. W., "Active Sites for Nucleate Boiling," *Chem, Engng. Prog. Symp., Ser.*, Vol. 55–29, 1959, pp. 103–110.

5 Gould, R. K., "Simple Method for Calibrating Small Omnidirectional Hydrophones," *J. Acoust. Soc. Amer.*, Vol. 43, 1968, pp. 1185–1186.

6 Hirth, J. P. and Pound, G. M., *Condensation and Evaporation*, Pergamon Press, Oxford, 1963.

7 Holl, J. W., "Nuclei and Cavitation," *Trans. ASME* Vol. 92, 1970, pp. 681–688.

8 Mori, Y., Hijikata, K. and Nagatani, T., "Effect of Dissolved Gas on Bubble Nucleation," *Int. J. Heat Mass Transfer*, Vol. 19, 1976, pp. 1153–1159.

9 Swanger, L. A. and Rhines, W. C., "On the Necessary Conditions for Homogeneous Nucleation of Gas Bubbles," *J. Cryst, Growth*, Vol. 12, 1972, pp. 323–326.

10 Hirth, J. P., Pound, G. M. and Pierre, G. R., "Bubble Nucleation," *Metall. Trans.*, Vol. 1, 1970, pp. 939–945.

11 Apfel, R. E., "A Novel Technique for Measuring the Strength of Liquids," *J. Acous. Soc. Amer.*, Vol. 49, 1971, pp. 145–155.

12 Ward, C. A., Balarkrishnan, A. and Hooper, F. C., "On Thermodynamics of Nucleation in Weak Gas-Liquid Solutions," *Trans. ASME*, Vol. 92, 1970, pp. 695–701.

13 Landau, L. D. and Lifshitz, E. M., *Fluid Mechanics*, Pergamon Press, Oxford, 1975.

14 Foch, J., "Stochastic Equations for Fluid Mixtures," *Phys. Fluids*, Vol. 14, 1971, pp. 893–897.

C. P. C. Wong
G. C. Vliet
P. S. Schmidt

Department of Mechanical Engineering,
University of Texas, Austin,
Austin, Tex.

Magnetic Field Effects on Bubble Growth in Boiling Liquid Metals

A theoretical analysis of bubble growth in superheated liquid metals shows that in the presence of a strong magnetic field, the growing bubble would assume an elongated shape and the volume would be less than that for the nonmagnetic case. As time progresses and for higher field strengths the bubble becomes more elongated. The analytical results are used to estimate the effect of strong magnetic fields on nucleate boiling heat transfer.

Introduction

In the conceptual development of fusion reactors, four coolants are being proposed as heat transfer media: metal lithium, lithium salt, helium, and boiling potassium. A number of conceptual design studies [1–4] have been carried out considering Li or Li_2BeF_4 (flibe) in forced convection. Li has the drawback that the flow rate must be rather high to achieve the required heat absorption without excessive temperature rise, and pumping losses due to magnetohydrodynamic effects may be excessive [5], whereas, flibe may provide a marginal tritium breeding ratio due to parasitic neutron capture and may have a chemical corrosion problem. High pressure helium has also been considered as a coolant [6–8] because of its chemical inertness, easy applicability to thermal conversion systems, and its negligible interaction with a magnetic field. Conceptual fusion reactors have been designed [9, 10] on the basis of helium as a coolant. However, helium requires a large blanket volume for coolant passages because of its low density, and it requires large compressor power.

The possibility of using a boiling liquid metal as the heat transfer medium has received some attention. Liquid metals have extremely high heat transfer coefficients, which means small coolant volume, and the enthalpy absorbed in the phase change means reduced flow rates. They also have low vapor pressures, and among the pure alkali metals, potassium has the lowest boiling point. Leverette [11] and Fraas [12] have suggested the possibility of using boiling potassium in a sort of "secondary loop" integrated into the blanket structure. Parkin, et al. [13] did a preliminary design of a boiling potassium heat removal system for fusion reactors. They compared high and low pressure helium with boiling potassium and showed that boiling potassium has certain advantages. A major unknown however is the effect of magnetic fields on the nucleate boiling characteristics of liquid metals, which are electrically conducting. The generation of a Lorentz force would definitely affect the movement of the conducting fluid, and thus the movement and growth of boiling bubbles.

Faber and Hsu [14] performed experiments with pool boiling of mercury in magnetic fields up to 6 weber/m^2 oriented normal to the boiling surface. They noted a marked decrease in the effective heat transfer coefficient (heat flux per degree of surface superheat) at modest heat fluxes with increasing magnetic field. However at high fluxes their results exhibit a progressively smaller effect of magnetic field. Fraas, et al. [15] have performed tests with potassium boiling on a cylindrical rod in transverse fields up to 6 webers/m^2, and noted relatively little effect from the magnetic field. Some simulated single bubble growth experiments have been conducted by the authors (unpublished) which involved bubbling argon through a small aperture into the bottom of a glass vessel containing NaK, both in the presence and in the absence of a magnetic field. From motion picture records, the bubble departure frequency was found to decrease by 20 to 40 percent for fields up to 0.9 webers/m^2. Wagner, et al. [16] did an analytical study of the effect on bubble growth of a spherically symmetric magnetic field using a spherical bubble growth model. They showed that the magnetic field has definite effects on bubble growth, and they present estimates of the effects of magnetic fields on nucleate boiling heat transfer.

In order to obtain a more precise understanding of the effects of magnetic fields on isolated bubble growth in liquid metals, an analytical model is presented which considers the growth of an ellipsoidal bubble and solves the integrated forms of the conservation relations. The results are then used to estimate the effect on nucleate boiling heat transfer. This paper is a summary of a portion of the work of Wong [17].

Analytical Study of Bubble Growth in Superheated Liquid-Metal Under a Uniform Magnetic Field

An order of magnitude analysis was conducted based on the spherically symmetric bubble growth momentum equation to assess the importance of the different physical phenomena on bubble growth in the presence of a magnetic field. Some of the more important results are: (1) the magnetic body force becomes relatively more dominant as time increases, (2) the viscous effect is relatively unimportant, and (3) except at the initial stage, the surface tension effect becomes less important and ultimately becomes negligible. In general it can be stated that for alkaline metals (all of which have similar physical properties to potassium), when the magnetic field strengths are high,

Contributed by the Heat Transfer Division for publication in the JOURNAL OF HEAT TRANSFER. Manuscript received by the Heat Transfer Division April 12, 1978.

the magnetic body force has a dominant effect on boiling bubble growth.

In the absence of a magnetic field, the bubble growth in superheated liquid metals will be similar to that of an electrical nonconducting liquid, that is, spherical growth will prevail. However, in the presence of a magnetic field, Fig. 1, there results a magnetic body force which opposes fluid motion transverse to magnetic field lines. This will result in a distortion of the bubble from spherical symmetry, being elongated in the direction of the imposed field. Simultaneously the heat transfer to the interface will be affected by the relative increase in surface to volume ratio. The following analysis treats the asymmetric growth of the bubble, including the influence of nonspherical shape on the thermal energy equation. Viscous effects were shown to be negligible and are neglected.

Because the Lorentz force exhibits symmetry about an axis aligned with the magnetic field, an ellipsoidal bubble shape as defined by Fig. 1 is a reasonable choice of geometry, and is thus assumed for the problem under consideration. The coordinate system is a cylindrical geometry with magnetic field in the z-direction. With this choice of coordinate, the problem becomes a two-dimensional problem with spatial variables r and z and bubble interface variables $R(t)$ and $Z(t)$ along the respective r and z axes. The momentum equations in the fluid, neglecting viscous and gravitational terms, are given by:

$$\rho_\ell \left(\frac{\partial u}{\partial t} + u\frac{\partial u}{\partial r}\right) = -\frac{\partial P}{\partial r} - \sigma_\ell B^2 u \tag{1}$$

and

$$\rho_\ell \left(\frac{\partial w}{\partial t} + w\frac{\partial w}{\partial z}\right) = -\frac{\partial P}{\partial z} \tag{2}$$

The continuity equation is given by:

$$\frac{u}{r} + \frac{\partial u}{\partial r} + \frac{\partial w}{\partial z} = 0$$

from which it can be shown that for spherical growth, the liquid velocity is:

$$u = \left(\frac{R}{r}\right)^2 \dot{R}$$

while for (infinite) cylindrical growth, the liquid velocity would be:

$$u = \left(\frac{R}{r}\right) \dot{R}$$

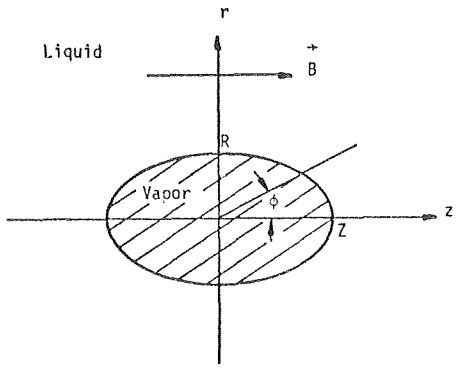

Fig. 1 Bubble and magnetic field configuration

Considering these limiting variations, this study assumes that

$$\bar{u} = \left(\frac{R}{r}\right)^n \dot{R} \tag{3}$$

and

$$\bar{w} = \left(\frac{Z}{z}\right)^m \dot{Z} \tag{4}$$

where $\lim_{z\to 0} u = \bar{u}$ and $\lim_{r\to 0} w = \bar{w}$. That is, R and Z represent the liquid-vapor interface points along the r and z axes respectively, as shown in Fig. 1, and $\dot{R}$ and $\dot{Z}$ are the interface velocities at these locations. Equations (3) and (4) determine the spatial dependence of $\bar{u}$ and $\bar{w}$ in the liquid along the r and z axes, where n and m are time dependent functions to be determined from the equations of continuity. It is to be noted that this velocity field, which is generally consistent with the physical problem, has been assumed in lieu of an actual solution of the liquid velocity field.

The analysis assumes that u and w are continuous functions of the spatial and time variables in order to obtain the limiting momentum and continuity equations along the r and z axes. Taking the limit as $z \to 0$ and $r \to R$, the continuity equation becomes:

$$\frac{\dot{R}}{R}(1-n) + \lim_{z\to 0}\frac{\partial w}{\partial z} = 0 \tag{5}$$

Nomenclature

a_ℓ = thermal diffusivity of liquid
A^* = a parameter, $(h_{fg}\rho_v/\rho_\ell T_{sat})$
A_E = area of ellipsoid
B = scalar value of magnetic field strength
h_{fg} = latent heat of evaporation
k_ℓ = liquid thermal conductivity
m = a parameter, $m = 2\,Z\dot{R}/\dot{Z}R$
n = a parameter, $n = 1 + \dot{Z}R/Z\dot{R}$
Nu = Nusselt number
Nu_B = Nusselt number with magnetic field
Nu_0 = Nusselt number without magnetic field
P = pressure in liquid
ΔP = pressure difference between vapor and liquid
Pr = Prandtl number
r = radial coordinate
r_p = radius perpendicular to bubble surface
R = bubble radius or vapor-liquid interface on the r-axis
$\dot{R}$ = first time derivative of R
$\ddot{R}$ = second time derivative of R
Re_0 = Reynolds number without magnetic field
Re_B = Reynolds number with magnetic field
R_E = equivalent radius, $(R^2Z)^{1/3}$
$\dot{R}_E$ = time rate change of R_E
R_s = spherical radius
t = time
t_0 = initial time
T = liquid temperature
T_v = vapor temperature
T_0 = liquid initial uniform temperature
T_{sat} = saturation temperature at P
ΔT = initial liquid superheat, $T_0 - T_{sat}$
u = radial velocity
$\bar{u}$ = radial velocity on r axis
V_E = volume of ellipsoid
V_0 = volume of bubble for no magnetic field
w = z-direction velocity
$\bar{w}$ = z-direction velocity on z axis
z = z-coordinate
Z = vapor-liquid interface on z-axis
$\dot{Z}$ = first time derivative of Z
$\ddot{Z}$ = second time derivative of Z

Subcripts

ϕ = angular variable
ϵ = eccentricity of ellipsoid
ρ_ℓ = liquid density
ρ_r = radius of curvature at R, $\dfrac{2RZ^2}{R^2+Z^2}$
ρ_v = vapor density
ρ_z = radius of curvature at Z, R^2/Z
$\rho_{rz} = (\rho_z{}^2\cos^2\phi + \rho_r{}^2\sin^2\phi)^{1/2}$
σ_ℓ = electric conductivity
σ_s = surface tension

Similarly, taking the limit as $r \to 0$ and $z \to Z$, the continuity equation becomes:

$$2 \lim_{r \to 0} \frac{\partial u}{\partial r} - \frac{\dot{Z}}{Z} m = 0 \tag{6}$$

where l'Hôpital's rule has been applied. The problems are then to find

$$\lim_{z \to 0} \frac{\partial w}{\partial z} \quad \text{and} \quad \lim_{r \to 0} \frac{\partial u}{\partial r}.$$

Referring to Fig. 2, the parametric representation of an ellipse can be obtained:

$$z' = Z \cos \phi, \quad z' = z$$

$$r' = Z \sin \phi, \quad \text{and} \quad r' = \frac{Z}{R} r$$

therefore $r = R \sin \phi$.

By decomposition of the velocity on the bubble surface,

$$u = \dot{R} \sin \phi, \quad \text{implies } u = \frac{\dot{R}}{R} r$$

$$w = \dot{Z} \cos \phi, \quad \text{implies } w = \frac{\dot{Z}}{Z} z$$

therefore,

$$\lim_{z \to 0} \frac{\partial w}{\partial z} = \frac{\dot{Z}}{Z} \quad \text{and} \quad \lim_{r \to 0} \frac{\partial u}{\partial r} = \frac{\dot{R}}{R}. \tag{7}$$

Equation (7) can be substituted into equations (5) and (6) respectively; thus n and m can be solved as

$$n = 1 + \frac{\dot{Z}R}{Z\dot{R}} \quad \text{and} \quad m = 2 \frac{Z\dot{R}}{\dot{Z}R} \tag{8}$$

Equations (3, 4) and (8) represent the spatial and temporal form of $\bar{u}$ and $\bar{w}$.

Taking the limit as $z \to 0$ of equation (1), substituting the spatial dependence of $\bar{u}$ and integrating the spatial variable r, from $r = R$ to $r = \infty$, the equation becomes:

$$R\ddot{R} + \frac{(n+1)}{2} \dot{R}^2 - \frac{R\dot{R}}{(n-1)} \frac{dn}{dt}$$

$$= A^*(T_v - T_{\text{sat}})(n-1) - \frac{2\sigma_s}{\rho_\ell} \left(\frac{1}{\rho_r}\right) (n-1) - \frac{\sigma_\ell B^2}{\rho_\ell} R\dot{R} \tag{9}$$

Similarly, taking the limit as $r \to 0$ of equation (2) making use of equation (4) and integrating z from $z = Z$ to $z = \infty$, one obtains:

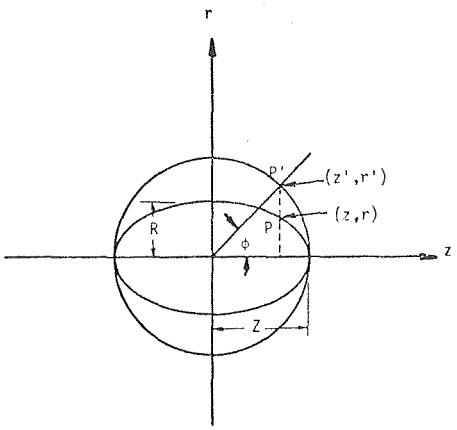

Fig. 2 Parametric representation of an ellipse

$$Z\ddot{Z} + \frac{(m+1)}{2} \dot{Z}^2 - \frac{Z\dot{Z}}{(m-1)} \frac{dm}{dt}$$

$$= A^*(T_v - T_{\text{sat}})(m-1) - \frac{2\sigma_s}{\rho_\ell} \left(\frac{1}{\rho_z}\right) (m-1) \tag{10}$$

where the Clausius-Clapeyron equation has been introduced. In addition, the surface force is approximated by defining ρ_r and ρ_z which are the radii of curvature of the bubble at R and Z, respectively:

$$\rho_r = \frac{2RZ^2}{R^2 + Z^2} \quad \text{and} \quad \rho_z = \frac{R^2}{Z}$$

As was determined from dimensional analysis and from later results, the surface tension effects are negligible, thus the surface tension terms will be dropped from the rest of the analysis.

The unknown in equations (9) and (10) is the vapor temperature, T_v, which must be determined from the energy conservation equation. Using the equation of conservation of thermal energy at the bubble interface, the rate of vapor generation (volume growth rate) can be expressed in terms of the heat conduction through the liquid to the interface:

$$V_E \rho_v h_{fg} = \oint k_\ell \left.\frac{\partial T}{\partial r_p}\right|_{\text{surface}} dA_E \tag{11}$$

where the integral is of the thermal gradient normal to the interface over the ellipsoidal bubble surface. The temperature gradient at a growing spherical surface, as given by Carslaw and Jaeger [18] and Zuber [19] is:

$$\left.\frac{\partial T}{\partial r_p}\right|_{r=R_s} = (T_0 - T_v) \left[\frac{1}{\sqrt{\pi a_\ell t}} + \frac{1}{R_s}\right] \tag{12}$$

For the ellipsoidal bubble we use the approximation

$$\left.\frac{\partial T}{\partial r_p}\right|_{\text{surface}} = (T_0 - T_v) \left[\frac{1}{\sqrt{\pi a_\ell t}} + \frac{1}{\rho_{rz}}\right] \tag{13}$$

where

$$\rho_{rz} = (\rho_z{}^2 \cos^2 \phi + \rho_r{}^2 \sin^2 \phi)^{1/2}$$

The assumptions of negligible surface tension effect and spatially uniform vapor temperature and pressure inside the bubble have also been made. Correction for initial-to-final vapor density ratio [20] has not been taken into account. Equation (13) is used in the integration of the right hand side of equation (11) and the result is closely approximated by:

$$\dot{V}_E = 2R\dot{R}Z + R^2\dot{Z} \simeq \frac{3k_\ell}{\rho_v h_{fg}} (T_0 - T_v) \times \left| \frac{A_E}{4\pi\sqrt{\pi a_\ell t}} + \frac{RZ}{\rho_r} \right| \tag{14}$$

where $A_E = 2\pi(R^2 + RZ \sin^{-1} \epsilon/\epsilon)$ is the area, and ϵ is the eccentricity of the prolate spheroid. The vapor temperature T_v is then solved from equation (14) and substituted into equations (9) and (10), resulting in two coupled second order ordinary differential equations which can be solved numerically with proper initial conditions.

The initial conditions chosen for the calculations are:

$$R(t_0) = Z(t_0) = \frac{2\sigma_s}{\Delta P} \tag{15}$$

$$\dot{R}(t_0) = \dot{Z}(t_0) = \left(\frac{2}{3} \frac{\Delta P}{\rho_\ell}\right)^{1/2} \tag{16}$$

where $t_0 = R(t_0)/\dot{R}(t_0)$ and

$$\Delta P = \frac{(T_0 - T_{\text{sat}})\rho_v h_{fg}}{T_{\text{sat}}}$$

is the Clausius-Clapeyron relation. Physically, these initial conditions imply spherical growth at $t = t_0$. When the bubble radius is slightly larger than the equilibrium radius, $R(t_0) = 2\sigma_s/\Delta P$, the bubble expands with an initially spherically symmetric velocity $\dot{R}(t_0)$. Equation (16) represents the inertially controlled regime of bubble growth, where ΔP is maximum.

Equations (9) and (10) were solved by the eighth order Runge-

Kutta numerical method. The results are presented in the following section.

Discussion of Theoretical Results

Nonmagnetic, Spherical Bubble Growth Results. While the present model allows nonsymmetrical bubble growth in the presence of a magnetic field, results from it for symmetrical growth (no field) were obtained for comparison with other available solutions. Fig. 3 shows the results using the present model for the growth of a spherical bubble in sodium at 100°C superheat and 1.7 atmospheres pressure for the case of $B = 0$. These theoretical results are compared with some theoretical and experimental results from the literature [21–23]. The results of the present study agree very well with the other calculations, which are valid for the inertially and thermally controlled regimes of spherical bubble growth.

Magnetic Field Bubble Growth Results. The numerical model was used to predict the growth of vapor bubbles in superheated alkali metals in magnetic fields. Fig. 4 presents the aspect ratios of vapor bubbles growing in superheated 11.1°C (20°F) potassium at 2 atmospheres pressure under different magnetic field intensities. The aspect ratio (Z/R) of the ellipsoid is seen to be a function of magnetic field and time during growth. As the magnetic field strength increases, the bubble becomes more elongated. The presence of the magnetic body force will distort the bubble, and in turn affect the heat transfer due to the relative increase in surface to volume ratio of the bubble. The Z/R curves are seen to not exhibit a monotonically increasing effect of magnetic field at high magnetic fields.

Fig. 5 shows the results of Fig. 4, over a small range of magnetic field strength (from 0 to 20 weber/m^2). These field strengths would be more applicable for probable future fusion power reactors. The curves show the effects of magnetic field on potassium vapor bubble aspect ratio to be quite linear for magnetic fields less than 15 weber/m^2.

Fig. 6 shows the effects of magnetic field and time on bubble volume for a bubble growing in potassium at a specific superheat, expressed as the ratio of ellipsoidal volume to spherical (zero magnetic field) volume. The field clearly reduces the ralative bubble volume as the bubbles grow. The V_E/V_0 curves are seen to exhibit a nonmonotonic behavior for large growth times. For reference, the volume of a spherical bubble (nonmagnetic case) as a function of time is also

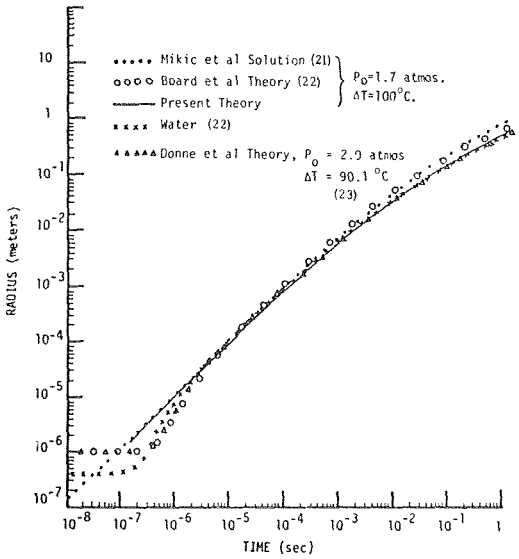

Fig. 3 Sodium vapor bubble growth in zero magnetic field

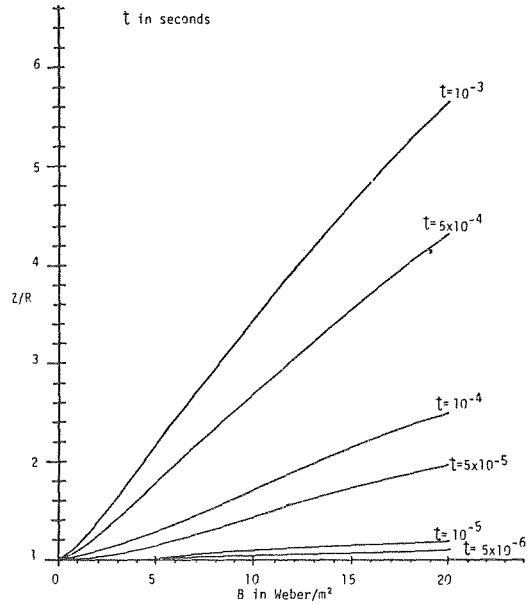

Fig. 5 Aspect ratio Z/R versus magnetic fields of $0 \leq B$ 20 weber/m^2 for potassium

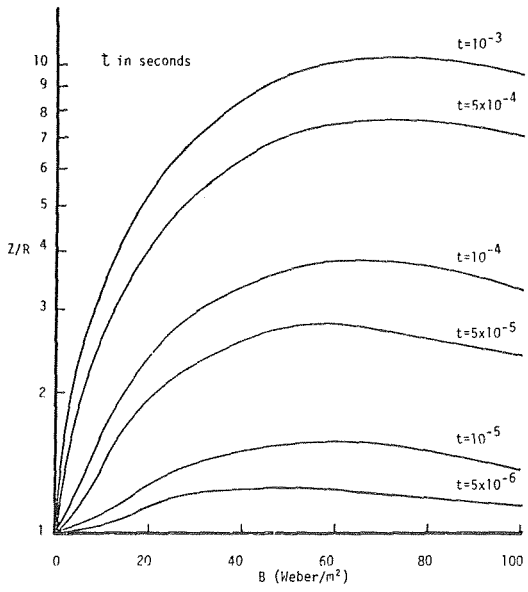

Fig. 4 Aspect ratio Z/R versus magnetic field for potassium

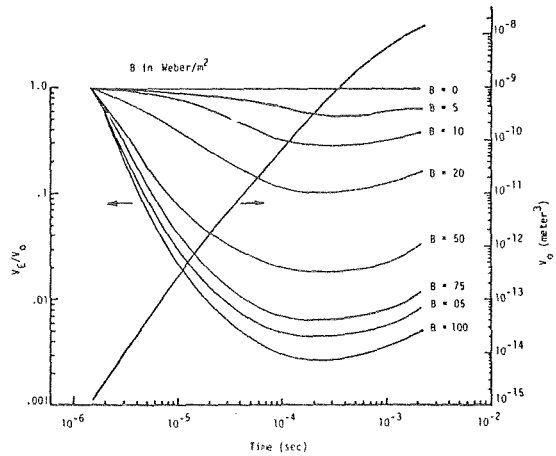

Fig. 6 Volume ratio V_E/V_0 and spherical volume growth, V_0, as a function of magnetic field for potassium at 11.1°C (20°F) superheat

shown in Fig. 6 for potassium at this superheat. Fig. 7 presents the results on an expanded scale for magnetic field strengths up to 20 weber/m^2. The nonmonotonic behavior of the curves at large growth times is illustrated quite clearly.

The present results show the basic behavior of a single bubble growing in an infinite superheated fluid under uniform magnetic fields. Of ultimate importance, however, is the effect of magnetic fields on the nucleate boiling heat transfer and on the critical heat flux. While the present results emphasize isolated bubble growth, an estimation of the effect of magnetic fields on the nucleate boiling heat transfer for liquid metals based on the results is presented below.

Heat Transfer in Liquid Metals

Forster and Zuber [24] formed a time independent boiling heat transfer model based on the bubble Reynolds number where:

$$\mathrm{Nu} \propto \mathrm{Re}^{0.62}\mathrm{Pr}^{1/3} \tag{17}$$

and $\mathrm{Re} \propto R_s\dot{R}_s$ for spherical bubble growth. Note that for spherical bubble growth in the asymptotic (diffusion) growth regime $R_s\dot{R}_s$ is constant and thus Nu is time independent. Assuming an extension of this boiling heat transfer model to the present study, an equivalent spherical bubble of radius R_E is defined:

$$R_E = (R^2Z)^{1/3} \tag{18}$$

where $4\pi/3\ R^2Z$ is the volume of the ellipsoid. Accordingly, the equivalent bubble radial growth rate is:

$$\dot{R}_E = \left(\frac{2\dot{R}}{R} + \frac{\dot{Z}}{Z}\right)\frac{R_E}{3}$$

Thus, for a nonspherical bubble growing in the presence of a magnetic field, $\mathrm{Re}_B \propto R_E\dot{R}_E$ and $\mathrm{Nu}_B \propto \mathrm{Re}_B{}^{0.63}$, and therefore the following approximation results:

$$\mathrm{Nu}_B/\mathrm{Nu}_0 = \left(\frac{\mathrm{Re}_B}{\mathrm{Re}_0}\right)^{0.62}$$

where the subscripts refer to with and without a B field respectively, and the Prandtl number disappears as it is not affected by the magnetic field.

Fig. 8 presents Nu as a function of time for different superheats and magnetic field strengths, based on the potassium bubble growth data of Figs. 4–7. In the absence of a magnetic field (top and bottom curves) and in the asymptotic (diffusion) growth regime Nu_0 is seen to become time independent. However, in the presence of a magnetic field (middle curves) Nu_B is time dependent. Comparative values of Nu_0 and Nu_B could be taken at a chosen time during the growth period of both bubbles, or at a specified bubble diameter such as the breakoff diameter.

As one comparison, a time is selected such that the spherical growth case (nonmagnetic) would already be in the asymptotic regime. Such a comparison would be conservative because Nu_B is still increasing as shown in Fig. 8. Fig. 9 presents an estimate of $\mathrm{Nu}_B/\mathrm{Nu}_0$ as a function of potassium superheat under different B fields, at 2 atmospheres pressure and at the selected time of $t = 10^{-3}$ s. The results show that $\mathrm{Nu}_B/\mathrm{Nu}_0$ decreases as B increases, and the curves for different magnetic field intensities approach different asymptotes. Fig. 10 shows the variations of $\mathrm{Nu}_B/\mathrm{Nu}_0$ as a function of B for potassium at $t = 10^{-3}$ s, cross-plotted from Fig. 9. Fig. 10 indicates the effect to be essentially a linear decrease in $\mathrm{Nu}_B/\mathrm{Nu}_0$ with magnetic field over the range indicated.

Based on Figs. 9 and 10, the boiling curve for potassium should shift to the right as magnetic field intensity increases, decreasing somewhat the effectiveness of boiling potassium as a heat transfer medium.

Another basis for the relative magnetic field effect on nucleate boiling based on single bubble growth results might be to evaluate the Nusselt number at a specific bubble volume instead of at a specific time of growth. Fig. 11 presents such results for $\Delta T = 12°\mathrm{C}$ and $\Delta T = 20°\mathrm{C}$. The volumes are chosen to be equal to the bubble volumes occurring at the asymptotic Nusselt number condition for the respective superheats at zero magnetic field. For comparison, the Nusselt numbers obtained at the same superheats based on a specific time ($t = 10^{-3}$ s) are also presented in Fig. 11. The approach of se-

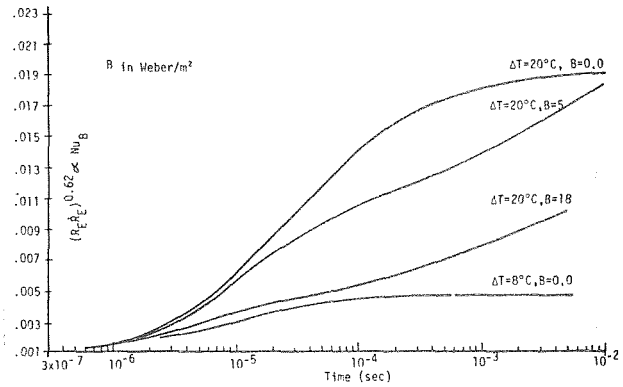

Fig. 8 Estimated Nusselt Number versus time under different superheats and magnetic field strengths for potassium

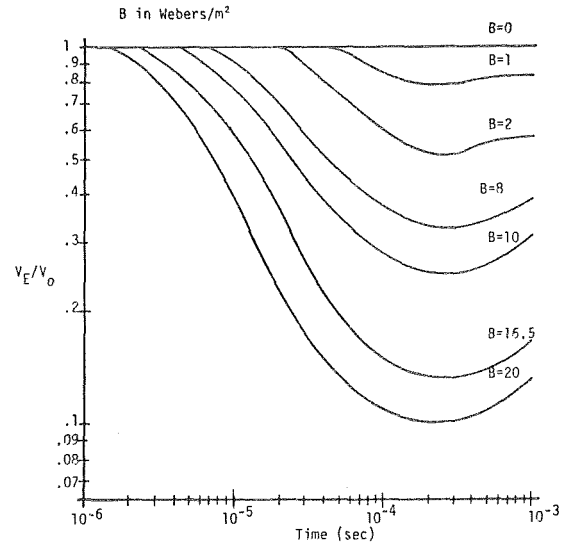

Fig. 7 Volume ratio V_E/V_0, versus time for potassium at 11.1°C superheat and for $B \leq 20$ weber/m^2

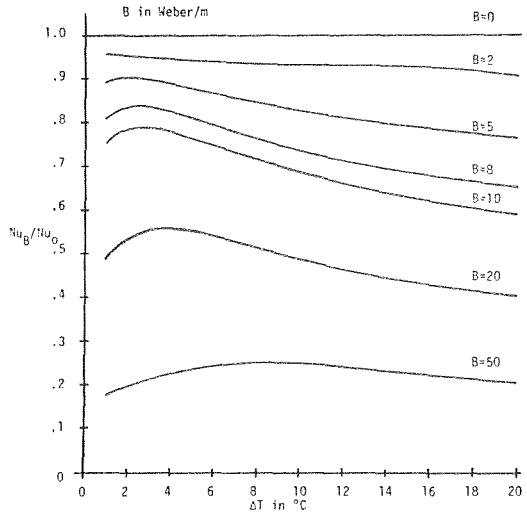

Fig. 9 Estimated effect of superheat and magnetic field on Nusselt number for potassium (based on selected growth time)

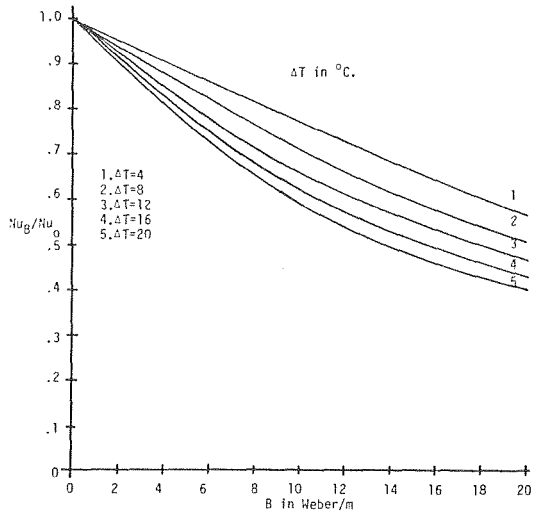

Fig. 10 Estimated effect of superheat and modest magnetic field on Nusselt Number for potassium (based on selected growth time)

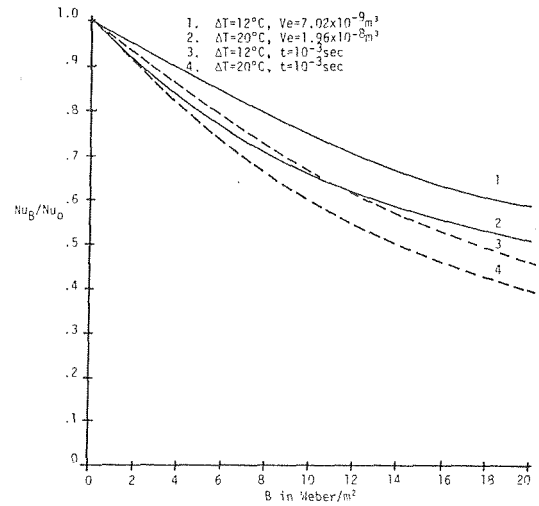

Fig. 11 Estimated effect of maagnetic field on Nusselt Number for potassium (based on selected bubble volume)

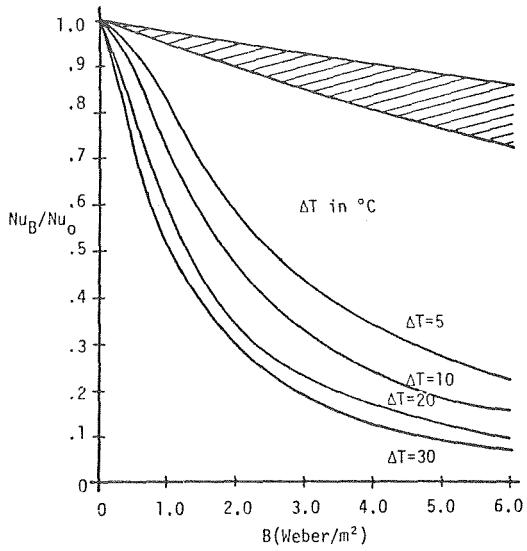

Fig. 12 Comparison of present results and those of Wagner and Lykoudis [16] for potassium. (Shaded area represents range of present results for $4 \leq \Delta T \leq 20$°C.)

lecting a specific time predicts a greater effect on nucleate boiling; however the results are not markedly different. It is considered that the effect based on similar volumes has more physical significance.

The only theoretical analyses of the effect of magnetic field on nucleate boiling heat transfer available in the literature are by Wagner, et al. [16] and Lykoudis [25]. A comparison of the Wagner and Lykoudis [16] results with the present results is presented in Fig. 12 for potassium over ranges of $0 < B < 6$ webers/m^2 and $4 < \Delta T < 20$°C. It is seen that the results of [16] predict a considerably stronger effect than the results obtained from the present study. The reason for this difference is that the spherically symmetric field assumed in [16] restricts bubble growth in all directions and thus presumably overestimates the effect of the magnetic field on bubble growth and on heat transfer.

In the experimental investigation conducted by Faber and Hsu [14] with mercury they found that, at 6 weber/m^2 and 100°C superheat, the magnetic field effect is quite significant at moderate nucleate boiling heat fluxes. From Fig. 7 of their paper the heat flux at 6 weber/m^2 is seen to be approximately 0.17 of that for zero field at the same superheat. The results from the present ellipsoidal bubble growth mode, under similar superheat and magnetic field strength, predict this ratio to be approximately 0.18. The almost identical value is presumed to be fortuitous, since the bubble growth results are for a uniform liquid superheat, whereas boiling occurs in a strong superheat gradient. At higher nucleate boiling heat fluxes (near the heat flux limit of their experiments) the Faber and Hsu data exhibit little effect of magnetic field on nucleate boiling. This variable effect at different heat fluxes is presently unexplained. It is expected however that using the isolated bubble growth results to predict nucleate boiling heat transfer becomes less justifiable as the critical heat flux is approached.

The present study provides a much improved model and results for isolated bubble growth in electrically conductive liquids in magnetic fields, as well as valuable insight into this boiling phenomenon. However, more refined and thorough experimental studies, as well as a more exact model, are still needed to confirm the magnitude of the effect of magnetic field on nucleate boiling heat transfer for liquid metals.

Conclusion

The present analytical investigation, is directed primarily toward isolated bubble growth in superheated liquid metals in magnetic fields. For alkali metals in strong magnetic fields the results show that growing bubbles will distort markedly from a spherical shape, being elongated in the direction of the field. The aspect ratio of the elongated (ellipsoidal) bubble is increased and the volume growth rate is suppressed with increasing field. The aspect ratio of the bubble also increases with time during the growth period.

These isolated bubble growth results, when used to estimate the effect on nucleate boiling heat transfer, suggest that magnetic fields typical of fusion power reactors would reduce the nucleate boiling heat transfer coefficient for alkali metals, though probably not so much as to eliminate it as a potential cooling medium in fusion power reactors. It may be speculated that the magnetic field would also have an effect on the critical heat flux for boiling alkali metals, though the magnitude is unknown.

Further experimental studies on the nucleate boiling and critical heat flux as well as more accurate analytical models are needed to confidently assess the effect of magnetic fields on the nucleate boiling and critical heat flux for liquid metals.

Acknowledgments

These studies were supported by grants from the Texas Atomic Energy Research Foundation (TAERF) and the National Science Foundation (NSF).

References

1 Grimes, W. R., and Cantor, S., "Molten Salts as Blanket Fluids in Controlled Fusion Reactors," USAEC Report ORNL-TM-4047, Oak Ridge National Laboratory, Dec., 1972.

2 Hancox, R., and Hunt, C. R., "The Use of Liquid Lithium as Coolant in a Fusion Reactor," Part I, UKAEA Research Group, Culham Laboratory, CLM-R115 Abington, Oct., 1971.

3 Werner, R. W., "Module Approach to Blanket Design—A Vacuum Wall Free Blanket Using Heat Pipes," in *Proceedings,* Nuclear Fusion Reactor Conference, UKAEA, Culham Laboratory, Abington, Berkshire, England, Sept., 17–19, 1969, pp. 536–557.

4 Steiner, D., "The Nuclear Performance of Fusion Reactor Blankets," *Nuclear Applications and Technology,* Vol. 9, July 1970, pp. 83–92.

5 Hoffman, M. A., and Carlson, G. A., "Calculation Techniques for Estimating the Pressure Losses for Conducting Fluid Flows in Magnetic Fields," UCRL-51010, Lawrence Radiation Laboratory, Feb., 4, 1971.

6 Fraas, A. P., "Problems in Coupling a Gas Turbine to a Thermonuclear Reactor," Paper T2-GT-98, ASME, 1971.

7 Hopkins, G. R., and Melese-d'Hospital, G., "Direct Helium Cooling Cycles for a Fusion Reactor," in *Proceedings,* Nuclear Fusion Reactor Conference, UKAEA, Culham Laboratory, Abington, Berkshire, England, Sept. 17–19, 1969, pp. 522–535.

8 Forster, S., "The Closed Helium Turbine Cycle with a Fusion Reactor as Energy Source," Paper T2-Wa/Ener 10, ASME, 1972.

9 Conn, R. W., et al., "UWMAK-II, A Conceptual Tokamak Reactor Design," UWFDM-112, Fusion Technology Program, The University of Wisconsin, Madison, Wisconsin, Oct., 1975.

10 Davis, J. W., et al., "Major Features of D-T Tokamak Fusion Reactor Systems," EPRI 472-1, Feb., 1976.

11 Leverette, S. J., "An Investigation of the Temperature Distribution in the Lithium Blanket of a Fusion Reactor," ORNL-TM-3701, May 1972.

12 Fraas, A. D., "Analysis of a Recirculating Lithium Blanket Designed to Give a Low Magnetohydrodynamic Pumping Power Requirement," ORNL-TM-3756, Sept., 1972.

13 Parkin, J. R., Schmidt, P. S., and Vliet, G. C., "Design of a Boiling Potassium Heat Removal System for Fusion Reactors," *Proceedings of the First Topical Meeting on the Technology of Controlled Nuclear Fusion,* April 1974, Vol. I, pp. 664–676.

14 Faber, O. C., and Hsu, Y. Y., "The Effect of a Vertical Magnetic Induction on the Nucleate Boiling of Mercury Over a Horizontal Surface," *Chemical Engr. Progress, Symposium Series,* No. 82, Vol. 64, pp. 33–41.

15 Fraas, A. P., et al., "Effect of a Strong Magnetic Field on Boiling of Potassium," ORNL-TM4218, 1974.

16 Wagner, P. S., and Lykoudis, P. S., "The Effect of Liquid Inertia on Bubble Growth in the Presence of a Magnetic Field," National Heat Transfer Conference, St. Louis, Aug., 1976.

17 Wong, Clement P., "Analysis of Bubble Growth and Boiling Heat Transfer for Liquid Metals in Magnetic Fields," Ph.D. Dissertation, University of Texas, Austin, Texas, May 1977.

18 Carslaw, H. S., and Jaeger, J. C., *Conduction of Heat in Liquids,* Oxford, The Clarendon Press, 1959.

19 Zuber, N., "Hydrodynamics Aspects of Boiling Heat Transfer," USAEC Report AECU-4439 (1959). (Ph.D. Thesis, University of California, Los Angeles).

20 Theofanous, T. C., and Patel, P. D., "Universal Relations for Bubble Growth," *Int. J. Heat Mass Transfer,* Vol. 19, 1976, pp. 425–429.

21 Mikic, B. B., "On Bubble Growth Rates," *Int. J. Heat Transfer,* Vol. 13, 1970, pp. 657.

22 Board, S. J., and Duffey, R. B., "Spherical Vapor Bubble Growth in Superheated Liquids," *Chemical Engineering Science,* Vol. 26, 1971, pp. 263–274.

23 Dome, M. D., and Ferranti, M. P., "The Growth of Vapor Bubbles in Superheated Sodium," *Int. J. Heat Transfer,* Vol. 18, 1975, pp. 477–493.

23 Forster, H. K., and Zuber, N., "Dynamics of Vapor Bubbles and Boiling Heat Transfer," *A.I.Ch.E.J.,* Vol. 1, 1955, pp. 531–535.

25 Lykoudis, P. S., "Bubble Growth in the Presence of a Magnetic Field," *Int. J. Heat Mass Transfer,* Vol. 19, 1976, pp. 1357–1362.

26 Colver, C. P., and Balzhiser, R. E., "A Study of Saturated Pool Boiling Potassium Up to Burnout Heat Fluxes," *Chemical Engineering Progress, Symposium Series,* No. 59, Vol. 61, 1965, pp. 253–263.

27 Wichner, R. P., and Hoffman, H. W., "Vapor Bubble Growth Rates in Superheated Liquid Metals," ORNL-TM-1413, 1966.

J. H. Lienhard
Professor.
Fellow ASME

Md. Alamgir
Research Asst.

M. Trela
Visiting Scientist[2]

Boiling and Phase Change Laboratory,
Mechanical Engineering Dept.,
University of Kentucky,
Lexington, KY 40506

Early Response of Hot Water to Sudden Release from High Pressure[1]

The very early stages of blowdown are observed with the aid of a novel quick-opening mechanism. Water at pressures and temperatures up to PWR conditions is released from a long, one-half in. (1.27 cm) ID pipe. Depressurization rates up to 1.62 × 10^6 atm/s are achieved. As a consequence of the rapidity of depressurization, the water reaches pressures far below saturation (even approaching the spinodal line) before nucleation occurs. The performance of the opening device is described quantitatively, and implications of the response of the water are discussed in relation to nuclear safety problems.

Introduction

The problem of predicting the response of nuclear reactors to various hypothetical pipe breaks is very important in assessing nuclear safety. The problem has, in turn, spawned a number of fundamental studies of suddenly initiated blowdown from pipes. Relatively little had been done with this problem before the end of the 1960's. Prior to 1971 Höppner and Schrock [1] looked at blowdown from relatively low pressures. And in 1970 there appeared a variety of studies done at much higher pressures—up to Pressurized Water Reactor conditions [2, 3, 4, 5, 6]. The most notable of these was the work of Edwards and O'Brien [2] which has been the point of reference for a great deal of subsequent analysis.

These experiments had certain things in common. They all were initiated by breaking a diaphragm or shattering a glass disc. They generally achieved most of the initial depressurization within one-half to one millisecond at rates of depressurization up to about 0.2 × 10^6 atm/s.

Another feature they exhibited was that the depressurization traces undershot the saturation pressure by very little in some cases and by a great deal in others before nucleation occurred. The work of Skripov and his coworkers in very clean liquids (see, e.g., [7, 8]) shows clearly that the extent to which it is possible to superheat a liquid (or depressurize it) beyond the saturation point depends strongly on how quickly it is done. This should be the case in reactor coolants as well. If experiments are to replicate the circumstances surrounding, say, a pipe fracture or other very sudden accident, the speed with which they are done should prove to be quite important. Thus, we wish to study higher speeds of depressurization than have previously been attained in the laboratory. By doing this we anticipate reaching greater pressure undershoots than have previously been attained. This, in turn, should put a considerably different initial condition on the subsequent blowdown process.

The purpose of this paper is therefore to describe the results of a rapid depressurization experiment in which the initial response of the liquid is emphasized.

The Experiment

The apparatus for the present work incorporates a quick-opening plug mechanism[3] developed by G. S. Borkar [9]. It is described fully along with the initial experimental results in [10].

Fig. 1 shows a pictorial layout of the apparatus. It presently involves a one half in. (1.27 cm) ID pipe; however, we are currently building a two in. (5.08 cm) replica of it to test our belief that scaling effects are not important. The apparatus incorporates a fairly conventional nitrogen system for pressurizing double-distilled water which has been degassed by boiling it for one half hour. The pressurization system is quite far from the test section so there is no problem of forcing N_2 into solution with the test liquid. The water is drawn into the system by a vacuum pump at an absolute pressure between 0.04 and 0.07 atm. We measured the oxygen content of the degassed water and found it to be about 0.8 mg/ltr of water or 10 percent of saturation at 20°C.

[1] The present work was done under support of the Electric Power Research Institute (Contract No. RP-687-1) with B. Sehgal as Contract Manager.

[2] Presently at Instytut Maszyn Przepływowych, Gdańsk, Poland.

Contributed by the Heat Transfer Division for publication in the JOURNAL OF HEAT TRANSFER. Manuscript received by the Heat Transfer Division November 11, 1977.

[3] The Electric Power Research Institute is applying for a patent on this mechanism.

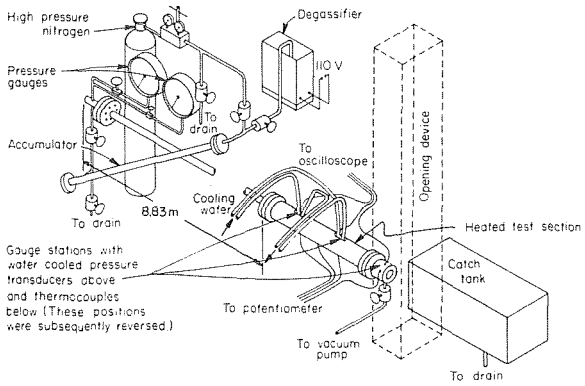

Fig. 1 Pictorial view of apparatus (opening device is shown in Fig. 2)

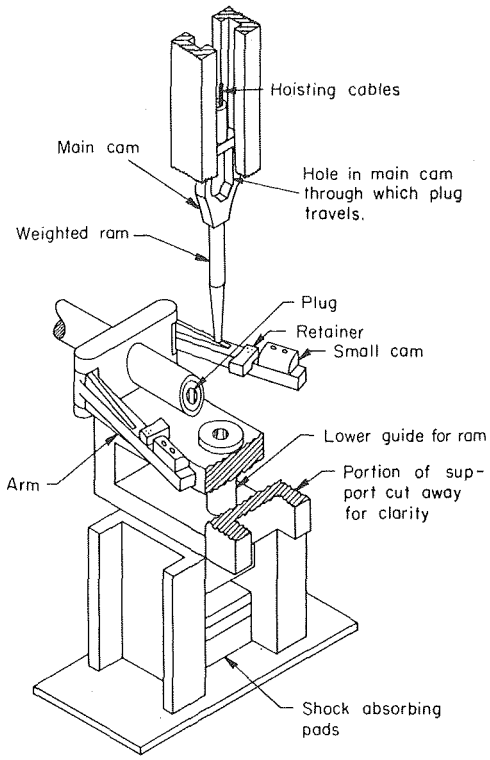

Fig. 2 Pictorial view of lower portion of opening device

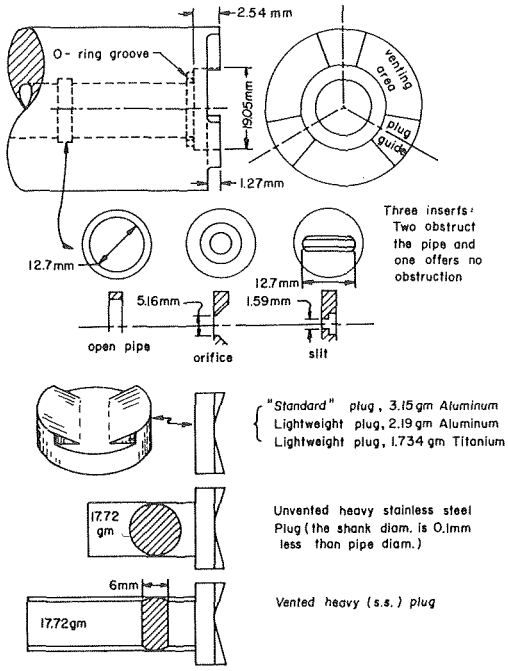

Fig. 3 Configuration of open end of pipe, obstructive inserts, and plugs

The one half in. pipe configuration consists of an unheated length of 8.83 m behind a heated test section approximately two m in length. The purpose of the long run of cold pipe is to prevent the reflected rarefaction wave from returning to the test section until the initial depressurization has occurred. Resistance heaters are used to bring the test section to a temperature which is uniform to within about ± five percent of the absolute temperature before the depressurization is triggered. Temperatures at the pressure transducers were obtained by plotting the axial temperature profile and interpolating.

Fig. 2 shows the simple quick-opening plug release device: a weighted cam drops from a height of almost three m. This cam engages two mating cams on arms which hold a light-weight plug in position. The arms are driven apart with constant acceleration and they clear the edges of the plug almost simultaneously. The plug then pops out under pressure of the liquid in the pipe. Reference [10] gives details of the design and shaping of this arrangement, as well as additional details as to instrument errors.

Fig. 3 shows, at the top, the recess into which all plugs were fit. The arrangement is contrived to guide the motion of the plugs for at least 2.54 mm, but to vent the liquid after 1.27 mm. Provision is also made

Nomenclature

A, A_e, A_p = cross-sectional area. A_e at exit plane of pipe (equal to plug area). A_p for the pipe itself

a = constant in equation (7)

c, $\bar{c}$ = velocity of propagation (equal to sound speed in a single medium). $\bar{c}$ is a mean c, defined in equation (5)

E = modulus of elasticity

m = mass of plug divided by A_p

p, p_{qs} = pressure. The quasistatic pressure established soon after depressurization

T, T_s = temperature. Saturation temperature

t = time

v = specific volume

v_p = velocity of plug

ΔT_{r_m} = difference between a spinodal temperature and the saturation temperature at the same pressure. Also used to denote the difference between a nucleation temperature and the saturation temperature at the same pressure.

δ = time required for an arbitrary 80% of depressurization to occur

κ = isothermal compressibility

ρ = density

Σ, Σ' = rate of depressurization during δ. Rate of depressurization between p_{sat} and p_{min}

τ = a characteristic time constant for depressurization, $m\kappa c A_p/A_e$

Subscripts

c = denotes a critical property

i = denotes a property of water prior to depressurization

min = denotes a property evaluated at the pressure of the nucleation point

r = denotes a "reduced" property—one divided by its value at the critical point.

sat = denotes a property of saturated liquid

s, w = denote properties of stainless steel and water, respectively

1, 2 = denote properties at the first and second transducers, respectively

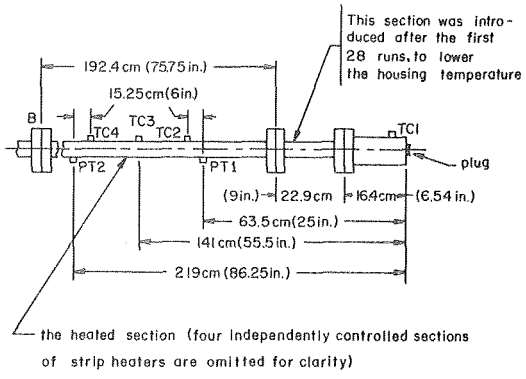

Fig. 4 **Dimensions of the test section. *TC* and *PT* designate the thermocouples and pressure transducers, respectively. (This figure includes two design changes not shown in Fig. 1: A cool section behind the housing and a relocation of *TC*'s and *PT*'s.)**

for including two obstructions of equal area (0.209 cm^2)—an orifice and a slit, as shown—in the pipe. Five types of plugs were employed and they are shown at the bottom of the figure. All had slanted surfaces on top so the retainers (shown in Fig. 2) would slide normal to the axis of rotation of the arms.

The basic plug was aluminum and weighed 3.15 g. Two lighter plugs and two heavier plugs (described at the bottom of the figure) were also used. Note that the heavy plugs are both of the same weight, but one will obstruct the escape of water until it has moved 25.4 mm while the other will vent water after 1.27 mm of travel owing to its cut-away cross section. One should note that our lightest plugs are not much heavier than the equivalent burst-diaphragm would have to be to withhold the pressure. Furthermore, no energy must be consumed to tear our plugs apart.

Fig. 4 shows the test section with locations of the piezoelectric pressure transducers (*PT*'s) and chromel-alumel thermocouples (*TC*'s) specified. The pressure transducers were flush-mounted with the inner wall of the pipe. A few original runs were made with the water cooled *PT*'s located above the *TC*'s. This of course led to some local cooling of the *TC*'s which we corrected with the positioning shown in Fig. 4. It was also necessary to cool the housing by introducing a short water-cooled section of pipe as shown in Fig. 4. Without this, the hot end of the pipe expanded against the cold arms and caused binding. (We are presently building our 5.08 cm. ID pipe with the arms separated from the pipe to avoid this problem.)

Analysis of Results

The basic data output of these tests was the pair of oscilloscope traces from *PT*1 and *PT*2. An illustrative set of such traces is shown in Fig. 5.

Characteristics of the Traces. Each trace exhibits minimal pressure oscillations on the LHS prior to plug release. These are generated as the retainers move across the plug face. The initial depressurization is a little slow—possibly as a result of binding or chattering when the plug starts to move. Most of the depressurization then occurs at great speed. We define the time of opening, δ, as the time for 80 percent of depressurization to occur. And we define the rate of depressurization, Σ, as the slope of the pressure trace in this range.

The pressure reaches a minimum below the local saturation pressure, p_{sat}, at which flashing occurs in the hot water traces. In the cold water traces this minimum is a negative pressure. In all but the highest pressure and temperature cases, flashing is followed by a sudden pressure recovery, to a value below the local saturation pressure. All this appears at the first transducer before the plug has vented. This pressure stabilizes sometime after about ten ms at a quasi-static pressure which we shall call p_{qs}. It turns out in the present experiments that

$$\frac{p_{sat} - p_{qs}}{p_{sat}} = 0.306 \pm 0.050 \qquad (1)$$

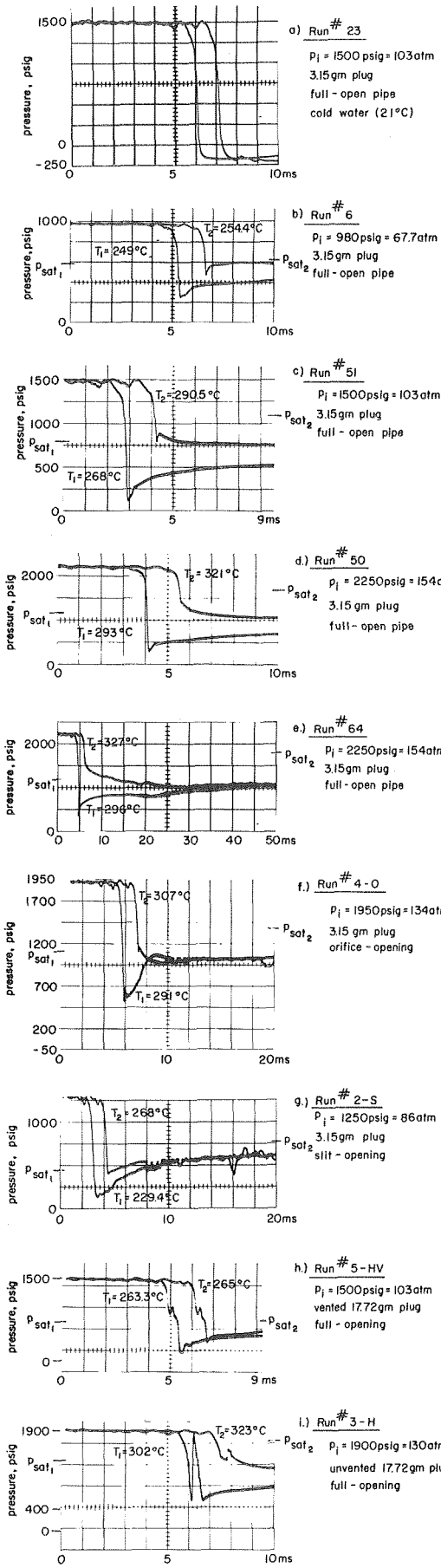

Fig. 5 **Oscilloscope pressure-time histories for nine blowdown events under different circumstances (trace on left is *PT*-1, trace on right is *PT*-2.)**

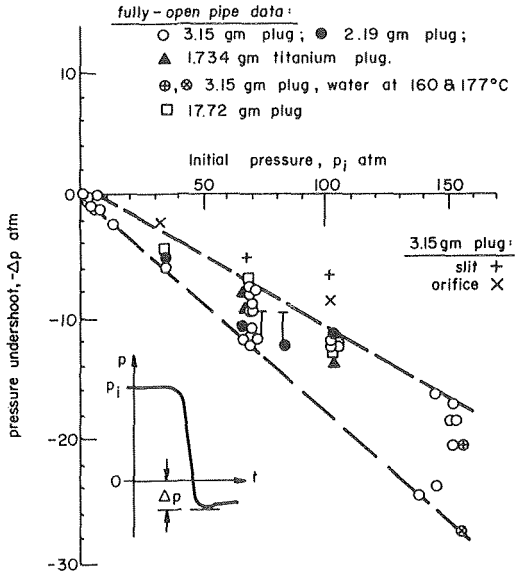

Fig. 6 Maximum tension endured by water during pressure undershoot

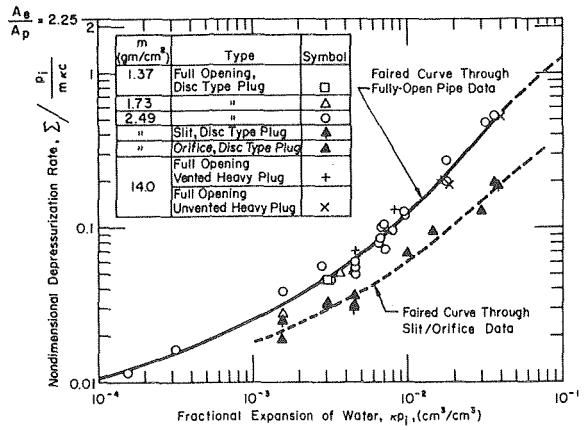

Fig. 7 Variation of nondimensional depressurization rate with fractional expansion of water

We have focused attention on the early response to depressurization in the present study. Therefore few of the traces have a 20 ms range or greater. Figs. 5(e), 5(f), and 5(g) are such traces and they show the reflection wave returning from the blind end of the pipe, 12 or 13 ms after the pipe is opened. Since the returning wave must pass through a two-phase mixture to reach $PT1$, it is greatly slowed down and does not arrive in time to appear on the traces.

The Cold Water Tests. A series of cold water tests permitted us to make final adjustments of the release mechanism and to establish reference opening characteristics. It turned out that for the 3.15 g plugs, Σ increased from 0.2 M-atm/s at 68 atm to 0.8 M-atm/s at 154 atm, and δ ranged from 0.4 ms to 0.25 ms in the same range.

The most interesting aspect of these tests was that the water was put under negative pressure, or tension, during depressurization. We believe this to occur because the plug and the water just behind it (outside of the pipe) accelerate rapidly while the increasingly long column of depressurized water inside the pipe is retarded both by its own mass and/or viscosity. Thus, we are pretty sure that the moving plug suddenly must pull upon (or "jerk") the liquid behind it. Of course, this only occurs when κp_i is small and when the venting is not immediate. Fig. 6 shows the resulting liquid tensions observed in our tests. All points (including two warm water points), with the exception of the slit and orifice points, reach a tension equal in magnitude to

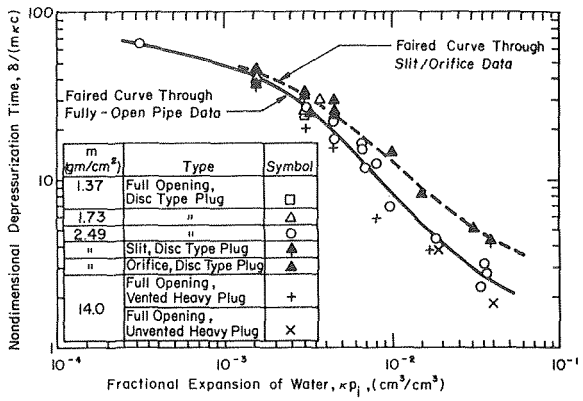

Fig. 8 Variation of nondimensional depressurization time with fractional expansion of water

about one-seventh of the initial pressure. The slits and orifices inhibit the initial impulses on the plug and result in less pressure undershoot.

The Rate of Depressurization. It will be helpful for purposes of data reduction if we identify a characteristic rate of depressurization and opening time in terms of the important system variables. We do this by writing a highly simplified theory of the rate of depressurization. Newton's second law says that the local pressure behind the plug, p, is:

$$pA_e = mA_p \frac{dv_p}{dt} \tag{2}$$

where v_p is the instantaneous speed of the plug, m is the mass of the plug divided by the cross-sectional area of the pipe, A_p, and A_e is the *exit area*, $\pi(1.905)^2/4$ cm^2 (see upper left-hand picture in Fig. 3).

The speed of the plug, v_p, must equal the speed of the liquid which has expanded as a result of the rarefaction front passing through it:

$$v_p = \kappa c(p_i - p) \tag{3}$$

where κ is the isothermal compressibility of the water and c is the speed of sound in the compressed water. Combining equations (2) and (3) we find

$$\frac{dp}{dt} = -\frac{p}{\tau}; \text{ time constant, } \tau \equiv \frac{m\kappa cA_p}{A_e} \tag{4}$$

Thus we nondimensionalize δ with τ and Σ with p_i/τ. It is consistent with the Buckingham Pi-theorem to look for a correlation of each of these variables with the single independent variable, κp_i. This term characterizes the maximum possible fractional expansion of the liquid. The existing observations of Σ and δ are plotted in Figs. 7 and 8 in this nondimensionalization.

Fig. 9 shows how we made these measurements. It should be noted that a second rate of depressurization, Σ', is defined for the superheated liquid regime—between p_{sat} and the flashing point, p_{min}. This will be used later in another context. The heavy plugs often led to a saw-tooth depressurization curve. In this case we were able to identify an envelope in which pieces of the same slope recurred. The values of Σ obtained thus were used in Fig. 7. The measurements of Σ and δ were generally accurate within ±15 percent.

The data for all of the open pipe configurations correlate very well in Figs. 7 and 8, regardless of the plug used. As the fractional expansion of water increases, the correlation model (which takes the liquid to be weightless) becomes increasingly correct. The dimensionless depressurization rate accordingly approaches the theoretical limit of $A_e/A_p = 2.25$. The constricted pipe configurations are not dimensionally similar to the open pipe, and data for these cases do not lie on the same correlation curve.

Speed of the Rarefaction Wave. Two kinds of interaction between the pipe and the liquid can cause the rarefaction wave to move at a speed different from the local speed of sound in the liquid: 1) The

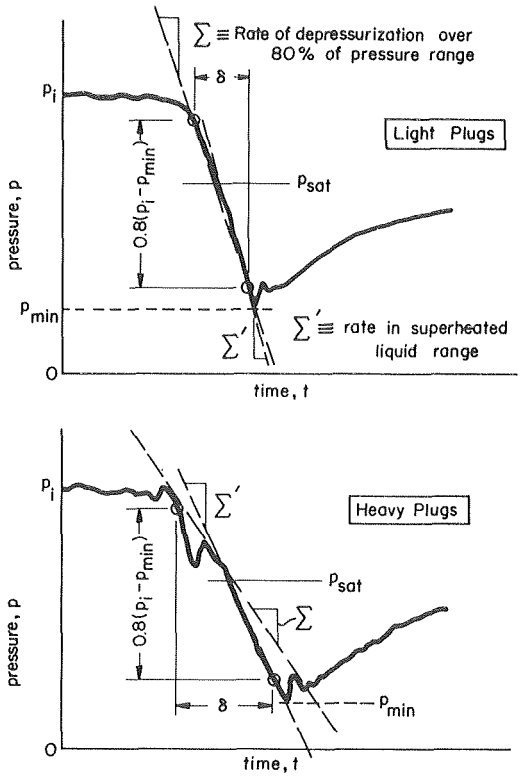

Fig. 9 The measurement of Σ and δ from oscilloscope traces for both light and heavy plugs

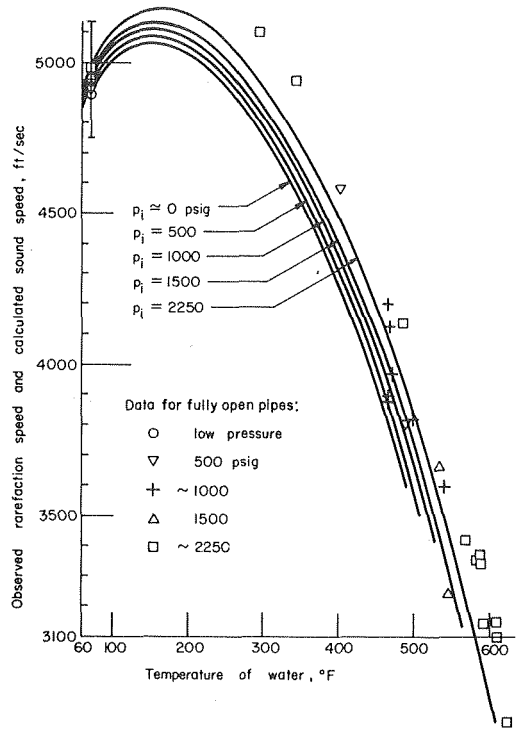

Fig. 10 The speed of sound in hot water

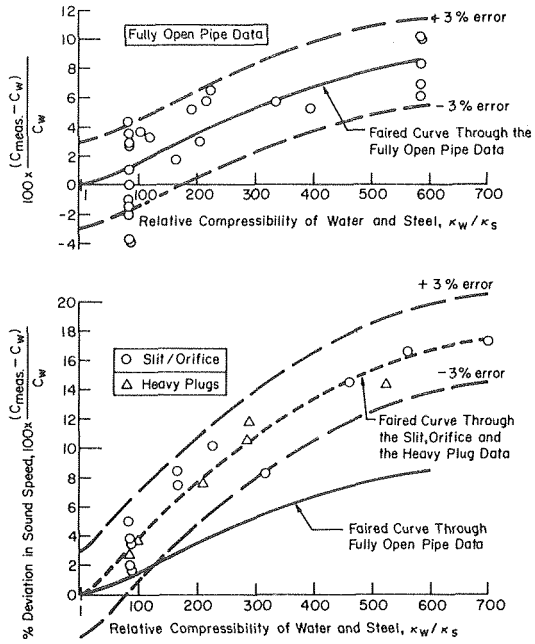

Fig. 11 Deviation of measured rarefaction speed from the calculated sound speed of water for the fully open and the constricted pipe

pipe shrinks a little as the rarefaction passes and relieves the internal pressure. The momentum and continuity equations then require that the wave be slightly slowed. In the present tests the pipe wall thickness (0.635 cm) was equal to the inside radius of the pipe. This effect is negligible in such a thick pipe. 2) When two media are bonded together, a rarefaction traveling along the bond will move at a mean sound speed $\bar{c}$. The rationale and experiments of McGlaun [11] indicate that the well known area-rule applies in the form:

$$\bar{c} = \sqrt{\frac{E_s A_s + E_w A_w}{\rho_s A_s + \rho_w A_w}} \tag{5}$$

where E, A, and ρ denote the modulus of elasticity, cross-sectional area, and density of two materials designated as s and w. Noting that $c_w = \sqrt{E_w/\rho_w}$ we rewrite equation (5) as

$$\frac{\bar{c}}{c_w} = \sqrt{\frac{1 + (E_s/E_w)(A_s/A_w)}{1 + (\rho_s/\rho_w)(A_s/A_w)}} \tag{5a}$$

The problem is that in a water pipe, bonding between water (w) and steel (s) is only present insofar as a shear stress is brought to bear by any movement of the water relative to the pipe. Such movement increases as the expansion of the water relative to that of the pipe, κ_w/κ_s. This ratio and those that appear in equation (5a) should thus dictate $c_{measured}/c_w$. But A_s/A_w and ρ_s/ρ_w change very little in the present tests and E_s/E_w is the reciprocal of κ_w/κ_s. Thus we finally look for a correlation of the type:

$$\frac{c_{measured}}{c_w} = f(\kappa_w/\kappa_s) \tag{6}$$

The speed of the rarefaction was measured from the oscilloscope traces for the various runs. An error analysis showed that the accuracy of the measurement was ± three percent of c_w. The speed of sound in water, c_w, was calculated from the complete equation of state for water given by the 1967 E.R.A Steam Tables [12].[4] We present the calculated values of c_w in Fig. 10, along with observed sound speeds in the pipe, with unrestricted openings. The deviations of $c_{measured}$ from c_w are plotted for the restricted, as well as fully open, pipes in Fig. 11. Fig. 11 shows that the measured rarefaction wave moves significantly faster than c_w.

If the bonding between water and pipe were perfect, ($c_{measured} - c_w$) would equal about $2c_w$. For the fully open pipe it reaches about 0.08 c_w, which, though much smaller, is not to be ignored. With the

[4] We are grateful to Amir Karimi for this calculation.

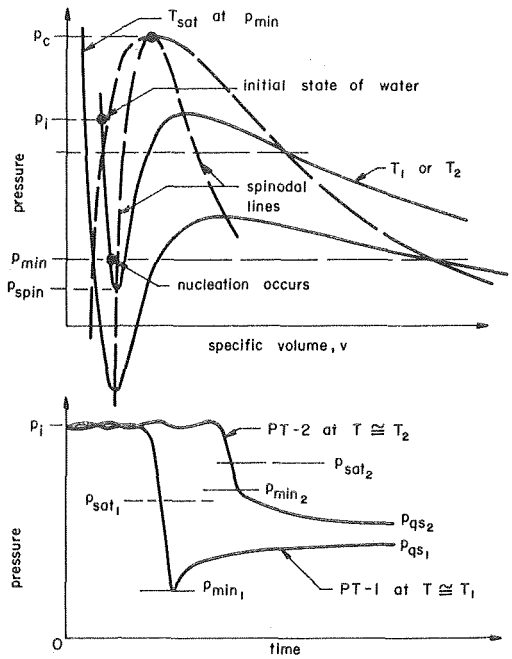

Fig. 12 Relation between pressure traces and the equation of state for water, during depressurization

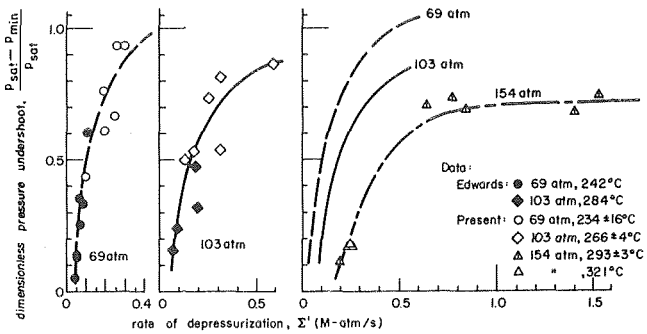

Fig. 13 The observed increase of pressure undershoot with rate of depressurization

various constrictions in the end of the pipe (slits, orifices, and heavy plugs) the water is forcibly "bonded" to the pipe and ($c_{measured} - c_w$) rises to 0.18 c_w.

This effect should diminish in larger, thinner pipes, as A_s/A_w decreases.

Pressure Undershoot

The previous discussion shows that different depressurization experiments might reduce the pressure at quite different rates. This means that different kinds of accidents might likewise result in different behavior. Of course, the rate is a strong function of initial pressure and temperature but it also varies with the mechanical features of opening.

The most important rate-dependent feature of the process is the pressure undershoot, ($p_{sat} - p_{min}$). If flashing occurs near the saturation point, then the subsequent blowdown process will be subjected to a markedly different initial condition than it will if flashing is delayed until a much lower pressure is reached. To deal with the undershoot phenomenon we must first consider some aspects of the superheated liquid state.

The Approach to the Spinodal Line. Fig. 12 relates the p-v diagram for water to a typical high-pressure oscilloscope trace. A depressurization process moves from the initial point to the flashing point along a line of constant entropy. Actually isentropic lines lie within 2.7°C of isothermal lines in all the present tests. (This calculation is based on conventional thermodynamics and a reasonable approximation to the equation of state in the superheated liquid regime.) We do not distinguish between isentropic and isothermal lines in Fig. 12. However, when we report temperatures at the flashing point, they have been corrected to values slightly below T_i.

The p-v diagram includes the spinodal lines or loci of limiting liquid superheat. This is the boundary above which flashing must occur, no matter what the process is. The liquid spinodal line cannot be absolutely reached in any experiment. Nevertheless the data of Skripov et al. [13, 14] for many liquids come extremely close to defining it (see discussion in [8]). Lienhard's corresponding states correlation [15] of these data is:

$$\Delta T_{r_m} = (1 - T_{r_s}) - a(1 - T_{r_s}^8) \tag{7}$$

where ΔT_{r_m} is the difference between any reduced spinodal temperature and the reduced saturation temperature, T_{r_s}, at the same pressure, and a is a constant.

The constant, a, was given in [15] as 0.095. However, we are interested in the particular fluid, water, for which a should differ slightly. Mr. A. Karimi of this laboratory has been attempting to locate the spinodal line and other p, v, T data for water by a constrained extrapolation of subcooled water data. This extrapolation and the theory of Furth (see [8]) agree approximately upon a liquid spinodal line which is well represented by equation (7) with $a \simeq 0.07$. This is presently our best knowledge of the spinodal line for water.

Any depressurization process will result in flashing somewhere between p_{sat} and $p_{spinodal}$, depending on the cleanliness of the water and the rapidity of the process. (In this connection we should note that it is probable that the second transducer registers nucleation which has occurred between $PT1$ and $PT2$.) We now wish to ask how close to the spinodal line flashing occurs in a depressurization process.

The Rate-Dependence of p_{min}. Fig. 13 shows dimensionless values of the pressure undershoot from both Edwards' and our experiments as a function of the local rate of depressurization in the superheated liquid,[5] Σ'. Results are shown for three initial pressure levels and only one fairly narrow range of initial temperatures at each pressure. Edwards' and our data superpose on these coordinates even though his pipe (7.32 cm ID) is almost six times larger than ours.

The results show that, particularly at slower opening speeds, the pressure undershoot is very sensitive to Σ'. The pressure undershoot appears to tend asymptotically toward a limit as Σ' is increased. But it only appears to reach that limit when T_i and p_i are on the order of *PWR* conditions. This is understandable since only under those conditions does p_{min} remain *positive* at the spinodal line. In the other cases it would be necessary to rapidly depressurize to extreme tensile stresses to reach the spinodal line.

Finally it is instructive to compare the results of these initially high pressure and temperature processes with the spinodal limit. Fig. 14 shows experimental values of ΔT_{r_m}. This is the temperature where flashing occurs (at p_{min}) minus the saturation temperature at that same pressure. The corresponding spinodal limit is plotted for comparison.

We see that the data from $PT1$ (at which the fastest values of Σ' were observed) generally come within 65 percent of the limit, while the slower values of Σ' from $PT2$ give lower superheat. This is precisely what we would expect from Fig. 13. Further superheating is prevented by the ultimate imperfections of cleaning and preparation of our system, and the history of pressurization as it will be limited in a prototype reactor as well. It is no longer limited by Σ' as it is at lower pressures.

[5] We are grateful to Mr. C. Y. Kan for his help in data reduction for Figs. 13 and 14.

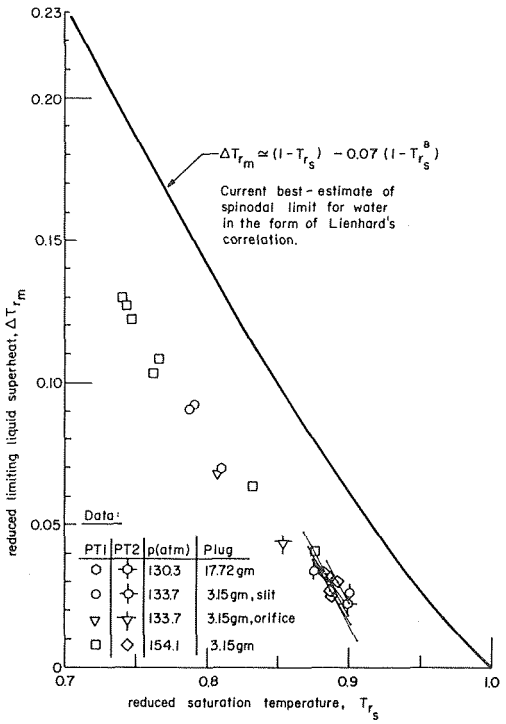

Fig. 14 Comparison of measured superheat limit with spinodal limit

Conclusions, Implications, and Problems

1 The first results of a very rapid early depressurization experiment are presented. They serve to suggest that the results of rapid blowdown tests might be strongly influenced by the rate of depressurization *prior to nucleation.*

2 A dimensionless rate of opening for this device is defined and correlated in general as a function of κp_i.

3 It is shown that the speed of propagation of rarefaction waves in water can be significantly faster than the speed of sound if the water is contained in a heavy pipe.

4 For all but *PWR* conditions the undershoot is strongly dependent on the rate of depressurization. Under *PWR* conditions, flashing occurs in our system at maximum superheats that reach about 65 percent of the spinodal limit.

5 The existing pressure traces do not indicate that any serious pressure fluctuations are introduced when Σ' is very large. The worst fluctuation observed in the present experiments occurred in run 3-i (see Fig. 5).

6 The inherent dependence of the pressure undershoot on Σ' suggests that the character of a pipe breach will dictate the initial condition for the subsequent blowdown process. None of the existing blowdown codes include any information as to the properties of superheated water or the limit of superheat. Some have been made to replicate Edwards' undershoot with the help of empirical adjustments, however. It would be instructive if someone could systematically investigate the dependence of the subsequent process on this initial condition.

7 The influence of two important variables on pressure undershoot—water condition and size—have not been investigated here. It is possible, though unlikely, that ours and Edwards' data can be correlated in Fig. 13 because of the fortuitous offsetting influences of these two variables.

References

1 Höppner, G., "Experimental Study of Phenomena Affecting Loss of Coolant Accident," Ph.D. Dissertation, University of California, Berkeley, 1971.

2 Edwards, A. R.; and O'Brien, T. P.; "Studies of Phenomena Connected with the Depressurization of Water Reactors," *Journal of the British Nuclear Energy Society*, Vol. 9, April 1970, pp 125–135.

3 Brockett, G. F.; Curet, H. D.; and Heiselmann, H. W.; "Experimental Investigations of Reactor System Blowdown," IN-1348, Idaho Nuclear Corporation, 1970.

4 Allemann, R. .; McElfresh, A. J.; Neuls, A. S.; Townsend, W. C.; Wilburn, N. P.; and Witherspoon, M. E.; "Experimental High Enthalpy Water Blowdown from a Simple Vessel through a Bottom Outlet," BNWL-1411 UC-80, Battelle Memorial Inst., 1970.

5 White, R. F., "Results of Two-Phase Blowdown Experiments Part 1: Straight Tube Test Section," AECL-3664, Chalk River Lab., 1970.

6 Gallagher, E. V., "Water Decompression Analysis for Blowdown of Nuclear Reactors," IITRI-578-P-21-30, IIT Research Institute, Chicago, 1970.

7 Skripov, V., *Metastabil'naya Zhidkost'*, Moskva, "Nauka,", 1972 (Translated as: *Metastable Liquids*, Halsted Press, John Wiley and Sons Inc., New York, 1974.)

8 Skripov, V., et al.; "Superheated Liquids: Thermophysical Properties, Homogeneous Nucleation and Explosive Boiling-Up" ASME Paper No. 77-HT-87, AIChE-ASME Heat Trans. Conf., Salt Lake City, August 15–17, 1977.

9 Borkar, G. S.; *Design of a Rapid, Hot-Water Depressurization Experiment*, M.S. Thesis, Univ. of Kentucky, May 1977.

10 Borkar, G. S.; Trela, M.; Lienhard, J. H.; "A Rapid Hot-Water Depressurization Experiment," Elect. Pwr. Res. Inst. (EPRI Report NP-527, Dec. 1977).

11 McGlaun, J. M., "Axisymmetric Waves in a Composite Cylinder," M.S. Thesis, University of Kentucky, 1975.

12 Meyer, A., McClintock, R. B., Silvestri, G. J., Spencer, R. C., Jr., *Thermodynamics and Transport Properties of Steam*, the 1967 ASME Steam, Am. Soc. Mech. Engrs., New York, 1967, p. 58.

13 Skripov, V. P., and Pavlov, P. A., "Explosive Boiling of Liquids and Fluctuation Nucleus Formation," *Teplofizika Vysokih Temp.*, Vol. 8, No. 4, 1970, pp. 833–839.

14 Pavlov, P. A., and Skripov, V. P., "Kinetics of Spontaneous Nucleation in Strongly Heated Liquids," *Teplofizika Vysokih Temp.*, Vol. 8, No. 3, 1970, pp. 579–585.

15 Lienhard, J. H., "Correlation for the Limiting Liquid Superheat," *Chem. Engr. Sci.*, Vol. 31, 1976, pp. 847–849.

D. C. Look
Associate Professor,
Mem. ASME

H. F. Nelson
Associate Professor

A. L. Crosbie
Professor,
Mem. ASME

R. L. Dougherty
Graduate Student.

Thermal Radiative Transfer Group,
Department of Mechanical and Aerospace Engineering,
University of Missouri-Rolla,
Rolla, MO.

Two-Dimensional Multiple Scattering: Comparison of Theory with Experiment

Theoretical and experimental multiple scattering results are compared for a two-dimensional geometry. The two-dimensional model predicts the radial distribution of the radiation leaving a semi-infinite isotropically scattering cylindrical medium exposed to collimated radiation. The results show that the intensity leaving the media can be expressed as a universal function of the optical radius. The experimental results are obtained using a He–Ne laser beam incident normal to the surface of a tank of distilled water which contains scattering centers (latex paint). The agreement between theory and experiment is good.

Introduction

Scattering of electromagnetic radiation is important in many fields such as visibility, meteorology, astrophysics, biology, remote sensing, and laser interaction. Multiple scattering becomes important as the number density of scattering centers, scattering cross section or path length increases. In many of these situations, the transfer is also multi-dimensional in character. Examples are dispersion of a source of illumination (searchlight problem), attenuation of radiation from a bolt of lightning by the falling droplets of rain, and dispersion of laser radiation in passage through a scattering medium.

A comprehensive review [1] of the theoretical work in multi-dimensional radiative transfer involving multiple scattering reveals that most investigators considered a planar medium exposed to spatially varying incident radiation. Most of the solution techniques involved some kind of approximation in the formulation, i.e., diffusion approximation, small angle scattering approximation. The Monte Carlo approach was often employed. Very few numerical results are available. The two most apropriate references for the current investigation are Hunt [2] and Beckett, Foster, Hutson and Moss [3]. Both considered a finite planar medium exposed to a radially varying source of collimated radiation. Only Beckett, et al. [3] presented numerical results. However, these were for the intensity transmitted through a finite medium.

Most of the experimental work [4] has been done by the Russians, and their emphasis has been on study of transmission of narrow light beams in milk-nigrosine-water solutions. Recently, Look and Tripses [4] reported preliminary experimental results of the radial distribution of back scattered laser radiation from dilute suspensions of latex paint in water. The results were preliminary because the detector was not calibrated and the scattering coefficient of the paint was unknown.

The most significant studies of combined experimental and theoretical multiple scattering investigations that appear in the literature are those of Sarofim, et al. [5–9]. These investigations were primarily concerned with bidirectional reflectance from a layer of water containing spherical latex particles of uniform size. However, they only considered one-dimensional radiative transfer. Howard and Novotny [10] reported a similar study using a polydisperse, nonspherical suspension of titanium dioxide particles in glycerol. One Russian paper [11] compared experimental and theoretical results for transmission using the small angle approximation. In general, all of the theoretical and experimental comparisons reported in the literature show good agreement.

The objective of this paper is to present a coordinated experimental and theoretical analysis of two-dimensional multiple scattering. The experimental setup consisted of a laser beam directed perpendicularly into the upper surface of a tank of distilled water. White latex paint was introduced into the water to produce the scattering centers. The scattered radiation that emerged from the upper surface of the water in the normal direction was measured as a function of the radial distance from the incident laser beam. The theoretical analysis was based on the two-dimensional radiative transport equation.

[1] Research supported in part by the National Science Foundation Grant No. NSF ENG 74-22107.

Contributed by the Heat Transfer Division of THE AMERICAN SOCIETY OF MECHANICAL ENGINEERS and presented at the AIChE/Heat Transfer Conference, Salt Lake City, Utah, August 15–17, 1977. Manuscript received by the Heat Transfer Division July 12, 1977. Paper No. 77-HT-48.

Theoretical and Experimental Formulation

Theoretical Analysis. The theoretical development for two-dimensional scattering in a semi-infinite medium is based on the solutions of the radiative transfer equation under the following assumptions: 1) steady state, 2) coherent scattering, 3) negligible interference and polarization effects, 4) homogeneous media, 5) nonemitting and nonabsorbing media, 6) isotropic scattering and 7) refractive index of unity. The last two assumptions are open to question; however, they significantly reduce the numerical complexity. In addition, these two assumptions are somewhat justified by one-dimensional multiple scattering study of Giovanelli [13] in which the intensity reflected by a semi-infinite scattering medium exposed to collimated radiation was calculated. For pure scattering and normal incidence, the intensity reflected normal to the surface is weakly dependent on refractive index and the scattering phase function. The validity of extending this conclusion to the two-dimensional geometry must await further investigation. In [14], the results for the strong forward scattering case, that is, the scattering phase function, was modeled as being composed of a spike superimposed on an isotropic background, are shown to be equivalent to the isotropic case for pure scattering.

In general, the incident intensity is a function of direction (μ, ϕ) and location (r, Ψ), and the problem is three-dimensional in character. However in this investigation, the incident intensity is assumed to be collimated and normal to the surface of the medium $[\delta(\mu - 1)\delta(\phi)]$ and is assumed to be independent of Ψ. Specifically, for a laser beam the radial variation is Gaussian [12], and the incident intensity is given by

$$I^+(\tau_r, \mu, \phi) = I_i\delta(\mu - 1)\delta(\phi)\exp(-\tau_r^2/\tau_{r0}^2)$$
$$= I_i\delta(\mu - 1)\delta(\phi)\exp(-r^2/r_0^2) \quad (1)$$

where

$$\tau_{r0} = NC_{sca}r_0 \quad (2a)$$

$$\tau_r = NC_{sca}r \quad (2b)$$

and N is the number density of scattering particles, C_{sca} is the scattering cross section, and r_0 is the effective beam radius. The Dirac delta function product, $\delta(\mu - 1)\delta(\phi)$, restricts the incident radiation to the normal direction. For this intensity distribution, the incident radiative flux is $\int_0^{2\pi}\int_0^1 I^+(\tau_r, \mu, \phi)\mu d\mu d\phi = I_i\exp(-r^2/r_0^2)$. Thus, the magnitude of the incident flux at the center of the beam is equal to I_i. The azimuthally symmetric (independent of Ψ) beam allows the isotropic source function to be expressed in terms of z and r.

The exact two-dimensional integral equation describing the source function is solved using the method of separation of variables and superposition. No mathematical approximation, such as Eddington's approximation, is employed. The intensity leaving the medium normal to the surface can be expressed as [14]

$$I_N(\tau_r) = I^-(\tau_r, \mu = 1, \phi)$$
$$= \frac{I_i}{8\pi}\tau_{r_0}^2\int_0^\infty \beta J_0(\beta\tau_r)\exp\left(-\frac{1}{4}\beta^2\tau_{r_0}^2\right)R(\beta)d\beta \quad (3)$$

The quantity $J_0(\beta\tau_r)R(\beta)/4\pi$ would be the intensity leaving normal to the medium; if it were exposed to collimated radiation with a radial variation in the form of a Bessel function, i.e., $J_0(\beta\tau_r)\delta(\mu - 1)\delta(\phi)$. The Bessel function boundary condition is used to separable variables. The quantity β can be referred to as the spatial frequency of this boundary condition. When $\beta = 0$, the incident radiation is radially uniform, and the problem is one-dimensional. The interested reader is referred to [14] for the complete details.

By letting $x = \beta\tau_r$, equation (3) can be written as

$$I_N(\tau_r) = \frac{I_i}{8\pi}\left(\frac{r_0}{r}\right)^2\int_0^\infty xJ_0(x)\exp\left[-\frac{1}{4}\left(\frac{r_0}{r}\right)^2x^2\right]R(x/\tau_r)dx \quad (4)$$

When r/r_0 is large the exponential term can be approximated by unity and the intensity can be expressed in terms of a universal function of τ_r, i.e.,

$$I_N(\tau_r) = I_i\left(\frac{r_0}{r}\right)^2 g(\tau_r) \quad (5)$$

where

$$g(\tau_r) = \frac{1}{8\pi}\int_0^\infty xJ_0(x)R(x/\tau_r)dx \quad (6)$$

Equation (4) has been evaluated numerically for a wide range of parameters [14]. Fig. 1 is typical of the numerical results and shows the normalized intensity I_N/I_i leaving a semi-infinite, pure scattering medium in the normal direction as a function of τ_{r_0}, for several radial distances from the beam τ_r/τ_{r_0}. Comparison of the results obtained from equations (4) and (5) reveals that approximation is valid to within one percent when $r/r_0 > 10$. The expression for the intensity leaving the medium in other directions is much more complex and was not evaluated. However, the flux and power leaving the medium were calculated [14]. As expected, for conservative scattering, the power leaving is $I_i\pi r_0^2$.

The emerging intensity distribution with τ_{r_0} can be explained in the following manner if one recalls equation (2). For a fixed laser beam radius, changing τ_{r_0} represents changing particle concentrations in the scattering medium. At zero concentration of scattering particles, no scattered radiation will leave the upper surface of the medium. As the number of scattering centers is increased, the probability of a

Nomenclature

c = effective scattering coefficient (see equation 19)
C_{sca} = scattering cross section
d = scattering particle diameter
$I_N(\tau_r)$ = theoretically predicted intensity leaving the medium normal to the surface, $I^-(\tau_r, 1, \phi)$
I_{exp} = experimentally measured intensity leaving the medium normal to the surface
I_i = see equation (1)
$I^+(\tau_r, \mu, \phi)$ = intensity incident on the medium
$I^-(\tau_r, \mu, \phi)$ = intensity leaving the medium
$J_0(x)$ = zeroth order Bessel function
L = depth of water in the tank
N = particle number density
P = detected power
P_i = incident power on the medium, $I_i\pi r_0^2$
r = radial distance from center of incident (laser) beam
r_0 = effective radius of incident (laser) beam
R_0 = inside radius of the barrel
T = effective transmittance of the barrel
V = voltage reading of the detector
z = distance into the media (normal to surface)
$\delta(x)$ = Dirac delta function, i.e., $\int_a^b f(x)\delta(x - x_0)dx = f(x_0)$ where $a \leqslant x_0 \leqslant b$
θ = polar angle, used to specify the direction of the intensity, measured between the intensity and the normal to the $r - \Phi$ plane
θ_m = generation angle of detector system acceptance cone
$\bar{\theta}$ = effective acceptance angle of detector system acceptance cone
λ = wavelength of the laser
$\mu = \cos\theta$
ξ = paint volume concentration
τ_r = radial optical coordinate, $NC_{sca}r$
τ_{r_0} = effective optical radius of incident (laser) beam, $NC_{sca}r_0$
ϕ = azimuthal angle, used to specify the direction of the intensity, measured between the projection of the intensity on the r-Ψ plane and the r-axis
Ψ = azimuthal angle, used to specify the location of a point in the medium, measured around the z-axis
$\Delta\omega$ = solid angle

photon being scattered out of the medium increases and increasing amounts of radiation emerge. The scattering will be predominantly double scattering, because the single scattered radiation cannot leave normal to the surface outside of the beam. As the concentration of scattering particles is increased, the probability of scattering events becomes so large that the radiation cannot effectively reach the position r/r_0. This causes the emerging intensity to reach maximum and begin to decrease at the given position r/r_0. For further increases in scattering concentrations, the number of scattering events increases causing the radiation at the given r/r_0 to decrease further. The maximum intensity is $0.04331\ I_i(r_0/r)^2$ and occurs at $\tau_r = 3.345$ or $\tau_{r_0} = 3.345(r_0/r)$. Combining these two expressions yields the following relation for the maximum intensity

$$I_{max}/I_i = 0.003871\ \tau_{r_0}^2 \tag{7}$$

Laboratory Setup. The laboratory apparatus used to obtain the measurements of scattered radiation is shown schematically in Fig. 2. The main component of the source assembly was 50 mw He-Ne laser. Mirrors were used to direct the laser beam into the tank assembly perpendicular to the surface of the water. The tank assembly consisted of a five gallon rectangular smooth surfaced glass tank (21 cm wide, 35 cm long and 25 cm high) with a cylindrical light trap at the bottom to eliminate reflection of the laser beam. The entire bottom of the tank and all surfaces of the trap were sprayed with the highly absorbing, diffusely reflecting 3M flat black paint. The detector consisted of a fiber optics bundle enclosed in a pipe. The detection end of the bundle had an acceptance angle of 28 deg. The acceptance angle was defined as the angle for which the energy decreases from 100 percent (for normal incidence) to one percent. To reduce the angular acceptance, a barrel was attached to the end of the pipe. All surfaces of this barrel were also covered with the aforementioned 3M flat black paint. As was discussed [4], this essentially eliminated any effective intra-barrel reflections. The barrel reduced the acceptance angle to four deg. This result agreed favorably with the analytical calculation for the acceptance angle. The power accepted by the fiber optics bundle was transported to the photomultiplier and the voltage drop across the load resistor of the photomultiplier was recorded as a function of detector position, r.

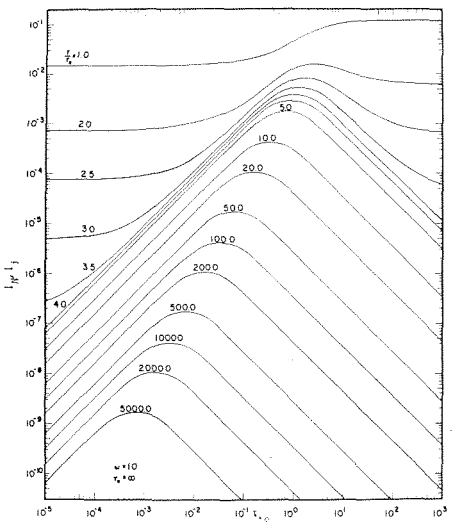

Fig. 1 Theoretical scattered intensity leaving the medium as a function of τ_{r_0} for several radial distances from the incident beam (r/r_0).

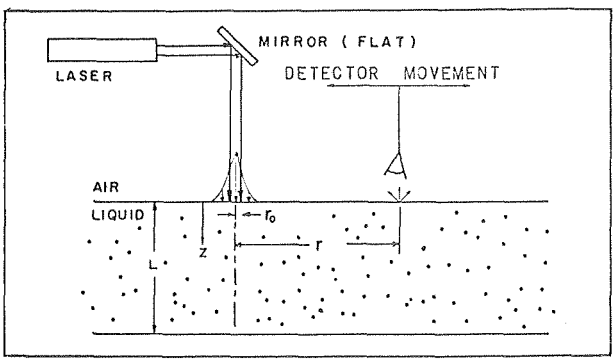

Fig. 2 Schematic of experimental setup.

When the number density of the scattering centers is small, the water in the tank obviously cannot be characterized as a semi-infinite media: however, for this case only single and double scattering are important. When the number density of scattering centers is large, multiple scattering is important and the water in the tank may be characterized as semi-infinite. The painted bottom and the trap minimize reflection from the bottom. In addition, the walls of the tank, being smooth glass, reflect specularly. Using Fresnel's relations, this interface reflects less than five percent. Tests were run to determine the wall effects by acquiring data with the laser incidence position shifted toward a wall of the tank. The result was that the walls of the tank were far enough from the scattering volume of interest that the reflectance of the tank walls was negligible. Thus, the experimental set-up simulated the theoretical situation.

Data Acquisition Procedure. Starting with distilled water, the amount of radiation scattered normally out of the water was recorded as the probe of the detector assembly was moved radially from the center of the laser beam. Once the data set was taken, more scattering centers were thoroughly mixed into the water and the process was repeated. White latex paint was used for the scattering centers primarily because uniform sized latex particles are extremely expensive. Because of the wide variation of sizes and indices of refraction of the particles in the paint, the paint was modeled as isotropic. Latex paint contains components whose average sizes are [15]: latex—0.7 micron, titanium dioxide—0.2 to 0.3 microns, extender pigment, calcium carbonate—1.4 microns (average), silica, etc. Examination of the particle sizes would suggest that the particles scatter predominantly in the forward direction (based upon Mie Theory). If the concentration of the particles were available, one could calculate the scattering phase function and scattering and absorption coefficients. However, no data concerning the particle concentrations were available from the manufacturer. As an alternative, the extinction coefficient was measured using transmission values obtained by a spectrophotometer.

Even though some of the particles of the paint are large, no settling or other discernable time variations were noticed for several hours. This observation was justified by the acquisition of data for various concentrations at several time intervals. That is for a given concentration (thoroughly mixed) a data set was acquired in 15 min or less. Without remixing, the data was reacquired after time intervals from 30 to 60 min. In addition, this given concentration was allowed to sit undisturbed for more than 48 hrs. It was then remixed and a data set reacquired. The result was that there was essentially no difference in the data for all cases.

The raw data of this study were adjusted slightly before plotting. That is, the photomultiplier tube (PMT) dark current level was subtracted from the voltage measurements and the location of the center of the laser beam was subtracted from the position reading of the detector.

In order to tie the theory and experimental results together, one needs, 1) a relationship between detected voltage V and emerging intensity I_N, 2) a relationship between particle concentration N and optical thickness τ_r and 3) the power of the incident laser beam. These relationships are discussed in the next section.

Relation of Experiment to Theory

In order to relate the raw experimental values to the theoretical results, one must analyze what the detection system "sees." Fig. 3 illustrates the "seeing portion" of the detection system. The intensity

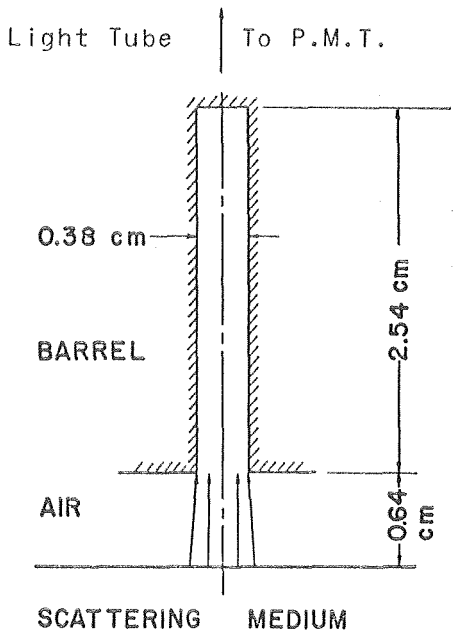

Fig. 3 Drawing of the barrel.

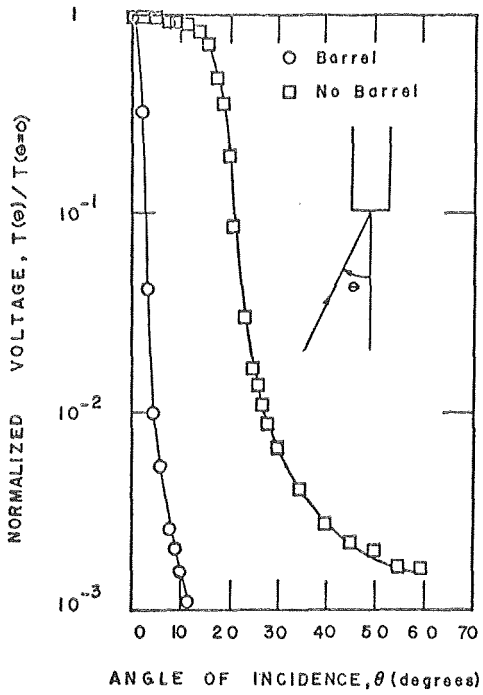

Fig. 4 Angular acceptance curve of the barrel and no-barrel configuration.

of the scattered radiation which eventually gets to the PMT is inversely proportional to the area (πR_0^2) and the solid angle $\Delta\omega$ and directly proportional to the detected power (in watts)

$$I_{\text{exp}} = \frac{P}{\pi R_0^2 \Delta\omega} \tag{8}$$

The value of $\Delta\omega$ may be determined from the acceptance angle of the detection system, i.e.,

$$\Delta\omega = 2\pi(1 - \cos\theta_m). \tag{9}$$

The actual power producing the intensity must be related to the measured voltage. From an independent laboratory experiment the conversion factor, which is gain dependent, is 2.0×10^{-7} watts/volt. Therefore,

$$I_{\text{exp}} = \frac{V\ 10^{-7}}{\pi^2 R_0^2(1 - \cos\theta_m)} \tag{10}$$

where V is the voltage reading in volts.

Using the Gaussian distribution given by equation (1) the power incident on the water, P_i, is

$$P_i = 2\pi \int_0^\infty \left[\int_0^{2\pi} \int_0^1 I^+(\tau_r, \mu, \phi)\mu d\mu d\phi \right] rdr = \pi r_0^2 I_i. \tag{11}$$

P_i was measured with a Jodon model 450B optical power meter. Typically this measured value of P_i was from 18 to 20 μW. Thus, the experimental equivalent of the ratio $I_N(\tau_r)/I_i$ becomes

$$\frac{I_{\text{exp}}}{I_i} = \frac{r_0^2 V\ 10^{-7}}{\pi R_0^2 P_i(1 - \cos\theta_m)} \tag{12}$$

Tests were run [4] to insure that the flux distribution of the incident laser beam was Gaussian. The flux passing through a narrow slit was measured as the slit was moved across the laser beam. This yielded a distribution from which it was possible to determine the value of r_0. It was defined as the radial distance where the ratio of the flux received to that at center of the beam was $1/e$. The value of r_0 was estimated to be 0.1 cm. The effective radius of the incident laser beam was defined differently in [4].

Equation (12) is complete except for the interpretation of θ_m. We have tacitly assumed in this derivation that the power detected would be a constant with respect to angle of incidence of the fiber optics bundle. This is not the case. The power transmitted depends on angle as shown in Fig. 4. The characteristics of this barrel are discussed in detail in [4]. The effective acceptance angle is defined as

$$T(\theta = 0)(1 - \cos^2\bar{\theta}) = 2\int_0^{\theta_m} T(\theta)\cos\theta \sin\theta d\theta. \tag{13}$$

Assuming θ_m is small ($\sin\theta \simeq \theta$ and $\cos\theta \simeq 1 - \theta^2/2$), equation (13) becomes

$$\bar{\theta}^2 = 2\int_0^{\theta_m} \frac{T(\theta)}{T(\theta = 0)} \theta d\theta. \tag{14}$$

Using the values of $T(\theta)/T(\theta = 0)$ from Fig. 4, a $\bar{\theta}$ of 2.75 deg (0.048 rad) was computed for the barrel configuration.

Therefore, equation (12) becomes

$$\frac{I_{\text{exp}}}{I_i} = \frac{r_0^2\ V\ 10^{-7}}{\pi R_0^2 P_i(1 - \cos\bar{\theta})} = \frac{2}{\pi}\left[\frac{r_0}{\bar{\theta} R_0}\right]^2 \left(\frac{V}{P_i}\right) 10^{-7} \tag{15}$$

R_0 and r_0 were measured [4] to be 0.190 cm and 0.1 cm respectively. This equation becomes

$$\frac{I_{\text{exp}}}{I_i} = 7.7 \times 10^{-6} \frac{V}{P_i} \tag{16}$$

when the values of the various parameters are inserted where V is in volts and P_i is in watts. Inspection of equation (15) reveals that the experimentally determined intensity is very sensitive to the values of r_0, R_0 and $\bar{\theta}$. The sensitivity of the results to r_0 can be eliminated by comparing the experimental results with equation (5), i.e.,

$$\frac{r^2 I_{\text{exp}}}{r_0^2 I_i} = 7.7 \times 10^{-4} \left(\frac{V}{P_i}\right) r^2 \tag{17}$$

In order to obtain values of the optical thickness, the scattering cross section for paint had to be determined. It is convenient to write τ_r in terms of the paint volume concentration ξ (volume of latex paint per unit volume of water plus latex paint) and the effective scattering coefficient, c. Thus, one can write

$$\xi = N\pi d^3/6 \tag{18}$$

where d is the effective particle diameter. This allows the optical thickness to be written as

$$\tau_r = \xi[6C_{sca}/\pi d^3]r = \xi c r \tag{19}$$

where c is the scattering cross section divided by the effective particle

volume. The value of c was determined by making transmission measurements through aqueous solutions containing known concentrations of scattering particles with spectrophotometer. The value of c that was obtained at $\lambda = 0.6328$ microns (λ measured in air) was 8390 cm^{-1} for latex paint. The same experimental process yielded experimental values for latex spheres which agreed well with Mie Theory calculations of the cross section.

An effective value of c equal to 839 cm^{-1} was used to correlate the experimental and theoretical results reported herein. The reason for the good agreement is probably because strong forward scattering of paint effectively reduces the scattering coefficient [14, 16, 17].

Results and Discussion

Figs. 5–7 show representative results of the comparisons of the experimental data to the theory. The experiments were all carried out with a He-Ne laser ($\lambda = 0.6328$ microns). The tank was filled with 15,820 cm^3 of distilled water, which yielded a water depth of 21.6 cm. Latex paint was used to produce the scattering centers. The size of the detection system was such that the minimum radial position for which data could be taken was about 0.95 cm away from the center of the incident laser beam. This restricts r/r_0 to be greater than 10. The lower end of the barrel was 0.64 cm above the water surface.

Fig. 5 presents the influence of changing the concentration of scatterers. It shows the experimental and theoretical results for the nondimensional scattered intensity as a function of the radial optical distance from the center of the incident laser beam for a representative set of paint concentrations (τ_{r_0} values). For small values of τ_r and τ_{r_0} the experimental intensity is larger than the predicted value. This behavior can be explained by considering reflection off the bottom. If the tank bottom was perfectly absorbing, the finite optical depth ($NC_{sca}L$) would reduce the number of scattering events as compared to the semi-infinite case. Consequently, the detected intensity would be less. Therefore, the increase in intensity is due to reflection off the bottom of the tank. The light trap is unable to completely absorb all the laser radiation that reaches the bottom. At larger values of τ_r, the experimental and theoretical results agree very well. One should also note that the scattered radiation intensity leaving normal to the upper surface of the medium decreases rapidly as τ_r increases for each constant value of concentration (τ_{r_0}).

Fig. 6 illustrates data similar to those of Fig. 5, except that the scattered intensity is plotted as a function of concentration (τ_{r_0}) at several constant values of r/r_0 so that it may be compared to the results of equation (5). Close to the incident beam and at small values τ_{r_0} the experimentally detected intensity is larger than the theoretical predictions, because of reflection off the bottom. At large values of τ_{r_0} and r/r_0 the experimental data are lower than the theoretical predictions because of absorption by the latex paint (the albedo is not exactly equal to one). For other than these situations, the experimental and theoretical results compare favorably, except that the experimental data peak at smaller values of τ_{r_0} than the theory predicts. Reasons for this behavior are discussed below. One should note, as discussed earlier, the scattered intensity goes through a maximum as the concentration of scattering particles increases.

The value of τ_{r_0} where the maximum scattered normal intensity occurs is shown in Fig. 7. The relationship between the maximum value of the scattered intensity and τ_{r_0} as given by equation (7) is plotted in Fig. 7 as the solid line. The experimental values shown on Fig. 7 were taken from graphs like that of Fig. 6. Each of the experimental points shown represents a different value of r/r_0. The comparison of the theory and experiment as shown in Fig. 7 is fair; however, the slopes of the theoretical and experimental data are about the same. Plotting the theoretical and experimental results in this manner vividly points out their differences. The reason for the poor agreement is due to a combination of things such as: 1) inaccurate estimates of peak intensities from experimental data, 2) inaccurate measurements of the concentrations of paint (ξ), 3) inaccurate cross section value for paint, (c), 4) inaccurate value of $\bar{\theta}$, 5) absorption of the latex paint, 6) inadequate theoretical model which has assumed nonabsorbing isotropic scattering particles and a refractive index of unity.

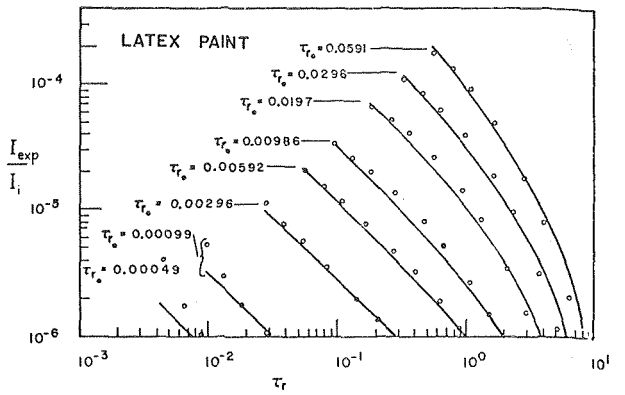

Fig. 5 The effect of changing the scatter concentration on the intensity leaving the surface as a function of the radial optical distance from the center of the incident laser beam. The solid lines are the theoretical results and the circles are the experimental data.

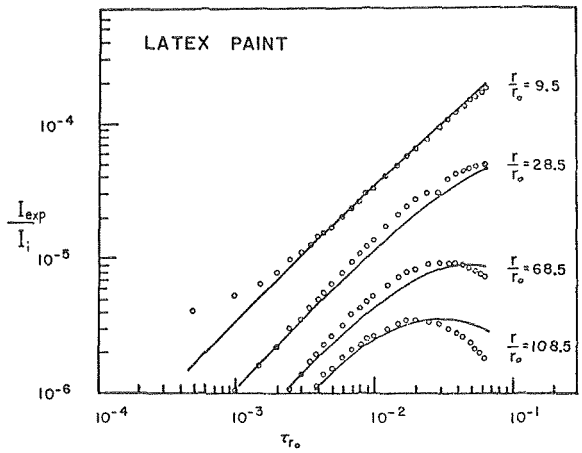

Fig. 6 Intensity leaving the medium as a function of τ_{r_0} for several values of r/r_0. The solid lines represent the theoretical data and the circles the experimental data.

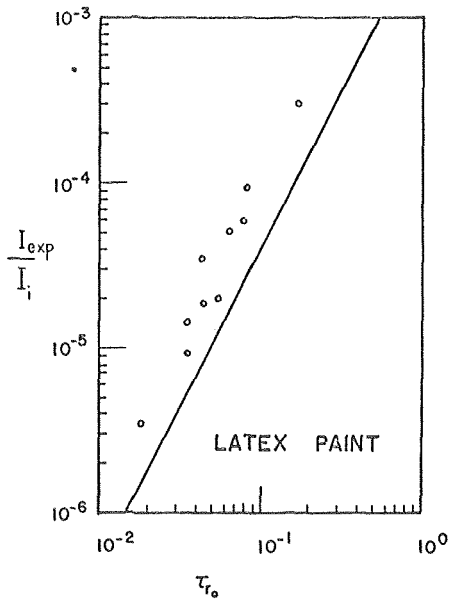

Fig. 7 The maximum value of the radial distribution of the intensity leaving the surface of the scattering medium as a function of τ_{r_0}. The solid line represents the theoretical results and the circles represent the experimental data.

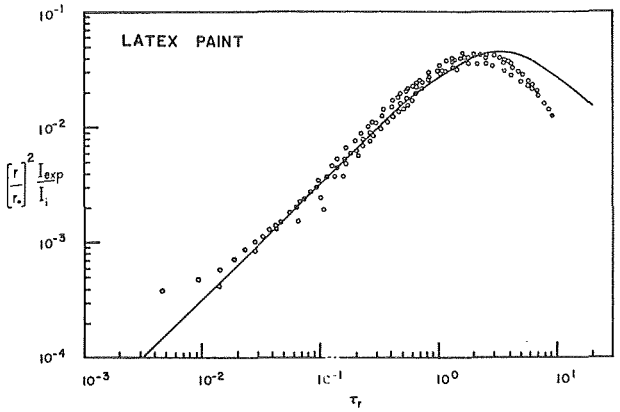

Fig. 8 The universal function $g(\tau_r)$ versus τ_r. The solid line represents the theoretical results and the circles represent the experimental data.

Analysis of the theoretical data as shown in Fig. 1 yields the relationship given as equation (5) that reduces all of the data to a single curve. This curve is presented as Fig. 8 where $(r/r_0)^2 I_{exp}/I_i$ is plotted as a function of τ_r. In this presentation, one loses the discrimination of the effects of the individual concentrations. One can see that the experimental results compare well with the theoretical values except at very small τ_r and large τ_r. At small τ_r (i.e., small paint concentrations) the finite depth of the experimental medium negates the semi-infinite depth assumption of the theory. At large τ_r (i.e., large paint concentrations) absorption by latex paint negates the pure scattering assumption of the theory.

Summary

A comparison of theoretical and experimental results of two dimensional, multiple scattering is presented. The results point out the importance of considering multiple-scattering and multi-dimensional analysis, since single scattering analysis predicts zero intensity leaving normal to the medium. The agreement between experiment and theory is good.

An interesting feature of this study is that the intensity leaving the medium can be expressed in terms of a universal function $g(\tau_r)$. Thus, instead of taking data for various particle concentrations, data can be obtained for one particle concentration and plotted in the form of Fig. 8. This yields essentially all information about the intensity leaving the scattering medium in the normal direction. The theoretical maximum of the universal function $g(\tau_r)$ occurs at $\tau_r = 3.345$; therefore, from the experimental results the scattering coefficient of the medium can be estimated. The location of the maximum does not require a highly calibrated detector. This result should be of great interest in remote sensing.

Comparison of the isotropic scattering theory with the results of the experiment reveal excellent agreement for latex paint. Probably, the reason the isotropic model agrees so well is because the paint can be characterized by a phase function with a strong forward component and an isotropic background and the results for this phase function are identical to the isotropic results when the albedo is unity [14]. The main disagreement occurs in the location of the maximum in the curve of Fig. 8. This disagreement is probably due to anisotropic scattering and the assumption of a refractive index of unity. Only further theoretical work coupled with controlled experiments will resolve these questions.

Multi-dimensional, multiple scattering radiative transfer offers many interesting challenges for future work. The effects of anisotropic scattering, refractive index of the media, finite depth (thus reflection characteristics of the bottom) and absorption by the particles should be investigated. Also, the difference in the location of the theoretical and experimental maximum of the universal function $g(\tau_r)$ needs further investigation.

Acknowledgment

The authors wish to acknowledge the support of the National Science Foundation Grant No. NSF ENG 74-22107 for the support of this research.

References

1 Crosbie, A. L., and Linsenbardt, T. L., "Two-Dimensional Isotropic Scattering in a Semi-Infinite Medium," *Journal of Quantitative Spectroscopy and Radiative Transfer*, Vol. 19, No. 3, 1978, pp. 257–284.

2 Hunt, G. E., "The Transport Equation of Radiative Transfer with Axial Symmetry," SIAM *Journal of Applied Mathematics*, Vol. 16, No. 1, 1968, pp. 228–237.

3 Beckett, P., Foster, P. J., Hutson, V., and Moss, R. L., "Radiative Transfer for a Cylindrical Beam Scattered Isotropically," *Journal of Quantitative Spectroscopy and Radiative Transfer*, Vol. 14, No. 11, Nov. 1974, pp. 1115–1126.

4 Look, D. C., and Tripses, J. G., "Preliminary Study of Two-Dimensional Multiple Scattering," *Letters in Heat and Mass Transfer*, Vol. 4, No. 2, 1977, pp. 129–139.

5 Hottel, H. C., Sarofim, A. F., Evans, L. B., and Vasalos, I. A., "Radiative Transfer in Anisotropically Scattering Media: Allowance for Fresnel Reflection at the Boundaries," ASME JOURNAL OF HEAT TRANSFER, Vol. 90, Feb. 1968, pp. 56–62.

6 Sarofim, A. F., Hottel, H. C., and Fahimian, E. J., "Scattering of Radiation by Particle Layers," *AIAA Journal*, Vol. 6, No. 12, 1968, pp. 2262–2266.

7 Hottel, H. C., Sarofim, A. F., Dalzell, W. H., and Vasolos, I. A., "Optical Properties of Coatings: Effect of Pigment Concentration," *AIAA Journal*, Vol. 9, No. 10, Oct. 1961, 1895–1898.

8 Hottel, H. C., Sarofim, A. F., Vasalos, I. A., and Dalzell, W. H., "Multiple Scatter: Comparison of Theory with Experiment," ASME JOURNAL OF HEAT TRANSFER, Vol. 92, May 1970, pp. 285–291.

9 Sarofim, A. F., Vasalos, I. A., and Jeje, A. A., "Experimental and Theoretical Study of Absorption in an Anisotropically Scattering Medium," *ASME Paper*, 71-HT-20, 1971.

10 Howard, F. H., and Novotny, J. L., "Reflectance of a Scattering Medium Containing Polydisperse Nonspherical Particles," *Proceedings of the 5th International Heat Transfer Conference*, Vol. 1, Sept. 1974.

11 Bravo-Zhivotoskiy, D. M., Dolin, L. S., Luchinin, A. G., and Savel'yev, V. A., "Structure of a Narrow Light Beam in Sea Water," *Atmospheric and Ocean Physics*, Vol. 5, No. 2, 1964, pp. 160–167.

12 Ready, J. T., *Effects of High-Power Laser Radiation*, New York, Academic Press, 1971.

13 Giovanelli, R. G., "Reflection by Semi-Infinite Diffusers," *Optica Acta*, Vol. 2, No. 4, Dec. 1955, pp. 153–162.

14 Crosbie, A. L., and Dougherty, R. L., "Two-Dimensional Isotropic Scattering in a Semi-Infinite Cylindrical Medium," to appear in *Journal of Quantitative Spectroscopy and Radiative Transfer*, 1978.

15 Mr. Norman Beck of W. L. Industries, West Calwell, New Jersey, 07006, provided the data, 1976.

16 Blevin, W. R. and Brown, W. J., "Light-Scattering Properties of Pigment Suspensions," *Journal of the Optical Society of America*, Vol. 51, No. 9, 1961, pp. 975–982.

17 Joseph, J. H., Wiscombe, W. J. and Weinman, J. A., "The Delta-Function Approximation for Radiative Flux Transfer," *Journal of the Atmospheric Sciences*, Vol. 33, No. 12, 1976, pp. 2452–2459.

S. S. Tsai
Department of Nuclear Energy,
Brookhaven National Laboratory,
Upton, N. Y. 11973

S. H. Chan
Energetics Department,
University of Wisconsin,
Milwaukee, WI 53201

Multi-Dimensional Radiative Transfer in Nongray Gases—General Formulation and the Bulk Radiative Exchange Approximation[1]

The present paper presents a general formulation of the radiative heat flux and its divergence for multi-dimensional radiative problems involving nongray absorbing-emitting gases. The expressions obtained are in terms of total band absorptance rather than the spectral absorption coefficient. Thus the frequency integration is eliminated, and the expressions are more compact. They avoid the necessity of detailed spectral absorption coefficient data for radiative transfer computations. Also presented is the bulk radiative exchange approximation together with its refinement. It is proposed to circumvent the mathematical complexity inherently imbedded in nongray multidimensional problems. The approximation, which is valid in the optically thin and thick limits, is found to be general and useful, not only because of its simplicity, but also because of its accuracy in all optical conditions.

1. Introduction

The process of radiative transfer through an absorbing-emitting medium is quite complicated. This is due to the fact that radiative transport is essentially an "action at a distance" type of process. In other words, any elemental medium not only exchanges radiant energy with all other elements but also with its bounding surfaces. This results in complicated expressions for the radiative flux and its divergence, involving integrations with respect to frequency, spatial coordinates, and solid angle. In a rigorous formulation of the divergence of the radiative flux, it is expressed in terms of the spectral intensity, which satisfies the radiative transfer equation. The spectral absorption coefficient appearing in the transfer equation is a complex, irregular function of frequency, which renders the calculation of the radiative flux and its divergence a formidable task. Consequently, the applicability and validity of infrared radiative transfer analyses depend largely on the simplicity and accuracy of the absorption model for the spectral absorption coefficient.

The gray gas approximation is the first attempt to reduce the complexity of radiative transfer problems by assuming that the absorption coefficient is independent of frequency. This simplifies greatly the formulation of radiative transfer problems and makes the differential approximation to the exact formulation possible. Considerable works have been focused on establishing suitable models for the spectral absorption coefficient. The total emissivity [1], modified emissivity [2], and transmission functions [3] have been employed to treat nongray radiative transfer problems. A recent research trend is to formulate nongray radiative transfer problems in terms of the total band absorptance [4–6], which is a well correlated function and more convenient to use than the spectral absorption coefficient.

More recently, the total band absorptance has been integrated with respect to solid angle for any geometries to form a single quantity termed as the geometric band absorptance [7] or slab band absorptance [8]. Naturally, it is more useful than the total band absorptance in the formulation of nongray radiative transfer, as it can eliminate both the frequency and solid angle integrals. The utility of the total band absorptance and the slab band absorptance in analyzing infrared radiation problems have since been well recognized [9–12].

Most of the existing methods for nongray gases are too cumbersome and impractical for use in all but the simplest case of one-dimensional problems. In view of such difficulties, Chan [13] has proposed a decay time approximation, aiming to treat nongray and geometrically complicated problems of engineering interest. The divergence of the radiative flux is explicitly expressed in terms of temperature in a

---

[1] Taken from the dissertation submitted to the Faculty of the Polytechnic Institute of New York in partial fulfillment of the requirements for the degree of Doctor of Philosophy (Mechanical Engineering), 1976.

Contributed by the Heat Transfer Division of THE AMERICAN SOCIETY OF MECHANICAL ENGINEERS and presented at the AIChE/ASME Heat Transfer Conference, Salt Lake City, Utah, August 15–17, 1977. Manuscript received by the Heat Transfer Division February 10, 1977. Paper No. 77-HT-51.

simple algebraic form. Though it provides good qualitative results, it has not been able to yield good quantitative results, as has also been noted by Cess [14].

A review of the previous works on nongray radiative transfer reveals the following deficiencies: first, the radiative flux for nongray gases has been formulated in terms of the total band absorptance for one-dimensional planar geometry but the formulation has not been extended to general three-dimensional geometries; secondly, it is the divergence of the radiative flux rather than the radiative flux itself which is needed in the energy equation. Nevertheless, the conventional practice tends to formulate the radiative flux first and then take the divergence of the radiative flux expression. In one-dimensional problems, this procedure can often be carried out, but this is not necessarily the case in two or three-dimensional problems. In fact, for multi-dimensional systems, the differentiation of the radiative flux with respect to spatial coordinates is always tedious and complicated, if not totally impossible. Finally, the complicated integral form of the divergence of the radiative flux, once introduced into the energy equation involving other modes of energy transfer, usually results in an integro-differential equation. For a gray gas, the integro-differential equation can be simplified to a differential equation by approximating the angular variation of the spectral intensity. However, the same kind of practice is not useful in nongray gas analysis since, in addition to angular dependence, the frequency dependence of the spectral intensity is almost impossible to approximate. Consequently, many gray gas techniques are either inapplicable or inadequate for solving nongray radiative transfer problems. Approximate methods for nongray gases are relatively rare, and the solution of nongray problems often has to resort to numerical techniques.

In view of the aforementioned deficiencies, we are aiming to provide:

1. a general formulation of the radiative heat flux and its divergence for absorbing-emitting nongray gases in terms of the total band absorptance for multi-dimensional configurations,
2. an approximate method that can greatly reduce the mathematical complexity of nongray, multidimensional problems,
3. analytical solutions based on the proposed method.

The first two are presented here while the last is to be reported later on.

2. A General Formulation of the Radiative Heat Flux and its Divergence

2.1. Equations of Radiative Transfer. Consider an absorbing, emitting, scattering medium confined within solid walls of arbitrary configuration as shown in Fig. 1. The confining walls may be an enclosure or a long channel, and the gas in local thermodynamic equilibrium may be at rest in the closure or flowing through the channel. A beam of intensity $I_\nu(r, \Omega)$, traveling in the direction $\vec{\ell}$, satisfies the equation of radiative transfer

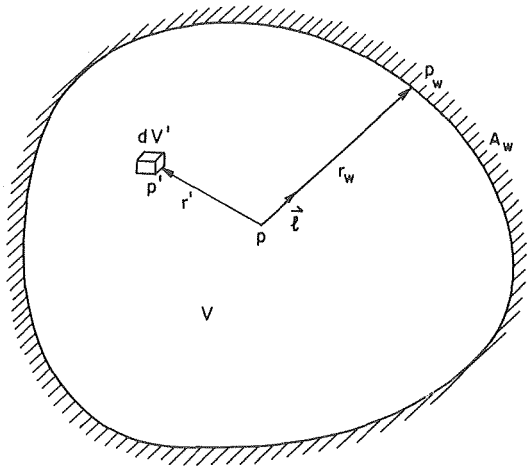

Fig. 1 Physical model and coordinate system

$$\vec{\ell} \cdot \nabla I_\nu = \gamma_\nu \hat{I}_\nu + K_\nu I_{b\nu} - \beta_\nu I_\nu \tag{1}$$

where $\hat{I}_\nu$ is the mean spectral intensity, $I_{b\nu}$ is the spectral Planck function, γ_ν is the spectral scattering coefficient, K_ν is the spectral absorption coefficient, and β_ν is the spectral extinction coefficient. The present study is concerned with absorbing-emitting gases whose scattering effect is neglected. Then the formal solution to the equation of radiative transfer is

$$I_\nu(p) = I_\nu(p_w) e^{-\int_0^{r_w} K_\nu(\xi) d\xi} + \int_0^{r_w} K_\nu(p') I_{b\nu}(p') e^{-\int_0^{r'} K_\nu(\xi) d\xi} dr' \tag{2}$$

where the first term on the right side represents the contribution from the wall to the intensity at p and the second term the contribution from the intervening gases between p and p_w. In equation (2), the origin of the coordinate system is chosen at the point p.

2.2. Total Band Absorptance and Geometric Band Absorptance. For molecular gases with discrete rotational-vibrational bands, the total band absorptance is defined as

Nomenclature

A = total band absorptance
A_0 = band width parameter
A_g = slab or geometric band absorptance
A_w = surface area
B = line width parameter
C_0 = correlation parameter
C_p = specific heat at constant pressure
$E_{\nu c}$ = Planck function evaluated at ν_c ($= \pi I_{b\nu c}$)
$E_b = \sigma T^4$
E_n = exponential integrals, $\int_0^1 \mu^{n-2} e^{-u/\mu} d\mu$
$f = 2.94 (1 - \exp(-2.60\beta))$
h = distance between two parallel walls
$I = \int_0^\infty I_\nu (p_w)\, d\nu$
I_ν = spectral intensity
$\hat{I}_\nu$ = spectral mean intensity, $\int_{4\pi} I_\nu d\Omega$
$I_{b\nu}$ = spectral Planck function
$I_{\nu c}$ = spectral intensity evaluated at ν_c
$I_{b\nu c}$ = spectral Planck function evaluated at ν_c
K_ν = spectral absorption coefficient
K = thermal conductivity
$\vec{\ell}$ = unit vector in the direction of $\overline{pp}_w$
L_m = mean beam length
p = a point or pressure
p_w = a point on the walls
p_e = total pressure
p_ξ = a point within the gas
$\vec{q}_r$ = radiative heat flux
r_w = distance between the point p and the point p_w
S = total band intensity
t = time
t_r = radiative decay time
T = temperature
T_1, T_2, T_w = temperature at the two parallel walls
u = optical coordinate, Spx/A_0
u_h = optical thickness, Sph/A_0
V = volume
x = physical coordinate measured from wall 1
β = line structure parameter, $B^2 p_e$
β_ν = extinction coefficient
γ = Euler-Maclaurin number, 0.5772156
γ_ν = scattering coefficient
ρ = density
Ω = solid angle
μ = cosine of the angle made by the direction of propagation of radiation and x coordinate or dynamic viscosity
σ = Stefan-Boltzmann constant
ν_c = frequency at the band center

Superscript

$'$ = refers to any point in the gas or differentiation with respect to the argument indicated.

$$A(r) = \int_{\Delta\nu} (1 - e^{-\int_0^r K_\nu(\xi)d\xi})\, d\nu \tag{3}$$

There are numerous explicit expressions for the total band absorptance in infrared radiation [4–6]. For example, according to the widely used Edwards exponential band model, the total band absorptance for overlapping line bands is given by

$$A(u) = A_0(\ell nu + E_1(u) + \gamma) \tag{4}$$

where u is the optical coordinate, γ is the Euler-Maclaurin number, and E_n is the exponential integral.

When the total band absorptance is integrated over the whole body of the radiating medium, the resulting quantity is termed as the geometric band absorptance [7],

$$A_g(r) = \frac{1}{\pi}\int_{4\pi} A(r)\cos\theta_i d\Omega$$

$$= \int_A \frac{\mu_i\mu_j}{\pi r^2}\int_{\text{band}} (1 - e^{-\rho kr})d\nu dA_j \tag{5}$$

where r is the distance between the area element dA_i at the origin p and the area element dA_j at the boundary; μ_i and μ_j are the cosines of the angles between r and the normal to dA_i and dA_j, respectively. Explicit expressions are available for a slab geometry [8, 15] as well as arbitrary geometries [7]. For the slab geometry, equation (5) reduces to the Edwards's slab band absorptance,

$$A_g(u) \equiv \int_0^1 A(u/\mu)2\mu d\mu \tag{6}$$

2.3. Formulation of the Divergence of the Radiative Flux. From equation (1) and the definition of the radiative flux

$$\hat{q}_r \equiv \int_{4\pi}\int_0^\infty \hat{\ell} I_\nu d\nu d\Omega, \tag{7}$$

the divergence of the radiative flux can be formulated as

$$\nabla\cdot\hat{q}_r = \int_{4\pi}\int_0^\infty K_\nu(I_{b\nu} - I_\nu)d\nu d\Omega$$

Upon substituting I_ν from equation (2), the resulting equation is

$$\nabla\cdot\hat{q}_r = 4\pi\int_0^\infty K_\nu(p)I_{b\nu}(p)d\nu$$

$$- \int_{4\pi}\int_0^\infty K_\nu(p)I_\nu(p_w)e^{-\int_0^{r_w} K_\nu(\xi)d\xi}\, d\nu d\Omega$$

$$- \int_{4\pi}\int_0^\infty\int_0^{r_w} K_\nu(p)K_\nu(p')I_{b\nu}(p')e^{-\int_0^{r'} K_\nu(\xi)d\xi}\, dr' d\nu d\Omega \tag{8}$$

The above equation is complex and cumbersome for use in radiation transfer calculations. A simpler form of $\nabla\cdot\hat{q}_r$ using the total band absorptance is developed next.

For the sake of simplicity in notation, it is assumed that the molecular gas has only one vibrational-rotational band. The following analysis is also applicable to the gas having more than one band. Since the Planck function within a wide band can usually be approximated by its value at the band center, equation (8) becomes

$$\nabla\cdot\hat{q}_r = 4\pi I_{b\nu c}(p)\int_{\Delta\nu} K_\nu(p)d\nu$$

$$- \int_{4\pi} I_{\nu c}(p_w)\int_{\Delta\nu} K_\nu(p)e^{-\int_0^{r_w} K_\nu(\xi)d\xi}\, d\nu d\Omega$$

$$- \int_{4\pi}\int_0^{r_w} I_{b\nu c}(p')\int_{\Delta\nu} K_\nu(p)K(p')e^{-\int_0^{r'} K_\nu(\xi)d\xi}\, d\nu dr' d\Omega \tag{9}$$

Employing the frequently used assumption that K_ν is a weak function of temperature, it reduces to

$$\nabla\cdot\hat{q}_r = 4\pi I_{b\nu c}(p)\left(\int_{\Delta\nu} K_\nu d\nu\right)$$

$$- \int_{4\pi} I_{\nu c}(p_w)\left(\int_{\Delta\nu} K_\nu(p_w)e^{-\int_0^{r_w} K_\nu(\xi)d\xi}\, d\nu\right) d\Omega$$

$$- \int_{4\pi}\int_0^{r_w} I_{b\nu c}(p')\left(\int_{\Delta\nu} K_\nu{}^2(p')e^{-\int_0^{r'} K_\nu(\xi)d\xi}\, d\nu\right) dr' d\Omega \tag{10}$$

The bracketed terms can be replaced by the total band absorptance and its derivatives as

$$\int_{\Delta\nu} K_\nu d\nu = A'(0) \tag{11a}$$

$$\int_{\Delta\nu} K_\nu(p_w)e^{-\int_0^{r_w} K_\nu(\xi)d\xi}\, d\nu = A'(r_w) \tag{11b}$$

and

$$\int_{\Delta\nu} K_\nu{}^2(p')e^{-\int_0^{r'} K_\nu(\xi)d\xi}\, d\nu = -A''(r') \tag{11c}$$

Substituting equations (11a) through (11c) into equation (10), we have

$$\nabla\cdot\hat{q}_r = 4\pi I_{b\nu c}(p)A'(0) - \int_{4\pi} I_{\nu c}(p_w)A'(r_w)d\Omega$$

$$+ \int_{4\pi}\int_0^{r_w} I_{b\nu c}(p')A''(r')dr'd\Omega \tag{12}$$

Note that the first term in equation (12) can be written as

$$4\pi I_{b\nu c}(p)A'(0) = \int_{4\pi} I_{b\nu c}(p)A'(0)d\Omega$$

$$= \int_{4\pi} I_{b\nu c}(p)A'(r_w)d\Omega + \int_{4\pi} I_{b\nu c}(p)(A'(0) - A'(r_w))d\Omega$$

$$= \int_{4\pi} I_{b\nu c}(p)A'(r_w)d\Omega - \int_{4\pi}\int_0^{r_w} I_{b\nu c}(p)A''(r')\, dr' d\Omega \tag{13}$$

Introducing equation (13) into equation (12) results in

$$\nabla\cdot\hat{q}_r = \int_{4\pi}(I_{b\nu c}(p) - I_{\nu c}(p_w))A'(r_w)d\Omega$$

$$- \int_{4\pi}\int_0^{r_w}(I_{b\nu c}(p) - I_{b\nu c}(p'))A''(r')dr'd\Omega \tag{14}$$

The physical meaning of the above equation is clear. The first term on the right side gives the net exchange of radiant energy between the gas element at p and the walls while the last term gives the net exchange between the gas element at p and the other gas elements. Upon partial integration of the last term, equation (14) can be expressed in terms of the first derivative of the total band absorptance as

$$\nabla\cdot\hat{q}_r = \int_{4\pi}(I_{b\nu c}(p_w) - I_{\nu c}(p_w))A'(r_w)d\Omega$$

$$- \int_{4\pi}\int_0^{r_w}\frac{\partial I_{b\nu c}(p')}{\partial r'}A'(r')dr'd\Omega \tag{15}$$

This form of $\nabla\cdot\hat{q}_r$ is more desirable than equation (14) for problems involving black bounding walls with no temperature jumps, because the first term vanishes in this case.

Either equation (14) or (15) is applicable to multi-dimensional problems of radiative transfer in nongray gases. The troublesome absorption coefficient which varies rapidly and irregularly with frequency has been replaced by a well behaved and correlated function—the total band absorptance. The advantage of employing the total band absorptance is well known in recent studies of one-dimensional nongray gas between two parallel plates [10, 16].

For later reference, equation (14) is written in Cartesian coordinate system for planar geometry bounded by two parallel black walls at nonuniform temperatures as shown in Fig. 2,

$$\nabla\cdot\hat{q}_r = [A_g'(x) + A_g'(h - x)]\cdot E_{\nu c}(x, y, z)$$

$$- \int_{-\infty}^{\infty}\int_{-\infty}^{\infty} E_{\nu c}[T_1(y', z')]A'(r_1)\frac{x}{\pi r_1{}^3}dy'dz'$$

$$- \int_{-\infty}^{\infty}\int_{-\infty}^{\infty} E_{\nu c}[T_2(y', z')]A'(r_2)\frac{h - x}{\pi r_2{}^3}dy'dz'$$

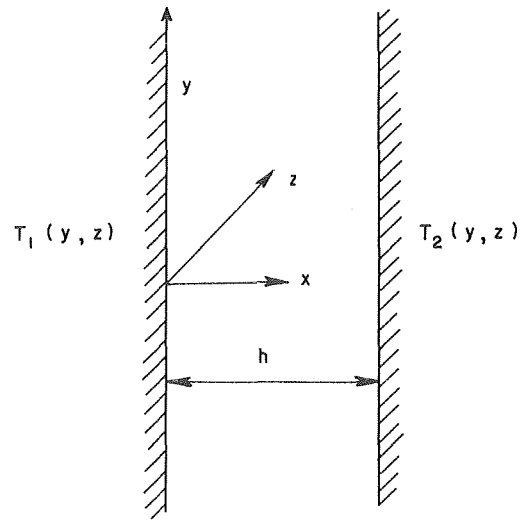

Fig. 2 Parallel plate coordinate system

$$- \int_{-\infty}^{\infty}\int_{-\infty}^{\infty}\int_{0}^{h} [E_{\nu c}(x,y,z) - E_{\nu c}(x',y',z')] \times \frac{A''(r')}{\pi(r')^2}\,dx'dy'dz' \quad (16a)$$

where

$$A_g'(x) \equiv dA_g(x)/dx$$

and

$$r_1 = [x^2 + (y-y')^2 + (z-z')^2]^{1/2}$$
$$r_2 = [(x-h)^2 + (y-y')^2 + (z-z')^2]^{1/2}$$
$$r' = [(x-x')^2 + (y-y')^2 + (z-z')^2]^{1/2}.$$

The x coordinate is normal to the wall and y and z coordinates are in a plane parallel to the wall. For one-dimensional cases where the walls are at two different but uniform temperatures, equation (16a) reduces to

$$\nabla\cdot\vec{q}_r = (E_{\nu c}(T) - E_{\nu c}(T_1))A_g'(x) + (E_{\nu c}(T) - E_{\nu c}(T_2))A_g'(h-x) - \int_0^x (E_{\nu c}(T) - E_{\nu c}(T'))A_g''(x-x')dx' - \int_x^h (E_{\nu c}(T) - E_{\nu c}(T'))A_g''(x'-x)dx' \quad (16b)$$

2.4. Bulk Radiative Exchange. It is interesting to note that there exists a simple expression for the net exchange of radiative energy between the entire gas volume and its surroundings. By changing the second term on the right side from spatial and solid angle integrals to volume integral, equation (14) becomes

$$\nabla\cdot\vec{q}_r = \int_{4\pi}(I_{b\nu c}(p) - I_{\nu c}(p_w))A'(r_w)d\Omega - \int_V (I_{b\nu c}(p) - I_{b\nu c}(p'))\frac{A''(r')}{(r')^2}dV' \quad (17)$$

Integrating both sides of equation (17) with respect to volume, the last term drops out because in the integration it contains the pair elements like $(I_{b\nu c}(p) - I_{b\nu c}(p'))A''(r')/(r')^2dV'dV$ and $(I_{b\nu c}(p') - I_{b\nu c}(p))A''(r')/(r')^2dVdV'$, which cancel each other. Therefore, equation (17) reduces to

$$\int_v \nabla\cdot\vec{q}_r dV = \int_V\int_{4\pi}(I_{b\nu c}(p) - I_{\nu c}(p_w))A'(r_w)d\Omega dV \quad (18)$$

Equation (18) simply states that the net energy transferred out of a gas volume V through radiation is equal to the sum of net exchange of energy between each individual gas element and its bounding surfaces. If the integrand in equation (18) is a continuous function of coordinates, then according to the mean value theorem, there exists a point p_ξ in the gas such that

$$(\nabla\cdot\vec{q}_r)_{p=p_\xi} = \int_{4\pi}(I_{b\nu c}(p_\xi) - I_{\nu c}(p_w))A'(r_w)d\Omega \quad (19)$$

In comparing equation (19) to equation (17), we see that within a system of any optical thickness, there always exists a location at which the gas-to-gas radiation exchange is identically zero. This will serve as a basis for the approximation to be proposed in the next section.

The averaged $\nabla\cdot\vec{q}_r$ follows immediately from equation (18) as

$$(\nabla\cdot\vec{q}_r)_{\text{avg.}} \equiv \frac{1}{V}\int_V \nabla\cdot\vec{q}_r dV = \frac{1}{V}\int_V\int_{4\pi}(I_{b\nu c}(p) - I_{\nu c}(p_w))A'(r_w)d\Omega dV \quad (20)$$

Under the conditions that the temperature variation is small over the entire radiation field and radiosity is uniform, we can make use of the slab band absorptance and Chan's approximation [7], $A_g = A(L_m)$, reducing equation (20) to

$$(\nabla\cdot\vec{q}_r)_{\text{avg.}} = (I_{b\nu c}(p) - I_{\nu c}(p_w))\frac{\pi A(L_m)A_w}{V} \quad (21)$$

where L_m is the equivalent mean beam length of the configuration under consideration. Equation (21) is the same as the decay time approximation used in the astrophysical and meteorological literature.

2.5. Formulation of the Radiative Flux. For completeness, a similar formulation of the radiative flux itself is also presented. Referring to Fig. 1, the radiative flux at the point p in the direction of $\vec{\ell}$ is

$$\vec{q}_r = \int_{4\pi}\int_0^\infty I_\nu\vec{\ell}\,d\nu d\Omega = \int_{4\pi}\int_0^\infty I_\nu(p_w)e^{-\int_0^{r_w}K_\nu(\xi)d\xi}\,\vec{\ell}\,d\nu d\Omega + \int_{4\pi}\int_0^\infty\int_0^{r_w} K_\nu(p')I_{b\nu}(p')e^{-\int_0^{r'}K_\nu(\xi)d\xi}\,\vec{\ell}\,dr'd\nu d\Omega \quad (22)$$

The first term in equation (22) represents the radiative flux at the point p contributed by the emission and reflection from the walls while the second term by the emission from the gas. Employing the total band absorptance, equation (22) yields

$$\vec{q}_r = \int_{4\pi} I(p_w)\vec{\ell}\,d\Omega - \int_{4\pi} I_{\nu c}(p_w)A(r_w)\vec{\ell}\,d\Omega + \int_{4\pi}\int_0^{r_w} I_{b\nu c}(p')A'(r')\vec{\ell}\,dr'd\Omega \quad (23)$$

where

$$I(p_w) = \int_0^\infty I_\nu(p_w)d\nu$$

In equation (23), the first term on the right side represents the radiative flux which could exist if the gas were absent; the second gives the portion of the wall radiation which is absorbed by the gas and the last term indicates the emission from the gas which arrives at the point p. Alternatively, with partial integration of the last term, equation (23) becomes

$$\vec{q}_r = \int_{4\pi} I(p_w)\vec{\ell}\,d\Omega + \int_{4\pi}(I_{b\nu c}(p_w) - I_{\nu c}(p_w))A(r_w)\vec{\ell}\,d\Omega - \int_{4\pi}\int_0^{r_w}\frac{\partial I_{b\nu c}(p')}{\partial r'}A(r')\vec{\ell}\,dr'd\Omega \quad (24)$$

For radiative transfer problems with black walls and no temperature jumps at the walls, the second term drops out and, consequently, equation (24) is simpler than equation (23). Again, for nongray planar

systems with black walls at different uniform temperatures, the radiative flux reduces to

$$q_r = E_b(T_1) - E_b(T_2) - (E_{\nu c}(T_1)A_g(x) - E_{\nu c}(T_2)A_g(h-x)) + \int_0^x E_{\nu c}(T')A_g'(x-x')dx' - \int_x^h E_{\nu c}(T')A_g'(x'-x)dx' \quad (25)$$

where $E_b(T_1) = \sigma T_1^4$ and $E_b(T_2) = \sigma T_2^4$ and q_r is the component of the radiative flux normal to two parallel walls.

3. The Bulk Radiative Exchange Approximation

3.1. The Bulk Radiative Exchange Approximation. Upon the substitution of the expression for the divergence of the radiative flux into an energy equation, the temperature field within the gas can be found. However, the resulting energy equation is generally too complicated to allow for analytical solutions even for the simplest case of one-dimensional problems and often it must resort to elaborate numerical schemes which are time-consuming and not necessarily accurate. Therefore, it is desirable to have an approximate expression for $\nabla\cdot\vec{q}_r$ which can greatly simplify the energy equation.

An inspection of equations (14) and (19) suggests that

$$\nabla\cdot\vec{q}_r(p) = \int_{4\pi} (I_{b\nu c}(p) - I_{\nu c}(p_w))A'(r_w)\,d\Omega \quad (26)$$

may be a good approximation under certain conditions. Indeed, this is the case for the optically thin limit because the gas-to-gas exchange approaches zero in this limit. This can be easily seen from equation (14) where the kernel $A''(r')$ is an order smaller than the other kernel $A'(r_w)$ in the optically thin limit. For any other optical conditions, equation (19) has demonstrated that the above approximation is exact at at least one location within the system of interest. Furthermore, as shown in equation (20), the average of the above approximation for $\nabla\cdot\vec{q}_r$ over the entire gas volume yields an identical result as that using the exact expression. Therefore, it assures the approximation to be qualitatively, if not quantitatively, correct for optical conditions other than the optically thin limit. It should be noted that the present approximation is different and better than the conventional optically thin limit approximation which can be obtained by replacing the term $A'(r_w)$ in equation (26) by the absorption coefficient. Since the absorption coefficient corresponds to a limiting value of $A'(r_w)$ when the path length approaches zero, the present approximation, equation (26), which is termed as the bulk radiative exchange approximation, is expected to be more general and applicable to a wider range of optical thickness than the optically thin approximation, as the latter neglects the gaseous self-absorption but not the present approximation.

The ability of a local gas element to transport energy by radiation should depend on not only its emissive power but also some function of the local optical length such as $A'(r_w)$, which varies from point to point. The present approximation does account for such a variation, but not the decay time approximation equation (21), because the latter contains the quantity $A(L_m)$, which is constant for a given system. Consequently, the bulk radiative exchange approximation is also expected to yield better results than the decay time approximation.

It is interesting to point out that for black walls with a given nonuniform temperature, $I_{\nu c}(p_w)$ is known. Then, the bulk exchange approximation is not an integral equation; it is an algebraic equation.

The largest error which might arise in the application of the approximation occurs when the system of interest is optically thick. In this case, the gas-to-gas exchange term may become appreciable in comparison with the gas-to-wall exchange term. In the following section, an attempt is made to incorporate the gas-to-gas exchange term to improve equation (26).

Before proceeding to the next section, it is noted that, for one-dimensional parallel plate systems with black walls, equations (26) and (16b) reduce to

$$\nabla\cdot\vec{q}_r \cong (E_{\nu c}(T) - E_{\nu c}(T_1))A_g'(x) + (E_{\nu c}(T) - E_{\nu c}(T_2))A_g'(h-x) \quad (27)$$

3.2. The Refined Bulk Radiative Exchange Approximation. As indicated in the preceding section, the gas-to-gas exchange term in equation (14) becomes significant in the optically thick limit. In fact, the bulk radiative exchange approximation can be easily improved by retaining the first few terms in a Taylor's series expansion of the gas-to-gas exchange term. In a somewhat different context, Sparrow and Cess [17] have discussed Taylor's series expansion technique for treating integral equations. Also Anderson and Viskanta [18] have obtained a radiative conductivity for combined conduction and radiation in nongray media by a similar technique.

An inspection of equation (14) reveals that the kernel A'' of the second term has a logarithmic singularity when the optical thickness approaches zero and decreases as $-1/r'^2$ when the optical thickness becomes large. Therefore, only the gas elements immediately adjacent to the point p can contribute substantially to the radiative exchange with the element at p, making the Taylor's series expansion technique attractive. A Taylor's series expansion about p of the Planck function in the integrand of the second term in equation (14) is sufficient to insure a good approximation to the original equation when the first few terms are retained. Accordingly, a Taylor's series expansion of $I_{b\nu c}(p')$ around the point p gives

$$I_{b\nu c}(p') = I_{b\nu c}(p) + \left.\frac{\partial I_{b\nu c}}{\partial r'}\right|_{p'=p} r' + \left.\frac{\partial^2 I_{b\nu c}}{\partial (r')^2}\right|_{p'=p} \frac{(r')^2}{2!} + \ldots$$

Substituting this expression into equation (14), we have

$$\nabla\cdot\vec{q}_r(p) = \int_{4\pi} [I_{b\nu c}(p) - I_{\nu c}(p_w)]A'(r_w)d\Omega + \int_{4\pi} [r_w A'(r_w) - A(r_w)] \left.\frac{\partial I_{b\nu c}}{\partial r'}\right|_p d\Omega + \int_{4\pi} \left(\frac{r_w^2}{2}A'(r_w) - r_w A(r_w) + \int_0^{r_w} A(r')dr'\right) \left.\frac{\partial^2 I_{b\nu c}}{\partial (r')^2}\right|_p d\Omega \quad (28)$$

In the optically thin limit, all the integration terms except the first vanish. If only the first term is retained, it reduces to the bulk radiative exchange approximation discussed above. Since such an approximation is quantitatively correct in the optically thin limit and, for any other optical conditions, at least qualitatively correct, the addition of the other terms appearing in equation (28) will undoubtedly further improve the accuracy of the approximation.

An order of magnitude consideration of equation (28) will provide some knowledge about the magnitude of the terms in the Taylor's series expansion. In the optically thin limit, all the coefficients in the square brackets, except that of the first term in equation (28), vanish as expected. On the other hand, in the optically thick limit, i.e., large u, it can be readily shown that

$$\text{second term} = 0\left(\frac{\ell n u}{u}\right) \gg \text{third term} = 0\left(\frac{1}{u}\right)$$

and that the terms after the third are even smaller. Therefore, the series converges extremely rapidly and, in the truly optically thick condition, only the second term involving the first derivative of $I_{b\nu c}$ needs to be retained.

Again for later applications, equation (28) for planar systems with black walls is written explicitly as

$$\nabla\cdot\vec{q}_r \cong (E_{\nu c}(T) - E_{\nu c}(T_1))A_g'(x) + (E_{\nu c}(T) - E_{\nu c}(T_2))A_g'(h-x) + ((h-x)A_g'(h-x) - A_g(h-x) - xA_g'(x) + A_g(x))\frac{dE_{\nu c}}{dx} + \left(\frac{1}{2}(h-x)^2A_g'(h-x) - (h-x)A_g(h-x) + A_g{}^i(h-x) + \frac{1}{2}x^2A_g'(x) - xA_g(x) + A_g{}^i(x)\right)\frac{d^2E_{\nu c}}{dx^2} \quad (29)$$

where

$$A_g{}^i(x) = \int_0^x A_g(x)dx.$$

It should be pointed out that, instead of integral equations, the bulk radiative exchange approximation, equation (27), is an algebraic equation and the refined approximation, equation (29), is a differential equation. Equation (27) is exact in the optically thin limit which by no means is the same as the conventional optical thin approximation. The latter accounts for only emission but neglects the gaseous self-absorption while the present approximation does account for self-absorption. Furthermore, for other optical conditions, equation (27) is exact at one location within the gas body and at other locations at least qualitatively correct as well. Thus, the present approximation without any refinement is far superior than the conventional one. A retention of one additional term will make it correct also in the optically thick limit. With two additional terms, excellent results can be expected even in intermediate optical conditions.

For completeness, the same technique is used to expand equation (23) into series. Upon expanding $I_{b\nu c}(p')$ into a Taylor's series around point p and substituting into the third term on the right side of equation (23), we have

$$\vec{q}_r = \int_{4\pi} I(p_w)\vec{\ell}d\Omega + \int_{4\pi} (I_{b\nu c}(\bar{p}) - I_{\nu c}(p_w))A(r_w)\vec{\ell}d\Omega + \int_{4\pi} \left(r_w A(r_w) - \int_0^{r_w} A(r')dr'\right) \left.\frac{\partial I_{b\nu c}}{\partial r'}\right|_p \vec{\ell}d\Omega + \ldots . \quad (30)$$

Nevertheless, the series does not converge as rapidly as that of $(\nabla\cdot\vec{q}_r)$ and is not as useful. For one-dimensional planar systems with black walls, it reduces to the form

$$q_r \cong E_b(T_1) - E_b(T_2) + (E_{\nu c}(T) - E_{\nu c}(T_1))A_g(x) - (E_{\nu c}(T) - E_{\nu c}(T_2))A_g(h-x) + (-xA_g(x) - (h-x)A_g(h-x) + A_g{}^i(h-x) + A_g{}^i(x))\frac{dE_{\nu c}}{dx} \quad (31)$$

4. Conclusions

The radiative flux and its divergence have been formulated in terms of the total band absorptance for multi-dimensional problems involving nongray radiating gases. For planar geometry, the slab band absorptance is utilized and the resulting expressions are even more compact.

Derived from the expressions is the bulk radiative exchange approximation which is proposed to handle general nongray multidimensional problems as it can greatly reduce the associated mathematical difficulties by simplifying the original integral equation to algebraic or differential equation. The bulk radiative exchange approximation with its refinement is valid in the optically thin and thick limits. In the intermediate range, the approximation has been shown to be at least qualitatively correct. Therefore, we can expect the approximation to provide remarkable results for all optical conditions as to be demonstrated in subsequent papers.

References

1 Gille, J., and Goody, R., "Convection in a Radiating Gas," *J. Fluid Mechanics*, Vol. 20, 1964, p. 47.

2 Goody, R. M., *Atmospheric Radiation*, Oxford Univ. Press, 1964.

3 Mandell, "Transmission Functions in the Numerical Solution of Radiative Heat Transfer Problems," *JQSRT*, Vol. 11, 1971, 1741–1748.

4 Edwards, D. K., and Menard, W. A., "Comparison of Models for Correlation of Total Band Absorptance," *Applied Optics*, Vol. 3, 1964, pp. 621–625.

5 Tien, C. L., and Lowder, J. E., "A Correlation for Total Band Absorptance of Radiating Gases," *Int. J. Heat Transfer*, Vol. 9, 1966, pp. 698–701.

6 Hsieh, T. C., and Grief, R., "Theoretical Determination of the Absorption Coefficient and the Total Band Absorptance Including a Specific Application to Carbon Monoxide," *Int. J. Heat Mass Transfer*, Vol. 15, 1972, pp. 1477–1487.

7 Chan, S. H., "Geometric Band Absorptance of a Nongray Gas with Arbitrary Configurations," *Int. J. Heat Mass Transfer*, Vol. 17, 1974, pp. 381–383.

8 Edwards, D. K., and Balakishnan, A., "Slab Band Absorptance for Molecular Gas Radiation," *JQSRT*, Vol. 12, 1972, pp. 1379–1387.

9 Wang, L. S., "An Integral Equation of Radiating Equilibrium in Infrared Radiating Gases," *JQSRT*, Vol. 8, 1968, p. 851.

10 Cess, R. D., and Tiwari, S. N., "The Large Path Length Limit for Infrared Gaseous Radiation," *Appl. Sci. Res.*, 19, 1968, pp. 439–449.

11 Cess, R. D., and Tiwari, S. N., "The Interaction of Thermal Conduction and Infrared Gaseous Radiation," *Appl. Sci. Res.*, 20, 1969, pp. 25–38.

12 Mighdoll, P., and Cess, R. D., "Infrared radiative equilibrium under large path length conditions," *AIAA*, Vol. 6, 1968, pp. 1778–1779.

13 Chan, S. H., "Radiative Decay Time of a Nongray Medium With Arbitrary Configuration," *JQSRT*, Vol. 13, 1973, pp. 1233–1236.

14 Cess, R. D., and Ramanathan, V., "The Applicability of an Approximate Expression for Radiative Heating," *JQSRT*, Vol. 13, 1973, pp. 79–81.

15 Lin, C. C., and Chan, S. H., "A General Slab Band Absorptance for Infrared Radiating Gases," ASME JOURNAL OF HEAT TRANSFER, Vol. 97, No. 3, 1975, pp. 478–480.

16 Cess, R. D., Minghdoll, P., and Tiwari, S. N., "Infrared Radiative Heat Transfer in Nongray Gases," *Int. J. Heat Mass Transfer*, Vol. 10, 1967, 1521–1532.

17 Sparrow, E. M., and Cess, R. D., *Radiative Heat Transfer*, Brooks/Cole, Belmont, Ca., 1966.

18 Anderson, E. E., and Viskanta, R., "Effective Conductivity for Conduction—Radiation by Taylor Series Expansion," *Int. J. Heat Mass Transfer*, Vol. 14, 1971, pp. 1216–1220.

J. H. Lienhard
Fellow ASME

A. H. Karimi
Boiling and Phase Change Laboratory,
Mechanical Engineering Department,
University of Kentucky,
Lexington, Kentucky 40506
Student Mem. ASME

Corresponding States Correlations of the Extreme Liquid Superheat and Vapor Subcooling

A variety of corresponding states correlations are made for the maximum or minimum nucleation temperatures obtained in many experiments by many workers. These correlations reveal: 1) That the best correlation occurs when the reduced liquid superheat is plotted against the reduced saturation temperature; and 2) that liquid superheat data correlate well and appear to fall near the spinodal line, while vapor subcooling data correlate poorly and fall far from the spinodal line. It is suggested that the published vapor subcooling results have been inferred in invalid ways from the data. It is therefore not presently possible to know whether existing vapor nucleation temperatures are actually far from the spinodal line, or incorrect.

Introduction

Interest in locating the line of maximum liquid superheat lay fallow for many decades after the pioneering work of Kenrick, et al. [1]. This interest has been revived since the late 1950's by the intense phase-change processes occurring in nuclear reactors and other modern equipment. Skripov, et al. [2, 3] have probably done more to define the liquid spinodal line than any other group.

The last two decades have also seen a rising interest in locating the line of maximum subcooling. Yellott [4] observed the limits of water-vapor subcooling as early as 1934. He was interested in erosive condensation in the low pressure stages of steam turbines—a process that has continued to receive attention. An additional concern with "condensation shocks" in other applications has continued to spur this work, and indeed, it has gained momentum in the last dozen years. Brief reviews of these efforts are given up to 1965 by Pouring [5] and to 1975 by Barschdorff [6]. There are several methods for bringing vapor to extreme values of subcooling, e.g.:

1 Isentropic expansion in converging-diverging nozzles brings superheated vapor to a point of maximum subcooling at which droplets form. The vapor may be pure, or mixed with "noncondensible" carrier gas. We shall present data obtained in this way by Pouring [5], Wegener and Pouring [7], Wegener, Clumpner, and Wu [8], Dawson, Willson, Hill, and Russell [9], Jaeger, Willson, Hill, and Russell [10], Kremmer and Okorounmu [11], Faro, Small, and Hill [12], Arthur [13], Binnie and Woods [14], Gyarmathy and Meyer [15], Head [16], and Willmarth and Nagamatsu [17].

2 A rarefaction wave passes through slightly superheated vapor in a shock tube bringing it to a subcooled state at which condensation suddenly occurs. We shall present Barschdorff's [6] data for pure vapors mixed with a noncondensible carrier.

3 A "diffusion cloud chamber" contains vapor and a noncondensible carrier in a one-dimensional thermally stratified chamber, condensing at the top and evaporating at the bottom. Owing to the character of the vapor-pressure curve the vapor reaches a maximum subcooling at a point in between. Here, a condensation cloud appears. We shall present data, obtained in this way by Katz [18], Heist and Reiss [19], and Katz, Scoppa, Kumar, and Mirabel [20].

It is customary to rationalize measurements of either of the limiting temperatures with some form of the nucleation theories of Volmer and Döring [21]. These are kinetic theories which anticipate that nucleation will occur when the thermodynamic potential barrier is on the order of the molecular kinetic energy. Furthermore, since these theories are probabilistic, they suggest that the limiting superheat or subcooling will decrease both with volume of the fluid and with the duration of exposure of the fluid to that temperature. To employ such theories one must introduce an experimentally determined nucleation rate. When this rate is on the order of $100/cm^3s$, a clean fluid will persist indefinitely. Nucleation limits occur when it is on the order of $10^{18}/cm^3s$. The nucleation described by such theories is called "homogeneous" in that it does not involve any foreign elements in the fluid. Of course, all real nucleation might be viewed as inhomogeneous since it needs molecular fluctuations to occur.

The problem we wish to address is that of finding out whether or not actual "homogeneous" nucleation approaches the spinodal line in the most rapid depressurization or heating processes. This in turn raises the question of specifying what the word "spinodal" means in relation to a real fluid for which the equation of state is not known. When we speak of the spinodal, we presume the following things about a real fluid.

Contributed by the Heat Transfer Division of THE AMERICAN SOCIETY OF MECHANICAL ENGINEERS and presented at the AIChE/ASME Heat Transfer Conference, Salt Lake City, Utah, August 15–17, 1977. Manuscript received by the Heat Division April 7, 1978. Paper No. 77-HT-20.

1 There is a unique p-v-T (pressure, volume, temperature) surface associated with any real fluid, which *includes* the hard-to-observe metastable regime and the unobservable unstable regime.

2 This surface has one locus of local maxima and one locus of local minima between the coexistence curves, defined by $(\partial p/\partial v)_T = 0$.

3 Real nucleation points lie on this surface in the regions of negative $(\partial p/\partial v)_T$.

4 This surface satisfies the Maxwell-Gibbs condition, $\int_f^g v dp = 0$, where f and g denote the saturated liquid and vapor curves.

5 All features of the p-v-T surface, including the spinodal lines, obey the law of corresponding states which says that there exists a universal surface of the form:

$$p_r = p_r(v_r, T_r, \text{a molecular parameter}) \tag{1}$$

where p_r, v_r, and T_r are p, v, and T divided by their critical values p_c, v_c, and T_c. The molecular parameter might be a Pitzer or Riedel factor, or simply the critical compressibility, $Z_c = p_c v_c/RT_c$, where R is the ideal gas constant.

6 A very careful measurement of the extreme subcooling or superheating can be viewed as an attempt to approach as closely as possible to the spinodal limit. This measurement must necessarily fall short of the spinodal line; but how far short is an open question, largely because the locations of the spinodal lines are not known precisely.

A Qualitative Use of van der Waals' Equation

Most attempts to represent real p-v-T surfaces accurately are based upon measurements in the stable regime and they do not provide accurate descriptions of the metastable and unstable regimes. However, Lienhard [22] recently showed that van der Waals' classic equation of state

$$p_r = \frac{8T_r}{3v_r - 1} - \frac{3}{v_r{}^2} \tag{2}$$

was an accurate member of the family of real fluids, equation (1).

Thus, we take the view that the van der Waals' equation is a legitimate representation of real behavior when $Z_c = 3/8$. It will not be accurate for the actual fluids which have smaller Z_c's, but it will correctly show the form and tendency of all aspects of real behavior. Both spinodal lines of a van der Waals fluid can be obtained by combining equation (2) with

$$T_{r_{sp}} = \frac{(3v_r - 1)^2}{4v_r{}^3} \tag{3}$$

It is also possible to calculate the van der Waals' vapor pressure curve by substituting it in the Maxwell-Gibbs criterion. The resulting vapor pressure curve is given by:

$$p_{r_s} = \frac{8T_{r_s}}{(v_{r_g} - v_{r_f})} \ln\left\{\frac{3v_{r_g} - 1}{3v_{r_f} - 1}\right\} - \frac{3}{v_{r_f} v_{r_g}} \tag{4}$$

where s denotes a saturation temperature or pressure.

Equations (2) and (3) specify the liquid and vapor spinodal temperatures $T_{r_{fsp}}$ and $T_{r_{gsp}}$ as a function of T_{r_s}. And equations (2) and (4) specify T_{r_s}. This trial-and-error calculation, originally done by hand for a few points, was recently redone on the computer by Ritchie [24], and Chen [25]. The resulting spinodal temperatures as given by van der Waals' equation are plotted as a function of T_{r_s} in Fig. 1.

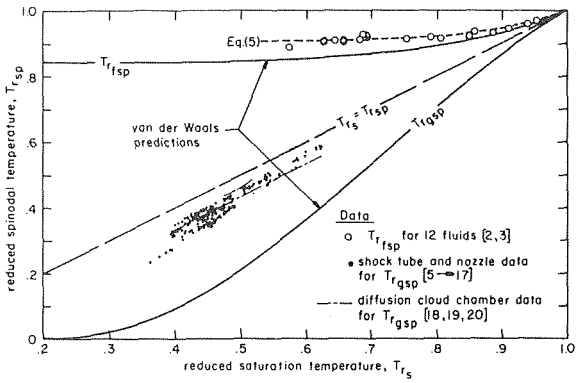

Fig. 1 Corresponding states correlations for $T_{r_{fsp}}$ and $T_{r_{gsp}}$

Corresponding States Correlations of the Data

We now return to our main problem—that of finding out whether or not nucleation occurs near the spinodal line. If nucleation data correlate, according to the law of corresponding states, on a line that has the same essential form as the van der Waals' spinodal line, then it will be a strong indication that homogeneous nucleation occurs near the spinodal line. Before actually making such a comparison it is well to consider what form of corresponding states correlation will be most successful.

Special note should be made of the fact that T_{r_s} is taken to be the independent variable in Fig. 1. The van der Waals reduced vapor pressure curve has already been observed (see [22] and [23]) to deviate very strongly from those of real gases with lower Z_c's. Furthermore, vapor-pressure data correlate badly on reduced coordinates even when the Z_c dependence is accounted. Since $p_s = f(T_s)$, one must always choose between p and T in correlating any property (such as T_{sp}) which is a unique function of the saturated state. Therefore, when we use the law of corresponding states to correlate any property which depends on T_{r_s} or p_{r_s} alone, we must expect a different correlation for either of the two variables we choose.

All of the nucleation data presented here will be correlated with T_{r_s}. In every case, a similar correlation has been attempted using p_{r_s} as the dependent variable and it has been found to be substantially worse than the one based on T_{r_s}. One such comparison has been published [26].

Early corresponding states correlations were made by Eberhart and Schnyders [27] and Eberhart, Kremsner and Blander [28] on $T_{r_{fsp}}$ versus T_{r_s} coordinates.[1] These correlations used older and sometimes restrictive sets of data. More recently Lienhard [26] correlated the full data of Skripov (which are probably the best measurements extant) for 12 substances and substantial ranges of T_{r_s} on $\Delta T_{r_{fsp}} \equiv (T_{r_{fsp}} - T_{r_s})$ versus T_{r_s} coordinates, and represented the correlation with:

$$\Delta T_{r_{fsp}} = 0.905 - T_{r_s} + 0.095 T_{r_s}{}^8 \tag{5}$$

[1] Note that we use the subscripts fsp and gsp to denote the nucleation temperatures as well as the spinodal temperature. It will be clear in the context which is being described.

Nomenclature

c_p, c_v = specific heat at constant pressure and at constant volume, respectively
p, p_r = pressure and reduced pressure, p/p_c, respectively
s = entropy
T, T_r = temperature and reduced temperature, T/T_c, respectively
v, v_r = volume and reduced volume, v/v_c, respectively
Z = compressibility factor, pv/RT
$\Delta T_{r_{gsp}} = (T_{r_s} - T_{r_{gsp}})$
$\Delta T_{r_{fsp}} = (T_{r_{fsp}} - T_{r_s})$
γ = specific heat ratio, c_p/c_v

Subscripts

c = a critical value
f, g = saturated liquid and vapor, respectively
fsp, gsp = liquid and vapor spinodal points or nucleation points, respectively, according to context
s = a saturation state
sp = a spinodal point

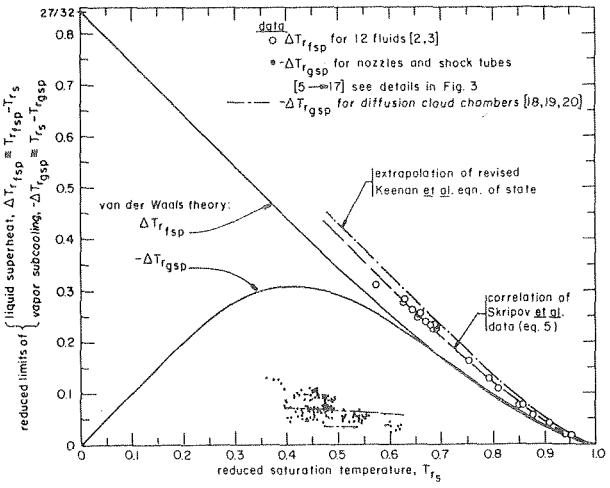

Fig. 2 Corresponding states correlations for $\Delta T_{r_{fsp}}$ and $-\Delta T_{r_{gsp}}$

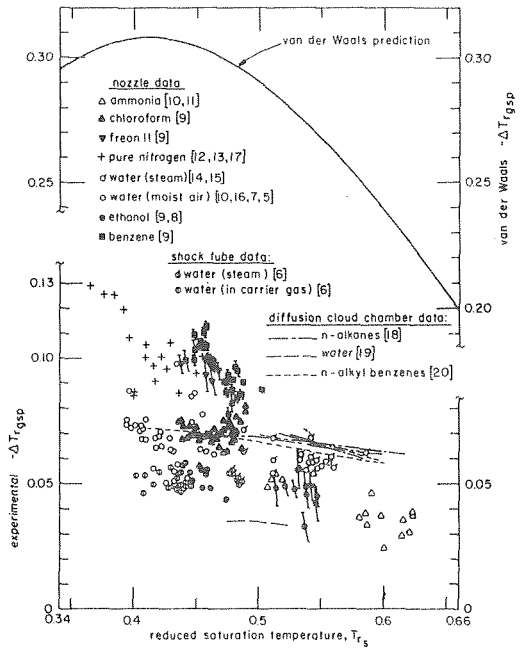

Fig. 3 Measured values of limiting vapor subcooling

Table 1 Effectiveness of Four Schemes of Correlation in Bringing Together Existing Nucleation Temperature Data

	Absolute variability of data in units of reduced temperature		
	liquids (Skripov, et al.)		
Coordinates	excl. H_2O	incl. H_2O	gases
$\Delta T_{r_{sp}}$ versus T_{r_s}	0.016	0.031	0.065
$T_{r_{sp}}$ versus T_{r_s}	0.018	0.034	0.065
$T_{r_{sp}}$ versus p_{r_s}	0.022	0.039	0.100
$\Delta T_{r_{sp}}$ versus p_{r_s}	0.048	0.048	0.200

Fig. 2 shows this correlation on the appropriate coordinates, along with the van der Waals' predictions (for $Z_c = 3/8$) and the data.

The measurements of the vapor nucleation temperature from [5–20] are shown in Figs. 1 and 2. Three things are immediately apparent: 1) The $T_{r_{gsp}}$ data deviate much farther from the van der Waals' prediction that the $T_{r_{fsp}}$ data do and they deviate toward the saturation line. 2) The data do not replicate the shape of the van der Waals' spinodal line, and 3) they exhibit far greater absolute scatter than the liquid nucleation data do.

Table 1 presents the absolute scatter of both sets of data in four different schemes of correlation. We see that the best correlation occurs in $\Delta T_{r_{sp}}$ versus T_{r_s} coordinates and that the liquid data correlate very well indeed. In comparing the liquid and vapor results, one might object that we are presenting data for only one method on the liquid side, and for several on the vapor side. However, the vapor data are so badly scattered among single methods as to scotch that objection.

We should also be aware that when the vapor data are rationalized by the molecular kinetic theory, nucleation density rates from as low as 1 cm^{-3} s^{-1} in diffusion cloud chambers, all the way to 10^{18} cm^{-3} s^{-1} in nozzle tests, must be used. The Skripov data for liquids correspond with about 10^{18} cm^{-3} s^{-1}. The $\Delta T_{r_{gsp}}$ data for nozzles suffer the full range of scatter in Fig. 3 even though they correspond with nucleation density rates that compare with those of Skripov.

Fig. 3 shows the $-\Delta T_{r_{gsp}}$ data from Fig. 2 in a greatly expanded scale on which individual points can be identified. These results show generally poor internal consistency. Both large and small values result from the same fluids. The shock-tube results are consistently low. It appears that $-T_{r_{gsp}}$ values for fluids with higher values of Z_c tend to be higher (in the direction of the van der Waals line) than those with lower Z_c's.

This plot suggests that no data have come anywhere near the vapor spinodal line. One might be tempted to blame dust particles, ions, or other heterogeneous elements for triggering early nucleation. But we believe that the experiments have been made with great care and that they probably come close to the real nucleation limit. On the one hand, there might be reasons (which we do not understand) why liquids can be heated almost all the way to their spinodal lines, but vapors cannot be cooled to their spinodal lines. On the other hand, there does appear to be a basic weakness in the vapor data reduction in all cases.

The Identification of the Nucleation Temperature

The nucleation temperatures were located by calculation rather than by direct measurement in all of the experiments that we report here. In the vapor expansion experiments it was usually argued that ideal gas relations would be valid owing to the low pressure involved (e.g., $10^{-5} \gtrsim p_r \gtrsim 5 \times 10^{-3}$).

However, the spinodal line is itself a manifestation of extreme nonideal behavior. It is the locus of points at which the van der Waals' attraction forces in a gas are equal to the molecular momentum and pressure forces. Indeed, it is easy to show that at low pressure the van der Waals' equation gives absolute values of the van der Waals' attraction and the pressure, which are equal.

By substituting equation (2) in $\partial p/\partial v|_s = \gamma\, \partial p/\partial v|_T$ (where s is the entropy and γ is the specific heat ratio, c_p/c_v), we obtain

$$\left.\frac{\partial \ln p_r}{\partial \ln v_r}\right|_s = -\gamma \left[\frac{1 - \dfrac{(3v_r - 1)^2}{4T_r v_r{}^3}}{1 - \dfrac{3v_r(3v_r - 1)}{8T_r v_r{}^3}}\right] \tag{6}$$

The bracketed term on the right shows how the conventional ideal gas relation for an isentropic process, pv^γ = constant, might be corrected for nonideality in accordance with van der Waals' equation. This term is unity in the ideal gas range and it decreases to zero at the spinodal line.

There is a second kind of misbehavior of pv^γ = constant in the neighborhood of the spinodal line: namely, that γ is not constant. It has been pointed out [30] that $(\partial T/\partial s)_p = T/c_p = 0$ on the spinodal lines; hence, c_p goes to infinity. At the same time c_v remains finite, so γ approaches infinity at the spinodal line.

The right hand side of equation (6) might thus be γ outside of the saturation region (before the expansion begins). As expansion continues into the two-phase region, we lack knowledge of c_p and c_v and are thus unable to predict the increase of γ. And the bracketed term

can be predicted only for the van der Waals substance—data do not exist for real substances in this region. At the spinodal line the right hand side of equation (6) is indeterminate and might assume any value from zero to infinity.

Actually, Gyarmathy, et al. [30] made steam expansion measurements and tried to rationalize them using an equation of state for steam. Unfortunately, no existing equation behaves well when extrapolated into the metastable region. In particular, they generally violate the Maxwell criterion if they are not used within about 25°C of the critical temperature.

More recently we have reconstructed the 50-constant equation of state of Keenan, et al. [31] requiring that it satisfy the Maxwell conditions (which the original equation does not do) and have thus created an equation which can be extrapolated to the liquid water spinodal line. That extrapolation is included in Fig. 2 and it lies just beyond the existing data. The precise location of the steam spinodal line is more sensitive to the choice of data points on which the equation is fit. Therefore we avoid plotting it for the moment and simply assert that, like the van der Waals vapor spinodal, it falls slightly above the relative liquid spinodal at high pressures and temperatures.

Other experiments made in carrier gases might appear to admit the use of ideal gas equations in their interpretation since the carrier gases are certainly ideal. However, the calculation cannot be completed in this case without introducing Dalton's law. The use of Dalton's law requires that the trace vapor *also* obey the ideal gas law, in a region that could hardly be less ideal.

Whatever experimental method has been used to date must unavoidably await knowledge of the properties of subcooled vapor before its results can be interpreted. That means that no one can say whether or not homogeneous nucleation occurs near the vapor spinodal line. The fact that it *does* occur near the *liquid* spinodal line forces us to admit the possibility that a valid interpretation of existing vapor data might place them closer together and nearer the spinodal line than they lie in Figs. 2 and 3.

Conclusions

1 Liquid nucleation temperatures are best correlated on $\Delta T_{r_{fsp}}$ versus T_{r_s} coordinates.

2 The state point associated with measured vapor nucleation data cannot be identified owing to presently incomplete property data. (Those reported in Figs. 1, 2, and 3 are based on unjustified uses of the ideal gas law.)

3 Homogeneous nucleation in liquids has been observed very near to the spinodal line.

4 Either the homogeneous nucleation of vapors occurs far from the spinodal line or else calculated values of $T_{r_{gsp}}$ are in error. It is not presently possible to tell which is the case.

Acknowledgment

This work has received partial support under Electric Power Research Institute contract RP687-1.

References

1 Kenrick, P. P., Gilbert, C. S., and Wismer, K. L., "The Superheating of Liquids," *Journal of Physical Chemistry,* Vol. 28, 1924, pp. 1297–1307.

2 Skirpov, V. P., and Pavlov, P. A., "Explosive Boiling of Liquids and Fluctuation Nucleus Formation," *Teplofizika Vysokih Temp.,* Vol. 8, No. 4, 1970, pp. 833–839.

3 Pavlov, P. A., and Skripov, V. P., "Kinetics of Spontaneous Nucleation in Strongly Heated Liquids," *Teplofizika Vysokih Temp.,* Vol. 8, No. 3, 1970, pp. 579–585.

4 Yellott, J. I., "Supersaturated Steam," *Engineering,* Vol. 137, 1934, p. 303.

5 Pouring, A. A., "Thermal Choking and Condensation in Nozzles," *The Physics of Fluids,* Vol. 8, No. 10, Oct. 1965, pp. 1802–1810.

6 Barschdorff, D., "Carrier Gas Effect on Homogeneous Nucleation of Water Vapor in a Shock Tube," *The Physics of Fluids,* Vol. 18, No. 5, May 1975, pp. 529–535.

7 Wegener, P. P., and Pouring, A. A., "Experiments on Condensation of Water Vapor by Homogeneous Nucleation in Nozzles," *The Physics of Fluids,* Vol. 7, No. 3, March 1964, pp. 352–361.

8 Wegener, P. P., Clumpner, J. A., and Wu, B. J. C., "Homogeneous Nucleation and Growth of Ethanol Drops in Supersonic Flow," *The Physics of Fluids,* Vol. 15, No. 11, Nov. 1972, pp. 1869–1876.

9 Dawson, D. B., Willson, E. J., Hill, P. G., and Russell, K. C., "Nucleation of Supersaturated Vapors in Nozzles. II. C_6H_6, $CHCl_3F$, and C_2H_5OH," *Journal of Chemical Physics,* Vol. 51, No. 12, Dec. 1969, pp. 5389–5396.

10 Jaeger, H. L., Willson, E. J., Hill, P. G., and Russell, K. C., "Nucleation of Supersaturated Vapors in Nozzles. I. H_2O and NH_3, *Journal of Chemical Physics,* Vol. 51, No. 12, Dec. 1969, pp. 5380–5388.

11 Kremmer, M., and Okorounmu, O., "Condensation of Ammonia Vapor During Rapid Expansion," Rept. No. 79, 1965, Massachusetts Institute of Technology, Gas Turbine Lab, Cambridge, MA.

12 Faro, I. D., Small, T. R., and Hill, F. K., "The Supersaturation of Nitrogen in a Hypersonic Wind Tunnel," *Journal of Applied Physics,* Vol. 23, 1952, pp. 40–43.

13 Arthur, P. D., "Effects of Impurities on the Supersaturation of Nitrogen in a Hypersonic Wind Tunnel," Ph.D. Thesis, 1952, California Institute of Technology, Pasadena, CA.

14 Binnie, A. M., and Woods, M. W., "The Pressure Distribution in a Convergent Divergent Steam Nozzle," *Proceedings,* Institution of Mechanical Engineers, (London), Vol. 138, p. 229.

15 Gyarmathy, G., and Meyer, H., "Spontane Kondensation," *ForschHft. Ver. Dt. Ing.,* Verlag, Dusseldorf, 1965, p. 508.

16 Head, R. M., "Investigations of Spontaneous Condensation Phenomena," Ph.D. Thesis, 1945, California Institute of Technology, Pasadena, CA.

17 Willmarth, W. W., and Nagamatsu, H. T., "The Condensation of Nitrogen in a Hypersonic Nozzle," *Journal of Applied Physics,* Vol. 23, 1952, pp. 1089–1095.

18 Katz, J. L., "Condensation of Supersaturated Vapor. I. The Homogeneous Nucleation of n-Alkanes," *Journal of Chemical Physics,* Vol. 52, No. 9, May 1970, pp. 4733–4748.

19 Heist, R. H., and Reiss, H., "Investigation of the Homogeneous Nucleation of Water Vapor Using a Diffusion Cloud Chamber," *Journal of Chemical Physics,* Vol. 59, No. 2, July 1973, pp 665–671.

20 Katz, J. L., Scoppa, C. J., Kumar, N. G., and Mirabel, P., "Condensation of a Supersaturated Vapor. II. The Homogeneous Nucleation of the n-Alkyl Benzenes," *Journal of Chemical Physics,* Vol. 62, No. 2, Jan. 1975, pp. 448–465.

21 See e.g.: Wegener, P. G., and Mack, L. M., "Condensation in Wind Tunnels," *Advances in Applied Mechanics,* (Dryden, H. L., and von Kármán, Th. eds.) Vol. 5, Academic Press, New York, 1958, pp. 307–447; or references 2 and 3.

22 Lienhard, J. H., "Relation between van der Waals' Fluid and Real Substances," *Iranian Journal of Science and Technology,* Vol. 5, No. 3-B, 1976, pp. 111–116.

23 Lienhard, J. H., and Schrock, V. E., "Generalized Displacement of the Nucleate Boiling Heat-Flux Curve, with Pressure Change," *International Journal of Heat and Mass Transfer,* Vol. 9, 1966, pp. 355–363.

24 Ritchie, B. W., unpublished computer program for T_{rfsp}, Chemical Engineering Department, University of Exeter, Exeter England. (Available on request.

25 Chen, S. L., unpublished computer program for T_{rgsp}, Mechanical Engineering Department, University of Kentucky, Lexington, KY. (Available on request.)

26 Lienhard, J. H., "Correlation for the Limiting Liquid Superheat," *Chemical Engineering Science,* Vol. 31, 1976, pp. 847–849.

27 Eberhart, J. G., and Schnyders, H. C., "Application of the Mechanical Stability Condition to the Prediction of the Limit of Superheat for Normal Alkanes, Ether, and Water," *Journal of Physical Chemistry,* Vol. 77, No. 23, 1973, pp. 2730–2734.

28 Eberhart, J. G., Kremsner, W., and Blander, M., "Metastability Limits of Superheated Liquids: Bubble Nucleation Temperatures of Hydrocarbons and Their Mixtures," *Journal of Colloid and Interface Science,* Vol. 50, No. 2, Feb. 1975, pp. 369–378.

29 Tien, C. L., and Lienhard, J. H. *Statistical Thermodynamics,* Holt, Rinehart and Winston, New York, 1971, p. 255.

30 Gyarmathy, G., Burkhard, H. P., Lesch, F., and Siegenthaler, A., "Spontaneous Condensation of Steam at High Pressure: First Experimental Results," *Conference Publications,* Institution of Mechanical Engineers, (London), No. 3, 1973, pp. 182–186.

31 Keenan, J. H., Keyes, F. G., Hill, P. G., and Moore, J. G., *Steam Tables,* John Wiley and Sons Inc., New York, 1969.

Min-Hsiun Lee[1]
Research Associate in Chemical Engineering,
Auburn University,
Auburn, Ala.

D. R. Jeng
Professor of Mechanical Engineering

K. J. De Witt
Professor of Chemical Engineering
The University of Toledo,
Toledo, Ohio

Laminar Boundary Layer Transfer over Rotating Bodies in Forced Flow

A procedure is described for the calculation of momentum and heat transfer rates through laminar boundary layers over rotating axisymmetric bodies in forced flow. By applying appropriate coordinate transformations and Merk's type of series, the governing momentum equations can be expressed as a set of coupled ordinary differential equations that depend on a wedge parameter and on a rotation parameter. For the energy equation, a set of ordinary differential equations is obtained which depend explicitly on the Prandtl number and implicitly on the aforementioned parameters. These equations are numerically integrated for a range of parameter values for the special case of a rotating sphere, and the local friction coefficient and the local Nusselt number are presented for values of the rotation parameter B = 1, 4, and 10 with Prandtl numbers of 1, 10, and 100. These results are then compared with previous theoretical results. It is also shown how the flow and heat transfer characteristics for a rotating disk can be readily obtained as a special case from the formulation for the rotating sphere. The disk results are also compared with previous theoretical and experimental studies.

Introduction

The flow and heat transfer characteristics of spinning bodies of revolution in a forced flow stream are important in the analysis of problems involving projectile motion, reentry missile behavior, fiber coating applications and rotary machine design. Up to the present time, only special cases in the above area have been investigated, and generalized analytical studies are unavailable due to the mathematical difficulties involved.

The flow and temperature fields for laminar forced flow impinging on a rotating disk have been investigated analytically by Hannah [1], Tifford and Chu [2], Schlichting and Truckenbrodt [3], Tien and Tsuji [4], Mabuchi, et al. [5], and Liu and Stewart [6]. Numerical results for several Prandtl numbers have also been obtained by Koh and Price [7]. Experimental data for heat transfer has been obtained by Koong and Blackshear [8] by means of a mass transfer analog corresponding to a Prandtl number of 2.4.

Heat transfer by convection in axisymmetric flow over an isothermal rotating cone has been investigated by Tien and Tsuji [9] by means of a perturbation and series expansion scheme for the two limiting cases of very slow and very fast rotation.

The flow field in the vicinity of a rotating sphere in a uniform flow stream with its axis of rotation parallel to the free stream velocity has been investigated by Hoskin [10]. Siekmann [11] utilized Hoskin's results for the flow field to analyze the thermal boundary layer for a similar problem. Both of these authors used the Blasius series method to solve their governing boundary layer equations. The drawback of the Blasius series method has been pointed out by Görtler [12].

More recently, Chao and Greif [13] used a quadratic velocity profile assumption to investigate the laminar forced convection heat transfer over rotating bodies with uniform or nonuniform surface temperature. Following a unique coordinate transformation, these authors were able to express the temperature field in terms of universal functions. In general, their solution is very effective for moderate or high Prandtl numbers and for small values of the rotation parameter. For small Prandtl numbers and large values of the rotation parameter, however, the quadratic velocity profile is inadequate for accurate determination of the temperature field. In recognizing this difficulty, Chao [14] has extended the analysis of [13] to incorporate more terms of the velocity profile in the solution of the energy equation. However, the accuracy of this resulting series has not been discussed other than for the case of a rotating disk.

In order to avoid the difficulties encountered by the previous methods, Merk's series [15] as refined by Chao and Fagbenle [16] is adopted in the present analysis. The analysis begins with the development of the procedure for solving the boundary layer equations for forced flow over any fairly arbitrary axisymmetrical rotating body. A numerical example involving the calculation of the momentum and heat transfer rates for the case of a rotating sphere will be illustrated. The results obtained by the present method are then compared with those of Hoskin [10], Siekmann [11], Chao and Greif [13] and Chao

[1] Formerly Graduate Assistant, Department of Chemical Engineering, The University of Toledo, Toledo, Ohio.

Contributed by the Heat Transfer Division for publication in the JOURNAL OF HEAT TRANSFER. Manuscript received by the Heat Transfer Division June 7, 1977

[14]. The method proposed in the present study offers several advantages: First of all, the simplifications introduced are mathematical in nature, and refinement of the calculation can be done in a straightforward manner by using more terms in the series solution. Secondly, the zeroth order solution provides reasonably accurate results for many engineering applications, and, finally, the method provides probably the most rapid and simple technique to predict the flow and heat transfer characteristics yet proposed in the literature.

Governing Equations and Solution Method

Consideration is given to steady, laminar, nondissipative, constant property, incompressible boundary layer flow around a rotating body placed in a uniform stream with its axis of rotation parallel to the free stream velocity. We choose nonrotating coordinates, x and y, with x representing the distance measured along a meridian curve from the forward stagnation point and y being measured normal to the surface of the rotating body. The quantity $r(x)$ is the radius of the body at the point x, u and v are the x and y components of the velocity, respectively, and w is the transverse velocity component due to spin of the body. Under the previously stated conditions, the boundary layer equations are:

$$\text{Continuity} \quad \frac{\partial}{\partial x}(ru) + \frac{\partial}{\partial y}(rv) = 0 \tag{1}$$

$$\text{Momentum} \quad u\frac{\partial u}{\partial x} + v\frac{\partial u}{\partial y} - \frac{w^2}{r}\frac{dr}{dx} = U_e\frac{dU_e}{dx} + \nu\frac{\partial^2 u}{\partial y^2} \tag{2}$$

$$u\frac{\partial w}{\partial x} + v\frac{\partial w}{\partial y} + \frac{uw}{r}\frac{dr}{dx} = \nu\frac{\partial^2 w}{\partial y^2} \tag{3}$$

with the boundary conditions

$$u = v = 0, w = r\Omega \quad \text{for } y = 0 \tag{4a}$$

$$u = U_e, v = w = 0 \quad \text{for } y \to \infty \tag{4b}$$

where $U_e(x)$ is the velocity of the mainstream at the edge of the boundary layer and Ω is the angular velocity of the rotating body which is assumed to be constant.

$$\text{Energy} \quad u\frac{\partial T}{\partial x} + v\frac{\partial T}{\partial y} = \alpha\frac{\partial^2 T}{\partial y^2} \tag{5}$$

with the boundary conditions

$$T = T_w \quad \text{for } y = 0 \tag{6a}$$

$$T = T_\infty \quad \text{for } y \to \infty \tag{6b}$$

where both T_w and T_∞ are constants.

To solve the set of partial differential equations (1, 2, 3, 5), we introduce a streamfunction $\psi(x, y)$ defined by

$$u = \frac{L}{r}\frac{\partial \psi}{\partial y}, \qquad v = -\frac{L}{r}\frac{\partial \psi}{\partial x} \tag{7}$$

such that the continuity equation (1) is identically satisfied, and where L is a characteristic length defined appropriately for the particular flow geometry involved in the problem. The (x, y) coordinates will now be transformed by writing

$$x \Rightarrow \xi = \int_0^x \frac{U_e(x)}{U_\infty}\left(\frac{r}{L}\right)^2\frac{dx}{L} \tag{8}$$

$$y \Rightarrow \eta = \left(\frac{\mathrm{Re}_L}{2\xi}\right)^{1/2}\frac{U_e}{U_\infty}\left(\frac{r}{L}\right)\frac{y}{L} \tag{9}$$

in which the Reynolds Number is defined as $\mathrm{Re}_L = U_\infty L/\nu$ and where U_∞ is the fluid approach velocity. A dimensionless stream function f is introduced such that

$$\psi(x, y) = U_\infty L\left(\frac{2\xi}{\mathrm{Re}_L}\right)^{1/2} f(\xi, \eta) \tag{10}$$

Using (8), (9), and (10), equation (7) becomes

$$u = U_e\frac{\partial f}{\partial \eta} \tag{11}$$

and

$$v = -\frac{r}{L}\frac{U_e}{(2\xi\mathrm{Re}_L)^{1/2}}\left\{f + 2\xi\frac{\partial f}{\partial \xi} + \left(\Lambda + \frac{2\xi}{r}\frac{dr}{d\xi} - 1\right)\eta\frac{\partial f}{\partial \eta}\right\} \tag{12}$$

where Λ is the wedge parameter and is defined by

$$\Lambda = \frac{2\xi}{U_e}\frac{dU_e}{d\xi} \tag{13}$$

We also define a dimensionless rotating velocity function $g(\xi, \eta)$ by

$$w(x, y) = r(x)\Omega g(\xi, \eta) \tag{14}$$

Substituting (11), (12), (13), and (14) into (2) and (3), the momentum equations become

$$f''' + ff'' + \Lambda(1 - f'^2) + \frac{2\xi}{r}\frac{dr}{d\xi}\left(\frac{r^2\Omega^2}{U_e{}^2}\right)g^2 = 2\xi\frac{\partial(f', f)}{\partial(\xi, \eta)} \tag{15}$$

$$g'' + fg' - gf'\left(\frac{4\xi}{r}\right)\frac{dr}{d\xi} = 2\xi\frac{\partial(g, f)}{\partial(\xi, \eta)} \tag{16}$$

with the boundary conditions

$$f = f' = 0, \quad g = 1, \quad \text{for } \eta = 0 \tag{17a}$$

$$f' = 1, \quad g = 0, \quad \text{for } \eta \to \infty \tag{17b}$$

The primes denote differentiation with respect to η, and $\partial(f', f)/\partial(\xi, \eta) = [f'\,\partial f'/\partial\xi - f''\,\partial f/\partial\xi]$ is the Jacobian.

Nomenclature

b_0, b_1, b_2, b_3 = coefficients defined in (23)
B = rotation parameter, $(2/3 \cdot R\Omega/U_\infty)^2$ for sphere
c_0, c_1, c_2, c_3 = coefficients defined in (24)
C_f = friction coefficient defined in (41)
f = dimensionless stream function, defined in (10)
g = dimensionless rotating velocity, defined in (14)
L = characteristic length for body
Nu = Nusselt number
Pr = Prandtl number = ν/α
r = radius of body at x
R = sphere radius
Re_R = Reynolds number = RU_∞/ν
T = temperature
u = velocity component in the x direction
U_e = velocity at outer edge of boundry layer
U_∞ = approach velocity
v = velocity component in y direction
w = velocity component in rotating direction
x = coordinate measured along surface from front stagnation point
z = coordinate measured in rotating direction
y = coordinate measured normal to x
α = thermal diffusivity
$\beta = x/R$
η = dimensionless y coordinate, defined in (9)
θ = dimensionless temperature, defined in (18)
Λ = wedge parameter, defined in (13)
ν = kinematic viscosity
ξ = dimensionless x coordinate, defined in (8)
ψ = stream function, defined in (7)
Ω = angular velocity

Subscripts

w = evaluated at wall
∞ = evaluated at approach conditions

Upon introducing a dimensionless temperature function, θ, defined by

$$\theta(\xi, \eta) = \frac{T - T_w}{T_\infty - T_w} \tag{18}$$

the thermal boundary layer equation (5) transforms to

$$\theta'' + \mathrm{Pr} f\theta' = 2\xi \,\mathrm{Pr}\, \frac{\partial(\theta, f)}{\partial(\xi, \eta)} \tag{19}$$

with the boundary conditions

$$\theta = 0 \text{ for } \eta = 0 \tag{20a}$$

$$\theta = 1 \text{ for } \eta \to \infty \tag{20b}$$

With the transformations thus being completed, we now have to solve equations (15), (16), and (19) with the boundary conditions (17(a), (b)) and (20(a), (b)), respectively. The dependent variables in these equations may be considered as functions of η and ξ, or of η and Λ, since Λ depends only on x, as does ξ, and there is a one-to-one correspondence between Λ and ξ. Hence one may regard Λ as a function of ξ or, conversely, ξ as a function of Λ, as suggested by Merk [15].

Following Chao and Fagbenle [16], we write solutions for f and g in the form of Merk's series as

$$f(\xi, \eta) = f_0(\Lambda, \eta) + 2\xi \frac{d\Lambda}{d\xi} f_1(\Lambda, \eta) + 4\xi^2 \frac{d^2\Lambda}{d\xi^2} f_2(\Lambda, \eta) + \left(2\xi \frac{d\Lambda}{d\xi}\right)^2 f_3(\Lambda, \eta) + \ldots \tag{21}$$

$$g(\xi, \eta) = g_0(\Lambda, \eta) + 2\xi \frac{d\Lambda}{d\xi} g_1(\Lambda, \eta) + 4\xi^2 \frac{d^2\Lambda}{d\xi^2} g_2(\Lambda, \eta) + \left(2\xi \frac{d\Lambda}{d\xi}\right)^2 g_3(\Lambda, \eta) + \ldots \tag{22}$$

The quantities $(2\xi/r)(dr/d\xi)r^2\Omega^2/U_e{}^2$ and $(4\xi/r)dr/d\xi$ in (15) and (16), respectively, are functions of x only, and since x can be inversely expressed in terms of Λ, these quantities can also be treated as functions of Λ. Therefore, the following expansions for these terms are proposed:

$$\frac{2\xi}{r}\frac{dr}{d\xi}\frac{r^2\Omega^2}{U_e{}^2} = \left(\frac{L\Omega}{U_\infty}\right)^2 \frac{2\xi}{r/L}\frac{d(r/L)}{d\xi}\left(\frac{r/L}{U_e/U_\infty}\right)^2 = \left(\frac{L\Omega}{U_\infty}\right)^2\left[b_0\Lambda + 2\xi\frac{d\Lambda}{d\xi}b_1 + 4\xi^2\frac{d^2\Lambda}{d\xi^2}b_2 + \left(2\xi\frac{d\Lambda}{d\xi}\right)^2 b_3 + \ldots\right] \tag{23}$$

and

$$\frac{4\xi}{r}\frac{dr}{d\xi} = \frac{4\xi}{r/L}\frac{d(r/L)}{d\xi} = c_0\Lambda + 2\xi\frac{\Lambda}{d\xi}c_1 + 4\xi^2\frac{d^2\Lambda}{d\xi^2}c_2 + \left(2\xi\frac{d\Lambda}{d\xi}\right)^2 c_3 + \ldots \tag{24}$$

where the b_n's and c_n's are defined as geometrical constant parameters to be determined either by a numerical fitting of the left hand sides of (23) and (24) to their respective right hand sides, or by analytical methods.

Upon substituting (21), (22), (23), and (24) into (15) and (16), and collecting terms free of $d\Lambda/d\xi$ and then terms common to $2\xi d\Lambda/d\xi$, $4\xi^2\, d^2\Lambda/d\xi^2 \ldots$, etc., one obtains a sequence of coupled ordinary differential equations. The first one in the sequence is

$$f_0''' + f_0 f_0'' + \Lambda[1 - (f_0')^2 + Bg_0{}^2] = 0 \tag{25}$$

$$g_0'' + f_0 g_0' - c_0\Lambda f_0' g_0 = 0 \tag{26}$$

with

$$f_0(\Lambda, 0) = f_0'(\Lambda, 0) = 0; \quad g_0(\Lambda, 0) = 1 \tag{27a}$$

$$f_0'(\Lambda, \infty) = 1; \quad g_0(\Lambda, \infty) = 0 \tag{27b}$$

where $B = b_0(L\Omega/U_\infty)^2$ and is a rotation parameter.

The differential equations for the remaining f_i and g_i are:

$$f_1''' + f_0 f_1'' - 2(1+\Lambda) f_0' f_1' + 3f_0'' f_1 + 2B\Lambda g_0 g_1 + \left(\frac{b_1}{b_0}\right) Bg_0{}^2 = \frac{\partial(f_0', f_0)}{\partial(\Lambda, \eta)} \tag{28}$$

$$g_1'' + f_0 g_1' - 2f_0' g_1 - c_0\Lambda(f_1' g_0 + g_1 f_0') - c_1 f_0' g_0 + 3f_1 g_0' = \frac{\partial(g_0, f_0)}{\partial(\Lambda, \eta)} \tag{29}$$

with

$$f_1(\Lambda, 0) = f_1'(\Lambda, 0) = g_1(\Lambda, 0) = 0 \tag{30a}$$

$$f_1'(\Lambda, \infty) = g_1(\Lambda, \infty) = 0 \tag{30b}$$

$$f_2''' + f_0 f_2'' - 2(2+\Lambda) f_0' f_2' + 5f_0'' f_2 + 2B\Lambda g_0 g_2 + \left(\frac{b_2}{b_0}\right) Bg_0{}^2 = f_0' f_1' - f_0'' f_1 \tag{31}$$

$$g_2'' + f_0 g_2' - 4f_0' g_2 - c_0\Lambda(g_0 f_2' + g_2 f_0') - c_2 f_0' g_0 + 5f_2 g_0' = f_0' g_1 - f_1 g_0' \tag{32}$$

with

$$f_2(\Lambda, 0) = f_2'(\Lambda, 0) = g_2(\Lambda, 0) = 0 \tag{33a}$$

$$f_2'(\Lambda, \infty) = g_2(\Lambda, \infty) = 0 \tag{33b}$$

etc.

For a given body geometry, the b_i's and c_i's are assumed to be known, and for any streamwise location x, Λ is fixed. Hence the above equations with their boundary conditions can be treated as simultaneous ordinary differential equations and solved successively with Λ and B regarded as parameters.

The accuracy of the above-mentioned method when applied to any specific geometry depends on how well the series on the right-hand sides of (23) and (24) represent the functions on the left-hand sides of (23) and (24). For an ellipsoid with small eccentricity or for a body which deviates only slightly from a sphere, two or three terms in the series are certainly sufficient. If more terms are required in the series for some particular geometry, such as for a rotating cone for which Λ is a constant and the left-hand sides of (23) and (24) are functions of x so that equations corresponding to (23) and (24) cannot be written, the following procedure is recommended. The terms

$$\frac{2\xi}{r}\frac{dr}{d\xi}\frac{\left(\frac{r^2}{L^2}\right)}{\left(\frac{U_e}{U_\infty}\right)^2}\left(\frac{L^2\Omega^2}{U_\infty{}^2}\right) \quad \text{and} \quad \frac{4\xi}{r}\frac{dr}{d\xi}$$

can be retained just as they are in (15) and (16), and one would use the similar series expansion as in (21) and (22). The resultant differential equations would then be functions of Λ and the aforementioned terms. For a given geometry the dependencies of these two terms on Λ are known and, for a specified Λ, their values are known. The differential equations can therefore be integrated as simultaneous ordinary differential equations with Λ and $L\Omega/U_\infty$ as parameters.

The appropriate series solution for (19) is analogous to that for (21) and (22). It is

$$\theta(\xi, \eta) = \theta_0(\Lambda, \eta) + 2\xi \frac{d\Lambda}{d\xi}\theta_1(\Lambda, \eta) + 4\xi^2 \frac{d^2\Lambda}{d\xi^2}\theta_2(\Lambda, \eta) + \left(2\xi\frac{d\Lambda}{d\xi}\right)^2 \theta_3(\Lambda, \eta) + \ldots \tag{34}$$

Substituting (34) and (21) into (19), followed by collection of terms free of $d\Lambda/d\xi$ and then successively terms common to $2\xi d\Lambda/d\xi$, $4\xi^2 d^2\Lambda/d\xi^2$, etc., yields

$$\mathrm{Pr}^{-1}\theta_0'' + f_0\theta_0' = 0 \tag{35}$$

with

$$\theta_0(\Lambda, 0) = 0; \quad \theta_0'(\Lambda, \infty) = 1 \tag{36}$$

$$\mathrm{Pr}^{-1}\theta_1'' + f_0\theta_1' - 2f_0'\theta_1 = \frac{\partial(\theta_0, f_0)}{\partial(\Lambda, \eta)} - 3f_1\theta_0' \tag{37}$$

with

$$\theta_1(\Lambda, 0) = \theta_1(\Lambda, \infty) = 0 \tag{38}$$

$$\mathrm{Pr}^{-1}\theta_2'' + f_0\theta_2' - 4f_0'\theta_2 = f_0'\theta_1 - f_1\theta_0' - 5f_2\theta_0' \tag{39}$$

with

$$\theta_2(\Lambda, 0) = \theta_2(\Lambda, \infty) = 0, \text{ etc.} \tag{40}$$

It is noticed that all θ_i's contain the Prandtl number as a parameter.

A numerical method of integration for these sets of equations (25–33, 35–40) has been developed and applied to a spherical geometry.

To conclude this section, we would like to point out that for rotating bodies having simple geometry, such as that of a disk, the right hand sides of (15), (16), and (19) are identically equal to zero and the terms $2\xi/r(dr/d\xi)r^2/U_e{}^2$ and $(4\xi/r)dr/d\xi$ on the left hand sides of (15) and (16), respectively, become constants. The solutions of these equations are then called the "similarity solution." For other geometries such as the rotating sphere, the right hand sides of (15), (16), and (19) do not vanish, and the numerical solution of f_0, g_0, and θ_0 are called the "local similarity solution" corresponding to the local value of the wedge parameter Λ at the location under consideration. In this sense, the remaining terms in the series expansion of (21), (22), and (34) may be interpreted as corrections to the local similarity solution.

When the solutions for the various f_i's, g_i's, and θ_i's are available, the significant boundary layer quantities, such as the local frictional coefficient and the local Nusselt number, can be readily obtained.

Defining the local frictional coefficient in the streamwise direction x by

$$C_f = \frac{\mu\left(\frac{\partial u}{\partial y}\right)_{y=0}}{\frac{1}{2}\rho U_\infty{}^2}$$

one finds, after transformation,

$$\frac{1}{2}C_f\,\mathrm{Re}_L{}^{1/2} = \left(\frac{r}{L}\right)\left(\frac{U_e}{U_\infty}\right)^2(2\xi)^{-1/2}\left[f_0''(\Lambda, 0) + 2\xi\frac{d\Lambda}{d\xi}f_1''(\Lambda, 0) + 4\xi^2\frac{d^2\Lambda}{d\xi^2}f_2''(\Lambda, 0) + \ldots\right] \tag{41}$$

One can also obtain the relationship

$$\mathrm{NuRe}_L{}^{-1/2} = \left(\frac{r}{L}\right)\frac{U_e}{U_\infty}(2\xi)^{-1/2}\left[\theta_0'(\Lambda, 0) + 2\xi\frac{d\Lambda}{d\xi}\theta_1'(\Lambda, 0) + 4\xi^2\frac{d^2\Lambda}{d\xi^2}\theta_2'(\Lambda, 0) + \ldots\right] \tag{42}$$

Numerical Integration for a Rotating Sphere

The simultaneous differential equations for the f_i's, g_i's, and θ_i's for a rotating sphere were integrated using a fourth-order Runge-Kutta procedure on the IBM 360/75. For this geometry it is found that $r/R = \sin x/R$, and from potential flow theory, $U_e/U_\infty = 1.5 \sin x/R$. Then the quantities $(r^2\Omega^2/U_e{}^2)(2\xi/r)dr/d\xi$ and $(4\xi/r)dr/d\xi$ can be expressed in the following simple form as

$$\frac{r^2\Omega^2}{U_e{}^2}\frac{2\xi}{r}\frac{dr}{d\xi} = \frac{4}{9}\left(\frac{R\Omega}{U_\infty}\right)^2\Lambda = B\Lambda \tag{43}$$

and

$$\frac{4\xi}{r}\frac{dr}{d\xi} = 2\Lambda \tag{44}$$

The geometrical parameters appearing in (23) and (24) or in (25–32) are $b_0 = 4/9$, $b_1 = b_2 = b_3 = \ldots = 0$, and $c_0 = 2$, $c_1 = c_2 = c_3 = \ldots = 0$. The radius of the sphere, R, is chosen for the characteristic length to replace L. The quantity $B = (2/3\,R\Omega/U_\infty)^2$ is called a rotation parameter and is a measure of the sphere spin relative to the mainstream velocity.

The complete details of the numerical integration procedure may be found in Lee [17], and will not be repeated here.

Computer printouts of the velocity functions f_i and g_i ($i = 0, 1, 2$) for Λ ranging from 0.1 to 0.5, and of the temperature functions θ_i ($i = 0, 1, 2$) for the same range of Λ and for Pr = 1.0, 10, and 100, are too lengthy to be included in this paper and may be obtained by writing to the authors. However, the velocity wall derivatives are given in Table 1 for rotation parameter values of 1, 4, and 10, respectively, and the temperature wall derivatives are given in Table 2 for the same rotation parameter values and for Prandtl numbers of 1, 10, and 100.

The calculation of the surface characteristics begins with an evaluation of the streamwise coordinate ξ and the wedge parameter Λ. As previously stated, for a spherical body we have $r/R = \sin x/R$ and $U_e/U_\infty = 3/2 \sin x/R$, so that ξ and Λ can be obtained and the determination of $2\xi d\,\Lambda/d\xi$ and of $4\xi\,d^2\Lambda/d\xi^2$ is straightforward. The needed values are

$$\xi = 1 - 1.5\cos\beta + 0.5\cos^3\beta \tag{45}$$

$$\Lambda = (4\cos\beta - 6\cos^2\beta + 2\cos^4\beta)/(3\sin^4\beta) \tag{46}$$

$$\frac{d\Lambda}{d\xi} = -\frac{8(1-\cos\beta)^3}{9\sin^8\beta} \tag{47}$$

$$\frac{d^2\Lambda}{d\xi^2} = \frac{-16}{27\sin^{12}\beta}(1-\cos\beta)^3(3-5\cos\beta) \tag{48}$$

where $\beta = x/R$. With the above information and the data in Tables 1 and 2, the local friction coefficient and the Nusselt number can be evaluated using (41) and (42) with the characteristic length being replaced by R. The series involved in these equations usually converged rapidly in regions not too far from the forward stagnation point, with somewhat slower convergence occurring as the distance from the forward stagnation point increased. It is possible that

Table 1 Wall derivatives of velocity functions for a rotating sphere

B	Wedge Parameter Λ	$f_0''(0)$	$g_0'(0)$	$f_1''(0) \times 10$	$g_1'(0) \times 10$	$f_2''(0) \times 10^2$	$g_2'(0) \times 10^2$
	0.500	1.1129	-0.7849	-0.3896	0.3994	0.3390	-0.4336
	0.495	1.1082	-0.7823	-0.3934	0.4018	0.3435	-0.4491
	0.480	1.0938	-0.7746	-0.4051	0.4090	0.3575	-0.4475
	0.450	1.0645	-0.7589	-0.4301	0.4242	0.3880	-0.4694
1	0.400	1.0139	-0.7320	-0.4779	0.4514	0.4472	-0.5089
	0.350	0.9609	-0.7042	-0.5348	0.4812	0.5196	-0.5527
	0.300	0.9051	-0.6754	-0.6034	0.5140	0.6092	-0.6011
	0.250	0.8461	-0.6454	-0.6876	0.5499	0.7218	-0.6540
	0.200	0.7831	-0.6140	-0.7925	0.5890	0.8659	-0.7113
	0.100	0.6421	-0.5464	-1.1028	0.6749	1.3074	-0.8317
	0.500	1.6233	-0.8463	-0.3911	0.3810	0.2296	-0.3962
	0.495	1.6152	-0.8434	-0.3966	0.3832	0.2355	-0.3991
	0.480	1.5909	-0.8345	-0.4138	0.3898	0.2541	-0.4080
	0.450	1.5411	-0.8165	-0.4513	0.4034	0.2955	-0.4264
4	0.400	1.4549	-0.7856	-0.5242	0.4275	0.3787	-0.4589
	0.350	1.3639	-0.7536	-0.6137	0.4532	0.4849	-0.4932
	0.300	1.2675	-0.7201	-0.7248	0.4802	0.6218	-0.5286
	0.250	1.1645	-0.6851	-0.8650	0.5079	0.8004	-0.5632
	0.200	1.0536	-0.6483	-1.0453	0.5347	1.0373	-0.5932
	0.100	0.7992	-0.5673	-1.6072	0.5680	1.8029	-0.5984
	0.500	2.5216	-0.9362	-0.4629	0.3835	0.1409	-0.3748
	0.495	2.5079	-0.9327	-0.4719	0.3856	0.1504	-0.3774
	0.480	2.4664	-0.9223	-0.5003	0.3921	0.1804	-0.3853
	0.450	2.3814	-0.9012	-0.5625	0.4053	0.2479	-0.4015
10	0.400	2.2338	-0.8649	-0.6851	0.4280	0.3867	-0.4289
	0.350	2.0776	-0.8271	-0.8377	0.4515	0.5676	-0.4559
	0.300	1.9111	-0.7874	-1.0303	0.4747	0.8057	-0.4801
	0.250	1.7325	-0.7457	-1.2771	0.4958	1.1223	-0.4973
	0.200	1.5388	-0.7013	-1.5999	0.5110	1.5496	-0.4987
	0.100	1.0873	-0.6015	-2.6398	0.4793	2.9682	-0.3536

eventually the series may become semi-divergent and thus require the use of the Euler summation technique [18], but this did not occur in the present study.

The computed wall friction results in the x direction, expressed as $1/2C_f\,\mathrm{Re}_R^{1/2}$, are summarized in Table 3 for values of B equal to 1, 4, and 10. The local heat transfer results, expressed as $\mathrm{NuRe}_R^{-1/2}$, are tabulated in Table 4 for B equal to 1, 4, and 10 and for Prandtl numbers of 1, 10, and 100. Additional data in Tables 3 and 4 illustrate the series results when only one term is used, as well as data from other sources for comparison purposes.

The dimensionless axial and rotating fluid velocities were calculated from (21) and (22) using the computed f_i's and g_i's, and are shown in Fig. 1 for $\Lambda = 0.3$, which corresponds to $x/R = 1.215$. It can be seen from the figure that the dimensionless axial velocity has a higher value for a higher rotation parameter B, which is due to centrifugal effects. The fluid which is forced outward in a radial direction is replaced by fluid entering in the axial direction.

Table 2 Sample of wall derivatives of temperature functions for a rotating sphere*

B	Wedge Parameter Λ	$\theta_0'(\Lambda,0)$	$\theta_1'(\Lambda,0) \times 10$	$-\theta_2'(\Lambda,0) \times 10^2$
		Pr = 1.0		
1	0.5	0.5536	0.1163	0.1969
	0.4	0.5437	0.1248	0.2138
	0.3	0.5318	0.1343	0.2325
	0.1	0.4977	0.1539	0.2728
4	0.5	0.5897	0.1820	0.2957
	0.4	0.5778	0.2025	0.3305
	0.3	0.5629	0.2280	0.3728
	0.1	0.5157	0.3162	0.5186
10	0.5	0.6432	0.2536	0.4040
	0.4	0.6287	0.2854	0.4511
	0.3	0.6100	0.3262	0.5083
	0.1	0.5453	0.4952	0.7469
		Pr = 10		
1	0.5	1.2911	0.3042	0.7268
	0.4	1.2595	0.3243	0.8055
	0.3	1.2219	0.3455	0.9030
	0.1	1.1158	0.3808	1.1976
4	0.5	1.4180	0.5018	1.0653
	0.4	1.3777	0.5536	1.2150
	0.3	1.3283	0.6176	1.4132
	0.1	1.1760	0.8342	2.1729
10	0.5	1.6003	0.7078	1.4469
	0.4	1.5493	0.7898	1.6709
	0.3	1.4852	0.8956	1.9765
	0.1	1.2734	1.3299	3.3299
		Pr = 100		
1	0.5	2.8796	0.7328	1.7807
	0.4	2.7995	0.7856	1.9829
	0.3	2.7048	0.8438	2.2390
	0.1	2.4387	0.9567	3.0542
4	0.5	3.2172	1.2009	2.6014
	0.4	3.1125	1.3316	2.9781
	0.3	2.9853	1.4971	3.4875
	0.1	2.5972	2.0745	5.5277
10	0.5	3.6860	1.6748	3.4829
	0.4	3.5523	1.8825	4.0405
	0.3	3.3865	2.1576	4.8197
	0.1	2.8477	3.3167	8.4307

* For more complete data please refer to [17].

Comparison with Previous Results

Many attempts have been made to develop a method of boundary layer analysis which can be applied to rotating bodies. In this section, the momentum and heat transfer results obtained by the present series technique are compared with the data calculated by other methods available in the literature. For the frictional coefficient, Hoskin [10] reported a Blasius type solution which was used to calculate the data included in Table 3. Our results using three terms in the series compare satisfactorily with Hoskin's data, the discrepancy being within 2.5 percent for the range of parameters studied. If the local similarity solution (one series term) is used, the discrepancy increases to 12 percent for $B = 1$, 15 percent for $B = 4$, and 18 percent for $B = 10$ for large x/R.

For comparison of our heat transfer results for the case of $B = 4$, Siekmann's [11] four-term Blasius-type series formula was used. We calculated $\mathrm{NuRe}_R^{-1/2}$ using Seikmann's equation for $B = 4$ and $\mathrm{Pr} = 1.0$, which is the only case considered in his analysis. The results are included in Table 4 and show excellent agreement with our results, for both our one-term and three-term series solutions, up to $x/R \leq 1.215$. For $x/R \geq 1.215$, his four-term results are very close to our one-term results, which suggests that the convergence of the Blasius series is slower than our series (42) for large x/R. Another heat transfer comparison is made in the same table with equations provided to us by Professor B. T. Chao [19] for $B = 1$ and 10. These equations were obtained by using the two-term velocity profile in the energy equation and the final series were expressed in terms of x/R. In general, the agreement is good for large Prandtl numbers; for $\mathrm{Pr} = 1$, the discrepancy is as high as 20.3 percent for $B = 10$. For a given Prandtl number, the discrepancy becomes larger for larger B. Therefore, for a small Prandtl number with a large rotation parameter, the use of the quadratic velocity profile in the analysis of the energy equation [13] is not adequate. In Table 4, the Nusselt numbers calculated by the series solution [13] in terms of curvature parameter ϵ_n's by retaining a three-term velocity distribution are also included for Pr = 1 and 10. For the case $\mathrm{Pr} = 1$, significant improvement is seen for both $B = 1$ and 10 as compared to our results. Some improvement is also noticed for the case of $\mathrm{Pr} = 10$. However, at the location $x/R = 1.374$, the results of the two-term velocity profile are closer to our value than are the three-term results. This may be attributed to the difference in the convergence characteristics of the series when it is expanded in terms of x/R or ϵ_n. It can also be seen that for $\mathrm{Pr} \geq 1$ and $x/R \leq 1.374$, one term in the series (42) is sufficient if the desired accuracy is not higher than 3.5 percent. It is also evident that the local heat transfer is augmented by the sphere rotation, which is understandable since we have seen that the axial velocity increases with rotation and therefore the local convective heat transfer is increased.

The flow and heat transfer characteristics of forced flow against an isothermal rotating disk can be readily obtained from the case for a rotating sphere. For the disk, $r = x$, $U_e/U_\infty = 2x/\pi R$, $B = (\pi R\Omega/2U_\infty)$, $\Lambda = 0.5$ (constant), and R is the disk radius. The local friction coefficient in the radial direction is defined in a form similar to that given by Tifford and Chu [2][2] as

[2] Unfortunately, the form of $C_f(\mathrm{Re}_x)^{1/2} = \tau_w/1/2\rho(C^2 + \Omega^2)x^2[(C^2 + \Omega^2)x^2/\nu]^{1/2}$ given in [2] is in error. Our C and B equal a and $(\omega/a)^2$ defined in [2], respectively.

Table 3 Local frictional coefficient, $\frac{1}{2} C_f\,\mathrm{Re}_R^{1/2}$, for a rotating sphere

$$\left(C_f = \tau_w / \tfrac{1}{2}\rho U_\infty^2,\ \mathrm{Re}_R = \frac{U_\infty R}{\nu}\right)$$

Wedge Parameter Λ	$\frac{x}{R}$	B = 1			B = 4			B = 10		
		Present 1 term	Results 3 terms	Hoskin[10] 4 terms	Present 1 term	Results 3 terms	Hoskin[10] 4 terms	Present 1 term	Results 3 terms	Hoskin[10] 4 terms
0.480	0.474	1.2485	1.2496	1.2497	1.8159	1.8170	1.8170	2.8153	2.8166	2.8165
0.400	0.951	1.8272	1.8403	1.8402	2.6217	2.6362	2.6359	4.0255	4.0444	4.0440
0.300	1.215	1.6797	1.7207	1.7203	2.3521	2.4023	2.4031	3.5466	3.6186	3.6218
0.200	1.374	1.3941	1.4780	1.4783	1.8754	1.9892	1.9953	2.7392	2.9144	2.9312
0.100	1.486	1.0814	1.2269	1.2336	1.3460	1.5644	1.5876	1.8314	2.1897	2.2451

Table 4 Values of Nu $Re_R^{-1/2}$ for a Rotating Sphere*

			Pr = 1				Pr = 10				Pr = 100		
B	Λ	x/R	Present 1 term	Results 3 terms	Chao and Greif [13]***	Chao [14]†	Present 1 term	Results 3 terms	Chao and Greif [13]	Chao [14]	Present 1 term	Results 3 terms	Chao and Greif[13]
1	0.500	0.0	.9588	.9588	.8904	.9589	2.2363	2.2363	2.2106	2.2364	4.9877	4.9878	4.9773
	0.400	0.951	.8026	.7998	.7567	.7792**	1.8593	1.8520	1.8350	1.8571**	4.1326	4.1151	4.1084
	0.300	1.215	.7020	.6961	.6716	.7064**	1.6129	1.5994	1.5914	1.6029**	3.5702	3.5375	3.5424
	0.200	1.374	.6256	.6171	.6078	.6275**	1.4226	1.4084	1.4099	1.4173**	3.1325	3.0981	3.1208
	0.100	1.486	.5608	.5510	.5560	.5557**	1.2573	1.2551	1.2650	1.2600**	2.7482	2.7444	2.7855
10	0.500	0.0	1.1141	1.1141	.6933	1.0914**	2.7718	2.7718	2.6376	2.7635	6.3844	6.3845	6.3358
	0.400	0.951	.9282	.9218	.6245	.9264**	2.2872	2.2695	2.1719	2.2722**	5.2440	5.2019	5.1696
	0.300	1.215	.8051	.7904	.5809	.8042**	1.9604	1.9234	1.8643	1.9363**	4.4700	4.3812	4.3873
	0.200	1.374	.7070	.6825	.5440	.7223**	1.6937	1.6434	1.6264	1.6640**	3.8333	3.7114	3.7899
	0.100	1.486	.6145	.5776	.5087	.5905**	1.4349	1.3912	1.4315	1.4180**	3.2090	3.1053	3.3050
					Siekmann [11] Blasius type series, 4 terms								
4	0.500	0.0	1.0214	1.0214	1.0214								
	0.400	0.951	.8529	.8484	.8485								
	0.300	1.215	.7430	.7328	.7362								
	0.200	1.374	.6575	.6414	.6528								
	0.100	1.486	.5811	.5593	.5868								

* More extensive data are available in [17]
** Euler Summation
*** Two term velocity prolife with the resulting series expanded in terms of x/R
† Three term velocity representation with the series in terms of ϵ_n functions

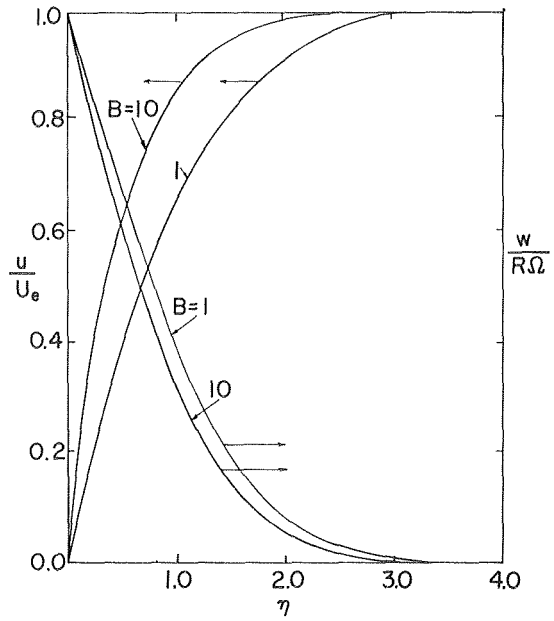

Fig. 1 U/U_e and $w/R\Omega$ versus η for $B = 1$ and 10 when $\Lambda = 0.3$ for a rotating sphere

$$C_f(\mathrm{Re}_x)^{1/2} = \frac{\tau_w}{\frac{1}{2}\rho(C^2+\Omega^2)x^2}\left[\frac{(C^2+\Omega^2)^{1/2}x^2}{\nu}\right]^{1/2}$$

$$= \frac{2^{3/2}}{(1+B)^{3/4}}[f_0''(\Lambda,0)]_{\Lambda=0.5} \quad (49)$$

where $C = 2U_\infty/\pi R$ and $\mathrm{Re}_x = [(C^2+\Omega^2)^{1/2}x^2/\nu]^{1/2}$. The values of $C_f(\mathrm{Re}_x)^{1/2}$ calculated from (49) for $B = 0$, 1, 4, and ∞ are 2.6239, 1.8717, 1.3734, and 1.020, respectively, as versus Tifford and Chu's values of 2.61, 1.83, 1.38, and 1.03. The data for two extreme cases, i.e., $B = 0$ and $B \to \infty$ are calculated using the values of a reported by Hannah [1]. Her a relates to our $[f_0''(\Lambda,0)]_{\Lambda=0.5}$ as

$$[f_0''(\Lambda,0)]_{\Lambda=0.5} = 2^{1/2}(1+B)^{3/4}a$$

The agreement is good between the two calculations.
If we compared the formula with that of Hannah in [1], our $[g_0'(\Lambda,0)]_{\Lambda=.5}$ is found to be related to b given in [1] by

Table 5 Comparison of Nusselt Number for forced flow against a rotating disk

Pr	B*	Present Analysis (50)	Tien and Tsuji [4]	Chao and Greif [13] Two term velocity representation	Chao [14] Three term velocity representation
1	1	0.6583	0.658	0.6113	0.659
	4	0.5577	0.557	0.432	0.548
10	1	1.5354	1.535	1.518	-
	4	1.3410	1.340	1.297	-

* $B^{1/2}$ is denoted by ω/C in [4, 13].

$$[g_0'(\Lambda,0)]_{\Lambda=.5} = 2^{-1/2}(1+B)^{1/4}b$$

Our values of $[g_0'(\Lambda,0)]_{\Lambda=.5}$ are in close agreement to b by the above relation.

The local Nusselt number may be written for a rotating disk in the form defined by Tien and Tsuji [4] as

$$\mathrm{Nu} = \frac{q_w \nu^{1/2}}{k(T_w - T_\infty)(C^2+\Omega^2)^{1/4}} = 2^{1/2}(1+B)^{-1/4}[\theta_0'(\Lambda,0)]|_{\Lambda=.5} \quad (50)$$

Equation (50) is similar to (17) of [4] and only differs by the factor $2^{1/2}(1+B)^{-1/4}$. A numerical comparison for Pr = 1 and 10 is given in Table 5, and it can be seen that our results agree with those of Tien and Tsuji to three decimal places. Using a quadratic velocity profile, Chao and Greif [13] reported an expression for the disk problem and their data are also given in Table 5. The discrepancy between the results indicates that, as for the rotating sphere, the quadratic velocity profile is not sufficient for small Prandtl numbers and large rotation parameters. Again, if the three-term velocity results are used, a significant improvement is seen.

It is of interest to compare our results for a rotating disk with the experimental data obtained by Koong and Blackshear [8]. For this purpose, values of $\theta_0'(0)$ for Pr = 2.4 were calculated, yielding 0.77005, 0.83102, and 0.92067 for $B = 1$, 4, and 10, respectively. The comparison is made in Fig. 2 with the Nusselt number defined in [8] plotted versus the rotational Reynolds number with several free stream velocity values, U_∞, that were used in their experiment being a parameter. In

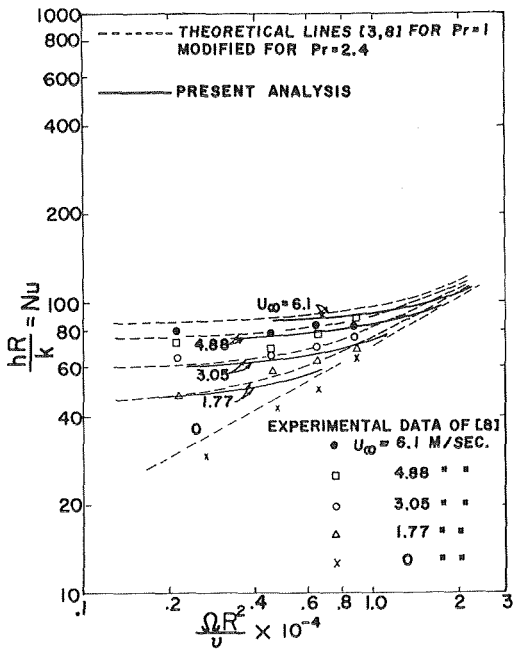

Fig. 2 Comparison of present analysis with experimental results for a rotating disk in forced flow. Pr = 2.4

their original paper, a comparison was also made with the theoretical results of Schlichting and Truckenbrodt [3] to which the appropriate Reynolds analogy for Pr = 1 had been applied and modified for Pr = 2.4. These results are also included in Fig. 2 as dotted lines. For a given U_∞, the Schlichting and Truckenbrodt data deviate from our results, especially for larger values of the rotational Reynolds number. This discrepancy may be attributed either to the integral method used in their analysis or to the modification of their data from a Prandtl number of 1.0 to 2.4 by the use of a correction which brings the $U_\infty = 0$ results into agreement with those of Sparrow and Gregg [20]. The experimental data of [8] quantitatively agree with our data except for the case of U_∞ = 6.1 M/s (20 ft/s). This discrepancy also becomes larger as the rotational Reynolds number increases.

References

1 Hannah, D. M., "Forced Flow Against a Rotating Disk," British Aeronautical Research Council Reports and Memoranda No. 2772, 1947.

2 Tifford, A. N., and Chu, S. T., "On the Flow Around a Rotating Disc in a Uniform Stream," *Journal of Aero. Sci.*, Vol. 19, 1952, pp. 184–285.

3 Schlichting, H., and Truckenbrodt, E., "The Flow Around a Rotating Disc in a Uniform Stream," *Reader's Forum, Journal of Aero. Sci.*, Vol. 18, No. 9, Sept. 1951, pp. 639–640.

4 Tien, C. L., and Tsuji, I. J., "Heat Transfer by Laminar Forced Flow Against a Non-Isothermal Rotating Disk," *Int. Journal of Heat and Mass Transfer*, Vol. 7, 1964, p. 247.

5 Mabuchi, I., Tanaka, T., and Sakakaibara, "Studies on the Convective Heat Transfer from a Rotating Disk," *Bulletin of JSME*, Vol. 10, No. 37, 1967.

6 Liu, K. T., and Stewart, W. E., "Asymptotic Solutions for Forced Convection from a Rotating Disk," *Int. Journal of Heat and Mass Transfer*, Vol. 14, 1971.

7 Koh, J. C. Y., and Price, J. F., "Nonsimilar Boundary Layer Heat Transfer of a Rotating Cone in Forced Flow," ASME JOURNAL OF HEAT TRANSFER, Vol. 89, 1967, p. 139.

8 Koong, S. S., and Blackshear, P. L., "Experimental Measurements of Mass Transfer from a Rotating Disk in a Uniform Stream," ASME JOURNAL OF HEAT TRANSFER, Vol. 87, 1965, p. 442.

9 Tien, C. L., and Tsuji, I. J., "A Theoretical Analysis of Laminar Forced Flow and Heat Transfer About A Rotating Cone," ASME JOURNAL OF HEAT TRANSFER, Vol. 87, 1965, p. 184.

10 Hoskin, N. E., "The Laminar Boundary Layer on a Rotating Sphere," in H. Görtler and W. Tollmien, 50 Jahre Grenzschichtforchung (*Friedr. Vieweg u. Sohn, Braunschweig*), 1955, pp. 127–131.

11 Siekmann, J., "The Calculation of the Thermal Laminar Boundary Layer on Rotating Sphere," Z. Angew. Math. Phys., Vol. 13, 1962, p. 468.

12 Görtler, H., "A New Series for the Calculation of Steady Laminar Boundary Layer Flows," *Journal of Math. Mech.*, Vol. 16, 1957, pp. 1–66.

13 Chao, B. T., and Greif, R., "Laminar Forced Convection Over Rotating Bodies," ASME JOURNAL OF HEAT TRANSFER, Vol. 96, 1974, pp. 463–466.

14 Chao, B. T., "An Analysis of Forced Convection Over Nonisothermal Surfaces via Universal Functions," Recent Advances in Engineering Science—Proceedings of the 14th Annual Meeting of the Society of Engineering Science, Lehigh Univ., 1977, pp. 471–483.

15 Merk, H. J., "Rapid Calculations for Boundary Layer Transfer Using Wedge Solutions and Asymptotic Expansions," *Journal of Fluid Mech.*, Vol. 5, 1959, pp. 460–480.

16 Chao, B. T., and Fagbenle, R. O., "On Merk's Method of Calculating Boundary Layer Transfer," *Int. Journal of Heat and Mass Transfer*, Vol. 17, 1974, pp. 223–240.

17 Lee, M. H., "Momentum and Heat Transfer Through Laminar Boundary Layers Over Rotating Bodies," Ph.D. Thesis, Engineering Science, College of Engineering, The University of Toledo, Toledo, Ohio, 1976.

18 Meksyn, D., *New Methods in Laminar Boundary Layer Theory*, Chapter 7, Pergamon Press, Oxford, 1961.

19 Private Communication, Prof. B. T. Chao, Dept. of Mechanical and Industrial Engineering, University of Illinois at Champaign-Urbana.

20 Sparrow, E. M., and Gregg, J. L., "Heat Transfer from a Rotating Disk to Fluids of Any Prandtl Number," ASME JOURNAL OF HEAT TRANSFER, Vol. 81, 1959, pp. 249–251.

J. R. Cannon[1]
Department of Mathematics,
The University of Texas,
Austin, Tex. 78712

P. C. DuChateau
Department of Mathematics,
Colorado State University,
Fort Collins, Colo. 80521

Determination of Unknown Coefficients in Parabolic Operators from Overspecified Initial-Boundary Data

Application of some asymptotic boundary behavior results for solutions of nonlinear parabolic initial boundary value problems is made to the determination of unknown coefficients and parameters in parabolic operators from overspecified boundary data. Some numerical results on the determination of parameters is presented and discussed.

1 Introduction

Let $u = u(x, t)$ denote the solution to the initial boundary value problem of the first kind

$$\frac{\partial u}{\partial t} = a(u)\frac{\partial^2 u}{\partial x^2}, \quad 0 < x < 1, \quad 0 < t \le T,$$
$$u(x, 0) = 0, \quad 0 \le x \le 1,$$
$$u(0, t) = f_1(t), \quad 0 < t \le T,$$
$$u(1, t) = f_2(t), \quad 0 < t \le T, \tag{1.1}$$

and let $v = v(x, t)$ denote the solution to the initial boundary value problem of the second kind

$$\frac{\partial v}{\partial t} = a(v)\frac{\partial^2 v}{\partial x^2}, \quad 0 < x < 1, \quad 0 < t \le T,$$
$$v(x, 0) = 0, \quad 0 \le x \le 1,$$
$$\frac{\partial v}{\partial x}(0, t) = g_1(t), \quad 0 < t \le T,$$
$$\frac{\partial v}{\partial x}(1, t) = g_2(t), \quad 0 < t \le T, \tag{1.2}$$

where $a = a(\cdot)$ is a known positive smooth function defined on $(-\infty, \infty)$ and where f_i, g_i, $i = 1, 2$, are known smooth functions which are defined on $0 \le t \le T$ and such that $f_i(0) = g_i(0) = 0$, $i = 1, 2$. In addition, let $U = U(x, t)$ denote the bounded solution of

$$\frac{\partial U}{\partial t} = a(U)\frac{\partial^2 U}{\partial x^2}, \quad 0 < x < \infty, \quad 0 < t \le T,$$
$$U(x, 0) = 0, \quad 0 \le x < \infty,$$
$$U(0, t) = f_1(t), \quad 0 < t \le T, \tag{1.3}$$

and let $V = V(x, t)$ denote the bounded solution of

$$\frac{\partial V}{\partial t} = a(V)\frac{\partial^2 V}{\partial x^2}, \quad 0 < x < \infty, \quad 0 < t \le T,$$
$$V(x, 0) = 0, \quad 0 \le x < \infty,$$
$$\frac{\partial V}{\partial x}(0, t) = g_1(t), \quad 0 < t \le T. \tag{1.4}$$

By the term *solution* we mean functions which possess continuous first derivatives with respect to x and t in the closure of the domain under consideration, which possess a continuous second derivative with respect to x in the considered domain, and which satisfy the given equation and specified initial and boundary conditions.

We assume the solutions u, v, U, and V exist and are unique. See [2, 5][2] for such results.

Setting

$$\alpha = a(0), \tag{1.5}$$

[1] This research was supported in part by the National Science Foundation.

Contributed by the Heat Transfer Division for publication in the JOURNAL OF HEAT TRANSFER. Manuscript received by the Heat Transfer Division November 9, 1977.

[2] Numbers in brackets designate References at end of paper.

let $u_\alpha = u_\alpha(x, t)$ denote the classical solution of the problem

$$\frac{\partial u_\alpha}{\partial t} = \alpha \frac{\partial^2 u_\alpha}{\partial x^2}, \quad 0 < x < 1, \quad 0 < t \le T,$$
$$u_\alpha(x, 0) = 0, \quad 0 \le x \le 1,$$
$$u_\alpha(0, t) = f_1(t), \quad 0 < t \le T,$$
$$u_\alpha(1, t) = f_2(t), \quad 0 < t \le T, \tag{1.6}$$

and let $v_\alpha = v_\alpha(x, t)$ denote the classical solution of the problem

$$\frac{\partial v_\alpha}{\partial t} = \alpha \frac{\partial^2 v_\alpha}{\partial x^2}, \quad 0 < x < 1, \quad 0 < t \le T,$$
$$v_\alpha(x, 0) = 0, \quad 0 \le x \le 1,$$
$$\frac{\partial v_\alpha}{\partial x}(0, t) = g_1(t), \quad 0 < t \le T,$$
$$\frac{\partial v_\alpha}{\partial x}(1, t) = g_2(t), \quad 0 < t \le T. \tag{1.7}$$

The existence and uniqueness of the classical solutions u_α and v_α can be found in [9]. Also, let $U_\alpha = U_\alpha(x, t)$ denote the bounded classical solution of

$$\frac{\partial U_\alpha}{\partial t} = \alpha \frac{\partial^2 U_\alpha}{\partial x^2}, \quad 0 < x < \infty, \quad 0 < t \le T,$$
$$U_\alpha(x, 0) = 0, \quad 0 \le x < \infty,$$
$$U_\alpha(0, t) = f_1(t), \quad 0 \le t \le T, \tag{1.8}$$

and let $V_\alpha = V_\alpha(x, t)$ denote the bounded classical solution of

$$\frac{\partial V_\alpha}{\partial t} = \alpha \frac{\partial^2 V_\alpha}{\partial x^2}, \quad 0 < x < \infty, \quad 0 < t \le T,$$
$$V_\alpha(x, 0) = 0, \quad 0 \le x < \infty,$$
$$\frac{\partial V_\alpha}{\partial x}(0, t) = g_1(t), \quad 0 < t \le T. \tag{1.9}$$

Formulas for the solution of (1.8) and the solution of (1.9) can also be found in [9].

In [1], we have shown that under certain assumptions upon the data f_i, and g_i, $i = 1, 2$, it follows that

$$\lim_{t \downarrow 0} \left\{ \frac{\partial u}{\partial x}(0, t) \Big/ \frac{\partial U}{\partial x}(0, t) \right\} = \lim_{t \downarrow 0} \left\{ \frac{\partial u}{\partial x}(0, t) \Big/ \frac{\partial u_\alpha}{\partial x}(0, t) \right\}$$
$$= \lim_{t \downarrow 0} \left\{ \frac{\partial u}{\partial x}(0, t) \Big/ \frac{\partial U_\alpha}{\partial x}(0, t) \right\} = \lim_{t \downarrow 0} \left\{ \frac{\partial U}{\partial x}(0, t) \Big/ \frac{\partial U_\alpha}{\partial x}(0, t) \right\}$$
$$= \lim_{t \downarrow 0} \left\{ \frac{\partial u_\alpha}{\partial x}(0, t) \Big/ \frac{\partial U_\alpha}{\partial x}(0, t) \right\} = 1, \tag{1.10}$$

and that

$$\lim_{t \downarrow 0} \frac{v(0, t)}{V(0, t)} = \lim_{t \downarrow 0} \frac{v(0, t)}{v_\alpha(0, t)} = \lim_{t \downarrow 0} \frac{v(0, t)}{V_\alpha(0, t)}$$
$$= \lim_{t \downarrow 0} \frac{V(0, t)}{V_\alpha(0, t)} = \lim_{t \downarrow 0} \frac{v_\alpha(0, t)}{V_\alpha(0, t)} = 1. \tag{1.11}$$

The proof of these results [1] employed a use of the maximum principle coupled with classical formulas for the heat equation.

The purpose of this paper is to apply the results (1.10) and (1.11). In the next section, we show how these results apply to a problem of determining an unknown coefficient in a parabolic operator from overspecified boundary data. In the third section, we apply these results to the determination of unknown parameters in a parabolic operator from overspecified boundary data. We conclude the paper with a discussion in the fourth section of some numerical experiments on the determination of unknown parameters in a parabolic operator.

2 Application to the Determination of an Unknown Coefficient

We consider the problem of finding the pair of functions $w = w(x, t)$ and $b = b(\cdot)$, where b is defined over the interval $I = [\inf w, \sup w]$ and is positive throughout I, such that (w, b) satisfies

$$\frac{\partial w}{\partial t} = \frac{\partial}{\partial x}\left(b(w) \frac{\partial w}{\partial x} \right), \quad 0 < x < \infty, \quad 0 < t \le T,$$
$$w(x, 0) = 0, \quad 0 \le x < \infty,$$
$$w(0, t) = f(t), \quad 0 < t \le T,$$
$$b(f(t)) \frac{\partial w}{\partial x}(0, t) = g(t), \quad 0 < t \le T, \tag{2.1}$$

where we assume that both f and g are smooth functions with $f' > 0$, $g' < 0$, $f(0) = 0$ and $g(0) = 0$. We do not give a precise definition of a solution of (2.1) since to solve (2.1) is beyond the scope of this presentation. In any case a weaker formulation of (2.1) can be obtained through the transformation

$$z = B(w) = \int_0^w b(\xi)\, d\xi. \tag{2.2}$$

Since $b > 0$, B is monotone increasing and B^{-1} exists. Equation (2.1) reduces to

$$\frac{\partial z}{\partial t} = b(B^{-1}(z)) \frac{\partial^2 z}{\partial x^2}, \quad 0 < x < \infty, \quad 0 < t \le T,$$
$$z(x, 0) = 0, \quad 0 \le x < \infty,$$
$$z(0, t) = B(f(t)), \quad 0 < t \le T,$$
$$\frac{\partial z}{\partial x}(0, t) = g(t), \quad 0 < t \le T. \tag{2.3}$$

Clearly any reasonable solution of (2.1) is a solution of (2.3) since less is required of b in (2.3) than in (2.1). Throughout this discussion, we shall assume that a solution of (2.3) is a smooth positive function b and a smooth function z which together satisfy (2.3).

Our purpose in this discussion is the application of the results of (1.10) and (1.11) to determine a necessary compatibility relationship between f and g. Set

$$\beta = b(0). \tag{2.4}$$

Since $z = 0$ if and only if $w = 0$, it follows that

$$b(B^{-1}(0)) = b(0) = \beta. \tag{2.5}$$

An application of (1.11) [see Theorem 6, 1] yields

$$\lim_{t \downarrow 0} \frac{B(f(t))}{V(0, t)} \cdot \frac{V(0, t)}{V_\beta(0, t)} = \lim_{t \downarrow 0} \frac{B(f(t))}{V_\beta(0, t)} = 1. \tag{2.6}$$

Consequently, we can define

$$h(t) = \frac{B(f(t))}{V_\beta(0, t)} \tag{2.7}$$

and note that $\lim_{t \downarrow 0} h(t) = 1$. Also,

$$h(t) = \frac{f(t)}{V_\beta(0, t)} \cdot \frac{1}{f(t)} B(f(t)), \tag{2.8}$$

and

$$\frac{f(t)}{V_\beta(0, t)} = h(t) \left\{ \frac{1}{f(t)} B(f(t)) \right\}^{-1}. \tag{2.9}$$

Since

$$\lim_{t \downarrow 0} h(t) = 1 \quad \text{and} \quad \lim_{t \downarrow 0} \frac{1}{f(t)} B(f) = \beta$$

we see that necessarily

$$\lim_{t \downarrow 0} \frac{f(t)}{V_\beta(0, t)} = \beta^{-1}. \tag{2.10}$$

Substituting

$$V_\beta(0, t) = -\beta^{1/2} \pi^{-1/2} \int_0^t \frac{g(\tau)}{\sqrt{(t - \tau)}}\, d\tau$$

into (2.10), we obtain

$$\beta = \left[\lim_{t\downarrow 0} \pi^{1/2} f(t) \left\{ -\int_0^t \frac{g(\eta)d\eta}{\sqrt{t-\eta}} \right\}^{-1} \right]^{-2}. \tag{2.11}$$

Theorem A

For a solution of (2.3) to exist with a b which is continuous and positive at zero, it is necessary that the

$$\lim_{t\downarrow 0} \pi^{1/2} f(t) \left\{ -\int_0^t \frac{g(\eta)d\eta}{\sqrt{t-\eta}} \right\}^{-1} \tag{2.12}$$

exists and is positive. If the limit (2.12) exists and is positive, then the value of b at zero is necessarily given by (2.11).

3 The Determination of Parameters in a Parabolic Operator

We consider the problem of determining the function $w = w(x, t)$ and the function $b(w) = \gamma + \mu w$, $\gamma > 0$, such that (w, b) satisfies the overdetermined system

$$\frac{\partial w}{\partial t} = \frac{\partial}{\partial x}\left(b(w)\frac{\partial w}{\partial x}\right), \quad 0 < x < 1/2, \quad 0 < t \le T,$$

$$w(x, 0) = 0, \quad 0 \le x \le 1/2,$$

$$w(0, t) = f(t), \quad 0 < t \le T,$$

$$w(1/2, t) = 0, \quad 0 < t \le T,$$

$$b(f(t))\frac{\partial w}{\partial x}(0, t) = g(t), \quad 0 < t \le T, \tag{3.1}$$

where we assume that both f and g are smooth functions with $f' > 0$, $g' < 0$, $f(0) = g(0) = 0$. Under the transformation

$$z = B(w) = \int_0^w b(\xi)d\xi, \tag{3.2}$$

(3.1) becomes

$$\frac{\partial z}{\partial t} = \sqrt{\gamma^2 + 2\mu z}\,\frac{\partial^2 z}{\partial x^2}, \quad 0 < x < 1/2, \quad 0 < t \le T,$$

$$z(x, 0) = 0, \quad 0 \le x \le 1/2,$$

$$z(1/2, t) = 0, \quad 0 < t \le T,$$

$$z(0, t) = \gamma f(t) + \frac{\mu}{2}[f(t)]^2, \quad 0 < t \le T,$$

$$\frac{\partial z}{\partial x}(0, t) = g(t), \quad 0 < t \le T. \tag{3.3}$$

We focus our attention upon determining the parameters γ and μ from the overspecification of boundary data in (3.3).

Now the function

$$z_\gamma(x, t) = -\int_0^t M(x, \gamma(t-\eta))g(\eta)\gamma d\eta + \int_0^t M(x-1, \gamma(t-\eta))g(\eta)\gamma d\eta \tag{3.4}$$

where

$$M(\xi, \sigma) = \pi^{-1/2}\sigma^{-1/2} \sum_{n=-\infty}^{\infty} \exp\left\{-\frac{(\xi+2n)^2}{4\sigma}\right\}, \quad \sigma > 0,$$

solves the problem

$$\frac{\partial z_\gamma}{\partial t} = \gamma\frac{\partial^2 z}{\partial x^2}, \quad 0 < x < 1/2, \quad 0 < t \le T,$$

$$z_\gamma(x, 0) = 0, \quad 0 \le x \le 1/2,$$

$$z_\gamma(1/2, 0) = 0, \quad 0 < t \le T,$$

$$\frac{\partial z_\gamma}{\partial x}(0, t) = g(t), \quad 0 < t \le T, \tag{3.5}$$

which influenced our choice of interval $0 < x < 1/2$ to consider in this section.

An application of (1.11) yields the result

$$\lim_{t\downarrow 0} \frac{z(0, t)}{Z_\gamma(0, t)} = 1, \tag{3.6}$$

where Z_γ is the bounded solution of

$$\frac{\partial Z_\gamma}{\partial t} = \gamma\frac{\partial^2 Z_\gamma}{\partial x^2}, \quad 0 < x < \infty, \quad 0 < t \le T,$$

$$Z_\gamma(x, 0) = 0, \quad 0 < x < \infty,$$

$$\frac{\partial Z_\gamma}{\partial x}(0, t) = g(t), \quad 0 < t \le T. \tag{3.7}$$

Actually, the employment of (3.6) has already been made in Theorem A of Section 2. From this we see that

$$\gamma = \left[\lim_{t\downarrow 0} \pi^{1/2} f(t) \left\{ -\int_0^t \frac{g(\eta)d\eta}{\sqrt{t-\eta}} \right\}^{-1} \right]^{-2}, \tag{3.8}$$

provided that

$$\lim_{t\downarrow 0} \pi^{1/2} f(t) \left\{ -\int_0^t \frac{g(\eta)d\eta}{\sqrt{t-\gamma}} \right\}^{-1} \tag{3.9}$$

exists and is positive. Hence, we have available the necessary condition on the data to determine one of the unknown parameters. We suppose that the limit in (3.9) exists and is positive. This determines γ and we can turn our attention to μ. Considering the equation

$$z(0, t) = \gamma f(t) + \frac{\mu}{2}(f(t))^2, \tag{3.10}$$

which results from substituting $w(0, t) = f(t)$ into (3.2) and performing the integration, we employ the fact that z depends upon μ to rewrite (3.10) as

$$\mu = 2\left\{\frac{z(0, t; \mu)}{(f(t))^2} - \frac{\gamma}{f(t)}\right\}, \tag{3.11}$$

where $z(0, t)$ has been written as $z(0, t; \mu)$ to reflect its dependence upon μ. Thus, the transformation

$$T\mu = 2\left\{\frac{z(0, t_*; \mu)}{(f(t_*))^2} - \frac{\gamma}{f(t_*)}\right\} \tag{3.12}$$

can be defined for a t_* at which f is different from zero. Elementary applications of the maximum principle [2, 3, 6, 7] yield the fact that $T\mu$ is continuous with respect to μ and that

$$|z(0, t_*; \mu)| \le \sup_{0\le t\le t_*} |g(t)|. \tag{3.13}$$

Hence, $T\mu$ is continuous and bounded uniformly in μ. Thus, the Brower fixed point theorem [8] may be applied and yields the existence of solutions of (3.11) for $t = t_*$. Uniqueness can be obtained from considering

$$\delta = \frac{(f(t_*))^2}{2} - \frac{\partial z}{\partial \mu}(0, t_*, \mu), \tag{3.14}$$

where

$$\delta \equiv \frac{d}{d\mu}(T\mu). \tag{3.15}$$

From (3.12), it is clear that the bound on $T\mu$ diminishes as $f(t_*)$ grows. Consequently, since $\partial z/\partial\mu(0, t_*, \mu)$, which depends only on g, is bounded on compact μ intervals, it follows that for $f(t_*)$ sufficiently large that $\delta > 0$ for μ throughout the interval into which μ is mapped by $T\mu$. Hence, $T\mu$ is monotone increasing and there is one and only one fixed point of (3.12). We can summarize the above as follows.

Theorem B

If $f' > 0$, $g' < 0$, $f(0) = g(0) = 0$ and

$$\lim_{t\downarrow 0} \pi^{1/2} f(t) \left\{ -\int_0^t \frac{g(\eta)d\eta}{\sqrt{t-\eta}} \right\}^{-1}$$

exists and is positive, then for the problem (3.3) γ is uniquely deter-

mined by (3.8). If the equation (3.10) is considered at only one point $t_* > 0$, then μ exists and is also unique if $f(t_*)$ is sufficiently large.

Remark

It is easy to extend the above results to the case of $b(w) = \Sigma_{n=0}^{N} c_n w^n$, $c_0 > 0$. In particular, c_0 is obtained via the same limit process. The constants c_n, $n = 1, \ldots, N$, are obtained via consideration of N equations selected from the boundary condition

$$z(0, t; c_1, \ldots, c_N) = c_0 f(t) + \frac{c_1}{2}(f(t))^2 + \ldots + \frac{c_N}{(N+1)}(f(t))^{N+1} \tag{3.16}$$

and an application of the Brower fixed point theorem. Unicity is unresolved as yet.

4 Discussion of Some Numerical Experiments

In the previous two sections we have indicated how the asymptotic results (1.10) and (1.11) could be applied to the problem of determining unknown parameters γ and μ such that functions $b(w) = \gamma + \mu w$ and $w = w(x, t)$ satisfy the equation and auxiliary conditions of (3.1). This section is devoted to discussing the results of some numerical experiments in which the parameters γ and μ are determined from the overspecified data of (3.1). Here, we consider a method that does not require the taking of a limit as $t \to 0$.

Applying the transformation (3.2) brings the problem (3.1) into the form (3.3) and it is in this form that the problem is analyzed numerically. To be precise, we study the problem of finding unknown parameters μ and γ, (where $\gamma > 0$), and an unknown function $z = z(x, t; \mu, \gamma)$ which satisfy

$$\frac{\partial z}{\partial t} = \sqrt{\gamma^2 + 2\mu z(x,t)}\,\frac{\partial^2 z}{\partial x^2}, \quad 0 < x < \tfrac{1}{2}, \quad t > 0,$$

$$z(x, 0) = 0, \quad 0 < x < \tfrac{1}{2},$$

$$\frac{\partial z}{\partial x}(0, t) = g(t), \quad z(\tfrac{1}{2}, t) = 0, \quad t > 0, \tag{4.1}$$

and the equation (3.10) which results from substituting $w(0, t) = f(t)$ into (3.2) and performing the integration:

$$z(0, t_*; \mu, \gamma) = \gamma f(t_*) + \tfrac{1}{2}\mu(f(t_*))^2, \tag{4.2}$$

where t_* denotes a given, positive constant (i.e. a particular instant in time) and f, g denote the measured data functions which conform to the hypotheses of Theorem B and where the parametric dependence of z on μ and γ is indicated above and below by writing $z = z(x, t; \mu, \gamma)$.

The "data" in these numerical experiments are generated in the following way. In the first experiment, which we shall refer to as experiment A, a positive value for t_* is chosen and remains fixed throughout the experiment. So-called "true values" of the parameters μ, γ are chosen, say they are denoted by γ_* and μ_*, and a data function $g_1(t)$ is selected, conforming to the hypotheses of Theorem B. The problem (4.1) is then solved numerically for $z(x, t)$ and, in particular, a value for $z(0, t_*)$ is computed. Finally, (4.2) is solved for the remaining piece of data $f_1(t_*)$. This procedure automatically generates data $g_1(t), f_1(t_*)$ which is consistent with the hypotheses of Theorem B. *In practice, this data would be determined experimentally and the values of the parameters γ_* and μ_* would, of course, be unknown.*

We proceed now as if the parameter values γ_*, μ_* are, in fact, unknown and seek to determine them from the data $g_1(t), f_1(t_*)$. The determination is carried out as follows.

We know, of course, that if we solve (4.1) with the true values γ_*, μ_* for the parameters γ, μ then the solution $z(x, t)$ will satisfy (4.2). On the other hand, there may be other pairs of values (γ, μ) such that the corresponding solution of (4.1) $z(x, t; \mu, \gamma)$ satisfies (4.2). Thus (4.2) defines (implicitly) a relation between μ and γ. To be more precise, for a given positive value of γ, say γ_1, we will write

$$\mu_1 = F(\gamma_1) \tag{4.3}$$

provided

$$z(0, t_*; \mu_1, \gamma_1) = \gamma_1 f_1(t_*) + \tfrac{1}{2}\mu_1(f_1(t_*))^2. \tag{4.4}$$

A graph for the relation F of (4.3) can be generated numerically by choosing a positive value for γ, say γ_1, choosing (somewhat arbitrarily) a value for μ and subsequently solving (4.1) numerically. Except in the event of a very fortuitous guess for μ, the relation (4.4) will not now be satisfied. Therefore, keeping $\gamma = \gamma_1$ fixed, we adjust the value of μ and solve the problem (4.1) again numerically, repeating this process until a value $\mu = \mu_1$ is found such that (4.4) holds. Repetition of this procedure for a succession of values $\gamma_1, \gamma_2, \ldots$ generates a sequence of points $(\gamma_1, \mu_1), (\gamma_2, \mu_2), \ldots$ on the graph of the relation

$$\mu = F_1(\gamma; t_*; f_1, g_1). \tag{4.5}$$

Included somewhere in this graph is the point (γ_*, μ_*).

The function F_1 in this experiment is naturally dependent on the data f_1 and g_1. We can, in fact, exploit this dependence by repeating the entire procedure from the beginning, keeping the values of t_*, μ_*, γ_* but choosing a new data function $g_2(t)$. Of course this new function $g = g_2(t)$ must still conform to the hypotheses of Theorem B. We determine in the same way as before a value $f_2(t_*)$ and generate numerically a new function,

$$\mu = F_2(\gamma; t_*; f_2, g_2). \tag{4.6}$$

The two graphs have in common the (presumably) unique point (γ_*, μ_*).

Fig. 1 shows a plot of μ versus γ for two distinct choices of the data function $g(t)$; i.e. Fig. 1 shows the graphs of F_1 and F_2. In this experiment we chose $\gamma_* = 1.0$ and $\mu_* = .10$ and it is clear from the figure that (1.0, .10) is the unique point of intersection of the two graphs.

A second numerical experiment, which we shall refer to as experiment B, is conducted in the following way. True values γ_* and μ_* are chosen for the unknown parameters γ and μ and a data function $g(t)$ is selected. A positive value t_1 is chosen for t_* and the remaining piece of data $f(t_1)$ is determined as before. Then, in much the same way that we numerically generated the graph for F_1 of (4.5) we generate a graph for the relation

$$\mu = G_1(\gamma; t_1; f, g). \tag{4.7}$$

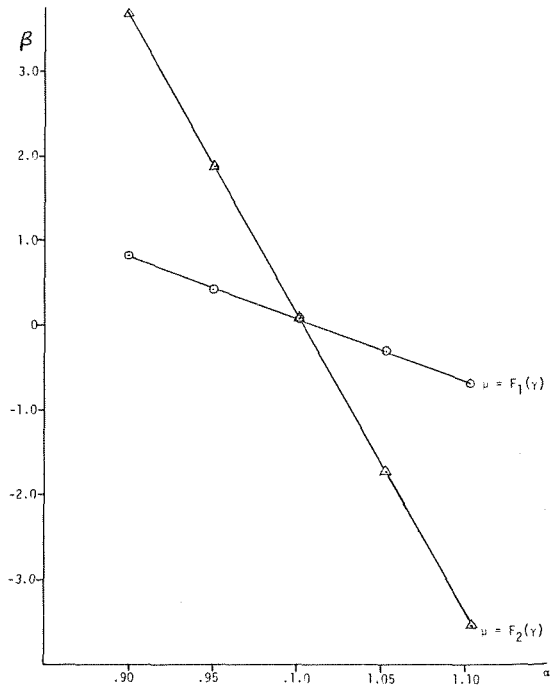

Fig. 1 μ versus γ for two choices of $g(t)$

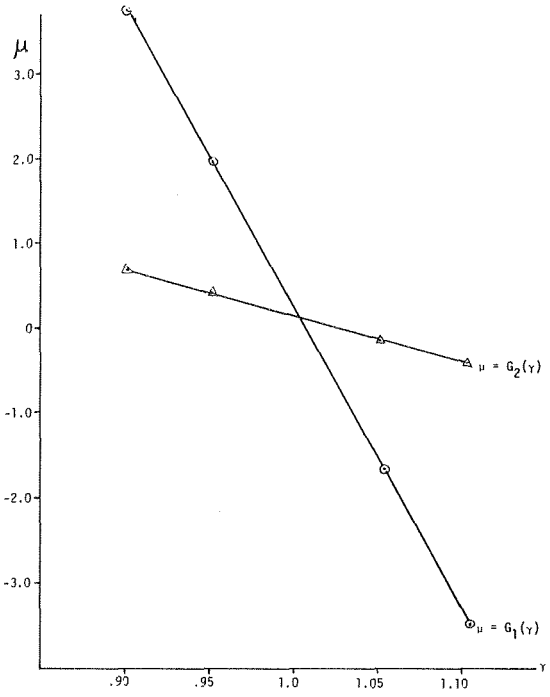

Fig. 2 μ versus γ for two choices of t_1

Then, keeping the same choices for μ_*, γ_* and g but selecting a new value t_2 for t_*, we determine the remaining piece of data $f(t_2)$ as before, and we generate a graph for a second relation

$$\mu = G_2(\gamma; t_2; f, g) \tag{4.8}$$

and, as before, the graphs of G_1 and G_2 contain the common point (γ_*, μ_*). Fig. 2 shows a plot of μ versus γ for two distinct choices of t_*; i.e., Fig. 2 shows the graphs of G_1 and G_2. The true values of μ and γ in experiment B were $\mu_* = .10$ and $\gamma_* = 1.0$. It is evident from Fig. 2 that (1.0, .10) is the unique point of intersection of the two graphs.

We should point out that implicit in the description of the numerical graph generating procedure is the assumption that

$$\left| \frac{\partial}{\partial \mu} (z(0, t_*)) \right| > 0. \tag{4.9}$$

From (4.2) we compute

$$\frac{\partial}{\partial \mu} [z(0, t_*)] = \tfrac{1}{2}(f(t_*))^2 + [\gamma + \mu f(t_*)] \frac{\partial}{\partial \mu} [f(t_*)].$$

Evaluating this expression numerically, it was found that (4.9) holds.

The results of experiments A and B indicate that determination of unknown parameters γ, μ from the overspecified data (4.2) is practically feasible. However, it is of interest to have some estimate of the sensitivity of the results to data error. In particular, it is of interest to know how errors in the measured values of $f(t_*)$, $g(t)$ affect the accuracy of the values for μ, γ determined by this procedure. Since the functional relationships between the involved quantities are quite complex, this analysis of error has been conducted numerically.

Table 1 displays the results for experiment A of inducing various levels of error in $f(t_*)$, in $g(t)$ and in both $f(t_*)$ and $g(t)$ simultaneously. Table 2 displays the analogous results for experiment B. The results in both cases indicate that the solutions (γ_*, μ_*) obtained by this procedure depend continuously on the data. Moreover, these results provide a basis for formulating a-posteriori estimates of the error.

Table 1 Error Level

$f_1(t_*)$	$f_2(t_*)$	$g_1(t)$	$g_2(t)$	γ	μ
0	0	0	0	1.0	.10
1%	1%	0	0	.981	.095
−1%	−1%	0	0	1.020	.105
−1%	1%	0	0	1.03	−.28
1%	−1%	0	0	.972	.46
2%	2%	0	0	.962	.11
−2%	−2%	0	0	1.038	.11
2%	−2%	0	0	1.058	−.60
−2%	2%	0	0	.94	.85
0	0	1%	1%	.985	.18
0	0	2%	2%	.967	.25
−2%	2%	2%	2%	1.03	−.30

Note: Error induced in $g(t)$ is a random function of t in the sense that the true $g(t)$ is multiplied by a factor $1 + \epsilon(t)$ where $\epsilon(t)$ is a random variable with mean zero and amplitude (positive, or negative) less than or equal to the value listed in the table.

Table 2 Error Level

$f(t_1)$	$f(t_2)$	$g(t)$	γ	μ
0	0	0	1.0	.10
1%	1%	0	.98	.125
−1%	1%	0	1.025	−.10
1%	−1%	0	.975	.30
0	0	2%	.99	.11
−1%	1%	1%	.983	.28

References

1 Cannon, J. R., and DuChateau, P. C., "Some Asymptotic Boundary Behavior of Solutions of Nonlinear Parabolic Initial Boundary Value Problems," to appear in *Journal of Mathematical Analysis and Applications*.

2 Friedman, A., *Partial Differential Equations of Parabolic Type*, Prentice Hall, Englewood Cliffs, N. J., 1964.

3 Friedman, A., "Remarks on the Maximum Principle for Parabolic Equations and its Applications," *Pacific J. Math.*, Vol. 8, 1958, pp. 201–211.

4 Kellogg, O. D., *Foundations of Potential Theory*, Dover Publications, N. Y., 1953, p. 265.

5 Ladyženskaja, O. A., Solonnikov, V. A., Vral'ceva, N. N., "Linear and Quasilinear Equations of Parabolic Type," *American Math. Soc.*, Providence, R. I., 1968.

6 Nirenberg, L., "A Strong Maximum Principle for Parabolic Equations," *Comm. Pure Appl. Math.*, Vol. 6, 1953, pp. 167–177.

7 Protter, M. H., and Weinberger, H. F., *Maximum Principles in Differential Equations*, Prentice Hall, Englewood Cliffs, N. J., 1967.

8 Vick, J., *Homology Theory*, Academic Press, N. Y., 1973, p. 28.

9 Widder, D. V., *The Heat Equation*, Academic Press, N. Y. 1975.

J. L. Hodges
The Hartford Graduate Center,
Hartford, Conn. 06120

R. C. Hoke
R. Bertrand
Exxon Research and Engineering Co.,
Linden, N. J. 07036

Prediction of Temperature Profiles in Fluid Bed Boilers[1]

Data acquired in the Exxon Research and Engineering Company's fluid bed boiler program indicate that the arrangement and orientation of internal boiler tubes has a strong effect on the measured bed temperature profile. Horizontally oriented tubes yield much steeper temperature gradients than do vertical tubes. Excessive vertical temperature gradients in coal fired fluid bed boilers can either limit coal feed rates or result in the formation of agglomerates of solid material which are destructive of bed internals. This study represents an attempt to understand the influence of orientation on vertical temperature profiles in fluid bed boilers. A back-mixing model for solids recirculation was developed and applied to the prediction of bed temperatures. Bubbling bed theory is not suitable for estimating solids circulation rates in pressurized beds of large particles with immersed tubes. However, by introducing the concept of a solids mixing height it was possible to estimate solid movement. The solids mixing height and vertical boiler tube dimensions were correlated in a manner which resulted in good agreement between theoretical and experimental bed temperature profiles. It is felt that this simple model may prove quite useful in the design of large scale commercial fluid bed boilers.

1 Introduction

The peak local temperature in fluid bed combustors is limited by the ash fusion temperature of the coal fired. Hot spots can result in the formation of clinkers which tend either to defluidize the bed or damage bed internals. Since an upper limit to bed temperature exists, a high temperature gradient will result in a low stack temperature, with a consequent reduction in the coal feed rate and the volumetric heat release rate within the bed.

Temperature profiles in fluid bed boilers are strongly influenced by the character of the bed internals. For example, it has been observed that beds with horizontally oriented cooling coils can have much steeper temperature gradients than beds with vertical coils [1]. There is a need, therefore, for a means of predicting expected temperature profiles within a fluid bed boiler of given coil geometry. This paper suggests one such method.

2 Development of the Theoretical Model

The temperature profile within a fluid bed combustor can depend on a number of physical and chemical phenomena: chemical reaction, heat and mass transfer in solid and gas phase, etc.

The theory of bubbling bed has been treated extensively in the literature [2–5]. According to the theory, the primary mechanism for axial solids movement is the entrainment of solids in the wake of an upward moving void, or "bubble." Mass conservation requires that solid material outside the wake (in the "emulsion" phase) rain downward through the upward moving emulsion gases. This is the means by which a pattern of solids recirculation is established within the bed. As the wake solids are carried upward there will be a continuous interchange (a cross-flow) of solids between emulsion and wake.

Since there is a net movement of gaseous material through the bed, both emulsion and bubble gases generally move upward (although gas back-mixing can occur at high superficial gas velocities). As with the solid material there is a continuous interchange between emulsion and bubble gas. Both solids and gas cross-flow tend to decrease with increasing superficial gas velocity.

Energy leaves the bed via a complex interaction between gas, solid and heat transfer surface [2, 3, 6]. Simultaneously, gas-gas and gas-solid contact will result, through combustion, in the liberation of heat throughout the bed [6–9]. The heat release rate will depend upon the rate at which fuel and oxidizer are brought together.

Recent studies have shown that diffusion is a major resistance for large carbon particles (greater than 1500 μ), whereas for smaller particles the combined effects of diffusion and chemical kinetics are important [10]. Except when running with a high excess air, there will generally not be enough oxygen in the emulsion gas to complete combustion. In this case the rate at which bubble gas is brought in contact with fuel (either in bubble phase, due to gas recirculation within the bubble wake, or in the emulsion phase due to bubble-emulsion-gas cross-flow) may influence the overall heat release rate.

It is clear that some simplifications will be necessary in order to develop a tractable theoretical model.

We have determined three distinct processes which affect overall

[1] This investigation was carried out under National Science Foundation Faculty Research participation Grant Number HES75-05125

Contributed by The Heat Transfer Division and presented at The ASME-AIChE Heat Transfer Conference, St. Louis, Missouri, August 9–11, 1976. Manuscript received by the Heat Transfer Division January 10, 1977. Paper No. 76-HT-66.

temperature levels, as well as the temperature profiles within the bed:

1 The extraction, or absorption of energy through heat transfer surface.
2 The release of energy throughout the bed due to the combustion of fuel.
3 The dispersal of energy throughout the bed as a result of solids and gas movement.

In summary, heat is released at the bottom of the bed and absorbed in the upper bed region. The rate at which energy is dispersed axially via solids movement determines the extent of the axial temperature gradient within the bed.

The analytical methods of treating each of the above mentioned is outlined as follows:

1 For the purpose of this analysis, experimentally determined values for the overall heat transfer coefficient were used in lieu of a detailed model for energy exchange between bed and boiler tube surface.
2 Heat release via combustion is a complex phenomenon, most likely involving mixing of fuel volatiles and air in the emulsion and bubble phases, gas-solid contact in both bubble and emulsion phases and chemical kinetics at the coal char surface. However, there is some experimental evidence to indicate that combustion in fluid bed reactors is restricted to a region near the coal feed point [11]. This would be particularly true for high volatile coals, since devolatilization and turbulent mixing are relatively fast processes. In contrast, the time scale for the combustion of the remaining char is comparatively long. However, the char combustion rate will go directly as the oxygen partial pressure, which is normally highest in the region near the distribution plate. When running with low excess air the oxygen concentration in the upper bed will be less by an order of magnitude than that near the coal feed point. Hence, even though the char is well-dispersed throughout the bed, most of the char will burn in the oxygen rich region near the distributor plate.
3 The dispersal of energy throughout the bed depends upon the flow characteristics of both solids and gas. A preliminary analysis, utilizing bubbling bed theory, indicated that under operating conditions typical of practical fluid bed boilers, solids recirculation rates are orders of magnitude higher than gas flow rates. The axial transfer of energy via direct gas convection is therefore less important than energy transfer due to solids movement. Gas flow, in that it influences solids movement, has a strong effect on axial energy transport. As a vehicle for direct energy transfer, the gas phase can be ignored. Neglecting gas phase energy transfer greatly simplifies the dispersion model since determination of heat transfer rates between bed solids and gas is not necessary.

The problem reduces to the prediction of solids transport rates and the use of those rates to determine the bed temperature profile. For this purpose a simple solids back-mixing model has been developed.

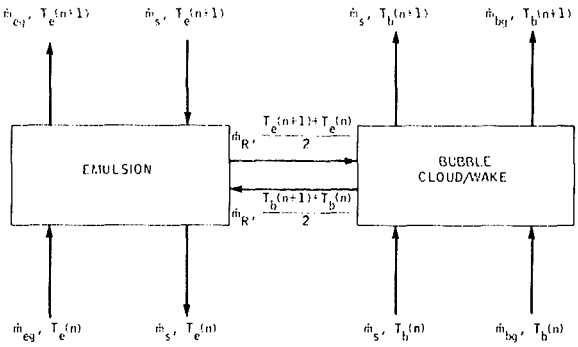

Fig. 1 Back-mixing model

3 Solids Back Mixing Model

The bed is divided into a set of N discreet horizontal sections. As indicated in Fig. 1, each section contains an emulsion phase and a bubble phase with associated cloud/wake.

Energy and mass flow into and out of a given section. Bubble gas moves upward, entering the control volume at some mass flow $\dot{m}_{bg}$. It leaves the volume at the same rate. Entering and leaving temperature are given by $T_b(n)$ and $T_b(n+1)$ respectively. Upward moving wake solids are carried through the volume at the solids recirculation rate $\dot{m}_s$. Differences in solids flow into and out of the control volume have been neglected. The bed composition is principally limestone (coal comprises about one percent of the bed material). Except during calcination, which occurs quickly when compared to the average stone residence time, the weight change of the stone is negligible and this assumption does not lead to serious error.

It has been assumed that wake solids and bubble gas are locally at the same temperature. As has been indicated, the actual choice for gas temperature is not critical since direct vertical gas phase energy transport is not significant compared to the solid.

Emulsion gas moves upward through the control volume at a mass flow $\dot{m}_{eg}$, entering at temperature $T_e(n)$ and leaving at $T_e(n+1)$.

Downward moving emulsion solids rain through the volume at the solids recirculation rate $\dot{m}_s$. Emulsion solids enter the volume at temperature $T_e(n+1)$ and leave at $T_e(n)$.

Solid material moves, within the control volume, from emulsion to wake at the solids cross-flow rate $\dot{m}_R$. This material enters the wake at the average emulsion temperature. Gas cross-flow has been neglected.

In this model it has been assumed that only the emulsion phase gives heat up to the cooling coils. While this assumption may not be particularly accurate, for the purpose of calculating heat loss to the cooling coils it has the advantage of being simple and does not lead to serious error, since the difference between the bubble and emulsion temperatures is usually small compared to the difference between the bed and cooling water temperatures.

Nomenclature

A = total cooling coil heat transfer surface
A_x = bed cross sectional area
C_g = specific heat of gas
C_s = specific heat of solids
d_b = bubble diameter
d_p = average particle diameter
h = overall bed heat transfer coefficient
h_m = mixing height
L_f = expanded bed height
L_{mf} = bed height at minimum fluidization
$\dot{m}_a$ = air flow rate
$\dot{m}_{bg}$ = bubble gas flow rate
$\dot{m}_c$ = coal feed rate
$\dot{m}_{eg}$ = emulsion gas flow rate
$\dot{m}_R$ = total bed cross-flow rate
$\dot{m}_{RL}$ = specific solids cross-flow rate
$\dot{m}_s$ = solids recirculation rate
Q_{ABS} = total rate of heat absorption by coils
Q_{IN} = heat input rate
T_a = inlet air temperature
T_b = bubble gas temperature
T_e = emulsion gas temperature
T_w = cooling water temperature
T_s = stack gas temperature
ΔH_c = heating value of coal
μ_g = gas viscosity
ρ_s = solids density
ρ_g = gas density
τ_R = solids sake residence time

An energy balance around a control volume containing bubble phase and associated cloud/wake yields

$$(\dot{m}_s C_s + \dot{m}_{bg} C_g)[T_b(n+1) - T_b(n)] + \frac{\dot{m}_R C_s}{2}[T_b(n+1) + T_b(n) - T_e(n+1) - T_e(n)] = 0 \quad (1)$$

An energy balance around a control volume containing emulsion phase yields

$$[\dot{m}_{eg} C_g + \dot{m}_s C_s][T_e(n+1) - T_e(n)] + \frac{\dot{m}_R C_s}{2}[T_e(n+1) + T_e(n) - T_b(n+1) - T_b(n)] = \dot{Q}_{ABS}(n) \quad (2)$$

defining the dimensionless parameters

$$\gamma = \frac{\dot{m}_R}{2\dot{m}_s} \qquad \phi = \frac{\dot{m}_{bg} C_g}{\dot{m}_s C_s} \qquad \theta = \frac{\dot{m}_{eg} C_g}{\dot{m}_s C_s}$$

and a normalized heat absorption

$$\dot{q}(n) = \frac{\dot{Q}_{ABS}(n)}{\dot{m}_s C_s}$$

gives

$$T_b(n+1) = \frac{1+\phi-\gamma}{1+\phi+\gamma} T_e(n) + \frac{\gamma}{1+\phi+\gamma}[T_e(n+1) + T_b(n)] \quad (3)$$

and

$$T_e(n+1) = \frac{\theta-\gamma-1}{\theta+\gamma-1} T_e(n) + \frac{\gamma}{\theta+\gamma-1}[T_b(n+1) + T_b(n)] + \frac{\dot{q}(n)}{\theta+\gamma-1} \quad (4)$$

The lower boundary condition is handled as follows. A control volume is constructed around the combustion zone, as indicated in Fig. 2. All heat release is assumed to be confined to this control volume.

Descending emulsion solids, having both given heat up to the boiler tubes and received energy via cross flow from hot ascending wake solids, enters the combustion zone at $T_e(1)$. If it is assumed that the thermal contact between emulsion solids and gas is good, the temperature of the emulsion gases leaving the combustion zone will be very close to $T_e(1)$. Upward moving wake solids and bubble gas leave the control volume at $T_b(1)$. Cool air enters at some initial air temperature T_a.

Applying the steady flow energy equation to this control volume;

$$Q_{in} = \dot{m}_c \Delta H_c = \dot{m}_{eg} C_g T_e(1) - \dot{m}_s C_s T_e(1) + \dot{m}_s C_s T_b(1) + \dot{m}_{bg} C_g T_b(1) - (\dot{m}_{eg} + \dot{m}_{bg}) C_g T_a \quad (5)$$

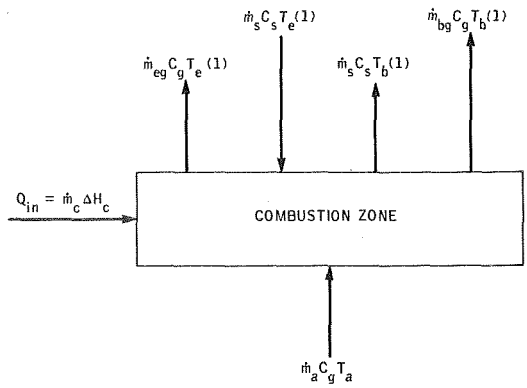

Fig. 2 Energy balance—combustion zone

and solving for $T_e(1)$,

$$T_e(1) = \frac{m_c \Delta H_c}{m_s C_s(\theta-1)} + \left(\frac{\theta+\gamma}{\theta-1}\right) T_a - \left(\frac{\gamma+1}{\theta-1}\right) T_c(1) \quad (6)$$

The dimensions of the combustion zone are somewhat arbitrary. In this analysis the combustion zone was assumed to extend from the distributor plate to the coal feed point. The model will not, of course, provide any information as to the temperature profile within the combustion zone. It simply defines the temperature at the zone boundaries. The treatment of the upper boundary condition follows. The leaving gas temperature is the average of the leaving bubble and emulsion temperatures.

$$T_s = \frac{\dot{m}_{eg} T_e(n) + \dot{m}_{bg} T_b(n)}{\dot{m}_{eg} + \dot{m}_{bg}} \quad (7)$$

The stack temperature may also be calculated from the overall heat balance

$$-\dot{m}_a C_g T_a + \dot{m}_a C_g T_s = \dot{m}_c \Delta H_c + Q_{ABS} \quad (8)$$

where

$$Q_{ABS} = hA(T_s - T_w) \quad (9)$$

Using the stack temperature in equation (9) in place of the average bed temperature greatly simplifies the problem and does not introduce serious error, providing bed temperature gradients are not too high.

For simplicity, entrance and exit gas flows were assumed equal. The exit gas flow will be about ten percent greater than the entrance gas flow. The effect of this assumption on the overall temperature profile will be small. The sensible heat loss due to solids leaving and entering the bed has also been neglected. Under normal conditions the solids feed rate would be much less than the solids circulation rate and this assumption will also lead to negligible error in the predicted temperature profile. Experimental heat balances on the Miniplant show the wall heat loss is low compared to heat absorption by the tubes and this loss has not been included in the overall heat balance. Then

$$T_s = \frac{\dot{m}_a C_g T_a + \dot{m}_c \Delta H_c - hAT_w}{\dot{m}_a C_g - hA} \quad (10)$$

equations (3), (4), (6), (7) and (10) completely specify the problem.

The equations were programmed for solution by digital computer. As a first step, the qualitative response of the system was evaluated over a range of operating conditions.

4 Back-Mixing Model—Parametric Analysis

The input data used in the calculations are based roughly on the operation of Exxon Research and Engineering Company's pressurized fluid bed boiler, referred to hereafter as the "Miniplant" [12]. Unless otherwise specified, these data are presented in Table 1.

Fig. 3 illustrates the effect of solids recirculation on bed temperature profile. As expected, increasing solids recirculation results in a flattening of the bed temperature profile.

Fig. 4 illustrates the effect of cross flow on bed temperature profile. The effect of increasing cross flow is to increase the bed temperature gradient. This result can be explained in the following manner. Solids recirculation, as defined, represents the flow, across an arbitrary horizontal plane, of either wake solids (in an upward direction) or

Table 1 Program input data

d_p	10^{-3} m
ρ_s	2250 kg/m^3
ρ_g	2.94 kg/m^3
μ_g	4.06×10^{-5} kg/m-s
A_x	0.08042 m^2
C_g	1009 Joule/kgK
ΔH_c	2.236×10^7 Joule/kg
T_w	438K
T_a	328K
C_s	962.8 Joule/K

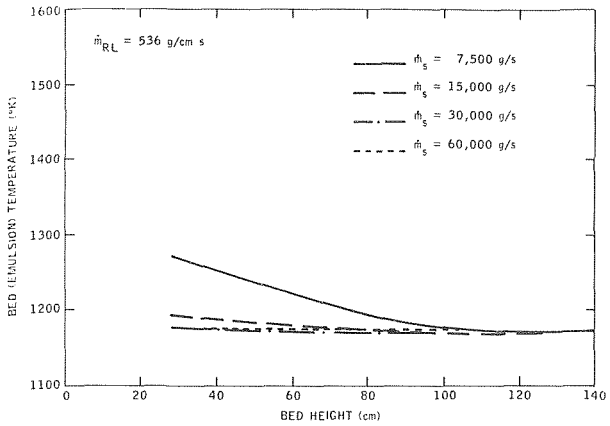

Fig. 3 Effect of solids recirculation on temperature distribution

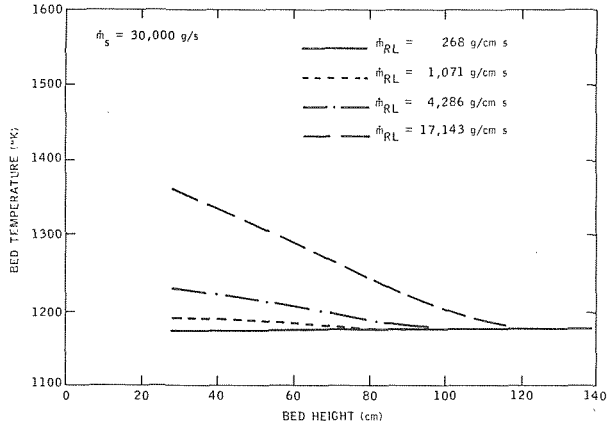

Fig. 4 Effect of solids interchange on temperature distribution

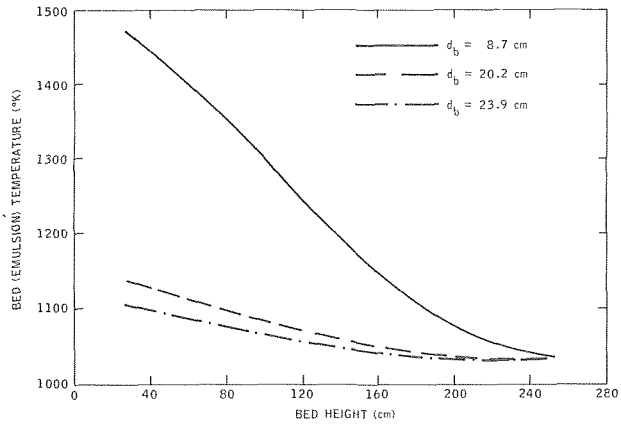

Fig. 5 Effect of bubble diameter on temperature profile

emulsion solids (in a downward direction). The solids cross flow, rather than representing the transfer of material *across* a horizontal plane, represents the movement of mass *between* two horizontal planes from one phase to another. The greater the distance separating the planes, the greater the cross flow. The parameter most useful is, therefore, not the total solids cross flow $\dot{m}_R$, but the specific solids cross flow, or cross flow per unit bed height, $\dot{m}_{RL}$, where

$$\dot{m}_{RL} = \dot{m}_s / L_f$$

It is possible to define a characteristic mixing height for the bed, h_m

$$h_m = \dot{m}_R / \dot{m}_{RL} \tag{11}$$

The physical significance of the mixing height is that if, at a given point in the bed, a solid particle is entrained in the wake of an upward moving bubble, that particle will most likely move from the wake back into the emulsion at a height h_m above the initial point of entrainment. The mixing height is related to the wake solids residence time by

$$\tau_R = \frac{h_m}{u_b} \tag{12}$$

A bed with low solids cross-flow will tend to have a large mixing height. That is, hot solids near the coal feed point will, when entrained by a bubble, move far up the bed before moving back into the emulsion phase. If the mixing height is low, hot wake solids will reenter emulsion at a point near their entry into the wake. The result is that the upward transport of energy via solids mixing is normally impeded by high solids cross-flow rates.

It has been observed that solids mixing in fluid beds can be adequately described by a simple turbulent diffusion model. From this perspective it can be seen that the solids mixing height is analogous to the Prandtl mixing length in turbulent flow theory [13]. The eddy diffusivity is proportional to the Prandtl mixing length. This is consistent with the observation that the model predicts an increase in the thermal homogeneity of the system with mixing height.

4 Bubbling Bed Theory and Solids Mixing

There is some doubt that the classic fast bubble theory is applicable to pressurized fluid beds of large particles with immersed tubes.

Recent work has been performed which seems to indicate that for the large particle sizes considered for fluid bed combustors the bed may operate in the slow bubble or transition regimes [14]. In addition, a so-called "turbulent flow" regime has been identified by some investigators which seems to be characterized by an absence of bubbles within the bed. Some data are available on solids movement in atmospheric beds of large particles without tubes, but it is not clear that these results can be applied to pressurized beds with densely packed tubes [15]. The flow regimes in atmospheric and pressurized fluid bed combustors are not well characterized at the present time.

In order to provide a qualitative idea of the effect of bubble size on bed temperature profile, fast bubble theory was used to estimate solids circulation and interchange rates. Results appear in Fig. 5. The model predicts that the average bed temperature gradient should decrease with increasing bubble size. These results can be interpreted by noting that solids circulation increases, and solids interchange decreases with bubble diameter. The solids mixing height (and bed eddy diffusivity) must therefore increase with bubble diameter.

5 Effect of Bed Geometry on Temperature Profile

A Correlation of Mixing Height and Baffle Dimensions. One might expect that the presence of baffling would complicate the problem of temperature profile prediction. Fortunately, the baffle geometry appears to control the rate at which solids mixing occurs and temperature profiles can be predicted when baffles are present in a simpler manner than is possible with open beds.

It is reasonable, in order to estimate solids recirculation rates, to equate bubble diameter to some characteristic horizontal bed dimension, such as the horizontal tube spacing. Kunii and Levenspiel present an expression for solids circulation as a function of bubble diameter which is equally valid for the fast bubble, slow bubble or transition regimes [3]. This expression has been used in the present analysis.

The solids cross flow rate and/or mixing height must be specified with more care, since the predicted temperature gradient is particularly sensitive to these parameters.

The "scale of turbulence" in FBC combustors is clearly influenced by the presence of immersed tubes in the bed. In extending the

analogy between mixing height and the Prandtl mixing length, it should be noted that turbulent flow theory establishes a precedent for relating the mixing height and characteristic physical bed dimensions. The mixing length concept has proven useful in analyzing mixing processes in the vicinity of turbulent jets, in the neighborhood of cylindrical arrays, etc., and it seems reasonable to extend this concept to predict solids movement in fluid beds in the presence of immersed tubes.

A tentative mechanism may be postulated whereby, as bubble and wake solids move upward and encounter horizontal surface, the wake solids are centrifuged out of the bubble phase and into emulsion phase. The structure of the bubble is destroyed and, as a new bubble is formed, emulsion solids are entrained in the bubble wake and transported upward until another horizontal surface in encountered. At this point, the process of wake/emulsion solids interchange continues.

This scheme presumes, of course, that the mixing height for a typical bubble in an open bed is much greater than the vertical baffle spacing, so that the bed dimensions, rather than the bubble properties, control the solids cross flow rate.

It seems reasonable to equate the mixing height with some typical vertical baffle dimension, such as vertical tube spacing. It is recognized that factors other than tube spacing almost certainly influence mixing height. However, in the absence of definitive data a more complex relation does not appear to be justified.

The vertical tube spacing of the horizontal coils previously installed in the Miniplant were of the order of seven to eight cm. The vertical coils presently installed are about 46 cm apart. Using these numbers for the mixing height and the other bed parameters cited in Table 2, the temperature profiles were calculated using the back-mixing model. The results are presented in Figs. 6 and 7.

Predicted temperature gradients for the vertical coil orientation range from 10–20°C/m (depending on the recirculation rate), as compared to measured values ranging from near zero to, in the extreme, 20°C/m. For this series of runs the steepest measured gradient was observed during a run in which, in order to reduce the bed gradient, the existing horizontal coils were simply rotated 90 deg. The mixing height in this instance would have been somewhere around 20 cm rather than the 46 cm used in this analysis. Theoretical gradients for the horizontal coils range from 50 to 75°C/m, as compared to measured values of about 40°C/m. As expected, theoretical temperature gradients were not particularly sensitive to the solids recirculation rate.

Table 2 Input data—parametric analysis

$\dot{m}_c$	0.0233 kg/s
h	350 Joule/m^{2}K
A	1.102 m^2
L_{mf}	1.27 m
L_f	2.54 m
$\dot{m}_a$	0.374 kg/s

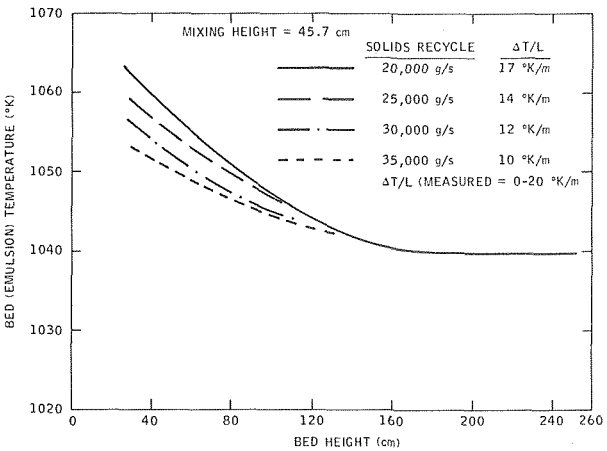

Fig. 6 Vertical coils—theoretical temperature profile

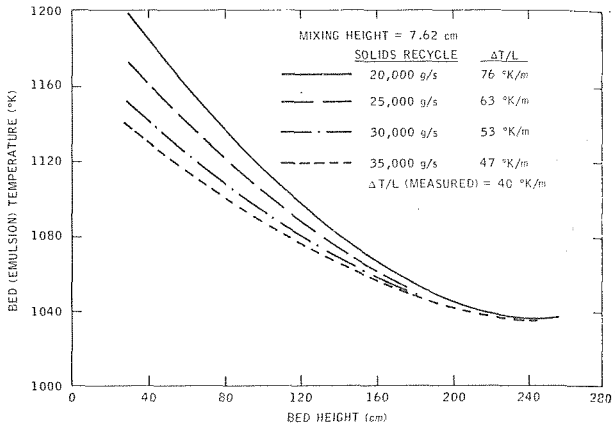

Fig. 7 Horizontal coils—theoretical temperature profile

The agreement between theory and experiment is very good, considering the simplicity of the model and the uncertainty of some of the input parameters.

B Effect of Coal Feed Rate on Temperature Profile. Miniplant operation has indicated that the bed temperature profile was more sensitive to coal feed rate with the horizontal coils installed than with the vertical coils.

Theoretical temperature profiles for different coal feed rates with horizontal coils appear in Fig. 8. Fig. 9 presents the same information for a vertical coil orientation. In both cases the excess air ranged from approximately 0 to 100. With the horizontal coils, the bed temperature gradient increased from 52.0 to 95.5° C/m as coal feed rate was increased. The range for the vertical coils was considerably less, (from 7.1 to 12.9°C/m) reflecting, at least in a qualitative sense, the physical situation.

It should be possible, as more data become available, to fit recirculation and cross flow rates for one data point and, by assuming that coal feed does not effect bed flow patterns, to use these fitted parameters to project peak bed temperatures under different load conditions.

C Theory versus Experiment. Theoretical temperature profiles have been compared with those measured in a recent Miniplant run. Pertinent data appear in Table 3. Results are presented in Fig. 10. The correlation is good. Although the model does not reflect the actual structure of the temperature profile, the overall theoretical gradient is close to the measured value. Structural differences can be attributed to the assumption of uniform fluid dynamic properties throughout the bed. In an actual bed significant spatial variations in solids circulation and interchange would be expected.

6 Conclusions

The agreement between theory and experiment seems to confirm that solids mixing plays the dominant role in the axial energy transfer process. The theory does, however, consistently over-estimate the measured gradient by a small, but significant margin. There seems to be only one explanation for this, namely the release of heat throughout the bed as a consequence of the combustion of of coal char. The model could be refined to include heat release due to combustion in the energy balance.

The mixing height is a useful concept for understanding the axial energy transport process, and for predicting temperature profiles in fluid beds. At the present time the mixing height cannot be obtained from bubble properties with any accuracy. In those instances where a bed has internals, and where solids mixing is influenced by these internals (i.e., when bubble diameter is of the order of baffle dimensions), the mixing height can be correlated with the internal bed dimensions.

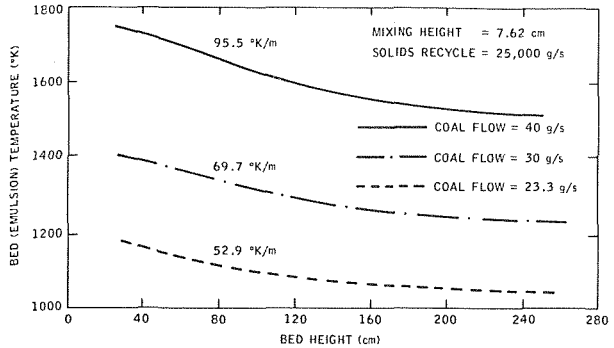

Fig. 8 Horizontal coils—effect of coal feed rate on temperature profile

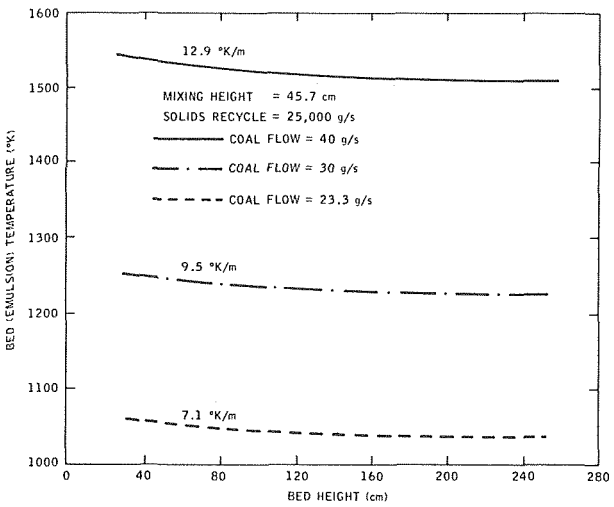

Fig. 9 Vertical coils—effect of coal feed rate on temperature profile

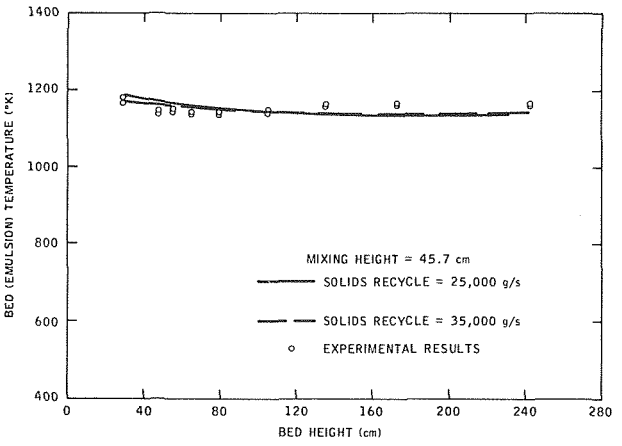

Fig. 10 Comparison of experimental and theoretical results

Table 3 Input data—comparison of theory and experiments

$\dot{m}_c = 0.0383$ kg/s
$h = 341$ Joule/m^{2}K
$A = 2.2037$ m^2
$L_{mf} = 1.58$ m
$L_f = 2.37$ m
$\dot{m}_a = 0.415$ kg/s

In the simple model proposed here, the mixing height was related to the vertical coil spacing. No account was taken of tube arrangements (i.e., staggered tubes versus in-line tubes). Clearly, the tube arrangements will influence solids flow and mixing height and some more work needs to be done in this area.

The model treats the mixing height as being constant throughout the bed. In practice, the mixing height in the lower bed will be different from the mixing height in the upper bed. In designing a fluid bed boiler, it is possible that the mixing height would be intentionally varied throughout the bed (in either an axial or, for large boilers, a radial direction) in order to optimally configure the system.

References

1 Hoke, R., and Bertrand, R., "Pressurized Fluidized Bed Combustion of Coal," Presented at The International Fluidized Bed Combustion Conference, London, England, Sept. 1975.

2 Davidson, J., and Harrison, D., *Fluidization,* Academic Press, 1971.

3 Kunii, D., and Levenspiel, O., *Fluidization Engineering,* Wiley, 1969.

4 Partridge, B., and Rowe, P., "Analysis of Gas Flow in a Bubbling Fluidized Bed When Cloud Formation Occurs," *Trans. Instn. Chem. Engrs.,* Vol. 44, 1966.

5 Chavarie, C., and Grace, J., "Performance Analysis of a Fluidized Bed Reactor. 1. Visible Flow Behavior," *Ind. Eng. Chem. Fundam.* Vol. 14, No. 2, 1975.

6 Vedamurthy, V., and Sastri, V., "An Analysis of the Conductive and Radiation Heat Transfer to the Walls of Fluidized Bed Combustion," *Int. Journal of Heat and Mass Transfer,* Vol. 17, 1974.

7 Partridge, B., and Rowe, P., "Chemical Reaction in a Bubbling Gas-Fluidized Bed," *Trans. Instn. Chem Engrs.,* Vol. 44, 1966.

8 Sergeant, G. and Smith, I., *Fuel,* Vol. 52, 1973.

9 Avedsian, M., and Davidson, J., "Combustion of Carbon Particles in a Fluidized Bed," *Trans. Instn. Chem. Engrs.,* Vol. 51, 1973.

10 Borghi, G., Sarofim, A., and Beer, J., "A Model of Coal Devolatilization and Combustion in Fluidized Bed," presented at the 70th Annual AICHE meeting, Nov. 1977.

11 Gibbs, B., and Beer, J., Private Communication.

12 Skopp, A., Nutkis, M., Hammons, G. A., and Bertrand, R., "Studies of Fluidized Lime-Bed Coal Combustion Desulfurization System," Final Report to the Environmental Protection Agency, Exxon Research and Engineering Company, Dec. 1971.

13 Schlichting, H., *Boundary Layer Theory,* McGraw-Hill Book Company, New York.

14 Louis, J., "Modeling of Fluidized Bed Combustion of Coal," Quarterly Technical Progress Report (No. 5) for the Period May 1, 1977–July 31, 1977, Massachusetts Institute of Technology, Energy Laboratory, Cambridge, Mass. (Prepared for ERDA under contract E (49-18)–2295.

15 Cranfield, R., "Solids Mixing in Fluidized Beds of Large Particles," presented at the 69th Annual AICHE Meeting, 1976.

J. G. Soland
Lt. USCG.
Ocean Engineering Department,
M.I.T.

W. M. Mack, Jr.
Project Engineer.
Foster-Miller Associates, Inc.,
Waltham, Mass.

W. M. Rohsenow
Professor of Mechanical Engineering.
Massachusetts Institute of Technology

Performance Ranking of Plate-Fin Heat Exchanger Surfaces

The Kays-London [4] way of presenting heat exchanger performance is modified to use the data in the simplified analysis of La Haye, et al. [5] which was extended to permit the ready comparison of the performance of the various plate-fin surfaces. Based on the four comparison criteria considered, the wavy finned 17.8-3/8 W surface of Kays-London is the best.

Introduction

The goal of any heat exchanger comparison method is to enable the designer to select from among the various enhanced surfaces that surface which is most beneficial. The comparison method should allow this selection to be made as easily and as accurately as possible.

Enhanced surfaces, particularly in the form of plate-fins, have been used in heat exchangers for many years. Attempts at comparing performance of various surfaces have also been made for many years. The more recent of these are by Bergles, et al. [1, 2].

La Haye, et al. [3] developed a method of comparing surfaces and used it to show how an effective uninterrupted flow length to diameter ratio could parametrically order the performance of surfaces. Further, Smith [4] developed a method similar to that presented here for comparing surfaces. Here, their comparison method is modified and used to compare the performance of all the Kays-London [5] plate finned surfaces, unfinned surfaces and sand roughened surfaces [6]. The method is universally applicable to any other heat exchanger surface as well.

Comparison Method

To simplify the comparison method, consider the performance of only one side of a plate-fin heat exchanger. This is equivalent to considering a heat exchanger with the controlling heat transfer resistance on one side—e.g., gas flow on the side of interest and condensing or boiling fluid on the other. We compare the performance of various finned and unfinned surfaces for the following quantities being the same:

1. ω, flow rate
2. $T_{h,\,in}$, hot fluid inlet temperature
3. $T_{c,\,in}$, cold fluid inlet temperature

Note also that the heat transfer resistance of the plate separating the two sides of the heat exchanger shall be considered to be negligible.

Kays and London [4], hereafter referred to as K-L, present data for many plate-fin surfaces in terms of heat transfer Colburn modulus, j, and friction factor, f, referred to the exposed area, A_T, as a function of Reynolds number, Re, based on the minimum free flow area, A_c.

The proposed comparison method converts these j and f magnitudes to the base plate area, A_b; hence, the effect of the fins is included in the new j_n and f_n based on A_b. Further, the new Reynolds number, Re_n, will be based on the open flow area, A_F, as though the fins were not present. This requires that the metal conductivity of the fins be specified in incorporating the effect of the fins into j_n.

The comparison of plate-fin performance is then converted to the same base that is currently used in comparing enhanced surfaces (such as those utilizing roughness, turbulence promoters, etc.) with plain, smooth surfaces.

Table 1 shows the proposed new definitions of the various quantities compared with the definitions used by K-L [4]. Note from Fig. 1, $D_n = 2b$ for either a finned or unfinned parallel plate passage.

To convert data of K-L to the new basis, the following ratios are obtained from the definitions, equations (1) through (10), and Fig. 1.

$$\frac{A_b}{A_T} = \frac{2aL}{\beta V} = \frac{2}{\beta b} \tag{11}$$

where $\beta \equiv A_T/V$

$$\frac{A_F}{A_c} = \frac{Lab}{A_T r_h} = \frac{1}{\beta r_h} \tag{12}$$

$$\frac{G_n}{G_c} = \frac{A_c}{A_F} = \beta r_h \tag{13}$$

$$\frac{\mathrm{Re}_n}{\mathrm{Re}} = \frac{D_n G_n}{4 r_h G_c} = \frac{\beta b}{2} \tag{14}$$

$$\frac{f_n}{f} = \frac{A_F A_T G_c{}^2}{A_c A_b G_n{}^2} = \frac{b}{2\beta^2 r_h{}^3} \tag{15}$$

Contributed by the Heat Transfer Division and presented at the Winter Annual Meeting, New York, N.Y., December 5–10, 1976. Revised manuscript received by the Heat Transfer Division July 1, 1977. Paper No. 76-WA/HT-31

Table 1 Definitions.

Kays and London [5]		Proposed	
$r_h \equiv \frac{A_c L}{A_T}$	(1a)	$D_n \equiv \frac{4A_F L}{A_b} = \frac{4V}{A_b}$	(1b)
$G_c \equiv \frac{\omega}{A_c}$	(2a)	$G_n \equiv \frac{\omega}{A_F}$	(2b)
$\mathrm{Re} \equiv \frac{4G_c r_h}{\mu}$	(3a)	$\mathrm{Re}_n \equiv \frac{G_n D_n}{\mu}$	(3b)
$f \equiv \frac{\Delta p_F}{\frac{L}{r_h}\frac{G_c^2}{2\rho g_0}}$	(4a)	$f_n \equiv \frac{\Delta p_F}{4\frac{L}{D_n}\frac{G_n^2}{2\rho g_0}}$	(4b)
$h \equiv \frac{q/\eta_0 A_T^*}{\Delta T}$	(5a)	$h_n \equiv \frac{q/A_b}{\Delta T}$	(5b)
$\mathrm{Nu} \equiv \frac{4r_h h}{k}$	(6a)	$\mathrm{Nu}_n \equiv \frac{h_n D_n}{k}$	(6b)
$j \equiv \frac{h}{G_c c_p}(\mathrm{Pr})^{2/3}$	(7a)	$j_n \equiv \frac{h_n}{G_n c_p}(\mathrm{Pr})^{2/3}$	(7b)
$^* \eta_0 \equiv \frac{A_{\mathrm{fin}}}{A_T}(1-\eta_f)$	(8)		
$\eta_f \equiv \frac{\tanh m\ell}{m\ell}$	(9)		
$m \equiv \sqrt{\frac{2}{\delta}\frac{h}{k_m}}$	(10a) thin sheet fins		
$m \equiv \sqrt{\frac{4}{\psi}\frac{h}{k_m}}$	(10b) circular pin fins		

$$\frac{j_n}{j} = \frac{h_n}{h}\frac{G_c}{G_n} = \frac{\eta_0 b}{2r_h} \tag{16}$$

These ratios were used to convert K-L data to the proposed f_n and j_n versus Re_n. Two assumptions were required in order to solve for the proper fin efficiency, η_f, required in the conversion. The heat exchanger used was constructed from aluminum ($k \simeq 100$ Btu/ft-hr°F) and the gas used was air at 90°F. Fig. 2 shows the two sets of curves on both bases for one of the K-L surfaces, namely their 6.2 plain plate-fin surface, Fig. 61 of [4].

The curve for f_n is unique for that surface but the j_n curve is only

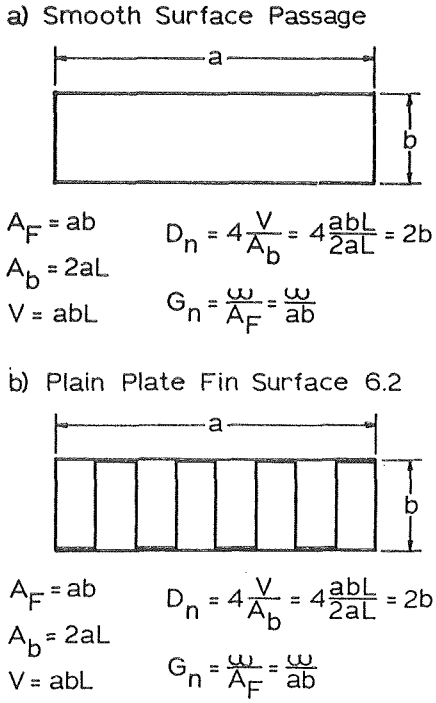

Fig. 1 Sample calculation of nominal diameter and mass flux for rectangular flow passages

Nomenclature

a = heat exchanger width
A_b = heat transfer area of base surface ignoring any enhancement; equals length times heated perimeter
A_c = minimum free flow area
A_f = frontal area of heat exchanger core
A_F = flow area ignoring any enhancing surfaces
A_T = total heat transfer area
b = plate spacing
c_p = specific heat
D_n = nominal diameter; defined by (1b)
e = roughness height for a granular surface
f = friction factor based on total area (A_T); defined by (4a)
f_n = friction factor based on base area (A_b); defined by (4b)
f_s = friction factor for a smooth surface; defined by (22)
g_0 = conversion factor (= 32.174 lbm-ft/lbf-s^2)
G_c = mass flux based on minimum free flow area; defined by (2a)
G_n = mass flux based on free flow area (A_F); defined by (2b)
h = heat transfer coefficient based on total area (A_T); defined by (5a)
h_n = heat transfer coefficient based on base area (A_b); defined by (5b)
j = Colburn factor based on total area (A_T); defined by (7a)
j_n = Colburn factor based on base area (A_b); defined by (7b)
j_s = Colburn factor for smooth surface; defined by (27)
k = thermal conductivity
ℓ = fin length from root to center (=$b/2$)
L = heat exchanger length
m = component of fin efficiency (η_f); defined by (10)
NTU = number of transfer units; = $Ah_n/\omega c_p$
p = pressure
P = pumping power
q = heat transfer rate
q/A = heat flux
r_h = hydraulic radius; defined by (1a)
T = temperature
U = overall heat transfer coefficient
V = heat exchanger volume on one side
Nu = Nusselt number; defined by (6a)
Nu_n = Nusselt number; defined by (6b)
Pr = Prandtl number
Re = Reynolds number based on minimum free flow area (A_c); defined by (3a)
Re_n = Reynolds number based on free flow area (A_F); defined by (3b)
β = ratio of total heat transfer area (A_T) to volume (V)
Δp_F = friction pressure drop
ω = mass flow rate
η_f = fin efficiency; defined by (9)
η_0 = total surface temperature effectiveness; defined by (8)
μ = viscosity
ρ = density
ϵ = heat exchanger effectiveness
δ = fin thickness
ψ = pin diameter

Subscripts

a = case a parameter (Shape, V = const.)
b = case b parametet (P, V = const.)
c = case c parameter (NTU, P = const.)
d = case d parameter (NTU, V = const.)
e = enhanced surface
m = heat exchanger metal
s = smooth surface

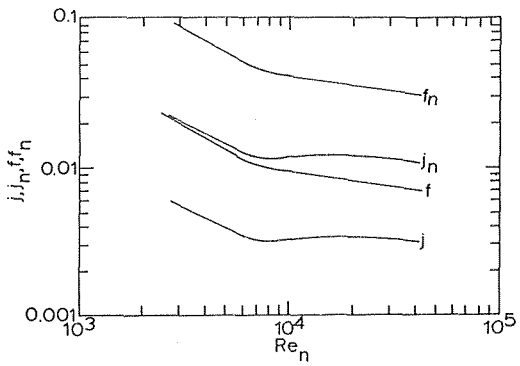

Fig. 2 Comparison of colburn *j* factors (*j* and j_n), and comparison of friction factors (*f* and f_n)

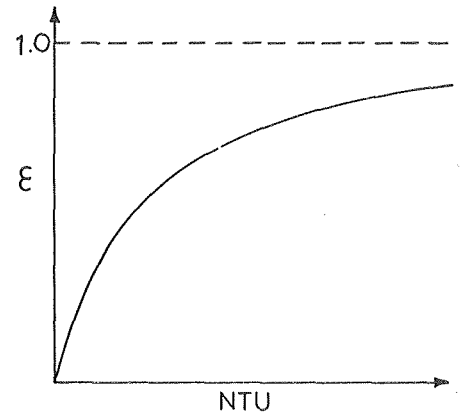

Fig. 3 Typical plot of heat exchanger effectiveness, ϵ, versus number of transfer units, *NTU*

for fins of aluminium. There would be a family of j_n curves for various fin material conductivities.

For any heat exchanger, the fluid pumping power per unit volume on one side is given by:

$$\frac{P}{V} = \frac{\omega \Delta p_f}{\rho V} = \frac{2\mu^3}{g_0 \rho^2} \frac{f_n \mathrm{Re}_n{}^3}{D_n{}^4} \propto f_n \mathrm{Re}_n{}^3 / D_n{}^4 \tag{17}$$

Since for the same fluid at the same temperature level, μ and ρ are constant.

The heat transfer for any heat exchanger is given by:

$$q = \epsilon (T_{h,\,\mathrm{in}} - T_{c,\,\mathrm{inc}}) \omega c_p \tag{18}$$

For any given flow arrangement, there exists a curve similar to that in Fig. 3 which relates ϵ to *NTU*, where $NTU = Ah_n/\omega c_p$.

This relationship between ϵ and *NTU* is always monotonically increasing. If fluid properties and flow rate are held constant, an increase in Ah_n results in an increase in *NTU* which results in an increase in ϵ and a higher heat transfer rate, *q*. Therefore, knowledge of either Ah_n or *NTU* will allow determination of the heat transfer rate. Thus the ratios Ah_n/V and NTU/V are quantities of interest:

$$\frac{NTU}{V} = \frac{Ah_n}{V \omega c_p} = \frac{4\mu}{\mathrm{Pr}^{2/3}} \frac{j_n \mathrm{Re}_m}{\omega D_n{}^2} \propto \frac{j_n \mathrm{Re}_n}{D_n{}^2} \tag{19}$$

for the same fluid at the same temperature levels, c_p, μ, and Pr are constant, and for the same flow rate, ω.

Similarly

$$\frac{Ah_n}{V} = \frac{4 c_p \mu}{\mathrm{Pr}^{2/3}} \frac{j_n \mathrm{Re}_n}{D_n{}^2} \propto \frac{j_n \mathrm{Re}_n}{D_n{}^2} \tag{20}$$

With enhanced surface data in the form f_n versus Re_n and j_n versus Re_n, it is a simple matter to construct the performance parameters $f_n \mathrm{Re}_n{}^3/D_n{}^4$ and $j_n \mathrm{Re}_n/D_n{}^2$, and to plot them as in Fig. 4. Different curves will result for different surfaces. Curves for two surfaces shown schematically in Fig. 4 will be used to demonstrate the use of these curves in determining heat exchanger relative performance. All comparisons will be made for the same ω, $T_{c,\,\mathrm{in}}$, $T_{h,\,\mathrm{in}}$. This implies that any comparison which results in the same value for NTU/V will also have the same q/V.

The schematic curves of Fig. 4 should, for the real surfaces, have a scale of Re_n magnitudes labelled along each curve when constructing them.

Point 0 has been selected on surface 1 of Fig. 4. It may lie anywhere on the surface 1 performance curve and represent a reference heat exchanger having the following specifications: P_0, NTU_0, q_o, L_0, $A_{F,0}$, V_0, where the subscript zero refers to surface 1. Diagramatically, the shape of the reference exchanger is labelled 0 in Fig. 5.

Four different performance comparisons are immediately available from Fig. 4 and are indicated by points *a*, *b*, *c*, and *d* on surface 2. Here the curve for surface 2 lies above the curve for surface 1 in Fig. 4.

Case a. Same heat exchanger shape and volume ($L_a = L_0$, $V_a = V_0$, $A_{F,a} = A_{F,0}$).

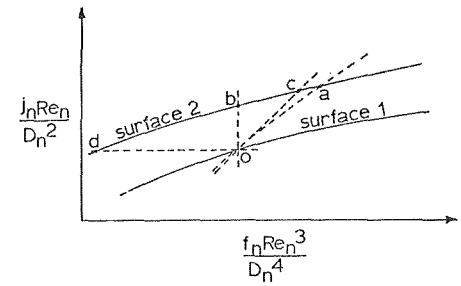

Fig. 4 Performance parameter curves for two surfaces showing points used in sample comparisons

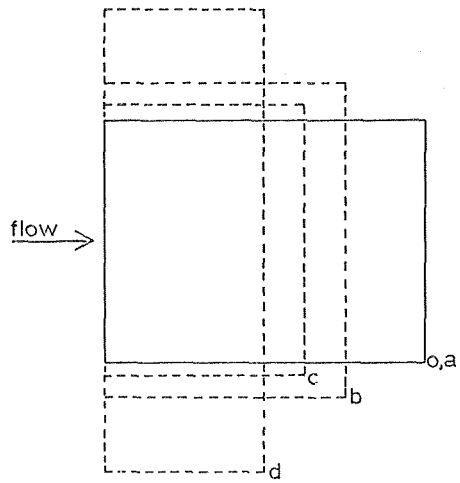

Fig. 5 Relative heat exchanger shape for sample comparisons assuming unit height

This case represents a comparison of points 0 and *a* of Fig. 4 where:

$$\mathrm{Re}_{na} = \mathrm{Re}_{n0} \times \frac{D_{na}}{D_{n0}}$$

since the flow rate (ω) and the frontal area (A_F) are fixed. The results of this comparison are easily obtained as the ratios of the ordinate values and abscissa values and their general nature are shown schematically in Fig. 6(a). Fig. 5 shows the same heat exchanger shape for this case. Fig. 6(a) shows schematically the magnitude of the increase in pumping power and the heat transfer when using surface 2 instead of surface 1 in the same shape heat exchanger.

Case b. Same heat exchanger volume and pumping power. ($V_b = V_0$, $P_b = P_0$).

This case represents a comparison of points 0 and b in Fig. 4 since a vertical line in the performance plot has a fixed value of power per unit volume. This comparison yields the NTU ratio of the two heat exchangers and is easily obtained as the ratio of the ordinate values at 0 and b. Results are shown schematically in Fig. 6(b) and shows the magnitude of the increase in the NTU for the same pumping power for surface 2 compared with surface 1. The relative shape for this case is shown in Fig. 5. Since surface 2 has higher friction, the same pumping power will be obtained for a smaller Reynolds number, i.e., $Re_b < Re_0$. This causes the frontal area to increase, $A_{F,b} > A_{F,0}$, while the same volume requires the length to decrease, $L_b < L_0$.

Case c. Same pumping power and number of transfer units. ($P_c = P_0$, $NTU_c = NTU_0$ (or $q_c = q_0$)).

This case represents a comparison of the heat exchanger size required for the same "job"—a job being defined as the same pumping power resulting in the same heat transfer rate. This comparison is a line having a slope of 1 in Fig. 4 (i.e., points 0 and c), since each axis is inversely proportional to the volume (NTU and P are constant). This results in the ratio of the heat exchanger volume required for the two surfaces obtained as the ratio of either the abscissas or the ordinates at points 0 and c. As long as surface 2 lies above surface 1, the result will be a smaller volume required to do the same job. The resulting reduction in volume for surface 2 is shown in Fig. 6(c) and the relative shape is shown in Fig. 5.

Case d. Same volume and number of transfer units. ($V_d = V_0$, $NTU_d = NTU_0$ (or $q_d = q_0$)).

This case compares the pumping power required by surface 2 to that required by surface 1 for the case when both heat exchangers yield the same overall heat transfer performance. It is obtained as the ratio of the abscissas of points 0 and d in Fig. 4, since a horizontal line on the performance plot has a constant value of NTU/V. The results are illustrated in Fig. 6(d); they show the decreased pumping power required for surface 2. The surface 2 Reynolds number is the smallest of all four cases and consequently, the flow area is the largest. Since the volume is the same as the surface 1 exchanger volume, the length must decrease and the general shape is shown as d in Fig. 5.

Thus for a very simply constructed plot of $j_n Re_n/d_n{}^2$ versus $f_n Re_n{}^3/D_n{}^4$, it is possible to obtain useful performance comparisons between two heat exchangers for four different criteria.

Cases b, c, and d are the same conceptually as criteria 3, 5, and 4 of Bergles [2].

Comparison of Kays and London Plate-Fin Surfaces

All of the plate-fin surfaces were plotted as performance curves of $j_n Re_n/D_n{}^2$ versus $f_n Re_n{}^3/D_n{}^4$, for the same ω, $T_{c,\,in}$ and $T_{h,\,in}$. This is a plot equivalent to NTU/V versus P/V.

K-L data are available for various finned surfaces having about nine different nominal diameters between 0.50 in. (12.7 mm) and 1.646 in. (41.8 mm) (b = 0.25 in. (6.4 mm) to 0.823 in. (20.9 mm)). For each nominal diameter, all of the finned surfaces were plotted as shown in Fig. 7. However, in Fig. 7, only the highest performance curve at each plate spacing is shown.

Table 2 lists all of the K-L plate-fin surfaces by type and surface designation. Due to the large number of surfaces used in the calculations, Figs. 7 and 10 will use the surface numbering system which is listed in the right hand column of Table 2.

All of the plate-fin surfaces were then compared to smooth surfaces having no enhancements and having the same nominal diameter (D_n), (or plate spacing (b)), as the plate-fin surface being compared. This was accomplished using all plate-fin surfaces having a common nominal diameter of 0.50 in. (12.7 mm) (b = 0.25 in. (6.4 mm)). This was chosen due to the quantity of data available. There are 17 surfaces having this nominal diameter, whereas, the next nominal diameter (D_n = 0.82 in. (20.8 mm)) has data for only three different surfaces. The subscript e will be used to denote the enhanced surface and the subscript s will be used to denote the smooth surface.

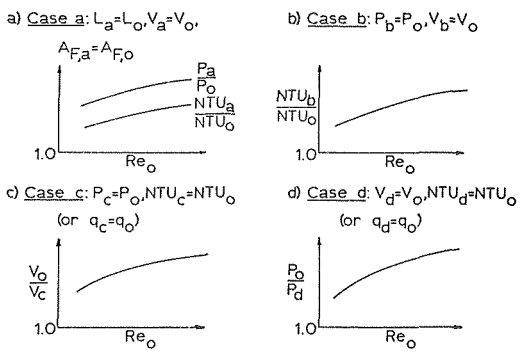

Fig. 6 Typical performance comparison results

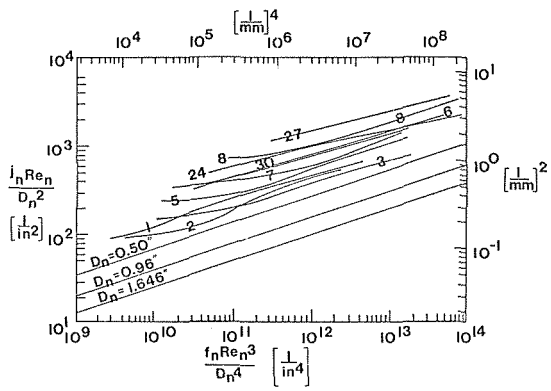

Fig. 7 Performance parameter curve for plate-fin surfaces. Note: Only the best surface is shown for each plate spacing, and the pin-fin surfaces.

Table 2 Kays and London Plate Fin Surfaces.

General Surface Type	Plate Spacing b, in. (mm)	Surface Designation	Surface Numbered in Figures as:
Plain plate-fin	0.47 (11.9)	5.3	1
	0.41 (10.4)	6.2	2
	0.82 (20.8)	9.03	3
	0.25 (6.4)	11.1	4
	0.48 (12.2)	11.1(a)	5
	0.33 (8.4)	14.77	6
	0.42 (10.7)	15.08	7
	0.25 (6.4)	19.86	8
Louvered plate-fin	0.25 (6.4)	3/8 − 6.06	9
	0.25 (6.4)	3/8(a) − 6.06	10
	0.25 (6.4)	1/2 − 6.06	11
	0.25 (6.4)	1/2(a) − 6.06	12
	0.25 (6.4)	3/8 − 8.7	13
	0.25 (6.4)	3/8(a) − 8.7	14
	0.25 (6.4)	3/16 − 11.1	15
	0.25 (6.4)	1/4 − 11.1	16
	0.25 (6.4)	1/4(b) − 11.1	17
	0.25 (6.4)	3/8 − 11.1	18
	0.25 (6.4)	3/8(b) − 11.1	19
	0.25 (6.4)	1/2 − 11.1	20
	0.25 (6.4)	3/4 − 11.1	21
	0.25 (6.4)	3/4(b) − 11.1	22
Strip-fin plate-fin	0.25 (6.4)	1/4(s) − 11.1	23
	0.49 (12.5)	3/32 − 12.22	24
	0.41 (10.4)	1/8 − 15.2	25
wavy-fin plate-fin	0.41 (10.4)	11.44 − 3/8W	26
	0.41 (10.4)	17.8 − 3/8W	27
pin-fin plate-fin	0.24 (6.1)	AP-1	28
	0.40 (10.2)	AP-2	29
	0.75 (19.1)	PF-3	30
	0.50 (12.7)	PF-4(F)	31
	0.51 (13.0)	PF-9(F)	32

See Fig. 8 for additional surface.

Smooth surface $j_n Re_n/D_n{}^2$ calculations were completed utilizing the Colburn correlation for forced-convection, turbulent flow in tubes with the appropriate nominal diameter (D_n) from [8]. This reduces to:

$$j_s \equiv 0.023\ Re^{-0.2} \quad \text{or} \quad j_s Re_n = 0.023\ Re_n{}^{0.8} \tag{21}$$

For a smooth surface $h = h_n$, $G = G_n$, $Re = Re_n$ and $f = f_n$.

Smooth surface $f_n Re_n{}^3/D_n{}^4$ was calculated as follows:

$$f_s \cong .0791\ Re_n{}^{-0.25} \quad \text{or} \quad f_s Re_n{}^3 = .0791\ Re_n{}^{2.75} \tag{22}$$

Combining (21) and (22) to obtain the equation for the smooth surface leads to:

$$\frac{j_s Re_n}{D_n{}^2} = \frac{.0481}{D_n{}^{.836}} \left[\frac{f_s Re_n{}^3}{D_n{}^4}\right]^{0.291} \tag{23}$$

These lines were calculated for three nominal diameters (0.50 in. (12.7 mm), 094 in. (23.9 mm), 1.646 in. (41.8 mm)) which span the range of values for the K-L surfaces and are shown on Fig. 7 as the three straight lines at the bottom of the figure.

Calculations were also made for the five pin-fin surfaces of [5]. Only the best of these surfaces is shown in Fig. 7. Surfaces 28, 29, 31 all follow surface 30 of Fig. 7 while surface 32 lies atop surface 1.

For all of the surfaces studied, specific performance comparison curves represented by the schematic curves shown in Fig. 6 were plotted for all of the surfaces for cases *a*, *b*, *c*, and *d*. They are presented in [7] and [8] but are omitted here. It is sufficient here to realize that the surfaces which lie higher on the plot of Fig. 7 give the better performance for all four cases.

Comparison of Some Other Plate-Fin Surfaces

The same procedure was applied to some other surfaces [9, 10, 11] shown in Fig. 8. The results are shown in Fig. 9, [12], where curve 27 is reproduced for comparison from Fig. 7. These surfaces lie below surface 27 except for surface 5-1.

Comparison with Sand Grained Roughness Surfaces

Many enhanced surfaces have been designed to increase the performance of heat exchangers. Dipprey and Saberski [6] determined the heat transfer coefficient and friction factor experimentally for rough tubes containing a granular type surface with roughness-height-to-diameter ratios (e/D) ranging from 0.0024 to 0.049. The best of these surfaces from the standpoint of higher heat transfer coefficients for lower friction factors (i.e., $e/D = 0.049$) was converted to the proposed performance parameters [7].

Fig. 10 contains a plot of the performance parameters $j_n Re_n/D_n{}^2$ versus $f_n Re_n{}^3/D_n{}^4$ for the Dipprey and Saberski surface using D_n = 0.50 in. (12.7 mm), as well as the best two K-L plate-fin surfaces having D_n = 0.82 in. (20.8 mm) and 0.50 in. (12.7 mm), respectively. Also shown is the smooth surface performance curve for D_n = 0.50 in. (12.7 mm). On this comparison basis the sand roughened surface is better than the smooth surface but falls well below the best of the K-L surfaces, 27.

Results of Comparison

The higher a curve lies on the performance curve of $j_n Re_n/D_n{}^2$ versus $f_n Re_n{}^3/D_n{}^4$ the better the surface performance. Inspection of the curves for all surfaces suggests that the following surfaces, or groups of surfaces are best in order of decreasing performance.

Ranking Number	Surface Number
1	27
2	25
3–11	8, 15–20, 23, 26
12–14	21, 22, 24
15–20	13, 14, 28–31
21	6
22–27	4, 7, 9–12
28	5
29–30	1, 32
31–32	2, 3

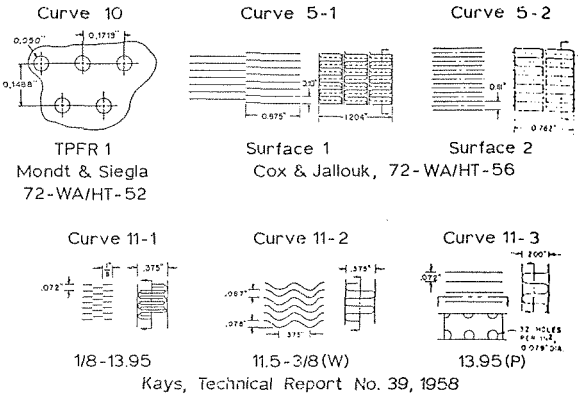

Fig. 8 Geometry of other plate fin surfaces investigated

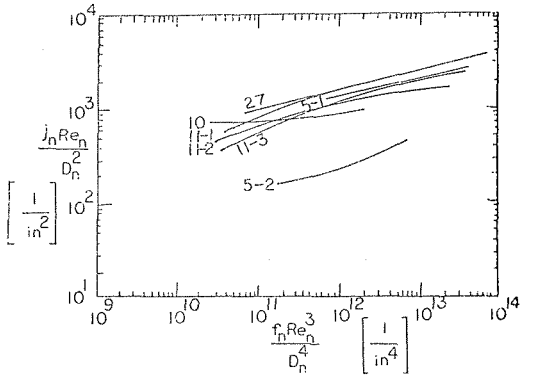

Fig. 9 Performance curves for surfaces shown in Fig. 8, [12]

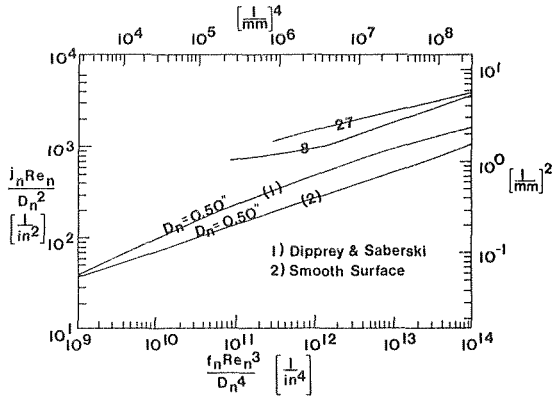

Fig. 10 Performance parameter curves for best plate-fin surfaces and Dipprey and Saberski (3) e/D = 0.049 surface

It should be remembered that "best" here is based on performance criteria as stated in cases *a*, *b*, *c*, and *d*. The high density fin surface usually results in larger frontal areas and shorter path lengths, Fig. 5. In some cases the resulting exchanger shapes would be unacceptable for a particular application; so the designer may be forced to select surfaces that lie lower on the performance parameter graph.

The comparisons here were made only for aluminium fins. Changing the fin material to copper or steel may rearrange the rank ordering of some of the surfaces. This has not been investigated. The same procedure, however, would be used.

Entrance and exit losses have not been included. These would want to be considered for the shorter passage length exchangers.

In addition the designer considers the cost of the exchanger system. This involves not only the cost of the surface but the cost of the

ducting which changes as the overall heat exchanger changes.

The comparisons here focus on one side of the exchangers assuming the thermal resistance on the other side is negligible. Sheldon [12] made sample comparisons for case c for cross-flow exchangers with the same air flow rates, ω, on the hot and cold sides. Exchangers were sized for a specific case with surface 23 on both sides and surface 27 on both sides. The volume reduction for the 27 surfaces from the 23 surfaces was 50 percent. Making the same comparison with negligible thermal resistance on one side the volume reduction of other side (surfaces 23 to 27) was 53 percent.

The simple comparisons made here should provide a reasonable guide to designers in selecting surfaces.

Conclusions

1 The comparison method of La Haye, et al. and Smith [4] was modified to compare heat exchanger performances on four different bases:

a. Same shape and volume of heat exchanger.
b. Same exchanger volume and pumping power.
c. Same pumping power and *NTU*.
d. Same volume and *NTU*.

2 All of Kays-London plate-fin surfaces, unfinned surfaces and a sand roughened surface and a few additional surfaces, Fig. 8, were compared on the above bases.

3 The best surface of those compared is found to be in the wavy-fin plate-fin 17.8 – 3/8 W with plate spacing of 0.41 in. (10.4 mm).

4 The designer may not always chose this best surface since he must consider the shape of the space envelope available, costs of surfaces and entrance and exit losses in short path length designs.

References

1 Bergles, A. E., Bunn, R. L., and Junkhan, G. H., "Extended Performance Evaluation Criteria for Enhanced Heat Transfer Surfaces," *Letters in Heat and Mass Transfer*, Vol. I, No. 2, 1974.

2 Bergles, A. E., Blumenkrantz, A. R., and Taborek, J., AIChE Reprint 9 for 13th National Heat Transfer Conference, 1972; Paper FC6.3 for Fifth International Heat Transfer Conference, 1974.

3 La Haye, P. G., Neugebauer, F. J., and Sakhuja, R. K., "A Generalized Prediction of Heat Transfer Surfaces," ASME JOURNAL OF HEAT TRANSFER, November 1974, Vol. 96, pp. 511–517.

4 Smith, J. L., Jr., "Prediction of Heat Transfer and Friction Factor Data for Heat Exchanger Design," ASME Paper 66-WA/HT-59.

5 Kays, W. M., and London, A. L., *Compact Heat Exchangers*, 2nd Edition, McGraw Hill Book Co., New York (1964).

6 Dipprey, D. F., and Sabersky, R. H., "Heat and Momentum Transfer in Smooth and Rough Tubes at Various Prandtl Numbers," *International Journal of Heat and Mass Transfer*, Vol. 6, 1963.

7 Mack, W. M., Jr., "Evaluation of the Heat Transfer Performance of Three Enhanced Surfaces Including an Enhanced Surface Heat Exchanger Performance Comparison Method," Sc.D. Thesis, Massachusetts Institute of Technology, 1974.

8 Soland, J. G., Mack, W. M., and Rohsenow, W. M., "Performance Ranking of Plate-Fin Heat Exchanger Surfaces," ASME Paper 76-WA/HT-31.

9 Mondt, J. R., and Siegla, D. C., "Performance of Perforated Heat Exchanger Surfaces," ASME Paper 72-WA/HT-52, Nov. 1972.

10 Cox, B., and Jallouk, P. A., "Methods for Evaluating Performance of Compact Surfaces," ASME Paper 72-WA/HT-56, Nov. 1972.

11 Kays, W. M., "Heat Transfer and Flow Friction of Wavy Fin, Strip Fin and Perforated Fin Surfaces," M. E. Dept., Stanford University, Technical Report No. 39, October, 1958.

12 Sheldon, G. E., "Heat Exchanger Performance Ranking," Ocean Engrg. Dept., M.I.T., M.E. Thesis, May 1976.

J. M. Bentley
T. K. Snyder
L. R. Glicksman
W. M. Rohsenow

Department of Mechanical Engineering,
Massachusetts Institute of Technology,
Cambridge, Mass. 02139

An Experimental and Analytical Study of a Unique Wet/Dry Surface for Cooling Towers

An advanced wet/dry heat transfer surface has been developed for power plant cooling towers eliminating the need for conventional dry surface. Hot water to be cooled is channeled down grooves in the surface; the balance of the surface is dry and acts like a fin. The cooling air passes over the surface in cross-flow. Since the grooves occupy only a small fraction of the surface area, a majority of the heat transfer is by sensible heat transfer. In the experimental apparatus the wet surface area was five percent of the total area and the heat transfer by evaporation varied between 20 and 40 percent of the total heat transfer. An analytical model indicated that the yearly water consumption of a cooling tower with the new wet/dry surface would be less than half that of a conventional wet cooling tower and fog plumes would be eliminated.

1 Introduction

A major problem in the generation of electric power is that of so-called waste heat rejection. Environmental considerations have restricted the use of once-through cooling systems which reject condenser heat directly to a natural water body. A commonly used alternative, an evaporative cooling system, requires a large supply of fresh water, and under certain ambient conditions the wet tower can produce local fogging and icing conditions which could be hazardous to nearby highways or airports.

A completely closed (or dry) cooling system, while having small direct environmental impact, has an initial capital cost several times that of the above alternatives and a dry-cooled power plant suffers a large loss in capacity during periods of high temperature when electrical demand is at its highest.

One effort to avoid these drawbacks involves a hybrid system of evaporative (wet) and dry components. The dry cooling capacity is used alone for most of the year with the wet helper components assisting during peak load and/or high ambient temperature conditions. This design provides significant savings in water consumption over a purely evaporative system and in capital investment and electrical production costs over a completely dry system. For example, a hybrid system which uses 40 percent of the water consumption of a totally wet system has a total evaluated cost (capital plus operating costs) approximately one-half that of a dry system [1]. However, the conventional dry surface is still very expensive and is subject to corrosion from the effluent of the nearby evaporative units. Also there is an increased need for system control and monitoring, and containment of makeup water for use by the wet towers during the peaking conditions may be a problem.

One such system has been purchased by the Public Service Company of New Mexico for use at their San Juan facility. Expected to be operational by 1981, the units are designed to save 60 percent of the water consumed annually by evaporative towers [1].

The Wet-Dry Concept. The advanced wet-dry concept discussed here attempts to achieve reduced cost and water consumption with one simple heat transfer surface design. (See Fig. 1.) This design restricts the water surface area by channeling the hot water into grooves on a series of inclined metallic plates within the tower. The surface can be used in a tower similar in design to a conventional wet tower with hot water sprayed on the plates from above and cooling air induced between the parallel plates by a fan or by natural draft. Cooling air flowing over the plates removes heat both through evaporation at the water surface and by convection from the dry plate surface which acts as a fin. Heat is also transferred to the air from the back of the plate which is completely dry. Evaporation is thus kept small by the reduced water-air interface, while the elimination of piping, headers, etc. cuts the cost of the dry heat transfer surface. Further advantages were seen in the possibilities of fog avoidance, high ambient temperature performance and retrofitting of existing wet tower cells.

Early work on plate design and testing has included visualization of water flow over various surface configurations [2, 3, 4]. A counterflow heat transfer model was built and tested, demonstrating reduced evaporation rates at high ambient temperature conditions. Design considerations and experience with the counterflow model have suggested that crossflow air-water design would be best for simplicity and low cost. Accordingly, the original apparatus has been modified to conduct crossflow experiments.

The experimental test program and results are presented below. These results will be compared to a numerical solution for the combined heat and mass transfer in the test section. The validated nu-

Contributed by the Heat Transfer Division for publication in the JOURNAL OF HEAT TRANSFER. *Manuscript received by the Heat Transfer Division* October 5, 1977.

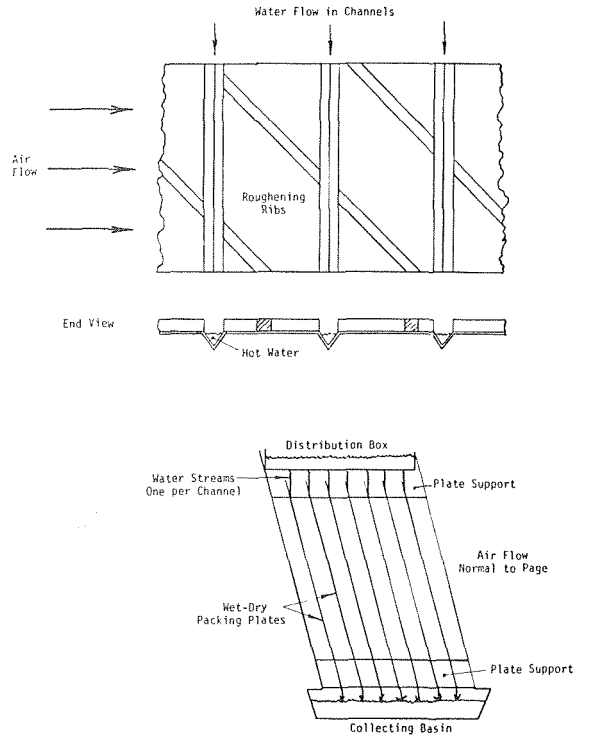

Fig. 1 Wet-dry surface and test apparatus

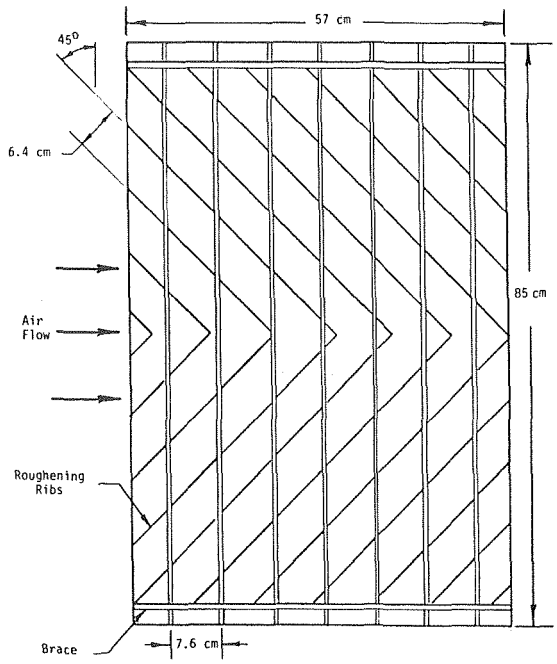

Fig. 2 Crossflow packing plate

merical model will then be used to predict the overall performance of cooling towers incorporating the advanced design and these will be compared to conventional towers.

2 Experimental Apparatus

The crossflow model heat transfer test apparatus consists of a packing section containing seven plates. The plate material is 0.64 mm (0.025 in.) thick anodized aluminum which was formed with a hydraulic press. Roughening ribs made of ¼ in. bar stock were attached to the upper surface of the plate to augment the heat transfer properties (see Fig. 2). The angle of attack, rib height, and spacing were established to optimize the heat transfer to pressure drop ratio for the dry surface as found by Han [5]. For the same friction power, the surface with the repeated rib has a heat transfer coefficient approximately twice that of a smooth surface. The individual plates used for testing purposes measure 85 cm (33½ in.) high × 57 cm (22¼ in.) wide and contain seven equally spaced grooves for water flow. The total area available for heat transfer was 6.78 m^2. Photographs were used to establish that five percent of the total surface area was covered by water. If the included angle formed by the sides of the water channel remains constant, varying the channel depth should not affect the percent wet area unless the channel becomes so shallow that the water overflows it.

The plates are arranged in the packing at a 10 deg angle from the vertical and spaced 3.8 cm (1.5 in.) apart on center. Air flow baffles set at the top and bottom of the packing section serve to eliminate air flow over the water distribution and collection areas. The air flow area is thus a parallelogram 67 cm (26.3 in.) high × 31 cm (12.4 in.) wide. The total air flow area is 2200 cm^2 (2⅓ ft^2). The clearance between the side wall and the plate adjacent to it was adjusted so that the air velocity through this gap was equal to the air velocity between the plates in the center of the test section. Maximum air velocity over the plate was 3.7 m/s (12 ft/s) provided by a 0.37 kw (½ hp) induced draft fan.

Water is fed into the channels from a distribution box set above the packing section. Individual holes were drilled for each channel, a design which works well on a small test scale, but will have to be

Nomenclature

C = flow stream capacity rate ($\dot{m}c_p$), J/s K
c_p = heat capacity, J/kg K
h_d = dry surface heat transfer coefficient, W/m^2 °C
h_ℓ = wet surface heat transfer coefficient, W/m^2 °C
h_D = wet surface mass transfer coefficient, cm/s
$h_{fg}{}^T$ = latent heat of vaporization of water at T, J/kg
$h_{fg}{}^0$ = latent heat of vaporization of water at T_0, J/kg
k = plate thermal conductivity, W/m °C
$\dot{m}$ = mass flow rate, kg/s
Pr = Prandtl Number
Q = heat transfer rate, Watts
Re = Reynolds Number
t = plate thickness, mm
T = temperature, °C
T_0 = reference temperature, °C
Z = length of fin, cm
$W.C.$ = water consumption, ℓ/yr
$W.C._{wet}$ = consumption of wet tower, ℓ/yr
$W.C._0$ = water consumption of a wet tower with a constant air inlet temperature of 32°C throughout year, ℓ/yr
η_f = fin efficiency
ρ = density, kg/m^3

Subscripts

a = air
d = dry plate
in = inlet
ℓ = liquid (water)
mix = mixture (air-water vapor)
out = outlet
v = water vapor

simplified for an actual system. An improved design which elimates the need for the distribution plates is currently under test. A catch basin approximately one in. below the plates collected the cooled water from the bottom of the plates. Air flow over the free water surface is hindered by rubber skirts attached to the air flow baffles and allowed to hang into the basin.

Maximum waterflow rate was found to be about 26 gm/s/channel (0.7 lbm/min/channel) or 1.28 kg/s (35 lbm/min) for the test apparatus. Hot water temperature was variable from 27 to 71°C (80 to 160°F) but cooling air temperature and humidity depended on the ambient conditions available in the laboratory. The wet surface area of the plates was determined by assuming that the water streams completely wetted the vee in each trough. This assumption was based on visual observation of the plates under varying water loading. There were 45 copper-constantan thermocouples to scan the air and water temperatures through the apparatus. Due to the small percentage of the water flow which was evaporated, it was impossible to measure the evaporation rate accurately by the change in water flow rates through the test section. Rather, the moisture content of the air flow was measured with an optical dewpoint hygrometer. Rotometers were used to measure the water flow rate and a traversing pitot tube was used to measure the air flow rate. From these parameters the enthalpy changes for both water and air can be calculated as well as the evaporation rate and the total heat transfer rate.

3 Analysis

The crossflow wet-dry concept was modeled numerically. This model divides the plate area into a number of equal sized square sueections each assumed to have constant properties. The program starts in the upper corner where both air and water inlet conditions are known and calculates that subsection's outlet conditions as described below. Using these outlet flow conditions as inlets to the adjacent subsection, the program moves over the entire grid.

The heat and mass transfer calculation within each subsection is performed assuming small property change within the subsection. Convective heat transfer from the dry plate surface was determined by first modeling the plate as a fin (Fig. 3), with the base at the inlet water temperature.

Fin efficiency was calculated from the physical properties of the packing plate and the surface heat transfer correlation for ribbed surfaces presented in [5]. The plate thickness was selected so that the fin efficiency was 0.8 (the heat transfer from the fin was 80 percent of that from a plate whose entire surface is at the temperature of the water). On the other side of the plate the surface directly under the water trough is treated as being at the water temperature. The water surface is assumed to be at the bulk water temperature. Convective heat transfer from these areas was calculated with the same heat transfer correlation, adjusted as described below.

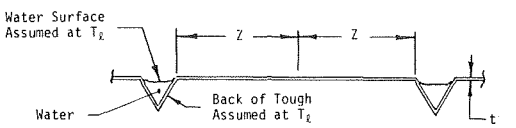

(A) Packing Plate Cross Section

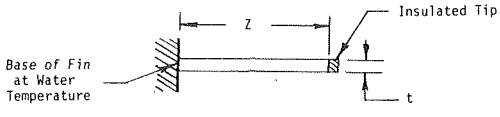

(B) Approximated Fin Model

Fin Efficiency, η_f = Actual Heat Transfer / Heat which would be transferred if entire fin area were at the base temperature.

$$\eta_f = \frac{\tanh Z\sqrt{2h_{dp}/kt}}{Z\sqrt{2h_{dp}/kt}}$$

For very wide fins, Ref. 5

Fig. 3 Model of packing plate as a fin

Evaporation from the water surface is calculated by using a mass transfer coefficient which is related to the heat transfer coefficient and physical properties of air and water by the Chilton-Colburn analogy [6].

$$h_D = \frac{h_d}{(\rho c_{p_a})}\left(\frac{\mathrm{Pr}}{Sc}\right)^{2/3} \tag{1}$$

At the water surface, the evaporation is given as

$$d\dot{m}_\ell = h_D dA_\ell(\rho_{w_{\mathrm{sat}}} - \rho_a) \tag{2}$$

where $\rho_{w_{\mathrm{sat}}}$ is the water vapor concentration at saturation conditions corresponding to the bulk water temperature and ρ_a is the concentration of water vapor in the bulk air flow. The energy transfer due to evaporation is thus:

$$dQ_{\mathrm{evap}} = d\dot{m}_\ell[h_{fg} + c_{p\ell}(T_{\ell_{\mathrm{in}}} - T_0)] \tag{3}$$

where T_0 is the reference temperature at which the enthalpy of liquid water is taken to zero. The convective heat transfer from the wet and dry surface is:

$$dQ_{\mathrm{conv}} = [\eta_f h_d dA_d + h_\ell dA_\ell](T_\ell - T_a) \tag{4}$$

By changing the ratio of water surface area to total surface area the ratio of energy transfer by evaporation to convection can be altered. Adding up the convective and evaporative heat transfer gives the total heat transfer for the individual grid section. For the water stream,

$$-dQ_\ell = dQ_{\mathrm{evap}} + dQ_{\mathrm{conv}} \tag{5}$$

The temperature change for water in a subsection is

$$dT_\ell = [-dQ_\ell + d\dot{m}_\ell c_{p\ell}(T_{\ell_{\mathrm{in}}} - T_0)]/\dot{m}_{\ell_{\mathrm{out}}} c_p \tag{6}$$

The humidity change is

$$dw = -d\dot{m}_\ell/\dot{m}_a \tag{7}$$

and the air temperature change is given by

$$dT_a = \frac{-dQ_\ell - dw\dot{m}_a[h_{fg}{}^0 + c_{p_v}(T_{a_{\mathrm{out}}} - T_0)]}{\dot{m}_a(c_{p_a} + w_{\mathrm{in}} c_{p_v})} \tag{8}$$

These changes are added to the inlet conditions to find the outlet properties of the air and water flows. This development is similar to that presented by Yadiogoroglu [7] for water surface modified for the additional dry surface contribution.

The average heat transfer coefficient is calculated from the correlation for ribbed surfaces shown in [5]. When the local heat and mass transfer at the water surface was calculated from the average value for ribbed surfaces, the results were somewhat erroneous. This discrepancy is caused by the proximity of the water channels to ribs, the distortion of the water surface by the air shear stress and variations of the extent of water wetting in the vee groove. It was found in the initial tests that when the heat and mass transfer coefficients were increased by twenty three percent over those calculated from the average coefficients for the ribbed surface, better agreement was achieved. This correction was used throughout the program.

When the repeated rib roughened surface is compared to typical dry tower surfaces, e.g., finned tubes, having the same hydraulic diameter, the rib roughened surface provides about a 20 percent improvement in heat transfer at the same fan power. However, surfaces cannot be evaluated solely on this basis. In order to minimize frontal area for the wet/dry configurations rather wide plates, in the direction of air flow, are needed. Due to the limited head provided by the fan, a relatively large plate spacing is needed reducing the heat transfer coefficient obtained from the plate surface. Table 1 illustrates how variations in the plate design characteristics alter the overall performance. By the use of cells which have different channel spacings,

and thus different wet to total area ratios, the water consumption of the units can be altered. If cells with two different surface designs are used at one plant, then by appropriate control of the cells the water consumption can be varied with load and weather conditions.

4 Experimental Results and Comparison with the Analysis

To establish the validity of the above analysis, model tower performance was measured under a number of operating conditions and compared with the computer simulation. An energy balance calculation between the air and water flow streams provided a check on the experimental procedure. Calculations [3] showed a maximum uncertainty of 15 percent. In fact, the maximum observed error in the energy balance for 14 test runs was 16 percent with the median being about 10 percent. The measured air-side energy change was consistently higher than the water-side. This was attributed to bias in the water temperature and air flow rate.

A scan of the outlet trough temperatures of one packing plate indicated that this reading may have been low, but as the scan covered only by one plate and could not be done for all test runs, the results were not used in calculating the values of Table 2. Another possible source of consistent error is the possibility of uneven air flow through the packing section. Care was taken during the model construction to minimize this occurrence, but small irregularities in plate support and spacing may have allowed air to bypass the exit air-side thermocouples causing a consistently high measurement. End effects due to the presence of a large water-free surface in the collecting trough and at the outlet points of the hot water distribution box were noticeable in the test data and very likely contributed to an increased evaporative heat transfer rate.

Typical inlet conditions to the model tower were inlet water temperature of 43°C (110°F), inlet air at 13°C (55°F), 4.844×10^{-3} lb_mH_2O/lb_m dry air, air and water mass flows of 4.2 and 0.84 kg/s (114 and 23 lb_m/min), respectively. For these conditions the air temperature change was 8°C (14°F) and water temperature change 12°C (21°F) indicating a relatively low exchanger effectiveness for these test conditions.

The test results are tabulated in Table 2 and are compared with the numerical predictions.

Comparison of data runs such as this with the computer model predictions established the validity of the analogy. In only two of the fourteen tests did the predictions vary from the measured values by amounts greater than the difference in the measured energy change between the air side and water side. In these two cases performance measurements at high water flow rates were attempted and the observed water streams overflowed their channels and increased the ratio of wet to dry surface area over what was assumed in the program.

Fig. 4 shows the effect of inlet air temperature and inlet water temperature levels on the heat transfer rate and the percent energy transfer by evaporation. For a fixed air temperature, increases in the inlet water temperature have two effects: they increase the initial dry

Table 1 Wet/dry performance for designs with different channel spacings and different plate widths

Plate Width	Number of Channels	Spacing Between Channels (in.)	Spacing Between Channels (cm)	Q_{Total}/A W/m²	Q_{Evap}/A W/m²	Q_{Evap}/Q_{Total}
10 ft	40	3	7.6	1126	508	45.2%
10	80	1.5	3.8	1776	1025	57.5%
10	20	6	15.2	681	249	36.5%
5	20	3	7.6	1268	502	39.7%
15	60	3	7.6	1022	511	50.0%

For All Cases

$T_{water_{in}} = 119.8°F = 48.8°C$
$T_{air_{in}} = 87.4°F = 30.8°C$
$V_{air_{in}} = 11.1$ ft/s = 3.4 m/s
Specific $Humidity_{in} = 0.0188$ lb/lb = .0188 kg/kg
Plate Thickness = 0.025 in. = .064 cm

Table 2

Run	No. 1		No. 2		No. 3		No. 4		No. 5	
	Test	Theory	Test	Theory	Test	Theory	Test	Theory	Test	Theory
Air Flow Rate kg/min	49.2		49.8		49.8		51.2		51.7	
Inlet Water Flow Rate, kg/min	9.3		9.5		9.5		16.9		14.2	
Inlet Air Temperature, °C	26.2		26.3		26.1		21.6		24.9	
Inlet Air Humidity, kg/kg × 10^3	3.183		3.163		2.850		3.505		3.849	
Inlet Water Temperature, °C	70.4		62.5		54.1		59.0		50.8	
Average Heat Transfer Rate, Kw	11.0	11.4	8.8	9.1	6.4	6.8	10.4	9.6	6.9	6.5
Evaporative Heat Transfer, Kw	4.9	4.6	3.6	3.5	2.6	2.5	4.5	3.3	3.1	2.3
Percent Evaporative Heat Transfer	44	40.3	41	39	39	37	43	34	45	35

Run	No. 6		No. 7		No. 8		No. 9		No. 10	
Air Flow Rate, kg/min	51.4		51.6		52.4		54.2		54.1	
Inlet Water Flow Rate, kg/min	10.8		10.8		10.4		9.4		9.4	
Inlet Air Temperature, °C	14.4		13.6		13.2		2.0		−0.7	
Inlet Air Humidity, kg/kg × 10^3	4.894		4.844		.3807		.4180		.4117	
Inlet Water Temperature, °C	63.9		58.1		42.9		48.6		50.9	
Average Heat Transfer Rate, Kw	11.0	11.3	9.7	9.8	5.6	6.0	8.6	8.9	10.2	10.4
Evaporative Heat Transfer, Kw	3.8	3.5	3.0	2.8	1.5	1.4	1.8	1.7	2.2	2.1
Percent Evaporative Heat Transfer	34	31	31	28	28	23	21	19	22	20

Run	No. 11		No. 12		No. 13		No. 14	
	Test	Theory	Test	Theory	Test	Theory	Test	Theory
Air Flow Rate, kg/min	53.8		53.5		30.0		29.9	
Inlet Water Flow Rate kg/min	9.5		9.4		9.5		9.5	
Inlet Air Temperature, °C	−1.6		−2.0		27.2		27.2	
Inlet Air Humidity kg/kg × 10^3	.4117		.4244		4.648		4.648	
Inlet Water Temperature, °C	58.4		63.0		73.5		55.9	
Average Heat Transfer Rate, Kw	11.7	11.9	13.2	13.2	9.3	9.4	5.4	5.3
Evaporative Heat Transfer, Kw	2.6	2.6	3.4	3.0	4.1	3.9	2.3	2.0
Percent Evaporative Heat Transfer	22	21	25	23	44	41	42	37

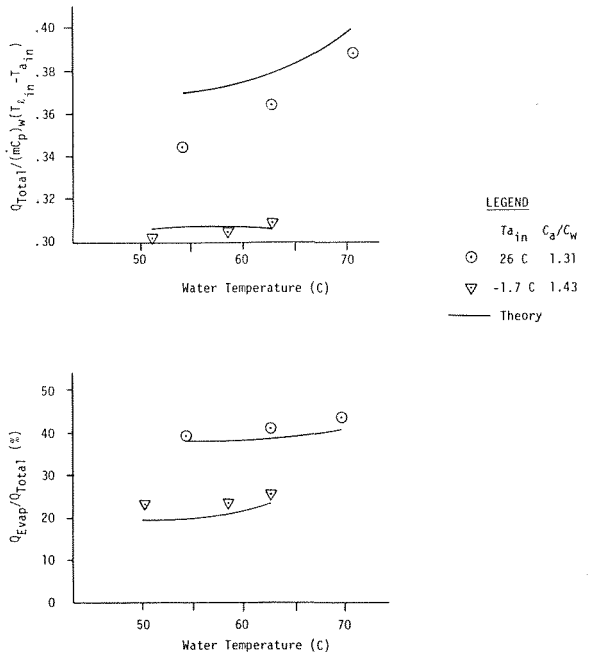

Fig. 4 Comparison of model theory and test results

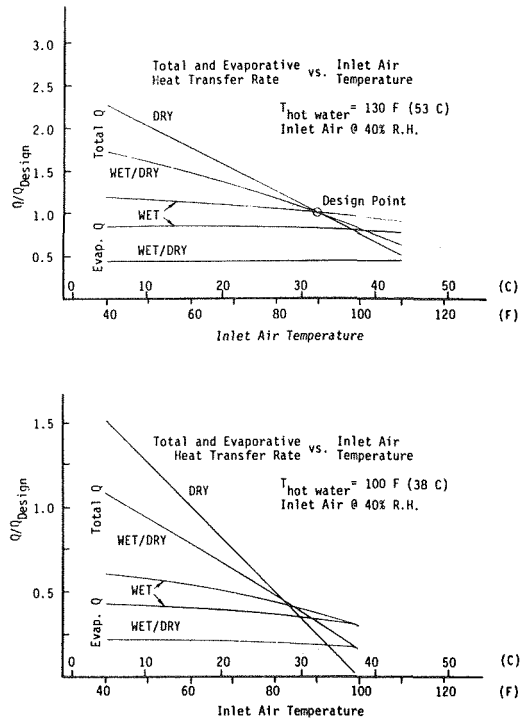

Fig. 5 Comparison of wet/dry performance with conventional wet and dry towers

bulb temperature difference, thereby increasing the convective heat transfer, and they also increase the saturation vapor pressure thus increasing evaporation. It is the latter effect which causes the nondimensional Q to rise. Note at low air temperature levels evaporation is severely reduced and the effect of changing the water temperature is diminished. For a fixed design the ratio of evaporative to total heat transfer is a very strong function of the inlet air temperature and a weak function of the inlet water temperature.

The plate was subdivided for these calculations into 625 subsections arranged in a square 25 × 25. The agreement between the data and predictions indicate the accuracy of the computer method and the correlations used for heat and mass transfer coefficients.

5 Comparisons with Conventional Towers

The computer model can be used as a tool to compare the performance of a tower using the new surface design which will be designated the wet/dry tower, to more conventional wet and dry cooling towers. Fig. 5 shows a comparison of the off-design performance of the three types of towers. The wet/dry tower is assumed to have 5 percent wet surface area. The major energy transfer mechanism in the wet tower is evaporation, about 80 percent of the energy transfer is by evaporation. The driving potential is the water vapor concentration difference between saturated water conditions and bulk air conditions. This difference is a weak function of inlet air conditions until very high inlet humidities and air temperatures are reached, thus the evaporative tower exhibits the smallest capacity decrease with increasing ambient temperatures. The wet/dry tower exhibits a behavior between the conventional wet and dry towers. As the percent wet area is increased, the wet/dry tower approaches wet tower performance. The curves in Fig. 5 are normalized to a fixed design temperature. Although it is not shown in Fig. 5, it must be remembered that at the same design heat rejection rate, the wet tower will require the least surface area and the dry tower the most area.

Fig. 6 shows the relative humidity of the exhaust air of the wet and wet/dry tower assuming the inlet air is at 90 percent relative humidity. As the exhaust relative humidity increases toward 100 percent, there is increased potential for fogging to occur. Note the low exhaust relative humidities for the wet/dry tower which indicate that fogging will not occur.

The annual water consumption of the wet/dry tower was compared

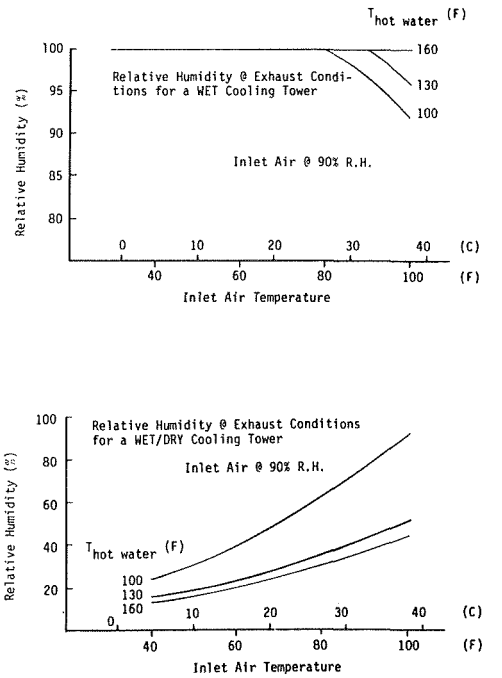

Fig. 6 Relative humidity at the exhaust of wet/dry and conventional wet towers

to that of a wet tower and a combined system of wet plus dry cooling towers for equal design cooling capacity. Figs. 7 and 8 illustrate the results for four different locations. $W.C._0$ is a common datum used to nondimensionalize the water consumption rates for the different towers. The figure beside the dry tower indicates the dry bulb temperature at which the dry tower can carry the entire cooling load of the power plant. Note that a combination of a wet/dry tower with a dry tower has a considerably lower water consumption rate than a

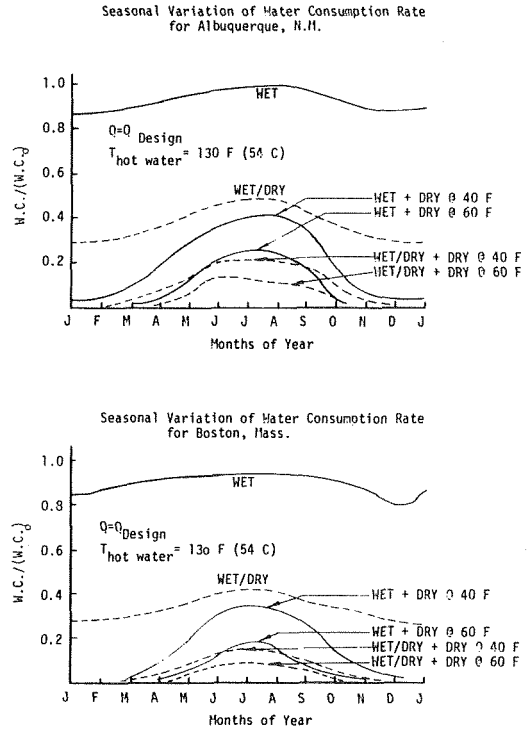

Fig. 7 Seasonal water consumption

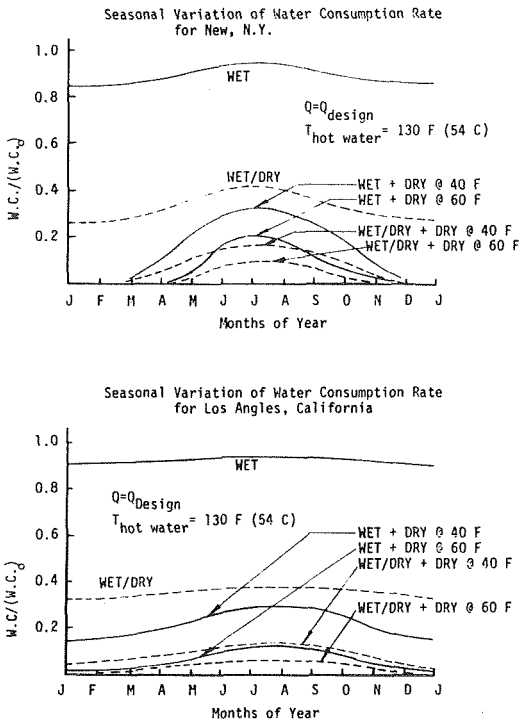

Fig. 8 Seasonal water consumption

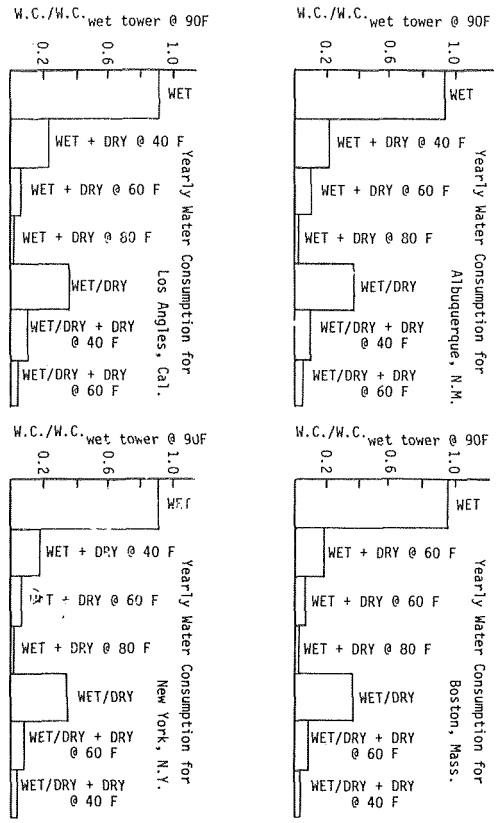

Fig. 9 Yearly water consumption

combined wet plus dry tower. For a fixed maximum or total yearly water consumption, a wet/dry plus dry tower system requires a much smaller dry tower than a wet plus dry system. Fig. 9 illustrates the total yearly water consumption for various systems.

For a utility with a large summer peak, the wet/dry tower can be used with a wet topping unit to reduce lost capacity penalities.

Conclusions

Experimental results have proven the effectiveness of the wet/dry plate concept in reducing cooling system evaporation. Good agreement was achieved between the test results and the numerical model. Studies using the numerical model have predicted a yearly water savings of 60 to 65 percent over a purely evaporative tower system. In addition, the possibility of site fogging has been eliminated.

Initial cost estimation [4] has shown the wet/dry plate concept to be competitive with presently available reduced-evaporation alternatives.

Additional work is underway on the problems of water distribution and collection as well as plate manufacture and on-site construction. Finally, tests and analyses of the advanced wet/dry cooling tower concept have shown it to be an effective, simplified and competitive method of rejecting condenser heat to the atmosphere at a reduced rate of water evaporation.

Acknowledgment

This research has been supported by the Division of Reactor Research and Development, Energy Research and Development Administration. Particular thanks are due to the suggestions and discussions by Mr. W. Savage.

References

1 United Engineers and Constructors, *Wet-Dry Cooling Tower Costs*, (Wash-1360), Dec. 1974.

2 Curcio, J. L., et al., "Advanced Dry Cooling Tower Concept," Energy Lab Report No. MIT-EL75-023, Heat Transfer Lab Report No. 82267-95, Department of Mechanical Engineering, MIT; Sept. 30, 1975.

3 Giebler, M. M., "Analysis and Testing of an Advanced Wet-Dry Cooling Tower Concept," S. M. Thesis, Department of Mechanical Engineering, MIT, Feb. 1976.

4 Snyder, T. K., et. al., "Advanced Wet-Dry Cooling Tower Concept," Energy Lab Report No. MIT-EL77-002, Heat Transfer Lab Report No. 83307-99, Department of Mechanical Engineering, MIT, Feb. 1977.

5 Han, Je-Chin, "Convective Heat Transfer in Channels Using Repeated Rib Roughness," Sc.D. Thesis, Department of Mechanical Engineering, MIT, Sept. 1976.
6 Rohsenow, W. M., Choi, H. Y., *Heat, Mass and Momentum Transfer*, Prentice-Hall, Inc., 1961.
7 Yadigaroglu, G., and Pastor, E. J., "An Investigation of the Accuracy of the Merkel Equation for Evaporative Cooling Tower Calculations, AIAA Paper No. 74-756, ASME Paper No. 74-T-59, 1974.

M. Nikanjam[1]
R. Greif

University of California, Berkeley
Department of Mechanical Engineering
and Lawrence Berkeley Laboratory,
Berkeley, California 94720

Heat Transfer During Piston Compression

An experimental and theoretical study has been carried out to determine the unsteady heat transfer from a nonreacting gas to the end wall of a channel during the piston compression of a single stroke. A thin platinum film resistance thermometer records the surface temperature of the wall during the compression. A conduction analysis in the wall, subject to the measured surface temperature variation, then yields the unsteady heat flux. A separate analysis based on the solution of the laminar boundary layer equations in the gas provides an independent determination of the heat flux. The two results are shown to be in good agreement. This is true for measurements that were made in air and in argon. Results for the heat transfer coefficient as a function of time are also presented and exhibit a nonmonotonic variation.

Introduction

The determination of the heat transfer from a gas to an enclosure during piston compression represents a problem that is of considerable practical importance as well as being one of fundamental interest. With respect to internal combustion engines, wall heat transfer processes are critical to the quenching of wall reactions leading to high hydrocarbon emissions, the durability of engine components, the loss of energy leading to decreased efficiency, etc. [1–5]. The transient, variable volume (moving surface), variable pressure aspects of the compression process result in complex phenomena that are difficult to appraise (for example, refer to [6–9]).

The present experiments were carried out in a single pulse, compression-expansion apparatus [8]. The work is an experimental and theoretical study of the unsteady end wall heat transfer during piston compression. The measurements were carried out during the compression stroke of a single pulse.

Experimental Apparatus and Measurements

The present set of measurements was carried out to determine the heat transfer from a gas to the wall of a channel of square cross section during piston compression. The apparatus used was a stainless steel enclosure that was fitted with a pneumatically operated piston (cf. Oppenheim, et al. [8]). There are three main elements in the apparatus: the compression chamber or test section, the driving chamber and the displacement control chamber. The chambers are separated from each other by bearings and seals, and contain separate pistons which are connected by an adjustable shaft (Fig. 1).

The test section has four ports on the top and four ports on the bottom walls. The chamber can be purged and filled through these ports which may also be used for temperature and pressure measurements. The end block of the chamber also has a port which may be adjusted to allow for a variety of configurations. The test section, 38 mm × 38 mm, contains an aluminum piston that is fitted with teflon seals. The test piston is connected by an aluminum rod to another piston in the driving chamber. The driving force for this piston is provided by the pressure difference across the piston. The pressure is supplied from compressed gas stored in a large tank near the apparatus. The flow through the driving chamber is controlled by a system of solenoid valves that are operated electronically.

The displacement control chamber is filled with oil and contains a series of snubbers which vary in inside diameter. The controlling piston in this snubber section, which is connected to the driver piston, moves first in an area of increasing cross section, then in a constant area and finally into a region of decreasing cross-sectional area. The snubbers can be changed to provide for different trajectories and strokes. A typical stroke for the present experiments was 5 in. (130 mm) with a compression ratio of 8 and a time interval of 30 ms.

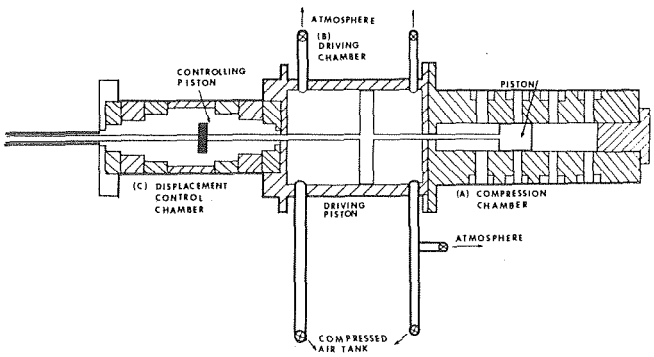

Fig. 1 Experimental apparatus including (a) compression chamber, (b) driving chamber and (c) displacement control chamber

[1] Present address: Union Carbide Corporation, Bound Brook, New Jersey.

Contributed by the Heat Transfer Division for publication in the JOURNAL OF HEAT TRANSFER. Manuscript received by the Heat Transfer Division October 21, 1977.

The main shaft extends beyond the snubber section and is fitted with a steel rack with a set of teeth. Opposite the shaft is a magnetic pickup that senses the teeth as they pass by. The corresponding change in voltage is then recorded as a function of time (Fig. 2) which yields the piston displacement as a function of time. To determine the pressure in the test section as a function of time, a Kistler pressure transducer (SN 52036) was placed in one of the ports. The output is shown in Fig. 2.

To measure the temperature of the wall as a function of time, a thin-film resistance thermometer was used. This gauge was built to fit the end block, and also the side wall of the test section, and was mounted flush with the wall to avoid disturbing the flow. The resistance thermometer consisted of a thin platinum film on an insulated backing. In the present experiments platinum was painted on a machinable glass-ceramic base (Macor, made by Corning Glass Works). The gauge was then baked in an oven to a temperature of 750°C to drive off the volatile constituents and to obtain a good metal-glass bond. Typically, the films had a resistance of 100 ohms with typical dimensions 1.3 cm × 0.3 cm.

The resistance thermometer was connected as the active element in a d-c bridge. A temperature change caused a change in resistance of the platinum film which caused an unbalance in the bridge. The resulting voltage was then amplified and displayed on a Tektronix oscilloscope (Fig. 2). For calibration purposes the resistance thermometer was placed in an enclosure that was thermally controlled and the voltage output of the bridge was recorded as a function of the temperature. The calibration tests were performed before and after the experiments and no changes were observed.

Numerous studies have been carried out with thin-film resistance thermometers [10–21]. These studies have demonstrated the durability of these gauges and their rapid response times. Indeed, calculations give a response time that is less than one μs and this has been confirmed by measurements that were made with these gauges in a shock tube. One important application has been in the determination of the wall heat flux based on the measured surface temperature histories. The evaluation of the heat flux is dependent on the properties of the insulating base, in particular on the parameter $(\rho ck)^{1/2}$. The value of this parameter obtained directly from experimental gauge measurements for a pyrex base [13, 16, 21] is 0.036 cal/cm^2°C s$^{1/2}$ (0.151 watt s$^{1/2}$/cm^{2}K) which is in very good agreement with the value calculated from the bulk properties of pyrex; namely, 0.035 cal/cm^2°C s$^{1/2}$ (0.146 watt s$^{1/2}$/cm^{2}K). The value of $(\rho ck)^{1/2}$ for Macor based on the values of the bulk properties [22] is 0.033 cal/cm^2°C s$^{1/2}$ (0.138 watt s$^{1/2}$/cm^{2}K) and this is the value that has been used in the present experiments.

Analysis

The determination of the heat flux during piston compression is based on the measured surface temperature of a thermally infinite solid (Macor) that is initially at a constant temperature. The solution for the wall heat flux is given by [16]:

$$q_{w,s} = \left(\frac{k\rho c}{\pi}\right)^{1/2} \int_0^t \frac{1}{(t-\bar{t})^{1/2}} \frac{dT_w}{d\bar{t}}\, d\bar{t} \tag{1}$$

To perform the numerical calculations for the heat flux it is more convenient to use the following form of equation (1) [16]:

$$q_{w,s} = \left(\frac{k\rho c}{\pi}\right)^{1/2} \left\{\frac{T_w(t) - T_i}{t^{1/2}} + \frac{1}{2}\int_0^t \frac{T_w(t) - T_w(\bar{t})}{(t-\bar{t})^{3/2}}\, d\bar{t}\right\} \tag{2}$$

which does not involve measurement of slopes.

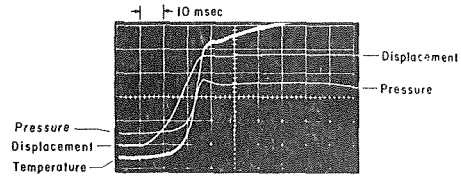

Fig. 2 Typical oscillogram for surface temperature, displacement and pressure measurements

An alternative approach for the determination of the wall heat flux is based on a solution of the conservation equations in the gas as applied to the thin boundary layer near the end wall. Neglecting viscous dissipation and taking the pressure to be uniform yields the following one-dimensional equations of continuity and energy:

$$\frac{\partial \rho}{\partial t} + \frac{\partial(\rho u)}{\partial x} = 0 \tag{3}$$

$$\rho c_p \left[\frac{\partial T}{\partial t} + \frac{u\partial T}{\partial x}\right] = \frac{dp_\infty}{dt} + \frac{\partial}{\partial x}\left(k\frac{\partial T}{\partial x}\right) \tag{4}$$

where x is the coordinate perpendicular to the wall. These are the same equations used by Isshiki and Nishiwaki [20] in their study of the effects of cyclic changes in an internal combustion engine and their analysis is used below. (For the simpler constant pressure problem refer to [18].) The continuity equation is satisfied by a stream coordinate ψ according to

$$\frac{\rho}{\rho_i} = \frac{\partial \psi}{\partial x}, \quad \frac{\rho u}{\rho_i} = -\frac{\partial \psi}{\partial t} \tag{5}$$

where ρ_i is the initial density (or a density at a specified state) of the gas. Using the ideal gas law, $p_\infty = \rho RT$ and a linear thermal conductivity variation with respect to temperature, the energy equation in ψ, t coordinates becomes:

$$\frac{\partial T}{\partial t} = \frac{\gamma - 1}{\gamma}\frac{T}{p_\infty}\frac{dp_\infty}{dt} + \alpha_i \frac{p_\infty}{p_i}\frac{\partial^2 T}{\partial \psi^2} \tag{6}$$

The transformation $d\tau = (p_\infty/p_i)dt$ [20] then yields

$$\frac{\partial T}{\partial \tau} = \frac{\gamma - 1}{\gamma}\frac{T}{p_\infty}\frac{dp_\infty}{d\tau} + \alpha_i \frac{\partial^2 T}{\partial \psi^2} \tag{7}$$

The gas outside the boundary layer is assumed to be compressed isentropically so that $p_\infty/p_i = (T_\infty/T_i)^{\gamma/(\gamma-1)}$. Making this substitution yields

$$\frac{\partial T}{\partial \tau} = \frac{T}{T_\infty}\frac{dT_\infty}{d\tau} + \alpha_i \frac{\partial^2 T}{\partial \psi^2} \tag{8}$$

Then, introducing the variable $\phi = T/T_\infty$ into equation (8) gives [20]

Nomenclature

c = specific heat of solid
c_p = specific heat of gas
h = heat transfer coefficient
k = thermal conductivity
p = gas pressure
q = heat flux
R = gas constant
t = time
T = temperature
u = gas velocity
V = volume
x = coordinate normal to wall
$\alpha = k/\rho c_p$ = thermal diffusivity
γ = ratio of the specific heats
$\phi = \dfrac{T}{T_\infty}$ = temperature ratio
ρ = density
ψ = stream coordinate
τ = transformed time

Subscripts

g = gas
i = initial
s = solid
w = wall
∞ = outside boundary layer

$$\frac{\partial \phi}{\partial \tau} = \alpha_i \frac{\partial^2 \phi}{\partial \psi^2} \tag{9}$$

subject to the conditions

$$\phi(\psi, 0) = 1$$
$$\phi(0, \tau) = T_w/T_\infty = T_w/T_i(V_i/V)^{\gamma-1} = \phi_w \tag{10}$$
$$\phi(\infty, \tau) = 1$$

Note that the wall location corresponds to $\psi = 0$.
The solution for the wall heat flux is then given by [16]:

$$q_{w,g} = +k_w \left.\frac{\partial T}{\partial x}\right|_{x=0} = -\frac{k_w \rho_w T_\infty}{\rho_i (\pi \alpha_i)^{1/2}} \int_0^\tau \frac{1}{(\tau - \bar{\tau})^{1/2}} \frac{d\phi_w}{d\bar{\tau}} d\bar{\tau} \tag{11}$$

or

$$q_{w,g} = -\frac{k_w \rho_w T_\infty}{\rho_i (\pi \alpha_i)^{1/2}} \left\{ \frac{\phi_w(\tau) - 1}{\tau^{1/2}} + \frac{1}{2} \int_0^\tau \frac{\phi_w(\tau) - \phi_w(\bar{\tau})}{(\tau - \bar{\tau})^{3/2}} d\bar{\tau} \right\} \tag{12}$$

Results and Discussion

Experiments were carried out in air and in argon with the thin film gauge placed at the end wall of the compression chamber. Typical results for the unsteady heat flux as determined from both the solution of the conduction equation in the solid, $q_{w,s}$, and the solution of the laminar boundary layer conservation equations in the gas, $q_{w,g}$, are presented in Figs. 3 and 4. The results for the heat flux from these

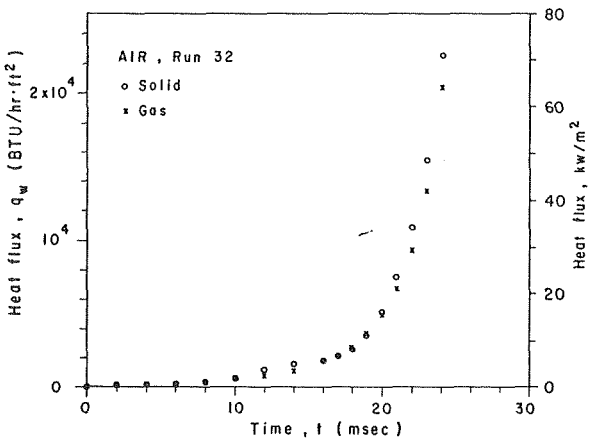

Fig. 3 Heat flux variation

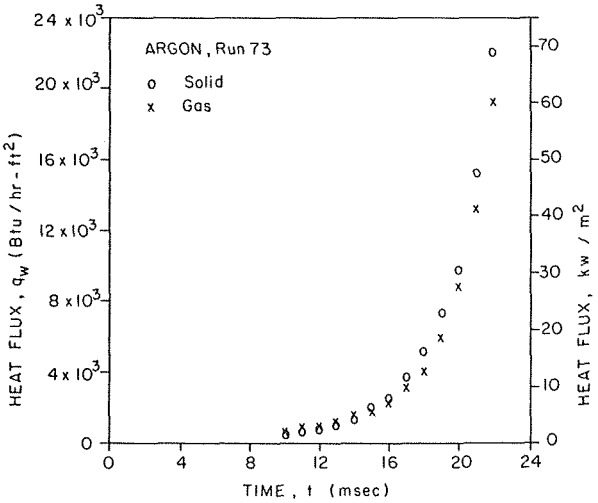

Fig. 4 Heat flux variation

two independent methods are seen to be in good agreement although we do have more confidence in the result based on the conduction analysis in the solid. This is because the calculation for $q_{w,s}$ only depends on the variation of the wall temperature, T_w, and the constant properties of the solid. In contrast, the calculation for $q_{w,g}$ requires the specification of the variation of the thermal conductivity of the gas with respect to temperature, the piston trajectory, that is, the volume of the compressed gas as a function of time, etc. It is noted that the determination of $q_{w,s}$ is influenced by the value of the parameter $(\rho ck)^{1/2}$, the nonzero thickness of the platinum film and the sensitivity of the gauge. On the basis of numerous investigations it has been concluded that the heat flux can be determined to an accuracy from ±5 to ±15 percent [16].

In the determination of the heat flux $q_{w,g}$, the dependent variable was shown to be $\phi_w = T_w/T_\infty = T_w/T_i(V_i/V)^{\gamma-1}$. Calculations were carried out for constant and for time varying values of the wall temperature, but because the variation in the wall temperature was small in comparison to the much larger variation of T_∞, the results were essentially the same. There are many applications when the variation in T_w is small and is not measured (so that the conduction analysis in the solid cannot then be used as the basis for determining the heat flux). Hence, for these applications $q_{w,g}$ (which is in good agreement with $q_{w,s}$) provides the basis for calculating the heat flux. In detail, for $\phi_w(\tau) = T_w(\tau)/T_\infty(\tau) \simeq \text{constant}/T_\infty(\tau)$, equation (12) becomes

$$q_{w,g} = \frac{-k_w \rho_w}{\rho_i (\pi \alpha_i)^{1/2}} \left\{ \frac{T_w - T_\infty(\tau)}{\tau^{1/2}} + \frac{T_\infty(\tau) T_w}{2} \int_0^\tau \frac{T_\infty^{-1}(\tau) - T_\infty^{-1}(\bar{\tau})}{(\tau - \bar{\tau})^{3/2}} d\bar{\tau} \right\} \tag{13}$$

so that the heat flux is determined solely from the variation of T_∞.

Of particular interest is the result for the heat transfer coefficient during piston compression which is obtained from the relation

$$h = \frac{q_{w,s}}{T_\infty - T_w} = \frac{1}{T_\infty(t) - T_w(t)} \left(\frac{k\rho c}{\pi}\right)^{1/2} \left\{ \frac{T_w(t) - T_i}{t^{1/2}} + \frac{1}{2} \int_0^t \frac{T_w(t) - T_w(\bar{t})}{(t - \bar{t})^{3/2}} d\bar{t} \right\} \tag{14}$$

The results for h are presented in Figs. 5 and 6 along with the values for V/V_i, T_∞, T_w and $q_{w,s}$. The values for h based on $q_{w,g}$ are in good agreement with those based on $q_{w,s}$ and are therefore not shown. Note that the heat transfer coefficient first decreases with time but as the compression continues, h reaches a minimum value and then increases with time. At the beginning of the compression the increase in the boundary layer thickness causes the heat transfer coefficient to decrease with time. However, as the compression continues work done by the piston and the convective transport (in the boundary layer towards the wall) become more important, finally causing the heat transfer coefficient to increase as shown in Figs. 5 and 6. For completeness, it is noted that the convective transport is a result of the drop in the gas temperature between the outer region and the region near the wall and the associated increase in density near the wall. Indeed, the density increase is brought about by the convection of the gas towards the wall. Reference to [18] should also be made which considers this effect in respect to a constant pressure problem.

It is noted that under ideal conditions the piston should come to a smooth stop at the end of the compression stroke. However, in practice the piston rebounds near the end of the stroke. This is accompanied by a decrease in the pressure which is followed by a slight rise as the piston completes the compression and then comes to the final position (Fig. 2).

In closing it is pointed out that there is some effect due to mixing in the gas resulting from the vortex that forms at the piston-wall interface [6–8]. This effect is directly reflected in the result for the heat flux from the conduction analysis in the solid via the measured wall temperature variation. However, in the boundary layer conservation equations in the gas any mixing effect must also be included as an additional convective transport mechanism. The omission of this contribution is consistent with the slightly smaller results obtained

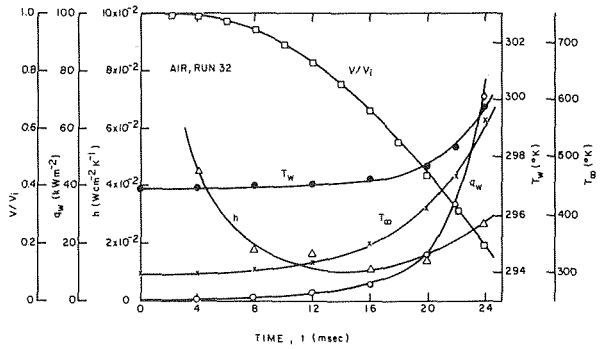

Fig. 5 Measured and calculated variables

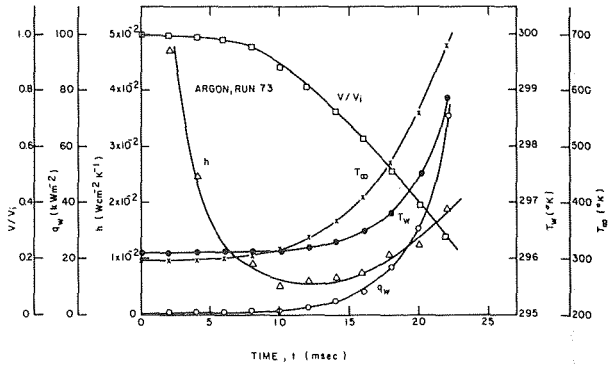

Fig. 6 Measured and calculated variables

for $q_{w,g}$ in comparison to $q_{w,s}$. Furthermore, the velocity of the piston directly imparts a velocity to the gas which has also been omitted in the boundary layer analysis. This is (also) consistent with the slightly smaller results for $q_{w,g}$.

Conclusions

The unsteady wall heat flux during piston compression of a single stroke has been determined by two independent methods. The heat transfer based on the laminar boundary layer equations and the piston trajectory yields results that are in good agreement with the flux obtained from the conduction analysis in the solid. This is true for end wall measurements that were made in air and in argon. Results for the heat transfer coefficient for all cases exhibit a nonmonotonic variation with respect to time.

Acknowledgment

The authors acknowledge with appreciation the support of this research by the National Science Foundation under NSF/RANN Grant AER-76-08727 and by the U.S. Energy Research and Development Administration under Contract W-7405-ENG-48.

References

1 Overbye, V. D., Bennethum, J. E., Uyehara, O. A., and Myers, P. S., "Unsteady Heat Transfer in Engines," Society of Automotive Engineers Transactions, Vol. 69, 1961, pp. 461–494.

2 Annand, W. J. D., "Heat Transfer in the Cylinders of Reciprocating Internal Combustion Engines," *Proc. I. Mech. E.*, Vol. 117, 1963.

3 LeFeuvre, T., Myers, P. S., and Uyehara, O. A., "Experimental Instantaneous Heat Fluxes in a Diesel Engine and their Correlation," *Society of Automotive Engineers Transactions*, Vol. 78, 1969, 690464, pp. 1717–1738.

4 Dao, K., Uyehara, O. A., and Myers, P. S., "Heat Transfer Rates at Gas-Wall Interfaces in Motored Piston Engines," *Society of Automotive Engineers Transactions*, Vol. 82, 730632, 1974, pp. 2237–2258.

5 Chong, M. S., Milkins, E. E., and Watson, H. C., "The Prediction of Heat and Mass Transfer During Compression and Expansion in I.C. Engines," Society of Automotive Engineers, 760761, 1976.

6 Tabaczynski, R. J., Hoult, D. P., and Keck, J. C., "High Reynolds Number Flow in a Moving Corner," *J. Fluid Mech.*, Vol. 42, 1970, pp. 249–256.

7 Daneshyar, H., Fuller, D. E., and Decker, B. E. L., "Vortex Motion Induced by the Piston of an Internal Combustion Engine," *Int. J. Mech. Sci.*, Vol. 15, 1973, pp. 381–390.

8 Oppenheim, A. K., Chang, R. K., Teichman, K., Smith, O. I., Sawyer, R. F., Ham, K., and Stewart, H. E., "A Cinematographic Study of Combustion in an Enclosure Filled with a Reciprocating Piston," Conference on Stratified Charge Engines, London, England, 1976.

9 Witze, P. O., "Hot-Wire Measurements of the Turbulent Structure in a Motored Spark-Ignition Engine," AIAA Paper No. 76-37, 1976.

10 Pfriem, H., "Zur Messung Schnell Wechselnder Temperatures in des Zylinderwand von Kolbenmaschiesen," *Forschung Ing.-West.*, Bd. 6, Heft 4, 1935, pp. 195–201.

11 Meier, A., "Recording Rapidly Changing Cylinder-Wall Temperatures," translation, NACA TM 1013, 1939.

12 Rabinowicz, J., Jessey, M. E., and Bartsch, C. A., "Resistance Thermometer for Heat Transfer Measurement in a Shock Tube," GALCIT Hypersonic Research Project Memo, 33, Guggenheim Aeronautical Laboratory, California Institute of Technology, July 1956.

13 Vidal, R., "Model Instrumentation Techniques for Heat Transfer and Force Measurements in a Hypersonic Shock Tunnel," Report AD 917-A-1, Buffalo, N.Y., Cornell Aeronautical Laboratory, Inc., 1956.

14 Bromberg, R., "Use of the Shock Tube Wall Boundary Layer in Heat Transfer Studies," *Jet Propulsion*, Vol. 26, Sept. 1956, pp. 737–740.

15 Rose, P. H., and Stark, W. I., "Stagnation Point Heat Transfer Measurements in Air at High Temperature," *Research Note* 24, Everett, Mass., AVCO Research Laboratory, AVCO Manufacturing Corp., Dec. 1956.

16 Hall, J. G. and Hertzberg, A., "Recent Advances in Transient Surface Temperature Thermomentry," *Jet Propulsion*, Vol. 28, 1958, pp. 719–723.

17 Bogdan, L., "High-Temperature, Thin-Film Resistance Thermometers for Heat Transfer Measurement," NASA Contractor Report, NASA CR-26, April 1964.

18 Collins, D. J., Greif, R. and Bryson, A. E., "Measurements of the Thermal Conductivity of Helium in the Temperature Range 1600–6700 K," *Int. J. Heat Mass Transfer*, Vol. 8, 1965, pp. 1209–1216.

19 Collins, D. J., "Shock Tube Study for the Determination of the Thermal Conductivity of Neon, Argon, and Krypton," ASME JOURNAL OF HEAT TRANSFER, Vol. 88, 1966, pp. 52–56.

20 Isshiki, N. and Nishiwaki, N., "Study on Laminar Heat Transfer of Inside Gas with Cyclic Pressure Change on an Inner Wall of a Cylinder Head," 4th International Heat Transfer Conference, Paris-Versialles, 1970, FC 3.5, pp. 1–10.

21 Skinner, G. T., "Calibration of the Thin-Film Gauge Backing Materials," ARS J., Vol. 31, 1961.

22 Grossman, D. G., Corning Glass Works, personal communication; also, Pamphlet MGS 274-2.

A. Gany,
Post Doctoral Research Associate

L. H. Caveny,
Senior Professional Staff Member,
Mem. ASME

M. Summerfield
Professor of Aerospace Engineering,
Mem. ASME

Aerospace and Mechanical Sciences Department,
Princeton University,
Princeton, N.J.

Aerothermochemistry of Metal Erosion by Hot Reactive Gases

Analytical studies were conducted to investigate the mechanisms of metal erosion produced by short exposures (< 2 ms) to flowing high pressure (~ 350 MPa), high temperature (~ 3000 K) reactive gases. Previous experimental studies established that the intense heating during the short exposure produced melting and, when reactive gases were used, oxidation of the surface and enhanced erosion. The reactions were modeled as diffusion-limited, heterogeneous surface reactions which achieved equilibrium at the gas/metal interface. Calculated results for the sequential events of initial heating, surface reactions, and melting explained and correlated the experimental trends for Fe, Al, Ti, and Mo. Rapidly increasing erosion rates with increasing O_2 concentration are the result of the surface reactions between the metal and O_2. As O_2 concentration increases, the heating produced by the surface reaction exceeds the forced convective heating which, in turn, greatly enhances the melting rate.

Introduction

Subjecting metals and metal alloys to a stream of high-pressure (up to 350 MN/m^2) and high-temperature reactive gases (2500 to 3000 K) flowing at high Reynolds numbers (up to 5×10^6) produces regression rates (i.e., erosion) of the metal surface that are much higher than the rates calculated from the theory of inert melting. The exposure times considered in this study are generally very short, on the order of one to two milliseconds. In earlier papers [1,2] which presented experimental data of steel and aluminum, the regression rate augmentation was hypothesized to be a result of the chemical interaction between the metal and the high-speed gas flow. However, in the previous studies no effort was made to model the chemical interactions.

The interpretation of the gas-metal interactions in combustion gas experiments is always obscured to some degree by the simultaneous presence of a large number of gaseous species formed in combustion processes. The problems associated with large numbers of gaseous species (i.e., using combustion gases) were overcome by developing and using a ballistic compressor [3]. The ballistic compressor is a device that provides hot, high-pressure individual gases (or prescribed gas mixtures) which can be brought into contact with a metal specimen for the study of the interaction processes. This paper uses the results of experimental studies in which high-pressure and high-temperature flows of individual gases and gas mixtures interacted with steel alloy AISI 4340, aluminum alloy 6061-T6, and pure materials (e.g., Fe, Ti, and Mo) and interprets the experimental findings in terms of the aerothermochemistry of the gases interacting with the metals.

A number of investigations have been performed on the high-temperature oxidation (e.g., [4]), combustion (e.g., [5, 6, and 7]), and ignition (e.g., [8]) of metals in stagnant or low flow environments. The present study considers chemical reactions of metals in a very high-pressure and high-speed flow system. These reaction rates are extremely fast compared to those of [4–8]. The introduction of fluid dynamics in gas-metal reactions alters considerably the mechanisms of oxidation and combustion proposed for the stagnant atmosphere studies; the high-speed flow limits the build-up of oxide scales which normally offer some protection from further oxidation.

Experimental Approach

The ballistic compressor utilizes a reservoir of driver gas to drive a piston to compress adiabatically the desired test gas. In this manner, the apparatus produces a quantity of hot, high-pressure gas (e.g., 350 MN/m^2 and 3000 K) that flows through the choked test orifice. The pressure history of the test gas is monitored by a high-frequency Kistler 607 piezoelectric pressure transducer. A detailed description of the ballistic compressor is given in [3].

The high-pressure and high-temperature gases generated by the ballistic compressor are brought into contact with metal specimens by passing the gases through a small orifice, 0.066 cm diameter hole, in disks 0.25 cm thick (see configuration in Fig. 1). Either individual gases (e.g., H_2, N_2, and Ar) or gas mixtures (e.g., O_2/N_2, Ar/CO_2, and H_2/N_2) are used. However, this paper will concentrate on the effects produced by N_2 and O_2/N_2. Metal test specimen mass loss and regression depths (measured by a profilometer with 1 μm resolution)

Contributed by the Heat Transfer Division of THE AMERICAN SOCIETY OF MECHANICAL ENGINEERS and presented at the AIChE-ASME Heat Transfer Conference, Salt Lake City, Utah, August 15–17, 1977. Manuscript received by the Heat Transfer Division November 8, 1977. Paper No. 77-HT-12.

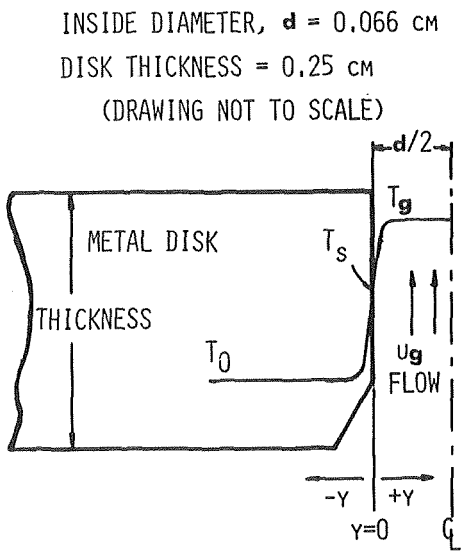

Fig. 1 Configuration and nomenclature of test specimen

are the primary quantitative data used to indicate the degree of the gas-metal interaction during exposure.

ANALYTICAL APPROACH

Outline of the Erosion Model. The extreme conditions of high-pressure and high-speed flow of reactive gases in the system produce situations under which the buildup of the oxide scales is limited and molten matter (of either oxide or metal), if formed, is very rapidly wiped off by the shear forces of the flow. Evidence of the formation of the melt layer and its removal is included and discussed in [2] and [9].

In stagnant or low-flow conditions it has been observed that some metals burn in the vapor phase while others are consumed by surface reactions [6, 7, 8]. Simple criteria such as the boiling point of the metal and its oxide have been used to categorize these processes. For example, those metals whose boiling temperature is lower than the boiling point of their oxide (e.g., aluminum) burn in the vapor phase. It is anticipated that others (e.g., iron and titanium) with boiling temperatures higher than the boiling temperature of the oxide burn on the surface [6, 8]. In the present case the situtation is quite different; therefore, the reaction mechanism is modified. The rapid removal of the molten layer prevents the temperature of the surface from exceeding the melting temperature of the metal, and the surface is exposed to the attack of reactive gases. Therefore, surface heterogeneous reactions between the metal and the reactive gases are expected for any metal under those conditions regardless of the criteria which are used to characterize the combustion of metals under low-flow conditions. This explanation is not inconsistent with the findings of Summerfield, et al. [9] for aluminum burning in the gas phase when aluminum is exposed to high-pressure, high-temperature combustion gas flows. Indeed, due to the wiping off of the molten aluminum from the surface, it is likely that droplets and vapors of the metal exist and also react in the flowing gases. For the conditions considered in this paper, reaction rates are assumed to be very fast in comparison to gas phase diffusion processes. The erosion is a result of both the chemical attack of the surface by reactive gases and the melting and melt-layer removal by the flow.

Physical Situation Considered in Model. The erosion process includes several steps in which successive and simultaneous heat transfer, surface reaction, and melting events take place. The relative importance of individual events depends on the severity of a particular pressure versus time program and the oxidizer concentration. Accordingly, the reader should keep in mind that in the discussion that follows, a specific type of exposure is being considered. The events which may occur at the surface of metal specimens and which have been included in the mathematical model are:

1 As the gases are compressed, they increase in temperature and flow through the orifice in the metal specimen. This is the beginning of the forced convective heating. (Fig. 2 will be used to illustrate the sequence of events.)

2 As the piston moves toward the end of the ballistic compressor (see Fig. 2 (a)), the rate of pressurization and rate of temperature rise accelerate rapidly toward their peak values (i.e., the point of maximum piston travel and minimum gas volume). During this period, the convective heating rate, q_g, accelerates rapidly, since both the free stream temperature and the convective heat transfer coefficient are increasing (see Figs. 2 (a) and (b)). For gases which contain a highly reactive oxidizer, heating due to surface reactions, q_r, becomes prominent above a threshold temperature (compare the results for N_2 and air in Fig. 2 (c)). For cases in which these reactions are very exothermic (e.g., when the reactive gas is oxygen), the heating due to surface reactions may be much greater than the nonreactive convective heating. As the metal and oxidizing species react, metallic oxides are formed (for discussions of oxide formation on steel, see [1 and 2]) and may be carried away by the shear forces of the high-speed flow. This is the first mode of material loss or erosion.

3 As the surface temperature continues to increase, the solidus or melting point is achieved. As the metal becomes mobile, it is carried away by the flow. This is the second mode of material loss.

4 After peak pressure is achieved (and the piston in the ballistic compressor reverses its direction), the gas temperature begins to decrease rapidly. Accordingly, q_g decreases rapidly. Indeed, for situations in which surface reactions are prominent, the gas temperature,

Nomenclature

c = specific heat, J/kg-K
c_p = gas specific heat at constant pressure, J/kg-K
C = molar concentration, kg-mol/m^3
d = hydraulic diameter, m
D = gas molar diffusivity, m^2/s
ΔG = Gibbs free energy per kg-mol of O_2, J
h = heat transfer coefficient, W/m^2-K
h_m = mass transfer coefficient, m/s
ΔH_R = enthalpy of reaction, J/kg-metal
J = mass flux on molar basis, kg-mol/m^2-s
K_p = equilibrium constant based on partial pressures, atm^{-1}
L = latent heat of fusion, J/kg
Me = metal
M = molecular or atomic weight, kg/kg-mol
$\mathrm{Nu} \equiv hd/\lambda_g$, Nusselt number
$\mathrm{Pr} \equiv \mu_g c_p/\lambda_g$, Prandtl number
p = pressure, Pa
q = heat flux, W/m^2
r = linear erosion rate, m/s
R_u = universal gas constant, J/kg-mol-K
$\mathrm{Re} \equiv \rho_g u_g d/\mu_g$, Reynolds number
$\mathrm{Sc} \equiv \mu_g/\rho_g D$, Schmidt number
$\mathrm{Sh} \equiv h_m d/D$, Sherwood number
t = time, s
T = temperature, K
T_m = metal melting temperature, K
u = axial gas flow velocity, m/s
x,y = stoichiometric coefficients
y = distance from metal surface, m
Y = molar fraction
λ = thermal conductivity, W/m-K
ν = stoichiometric ratio: mol-metal/mol-O_2
Ω = collision function
ρ = density, kg/m^3

Subscripts

g = gas, gas phase
ig = threshold temperature for surface reactions
ox = oxidizer
0 = initial conditions
r = chemical reaction
s = condensed phase surface
x,y = stoichiometric coefficients

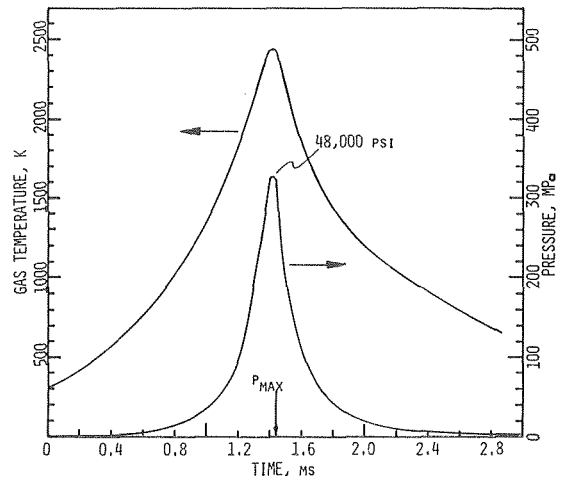

Fig. 2(a) Measured pressure versus time and calculated temperature versus time

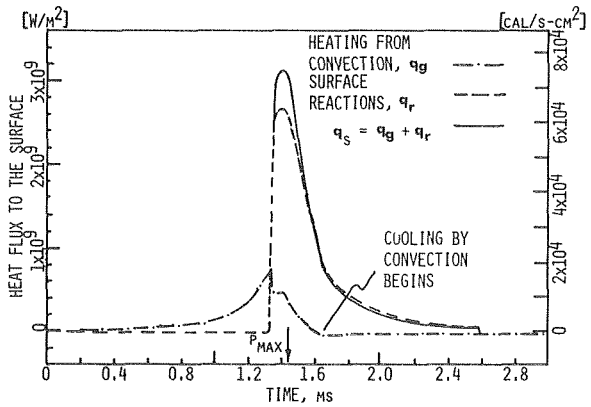

Fig. 2(b) Heating rates due to forced convection and surface reactions showing that surface reaction can be the primary source of heat transfer to the surface

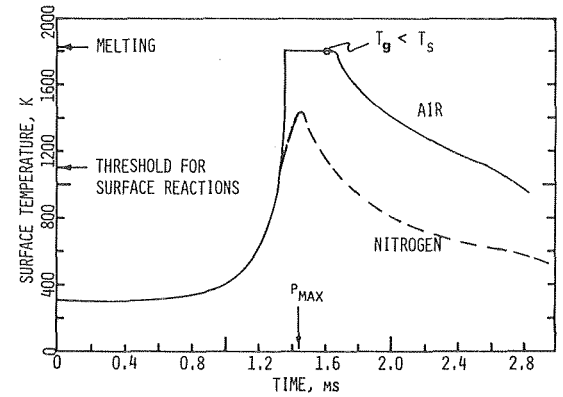

Fig. 2(c) Surface temperature versus time illustrating the onset of surface reactions and melting. Comparison of the results for air and N_2 illustrates the importance of considering the reaction processes

Fig. 2 Calculated results for AISI 4340 steel correponding to measured pressure versus time trace for air

T_g, will fall below the surface temperature, T_s. As pressure decreases, the surfaces temperature falls below the melting point and no further melting occurs.

5 As the surface temperature, gas temperature, and pressure decrease, the surface reaction rates diminish.

The pressure versus time programs and gas compositions were specified so that the net mass losses were relatively small, e.g., erosion depths of 2 to 20 μm are typical. The scales on the surface were observed using the two-piece specimen described in [1]. Scanning Electron Microscope images reveal a variety of very thin scale deposits. However, the scales that remain probably form near the end of the pressure cycle and are not subjected to high shear forces.

Formulation of Equations. Numerical solutions were obtained for the nonsteady heat conduction equation in the condensed (metal) phase (see geometry in Fig. 1):

$$\rho c \left(\frac{\partial T}{\partial t} + r\frac{\partial T}{\partial y}\right) = \frac{\partial}{\partial y}\left(\lambda \frac{\partial T}{\partial y}\right) \tag{1}$$

The symbols corresponding to the consensed phase are not subscripted. Since the depth heated is small compared to the other dimensions of the orifice, the one-dimensional form of equation (1) is a good approximation. As shown in Figs. 3 and 4, the thermal properties of metals are very temperature dependent. Thus, variable thermal properties were considered in the model. The thermal properties used in the calculations were taken from [10].

The initial condition is:

$$T = T_0 \quad \text{when } t = t_0 \tag{2}$$

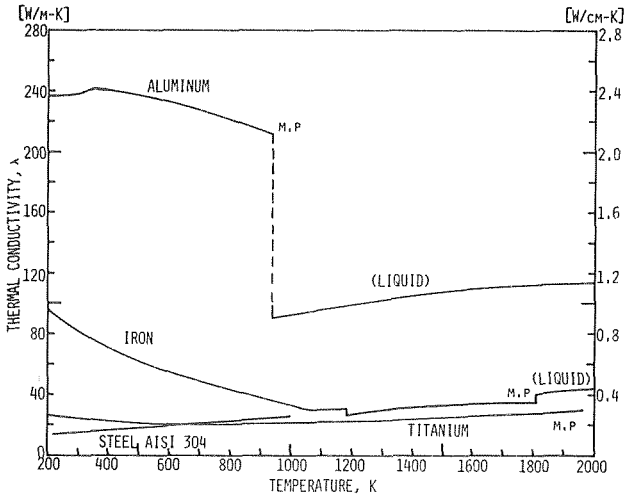

Fig. 3 Thermal conductivity of various metals and metallic alloys versus temperature

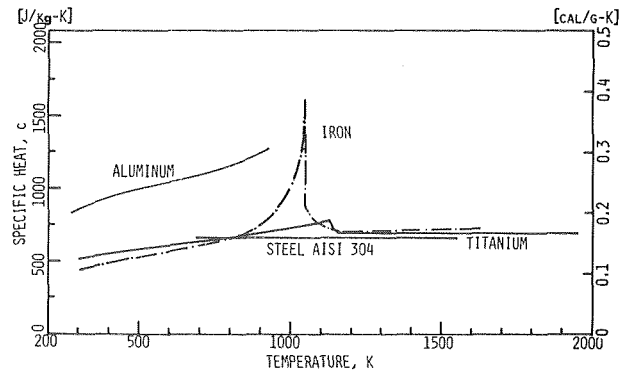

Fig. 4 Specific heat of various metals and metallic alloys versus temperature

The first surface boundary condition (at $y = 0$) is:

$$\lambda(\partial T/\partial y)_{y=0} = q_s \quad \text{when } T < T_m \tag{3a}$$

$$\lambda(\partial T/\partial y)_{y=0} = q_s - L\rho r \quad \text{when } T = T_m \tag{3b}$$

where q_s consists of the heat flux by convection, q_g, and the heat flux from the surface chemical reaction, q_r, i.e.,

$$q_s = q_g + q_r \tag{4}$$

In this system, which is characterized by high values of forced convection, radiative heat transfer is negligible and does not achieve more than a fraction of percent of the convective heating.

The second boundary condition is

$$y \to -\infty, T = T_0 \tag{5}$$

Heat and mass fluxes associated with turbulent boundary layer flows were used. The flow is turbulent according to the Reynolds number range (based on the orifice diameter) which typically varies from about $0.5 \cdot 10^6$ to $2 \cdot 10^6$ when the stagnation pressure increases from 50 to 300 MPa (the corresponding flow speed is about 600 to 1000 m/s). The heat transfer coefficient, h, corresponds to the following correlation for Nusselt number:

$$\mathrm{Nu} = 0.023\ \mathrm{Re}^{0.8}\mathrm{Pr}^{0.33} \tag{6}$$

where all the dimensionless numbers are based on the port hydraulic diameter, d, and the free stream gas properties. The convective heat flux is

$$q_g = h(T_g - T_s) \tag{7}$$

where T_g is the recovery temperature of the gas.

The use of the relationship developed for steady convection to calculate instantaneous values is justified, since the characteristic response times of the boundary layer in the actual system are about three orders of magnitude smaller than the typical exposure time.

Calculations of heat and mass transfer coefficients for the conditions of fully developed turbulent boundary layer were made neglecting the leading edge effects which were minimized by streamlining the orifice entrance (see Fig. 1). The actual length to diameter ratio of four produces a somewhat higher convection; in the very high Reynolds numbers involved, this increase is approximately 10–15 percent (see Deissler [11]) which is of the order of uncertainty expected in these types of heat and mass transfer calculations. It is believed that using the same approximation for the entire range of test conditions preserves the main trends being studied.

The surface reaction processes were modeled on the assumptions of heterogeneous surface reactions and chemical equilibrium between the metal and the oxidizer at the gas/metal interface. Thus, the entire process is controlled by the diffusion rate of the oxidizer through the boundary layer to the wall. The equilibrium partial pressure and the mole fraction of the oxidizer at the wall were related to the surface temperature through the appropriate chemical reaction.

When the reactive gas is oxygen, the chemical reaction with the metal, *Me*, has the following form

$$(2x/y)\ Me + O_2 \overset{K_p}{\rightleftharpoons} (2/y)\ Me_xO_y \tag{8}$$

and the expression for the equilibrium constant, K_p, is

$$K_p = 1/p_{O_2} \tag{9}$$

when both the metal and the oxide are in the condensed phase. Hence, the equilibrium partial pressure of the oxygen at the wall is

$$p_{O_2} = 1/K_p \tag{10}$$

The tendency for the reaction to occur is expressed by the Gibbs free energy, ΔG, which is temperature dependent. The equilibrium constant, K_p, is related to ΔG through the relationship

$$\Delta G = -R_u T \ln K_p \tag{11}$$

It appears that for all of the metal-oxygen systems examined ΔG is negative with high absolute values, and, hence, the values of K_p are very high in the temperature range up to the melting point (Fig. 5). The data used for these calculations were taken from [12 and 13]. These high values of K_p indicate that the reaction is basically unidirectional in the temperature range of interest and that the equilibrium oxygen partial pressure at the surface is comparatively low. Because of the relatively high temperature in the system, the gases were accounted for as ideal, although very high pressures are involved. The relative trends are expected to hold over the range of interest.

The mass transfer coefficient, h_m, is based on the Sherwood number, using

$$\mathrm{Sh} = 0.023\ \mathrm{Re}^{0.8}\mathrm{Sc}^{0.33} \tag{12}$$

The molar diffusivity of the oxygen, D, has a complex dependence on molecular interaction and collision functions [14]

$$D = 3.85 \times 10^{-4}\ T^{1.5}/(p\Omega) \tag{13}$$

with D in [m²/s] and p in [N/m²]. The collision function is approximated (in the range of interest) by

$$\Omega = 1.76 - 0.332 \log T \tag{14}$$

The mass flux of the oxidizer to the wall (moles per unit area and time) is

$$J_{ox} = h_m C(Y_{ox} - Y_{ox,s}) \tag{15}$$

where C and Y_{ox} are related to the free stream. Chemical equilibrium (or near equilibrium) conditions at the wall indicate that the heat flux to the wall due to surface chemical reaction, q_r, is directly dependent on the oxidizer mass flux to the wall:

$$q_r = J_{ox}(-\Delta H_R)_v M \tag{16}$$

The metal regression rate due to metal oxidation during the chemical reaction is

$$r = q_r/(-\Delta H_R \rho) \tag{17}$$

For most situations when melting occurs, the actual mass loss is primarily the result of the melting process and not the metal consumption by surface reactions, since the heat of reaction is much higher than the heat of fusion. Due to the high shearing forces of the flow, the melt is rapidly removed by flowing along the surface; thus, thermal resistance attributable to the melt layer is small. Once the

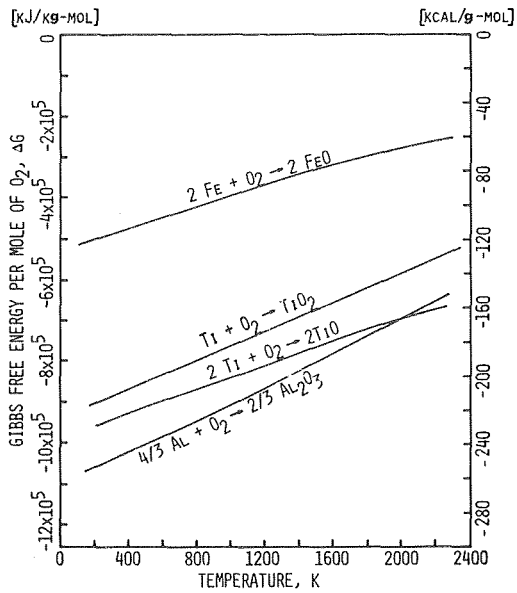

Fig. 5 Gibbs free energy dependence on temperature for metal-oxygen reactions shows that in the temperature range of interest the large negative values indicate high values of the equilibrium constants

surface reaches the melting temperature, the temperature does not increase further, and the excess of heat from the convective heat flux and chemical reaction causes melting of the metal surface. The erosion rate in this case is

$$r = [q_g + q_r - \lambda(\partial T/\partial y)_{y=0}]/L\rho \tag{18}$$

For each metal a threshold temperature less than the melting temperature was considered, below which chemical reactions are not significant.

Results and Discussion

Fig. 2, which was used as an example in the description of the model, shows a typical heating cycle employing air and steel alloy AISI 4340. The connection between increasing the oxygen concentration and the resulting increase in the duration of the melting process (Fig. 6) indicates that in high oxygen concentration the contribution of the heat transfer to the wall due to surface reaction becomes much higher than the heat flux by convection. For the particular duty cycle of Fig. 2, and when no reaction takes place (such as with N_2), the maximum wall temperature remains below the melting point. Accordingly, in that situation, the reactive action of the gases is a necessary condition to achieve melting. As can be seen from Fig. 7, high erosion rates are associated with high oxygen concentration.

The theoretical predictions of the total erosion are compared with the experimental data for several metals in Fig. 8. Good agreement was achieved both for aluminum, which is very reactive with oxygen, and for steel and iron, which are only moderately reactive. No closely relatable experimental data is available for titanium; however, evidence of high erosion (about one-half of that of aluminum) is included in [9]. In that case, the erosion was due to action of combustion gases, while the pressure, temperature, and flow conditions were similar to the present study.

The erosion process is affected by several parameters. With respect to metal properties, low thermal conductivity, melting point, and latent heat of fusion, as well as high heat of reaction and specific heat, all tend to increase erosion. Table 1 summarizes some of the thermophysical properties of the metals and alloys. However, the interplay among the various factors is complex. This complexity is due partially to the strong temperature dependence of some of these parameters (see thermal conductivity and specific heat in Figs. 3 and 4). Therefore, it is difficult to predict which factor is the dominant one without making the entire computation.

Taking into account the physical properties, one can explain the

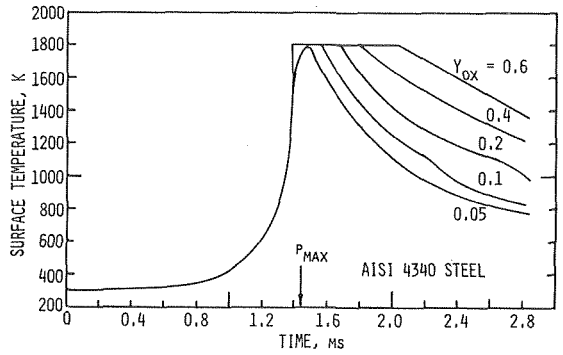

Fig. 6 Effect of O_2 concentration on surface temperature versus time showing that increasing the O_2 concentration greatly increases the heating rates

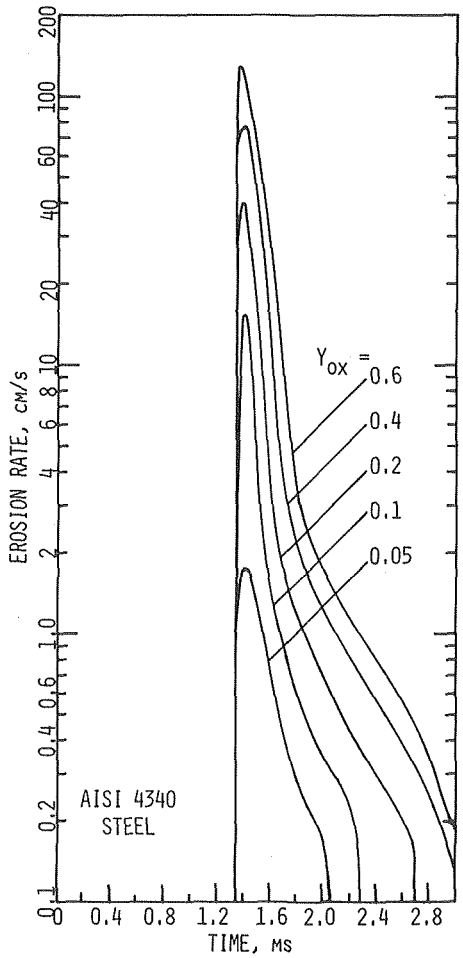

Fig. 7 Variation of erosion rate with time for various O_2 mole fractions. The rapidly increasing erosion rates with increasing O_2 concentration is attributed to the exothermic surface reactions between Fe and O_2

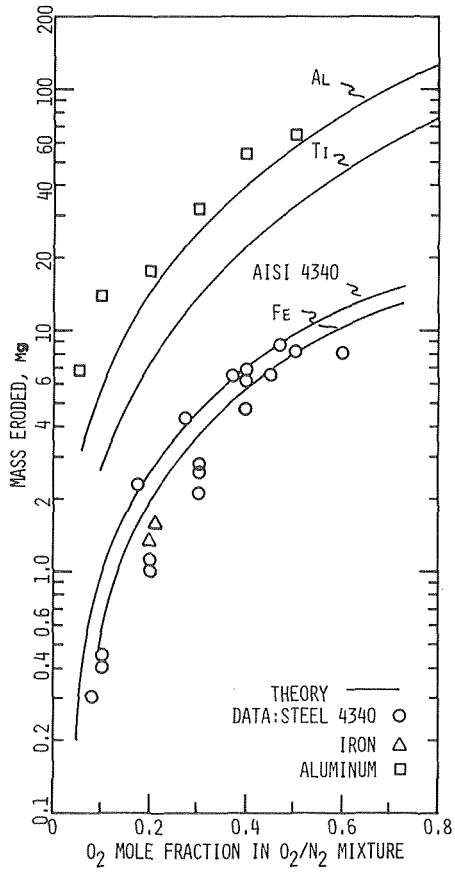

Fig. 8 Comparison of the experimental data and the theoretical results for erosion of various metals shows that the theoretical model describes the erosion of steel as well as the considerably higher erosion rates of aluminum

Table 1 Thermophysical properties of some metals and alloys

Metal or Alloy	Atomic Weight M	Density ρ[g/cm^3]	Melting Temp. T_{melt} [K]	Threshold Temp. T_{ig} [K]	Latent Heat of Fusion L [kJ/kg]	Enthalpy of Reaction with Oxygen $\Delta H_R \times 10^{-3}$ [kJ/kg-metal]	To Form
Iron	55.847	7.87	1810	1100	272	−4.73	FeO
Steel AISI 4340	—	7.86	1800	1100	274	−4.73	FeO
Steel AISI 304	—	8.02	1700	1100	274	−4.73	FeO
Aluminum	26.98	2.70	933	930	389	−31.00	Al_2O_3
Titanium	47.90	4.50	1953	1100	419	−10.93	TiO
						−19.95	TiO_2
Molybdenum	95.94	10.24	2883		253	−5.80	MoO_2

main results shown in Fig. 8. The high erosion of aluminum compared to that of steel is due to its high heat of reaction and low melting temperature. Titanium, whose melting point is high compared to aluminum, exhibits lower erosion, yet higher than that of steel because of its low thermal conductivity. Iron and steel exhibit relatively low erosion mainly because of their relatively low heats of reaction with O_2. Note that in low oxygen concentration (for iron and steel below five percent) the melting temperature is not achieved (Fig. 6). In such cases, relatively low erosion is expected, since the erosion is produced entirely by chemical reaction. No measureable erosion was observed for molybdenum due to its high melting point which is not achieved for the heating conditions being considered.

A threshold temperature, T_{ig}, has been introduced. This temperature is approximately the point above which an appreciable surface chemical reaction takes place. Since kinetic data for high heating rates are not available, there is uncertainy about this parameter. Due to high heating rates and shear force conditions in the present system, the ignition temperature concept used by Mellor and Glassman [8] cannot replace the threshold temperature. In the cases of steel and iron, T_{ig} was deduced from experimental results obtained over a range of peak pressures. The maximum calculated surface temperature corresponding to the experiment for which no erosion could be measured was taken as the threshold temperature. In the case of aluminum, the value of T_{ig} is assumed to be close to the metal melting point, since the mobility of the surface layer causes removal of the oxide protective shell and, thus, exposes the metal to chemical attack. Variations of T_{ig} by several hundred degrees produce changes of 10 to 20 percent in the calculated erosion.

The specific reactions and products related to the interaction between oxygen and the individual metals were chosen according to the following arguments: Phase diagrams of the iron-oxygen system [12, 13] as well as experimental findings [1] show that for the high temperature region (above 830 K) the most preferable oxidation product is wüstite, FeO. In the case of the aluminum-oxygen system, the assumption of very fast reaction rates leads to the conclusion that the main overall reaction product will be the most stable one, namely Al_2O_3. For purposes of this analysis, we considered the heat release associated with the overall reaction rather than the heat releases of the intermediate reaction steps. Both TiO and TiO_2 may exist in the temperature range of interest. However, both of these reactions yield similar erosion rates in the titanium-oxygen system.

The present model of diffusion-controlled equilibrium surface reaction (i.e., concentrating all of the heat release at the surface) yields the upper limit of erosion. Since the analytical and experimental results are in approximate agreement, one may conclude that the actual processes are well represented by the model.

Conclusions

The extreme conditions of high-pressure, high-temperature, and high-speed flow of reactive gases modify the mechanism of reaction between metals and gases as observed in low-pressure and stagnant or moderate flow systems. Surface reactions controlled by the gas phase diffusion process explain and correlate the erosion rates of oxygen-metal systems both in the case of metals which burn in the vapor phase under low flow conditions (e.g., aluminum) and metals which normally exhibit surface reactions (e.g., iron).

Erosion is the result of both surface reaction and melt removal by the flowing gases. The surface temperature does not exceed the melting point of the metal. The surface reactions contribute in two ways to the mass removal processes: (1) below the melting point the mass loss is attributed to oxidation and subsequent removal of the oxide, and (2) the oxidation is exothermic and, thus, augments the heat transfer rate. Indeed, at high oxidizer concentrations the heat transfer produced by the surface reactions exceeds the forced convective heating and, thus, greatly enhances the melting process.

Acknowledgment

This research is being sponsored by the U.S. Army Materials and Mechanics Research Center under Contract DAAA21-76-C-0069. The first author sincerely thanks the Lady Davis Foundation for awarding him a Post Doctoral Fellowship for partial support.

References

1 Alkidas, A. C., Christoe, C. W., Caveny, L. H., and Summerfield, M., "Erosive Effects of High Pressure and High Temperature Pure Gases on Steel," ASME *Journal of Engineering Materials and Technology*, Vol. 99, No. 3, July 1977, pp. 239–243.

2 Alkidas, A. C., Caveny, L. H., Summerfield, M., and Johnson, J. W., "Erosion of Steel Alloys by Hot Reactive Gases," *Proceedings of Symposium on Properties of High Temperature Alloys*, Electrochemical Society and the Metallurgical Society of AIME, 1976, pp. 199–212.

3 Alkidas, A. C., Plett, E. G., and Summerfield, M., "A Performance Study of Ballistic Compressor," *AIAA Journal*, Vol. 14, No. 12, Dec. 1976, pp. 1752–1758.

4 Kofstad, P., *High Temperature Oxidation of Metals*, John Wiley & Sons, Inc., New York, 1966.

5 Markstein, G. H., "Combustion of Metals," *AIAA Journal*, Vol. 1, No. 3, Mar 1963, pp. 550–562.

6 Glassman, I., "Combustion of Metals: Physical Considerations," *Solid Propellant Rocket Research, Progress in Astronautics and Aeronautics*, M. Summerfield, Ed., Academic Press, NY, 1960, pp. 253–258.

7 Brzustowski, T. A. and Glassman, I., "Spectroscopic Investigation of Metal Combustion," *Heterogeneous Combustion, Progress in Astronautics and Aeronautics*, H. G. Wolfhard, et al., eds., Academic Press, NY, 1964, pp. 41–73.

8 Mellor, A. M. and Glassman, I., "Heterogeneous Ignition of Metals: Model and Experiments," AMS Report No. 816, Aerospace and Mechanical Sciences Department, Princeton University, Princeton, NJ, 1967.

9 Plett, E. G., Alkidas, A. C., Shrader, R. E., and Summerfield, M., "Erosion of Metals by High Pressure Combustion Gases: Inert and Reactive Erosion," ASME JOURNAL OF HEAT TRANSFER, Vol. 97, No. 1, Feb 1975, pp. 110–115.

10 *Thermophysical Properties of Matter, The TPRC Data Series*, Touloukian, Y. S., Ed., IFI/Plenum, NY, 1970.

11 Deissler, R. G., "Turbulent Heat Transfer and Friction in the Entrance Regions of Smooth Passages," *Trans. ASME*, Vol. 77, 1955, pp. 1221–1233.

12 Fast, J. D., *Interaction of Metals and Gases, I: Thermodynamics and Phase Relations*, Academic Press, NY, 1965.

13 Muan, A. and Osborn, E. F., *Phase Equilibria Among Oxides in Steelmaking*, Addison-Wesley, Reading, MA, 1965.

14 Bird, R. B., Stewart, W. E., and Lightfoot, E. N., *Transport Phenomena*, John Wiley & Sons, Inc., 1960, p. 511.

journal of heat transfer

technical notes

This section contains shorter technical papers. These shorter papers will be subjected to the same review process as that for full papers.

Effect of Circumferential Wall Heat Conduction on Boundary Conditions for Heat Transfer in a Circular Tube

J. W. Baughn[1]

Nomenclature

d = tube average diameter
h = local heat transfer coefficient
$\bar{h}$ = average heat transfer coefficient
k = wall thermal conductivity
N_c = circumferential conduction number
P_w = wall conductance parameter $(hd/k)(d/t)$ of Morcos and Bergles
q_0'' = local heat flux on outside of tube
q_i'' = local heat flux on inside of tube
$\bar{q}_o''$ = average heat flux on outside of tube
q''' = volumetric heating in tube wall
δq = difference between sum of outside and volumetric heating and inside flux (viz., $q_0'' + q''' t - q_i''$)
r = radial coordinate
$\bar{r}$ = average radius
r_i = inside radius of tube
r_0 = outside radius of tube
s = path coordinate along tube
t = thickness of tube $(r_0 - r_i)$
T_B = bulk temperature of fluid
T = two-dimensional wall temperature, $T(r, \theta)$
T_i = wall temperature at inside of tube
T_w = one-dimensional wall temperature, $T_w(\theta)$
β = ratio of maximum to minimum heat flux on outside of tube
θ = circumferential coordinate

Introduction

In experimental studies of heat transfer to a fluid in a circular tube, it is usually necessary to determine the inside wall thermal boundary condition. In many cases the thermal boundary conditions may vary around the tube (nonuniform circumferential boundary conditions).

It is usually required that measurements be made at the outside of the tube (it is very difficult to measure temperature and heat flux at the inside wall). The desired thermal boundary conditions at the inside wall are then inferred by solving the heat conduction problem in the wall.

It is highly desirable to minimize the effect of circumferential heat conduction in the design of such experiments. In the present note an analysis is presented which determines both the criteria for minimizing circumferential wall conduction effects and the necessary condition for agreement between one-dimensional and two-dimensional solutions.

One-Dimensional Circumferential Conduction Number

Following Morcos and Bergles [1], the two-dimensional steady-state energy balance for the tube element shown in Fig. 1 yields,

$$r_0 q_0''(\theta) + \frac{r_0^2 - r_i^2}{2} q''' - h(\theta) r_i [T_i(\theta) - T_B] + \frac{d}{d\theta} \int_{r_i}^{r_0} \frac{k}{r} \frac{\partial T(r, \theta)}{\partial \theta} dr = 0 \quad (1)$$

If the radial wall temperature variation across a thin tube wall is neglected compared to the circumferential variation, we obtain the equation of Reynolds [2] with an extra term $(q''' t)$ for the volumetric (usually electric) heating of the tube.

$$\frac{kt}{\bar{r}^2} \frac{d^2 T_w(\theta)}{d\theta^2} - q_i''(\theta) + q_0''(\theta) + q''' t = 0 \quad (2)$$

where

$$q_i''(\theta) = h(\theta)[T_i(\theta) - T_B] \quad (3)$$

It is interesting to note that the criteria for the two-dimensional equation (1) to reduce to the one-dimensional equation (2) is

$$\frac{r_0^2 - r_i^2}{2r_0} \simeq t, \quad \frac{r_i}{r_0} \simeq 1$$

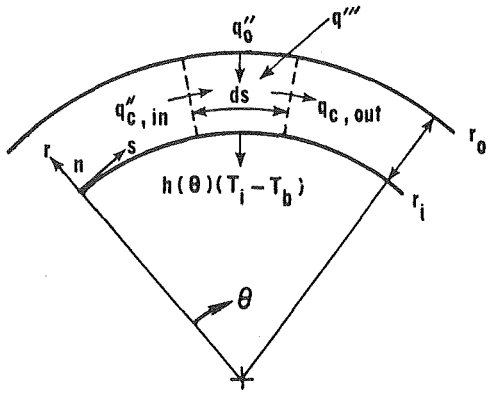

Fig. 1 Steady-state energy balance for a tube wall element

[1] Associate Professor, Department of Mechanical Engineering, University of California, Davis, Mem. ASME.

Contributed by the Heat Transfer Division of THE AMERICAN SOCIETY OF MECHANICAL ENGINEERS. Manuscript received by the Heat Transfer Division August 19, 1977.

and

$$\frac{1}{r_0}\frac{d}{d\theta}\int_{r_i}^{r_0}\frac{k}{r}\frac{\partial T}{\partial \theta}dr \simeq \frac{kt}{r^2}\frac{d^2T_w}{d\theta^2} \tag{4}$$

the first two conditions require that the pipe be thin (i.e., $t \ll r_i$). If this is the case the second condition reduces to

$$\int_{r_i}^{r_0}\frac{k}{r}\frac{\partial T(r,\theta)}{\partial \theta}dr \simeq \frac{kt}{\bar{r}}\frac{dT_w(\theta)}{d\theta} \tag{6}$$

which can be interpreted as a requirement that the circumferential heat flow around the pipe can be represented by the one-dimensional wall temperature $T_w(\theta)$.

Looking now at the one-dimensional solution, Morcos and Bergles further simplify equation (2) and (3) by replacing the local heat transfer coefficient $h(\theta)$ by an average value $\bar{h}$ and writing

$$\frac{q_0''(\theta)}{\bar{h}} + \frac{q'''t}{\bar{h}} - [T_i - T_B] + \frac{1}{P_w}\frac{\partial^2 T_i}{\partial \theta^2} = 0 \tag{7}$$

From this equation, it can be observed that small circumferential conduction, for which

$$q_0''(\theta) + q'''t \simeq \bar{h}[T_i - T_B] \tag{8}$$

is obtained when

$$\frac{1}{P_w}\frac{\partial^2 T_i}{\partial \theta^2} \ll \frac{q_0''(\theta) + q'''t}{\bar{h}} \tag{9}$$

while interesting this is not particularly useful to the experimenter.

To obtain a useful characteristic circumferential conduction number, note that the desired result is that the inside heat flux $q_i''(\theta)$ differ little from the sum of the outside and volumetric heat terms $q_0''(\theta) + q'''t$. Specifically we desire

$$\frac{\delta q}{q_0''(\theta) + q'''t} \ll 1 \tag{10}$$

where

$$\delta q = q_0''(\theta) + q'''t - q_i''(\theta)$$

Rearranging equation (2) and dividing by $q_0''(\theta) + q'''t$

$$\frac{q_0''(\theta) + q'''t - q_i''(\theta)}{q_0''(\theta) + q'''t} = \frac{kt}{(q_0''(\theta) + q'''t)}\bar{r}^2\frac{\partial^2 T_i}{\partial \theta^2} \tag{11}$$

and then noting that $q_i''(\theta) = h(\theta)[T_i - T_B]$ and defining

$$N_c(\theta) \equiv \left|\frac{\delta q}{q_0''(\theta) + q'''t}\right| \tag{12}$$

we can write

$$N_c(\theta) = \left|\frac{kt}{(q_0''(\theta) + q'''t)}\frac{1}{\bar{r}^2}\frac{d}{d\theta^2}\left[\frac{q_i''(\theta)}{H(\theta)}\right]\right| \tag{13}$$

The wall circumferential conduction number $N_c(\theta)$ represents the local fractional change in the inside wall boundary condition due to circumferential wall conduction. If a design minimizes this effect then $N_c(\theta) \ll 1$ and $q_i''(\theta) \simeq q_0''(\theta) + q'''t$ and we can write

$$N_c(\theta) = \left|\frac{kt}{q_0''(\theta) + q'''t}\frac{1}{\bar{r}^2}\frac{d^2}{d\theta^2}\left[\frac{q_0''(\theta) + q'''t}{h(\theta)}\right]\right| \tag{14}$$

As seen in the example below, equation (13) can be useful to the experimenters' efforts to minimize N_c. Furthermore, when $N_c \ll 1$, it is expected that the one-dimensional solution will accurately describe the circumferential conduction. A solution (such as Reynolds [2]) can then be used to correct data.

Example—One-Dimensional

To apply this circumferential conduction number we will select a simple but interesting example. Consider a tube with no volumetric heating. An outside heat flux boundary condition

$$q_0''(\theta) = \bar{q}_0''\left[1 + \frac{\beta - 1}{\beta + 1}\cos\theta\right] \tag{15}$$

is assumed with a uniform heat transfer coefficient inside the tube (i.e., $h(\theta) = h$). This condition might occur, for instance, where an external radiant heat source was used. It also can be simulated by use of a very thin conductive coating on an electrical insulating tube such as used by Morcos and Bergles [1] and presently in use by the author. Then equation (13) yields

$$N_c(\theta) = \frac{kt}{h\bar{r}^2}\frac{\cos\theta}{\dfrac{\beta + 1}{\beta - 1} + \cos\theta} \tag{16}$$

This is plotted with the imposed boundary condition in Fig. 2. The case of $\beta = \infty$ corresponds to a cosine distribution with no heating at the $\theta = 180$ deg position. In this case it is seen that at $\theta = 0$ deg, $N_c = 0.5\,kt/h\bar{r}^2$, which agrees with the example used by Reynolds [2]. Note that N_c approaches ∞ at $\theta = 180$ deg since any circumferential heat conduction results in an infinite fractional change at this position. For an experimental design with this boundary condition, it is desirable to select a tube such that

$$\frac{kt}{h\bar{r}^2}\frac{\cos\theta}{1 + \cos\theta} \ll 1 \tag{17}$$

at the local position θ of interest.

Two-Dimensional Solution

In general, two-dimensional conduction problems require a computer solution (or at least result in difficult infinite series solution). However, as it turns out, the example from the previous section with $\beta = \infty$ can be solved in closed form due to the orthogonality of the boundary condition. The boundary conditions are

$$q_0''(\theta) = k\frac{\partial T(r_0,\theta)}{\partial r} = \bar{q}_0''[1 + \cos\theta] \tag{18}$$

$$q_i''(\theta) = k\frac{\partial T(r_i,\theta)}{\partial r} = h[T_i(r_i,\theta) - T_B] \tag{19}$$

A series solution obtained by separation of variables for a similar set of boundary conditions is given by Arpaci [3] and with minor modifications yields

$$T(r,\theta) = a_0\left[\ln\frac{r}{r_i} + \frac{k}{\bar{h}r_i}\right]$$

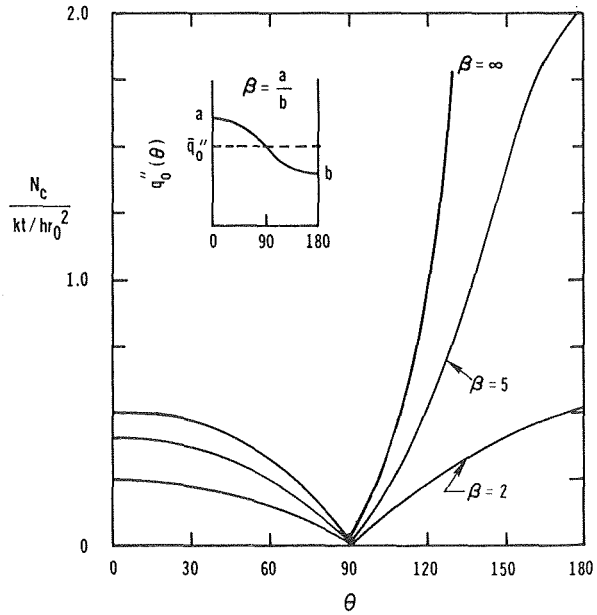

Fig. 2 Circumferential conduction number for one-dimensional solution

$$+\sum_{n=1}^{\infty} a_n \left[\left(\frac{r}{r_i}\right)^n + \left\{ \frac{1-\frac{hr_i}{kn}}{1+\frac{hr_i}{kn}} \right\} \left(\frac{r}{r_i}\right)^{-n} \right] \cos n\theta + T_B \quad (20)$$

where the coefficients are determined from the boundary conditions:

$$a_0 = \frac{\bar{q}_0'' r_0}{k}, \quad a_1 = \frac{\bar{q}_0'' r_0}{k} \left[\frac{r_0}{r_i} + \left\{ \frac{1-B}{1+B} \right\} \left(\frac{r_0}{r_i}\right)^{-1} \right]^{-1} \quad (21)$$

$$a_{n>1} = 0$$

where $B = hr_i/k$.

This last result, $a_{n>1} = 0$, is particularly fortuitous in this case and is due to the cosine distribution chosen. As a result, all the series terms become zero except for the first.

The circumferential conduction number, N_c, was defined in the one-dimensional case as

$$N_c = \frac{\delta q}{q_0''(\theta) + q''' t}$$

which for no volumetric heating became

$$\frac{q_0''(\theta) - q_i''(\theta)}{q_0''(\theta)}$$

In the two-dimensional case, it is desirable to include the effect of the reduced area on the inside of the tube such that

$$\delta q = q_0''(\theta) - \frac{r_i}{r_0} q_i''(\theta) \quad (22)$$

and

$$N_c = 1 - \frac{r_i}{r_0} \frac{q_i''(\theta)}{q_0''(\theta)} \quad (23)$$

Using equations (18)–(21) yields

$$N_c = 1 - \left[1 + \frac{\left(\frac{2B}{1+B}\right)\frac{r_i}{r_0}}{1 - \left(\frac{1-B}{1+B}\right)\left(\frac{r_0}{r_i}\right)^{-2}} \right] \frac{\cos\theta}{1+\cos\theta} \quad (24)$$

where B is a form of the Biot number and is hr_i/k here. A comparison of equation (24) to equation (16) shows that the distribution about θ is the same for the two-dimensional case here so we will consider only $\theta = 0$ which reduces to

$$N_c = \frac{1}{2} - \frac{\left(\frac{B}{1+B}\right)\left(\frac{r_0}{r_i}\right)^{-1}}{1 - \left(\frac{1-B}{1+B}\right)\left(\frac{r_0}{r_i}\right)^{-2}} \quad (25)$$

For a given value of r_0/r_i this is only a function of kt/hr_i^2 since

$$B = \frac{hr_i}{k} = \frac{(r_0/r_i) - 1}{\frac{kt}{hr_i^2}} \quad (26)$$

This is plotted in Fig. 3 for small values of $r_0/r_i - 1$.

Conclusion

The error due to circumferential heat conduction can be reduced by selection of low thermal conductivity materials, a thin wall, or a large radius. The criteria for minimizing this effect is a circumferential conduction number, which is a function of the wall properties and the boundary conditions. This parameter has been derived here and for a selected boundary condition has been compared to one and two-dimensional solutions. It is concluded that minimizing the circumferential conduction number both minimizes circumferential conduction and allows the remaining conduction to be described by the one-dimensional equation. This is demonstrated here only for a cosine distribution, however, it is expected that similar results hold for higher harmonics. These results can also be applied to external heat transfer from a cylinder where the significance of circumferential conduction has been recently demonstrated by Lee and Kakade [4].

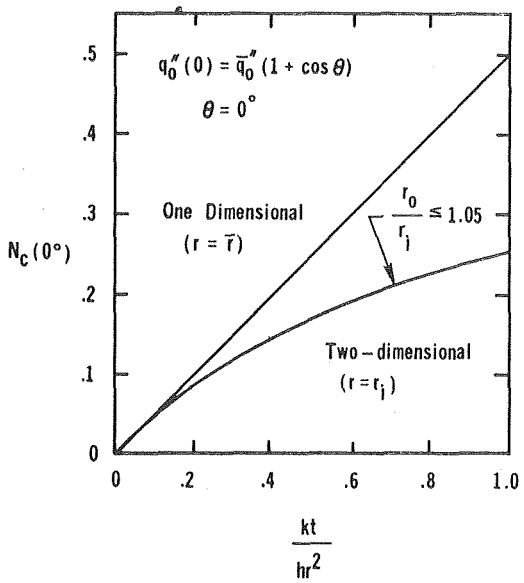

Fig. 3 Comparison of circumferential conduction number for one and two-dimensional solutions

References

1 Morcos, S. M., and Bergles, A. E., "Experimental Investigation of Combined Forced and Free Laminar Convection in Horizontal Tubes," ASME JOURNAL OF HEAT TRANSFER, May 1975, pp. 212–219.

2 Reynolds, W. C., "Effect of Wall Heat Conduction on Convection in a Circular Tube with Arbitrary Circumferential Heat Input," *International Journal of Heat and Mass Transfer*, Vol. 6, 1963, pp. 925–930.

3 Arpaci, V. S., *Conduction Heat Transfer*, Addison Wesley, 1966, pp. 228–230.

4 Lee Y., and Kakade, S. G., "Effect of Peripheral Wall Conduction on Heat Transfer from a Cylinder in Cross-Flow," *International Journal of Heat and Mass Transfer*, Vol. 19, 1976, pp. 1034–1037.

Acknowledgment

The assistance of my student, George R. Cunnington, in checking the two-dimensional solution is appreciated.

Heat Transfer in the Entrance Region of a Straight Channel: Laminar Flow with Uniform Wall Temperature

M. S. Bhatti[1] and C. W. Savery[2]

Nomenclature

$h = \dot{q}''_w/(T_w - T_0)$, local heat transfer coefficient

$h_m = \dot{q}''_w \ell n[(T_w - T_0)/(T_w - T_b)]/(T_b - T_0)$, mean heat transfer coefficient

$\mathrm{Nu} = ha/k$, local Nusselt number

$\mathrm{Nu}_m = h_m a/k$, mean Nusselt number

[1] Senior Engineer, Owens-Corning Fiberglas Corporation, Granville, Ohio, Mem. ASME.

[2] Assoc. Professor, Drexel University, Philadelphia, Pa., Mem. ASME.

Contributed by the Heat Transfer Division of THE AMERICAN SOCIETY OF MECHANICAL ENGINEERS. Manuscript received by the Heat Transfer Division September 30, 1977.

$$+\sum_{n=1}^{\infty} a_n \left[\left(\frac{r}{r_i}\right)^n + \left\{ \frac{1-\frac{hr_i}{kn}}{1+\frac{hr_i}{kn}} \right\} \left(\frac{r}{r_i}\right)^{-n} \right] \cos n\theta + T_B \quad (20)$$

where the coefficients are determined from the boundary conditions:

$$a_0 = \frac{\bar{q}_0'' r_0}{k}, \quad a_1 = \frac{\bar{q}_0'' r_0}{k} \left[\frac{r_0}{r_i} + \left\{ \frac{1-B}{1+B} \right\} \left(\frac{r_0}{r_i}\right)^{-1} \right]^{-1} \quad (21)$$

$$a_{n>1} = 0$$

where $B = hr_i/k$.

This last result, $a_{n>1} = 0$, is particularly fortuitous in this case and is due to the cosine distribution chosen. As a result, all the series terms become zero except for the first.

The circumferential conduction number, N_c, was defined in the one-dimensional case as

$$N_c = \frac{\delta q}{q_0''(\theta) + q''' t}$$

which for no volumetric heating became

$$\frac{q_0''(\theta) - q_i''(\theta)}{q_0''(\theta)}$$

In the two-dimensional case, it is desirable to include the effect of the reduced area on the inside of the tube such that

$$\delta q = q_0''(\theta) - \frac{r_i}{r_0} q_i''(\theta) \quad (22)$$

and

$$N_c = 1 - \frac{r_i}{r_0} \frac{q_i''(\theta)}{q_0''(\theta)} \quad (23)$$

Using equations (18)–(21) yields

$$N_c = 1 - \left[1 + \frac{\left(\frac{2B}{1+B}\right)\frac{r_i}{r_0}}{1 - \left(\frac{1-B}{1+B}\right)\left(\frac{r_0}{r_i}\right)^{-2}} \right] \frac{\cos\theta}{1+\cos\theta} \quad (24)$$

where B is a form of the Biot number and is hr_i/k here. A comparison of equation (24) to equation (16) shows that the distribution about θ is the same for the two-dimensional case here so we will consider only $\theta = 0$ which reduces to

$$N_c = \frac{1}{2} - \frac{\left(\frac{B}{1+B}\right)\left(\frac{r_0}{r_i}\right)^{-1}}{1 - \left(\frac{1-B}{1+B}\right)\left(\frac{r_0}{r_i}\right)^{-2}} \quad (25)$$

For a given value of r_0/r_i this is only a function of kt/hr_i^2 since

$$B = \frac{hr_i}{k} = \frac{(r_0/r_i) - 1}{\frac{kt}{hr_i^2}} \quad (26)$$

This is plotted in Fig. 3 for small values of $r_0/r_i - 1$.

Conclusion

The error due to circumferential heat conduction can be reduced by selection of low thermal conductivity materials, a thin wall, or a large radius. The criteria for minimizing this effect is a circumferential conduction number, which is a function of the wall properties and the boundary conditions. This parameter has been derived here and for a selected boundary condition has been compared to one and two-dimensional solutions. It is concluded that minimizing the circumferential conduction number both minimizes circumferential conduction and allows the remaining conduction to be described by the one-dimensional equation. This is demonstrated here only for a cosine distribution, however, it is expected that similar results hold for higher harmonics. These results can also be applied to external heat transfer from a cylinder where the significance of circumferential conduction has been recently demonstrated by Lee and Kakade [4].

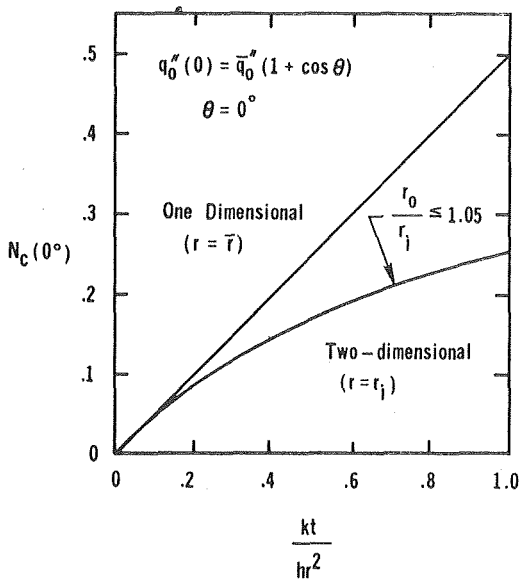

Fig. 3 Comparison of circumferential conduction number for one and two-dimensional solutions

References

1 Morcos, S. M., and Bergles, A. E., "Experimental Investigation of Combined Forced and Free Laminar Convection in Horizontal Tubes," ASME JOURNAL OF HEAT TRANSFER, May 1975, pp. 212–219.

2 Reynolds, W. C., "Effect of Wall Heat Conduction on Convection in a Circular Tube with Arbitrary Circumferential Heat Input," *International Journal of Heat and Mass Transfer*, Vol. 6, 1963, pp. 925–930.

3 Arpaci, V. S., *Conduction Heat Transfer*, Addison Wesley, 1966, pp. 228–230.

4 Lee Y., and Kakade, S. G., "Effect of Peripheral Wall Conduction on Heat Transfer from a Cylinder in Cross-Flow," *International Journal of Heat and Mass Transfer*, Vol. 19, 1976, pp. 1034–1037.

Acknowledgment

The assistance of my student, George R. Cunnington, in checking the two-dimensional solution is appreciated.

Heat Transfer in the Entrance Region of a Straight Channel: Laminar Flow with Uniform Wall Temperature

M. S. Bhatti[1] and C. W. Savery[2]

Nomenclature

$h = \dot{q}''_w/(T_w - T_0)$, local heat transfer coefficient

$h_m = \dot{q}''_w \ell n[(T_w - T_0)/(T_w - T_b)]/(T_b - T_0)$, mean heat transfer coefficient

$\mathrm{Nu} = ha/k$, local Nusselt number

$\mathrm{Nu}_m = h_m a/k$, mean Nusselt number

[1] Senior Engineer, Owens-Corning Fiberglas Corporation, Granville, Ohio, Mem. ASME.

[2] Assoc. Professor, Drexel University, Philadelphia, Pa., Mem. ASME.

Contributed by the Heat Transfer Division of THE AMERICAN SOCIETY OF MECHANICAL ENGINEERS. Manuscript received by the Heat Transfer Division September 30, 1977.

X_t = dimensionless thermal entrance length
X_0 = dimensionless axial distance at which flat plate solution is applied
The remainder of the symbols are defined in [1].

Introduction

Recently, Bhatti and Savery [1] developed a closed-form analytical solution to the problem of simultaneous development of velocity and temperature fields in a straight channel with uniform wall heat flux. Using an identical approach, a semi-analytic solution is developed to the problem of simultaneous development of velocity and temperature fields in a straight channel with uniform wall temperature. Because of its applications to compact heat exchangers, this problem has invoked several investigations. Sparrow [2] employed the Karman-Pohlhausen method to solve for the temperature field using all approximate momentum transfer analysis based on the application of Bernoulli's equation to the fluid core. Stephan [3] presented an approximate series solution for an isothermal circular tube as well as for a straight channel. Hwang and Fan [4] developed a finite difference solution using the point velocities presented earlier by Bodoia and Osterle. Mercer, et al. [5] also developed a finite difference solution and, in addition, reported experimental local and mean Nusselt numbers for air (Pr = 0.7). More recently, Lombardi and Sparrow [6] reported experimental local Nusselt numbers for a fluid with Pr = 2.5.

Analysis

The coordinate system chosen for the analysis is the same as in [1]. The thermal boundary layer growth along the channel wall will be determined from the integrated form of the energy equation given as equation (7) in [1].

The axial velocity profile within the boundary layer will be taken as the generalized Hagen-Poiseuille velocity distribution, equation (1) of [1]. The local hydrodynamic boundary layer thickness, δ, and the pressure gradient, (dp/dx), entering the generalized Hagen-Poiseuille velocity profile are given as simple functions of the dimensionless axial core velocity, U, by equations (2) and (3) of [1]. The variation of U with the dimensionless axial coordinate, X, is determined by the application of overall mechanical energy equation which leads to the ordinary differential equation (4) of [1], whose solution subject to the boundary condition that at $X = 0$, $U = 1$ is given by equation (5) of [1].

The temperature distribution required in the solution of the energy equation will be taken as

$$\frac{T - T_w}{T_0 - T_w} = \frac{1}{2}\left(\frac{y}{\delta_t}\right)\left[3 - \left(\frac{y}{\delta_t}\right)^2\right] \tag{1}$$

which satisfies the boundary conditions that at $y = 0$, $T = T_w$ and $(\partial^2 T/\partial y^2) = 0$. The latter condition arises from the process of satisfying the energy differential equation at the channel wall. Equation (1) also satisfies the boundary conditions that at $y = \delta_t$, $T = T_0$ and $(\partial T/\partial y) = 0$.

Bearing in mind that for fluids with $\Pr < 1$, $\delta_t > \delta$ and for fluids with $\Pr \geq 1$, $\delta_t \leq \delta$, we introduce equations (1), (2), and (3) of [1] together with equation (1) into the energy equation (7) of [1], carry out the indicated operations, and eventually obtain

$$\frac{d\zeta}{dU} = \frac{2\zeta^3(U-1)(513-297U) - 7\Pr U\zeta(3-2U)(45\zeta^4 - 40\zeta^3 + 15\zeta^2 - 1)}{7\Pr U(U-1)(3-2U)(45\zeta^4 - 15\zeta^2 + 3)} \tag{2}$$

applicable to fluids with $\Pr < 1$ and

$$\frac{d\zeta}{dU} = \frac{2(U-1)(513-297U) + 7\Pr U\zeta^3(3-2U)(5\zeta - 24)}{21\Pr U\zeta^2(U-1)(3-2U)(16-\zeta)} \tag{3}$$

applicable to fluids with $\Pr \geq 1$.

Equations (2) and (3) give the variation of the boundary layer shape factor, ζ, and hence of the thermal boundary layer thickness, δ_t, with U. Unfortunately, they cannot be integrated in closed form since the variables U and ζ are nonseparable. Therefore, a numerical integration is employed. The applicable boundary condition is that at $X = 0$, i.e., at $U = 1$, $\delta = \delta_t = 0$. The application of this boundary condition to equations (2) and (3) shows that at $U = 1$, $(d\zeta/dU) = \infty$. Thus, we are faced with the problem of finding an initial value to commence the numerical integration. To circumvent this difficulty, we shall invoke the flat plate solution in the neighborhood of the origin. To that end, we recall that the boundary layer shape factor for a flat plate is given by [2]

$$\zeta = 0.5[1 + (1.5/\Pr - 0.6)^{1/2}] \qquad (\Pr < 1) \tag{4}$$

$$\zeta = 1/\Pr^{1/3} \qquad (\Pr \geq 1) \tag{5}$$

The value of U varies from 1 at the origin to 1.5 at ∞ where the flow becomes hydrodynamically developed. For the purpose of picking a reasonable value of X_0 where the flat plate solution given by equations (4) and (5) applies, we shall arbitrarily take it to correspond to $U = 1.0005$. From equation (5) of [1], we see that $U = 1.0005$ corresponds to $X_0 = 3.2127 \times 10^{-10}$. With the question of the initial value settled, the numerical integration of equations (2) and (3) can be carried out in a straight-forward fashion by the application of the fourth order Runge-Kutta technique.

The heat transfer results will be presented in terms of local and mean Nusselt numbers. The bulk temperature, T_b, entering the definition of the mean Nusselt number, Nu_m, can be determined from the steady state energy equation in conjunction with equation (1) which leads to

$$\frac{T_b - T_0}{T_w - T_0} = \frac{3}{2\Pr}\int_0^X \frac{dX_1}{(\delta_t/a)} \tag{6}$$

Forming the Nusselt numbers,

$$\frac{1}{\mathrm{Nu}} = \frac{3}{2}\left(\frac{\delta_t}{a}\right) \tag{7}$$

$$\frac{1}{\mathrm{Nu}_m} = -\frac{X}{\Pr}\ell n\left[1 - \frac{3}{2\Pr}\int_0^X \frac{dX_1}{(\delta_t/a)}\right] \tag{8}$$

The integral appearing in equation (8) can be split into two integrals with the limits $0 \leq X \leq X_0$ and $X_0 \leq X \leq X_t$. The first of these integrals can be evaluated analytically with the help of equations (4) and (5) and by noting that the hydrodynamic boundary layer thickness for a flat plate is given by $(\delta/a) = 5\,X^{1/2}$. However, the second integral has to be evaluated numerically since between the limits $X_0 \leq X \leq X_t$, (δ_t/a) is determined as a function of X numerically via equations (2) and (3). IBM standard subroutine QSF [7] can be conveniently used to evaluate this integral, once the equidistantly tabulated values of U and (δ_t/a) become available from the solution of equations (2) and (3). The subroutine QSF evaluates the integrals by means of Simpson's rule together with Newton's 3/8 rule.

Results and Discussion

The heat transfer results are calculated for eleven fluids covering the Prandtl number range of 0.01–10,000. The previous investigators treated the Prandtl number range of 0.01–1000.

The numerical integration of equations (2) and (3) is carried out from $U = 1.0005$ using a step size of $\Delta U = 0.0025$. Beyond $U = 1.4955$, a step size of $\Delta U = 0.001$ is used. Near the channel inlet ($U \leq 1.0005$), the flat plate solution given by equations (4) and (5) is considered applicable. In order to estimate the truncation error for the analysis, the calculations were repeated for $\Pr = 0.7$ using a step size of $U = 0.005$. An error analysis then revealed that the truncation error for the values of ζ varied in the range of 0.0001–0.0003. Knowing the variation of ζ with U, the variation of ζ with X is calculated from equation (5) of [1]. Next, (δ/a) is calculated from equation (2) of [1] and (δ_t/a) is determined from the computed values of ζ and (δ/a). Finally, local and mean Nusselt numbers are calculated from equations (7) and (8). These results are displayed in Figs. 1 and 2. The local Nusselt numbers displayed in Fig. 1 approach an asymptotic value

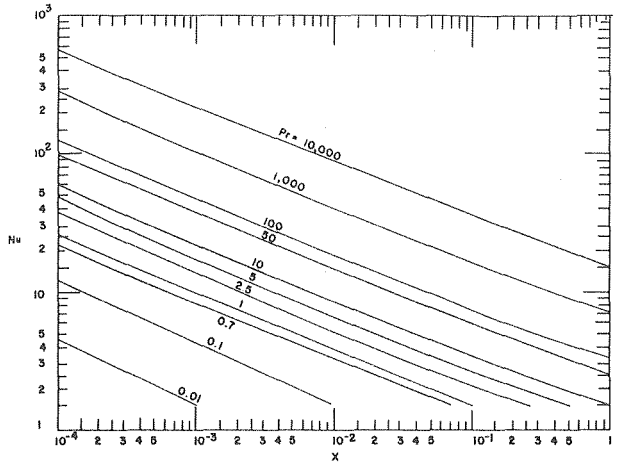

Fig. 1 Local Nusselt numbers in the entrance region of a straight channel

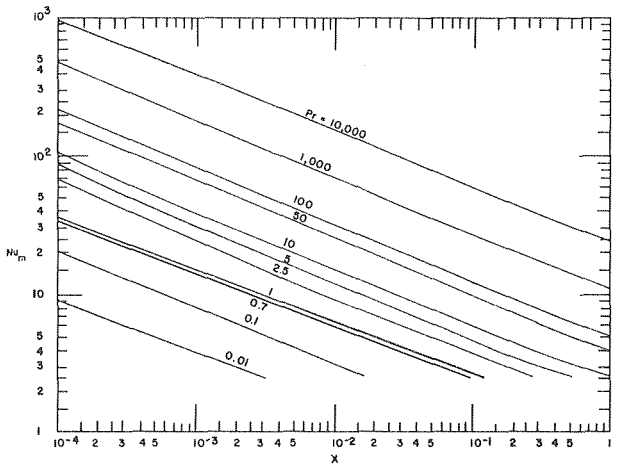

Fig. 2 Mean Nusselt numbers in the entrance region of a straight channel

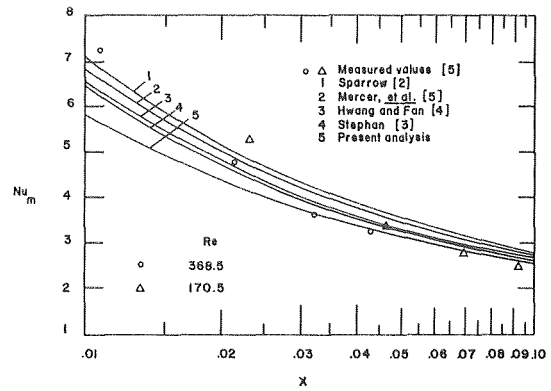

Fig. 3 Comparison of the mean Nusselt number predictions by various investigators

of 1.5, and the mean Nusselt numbers displayed in Fig. 2 approach an asymptotic value of 1.9.

Fig. 3 shows a comparison of the mean Nusselt number predictions of [2, 3, 4 and 5] and the present analysis with the measurements of [5] for air (Pr = 0.7). To accentuate the deviations from the measured values, the results are plotted on semi-log paper. The first three measurements appear to be in error due to the formation of finite boundary layer thicknesses at the inlet to the test channel [5]. The rest of the measurements are in overall best accord with the predictions of the present analysis, the maximum deviation being five percent. The variance between different analyses, especially in the neighborhood of the origin, appears to stem from the approximate manner in which various investigators accounted for the inertia effects in the momentum transfer analyses. If the finite difference analysis of [4] is accepted as a standard, then the analysis of [2], which uses Bernoulli's equation throughout the entrance region, appears to overestimate the inertia effects. On the other hand, present analysis (curve 5) employing generalized Hagen-Poiseuille velocity profile in conjunction with overall mechanical energy equation, appears to underestimate the inertia effects near the channel inlet. The varying degree of approximations inherent in the analyses of [3 and 5] likewise results in deviations from the analysis of [4].

The measurements of local Nusselt numbers for air (Pr = 0.7) reported in [5] are compared in Table 1 with the predictions of the present analysis, as well as with the predictions of the following correlating equation of [6]:

$$\mathrm{Nu} = 0.332\mathrm{Pr}^{1/2} X^{-1/2} \times (1 + 1.825\, X^{1/2})^{1/2} \left(1 + \frac{0.9125X^{1/2}}{1 + 1.825X^{1/2}}\right) \quad (9)$$

Table 1 Comparison of local Nusselt Number predictions with the measurements

X	Re	Measurements of [5]	Predictions of [6]	Predictions of present analysis
0.0107	368.5	3.230	3.348	3.122
0.0214	368.5	2.485	2.507	2.362
0.0231	170.5	2.250	2.428	2.290
0.0322	368.5	2.090	2.133	2.016
0.0428	368.5	1.870	1.893	1.789
0.0462	170.5	1.745	1.843	1.742
0.0694	170.5	1.515	1.588	1.497
0.0924	170.5	1.350	1.436	1.348

This equation is applicable in the Prandtl number range of 0.01–2 [2]. The tabulated predictions of [5] are rather sparse and therefore cannot be included in Table 1. The other investigators have not reported the local Nusselt numbers. Table 1 shows that the present analysis predictions agree to within five percent and those of [6] to within eight percent of the measurements.

Lombardi and Sparrow [6] have reported 130 measurements of the local Nusselt numbers in the range of $0.0088 < X < 0.48$ for a fluid with Pr = 2.5. For the most part, the predictions of equation (9) agree with the measured values within five percent. The predictions of the present analysis agree with those of equation (9) within one percent. Consequently, they display the same level of agreement with the measured values as equation (9).

Finally, from the computed values of the thermal boundary layer thicknesses, it is observed that the dimensionless thermal entrance length, X_t (the axial distance at which the thermal boundary layers growing from the opposite channel walls merge) is given by $X_t = 0.1020\mathrm{Pr}$ for all Prandtl number fluids. The corresponding relation for the case of uniform wall heat flux determined from the results of [1] is $X_t = 0.1393\mathrm{Pr}$.

Acknowledgments

Portions of this work were sponsored by the National Science Foundation under grant Nos. ENG 73-08 125 A01 and ENG 76-00159.

References

1 Bhatti, M. S., and Savery, C. W., "Heat Transfer in the Entrance Region of a Straight Channel: Laminar Flow with Uniform Wall Heat Flux," ASME JOURNAL OF HEAT TRANSFER, Vol. 99, Feb. 1977, pp. 142–144.

2 Sparrow, E. M., "Analysis of Laminar Forced Convection Heat Transfer in the Entrance Region of Flat Rectangular Ducts," NACA TN 3331, 1955.

3 Stephan, K., "Warmeubergang und Druckabfall bei nicht ausgebildeter Laminarstromung in Rohren und in ebenen Spalten," *Chemie—Ing. Techn.*, Vol. 31, No. 12, 1959, pp. 773–778.

4 Hwang, C. L., and Fan, L. T., "Finite Difference Analysis of Forced Convection Heat Transfer in Entrance Region of a Flat Rectangular Duct,"

Applied Scientific Research, Vol. 13, Sec. A, 1964, pp. 401–422.
5 Mercer, W. E., Pearce, W. M. and Hitchcock, J. E., "Laminar Forced Convection in the Entrance Region Between Parallel Flat Plates," ASME JOURNAL OF HEAT TRANSFER, Vol. 89, Aug. 1967, pp. 251–257.
6 Lombardi, G., and Sparrow, E. M., "Measurements of Local Transfer Coefficients for Developing Laminar Flow in Flat Rectangular Ducts," *International Journal of Heat and Mass Transfer*, Vol. 17, 1974, pp. 1135–1139.
7 IMB System/360 Scientific Subroutine Package, Version III, Edition GH20-0205-4, 1968, pp. 291–292.

Mixed Convection about a Sphere with Uniform Surface Heat Flux

A. Mucoglu[1] and T. S. Chen[1]

Nomenclature

C_f = local friction factor
F, f = reduced stream functions
g = gravitational acceleration
Gr^* = Grashof number, $g\beta q_w R^4/k\nu^2$
Gr = Grashof number, $g\beta(T_w - T_\infty)R^3/\nu^2$
k = thermal conductivity
Nu = local Nusselt number
Pr = Prandtl number
q_w = local surface heat transfer rate per unit area
R = radius of sphere
Re = Reynolds number
T = fluid temperature
T_w = wall temperature
T_∞ = free stream temperature
U = local free stream velocity
u, v = velocity components in x and y directions
u_∞ = undisturbed oncoming free stream velocity
x, y = dimensional coordinates as shown in inset of Fig. 3
X, Y = dimensionless coordinates
β = coefficient of thermal expansion
η = pseudo-similarity variable
θ = dimensionless temperature
Λ^* = forced-flow parameter, $\mathrm{Re}^2/|\mathrm{Gr}^*|^{4/5} = \Omega^{*-4/5}$
Λ_{UWT} = forced-flow parameter, $\mathrm{Re}^2/|\mathrm{Gr}| = 1/\Omega$
ν = kinematic viscosity
ξ = transformed axial coordinate
Φ = dimensionless temperature
ϕ = angular coordinate
ψ = stream function
Ω^* = buoyancy parameter, $|\mathrm{Gr}^*|\mathrm{Re}^{5/2}$
Ω_{UWT} = buoyancy parameter, $|\mathrm{Gr}|/\mathrm{Re}^2$

Introduction

Very recently, the present authors studied the problem of laminar mixed convection heat transfer from a sphere maintained at a uniform surface temperature [1] and presented local wall shear and surface heat transfer results for gases having a Prandtl number of 0.7, for both assisting and opposing flows. Their analysis and results encompassed the entire regime of mixed convection, ranging from pure forced convection to pure free convection. The present study is an extension of the previous work by the authors [1] and deals with mixed convection about a sphere with a prescribed uniform surface heat flux. As in the case of uniform wall temperature, the conservation equations of the boundary layers are reduced by a nonsimilarity transformation and the resulting system of equations are then solved by a finite-difference method. Numerical results are presented for a Prandtl number of 0.7. These results are also compared with those for the case of uniform wall temperature.

Analysis

The flow configuration and the coordinate system for the problem under consideration are depicted in the inset of Fig. 3. The forced flow is moving upward, while the gravity g acts downward in the opposite direction. A constant heat flux q_w is maintained at the surface of the sphere. If $q_w > 0$, the resulting buoyancy force will assist the forced flow. On the other hand, if $q_w < 0$, the buoyancy force will oppose the forced flow.

The conservation equations along with their boundary conditions for the present problem are identical to those given by equations (1)–(4) of [1], except that the uniform wall temperature condition therein is now replaced by the uniform surface heat flux condition $\partial T/\partial y = -q_w/k$ at $y = 0$. In addition, the analysis of the problem follows a pattern similar to that described in [1], with only minor changes, and its details are omitted here.

Forced-Flow Dominated Case. The transformed conservation equations for this case assume the form

$$f''' + \gamma(\xi)ff'' + \delta(\xi)(1 - f'^2) \pm \Omega^*\lambda(\xi)\theta = 2\xi\left(f'\frac{\partial f'}{\partial \xi} - f''\frac{\partial f}{\partial \xi}\right) \quad (1)$$

$$\frac{1}{Pr}\theta'' + \gamma(\xi)f\theta' = 2\xi\left(f'\frac{\partial \theta}{\partial \xi} - \theta'\frac{\partial f}{\partial \xi}\right) \quad (2)$$

$$f'(\xi, 0) = 0, f(\xi, 0) = 0, \theta'(\xi, 0) = -\sqrt{2\xi}/(U/u_\infty) \quad (3)$$

$$f'(\xi, \infty) = 1, \theta(\xi, \infty) = 0$$

in which ξ, η, $\gamma(\xi)$, $\delta(\xi)$, $\lambda(\xi)$ are as defined in [1], the primes denote partial differentiation with respect to η,

$$\theta(\xi, \eta) = [T(x, y) - T_\infty]\mathrm{Re}^{1/2}/(q_w R/k) \quad (4)$$

is the dimensionless temperature, and the plus and minus signs that appear in front of Ω^* in equation (1) are associated with assisting and opposing flows, respectively. In equation (1), the buoyancy parameter Ω^* has the expression

$$\Omega^* = |\mathrm{Gr}^*|/\mathrm{Re}^{5/2} \quad (5)$$

wherein the Grashof number Gr^* and the Reynolds number Re are defined, respectively, as

$$\mathrm{Gr}^* = g\beta q_w R^4/k\nu^2, \ \mathrm{Re} = u_\infty R/\nu \quad (6)$$

The physical quantities of interest are the local friction factor C_f, the local Nusselt number Nu, the velocity distribution $u/U = f'(\xi, \eta)$, and the temperature distribution $\theta(\xi, \eta)/\theta(\xi, 0)$. The first two quantities are as defined in reference [1] and now have the expressions

$$C_f\mathrm{Re}^{1/2} = \sqrt{2}[(U/u_\infty)^2/\xi^{1/2}]f''(\xi, 0), \ \mathrm{NuRe}^{-1/2} = 1/\theta(\xi, 0) \quad (7)$$

Buoyancy-Force Dominated Case. In this case one introduces the transformation variables

$$X = x/R, \ Y = (y/R)|\mathrm{Gr}|^{1/5} \quad (8)$$

along with the reduced stream function $F(X, Y)$ and the dimensionless temperature $\Phi(X, Y)$ defined, respectively, as

$$F(X, Y) = \frac{\psi(x, y)}{\nu X|\mathrm{Gr}|^{1/5}}, \ \Phi(X, Y) = \frac{[T(x, y) - T_\infty]|\mathrm{Gr}|^{1/5}}{q_w R/k} \quad (9)$$

With equations (8) and (9), the transformation of momentum and energy equations results in

[1] Department of Mechanical and Aerospace Engineering, University of Missouri–Rolla, Rolla, Mo.
Contributed by the Heat Transfer Division for publication in the JOURNAL OF HEAT TRANSFER. Manuscript received by the Heat Transfer Division December 14, 1977

Applied Scientific Research, Vol. 13, Sec. A, 1964, pp. 401–422.
5 Mercer, W. E., Pearce, W. M. and Hitchcock, J. E., "Laminar Forced Convection in the Entrance Region Between Parallel Flat Plates," ASME JOURNAL OF HEAT TRANSFER, Vol. 89, Aug. 1967, pp. 251–257.
6 Lombardi, G., and Sparrow, E. M., "Measurements of Local Transfer Coefficients for Developing Laminar Flow in Flat Rectangular Ducts," *International Journal of Heat and Mass Transfer*, Vol. 17, 1974, pp. 1135–1139.
7 IMB System/360 Scientific Subroutine Package, Version III, Edition GH20-0205-4, 1968, pp. 291–292.

Mixed Convection about a Sphere with Uniform Surface Heat Flux

A. Mucoglu[1] and T. S. Chen[1]

Nomenclature

C_f = local friction factor
F, f = reduced stream functions
g = gravitational acceleration
Gr^* = Grashof number, $g\beta q_w R^4/k\nu^2$
Gr = Grashof number, $g\beta(T_w - T_\infty)R^3/\nu^2$
k = thermal conductivity
Nu = local Nusselt number
Pr = Prandtl number
q_w = local surface heat transfer rate per unit area
R = radius of sphere
Re = Reynolds number
T = fluid temperature
T_w = wall temperature
T_∞ = free stream temperature
U = local free stream velocity
u, v = velocity components in x and y directions
u_∞ = undisturbed oncoming free stream velocity
x, y = dimensional coordinates as shown in inset of Fig. 3
X, Y = dimensionless coordinates
β = coefficient of thermal expansion
η = pseudo-similarity variable
θ = dimensionless temperature
Λ^* = forced-flow parameter, $\mathrm{Re}^2/|\mathrm{Gr}^*|^{4/5} = \Omega^{*-4/5}$
Λ_{UWT} = forced-flow parameter, $\mathrm{Re}^2/|\mathrm{Gr}| = 1/\Omega$
ν = kinematic viscosity
ξ = transformed axial coordinate
Φ = dimensionless temperature
ϕ = angular coordinate
ψ = stream function
Ω^* = buoyancy parameter, $|\mathrm{Gr}^*|\mathrm{Re}^{5/2}$
Ω_{UWT} = buoyancy parameter, $|\mathrm{Gr}|/\mathrm{Re}^2$

Introduction

Very recently, the present authors studied the problem of laminar mixed convection heat transfer from a sphere maintained at a uniform surface temperature [1] and presented local wall shear and surface heat transfer results for gases having a Prandtl number of 0.7, for both assisting and opposing flows. Their analysis and results encompassed the entire regime of mixed convection, ranging from pure forced convection to pure free convection. The present study is an extension of the previous work by the authors [1] and deals with mixed convection about a sphere with a prescribed uniform surface heat flux. As in the case of uniform wall temperature, the conservation equations of the boundary layers are reduced by a nonsimilarity transformation and the resulting system of equations are then solved by a finite-difference method. Numerical results are presented for a Prandtl number of 0.7. These results are also compared with those for the case of uniform wall temperature.

Analysis

The flow configuration and the coordinate system for the problem under consideration are depicted in the inset of Fig. 3. The forced flow is moving upward, while the gravity g acts downward in the opposite direction. A constant heat flux q_w is maintained at the surface of the sphere. If $q_w > 0$, the resulting buoyancy force will assist the forced flow. On the other hand, if $q_w < 0$, the buoyancy force will oppose the forced flow.

The conservation equations along with their boundary conditions for the present problem are identical to those given by equations (1)–(4) of [1], except that the uniform wall temperature condition therein is now replaced by the uniform surface heat flux condition $\partial T/\partial y = -q_w/k$ at $y = 0$. In addition, the analysis of the problem follows a pattern similar to that described in [1], with only minor changes, and its details are omitted here.

Forced-Flow Dominated Case. The transformed conservation equations for this case assume the form

$$f''' + \gamma(\xi)ff'' + \delta(\xi)(1 - f'^2) \pm \Omega^*\lambda(\xi)\theta = 2\xi\left(f'\frac{\partial f'}{\partial \xi} - f''\frac{\partial f}{\partial \xi}\right) \quad (1)$$

$$\frac{1}{Pr}\theta'' + \gamma(\xi)f\theta' = 2\xi\left(f'\frac{\partial \theta}{\partial \xi} - \theta'\frac{\partial f}{\partial \xi}\right) \quad (2)$$

$$f'(\xi, 0) = 0, f(\xi, 0) = 0, \theta'(\xi, 0) = -\sqrt{2\xi}/(U/u_\infty) \quad (3)$$

$$f'(\xi, \infty) = 1, \theta(\xi, \infty) = 0$$

in which ξ, η, $\gamma(\xi)$, $\delta(\xi)$, $\lambda(\xi)$ are as defined in [1], the primes denote partial differentiation with respect to η,

$$\theta(\xi, \eta) = [T(x, y) - T_\infty]\mathrm{Re}^{1/2}/(q_w R/k) \quad (4)$$

is the dimensionless temperature, and the plus and minus signs that appear in front of Ω^* in equation (1) are associated with assisting and opposing flows, respectively. In equation (1), the buoyancy parameter Ω^* has the expression

$$\Omega^* = |\mathrm{Gr}^*|/\mathrm{Re}^{5/2} \quad (5)$$

wherein the Grashof number Gr^* and the Reynolds number Re are defined, respectively, as

$$\mathrm{Gr}^* = g\beta q_w R^4/k\nu^2, \mathrm{Re} = u_\infty R/\nu \quad (6)$$

The physical quantities of interest are the local friction factor C_f, the local Nusselt number Nu, the velocity distribution $u/U = f'(\xi, \eta)$, and the temperature distribution $\theta(\xi, \eta)/\theta(\xi, 0)$. The first two quantities are as defined in reference [1] and now have the expressions

$$C_f\mathrm{Re}^{1/2} = \sqrt{2}[(U/u_\infty)^2/\xi^{1/2}]f''(\xi, 0), \mathrm{NuRe}^{-1/2} = 1/\theta(\xi, 0) \quad (7)$$

Buoyancy-Force Dominated Case. In this case one introduces the transformation variables

$$X = x/R, Y = (y/R)|\mathrm{Gr}|^{1/5} \quad (8)$$

along with the reduced stream function $F(X, Y)$ and the dimensionless temperature $\Phi(X, Y)$ defined, respectively, as

$$F(X, Y) = \frac{\psi(x, y)}{\nu X|\mathrm{Gr}|^{1/5}}, \Phi(X, Y) = \frac{[T(x, y) - T_\infty]|\mathrm{Gr}|^{1/5}}{q_w R/k} \quad (9)$$

With equations (8) and (9), the transformation of momentum and energy equations results in

[1] Department of Mechanical and Aerospace Engineering, University of Missouri–Rolla, Rolla, Mo.
Contributed by the Heat Transfer Division for publication in the JOURNAL OF HEAT TRANSFER. Manuscript received by the Heat Transfer Division December 14, 1977

$$F''' + \left(1 + \frac{X \cos X}{\sin X}\right) FF'' - F'^2 + \sigma(X)\Lambda^* + \frac{\sin X}{X}\Phi = X\left(F'\frac{\partial F'}{\partial X} - F''\frac{\partial F}{\partial X}\right) \quad (10)$$

$$\frac{1}{\mathrm{Pr}}\Phi'' + \left(1 + \frac{X \cos X}{\sin X}\right) \mathrm{F}\Phi' = \mathrm{X}\left(\mathrm{F}'\frac{\partial \Phi}{\partial \mathrm{X}} - \Phi'\frac{\partial \mathrm{F}}{\partial \mathrm{X}}\right) \quad (11)$$

$$F'(X, 0) = 0, F(X, 0) = 0$$

$$\Phi'(X, 0) = -1, F'(X, \infty) = \chi(X)\Lambda^{*1/2}, \Phi(X, \infty) = 0 \quad (12)$$

In the foregoing equations, the primes now stand for partial differentiation with respect to Y, $\sigma(X)$ and $\chi(X)$ are given by equation (31) of reference [1], and the forced-flow effects are represented by the parameter

$$\Lambda^* = \mathrm{Re}^2/|\mathrm{Gr}^*|^{4/5} = \Omega^{*-4/5} \quad (13)$$

The streamwise velocity distribution is given by $u/U = [X/(U/u_\infty)]F'(X, Y)/\Lambda^{*1/2}$ and the temperature distribution by $(T - T_\infty)/(T_w - T_\infty) = \Phi(X, Y)/\Phi(X, 0)$. The expressions for the local friction factor C_f and the local Nusselt number Nu are

$$C_f\mathrm{Re}^{1/2} = 2XF''(X, 0)/\Lambda^{*3/4}, \mathrm{NuRe}^{-1/2} = 1/[\Phi(X, 0)\Lambda^{*1/4}] \quad (14)$$

Results and Discussion

Equations (1–3) and (10–12) were solved by using an efficient and accurate finite-difference method [1], and numerical results were obtained for a Prandtl number of 0.7. The buoyancy force parameter $\mathrm{Gr}^*/\mathrm{Re}^{5/2}$ in the computations ranged from 0 (i.e., pure forced convection) to ∞ (i.e., pure free convection with $\mathrm{Re}^2/\mathrm{Gr}^{*4/5} = 0$) for assisting flow and from 0 to −2.0 for opposing flow. The local free stream velocity distributions $U(x)$ used in the computations are from the potential flow solution and from measured velocity distributions, as given in reference [1].

The angular distributions of the local wall shear stress $C_f\mathrm{Re}^{1/2}$ and the local Nusselt number $\mathrm{NuRe}^{-1/2}$ are shown, respectively, in Figs. 1 and 2. As in the case of uniform wall temperature [1], both the local wall shear and the local Nusselt number increase with increasing buoyancy force for assisting flow ($\mathrm{Gr}^*/\mathrm{Re}^{5/2} > 0$), with a resulting delay in the flow separation. This behavior is due to a favorable pressure gradient induced by the buoyancy forces that assist the forced flow. For opposing flow ($\mathrm{Gr}^*/\mathrm{Re}^{5/2} < 0$), on the other hand, the buoyancy forces induce an adverse pressure gradient and the local wall shear and Nusselt number decrease with increasing buoyancy force. As a result, the flow separation occurs earlier and moves toward the stagnation point. It is also interesting to note that for assisting flow with strong buoyancy forces (e.g., $\mathrm{Gr}^*/\mathrm{Re}^{5/2} \geq 20$), the local friction factor and Nusselt number tend to become less sensitive to the variation of the local free stream velocity distributions.

The angular distributions of the local Nusselt number in terms of $\mathrm{NuGr}^{*-1/5}$ for large buoyancy parameters ($5 \leq \mathrm{Gr}^*/\mathrm{Re}^{5/2} \leq \infty$) are shown in Fig. 3. The curve for $\mathrm{Gr}^*/\mathrm{Re}^{5/2} = \infty$ (i.e., $\mathrm{Re}^2/\mathrm{Gr}^{*4/5} = 0$) represents the case of pure free convection. As to be expected, the local Nusselt number becomes independent of the local free stream velocity distributions as $\mathrm{Gr}^*/\mathrm{Re}^{5/2}$ increases to ∞. Also shown in the figure is the curve from Chiang and coworkers [2] for pure free convection, which deviates from the present curve for $\mathrm{Gr}^*/\mathrm{Re}^{5/2} = \infty$ at large angular positions.

Next, the present local Nusselt number results for the uniform surface heat flux (UHF) will be compared with those for the uniform wall temperature (*UWT*) reported earlier by the present authors [1]. To compare directly the results between the *UHF* and *UWT* cases, it is necessary to define an equivalent buoyancy parameter Ω_e (or an equivalent forced-flow parameter Λ_e) between these two cases. This can be achieved by expressing the buoyancy parameter for the UWT case in terms of the local surface heat flux $q_w(x) = -k(\partial T/\partial y)_{y=0}$ as

$$\Omega_e = [g\beta|q_w(x)|R^4/k\nu^2]/\mathrm{Re}^{5/2} = |\mathrm{Gr}_e^*|/\mathrm{Re}^{5/2} \quad (15)$$

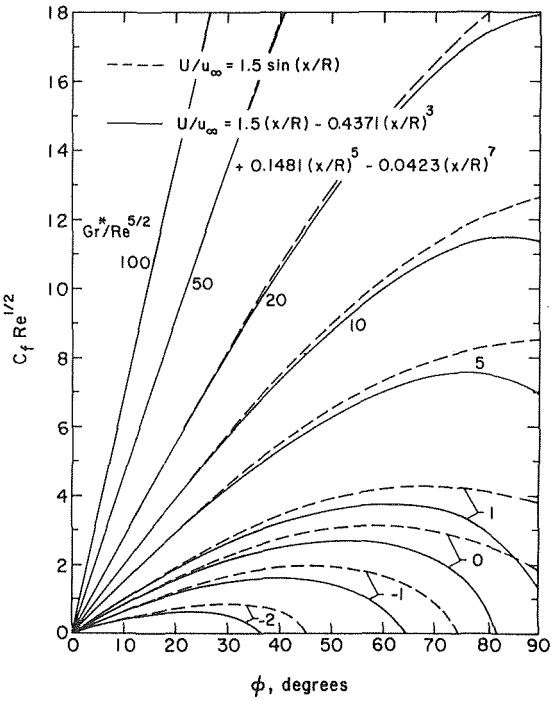

Fig. 1 Angular distributions of the local friction factor, Pr = 0.7

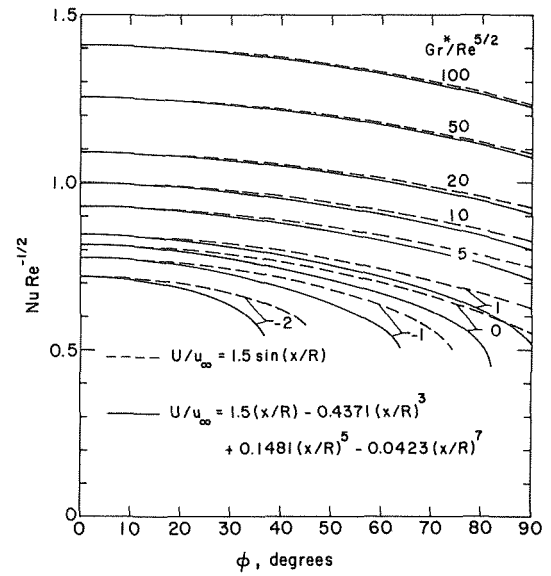

Fig. 2 Angular distributions of the local Nusselt number, Pr = 0.7

With the $q_w(x)$ expression for the forced-flow dominated case, one can arrive at

$$\Omega_e = \Omega_{UWT}\mathrm{Nu}_{UWT}\mathrm{Re}^{-1/2} \quad (16)$$

with

$$\Omega_{UWT} = |\mathrm{Gr}|/\mathrm{Re}^2, \mathrm{Gr} = g\beta(T_w - T_\infty)R^3/\nu^2 \quad (17)$$

In the same manner, one obtains for the buoyancy dominated case,

$$\Lambda_e = \Lambda_{UWT}{}^{4/5}[\mathrm{Nu}_{UWT}\mathrm{Re}^{-1/2}]^{-4/5} \quad (18)$$

wherein

$$\Lambda_{UWT} = \mathrm{Re}^2/|\mathrm{Gr}| = 1/\Omega_{UWT} \quad (19)$$

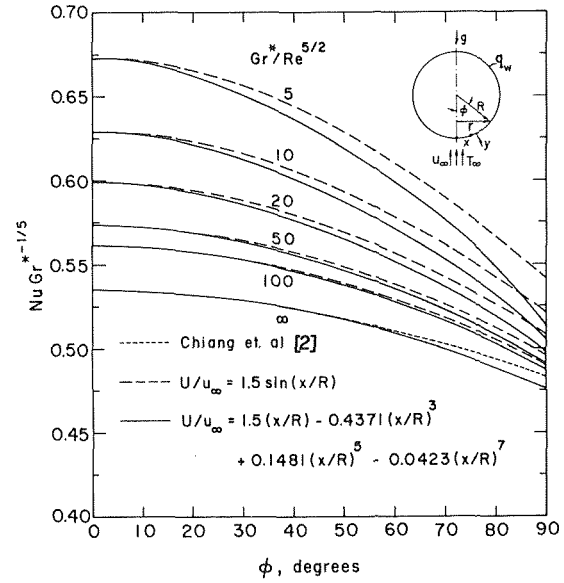

Fig. 3 Angular distributions of the local Nusselt number in terms of $NuGr^{*-1/5}$, Pr = 0.7

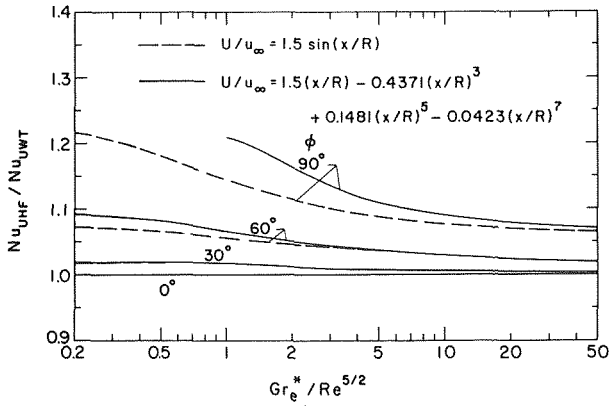

Fig. 4 A comparison of the local Nusselt numbers between uniform surface heat flux and uniform wall temperature

The Nusselt number ratio Nu_{UHF}/Nu_{UWT} can be determined when $\Omega_e = \Omega^*_{UHF}$ (or $\Lambda_e = \Lambda^*_{UHF}$). This Nusselt number ratio versus $Gr_e^*/Re^{5/2}$ is illustrated in Fig. 4 for the case of assisting flow at representative angular positions of ϕ = 0 deg, 30 deg, 60 deg, and 90 deg. As can be seen from the figure, the Nu_{UHF}/Nu_{UWT} ratio increases from unity as the angle ϕ increases from 0 deg. Thus, it can be concluded that for an equivalent buoyancy force effect, heating by uniform surface heat flux yields larger local Nusselt numbers than heating by uniform wall temperature.

Acknowledgments

The present study was supported by a grant from the National Science Foundation (NSF ENG 75-15033).

References

1 Chen, T. S. and Mucoglu, A., "Analysis of Mixed Forced and Free Convection About a Sphere," *International Journal of Heat and Mass Transfer*, Vol. 20, 1977, pp. 867–875.

2 Chiang, T., Ossin, A. and Tien, C. L., "Laminar Free Convection From a Sphere," ASME JOURNAL of HEAT TRNASFER, Vol. 86, 1964, pp. 537–542.

Radiation Augmented Fires within Enclosures

A. T. Modak[1] and M. K. Mathews[2]

Introduction

Considerable evidence [1] exists showing that the growth of fires of combustible materials within enclosures is controlled by the radiative energy transfer from the enclosure surfaces and from the layer of hot combustion products (soot particles, CO_2, H_2O, etc.) that accumulates near the ceiling.

This note develops a general mathematical formulation [2–5] for the radiative flux from the ceiling layer and enclosure surfaces to any arbitrarily located differential target element within the enclosure.

Mathematical Formulation

The ceiling layer of flames and combustion products is considered to be a slab [5] of uniform thickness. Since the primary infrared radiators in luminous flames are small soot particles ($\pi d/\lambda < 1/4$), neglecting scattering in the infrared (the important spectral region of interest) is justified. In the ceiling layer, the particles may be somewhat larger than in flames; nevertheless, the effect of scattering is still relatively small and is neglected. The layer is assumed to be a gray (absorption coefficient, k) isothermal (temperature, T) and homogeneous mixture of flames, soot particles, carbon dioxide, water vapor, etc., in thermodynamic equilibrium. For a ceiling layer consisting mainly of luminous flames and small soot particles, the gray assumption is satisfactory [3, 4]. The bounding enclosure surfaces are assumed to be black. Surfaces within the layer are characterized by a single uniform temperature, T_c. Each wall below the layer is assumed to be at a uniform temperature but is allowed to be at a different temperature from the other walls. Wall temperatures below the ceiling layer are characterized by T_a, T_b, etc.

For rays viewing the bounding enclosure surfaces within the ceiling layer, the radiance $N(\ell_c)$ for a path length, ℓ_c, is given by:

$$N(\ell_c) = \frac{\sigma T^4}{\pi}\left(1 - \left(1 - \frac{T_c^4}{T^4}\right)\exp(-k\ell_c)\right), \qquad (1)$$

where σ is the Stefan-Boltzmann constant.

The radiance for rays viewing the walls below the ceiling layer, at temperature T_a or T_b, is $N_a = \sigma T_a{}^4/\pi$ and $N_b = \sigma T_b{}^4/\pi$, respectively.

The radiative flux, $\dot{q}''$, from the ceiling layer and enclosure surfaces to a differential target surface element is given by [6]:

$$\dot{q}'' = \int_\Omega N \frac{(\vec{n}\cdot\vec{r}_0)}{r_0}\, d\Omega \text{ where } (\vec{n}\cdot\vec{r}_0) \geq 0. \qquad (2)$$

The unit normal $\vec{n}$, to the target element has the direction cosines u, v and w; $\vec{r}_0$ is the radius vector along the line of sight (ray) to the far edge of the ceiling layer; $(\vec{n}\cdot\vec{r}_0)$ represents the dot product of the two vectors and $d\Omega$ is the elemental solid angle subtended at the target element. The integration is performed over all solid angles with $(\vec{n}\cdot\vec{r}_0) \geq 0$.

The radiative flux from the ceiling layer and enclosure surfaces above[3] a target located within the enclosure is given by the sum of four fluxes from four rectangular parallelepipeds (boxes). The target is located at one corner of each box. Fig. 1 shows a detail of one of the parallelepipeds. The radiative flux, $\dot{q}_1''$, from the ceiling layer and

[1] Factory Mutual Research Corporation, Norwood, Mass. 02062.
[2] Factory Mutual Research Corporation, Norwood, Mass. 02062.
[3] The flux from below may be computed similarly.

Contributed by the Heat Transfer Division for publication in the JOURNAL OF HEAT TRANSFER. Manuscript received by the Heat Transfer Division April 26, 1978.

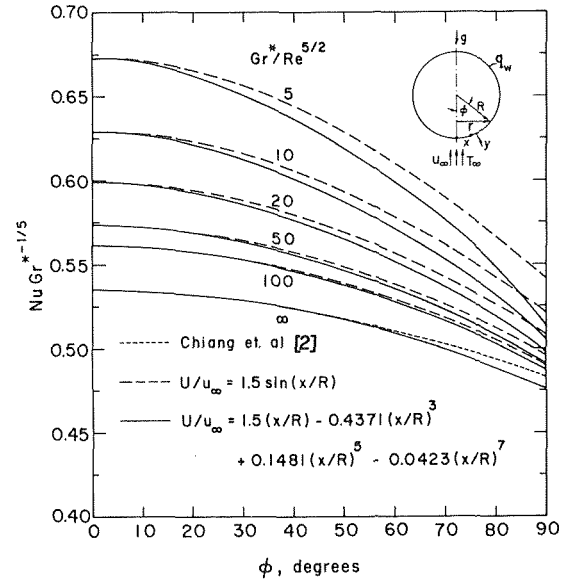

Fig. 3 Angular distributions of the local Nusselt number in terms of $NuGr^{*-1/5}$, Pr = 0.7

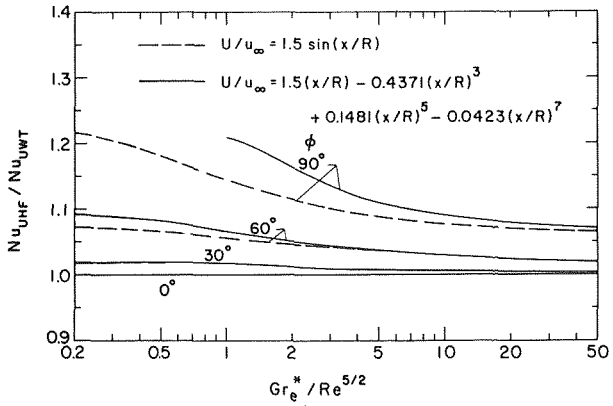

Fig. 4 A comparison of the local Nusselt numbers between uniform surface heat flux and uniform wall temperature

The Nusselt number ratio Nu_{UHF}/Nu_{UWT} can be determined when $\Omega_e = \Omega^*_{UHF}$ (or $\Lambda_e = \Lambda^*_{UHF}$). This Nusselt number ratio versus $Gr_e^*/Re^{5/2}$ is illustrated in Fig. 4 for the case of assisting flow at representative angular positions of $\phi = 0$ deg, 30 deg, 60 deg, and 90 deg. As can be seen from the figure, the Nu_{UHF}/Nu_{UWT} ratio increases from unity as the angle ϕ increases from 0 deg. Thus, it can be concluded that for an equivalent buoyancy force effect, heating by uniform surface heat flux yields larger local Nusselt numbers than heating by uniform wall temperature.

Acknowledgments

The present study was supported by a grant from the National Science Foundation (NSF ENG 75-15033).

References

1 Chen, T. S. and Mucoglu, A., "Analysis of Mixed Forced and Free Convection About a Sphere," *International Journal of Heat and Mass Transfer*, Vol. 20, 1977, pp. 867–875.

2 Chiang, T., Ossin, A. and Tien, C. L., "Laminar Free Convection From a Sphere," ASME JOURNAL of HEAT TRNASFER, Vol. 86, 1964, pp. 537–542.

Radiation Augmented Fires within Enclosures

A. T. Modak[1] and M. K. Mathews[2]

Introduction

Considerable evidence [1] exists showing that the growth of fires of combustible materials within enclosures is controlled by the radiative energy transfer from the enclosure surfaces and from the layer of hot combustion products (soot particles, CO_2, H_2O, etc.) that accumulates near the ceiling.

This note develops a general mathematical formulation [2–5] for the radiative flux from the ceiling layer and enclosure surfaces to any arbitrarily located differential target element within the enclosure.

Mathematical Formulation

The ceiling layer of flames and combustion products is considered to be a slab [5] of uniform thickness. Since the primary infrared radiators in luminous flames are small soot particles ($\pi d/\lambda < 1/4$), neglecting scattering in the infrared (the important spectral region of interest) is justified. In the ceiling layer, the particles may be somewhat larger than in flames; nevertheless, the effect of scattering is still relatively small and is neglected. The layer is assumed to be a gray (absorption coefficient, k) isothermal (temperature, T) and homogeneous mixture of flames, soot particles, carbon dioxide, water vapor, etc., in thermodynamic equilibrium. For a ceiling layer consisting mainly of luminous flames and small soot particles, the gray assumption is satisfactory [3, 4]. The bounding enclosure surfaces are assumed to be black. Surfaces within the layer are characterized by a single uniform temperature, T_c. Each wall below the layer is assumed to be at a uniform temperature but is allowed to be at a different temperature from the other walls. Wall temperatures below the ceiling layer are characterized by T_a, T_b, etc.

For rays viewing the bounding enclosure surfaces within the ceiling layer, the radiance $N(\ell_c)$ for a path length, ℓ_c, is given by:

$$N(\ell_c) = \frac{\sigma T^4}{\pi}\left(1 - \left(1 - \frac{T_c^4}{T^4}\right)\exp(-k\ell_c)\right), \qquad (1)$$

where σ is the Stefan-Boltzmann constant.

The radiance for rays viewing the walls below the ceiling layer, at temperature T_a or T_b, is $N_a = \sigma T_a{}^4/\pi$ and $N_b = \sigma T_b{}^4/\pi$, respectively.

The radiative flux, $\dot{q}''$, from the ceiling layer and enclosure surfaces to a differential target surface element is given by [6]:

$$\dot{q}'' = \int_\Omega N \frac{(\vec{n}\cdot\vec{r}_0)}{r_0}\, d\Omega \text{ where } (\vec{n}\cdot\vec{r}_0) \geq 0. \qquad (2)$$

The unit normal $\vec{n}$, to the target element has the direction cosines u, v and w; $\vec{r}_0$ is the radius vector along the line of sight (ray) to the far edge of the ceiling layer; $(\vec{n}\cdot\vec{r}_0)$ represents the dot product of the two vectors and $d\Omega$ is the elemental solid angle subtended at the target element. The integration is performed over all solid angles with $(\vec{n}\cdot\vec{r}_0) \geq 0$.

The radiative flux from the ceiling layer and enclosure surfaces above[3] a target located within the enclosure is given by the sum of four fluxes from four rectangular parallelepipeds (boxes). The target is located at one corner of each box. Fig. 1 shows a detail of one of the parallelepipeds. The radiative flux, $\dot{q}_1''$, from the ceiling layer and

[1] Factory Mutual Research Corporation, Norwood, Mass. 02062.

[2] Factory Mutual Research Corporation, Norwood, Mass. 02062.

[3] The flux from below may be computed similarly.

Contributed by the Heat Transfer Division for publication in the JOURNAL OF HEAT TRANSFER. Manuscript received by the Heat Transfer Division April 26, 1978.

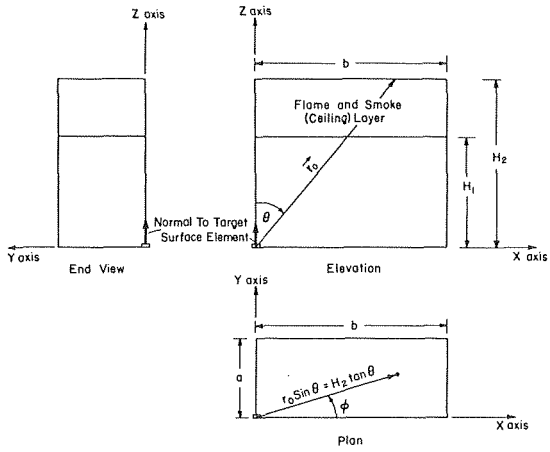

Fig. 1 Elevation, end and plan views of one rectangular parallelepiped. The origin of a Cartesian and spherical polar coordinate system is located at the target element.

enclosure surfaces in one of the parallelepipeds (of Fig. 1) is given by equation (2) and the equations for radiance, N. The path length, ℓ_c, through the ceiling layer is given by:

$$\ell_c = \frac{z_0 - H_1}{\cos\theta} \text{ for all values of } \phi; \tag{3}$$

z_0 is the vertical coordinate where the ray leaves the ceiling layer (outlet); H_1 and H_2 are the vertical coordinates of the lower and upper edges of the ceiling layer respectively; θ and ϕ are the polar and azimuthal angles, respectively, of a spherical polar coordinate system about the target element. The origin of a rectangular, Cartesian coordinate system is also located at the target element: $\theta = \pi/2$ and $\phi = 0$ represent the x-axis; $\theta = \pi/2$ and $\phi = \pi/2$, the y-axis; and $\theta = 0$, the z-axis of the Cartesian coordinate system; a and b are the depth along the y-axis and the breadth along the x-axis of the rectangular parallelepiped of Fig. 1. The x and y-axes are chosen such that $b \geq a$. The unit normal vector to the target, $\vec{n}$, the radius vector, $\vec{r}_0$, and the elemental solid angle, $d\Omega$, of equation (2) are defined by:

$$\vec{n} = \vec{i}u + \vec{j}v + \vec{k}w,$$

$$\vec{r}_0 = r_0(\vec{i}\sin\theta\cos\phi + \vec{j}\sin\theta\sin\phi + \vec{k}\cos\theta) \tag{4}$$

and

$$d\Omega = \sin\theta d\phi d\theta.$$

Substituting equations (1), (3) and (4) in equation (2) yields the flux, $\dot{q}_1''$:

$$\dot{q}_1'' = \frac{\sigma T^4}{\pi}\int_{\theta=0}^{\theta_3} d\theta \int_{\phi=\phi_\ell(\theta)}^{\phi_u(\theta)} \left\{1 - \left[1 - \frac{T_c{}^4}{T^4}\right]\exp\left[\frac{-k(z_0 - H_1)}{\cos\theta}\right]\right\}$$
$$\times \omega(\theta, \phi)d\phi + T_a{}^4\left(\Pi(\theta_2, \theta_3, 0, \phi_1) + \Pi\left(\theta_3, \frac{\pi}{2}, 0, \phi_2\right)\right)$$
$$+ T_b{}^4\left(\Pi\left(\theta_1, \theta_3, \phi_3, \frac{\pi}{2}\right) + \Pi\left(\theta_3, \frac{\pi}{2}, \phi_2, \frac{\pi}{2}\right)\right); \tag{5}$$

where

$$\omega(\theta, \phi) = (u\sin\theta\cos\phi + v\sin\theta\sin\phi + w\cos\theta)\sin\theta;$$

$$\Pi(\theta_\ell, \theta_u, \phi_\ell(\theta), \phi_u(\theta)) = \frac{\sigma}{\pi}\int_{\theta_\ell}^{\theta_u}\int_{\phi_\ell(\theta)}^{\phi_u(\theta)} \omega(\theta, \phi)d\phi d\theta;$$

θ_i and ϕ_i are defined in the following tabulation:

	θ_i and ϕ_i	
i	θ_i	ϕ_i
1	$\tan^{-1}\left(\frac{a}{H_1}\right)$	$\cos^{-1}\left(\frac{b}{H_1\tan\theta}\right)$
2	$\tan^{-1}\left(\frac{b}{H_1}\right)$	$\tan^{-1}\left(\frac{a}{b}\right)$
3	$\tan^{-1}\left(\frac{\sqrt{a^2+b^2}}{H_1}\right)$	$\sin^{-1}\left(\frac{a}{H_1\tan\theta}\right)$

The second term of equation (5) represents the radiative flux from the ceiling layer and from the enclosure surfaces bounding it that are within the ceiling layer. The other terms of equation (5) represent the radiative flux from the walls below the ceiling layer (at T_a and T_b). The upper and lower limits, $\phi_u(\theta)$ and $\phi_\ell(\theta)$ respectively, of the inner integration over the azimuthal angle, ϕ, are a function of the outer integration variable, θ. The limits of ϕ are:

$$\phi_\ell(\theta) = 0,\ \phi_u(\theta) = \frac{\pi}{2} \text{ for } 0 \leq \theta \leq \theta_1$$

$$\phi_\ell(\theta) = 0,\ \phi_u(\theta) = \phi_3 \text{ for } \theta_1 < \theta \leq \theta_2$$

$$\phi_\ell(\theta) = \phi_1,\ \phi_u(\theta) = \phi_3 \text{ for } \theta_2 < \theta \leq \theta_3 \tag{6}$$

The vertical coordinate, z_0, is a function of θ and ϕ:

$$z_0 = H_2 \text{ for } 0 \leq \theta \leq \tan^{-1}\left(\frac{a}{H_2}\right)$$
$$\phi_\ell(\theta) \leq \phi \leq \phi_u(\theta)$$

$$z_0 = \text{Minimum of } \left(\frac{b}{\tan\theta\cos\phi}, H_2\right) \text{ for } \tan^{-1}\left(\frac{a}{H_2}\right) < \theta \leq \theta_3 \tag{7}$$
$$\phi_\ell(\theta) \leq \phi \leq \phi_2$$

$$z_0 = \text{Minimum of } \left(\frac{a}{\tan\theta\sin\phi}, H_2\right) \text{ for } \tan^{-1}\left(\frac{a}{H_2}\right) < \theta \leq \theta_3$$
$$\phi_2 < \phi \leq \phi_u(\theta).$$

The double integrations of equation (5) may be evaluated numerically, e.g., using Simpson's rule.

Application

The radiative flux from the ceiling layer to the floor is obtained by using equation (5) for each of the four rectangular parellelepipeds, and the results are compared with heat flux measurements made in a full-scale fire test [5], using Gardon-type heat flux gauges located on the carpeted floor of a room containing bedroom furniture.

The fire test was performed at full scale on a 2.4 m wide × 3.7 m long × 2.4-m high bedroom containing a bed with a polyurethane mattress, a bureau, a desk, a television set, books, hanging curtains and some clothes. The room was ventilated by a single doorway 0.8 m wide × 2 m high. The fire was started by igniting a central spot on the surface of the polyurethane mattress with a match, and was allowed to grow past the time when the entire bedroom was involved in the fire (post-flashover). Then, the test was terminated by a manually actuated sprinkler.

Surface and gas temperatures, the absorption coefficient of the ceiling layer and heat fluxes were measured at several locations continuously from ignition to termination of the test. Measured heat fluxes were compared with calculated radiative heat fluxes from the ceiling layer and enclosure surfaces to the floor. The physical parameters required as inputs to this calculation are: 1) the temperature, T_c; 2) the thickness, $h(= H_2 - H_1)$; 3) the effective radiation temperature, T; 4) the gray absorption coeffficient, k, of the ceiling layer; and 5) the temperatures of the side walls below the layer.

These input parameters are obtained from surface and gas phase thermocouple measurements, visual observations and smoke radiance measurements made continuously during the fire test. The radiative flux from the enclosure walls below the ceiling layer was neglected ($T_a = T_b = 0$) in these comparisons; the simplification is reasonable since, in this particular fire, the flux due to the side walls of the enclosure below the ceiling layer was estimated to be negligible compared to flux from the ceiling layer itself.

The foregoing input parameters (T_c, h, T and k) were used to calculate the radiative flux from the ceiling layer to gauges on the floor at the front and rear of the bedroom. Columns 6 and 7 of Table 1 show calculated values and the range of measured values, respectively,

Table 1 Comparison of calculated and measured heat fluxes to floor in a full-scale room fire

1	2	3	4	5	6	7	8	9
					Comparison of Calculated and Measured Heat Fluxes to Floor			
					Front Guage		Rear Guage	
Time After Ignition Seconds	Average Temperature of Enclosure Surfaces Within the Ceiling Layer T_c, K (Input)	Thickness of Ceiling Layer[a] h, m $h = H_2 - H_1$ (Input)	Temperature of Ceiling Layer T, K (Input)	Absorption Coefficient of Ceiling Layer k, m^{-1} (Input)	Calculated Flux kW/m² (Output)	Measured Flux kW/m²	Calculated Flux kW/m² (Output)	Measured Flux kW/m²
351	386	1.1	868	0.079	1.7	2.2	1.6	3.3
354	401	1.1	913	0.11	2.6	2.6	2.4	3.7
357	420	1.1	1058	0.086	3.6	3.1	3.4	4.6
360	452	1.1	1205	0.077	5.2	4.5	4.9	6.7
363	495	1.1	1191	0.12	7.6	6.9	7.1	9.3
366	529	1.1	1169	0.20	11	9.2	10	11
369	562	1.1	1177	0.31	16	13	15	15
372	603	1.1	1182	0.49	22	20	21	22
411–420	996	1.6	1211	1.5	75	46–84	70	35–78
435–411	973	2.44	1260	1.5[b]	121	138[c]	119	14–29[d]

[a] Room height, $H_2 = 2.44$ m
[b] Measurements were unreliable; the absorption coefficient was assumed to be the same as for the second time period.
[c] Measured values exceeded the range of the instrument.
[d] Unreliable; rear heat flux gauge probably got covered with debris.

versus time after ignition for the front heat flux gauge; columns 8 and 9 show corresponding values for the rear gauge. Since all heat flux readings were near zero prior to 351 seconds, this period is not shown. The test was terminated at 444 seconds after ignition. Table 1 shows that the measurements are in reasonable agreement with calculated values.

Analytic Approximations

For special cases when two direction cosines equal zero and the third equals unity, the numerical calculations of equation (5) can be simplified to approximate and analytic, closed-form expressions,

The term $(1 - (1 - T_c^4/T^4)\exp(-k(z_0 - H_1)/\cos\theta))$ in the integrand of equation (5) represents an "emissivity" term for the ceiling layer. The double integral may be made analytic, by representing the emissivity factor in terms of an (optically thin) mean-beam-length, $L_m = 4V/A$ where V is the volume of the ceiling layer, $V = ab(H_2 - H_1)$ and A the total bounding surface area of the ceiling layer,

$$A = [2(H_2 - H_1)(a + b) + 2ab]:$$

$$L_m = \frac{2ab(H_2 - H_1)}{[(H_2 - H_1)(a + b) + ab]} \quad (8)$$

For a corner target which is parallel to the ceiling (i.e., $u = v = 0$ and $w = 1$), an analytic approximation to equation (5) is given by $\dot{q}_{1m}''$ (0, 0, 1):

$$\dot{q}_{1m}''(0,0,1) = \frac{\sigma T^4}{2\pi}\left(1 - \left(1 - \frac{T_c^4}{T^4}\right)e^{-kL_m}\right)\left(\frac{a}{\sqrt{H_1^2 + a^2}}\tan^{-1}\left(\frac{b}{\sqrt{H_1^2 + a^2}}\right) + \frac{b}{\sqrt{H_1^2 + b^2}}\tan^{-1}\left(\frac{a}{\sqrt{H_1^2 + b^2}}\right)\right)$$
$$+ \frac{\sigma T_a^4}{2\pi}\left(\tan^{-1}\left(\frac{a}{b}\right) - \frac{b}{\sqrt{H_1^2 + b^2}}\tan^{-1}\left(\frac{a}{\sqrt{H_1^2 + b^2}}\right)\right)$$
$$+ \frac{\sigma T_b^4}{2\pi}\left(\tan^{-1}\left(\frac{b}{a}\right) - \frac{a}{\sqrt{H_1^2 + a^2}}\tan^{-1}\left(\frac{b}{\sqrt{H_1^2 + a^2}}\right)\right), \quad (9)$$

where L_m is given by equation (8).

The accuracy of the beam-length approximation was compared with numerical calculations for a range of values of the parameters a, b, H_1, H_2, T and T_c. Fig. 2 shows a representative case where the radiative flux to the floor at room center is plotted versus non-dimensional layer thickness, parametric in non-dimensional absorption coefficient.

Fig. 2 shows that the analytic approximation is reasonable over a wide range of layer thickness and absorption coefficient. The analytic approximation is exact for $k = 0$ (no layer) and $k \to \infty$ (opaque layer). In realistic fires, the analytic approximation is generally accurate to

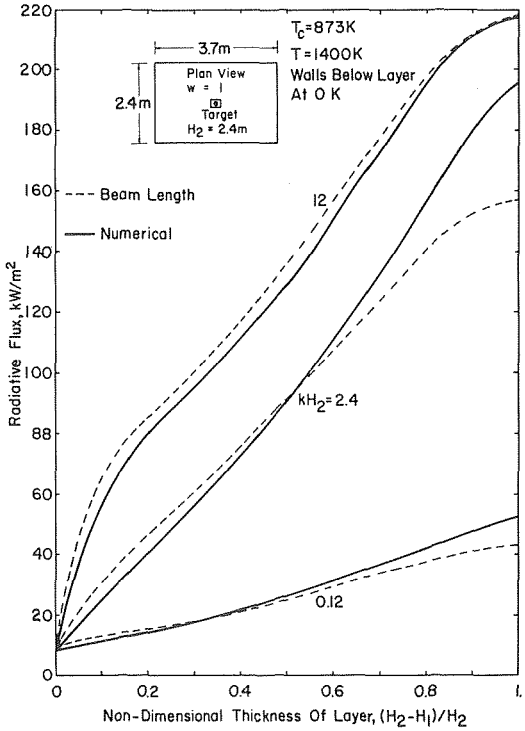

Fig. 2 Comparison of numerical and analytic calculations for radiative flux to the floor at the center of a room.

within ten percent of the numerical calculation. Analytic approximations for targets parallel to one of the side walls of the enclosure ($u = 0, v = 1, w = 0$ or $u = 1, v = 0, w = 0$) show [7] comparable accuracy when matched with numerical calculations. The approximations for such targets are not explicitly provided in this note, but can be readily derived in a manner analogous to equation (9).

The geometric mean beam length ($L_m = 4V/A$) is an optically thin approximation only valid for computing the flux to the bounding surface of a radiative medium. The justification for this simple approximation lies in its comparison with numerical calculations for a broad range of parameters. It is a satisfactory approximation for targets distant from the medium, provided the effect of distance is accounted for by means of a view factor (see equation (9)). Better

approximations have been provided [7] but only at the price of increased complexity, so that the usefulness of those approximations is limited.

References

1 Quintiere, J., Fire Standards and Safety, p. 131, ASTM special technical publication No. 614, A. F. Robertson, Ed., ASTM Philadelphia, Pa., NBS, Washington, D.C., 1976.

2 Cheng, P., Progress in Astronautics and Aeronautics, Vol. *31*, 1972, p. 269.

3 Markstein, G. H., "Radiative Properties of Plastic Fires," XVII Symposium (International) on Combustion, University of Leeds, England, Aug. 1978.

4 Buckius, R. O. and Tien, C. L., *Int. J. Heat Mass Transfer*, Vol. *20*, (1977), p. 93.

5 Alpert, R. L., Modak, A. T. and Newman, J. S., "The Third Full-Scale Bedroom Fire Test of the Home Fire Project (July 30, 1975) Volume I—Test Description and Experimental Data," Factory Mutual RESEARCH Corporation Technical Report Serial No. 21011.6, Oct. 1975, NTIS PB-253 314/AS.

6 Dayan, A. and Tien, C. L., *Combustion Science and Technology* Vol. *9*, 1974, p. 41.

7 Modak, A. T. and Mathews, M. K., Paper 77-HT-98, Seventeenth National ASME-AIChE Heat Transfer Conference, Salt Lake City, Utah, Aug. 1977.

Approximate Radiation Shape Factors between Two Spheres

J. D. Felske[1]

Introduction

The radiation shape factor between two spheres has been evaluated numerically and either plotted or tabulated by several investigators [1–4]. However, it would be useful to have a simple analytical expression which would be accurate over the entire parameter range. In [4], several approximate expressions were proposed and their regions of applicability defined. It was found, though, that the expressions became progressively more inaccurate as the sphere spacing was decreased and had a 12.1 percent error for the case of equal radius spheres which were just touching. The present work, on the other hand, develops a single analytical expression whose greatest discrepancy is only 5.8 percent for this extreme case.

Analysis

It is well known that the shape factor between two spheres of finite size and spacing is always greater than the shape factor calculated by replacing one by a point source [3, 4, 6]. The point source solution, however, is quite simple and therefore it would be advantageous to modify it to account for the finite size of the radiating sphere. The following modification was devised arbitrarily. In essence it implies that the kernel of the double area integration was separable.

The shape factor from sphere 1 to sphere 2 (see Fig. 1) is taken to be of the form:

$$F_{12} = F_{12}^{PS} f(R_1/c) \tag{1}$$

where F_{12}^{PS} is the shape factor if sphere 1 is infinitesimal (a point source) and $f(R_1/c)$ is a function which accounts for its actual finite size. The function f is arbitrarily assumed to be a function of only (R_1/c). The point source solution is developed in [6] and may also be found as 1/4 × equation (11) in [7]. The result is:

$$F_{12}^{PS} = [1 - \sqrt{1 - (R_2/c)^2}]/2 \tag{2}$$

Similarly, the shape factor from sphere 2 to sphere 1 would then be of the form:

$$F_{21} = F_{21}^{PS} f(R_2/c) \tag{3}$$

where

$$F_{21}^{PS} = [1 - \sqrt{1 - (R_1/c)^2}]/2 \tag{4}$$

and f is the same function as in equation (1)—the argument now being (R_2/c) instead of (R_1/c).

The function f may then be determined by applying the reciprocity relationship:

$$A_1 F_{12} = A_2 F_{21} \tag{5}$$

Substituting equations (1–4) and noting $A = 4\pi R^2$ yields:

$$\frac{f(R_1/c)}{f(R_2/c)} = \frac{R_2^2 [1 - \sqrt{1 - (R_1/c)^2}]}{R_1^2 [1 - \sqrt{1 - (R_2/c)^2}]}$$

This suggests the following form for f:

$$f(R/c) = C_0[1 - \sqrt{1 - (R/c)^2}]/(R/c)^2 \tag{6}$$

where the constant C_0 is determined from the condition that as $(R/c) \to 0$, the shape factor becomes identically the point source result. That is:

$$\lim_{(R/c)\to 0} f(R/c) = 1 \tag{7}$$

which then gives:

$$C_0 = 2$$

The approximate shape factor for all sphere sizes and spacings is then:

$$F_{12} = [1 - \sqrt{1 - (R_2/c)^2}][1 - \sqrt{1 - (R_1/c)^2}](c/R_1)^2 \tag{8}$$

For purposes of comparison with the numerical integration solution [4], the computations will be given as functions of the radius ratio (R_1/R_2) and the surface to surface spacing ratio (s/R_2). See Fig. 1 for the definition of s. That is,

$$F_{12} = F_{12}(R_1/c, R_2/c) = F_{12}(R_1/R_2, s/R_2)$$

where the center to center and surface to surface distances are related by

$$c = R_1 + R_2 + s \tag{9}$$

In Table 1, entries for values of s/R_2 to the left of the solid vertical lines are percentage differences between the closed form solution of equation (8) and the numerical integration results of [4]:

$$\text{percent diff} = 100 \times (F_{\text{equation(8)}} - F_{\text{num}})/F_{\text{num}} \tag{10}$$

Entries to the right of the solid vertical lines represent discrepancies of the approximations with respect to either the point-source or the modified-point-source solution depending upon which was more accurate [4]. (This latter type of comparison was necessary since the

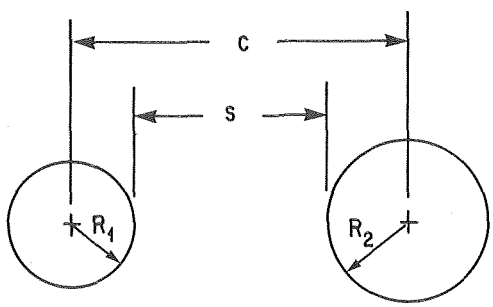

Fig. 1 Sphere geometry

[1] Asst. Professor, Department of Mechanical Engineering, State University of New York at Buffalo, Amherst, N.Y. 14260

Contributed by the Heat Transfer Division for publication in The JOURNAL OF HEAT TRANSFER. Manuscript received by the Heat Transfer Division October 27, 1977.

approximations have been provided [7] but only at the price of increased complexity, so that the usefulness of those approximations is limited.

References

1 Quintiere, J., Fire Standards and Safety, p. 131, ASTM special technical publication No. 614, A. F. Robertson, Ed., ASTM Philadelphia, Pa., NBS, Washington, D.C., 1976.

2 Cheng, P., Progress in Astronautics and Aeronautics, Vol. *31*, 1972, p. 269.

3 Markstein, G. H., "Radiative Properties of Plastic Fires," XVII Symposium (International) on Combustion, University of Leeds, England, Aug. 1978.

4 Buckius, R. O. and Tien, C. L., *Int. J. Heat Mass Transfer*, Vol. *20*, (1977), p. 93.

5 Alpert, R. L., Modak, A. T. and Newman, J. S., "The Third Full-Scale Bedroom Fire Test of the Home Fire Project (July 30, 1975) Volume I—Test Description and Experimental Data," Factory Mutual RESEARCH Corporation Technical Report Serial No. 21011.6, Oct. 1975, NTIS PB-253 314/AS.

6 Dayan, A. and Tien, C. L., *Combustion Science and Technology* Vol. *9*, 1974, p. 41.

7 Modak, A. T. and Mathews, M. K., Paper 77-HT-98, Seventeenth National ASME-AIChE Heat Transfer Conference, Salt Lake City, Utah, Aug. 1977.

Approximate Radiation Shape Factors between Two Spheres

J. D. Felske[1]

Introduction

The radiation shape factor between two spheres has been evaluated numerically and either plotted or tabulated by several investigators [1–4]. However, it would be useful to have a simple analytical expression which would be accurate over the entire parameter range. In [4], several approximate expressions were proposed and their regions of applicability defined. It was found, though, that the expressions became progressively more inaccurate as the sphere spacing was decreased and had a 12.1 percent error for the case of equal radius spheres which were just touching. The present work, on the other hand, develops a single analytical expression whose greatest discrepancy is only 5.8 percent for this extreme case.

Analysis

It is well known that the shape factor between two spheres of finite size and spacing is always greater than the shape factor calculated by replacing one by a point source [3, 4, 6]. The point source solution, however, is quite simple and therefore it would be advantageous to modify it to account for the finite size of the radiating sphere. The following modification was devised arbitrarily. In essence it implies that the kernel of the double area integration was separable.

The shape factor from sphere 1 to sphere 2 (see Fig. 1) is taken to be of the form:

$$F_{12} = F_{12}{}^{PS} f(R_1/c) \tag{1}$$

where $F_{12}{}^{PS}$ is the shape factor if sphere 1 is infinitesimal (a point source) and $f(R_1/c)$ is a function which accounts for its actual finite size. The function f is arbitrarily assumed to be a function of only (R_1/c). The point source solution is developed in [6] and may also be found as 1/4 × equation (11) in [7]. The result is:

$$F_{12}{}^{PS} = [1 - \sqrt{1 - (R_2/c)^2}]/2 \tag{2}$$

Similarly, the shape factor from sphere 2 to sphere 1 would then be of the form:

$$F_{21} = F_{21}{}^{PS} f(R_2/c) \tag{3}$$

where

$$F_{21}{}^{PS} = [1 - \sqrt{1 - (R_1/c)^2}]/2 \tag{4}$$

and f is the same function as in equation (1)—the argument now being (R_2/c) instead of (R_1/c).

The function f may then be determined by applying the reciprocity relationship:

$$A_1 F_{12} = A_2 F_{21} \tag{5}$$

Substituting equations (1–4) and noting $A = 4\pi R^2$ yields:

$$\frac{f(R_1/c)}{f(R_2/c)} = \frac{R_2{}^2 [1 - \sqrt{1 - (R_1/c)^2}]}{R_1{}^2 [1 - \sqrt{1 - (R_2/c)^2}]}$$

This suggests the following form for f:

$$f(R/c) = C_0[1 - \sqrt{1 - (R/c)^2}]/(R/c)^2 \tag{6}$$

where the constant C_0 is determined from the condition that as $(R/c) \to 0$, the shape factor becomes identically the point source result. That is:

$$\lim_{(R/c)\to 0} f(R/c) = 1 \tag{7}$$

which then gives:

$$C_0 = 2$$

The approximate shape factor for all sphere sizes and spacings is then:

$$F_{12} = [1 - \sqrt{1 - (R_2/c)^2}][1 - \sqrt{1 - (R_1/c)^2}](c/R_1)^2 \tag{8}$$

For purposes of comparison with the numerical integration solution [4], the computations will be given as functions of the radius ratio (R_1/R_2) and the surface to surface spacing ratio (s/R_2). See Fig. 1 for the definition of s. That is,

$$F_{12} = F_{12}(R_1/c, R_2/c) = F_{12}(R_1/R_2, s/R_2)$$

where the center to center and surface to surface distances are related by

$$c = R_1 + R_2 + s \tag{9}$$

In Table 1, entries for values of s/R_2 to the left of the solid vertical lines are percentage differences between the closed form solution of equation (8) and the numerical integration results of [4]:

$$\text{percent diff} = 100 \times (F_{\text{equation(8)}} - F_{\text{num}})/F_{\text{num}} \tag{10}$$

Entries to the right of the solid vertical lines represent discrepancies of the approximations with respect to either the point-source or the modified-point-source solution depending upon which was more accurate [4]. (This latter type of comparison was necessary since the

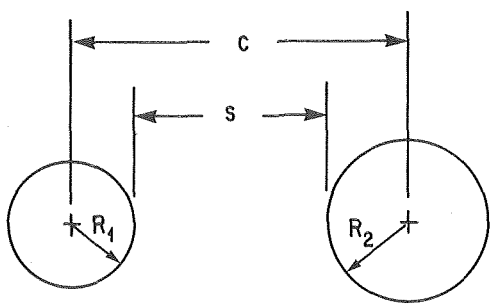

Fig. 1 Sphere geometry

[1] Asst. Professor, Department of Mechanical Engineering, State University of New York at Buffalo, Amherst, N.Y. 14260

Contributed by the Heat Transfer Division for publication in The JOURNAL OF HEAT TRANSFER. Manuscript received by the Heat Transfer Division October 27, 1977.

Table 1 Percent differences between the numerical integration solution [4] and: (a) equation (8), (b) point-source solution [4], and (c) modified point source solution [4]. See text for meaning of heavy vertical lines.

R_1/R_2		s/R_2 0.0	0.2	0.4	0.6	0.8	1.0	10.0
0.1	(a)	-2.6	-0.7	+0.1	+0.1	+0.1	+0.1	0.0
	(b)	-2.8	-0.8	0.0	0.0	0.0	0.0	0.0
	(c)	-31.0	-18.6	-12.6	-9.5	-7.4	-6.0	-0.2
0.2	(a)	-3.4	-1.4	-1.7	-0.4	+0.3	+0.2	0.0
	(b)	-4.0	-1.9	-2.1	-0.8	0.0	0.0	0.0
	(c)	-25.0	-16.2	-12.5	-8.8	-6.5	-5.3	-0.2
0.4	(a)	-4.8	-2.2	-1.1	-0.6	-0.5	-0.2	0.0
	(b)	-6.8	-3.8	-2.4	-1.6	-1.4	-0.9	0.0
	(c)	-19.1	-13.0	-9.5	-7.3	-6.0	-4.8	-0.2
0.6	(a)	-5.1	-2.4	-1.5	-0.9	0.0	-0.5	+0.1
	(b)	-8.6	-5.2	-3.8	-2.8	-1.6	-1.9	0.0
	(c)	-15.5	-10.7	-8.1	-6.3	-4.5	-4.4	-0.1
0.8	(a)	-5.6	-2.8	-1.6	-1.0	-0.7	-0.1	+0.1
	(b)	-10.6	-6.8	-5.0	-3.9	-3.1	-2.2	0.0
	(c)	-13.6	-9.3	-7.0	-5.5	-4.5	-3.4	-0.1
1.0	(a)	-5.8	-2.9	-1.8	-1.2	-0.9	+0.1	+0.1
	(b)	-12.1	-8.2	-6.2	-5.0	-4.1	-2.7	0.0
	(c)	-12.1	-8.2	-6.2	-5.0	-4.1	-2.7	0.0
2.0	(a)	-5.6	-3.3	-2.2	-1.4	-1.3	-1.1	+0.1
	(b)	-17.6	-13.9	-11.5	-9.7	-8.7	-7.7	-0.4
	(c)	-8.3	-5.8	-4.3	-3.4	-3.0	-2.6	-0.0
4.0	(a)	-3.6	-2.7	-2.4	-1.6	-1.2	-0.8	+0.1
	(b)	-22.6	-20.2	-18.4	-16.4	-14.8	-13.4	-1.7
	(c)	-4.6	-3.6	-3.2	-2.4	-1.9	-1.5	0.0
8.0	(a)	-3.5	-2.1	-1.6	-1.3	-0.9	-0.9	+0.1
	(b)	-29.6	-26.9	-24.9	-23.4	-21.9	-20.7	-4.6
	(c)	-3.8	-2.4	-1.8	-1.6	-1.2	-1.1	0.0
10.0	(a)	-2.6	-2.0	-1.4	-1.2	-0.8	-0.9	+0.1
	(b)	-31.0	-28.9	-27.0	-25.5	-24.1	-23.0	-6.0
	(c)	-2.8	-2.2	-1.5	-1.4	-1.0	-1.1	0.0

numerical computations given in [4] were only for points lying to the left of the solid vertical lines. Points lying to the right of these lines are stated in [4] as being represented to within 1 percent of the numerical solution by either the point-source solution or the modified-point-source solution depending upon the parameter range.)

From this table it is seen that the present results are generally more accurate than the two approximations of [4]. Also, for the most demanding case of equal radius spheres which are just touching, the present solution is only 5.8 percent in error as compared to errors of 12.1 percent resulting from each of the approximate solutions in [4]. Finally, it should be noted that the errors are generally largest for the case of zero sphere spacing but decrease rapidly to less than one percent with the present results converging to the results of the appropriate expression in [4] for large sphere spacings.

Conclusions

The shape factors between two spheres can be determined to a good approximation by employing the "separability" assumption given in equation (1). The resulting simple closed form expression, equation (8), is quite accurate over the entire range of sphere sizes and spacings including the region where acceptable results could have previously been obtained only by numerical integration.

References

1 Jones, L. R., "Diffuse Radiation View Factors Between Two Spheres," ASME JOURNAL OF HEAT TRANSFER, Vol. 87, No. 3, Aug. 1965, pp. 421–422.

2 Campbell, J. P., and McConnell, D. G., "Radiant-Interchange Configuration Factors for Spherical and Conical Surfaces to Spheres," NASA Tech. Note No. D-4457, 1968.

3 Juul, N. H., "Diffuse Configuration View Factors Between Two Spheres, and Their Limits," *Letters in Heat and Mass Transfer*, Vol. 3, pp. 205–212, 1976.

4 Juul, N. H., "Investigation of Approximate Methods for Calculation of the Diffuse Radiation Configuration View Factor Between Two Spheres," *Letters in Heat and Mass Transfer*, Vol. 3, pp. 513–522, 1976.

5 Siegel, R. and Howell, J. R., *Thermal Radiation Heat Transfer*, pp. 204–207, McGraw-Hill, N.Y., 1972.

6 Juul, N. H., "Applicability of Evaluating the View Factor by the Solid Angle in Radiation from Spheres or Infinitely Long Cylinders to Arbitrary Bodies," submitted to the *International Journal of Heat and Mass Transfer*.

7 Watts, R. G., "Radiant Heat Transfer to Earth Satellites," ASME JOURNAL OF HEAT TRANSFER, Vol. 87, No. 3, Aug. 1965, pp. 369–373.

Tube Wall Temperatures of an Eccentrically Located Horizontal Tube within a Narrow Annulus

R. W. Alperi[1]

Introduction

The problem considered in this technical note is that of a horizontal heated tube located eccentrically within another cylinder which forms an annular region for fluid flow such that a variable flow area (determined by the angle ψ) is formed (Figs. 1 and 2 indicate the geometry utilized in this analysis). The inner cylinder can be heated by using either an electrical power source or a hot water source. During operation of this system, it could be possible that the upper portion of the eccentric annulus (postulated to have the smallest clearance) could become vapor blanketed (dryout) while saturated boiling occurs over the remainder of the annular region. If such a situation occurred, the question arises as to what tube wall temperature distributions would be incurred using the two different types of heating sources. The answer to this question, namely, what is the temperature distribution of the heated tube wall when vapor blanketing of a portion of a narrow annular crevice occurs, when the two different possible heat sources are utilized, is the subject of this paper. Singley [1] has reported on experience in regard to steam generator tube support regions. Ishibashi and Nishikana [2] have also reported on the different flow regimes (coalesced and isolated bubble regions) that exist in vertical tubes with small clearances under different boiling situations. However, in general, the effects of boiling heat transfer in narrow annular spaces when eccentricity of the inner heated tube is present have not been extensively studied either analytically or experimentally; however, some completed studies have been reported by Rosenhow and Hartnett [3]. It should be noted that the cooling of individual insulated electrical cables can result [4] in a similar situation as is proposed here.

Analysis

Under the conditions proposed above, the upper region could be steam blanketed and have a small heat transfer coefficient (h_2) while the remainder of the annular area has local boiling and a high heat transfer coefficient (h_1). Two modes of heating the central tube, electrical heating and hot water heating are considered. For the case where the tube is heated by an electrical heater, the inside tube wall is assumed to have a constant heat flux as the boundary condition while the inside wall temperature is assumed to be constant when the tube is heated by a hot water energy source. Axial conduction effects are neglected in this analysis.

[1] Senior Engineer, Bettis Atomic Power Laboratory, Box 79, West Mifflin, PA 15122

Contributed by the Heat Transfer Division for publication in the JOURNAL OF HEAT TRANSFER. Manuscript received by the Heat Transfer Division August 19, 1977.

Table 1 Percent differences between the numerical integration solution [4] and: (a) equation (8), (b) point-source solution [4], and (c) modified point source solution [4]. See text for meaning of heavy vertical lines.

R_1/R_2	s/R_2	0.0	0.2	0.4	0.6	0.8	1.0	10.0
0.1	(a)	-2.6	-0.7	+0.1	+0.1	+0.1	+0.1	0.0
	(b)	-2.8	-0.8	0.0	0.0	0.0	0.0	0.0
	(c)	-31.0	-18.6	-12.6	-9.5	-7.4	-6.0	-0.2
0.2	(a)	-3.4	-1.4	-1.7	-0.4	+0.3	+0.2	0.0
	(b)	-4.0	-1.9	-2.1	-0.8	0.0	0.0	0.0
	(c)	-25.0	-16.2	-12.5	-8.8	-6.5	-5.3	-0.2
0.4	(a)	-4.8	-2.2	-1.1	-0.6	-0.5	-0.2	0.0
	(b)	-6.8	-3.8	-2.4	-1.6	-1.4	-0.9	0.0
	(c)	-19.1	-13.0	-9.5	-7.3	-6.0	-4.8	-0.2
0.6	(a)	-5.1	-2.4	-1.5	-0.9	0.0	-0.5	+0.1
	(b)	-8.6	-5.2	-3.8	-2.8	-1.6	-1.9	0.0
	(c)	-15.5	-10.7	-8.1	-6.3	-4.5	-4.4	-0.1
0.8	(a)	-5.6	-2.8	-1.6	-1.0	-0.7	-0.1	+0.1
	(b)	-10.6	-6.8	-5.0	-3.9	-3.1	-2.2	0.0
	(c)	-13.6	-9.3	-7.0	-5.5	-4.5	-3.4	-0.1
1.0	(a)	-5.8	-2.9	-1.8	-1.2	-0.9	+0.1	+0.1
	(b)	-12.1	-8.2	-6.2	-5.0	-4.1	-2.7	0.0
	(c)	-12.1	-8.2	-6.2	-5.0	-4.1	-2.7	0.0
2.0	(a)	-5.6	-3.3	-2.2	-1.4	-1.3	-1.1	+0.1
	(b)	-17.6	-13.9	-11.5	-9.7	-8.7	-7.7	-0.4
	(c)	-8.3	-5.8	-4.3	-3.4	-3.0	-2.6	-0.0
4.0	(a)	-3.6	-2.7	-2.4	-1.6	-1.2	-0.8	+0.1
	(b)	-22.6	-20.2	-18.4	-16.4	-14.8	-13.4	-1.7
	(c)	-4.6	-3.6	-3.2	-2.4	-1.9	-1.5	0.0
8.0	(a)	-3.5	-2.1	-1.6	-1.3	-0.9	-0.9	+0.1
	(b)	-29.6	-26.9	-24.9	-23.4	-21.9	-20.7	-4.6
	(c)	-3.8	-2.4	-1.8	-1.6	-1.2	-1.1	0.0
10.0	(a)	-2.6	-2.0	-1.4	-1.2	-0.8	-0.9	+0.1
	(b)	-31.0	-28.9	-27.0	-25.5	-24.1	-23.0	-6.0
	(c)	-2.8	-2.2	-1.5	-1.4	-1.0	-1.1	0.0

numerical computations given in [4] were only for points lying to the left of the solid vertical lines. Points lying to the right of these lines are stated in [4] as being represented to within 1 percent of the numerical solution by either the point-source solution or the modified-point-source solution depending upon the parameter range.)

From this table it is seen that the present results are generally more accurate than the two approximations of [4]. Also, for the most demanding case of equal radius spheres which are just touching, the present solution is only 5.8 percent in error as compared to errors of 12.1 percent resulting from each of the approximate solutions in [4]. Finally, it should be noted that the errors are generally largest for the case of zero sphere spacing but decrease rapidly to less than one percent with the present results converging to the results of the appropriate expression in [4] for large sphere spacings.

Conclusions

The shape factors between two spheres can be determined to a good approximation by employing the "separability" assumption given in equation (1). The resulting simple closed form expression, equation (8), is quite accurate over the entire range of sphere sizes and spacings including the region where acceptable results could have previously been obtained only by numerical integration.

References

1 Jones, L. R., "Diffuse Radiation View Factors Between Two Spheres," ASME JOURNAL OF HEAT TRANSFER, Vol. 87, No. 3, Aug. 1965, pp. 421–422.

2 Campbell, J. P., and McConnell, D. G., "Radiant-Interchange Configuration Factors for Spherical and Conical Surfaces to Spheres," NASA Tech. Note No. D-4457, 1968.

3 Juul, N. H., "Diffuse Configuration View Factors Between Two Spheres, and Their Limits," *Letters in Heat and Mass Transfer*, Vol. 3, pp. 205–212, 1976.

4 Juul, N. H., "Investigation of Approximate Methods for Calculation of the Diffuse Radiation Configuration View Factor Between Two Spheres," *Letters in Heat and Mass Transfer*, Vol. 3, pp. 513–522, 1976.

5 Siegel, R. and Howell, J. R., *Thermal Radiation Heat Transfer*, pp. 204–207, McGraw-Hill, N.Y., 1972.

6 Juul, N. H., "Applicability of Evaluating the View Factor by the Solid Angle in Radiation from Spheres or Infinitely Long Cylinders to Arbitrary Bodies," submitted to the *International Journal of Heat and Mass Transfer*.

7 Watts, R. G., "Radiant Heat Transfer to Earth Satellites," ASME JOURNAL OF HEAT TRANSFER, Vol. 87, No. 3, Aug. 1965, pp. 369–373.

Tube Wall Temperatures of an Eccentrically Located Horizontal Tube within a Narrow Annulus

R. W. Alperi[1]

Introduction

The problem considered in this technical note is that of a horizontal heated tube located eccentrically within another cylinder which forms an annular region for fluid flow such that a variable flow area (determined by the angle ψ) is formed (Figs. 1 and 2 indicate the geometry utilized in this analysis). The inner cylinder can be heated by using either an electrical power source or a hot water source. During operation of this system, it could be possible that the upper portion of the eccentric annulus (postulated to have the smallest clearance) could become vapor blanketed (dryout) while saturated boiling occurs over the remainder of the annular region. If such a situation occurred, the question arises as to what tube wall temperature distributions would be incurred using the two different types of heating sources. The answer to this question, namely, what is the temperature distribution of the heated tube wall when vapor blanketing of a portion of a narrow annular crevice occurs, when the two different possible heat sources are utilized, is the subject of this paper. Singley [1] has reported on experience in regard to steam generator tube support regions. Ishibashi and Nishikana [2] have also reported on the different flow regimes (coalesced and isolated bubble regions) that exist in vertical tubes with small clearances under different boiling situations. However, in general, the effects of boiling heat transfer in narrow annular spaces when eccentricity of the inner heated tube is present have not been extensively studied either analytically or experimentally; however, some completed studies have been reported by Rosenhow and Hartnett [3]. It should be noted that the cooling of individual insulated electrical cables can result [4] in a similar situation as is proposed here.

Analysis

Under the conditions proposed above, the upper region could be steam blanketed and have a small heat transfer coefficient (h_2) while the remainder of the annular area has local boiling and a high heat transfer coefficient (h_1). Two modes of heating the central tube, electrical heating and hot water heating are considered. For the case where the tube is heated by an electrical heater, the inside tube wall is assumed to have a constant heat flux as the boundary condition while the inside wall temperature is assumed to be constant when the tube is heated by a hot water energy source. Axial conduction effects are neglected in this analysis.

[1] Senior Engineer, Bettis Atomic Power Laboratory, Box 79, West Mifflin, PA 15122

Contributed by the Heat Transfer Division for publication in the JOURNAL OF HEAT TRANSFER. Manuscript received by the Heat Transfer Division August 19, 1977.

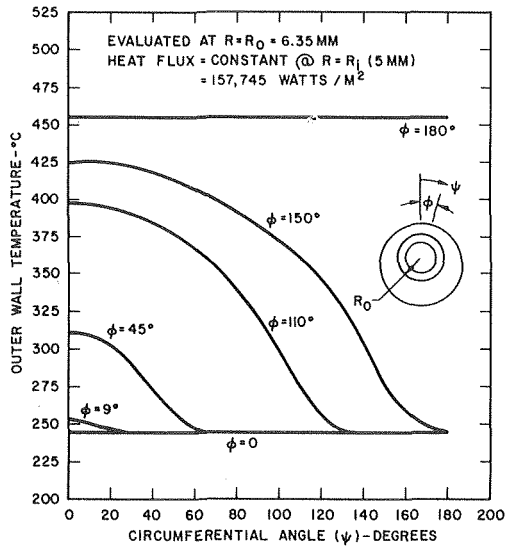

Fig. 1 Circumferential variation of wall temperature (constant heat flux)

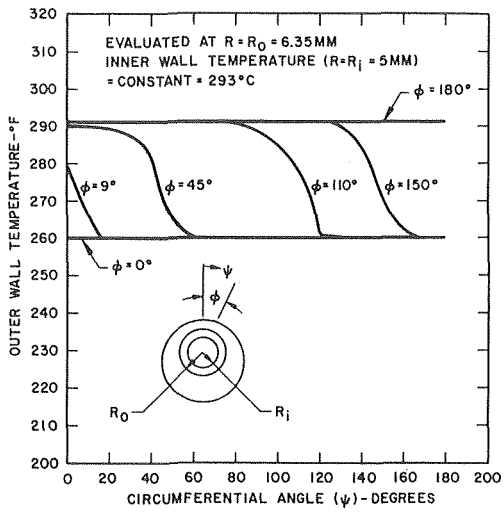

Fig. 2 Circumferential variation of wall temperature (constant wall temperature)

The governing equation for the steady-state temperature distribution in a tube which has a variable circumferential heat transfer coefficient along the outer radius is:

$$\frac{\partial^2 t}{\partial r^2} + \frac{1}{r}\frac{\partial t}{\partial r} + \frac{1}{r^2}\frac{\partial^2 t}{\partial \psi^2} = 0 \tag{1}$$

The boundary conditions for the two cases considered here are:

Electrically Heated

$$@\ R = R_i,\ -K\frac{\partial t}{\partial r} = q'' = \text{Constant}$$

$$@\ R = R_0,\ -\phi \leqslant \psi \leq \phi,\ -K\frac{\partial t}{\partial r} = h_2(t - t_\infty)$$

$$\left.\begin{matrix}\phi \leqslant \psi \leq \pi \\ -\pi \leqslant \psi \leq -\phi\end{matrix}\right\} -K\frac{\partial t}{\partial r} = h_1(t - t_\infty)$$

Hot Water Heated

$$@\ R = R_i,\ t = t_w = \text{Constant}$$

$$@\ R = R_0 \left\{\begin{matrix}\text{same as for} \\ \text{electrically} \\ \text{heated case}\end{matrix}\right. \tag{2}$$

The general solution for each case can be written as:

$$t = H_0 + H_1 \ln r + (H_2 \ln r + H_3)\psi + \sum_{m=1}^{\infty} \{A_m r^m + B_m r^{-m}\} \cos m\psi + \sum_{m=1}^{\infty} \{C_m r^m + D_m r^{-m}\} \sin m\psi \tag{3}$$

Each mode of heating the tube will be considered separately below wherein a standard Fourier Analysis technique was utilized to obtain a solution.

Electrically Heated Tube

Evaluating the above expression with the constant heat flux boundary condition for the electrically heated tube case at the inner boundary results in expressions for H_1 and A_m in terms of B_m. Hence, the expression for temperature becomes:

$$t = H_0 - \frac{q''Ri}{K}\ln r + \sum_{m=1}^{\infty} B_m\{r^m R_i^{-2m} + r^{-m}\}\cos m\psi \tag{4}$$

The above expression was evaluated at the outer boundary condition where the product of $h(t - t_\infty)$ was expanded in terms of a Fourier series for the two different regions assumed in this analysis and the coefficients of the like terms are equated to each other. The resulting coefficients are summarized in Table 1. As can be seen, there are $m = n$ equations that can be solved uniquely for the individual coefficients utilizing the constant term also shown in Table 1.

In Table 1, the following definitions are utilized:

$$\alpha_0 = H_0 - t_\infty - \frac{q''Ri}{K}\ln R_0$$

$$\alpha_m = R_0{}^m R_i{}^{-2m} + R_0{}^{-m} \tag{5}$$

$$\alpha_m{}^1 = R_0{}^{m-1} R_i{}^{-2m} - R_0{}^{-m-1}$$

The final solution for temperature can then be written as:

$$t = \alpha_0 + \sum_{m=1}^{\infty} B_m\{r^m R_i{}^{-2m} + r^{-m}\}\cos m\psi + t_\infty \tag{6}$$

Constant Wall Temperature

Evaluating the general solution for temperature (3) similarly for a constant wall temperature results in the following expression for temperature

$$t = t_\infty + \gamma_0 + \sum_{m=1}^{\infty} B_m(r^m R_i{}^{-2m} + r^{-m})\cos m\psi \tag{7}$$

where the coefficients of B_m and γ_0 are summarized in Table 2. The following definitions are utilized in Table 2:

$$\gamma_m = R_0{}^{-m} - R_i{}^{-2m} R_0{}^m$$

$$\gamma_0 = t_w - t_\infty + H_1 \ln\frac{R_0}{R_i} \tag{8}$$

$$\gamma_m{}^1 = R_0{}^{-m-1} + R_i{}^{-2m} R_0{}^{m-1}$$

Results

The temperature solutions were used to evaluate the tube wall temperatures for various degrees of vapor blanketing that might occur within the narrow annular crevice region. This was done by varying the vapor blanketing angle (ϕ) from 0 to π radians (concentric tubes with no vapor blanketing to being all vapor blanketed). Values of h_1 = 17,038.2 W/M²°C and h_2 = 567.9 W/M²°C were used for these calculations. The thermal conductivity utilized in these calculations was 17.3 W/M²°C. Temperature variations around the periphery for

Table 1 Summary of solution coefficients constant heat flux

a_0	B_1	B_2	B_3	B_4	B_n	CONSTANT
$\frac{-1}{\pi}\{(h_1-h_2)\phi - h_1\pi\}$	$\frac{-(h_1-h_2)a_1 \text{ SIN } \phi}{\pi}$	$\frac{-(h_1-h_2)a_2 \text{ SIN } 2\phi}{2\pi}$	$\frac{-(h_1-h_2)a_3 \text{ SIN } 3\phi}{3\pi}$	$\frac{-(h_1-h_2)a_4 \text{ SIN } 4\phi}{4\pi}$	$\frac{-(h_1-h_2)a_n \text{ SIN } n\phi}{n\pi}$	$\frac{q'' R_i}{R_0}$
$\frac{2(h_1-h_2) \text{ SIN } \phi}{\pi}$	$\frac{(h_1-h_2)a_1}{\pi}\left(\frac{\text{SIN } 2\phi}{2}+\phi\right)$ $-(h_1 a_1 + K a_1')$	$\frac{(h_1-h_2)a_2}{\pi}\left(\frac{\text{SIN } 3\phi}{3}+\text{SIN } \phi\right)$	$\frac{(h_1-h_2)a_3}{\pi}\left(\frac{\text{SIN } 4\phi}{4}+\frac{\text{SIN } 2\phi}{2}\right)$	$\frac{(h_1-h_2)a_4}{\pi}\left(\frac{\text{SIN } 5\phi}{5}+\frac{\text{SIN } 3\phi}{3}\right)$	$\frac{(h_1-h_2)a_n}{\pi}\left(\frac{\text{SIN } (n+1)\phi}{(n+1)}+\frac{\text{SIN } (n-1)\phi}{n-1}\right)$	0
$\frac{(h_1-h_2) \text{ SIN } 2\phi}{\pi}$	$\frac{(h_1-h_2)a_1}{\pi}\left(\frac{\text{SIN } 3\phi}{3}+\text{SIN } \phi\right)$	$\frac{(h_1-h_2)a_2}{\pi}\left(\frac{\text{SIN } 4\phi}{4}+\phi\right)$ $-(h_1 a_2 + 2K a_2')$	$\frac{(h_1-h_2)a_3}{\pi}\left(\frac{\text{SIN } 5\phi}{5}+\text{SIN } \phi\right)$	$\frac{(h_1-h_2)a_4}{\pi}\left(\frac{\text{SIN } 6\phi}{6}+\frac{\text{SIN } 2\phi}{2}\right)$	$\frac{(h_1-h_2)a_n}{\pi}\left(\frac{\text{SIN } (n+2)\phi}{n+2}+\frac{\text{SIN } (n-2)\phi}{n-2}\right)$	0
$\frac{2(h_1-h_2) \text{ SIN } 3\phi}{3\pi}$	$\frac{(h_1-h_2)a_1}{\pi}\left(\frac{\text{SIN } 4\phi}{4}+\frac{\text{SIN } 2\phi}{2}\right)$	$\frac{(h_1-h_2)a_2}{\pi}\left(\frac{\text{SIN } 5\phi}{5}+\text{SIN } \phi\right)$	$\frac{(h_1-h_2)a_3}{\pi}\left(\frac{\text{SIN } 6\phi}{6}+\phi\right)$ $-(h_1 a_3 + 3K a_3')$	$\frac{(h_1-h_2)a_4}{\pi}\left(\frac{\text{SIN } 7\phi}{7}+\text{SIN } \phi\right)$	$\frac{(h_1-h_2)a_n}{\pi}\left(\frac{\text{SIN } (n+3)\phi}{n+3}+\frac{\text{SIN } (n-3)\phi}{n-3}\right)$	0
⋮	⋮	⋮			⋮	
$\frac{2(h_1-h_2) \text{ SIN } m\phi}{m\pi}$	$\frac{(h_1-h_2)a_1}{\pi}\left(\frac{\text{SIN } (m+1)\phi}{m+1}+\frac{\text{SIN } (m-1)\phi}{m-1}\right)$	$\frac{(h_1-h_2)a_2}{\pi}\left(\frac{\text{SIN } (m+2)\phi}{m+2}+\frac{\text{SIN } (m-2)\phi}{m-2}\right)$			$\frac{(h_1-h_2)a_n}{\pi}\left\{\frac{\text{SIN } (n+m)\phi}{n+m}+\frac{\text{SIN } (n-m)\phi}{(n-m)}\right\}$	0
				IF $m=n$, $\frac{\text{SIN } (n-m)\phi}{n-m}=\phi$ AND ADDED TERM $-(h_1 a_n + nK a_n')$		

Table 2 Summary of solution coefficients constant wall temperature

γ_0	B_1	B_2	B_3	B_4	B_n	CONSTANT
$\frac{-1}{\pi}\left\{(h_1-h_2)\phi - h_1\pi - \frac{\pi K}{R_0 \ln \frac{R_0}{R_i}}\right\}$	$\frac{-(h_1-h_2)\gamma_1 \text{ SIN } \phi}{\pi}$	$\frac{-(h_1-h_2)\gamma_2 \text{ SIN } 2\phi}{2\pi}$	$\frac{-(h_1-h_2)\gamma_3 \text{ SIN } 3\phi}{3\pi}$	$\frac{-(h_1-h_2)\gamma_4 \text{ SIN } 4\phi}{4\pi}$	$\frac{-(h_1-h_2)\gamma_n \text{ SIN } n\phi}{n\pi}$	$\frac{K(t_w-t_\infty)}{R_0 \ln \frac{R_0}{R_i}}$
$\frac{2(h_1-h_2) \text{ SIN } \phi}{\pi}$	$\frac{(h_1-h_2)\gamma_1}{\pi}\left(\frac{\text{SIN } 2\phi}{2}+\phi\right)$ $-(h_1\gamma_1 - K\gamma_1')$	$\frac{(h_1-h_2)\gamma_2}{\pi}\left(\frac{\text{SIN } 3\phi}{3}+\text{SIN } \phi\right)$	$\frac{(h_1-h_2)\gamma_3}{\pi}\left(\frac{\text{SIN } 4\phi}{4}+\frac{\text{SIN } 2\phi}{2}\right)$	$\frac{(h_1-h_2)\gamma_4}{\pi}\left(\frac{\text{SIN } 5\phi}{5}+\frac{\text{SIN } 3\phi}{3}\right)$	$\frac{(h_1-h_2)\gamma_n}{\pi}\left(\frac{\text{SIN } (n+1)\phi}{(n+1)}+\frac{\text{SIN } (n-1)\phi}{n-1}\right)$	0
$\frac{(h_1-h_2) \text{ SIN } 2\phi}{\pi}$	$\frac{(h_1-h_2)\gamma_1}{\pi}\left(\frac{\text{SIN } 3\phi}{3}+\text{SIN } \phi\right)$	$\frac{(h_1-h_2)\gamma_2}{\pi}\left(\frac{\text{SIN } 4\phi}{4}+\phi\right)$ $-(h_1\gamma_2 - 2K\gamma_2')$	$\frac{(h_1-h_2)\gamma_3}{\pi}\left(\frac{\text{SIN } 5\phi}{5}+\text{SIN } \phi\right)$	$\frac{(h_1-h_2)\gamma_4}{\pi}\left(\frac{\text{SIN } 6\phi}{6}+\frac{\text{SIN } 2\phi}{2}\right)$	$\frac{(h_1-h_2)\gamma_n}{\pi}\left(\frac{\text{SIN } (n+2)\phi}{n+2}+\frac{\text{SIN } (n-2)\phi}{n-2}\right)$	0
$\frac{2(h_1-h_2) \text{ SIN } 3\phi}{3\pi}$	$\frac{(h_1-h_2)\gamma_1}{\pi}\left(\frac{\text{SIN } 4\phi}{4}+\frac{\text{SIN } 2\phi}{2}\right)$	$\frac{(h_1-h_2)\gamma_2}{\pi}\left(\frac{\text{SIN } 5\phi}{5}+\text{SIN } \phi\right)$	$\frac{(h_1-h_2)\gamma_3}{\pi}\left(\frac{\text{SIN } 6\phi}{6}+\phi\right)$ $-(h_1\gamma_3 - 3K\gamma_3')$	$\frac{(h_1-h_2)\gamma_4}{\pi}\left(\frac{\text{SIN } 7\phi}{7}+\text{SIN } \phi\right)$	$\frac{(h_1-h_2)\gamma_n}{\pi}\left(\frac{\text{SIN } (n+3)\phi}{n+3}+\frac{\text{SIN } (n-3)\phi}{n-3}\right)$	0
⋮	⋮	⋮			⋮	
$\frac{2(h_1-h_2) \text{ SIN } m\phi}{m\pi}$	$\frac{(h_1-h_2)\gamma_1}{\pi}\left(\frac{\text{SIN } (m+1)\phi}{m+1}+\frac{\text{SIN } (m-1)\phi}{m-1}\right)$	$\frac{(h_1-h_2)\gamma_2}{\pi}\left(\frac{\text{SIN } (m+2)\phi}{m+2}+\frac{\text{SIN } (m-2)\phi}{m-2}\right)$			$\frac{(h_1-h_2)\gamma_n}{\pi}\left\{\frac{\text{SIN } (n+m)\phi}{n+m}+\frac{\text{SIN } (n-m)\phi}{(n-m)}\right\}$	0
				IF $m=n$, $\frac{\text{SIN } (n-m)\phi}{n-m}=\phi$ AND ADDED TERM $-(h_1\gamma_n - nK\gamma_n')$		

typical cases of an electrically heated tube are shown in Fig. 1 and for the hot water heated tubes in Fig. 2. As can be seen, the temperature variations can be significant between the area of the vapor blanketing, and the region of local boiling although much more so for the electrically heated case. It is significant to note that the results indicate that the wall temperatures can vary significantly but thermocouples placed within the tube but not in the area of the vapor blanketing may not indicate any significant temperature changes have occurred. The calculated temperature profiles tend to indicate that a greater potential exists for electrically heated tube tests to have vapor blanketed regions than for hot water heated tube tests.

References

1 Singley, W. J., "Shippingport Atomic Power Station Steam Generator Tube Damage and Water Chemistry Control," WAPD-TM-1309, Jan. 1978

2 Ishibashi, E., and Nishikawa, K., "Saturated Boiling Heat Transfer in Narrow Spaces," *Int. Jl. of Heat Mass Transfer*, Vol. 12, 1969, pp. 863–894

3 Rosenhow, W. M., and Hartnett, J. P., *Handbook of Heat Transfer*, McGraw Hill Book Company, New York, pp. 7–107 to 7–110.

4 Chato, J. C., and Chern, S. Y., "The Effects of Non-Uniform Cooling on the Heat Transfer From an Insulated Electric Cable," ASME JOURNAL OF HEAT TRANSFER, Vol. 97, Aug. 1975, pp. 424–428

A Finite Element Thermal Analysis Procedure for Several Temperature-Dependent Parameters

E. A. Thornton[1] and A. R. Wieting[2]

Nomenclature

A = tube element conduction area
A_s = tube element surface convection area
c_p = fluid specific heat
h = convective heat transfer coefficient
$[J]$ = Jacobian matrix defined in equation (4)
k = thermal conductivity
$[K]$ = thermal conductance matrix
$[\overline{K}]$ = thermal conductance matrix for a unit thermal parameter
$[K^*]$ = nonsymmetric portion of the Jacobian matrix, defined in equation (5) or (12)
L = tube/fluid element length
$\dot{m}$ = fluid mass flow rate
N = number of element nodes
NC = number of component matrices
$\{Q\}$ = heat load vector
$\{R\}$ = residual heat load vector, defined in equation (6) or (14)
$\{T\}$ = temperature vector
$\{\Delta T\}$ = temperature increment vector, defined in equation (2)
T_a = average element temperature, defined in equation (8)
TP = thermal parameter

Subscripts

c = component matrix
e = element matrix
n = iteration number

Introduction

Steady-state conduction/convection thermal analysis of practical structures requires consideration of several temperature dependent thermal parameters. For example, a typical conduction/forced convection thermal analysis involves the independent variation of: (1) the thermal conductivity of the structure, (2) the fluid specific heat, and (3) the convective heat transfer coefficient. In a recent development of finite element methodology for steady state thermal analysis of convectively cooled structures [1] new finite elements were developed which incorporated these three parameters into single elements. The elements differ from past finite elements for steady-state thermal analysis [2] which have utilized only one temperature dependent thermal parameter (e.g., conductivity) per element.

Steady-state thermal analysis using finite elements with temperature dependent thermal parameters requires the solution of a nonlinear set of algebraic equations. One of the most popular solution methods in nonlinear analysis is the Newton-Raphson iteration technique. The Newton-Raphson method is discussed in a recent conduction heat transfer text [3] with reference to an algebraic equation, but no information is presented which shows the application of the method to a set of simultaneous nonlinear equations such as generated by either the finite difference or finite element methods. The method has been successfully applied to nonlinear structural analysis [4], and thermal analysis [5–7]. The applications to thermal analysis have been limited to finite elements involving only one temperature dependent parameter, e.g., the thermal conductivity. A well-known drawback of the conventional Newton-Raphson method is the need to recompute and factor the global conductance (stiffness) matrix at each iteration. Frequently, a modified Newton-Raphson method is used where the conductance matrix is held constant for several iterations and is recalculated only when the convergence rate deteriorates, [8].

The purpose of this paper is to present a finite element thermal analysis procedure for simple elements with several temperature dependent thermal parameters. The procedure is based on an application of the generalized Newton-Raphson technique presented in [5]. The conventional Newton-Raphson technique is used, but to achieve improved computational efficiency a procedure is developed in which element conductance matrices are computed once per unit thermal parameter. The procedure is demonstrated for a convectively cooled structure with three hypothetical, widely varying thermal parameters. Convergence rates of the calculated coolant and structural temperatures are presented and computational savings of the unit thermal parameter concept are discussed.

Analysis Procedure for Several Thermal Parameters

Finite element thermal analysis of a steady state conduction/forced convection problem with temperature dependent thermal parameters requires solution of a set of nonlinear, algebraic equations,

$$[K(T)]\{T\} = \{Q\} \tag{1}$$

where $[K(T)]$ is the temperature-dependent system conductance matrix, $\{T\}$ is the nodal temperature vector and $\{Q\}$ is the system nodal heat load vector. The heat load vector is assumed constant. This is a permissible assumption in many conduction/forced convection problems where heat loads normally arise from specified surface or convective heating and radiative exchanges are neglected.

The Newton-Raphson iterative solution algorithm for solving equation (1) is

$$[J]_n\{\Delta T\}_{n+1} = \{R\}_n \tag{2}$$

$$\{T\}_{n+1} = \{T\}_n + \{\Delta T\}_{n+1} \tag{3}$$

where $[J]_n$ is called in [5] the Jacobian matrix. In the present paper $[J]_n$ is called the system Jacobian matrix, and it is assembled from element Jacobian matrices. A typical term of an element Jacobian matrix is given by

$$(J_{ij})_e = (K_{ij})_e + (K_{ij}{}^*)_e \tag{4}$$

where

$$(K_{ij}{}^*)_e = \sum_{\ell=1}^{N} (\partial(K_{i\ell})_e/\partial T_j)\,(T_\ell)_e \tag{5}$$

and N is the number of element nodes; $(K_{ij})_e$ is a term of the element conductance matrix, $(K_{ij}{}^*)_e$ is a pseudo conductance term contributed by the Newton-Raphson technique and $(T_\ell)_e$ represents the element nodal temperatures. The terms in the Jacobian matrix depend on: (1) the element type (rod, quadrilateral, etc.), (2) the spatial variation of the thermal parameters within an element, and (3) the form of the temperature dependence of the thermal parameters.

The matrix $\{R\}_n$, (equation (2)), denotes the system residual nodal heat-load vector which is assembled from corresponding element vectors. A typical term of an element residual heat load vector is given by

$$(R_i)_e = (Q_i)_e - \sum_{\ell=1}^{N} (K_{i\ell})_e\,(T_\ell)_e. \tag{6}$$

The application of the Newton-Raphson technique to elements with several thermal parameters is based on two assumptions: (1) thermal parameters are constant within an element, and (2) an element thermal parameter depends only on the average element temperature. These assumptions are reasonable for lower order finite elements with simple temperature variations. Indeed, the assumption of constant thermal parameters within a discrete region is an accepted practice

[1] Assoc. Professor, Old Dominion University, Norfolk, Va. 23508, Mem. ASME.
[2] Research Engineer, NASA Langley Research Center, Hampton, Va. 23665.
Contributed by the Heat Transfer Division for publication in the JOURNAL OF HEAT TRANSFER.. Manuscript received by the Heat Transfer Division December 12, 1977.

in heat transfer analysis using the lumped-parameter approach. In conduction heat transfer higher-order finite elements offer computational advantages, and the thermal conductivity should be permitted to vary within the element, [5]. In such cases assumptions (1) and (2) are not valid.

Using assumption (1), an element conductance matrix associated with a typical thermal parameter can be expressed as a product of the thermal parameter and a unit conductance matrix. Furthermore, for an element with several thermal parameters the element conductance matrix can be expressed as the sum of such terms, one for each thermal parameter. For example, the element conductance matrix for a tube/fluid element [1] with two fluid nodes and two tube nodes is

$$[K]_e = k\begin{bmatrix} 0 & 0 & 0 & 0 \\ 0 & 0 & 0 & 0 \\ 0 & 0 & A/L & -A/L \\ 0 & 0 & -A/L & A/L \end{bmatrix} + h\begin{bmatrix} A_s/3 & A_s/6 & -A_s/6 & -A_s/3 \\ & A_s/3 & -A_s/3 & -A_s/6 \\ \text{Sym} & & A_s/3 & A_s/6 \\ & & & A_s/3 \end{bmatrix} + c_p\begin{bmatrix} -\dot{m}/2 & \dot{m}/2 & 0 & 0 \\ -\dot{m}/2 & \dot{m}/2 & 0 & 0 \\ 0 & 0 & 0 & 0 \\ 0 & 0 & 0 & 0 \end{bmatrix} \tag{7}$$

where k is the tube thermal conductivity, A is the tube conduction area and L is the element length; h is the convective heat transfer coefficient and A_s is the tube inner surface convection area; c_p is the fluid specific heat; and $\dot{m}$ is the fluid mass flow rate. Assumption (2) means that element thermal parameters such as k, h, and c_p in equation (7) are interpolated from tabulated data using an average element temperature T_a, computed from

$$T_a = 1/N \sum_{j=1}^{N} T_j \tag{8}$$

where T_j is the temperature of the jth node. In equation (8) N is the number of temperatures effecting the thermal parameter and T_j are the associated temperatures. For example, the tube thermal conductivity depends only on the two tube temperatures whereas h and c_p depend on the two fluid temperatures. For the simple, lower order, one and two dimensional elements used in this study the temperature averaging scheme presented in equation (8) has proven very satisfactory. For other two and three dimensional finite elements a weighted temperature average may be more desirable.

The Jacobian matrix (equation (4)) for an element with several thermal parameters is evaluated by resolving an element Jacobian into component matrices, one component matrix for each thermal parameter. Thus

$$[J]_e = \sum_{c=1}^{NC} [J]_c \tag{9}$$

where $[J]_c$ is a typical component Jacobian matrix and NC is the number of element thermal parameters. Each component Jacobian matrix is the sum of two terms as shown in equation (4). Using assumption (1), a typical component conductance matrix, the first term in equation (4), is

$$(K_{ij})_c = TP_c(\overline{K}_{ij})_c \tag{10}$$

where TP_c is a typical component thermal parameter (e.g., h, k, or c_p) and $(\overline{K}_{ij})_c$ is a unit conductance matrix (see equation (7)). Using assumption (2), the second term, the pseudo conductance matrix (equation (5)), may be written in terms of the average element temperature T_a. First, the chain rule of differentiation gives

$$(K_{ij}{}^*)_c = \sum_{\ell=1}^{N} (\partial T_a/\partial T_j)(d(K_{i\ell})_c/dT_a)(T_\ell)_e. \tag{11}$$

Then differentiating equations (8) and (10) and substituting into equation (11) yields

$$(K_{ij}{}^*)_c = 1/N(d(TP)_c/dT_a) \sum_{\ell=1}^{N} (\overline{K}_{i\ell})_c (T_\ell)_e. \tag{12}$$

Since the right hand side of equation (12) is independent of j, $(K_{ij}{}^*)_c$ is a matrix with equal columns. The quantity $d(TP)_c/dT_a$ represents the slope of the thermal parameter curve evaluated at the average element temperature. (In this paper, all parameters are assumed to vary in a piecewise linear manner with temperature.) Combining equations (10) and (12) gives an explicit equation for the terms of a component Jacobian matrix:

$$(J_{ij})_c = TP_c(\overline{K}_{ij})_c + 1/N\,(d(TP)_c/dT_a) \sum_{\ell=1}^{N} (\overline{K}_{i\ell})_c\,(T_\ell)_e. \tag{13}$$

The element residual heat load vector may be written in terms of components in a similar manner. The residual load for a typical component is then found by substituting equation (10) into equation (6) to obtain:

$$(R_i)_c = (Q_i)_c - TP_c \sum_{\ell=1}^{N} (\overline{K}_{i\ell})_c (T_\ell)_e. \tag{14}$$

Equations (13) and (14) are the basis for the solution procedure for several thermal parameters. These equations have the following computational conveniences: (1) they are valid for all element types independent of the element formulation, (2) element component conductance matrices need to be computed only once, and (3) they have common operations so that computations can be efficiently combined into a single subroutine.

In the computer program utilizing the procedure [9], element unit conductance matrix components are first formed for all elements. At each iteration Jacobian matrices and residual heat load vectors for each component are computed from the unit conductance matrices using equations (13) and (14). Component thermal parameters TP_c and $d(TP)_c/dT_a$ are computed from tabulated input data using linear interpolation. Component matrices are then simultaneously assembled into the system matrices. The system equations (2) are solved by a general banded equation solver because of the asymmetry of the Jacobian matrix. The iteration process is initiated by assuming a zero nodal temperature vector and terminated when the largest ΔT at a node (expressed as a percentage) is less than a specified convergence criterion.

Example

The solution procedure has been successfully applied to several convectively cooled structures, [1]. One of these applications was to a segment of a strut for a hydrogen cooled supersonic combustion ramjet (scramjet) engine, Fig. 1. The strut is heated by hot hydrogen flowing in internal manifolds and aerodynamically by external air flow. The structure is cooled by cold hydrogen flowing between the primary structure and the aerodynamic skin. The finite element model, Fig. 1, utilizes rod and quadrilateral conduction elements to

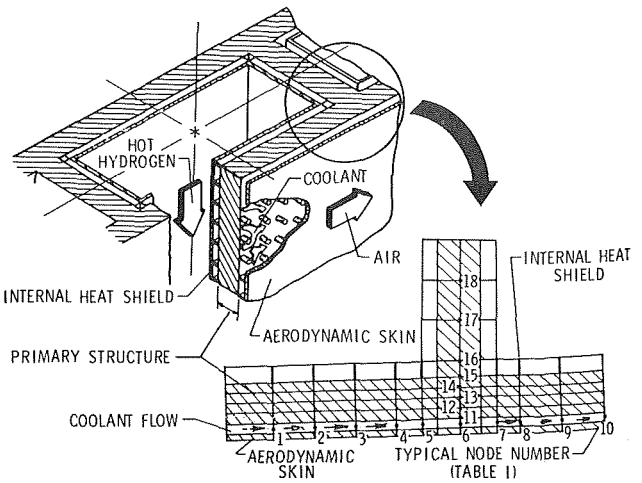

Fig. 1 Scramjet strut segment and finite element model

represent the heat shield, primary structure and aerodynamic skin and plate-fin/fluid elements to represent the coolant passage. The temperatures on the boundary of the region (except for the coolant outlet temperature) are specified. The temperature variations of three hypothetical thermal parameters are displayed in Fig. 2. Hypothetical parameters are used so that a significant variation of the thermal parameters will occur over the structural and fluid temperature ranges.

The finite element calculated temperatures at each iteration for selected nodes (Fig. 1) are presented in Table 1. The convergence rate is good; four iterations were required to meet the convergence criteria of 0.1 percent. The predominant thermal parameter is the convection coefficient h which increases by over 300 percent. Structural temperatures vary in successive iterations because of the simultaneous effects of an increasing heat loss to the coolant and a two-fold increase in the thermal conductivity. In [1], utilizing realistic thermal parameters, convergence was achieved in three iterations and calculated temperatures were in excellent agreement with results from a lumped parameter thermal analysis.

In this application (132 nodes, 98 elements) the initial formation of the element matrices required 25 percent of the CPU (Central Processing Units) time for the complete solution. If element matrices had been computed at every iteration the time for a complete solution would have increased by more than 60 percent. Thus, the Jacobian matrix computed from unit conductance matrices can result in significant savings in computer time.

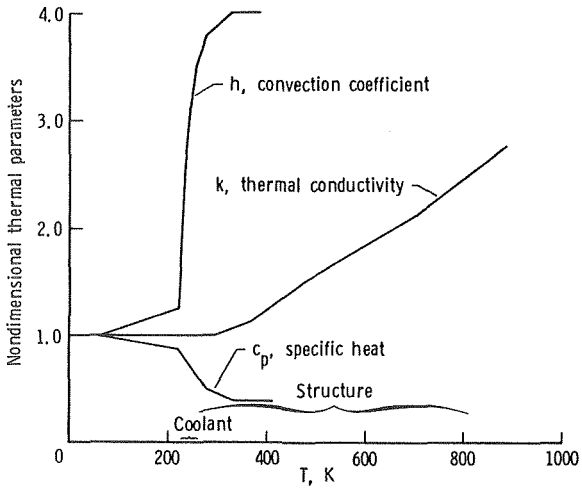

Fig. 2 Temperature variation of thermal parameters

Table 1 Finite element predicted temperatures

Nodes	Iteration 0	1	2	3,4
Coolant Temperatures, K				
1	223.7	225.2	225.5	225.6
2	225.3	228.6	228.9	229.0
3	226.9	232.3	233.3	233.4
4	228.7	236.3	237.6	237.8
5	229.9	239.3	241.2	241.6
6	231.4	244.1	244.8	247.2
7	233.4	249.2	252.7	253.0
8	234.4	251.7	255.0	255.4
9	236.1	256.0	259.7	259.9
10	237.9	260.0	262.7	263.0
Primary Structure Temperatures, K				
11	264.7	262.9	264.2	264.3
12	293.2	310.9	312.1	312.2
13	324.4	360.6	360.8	360.9
14	360.7	414.5	412.2	412.2
15	405.9	469.8	466.3	466.5
16	480.7	546.9	544.4	544.4
17	639.4	683.9	683.3	683.3
18	721.1	741.7	741.1	741.1

Concluding Remarks

A finite element thermal analysis procedure for elements with several temperature dependent thermal parameters is presented. The procedure, based on an application of the Newton-Raphson iteration technique, is formulated by resolving element matrices into component matrices, one component for each thermal parameter. Component conductance matrices are evaluated assuming constant thermal parameters within an element and are computed once per unit thermal parameter. Significant savings in computer time result from the unit thermal parameter concept. The solution procedure applied to a convectively cooled structure with significantly varying thermal parameters converged in four iterations.

The thermal analysis procedure has proven to be both an efficient and effective technique for nonlinear analysis of practical conduction/convection problems.

References

1 Thornton, E. A., and Wieting, A. R., "Finite Element Methodology for Thermal Analysis of Convectively Cooled Structures," Presented at the 15th Aerospace Sciences Meeting, Los Angeles, Ca, AIAA Paper No. 77-187, Jan. 1977.

2 Lee, H. P., "NASTRAN Thermal Analyzer, Vol. I: The NASTRAN Thermal Analyzer Manual," NASA Goddard Space Flight Center, X-322-76-16, Dec. 1975.

3 Myers, G., *Analytical Methods in Conduction Heat Transfer*, McGraw Hill Book Company, 1971, pp 308–309.

4 Tillerson, J. R.; Stricklin, J. A.; and Haisler, W. C., "Numerical Methods for the Solution of Nonlinear Problems in Structural Analysis," *Numerical Solution of Nonlinear Structural Problems*, Hartung, R. F. editor, ASME, 1973, pp. 67–101.

5 Lyness, J. F.; Owen, D. R. J.; and Zienkiewicz, O. C., "The Finite Element Analysis of Engineering Systems Governed by a Nonlinear Quasi-Harmonic Equation," *Journal of Computers and Structures*, Vol. 5, 1975, pp. 65–79.

6 Padovan, J., "Steady Conduction of Heat in Linear and Nonlinear Fully Anisotropic Media by Finite Elements," ASME JOURNAL OF HEAT TRANSFER, Aug. 1974, pp. 313–318.

7 Anderson, C. A.; and Zienkiewicz, O. C., "Spontaneous Ignition: Finite Element Solutions for Steady and Transient Conditions," ASME JOURNAL OF HEAT TRANSFER, Aug. 1974, pp. 398–404.

8 Stricklin, J. A. and Haisler, W. E., "Formulations and Solution Procedures for Nonlinear Structural Analysis," *Journal of Computers and Structures*, Vol. 7, No. 1, Feb. 1977, pp. 130.

9 Thornton, E. A., "TAPl: A Finite Element Program for Steady State Thermal Analysis of Convectively Cooled Structures," NASA CR-145069, Nov. 1976.

Temperatures in an Anisotropic Sheet Containing an Insulated Elliptical Hole

M. H. Sadd[1] and I. Miskioglu[2]

Introduction

It is well known that when the flow of heat is disturbed by some discontinuity (e.g., hole, void or crack), there will be a high elevation of the local temperature gradient around the discontinuity. Thermal disturbances of this type can produce sizeable thermal stresses and in some cases can cause material failure through crack propagation. A considerable amount of research has been devoted to such problems [1–14].

[1] Department of Mechanical Engineering, Mississippi State University, Mississippi State, MS 39762.

[2] Presently a graduate student at Iowa State University, Ames, Iowa.

Contributed by the Heat Transfer Division for publication in the JOURNAL OF HEAT TRANSFER. Manuscript received by the Heat Transfer Division February 21, 1978.

represent the heat shield, primary structure and aerodynamic skin and plate-fin/fluid elements to represent the coolant passage. The temperatures on the boundary of the region (except for the coolant outlet temperature) are specified. The temperature variations of three hypothetical thermal parameters are displayed in Fig. 2. Hypothetical parameters are used so that a significant variation of the thermal parameters will occur over the structural and fluid temperature ranges.

The finite element calculated temperatures at each iteration for selected nodes (Fig. 1) are presented in Table 1. The convergence rate is good; four iterations were required to meet the convergence criteria of 0.1 percent. The predominant thermal parameter is the convection coefficient h which increases by over 300 percent. Structural temperatures vary in successive iterations because of the simultaneous effects of an increasing heat loss to the coolant and a two-fold increase in the thermal conductivity. In [1], utilizing realistic thermal parameters, convergence was achieved in three iterations and calculated temperatures were in excellent agreement with results from a lumped parameter thermal analysis.

In this application (132 nodes, 98 elements) the initial formation of the element matrices required 25 percent of the CPU (Central Processing Units) time for the complete solution. If element matrices had been computed at every iteration the time for a complete solution would have increased by more than 60 percent. Thus, the Jacobian matrix computed from unit conductance matrices can result in significant savings in computer time.

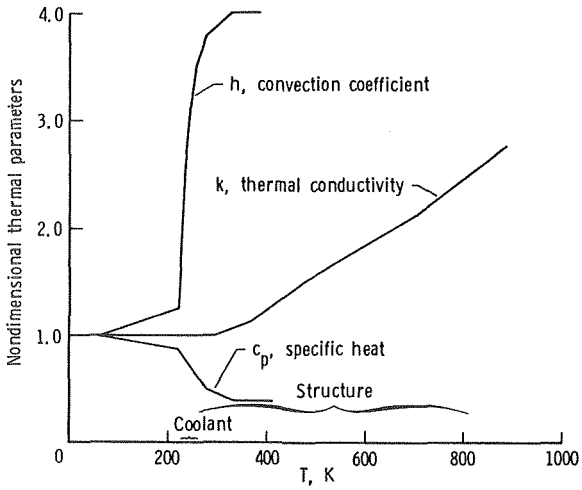

Fig. 2 Temperature variation of thermal parameters

Table 1 Finite element predicted temperatures

Nodes	Iteration 0	1	2	3,4
Coolant Temperatures, K				
1	223.7	225.2	225.5	225.6
2	225.3	228.6	228.9	229.0
3	226.9	232.3	233.3	233.4
4	228.7	236.3	237.6	237.8
5	229.9	239.3	241.2	241.6
6	231.4	244.1	244.8	247.2
7	233.4	249.2	252.7	253.0
8	234.4	251.7	255.0	255.4
9	236.1	256.0	259.7	259.9
10	237.9	260.0	262.7	263.0
Primary Structure Temperatures, K				
11	264.7	262.9	264.2	264.3
12	293.2	310.9	312.1	312.2
13	324.4	360.6	360.8	360.9
14	360.7	414.5	412.2	412.2
15	405.9	469.8	466.3	466.5
16	480.7	546.9	544.4	544.4
17	639.4	683.9	683.3	683.3
18	721.1	741.7	741.1	741.1

Concluding Remarks

A finite element thermal analysis procedure for elements with several temperature dependent thermal parameters is presented. The procedure, based on an application of the Newton-Raphson iteration technique, is formulated by resolving element matrices into component matrices, one component for each thermal parameter. Component conductance matrices are evaluated assuming constant thermal parameters within an element and are computed once per unit thermal parameter. Significant savings in computer time result from the unit thermal parameter concept. The solution procedure applied to a convectively cooled structure with significantly varying thermal parameters converged in four iterations.

The thermal analysis procedure has proven to be both an efficient and effective technique for nonlinear analysis of practical conduction/convection problems.

References

1 Thornton, E. A., and Wieting, A. R., "Finite Element Methodology for Thermal Analysis of Convectively Cooled Structures," Presented at the 15th Aerospace Sciences Meeting, Los Angeles, Ca, AIAA Paper No. 77-187, Jan. 1977.

2 Lee, H. P., "NASTRAN Thermal Analyzer, Vol. I: The NASTRAN Thermal Analyzer Manual," NASA Goddard Space Flight Center, X-322-76-16, Dec. 1975.

3 Myers, G., *Analytical Methods in Conduction Heat Transfer*, McGraw Hill Book Company, 1971, pp 308–309.

4 Tillerson, J. R.; Stricklin, J. A.; and Haisler, W. C., "Numerical Methods for the Solution of Nonlinear Problems in Structural Analysis," *Numerical Solution of Nonlinear Structural Problems*, Hartung, R. F. editor, ASME, 1973, pp. 67–101.

5 Lyness, J. F.; Owen, D. R. J.; and Zienkiewicz, O. C., "The Finite Element Analysis of Engineering Systems Governed by a Nonlinear Quasi-Harmonic Equation," *Journal of Computers and Structures*, Vol. 5, 1975, pp. 65–79.

6 Padovan, J., "Steady Conduction of Heat in Linear and Nonlinear Fully Anisotropic Media by Finite Elements," ASME JOURNAL OF HEAT TRANSFER, Aug. 1974, pp. 313–318.

7 Anderson, C. A.; and Zienkiewicz, O. C., "Spontaneous Ignition: Finite Element Solutions for Steady and Transient Conditions," ASME JOURNAL OF HEAT TRANSFER, Aug. 1974, pp. 398–404.

8 Stricklin, J. A. and Haisler, W. E., "Formulations and Solution Procedures for Nonlinear Structural Analysis," *Journal of Computers and Structures*, Vol. 7, No. 1, Feb. 1977, pp. 130.

9 Thornton, E. A., "TAPl: A Finite Element Program for Steady State Thermal Analysis of Convectively Cooled Structures," NASA CR-145069, Nov. 1976.

Temperatures in an Anisotropic Sheet Containing an Insulated Elliptical Hole

M. H. Sadd[1] and I. Miskioglu[2]

Introduction

It is well known that when the flow of heat is disturbed by some discontinuity (e.g., hole, void or crack), there will be a high elevation of the local temperature gradient around the discontinuity. Thermal disturbances of this type can produce sizeable thermal stresses and in some cases can cause material failure through crack propagation. A considerable amount of research has been devoted to such problems [1–14].

[1] Department of Mechanical Engineering, Mississippi State University, Mississippi State, MS 39762.

[2] Presently a graduate student at Iowa State University, Ames, Iowa.

Contributed by the Heat Transfer Division for publication in the JOURNAL OF HEAT TRANSFER. Manuscript received by the Heat Transfer Division February 21, 1978.

The majority of this research has been for isotropic materials. Only the very recent works by Murata and Atsumi [13] and Atkinson and Clements [14] have investigated anisotropic materials. The widespread use of composite materials in structural applications has caused a strong need for understanding anisotropic material behavior. Consequently information on thermal stress concentrations around material discontinuities in anisotropic bodies will have application in high-temperature composite materials.

This present note is concerned with the first part of a general uncoupled thermal stress problem for anisotropic media, i.e., a determination of the temperature distribution. Specifically the temperatures in an infinite anisotropic sheet containing an insulated elliptical hole will be determined. The problem has an identical formulation as the inclusion problem of Yang and Chou [15]. Results of this anisotropic study can be directly incorporated in a thermal stress analysis investigation, and can also be used in current fracture mechanics theories.

Temperature Problem

For anisotropic solids the thermal conductivity shows directional properties, and the heat flux vector $\underline{q}$, is not necessarily normal to an isothermal surface. For this case the generalized Fourier law of conduction would read

$$q_i = -k_{ij}\frac{\partial T}{\partial x_j}, \tag{1}$$

where the conductivity coefficients k_{ij} form a second order tensor. Note that for the isotropic case, $k_{ij} = k\delta_{ij}$, where δ_{ij} is the kronecker delta.

Using the general conduction law, equation (1), and the conservation of energy for steady-state conditions with no heat sources gives the heat conduction equation

$$k_{ij}\frac{\partial^2 T}{\partial x_i \partial x_j} = 0, \tag{2}$$

or written out in component form for two dimensions

$$k_{11}\frac{\partial^2 T}{\partial {x_1}^2} + 2k_{12}\frac{\partial^2 T}{\partial x_1 \partial x_2} + k_{22}\frac{\partial^2 T}{\partial {x_2}^2} = 0. \tag{3}$$

The temperature distribution problem will be to determine the steady state temperatures $T(x_1, x_2)$, in an infinite anisotropic plate lying in the x_1x_2-plane, which will be referred to as the z-plane. This plate is subjected to a uniform heat flux q_0, at infinity directed along the positive x_2 axis. The plate also contains an insulated elliptical hole whose major axis $2a$ and minor axis $2b$ lie along the x_1 and x_2 axes, respectively (see Fig. 1). Although the heat flow is directed perpendicular to the axis of the elliptical hole, the problem could also be easily solved for an inclined heat flow.

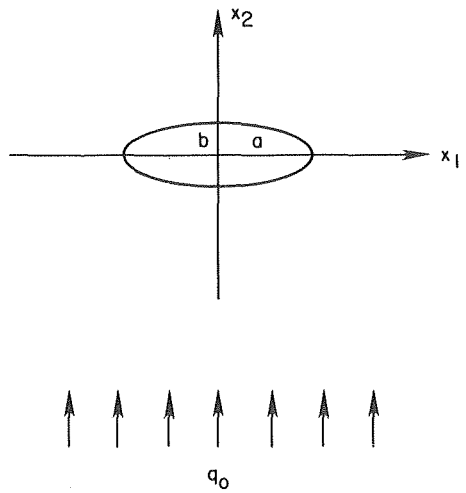

Fig. 1 Schematic of Heat flow around an insulated elliptical hole

Using the method of characteristics for linear partial differential equations of order two, the solution to equation (3) can be written in terms of two arbitrary functions T_1 and T_2,

$$T = T_1(x_1 + \mu_1 x_2) + T_2(x_1 + \mu_2 x_2), \tag{4}$$

where μ_1 and μ_2 are the roots of the characteristic equation associated with equation (3), which reads

$$k_{22}\mu^2 + 2k_{12}\mu + k_{11} = 0. \tag{5}$$

Solving the quadratic equation (5) gives

$$\mu_{1,2} = \frac{1}{k_{22}}[-k_{12} \pm \sqrt{{k_{12}}^2 - k_{11}k_{22}}]. \tag{6}$$

Since the homogeneous quadratic form

$$k_{11}\left(\frac{\partial T}{\partial x_1}\right)^2 + 2k_{12}\frac{\partial T}{\partial x_1}\frac{\partial T}{\partial x_2} + k_{22}\left(\frac{\partial T}{\partial x_2}\right)^2$$

is positive definite, it follows that $k_{11}k_{22} > {k_{12}}^2$, and so the roots of equation (6) become complex conjugates.

We can then write the solution form equation (4) as

$$T = T_1(z') + T_2(\bar{z}') \tag{7}$$

where $z' = x_1 + \mu_1 x_2$, and the superposed bar indicates complex conjugate. With the further restriction that T must be real, equation (7) becomes

$$T = T_1(z') + \overline{T}_1(\bar{z}') = 2\,\mathrm{Re}[T_1(z')]. \tag{8}$$

The boundary conditions for this problem read

$$\begin{aligned} &\underline{q} = (q_1, q_2) = (0, q_0), \text{ at infinity} \\ &\underline{q}\cdot\underline{n} = 0, \text{ on hole} \end{aligned} \tag{9}$$

where $\underline{n}$ is the unit normal vector on the elliptical hole. The condition at infinity $(9)_1$ gives

$$k_{11}\frac{\partial T}{\partial x_1} + k_{12}\frac{\partial T}{\partial x_2} = 0, \qquad k_{12}\frac{\partial T}{\partial x_1} + k_{22}\frac{\partial T}{\partial x_2} = -q_0.$$

Solving these equations for the temperature gradients yields

$$\frac{\partial T}{\partial x_1} = \frac{k_{12}}{k_{11}}\frac{q_0}{H}, \qquad \frac{\partial T}{\partial x_2} = -\frac{q_0}{H}, \qquad H = -\frac{{k_{12}}^2}{k_{11}} + k_{22}. \tag{10}$$

Following common methods used in ideal fluid mechanics [16], the solution of this problem is found by conformal mapping techniques. By employing the three mappings

$$z' = x_1 + \mu_1 x_2, \qquad s = \frac{z' + \sqrt{{z'}^2 - a^2 - {\mu_1}^2 b^2}}{a - i\mu_1 b}, \qquad f = s - \frac{1}{s}, \tag{11}$$

the exterior of the elliptical hole in the z-plane is mapped to the exterior of a unit circle in the s-plane which in turn is mapped onto the whole f-plane, cut from $-2i$ to $2i$.

The boundary condition $(9)_1$, specified by relation $(10)_2$, transforms in the f-plane to

$$\frac{dT_1}{df} = -\frac{m_1 q_0}{\mu_1 H}, \tag{12}$$

where $m_{1,2} = 1/2(a \mp i\mu_1 b)$. Recall this relation was valid far away from the hole, i.e., for large f. However, since the f-plane contains no discontinuity, relation (12) is actually valid everywhere in the f-plane. It should also be pointed out that boundary condition $(9)_2$ is also satisfied through this mapping procedure.

Using the previous ideas, equation (12) can then be simply integrated to obtain our solution. Integrating and using the transformations equation (11) yields[3]

[3] The constant of integration for equation (13) has been dropped since it has no effect on the heat flux conditions

$$T_1(z') = -\frac{m_1 q_0}{\mu_1 H}\left[\frac{z' + \sqrt{z'^2 - 4m_1m_2}}{2m_1} - \frac{z' - \sqrt{z'^2 - 4m_1m_2}}{2m_2}\right]. \quad (13)$$

For the limiting case of $b \to 0$, the ellipse becomes a line crack of lenght $2a$, and the temperature distribution, equation (13), becomes

$$T_1(z') = \frac{q_0}{\mu_1 H}\sqrt{z'^2 - a^2}. \quad (14)$$

For the isotropic limit ($\mu_1 = i$), the general temperature distribution (13) reduces to that found by Florence and Goodier [2].

Results and Conclusions

Results of the previous analysis are best seen by plotting the isotherm lines. A numerical routine was developed [17] to calculate the coordinates of the isotherms in the z-plane. For illustrative purposes the conductivity components are chosen as $k_{11} = 1.0$, $k_{12} = 1.0$ and $k_{22} = 2.0$ W/cm-K. Isotherms for three different ratios of minor to major axis, i.e., $b/a = 0.5, 0.2, 0.0$ are shown in Figs. 2, 3, and 4. Using equation (10), the temperature gradient for this case far away from the hole is $\nabla T = q_0(1, -1)$. Consequently the isotherms should be inclined 45 deg to the x_1 axis away from the discontinuity.

The figures clearly show the rapid temperature changes around the major sides of the ellipses. This is a local phenomenon; however, these large temperature gradients give rise to large thermal stresses. As the hole ratio $b/a \to 0$, the temperature gradient becomes singular at the crack tip, see equation (14). Therefore, especially for small b/a, the uniform flow of heat could initiate material fracture. A detailed stress analysis study of this problem is forthcoming.

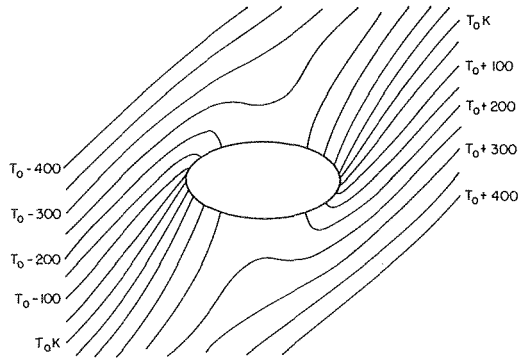

Fig. 2 Isotherms for $b/a = 0.5$; with $k_{11} = 1.0 = K_{12} = 1.0$, $k_{22} = 2.0$ W/cm-K, $q_0 = 10.0$ W/cm^2, T_0 = arbitrary reference temperature

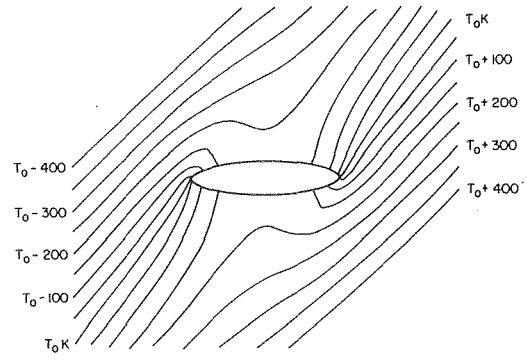

Fig. 3 Isotherms for $b/a = 0.2$; with $k_{11} = 1.0$, $k_{12} = 1.0$, $k_{22} = 2.0$ W/cm-K, $q_0 = 10.0$ W/cm^2, T_0 = arbitrary reference temperature

References

1 Florence, A. L. and Goodier, J. N., "Thermal Stress at Spherical Cavities and Circular Holes in Uniform Heat Flow," ASME *Journal of Applied Mechanics*, Vol. 26, 1959, p. 293.

2 Florence, A. L. and Goodier, J. N., "Thermal Stresses Due to Disturbance of Uniform Heat Flow by an Insulated Ovaloid Hole," ASME *Journal of Applied Mechanics*, Vol. 27, 1960, p. 635.

3 Florence, A. L. and Goodier, J. N., "Localized Thermal Stress at Holes, Cavities and Inclusions Disturbing Uniform Heat Flow," *Proc. Eleventh Int. Cong. Appl. Mech.*, Munich, 1964, p. 562.

4 Olesiak, Z. and Sneddon, I. N., "The Distribution of Thermal Stress in an Infinite Elastic Solid Containing a Penny-Shaped Crack," *Arch. Rat. Mech. Anal.*, Vol. 4, 1960, p. 238.

5 Sih, G. C., "On the Singular Character of Thermal Stresses Near a Crack Tip," ASME *Journal of Applied Mechanics*, Vol. 29, 1962, p. 587.

6 Bapu Rao, M. N., "Thermal Stresses Around an Insulated Crack in an Infinite Plate Subjected to a Uniform Heat Flow," *Int. Jour. Fracture*, Vol 7, 1976, p. 777.

7 Kassir, M. K. and Sih, G. C., "Three Dimensional Thermoelastic Problems of Planes of Discontinuities or Cracks in Solids," *Dev. Theo. Appl. Mech.*, Vol. 3, 1967, p. 167.

8 Kassir, M. K., "On the Distribution of Thermal Stresses Around an Elliptical Crack in an Infinite Solid," *Int. Jour. Eng. Sci.*, Vol. 7, 1969, p. 769.

9 Kassir, M. K., "Thermal Crack Propagation," ASME *Journal of Basic Engineering*, Vol. 92, 1971, p. 643.

10 Sekine, H., "Thermal Stress Singularities at Tips of a Crack in a Semi-Infinite Medium Under Uniform Heat Flow," *Eng. Fracture Mech.*, Vol. 7, 1975, p. 713.

11 Sekine, H., "Thermal Stresses Near Tips of an Insulated Line Crack in a Semi-Infinite Medium Under Uniform Heat Flow," *Eng. Fracture Mech.*, Vol. 9, 1977, p. 499.

12 Sekine, H., "Thermal Stress Problem for a Ribbon-Like Inclusion," *Letters Appl. Eng. Sci.*, Vol. 5, 1977, p. 51.

13 Murata, K. and Atsumi, A., "Thermal Stresses in a Transversely Isotropic Cylinder Containing a Penny-Shpaed Crack," *Letters Appl. Eng. Sci.*, Vol. 5, 1977, p. 173.

14 Atkinson, C. and Clements, D. L., "On Some Crack Problems in Anisotropic Thermoelasticity," *Int. Jour. Solids Structures*, Vol. 13, 1977, p. 855.

15 Yang, H. C. and Chou, Y. T., "Antiplane Strain Problems of an Elliptic Inclusion in an Anisotropic Medium," ASME *Journal of Applied Mechanics*, Vol. 44, 1977, p. 437.

16 Milne-Thomson, L. M., *Theoretical Hydrodynamics*, Macmillan, New York, 1960.

17 Miskioglu, I., "Thermal Stresses Around an Insulated Elliptical Hole in an Anisotropic Plate," M.S. Thesis, Mississippi State University, May 1978.

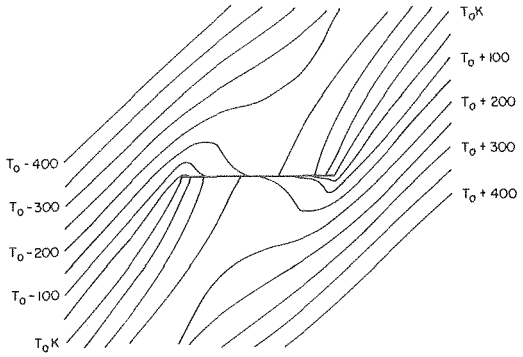

Fig. 4 Isotherms for $b/a = 0.0$; with $k_{11} = 1.0$, $k_{12} = 1.0$, $k_{22} = 2.0$ W/cm-K, $q_0 = 10.0$ W/cm^2, T_0 = arbitrary reference temperature

Heat Conduction in Axisymmetric Body-Duct Configuration

T. Miloh[1]

Nomenclature

a = radius of duct
A_n = coefficients, equation (4)
b = maximum radius of body
c = foci of spheroid and axial extent of source distribution

[1] School of Engineering, Tel-Aviv University, Tel-Aviv, Israel.

Contributed by the Heat Transfer Division for publication in the JOURNAL OF HEAT TRANSFER. Manuscript received by the Heat Transfer Division December 6, 1977.

$$T_1(z') = -\frac{m_1 q_0}{\mu_1 H}\left[\frac{z' + \sqrt{z'^2 - 4m_1m_2}}{2m_1} - \frac{z' - \sqrt{z'^2 - 4m_1m_2}}{2m_2}\right]. \quad (13)$$

For the limiting case of $b \to 0$, the ellipse becomes a line crack of lenght $2a$, and the temperature distribution, equation (13), becomes

$$T_1(z') = \frac{q_0}{\mu_1 H}\sqrt{z'^2 - a^2}. \quad (14)$$

For the isotropic limit ($\mu_1 = i$), the general temperature distribution (13) reduces to that found by Florence and Goodier [2].

Results and Conclusions

Results of the previous analysis are best seen by plotting the isotherm lines. A numerical routine was developed [17] to calculate the coordinates of the isotherms in the z-plane. For illustrative purposes the conductivity components are chosen as $k_{11} = 1.0$, $k_{12} = 1.0$ and $k_{22} = 2.0$ W/cm-K. Isotherms for three different ratios of minor to major axis, i.e., $b/a = 0.5, 0.2, 0.0$ are shown in Figs. 2, 3, and 4. Using equation (10), the temperature gradient for this case far away from the hole is $\nabla T = q_0(1, -1)$. Consequently the isotherms should be inclined 45 deg to the x_1 axis away from the discontinuity.

The figures clearly show the rapid temperature changes around the major sides of the ellipses. This is a local phenomenon; however, these large temperature gradients give rise to large thermal stresses. As the hole ratio $b/a \to 0$, the temperature gradient becomes singular at the crack tip, see equation (14). Therefore, especially for small b/a, the uniform flow of heat could initiate material fracture. A detailed stress analysis study of this problem is forthcoming.

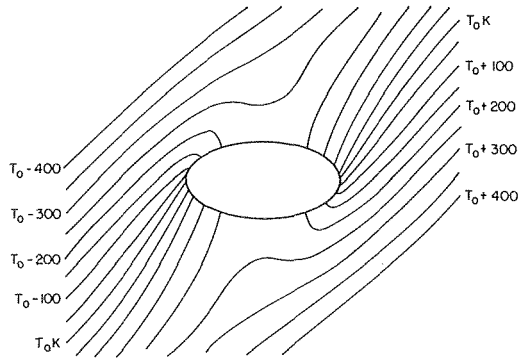

Fig. 2 Isotherms for $b/a = 0.5$; with $k_{11} = 1.0 = K_{12} = 1.0$, $k_{22} = 2.0$ W/cm-K, $q_0 = 10.0$ W/cm^2, T_0 = arbitrary reference temperature

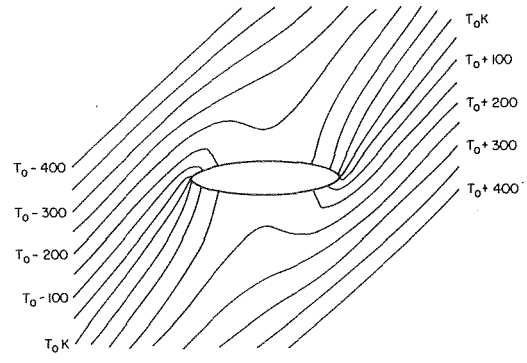

Fig. 3 Isotherms for $b/a = 0.2$; with $k_{11} = 1.0$, $k_{12} = 1.0$, $k_{22} = 2.0$ W/cm-K, $q_0 = 10.0$ W/cm^2, T_0 = arbitrary reference temperature

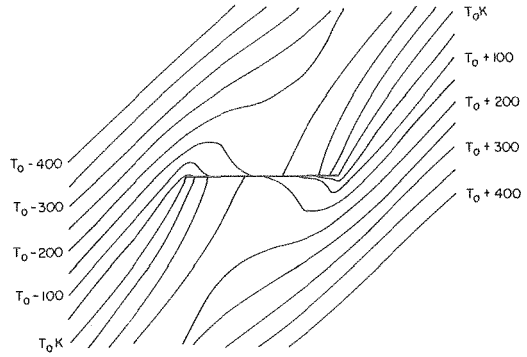

Fig. 4 Isotherms for $b/a = 0.0$; with $k_{11} = 1.0$, $k_{12} = 1.0$, $k_{22} = 2.0$ W/cm-K, $q_0 = 10.0$ W/cm^2, T_0 = arbitrary reference temperature

References

1 Florence, A. L. and Goodier, J. N., "Thermal Stress at Spherical Cavities and Circular Holes in Uniform Heat Flow," ASME *Journal of Applied Mechanics,* Vol. 26, 1959, p. 293.

2 Florence, A. L. and Goodier, J. N., "Thermal Stresses Due to Disturbance of Uniform Heat Flow by an Insulated Ovaloid Hole," ASME *Journal of Applied Mechanics,* Vol. 27, 1960, p. 635.

3 Florence, A. L. and Goodier, J. N., "Localized Thermal Stress at Holes, Cavities and Inclusions Disturbing Uniform Heat Flow," *Proc. Eleventh Int. Cong. Appl. Mech.,* Munich, 1964, p. 562.

4 Olesiak, Z. and Sneddon, I. N., "The Distribution of Thermal Stress in an Infinite Elastic Solid Containing a Penny-Shaped Crack," *Arch. Rat. Mech. Anal.,* Vol. 4, 1960, p. 238.

5 Sih, G. C., "On the Singular Character of Thermal Stresses Near a Crack Tip," ASME *Journal of Applied Mechanics,* Vol. 29, 1962, p. 587.

6 Bapu Rao, M. N., "Thermal Stresses Around an Insulated Crack in an Infinite Plate Subjected to a Uniform Heat Flow," *Int. Jour. Fracture,* Vol 7, 1976, p. 777.

7 Kassir, M. K. and Sih, G. C., "Three Dimensional Thermoelastic Problems of Planes of Discontinuities or Cracks in Solids," *Dev. Theo. Appl. Mech.,* Vol. 3, 1967, p. 167.

8 Kassir, M. K., "On the Distribution of Thermal Stresses Around an Elliptical Crack in an Infinite Solid," *Int. Jour. Eng. Sci.,* Vol. 7, 1969, p. 769.

9 Kassir, M. K., "Thermal Crack Propagation," ASME *Journal of Basic Engineering,* Vol. 92, 1971, p. 643.

10 Sekine, H., "Thermal Stress Singularities at Tips of a Crack in a Semi-Infinite Medium Under Uniform Heat Flow," *Eng. Fracture Mech.,* Vol. 7, 1975, p. 713.

11 Sekine, H., "Thermal Stresses Near Tips of an Insulated Line Crack in a Semi-Infinite Medium Under Uniform Heat Flow," *Eng. Fracture Mech.,* Vol. 9, 1977, p. 499.

12 Sekine, H., "Thermal Stress Problem for a Ribbon-Like Inclusion," *Letters Appl. Eng. Sci.,* Vol. 5, 1977, p. 51.

13 Murata, K. and Atsumi, A., "Thermal Stresses in a Transversely Isotropic Cylinder Containing a Penny-Shpaed Crack," *Letters Appl. Eng. Sci.,* Vol. 5, 1977, p. 173.

14 Atkinson, C. and Clements, D. L., "On Some Crack Problems in Anisotropic Thermoelasticity," *Int. Jour. Solids Structures,* Vol. 13, 1977, p. 855.

15 Yang, H. C. and Chou, Y. T., "Antiplane Strain Problems of an Elliptic Inclusion in an Anisotropic Medium," ASME *Journal of Applied Mechanics,* Vol. 44, 1977, p. 437.

16 Milne-Thomson, L. M., *Theoretical Hydrodynamics,* Macmillan, New York, 1960.

17 Miskioglu, I., "Thermal Stresses Around an Insulated Elliptical Hole in an Anisotropic Plate," M.S. Thesis, Mississippi State University, May 1978.

Heat Conduction in Axisymmetric Body-Duct Configuration

T. Miloh[1]

Nomenclature

a = radius of duct
A_n = coefficients, equation (4)
b = maximum radius of body
c = foci of spheroid and axial extent of source distribution

[1] School of Engineering, Tel-Aviv University, Tel-Aviv, Israel.

Contributed by the Heat Transfer Division for publication in the JOURNAL OF HEAT TRANSFER. Manuscript received by the Heat Transfer Division December 6, 1977.

C_n = coefficients, equation (14)
$D_n{}^m$ = coefficients, equation (17)
I_0 = modified Bessel function of first kind
j_n = spherical Bessel function
K_0 = modified Bessel function of second kind
k_t = thermal conductivity
M = axial source distribution
P_n = Legendre polynomials of first kind
q = heat flux, equation (7)
q_0 = heat flux for zero blockage
Q_n = Legendre polynomials of second kind
r = radial distance
r_c = radius of curvature
R = radius of sphere
T = temperature
T_1 = temperature of duct
T_2 = temperature of body
T^* = dimensionless temperature
x = distance along axis of symmetry
δ = Dirac delta function
μ = spheroidal coordinate
ρ = radial distance
ξ = axial distance
ζ = spheroidal coordinate
ζ_0 = inverse of spheroid eccentricity
ζ_b = equation of body, equation (6)

1 Introduction

A frequent configuration encountered in nuclear reactors is that of an elongated fuel element placed axisymmetrically inside a horizontal tube filled by a cool liquid. Very often liquid metals are used as coolants and under such circumstances the Peclet number is relatively small so that heat convection may be ignored with respect to heat conduction. The surface temperature of the fuel element is approximately constant and the wall of the duct is also maintained at constant temperature by an exterior cooling. An important engineering parameter in the design of such body-duct configuration is the flux of heat-conduction as a function of the blockage which is defined as the ratio between the maximum diameter of the central body and the diameter of the tube.

In the present paper a solution is presented for the temperature field in the duct and for the steady heat flux through its wall under the assumption of small Peclet numbers (no convection) and isothermal surfaces. The geometry of the problem is depicted in Fig. 1, where the heat flux from the slender body, given by $\rho = r(x)$, is determined as a function of the blockage ratio b/a and the temperature difference $T_2 - T_1$, between the body and the wall. Since the classical method of expansion in terms of orthogonal function can not be used in the present configuration, the method of Green's functions and the resulting integral equation is instead used. The integral equation, which is of the Fredholm type of the first kind, is solved by employing the collocation method. It is also shown that for spheroidal bodies an exact solution can be obtained, and for this reason the concept of using an "equivalent spheroid" is also advocated in this paper. A comparison between two numerical solutions for the heat flux for a spheroidal shape and for a sharp-edged fuel element is also presented.

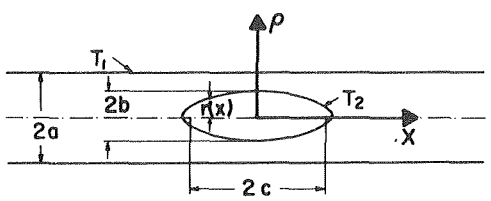

Fig. 1. Definition sketch for axisymmetric body-duct configuration

2 Formulation of the Problem

Consider a source of unit strength lying on the axis of a cylindrical duct. Let us define a cylindrical coordinate system (x, ρ) with its origin at the location of the source. Let a denote the radius of the isothermal circular tube of temperature T_1. The temperature field in the cylindrical duct is then given by

$$T(x, \rho) = T_1 - \frac{1}{\sqrt{x^2 + \rho^2}} + \frac{2}{\pi} \int_0^\infty \frac{K_0(ka)}{I_0(ka)} I_0(k\rho) \cos(kx) dk \quad (1)$$

which can be easily verified by employing the well-known relation ([1], p. 1261).

$$\frac{1}{\sqrt{x^2 + \rho^2}} = \frac{2}{\pi} \int_0^\infty K_0(k\rho) \cos(kx) dk. \quad (2)$$

Here K_0 and I_0 denote the zeroth order modified Bessel functions of the first and second kind respectively.

Let the equation of an isothermal axisymmetric body lying in the center of the duct be denoted by $\rho = r(x)$ and its surface temperature by T_2 (Fig. 1). It is convenient to select the origin at the center of the body and to normalize distances by c where $2c$ represents the distance between the body foci, hence the body may be generated by a distribution of sources $M(\xi)$ over that part of the x axis where $-1 < \xi < 1$. If the body has round ends the two extremes of the body should be at $\pm(1 + 1/2r_c)$ where r_c denote the radius of curvature at the endpoints. The integral equation for the determination of $M(\xi)$ is then

$$T_2 - T_1 = -\int_{-1}^{1} \frac{M(\xi) d\xi}{\sqrt{(x - \xi)^2 + r^2}} + \frac{2}{\pi} \int_{-1}^{1} \int_0^\infty M(\xi) \frac{K_0(ka)}{I_0(ka)} I_0(kr) \cos k(x - \xi) dk d\xi \quad (3)$$

which is a Fredholm integral equation of the first kind.

The numerical solution of (3) is very laborious. First, because of the peaking characteristics of the kernel of the single integral, the integration has to be carried out with special care mainly in the region where ξ is in the neighborhood of x (note that for the case where $x = \xi$ the kernel is infinitely large). Second, the numerical evaluation of the double integral is time consuming due to the oscillatory behaviour of the kernel. In order to overcome these difficulties it is suggested to expand $M(\xi)$ in terms of a Neumann series of Legendre polynomials,

$$M(\xi) = (T_2 - T_1) \sum_{n=0}^{\infty} A_n P_n(\xi) \quad (4)$$

where P_n denotes the nth order Legendre function of the first kind and A_n are coefficients to be determined.

It is convenient at this stage to define spheroidal coordinates μ and ζ which are related to the cylindrical coordinates x and ρ by the following transformation:

$$\rho^2 = (\zeta^2 - 1)(1 - \mu^2), \qquad x = \mu\zeta \quad (5)$$

The equation of the body surface, $\zeta_b(x)$ is then given by

$$2\zeta^2_b(x) = x^2 + r^2(x) + 1 + [(x^2 + r^2(x) + 1)^2 - 4x^2]^{1/2} \quad (6)$$

where $r(x)$ denotes the equation of the surface in cylindrical coordinates.

The selected form for the axial source distribution, (4) is particularly suitable for the computation of the heat-flux in the body-duct configuration. Denoting the coefficient of thermal conductivity of the medium by k_t, the total amount of heat-flux is given by

$$q = -k_t \int_S \frac{\partial T}{\partial n} dS \quad (7)$$

where S denotes the surface of the central body and n is the normal direction to the surface. By using the Gauss flux theorem equation (7) is expressed as

$$q = -8c\pi k_t (T_2 - T_1) A_0 \quad (8)$$

hence the heat-flux depends only on a single coefficient A_0 in the infinite sum (4).

3 Treatment of Single and Double Integrals

Following Morse and Fesbach [1] there exists the following expansion for the inverse of the distance between arbitrary two points in terms of Legendre functions

$$\frac{1}{\sqrt{(x-\xi)^2+r^2(x)}} = \sum_{n=0}^{\infty} (2n+1) P_n\left(\frac{x}{\zeta_b}\right) Q_n(\zeta_b) P_n(\xi) \tag{9}$$

where Q_n denotes the nth order Legendre function of the second kind.

Using the orthogonality properties of the Legendre polynomials, and after subsituting (4) and (9) in (3), yields

$$\int_{-1}^{1} \frac{M(\xi)d\xi}{[(x-\xi)^2+r^2(x)]^{1/2}} = 2(T_2-T_1) \sum_{n=0}^{\infty} A_n P_n\left(\frac{x}{\zeta_b}\right) Q_n(\zeta_b) \tag{10}$$

Similarly, the substitution of (4) into the double integral in (3) yields

$$\frac{2}{\pi}\int_{-1}^{1}\int_{0}^{\infty} M(\xi)\frac{K_0(ka)}{I_0(ka)} I_0(kr)\cos k(x-\xi)dkd\xi = \frac{4(T_2-T_1)}{\pi}\sum_{n=0}^{\infty} A_n i^n \int_0^{\infty}\frac{K_0(ka)}{I_0(ka)} I_0(kr)e^{-ikx} j_n(k)dk \tag{11}$$

where only the real part of (11) has to be considered. Here j_n denotes the nth order spherical Bessel function of the first kind defined by

$$j_n(k) = \frac{1}{2}(-1)^n \int_{-1}^{1} P_n(\xi) e^{ik\xi} d\xi \tag{12}$$

Combining (10) and (11) together with (3), renders the following infinite set of linear equations for the coefficients A_n:

$$\sum_{n=0}^{\infty} A_n C_n(x, r, a) = 1 \tag{13}$$

where

$$C_n(x,r,a) = -2P_n\left(\frac{x}{\zeta_b}\right) Q_n(\zeta_b) + \frac{4}{\pi} i^n \int_0^{\infty}\frac{K_0(ka)}{I_0(k0)} I_0(kr)e^{-ikx} j_n(k)dk \tag{14}$$

A method for solving equation (13) is to take only the first N terms in the infinite sum and to satisfy the equation at N chosen nodal points on the body. This is the so called collocation method. It is well known that the accuracy of this method is very sensitive to the choice of the nodal points and more points should be selected around the body-ends than over its center.

Once equation (13) has been solved for the coefficients A_n the dimensionless temperature $T^* = (T-T_1)/(T_2-T_1)$ in the duct is given by

$$T^*(x,\rho) = \sum_{n=0}^{\infty} A_n \left\{-2P_n\left(\frac{x}{\zeta}\right) Q_n(\zeta) + \frac{4}{\pi} i^n \int_0^{\infty}\frac{K_0(ka)}{I_0(ka)} I_0(k\rho) j_n(k) e^{-ikx} dk\right\} \tag{15}$$

where $\zeta(x, \rho)$ is defined in (5).

4 Simplifications for Spheroidal Bodies

The use of the collocation method introduces numerical inaccuracies into the solution and should be avoided, if possible. For the particular case where the central body is prolate spheroid, it can be shown that it is not necessary to use the collocation method and instead an exact solution can be obtained. Consider the spheroidal body given by $\zeta_b(x) = \zeta_0 = \text{const}$, where ζ_0 is the inverse of the spheroid eccentricity. Multiplying equation (13) by $P_m(\mu)$ and integrating over the range $1 > \mu > -1$, yields the following set of equations for A_n:

$$\sum_{n=0}^{\infty} A_{2n} D_{2n}{}^{2m}(a) = \delta(m), \qquad A_{2n+1} = 0. \tag{16}$$

where $\delta(m)$ is the Dirac delta function and

$$D_{2n}{}^{2m}(a) = -\frac{2}{4n+1} Q_{2n}(\zeta_0)\delta(m-n) + \frac{2}{\pi}(-1)^n \int_0^{\infty}\int_{-1}^{1} \times \frac{K_0(ka)}{I_0(ka)} I_0[k\sqrt{(\zeta_0^2-1)(1-\mu^2)}] e^{-ik\zeta_0\mu} j_{2n}(k) P_{2m}(\mu) d\mu dk \tag{17}$$

hence, in contrast with (13), the determination of the coefficients A_n is free of the choice of the nodal points. Equation (17) may be further simplified by employing the following relation [2]:

$$\int_{-1}^{1} P_m(\mu) I_0[k\sqrt{(\zeta_0^2-1)(1-\mu^2)}] e^{ik\zeta_0\mu} d\mu = 2i^m P_m(\zeta_0) j_m(k) \tag{18}$$

hence,

$$D_{2n}{}^{2m}(a) = -\frac{2}{4n+1} Q_{2n}(\zeta_0)\delta(m-n) + \frac{4}{\pi}(-1)^{m+n} P_{2m}(\zeta_0) \int_0^{\infty}\frac{K_0(ka)}{I_0(ka)} j_{2n}(k) j_{2m}(k) dk \tag{19}$$

For the case of "zero blockage" the radius of the pipe tends to infinity and the integral in the r.h.s. of (19) vanishes. Equation (16) can then be solved exactly yielding for the Neumann coefficients

$$A_m = -\frac{\delta(m)}{2Q_0(\zeta_0)} \tag{20}$$

and

$$q_0 = \frac{4c\pi k_t(T_2-T_1)}{Q_0(\zeta_0)} = 8c\pi k_t(T_2-T_1)\left[\log\frac{\zeta_0+1}{\zeta_0-1}\right]^{-1} \tag{21}$$

for the heat-flux from the surface of an isothermal spheroid at T_2 to an infinite medium of ambient temperature T_1. In the limit when $c \to 0$ and $\zeta_0 \to \infty$, the spheroid shrinks to a sphere with finite radius given by $R = c\zeta_0$, and equation (21) renders $q = 4\pi k_t R(T_2 - T_1)$.

5 Numerical Examples and Discussions

Numerical results are given for two axisymmetric central bodies with the same volume and same length to maximum-diameter ratio of $\sqrt{40}$; a spheroid with round edges and $\zeta_0 = \sqrt{40/30}$ and a sharp-edged body given by

$$r^2(x) = \frac{27}{640}\left(\frac{x+1+\alpha}{2+\alpha}\right)(1-x)^2, \qquad \alpha = \frac{54}{2533} \tag{22}$$

The two infinite sets of linear equations, namely (12) and (16) were solved by using the method of reduction [3] with 32 mesh points given by the Gauss 32 point quadrature formula. The amount of heat flux in the case of finite blockage depends only on a single coefficient A_0 of the infinite series and is given in equation (8). The relative increase of the heat flux due to the blockage effect q/q_0, is depicted in Fig. 2

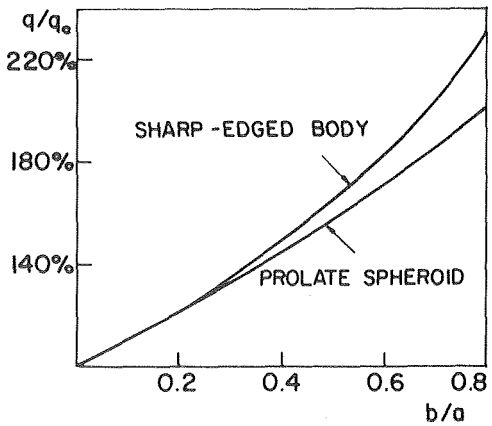

Fig. 2. Variation of heat-flux versus blockage for a prolate spheroid and a sharp-edged body

versus the blockage ratio b/a, for the spheroid and for the sharp-edged body. For $b/a = 0.2$, for example (20 percent blockage), the heat flux from the spheroid increases by 19 percent whereas the heat flux from the sharp-edged body increases by 21 percent. For a larger blockage ratio, say $b/a = 0.8$, the heat flux from the spheroid increases by as much as 100 percent and from the sharp-edged body by 130 percent.

Since the numerical solution for the spheroid is more efficient, yet more exact in the sense that it does not depend on the proper selection of the nodal points, it is also suggested that one use the concept of "equivalent spheroid." This concept is useful in the computation of an integral quantity such as the heat-flux from the surface of an arbitrary axisymmetric body. The idea is to replace the body by a proper spheroid with the same length and slenderness-ratio and to compute the heat flux for the spheroid rather than for the original body.

References

1 Morse, P. M. and Feshback, H., *Methods of Theoretical Physics*, McGraw-Hill, 1953.

2 Havelock, T. H., "Collected Papers on Hydrodynamics," U.S. Office of Naval Research, Government Printing Office, Washington, D.C., p. 591, 1963.

3 Kantarovich, L. V. and Krylov, V. L., "Approximate Methods of Higher Analysis," *Interscience*, 1958.

Closed Form Solutions for Certain Heat Conduction Problems

A. K. Naghdi[1]

Introduction

The exact closed form solutions have been derived for the problem of temperature distribution in an infinitely long circular cylindrical region subject to steady heat generation applied in a portion of the region as described in the following. The internal heat generation per unit time and volume q^*, which varies as a closed form polynomial only in the direction perpendicular to a plane parallel to the axis of the cylinder, exists on one side of the plane as shown in Fig. 1. We shall give as two examples, the cases of uniform heat generation in a portion of the cylinder, and concentrated heat source along a plane parallel to the axis of the cylinder.

Analysis

Let us consider a solid circular cylinder with radius R, and choose in its cross section sets of nondimensional rectangular and polar coordinate systems ξ, η, and ρ, θ as shown in Fig. 1. Here

$$\xi = \frac{X}{R}, \quad \eta = \frac{Y}{R}, \quad \rho = \frac{r}{R}. \tag{1}$$

It is assumed that there is no dependence of the properties of the material in the Z direction, and that the surface of the cylinder is kept at zero temperature. Since the heat conduction is two-dimensional, from this point we focus our attention only to the circular cross-sectional area. The governing differential equation for the temperature field T in the aforementioned cylinder of homogeneous isotropic material is given by

$$\nabla^2 T = p^*, \quad p^* = -\frac{R^2}{\kappa} q^* \tag{2}$$

in which κ is thermal conductivity, and ∇^2 is the two-dimensional Laplace operator.

Case I. Uniform Heat Generation on one Side of a Plane Parallel to the Axis of the Cylinder. For this case p^* can be written as

$$p^* = \bar{p} U(\xi - \xi_0), \tag{3}$$

in which $\bar{p}$ is a constant, ξ_0 is shown in Fig. 1, and

$$\left.\begin{aligned} U(\xi - \xi_0) &= 1 \quad \text{for } \xi \geq \xi_0, \\ U(\xi - \xi_0) &= 0 \quad \text{for } \xi < \xi_0. \end{aligned}\right\} \tag{4}$$

Let us substitute (3) in (2) and choose T_p as an η-independent particular integral of the differential equation to get

$$\frac{d^2 T_p}{d\xi^2} = \bar{p} U(\xi - \xi_0). \tag{5}$$

Integrating both sides of equation (5) twice, and considering that T_p and $\partial T_p/\partial \xi$ must be continuous at $\xi = \xi_0$, we obtain:

$$\left.\begin{aligned} T_p &= \frac{\bar{p}}{2}(\xi - \xi_0)^2 \quad \text{for } \xi \geq \xi_0, \\ T_p &= 0 \quad \text{for } \xi < \xi_0. \end{aligned}\right\} \tag{6}$$

In polar coordinate form, one can write relation (6) as

$$\left.\begin{aligned} T_p &= \frac{\bar{p}}{2}(\rho \cos\theta - \cos\theta_0)^2 \quad \text{for } \rho \cos\theta \geq \cos\theta_0 \\ T_p &= 0 \quad \text{for } \rho \cos\theta < \cos\theta_0 \end{aligned}\right\} \tag{7}$$

in which θ_0 is shown in Fig. 1.

Due to the symmetry with respect to the ξ axis, one can write the complementary solution T_c of equation (2) in the following polar coordinate form:

$$T_c = A_0 + A_1 \rho \cos\theta + \ldots + A_n \rho^n \cos n\theta + \ldots. \tag{8}$$

Here $A_0, A_1, \ldots A_n$ are the unknown constants to be determined from the boundary condition:

$$T = T_p + T_c = 0 \quad \text{at } \rho = 1. \tag{9}$$

Let us expand $T_p|_{\rho=1}$ in Fourier series with respect to θ and employ (9) to get

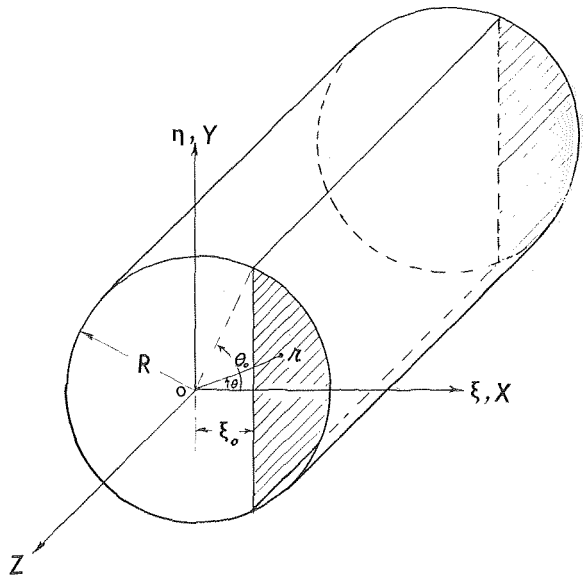

Fig. 1 Circular cylinder subjected to a heat source on one side of a plane parallel to the axis of the cylinder.

[1] Professor of Aeronautical-Astronautical Engineering and Mathematical Sciences, Indiana-Purdue University, Indianapolis, Ind. 46205

Contributed by the Heat Transfer Division for publication in the JOURNAL OF HEAT TRANSFER. Manuscript received by the Heat Transfer Division, October 17, 1977.

versus the blockage ratio b/a, for the spheroid and for the sharp-edged body. For $b/a = 0.2$, for example (20 percent blockage), the heat flux from the spheroid increases by 19 percent whereas the heat flux from the sharp-edged body increases by 21 percent. For a larger blockage ratio, say $b/a = 0.8$, the heat flux from the spheroid increases by as much as 100 percent and from the sharp-edged body by 130 percent.

Since the numerical solution for the spheroid is more efficient, yet more exact in the sense that it does not depend on the proper selection of the nodal points, it is also suggested that one use the concept of "equivalent spheroid." This concept is useful in the computation of an integral quantity such as the heat-flux from the surface of an arbitrary axisymmetric body. The idea is to replace the body by a proper spheroid with the same length and slenderness-ratio and to compute the heat flux for the spheroid rather than for the original body.

References

1 Morse, P. M. and Feshback, H., *Methods of Theoretical Physics*, McGraw-Hill, 1953.

2 Havelock, T. H., "Collected Papers on Hydrodynamics," U.S. Office of Naval Research, Government Printing Office, Washington, D.C., p. 591, 1963.

3 Kantarovich, L. V. and Krylov, V. L., "Approximate Methods of Higher Analysis," *Interscience*, 1958.

Closed Form Solutions for Certain Heat Conduction Problems

A. K. Naghdi[1]

Introduction

The exact closed form solutions have been derived for the problem of temperature distribution in an infinitely long circular cylindrical region subject to steady heat generation applied in a portion of the region as described in the following. The internal heat generation per unit time and volume q^*, which varies as a closed form polynomial only in the direction perpendicular to a plane parallel to the axis of the cylinder, exists on one side of the plane as shown in Fig. 1. We shall give as two examples, the cases of uniform heat generation in a portion of the cylinder, and concentrated heat source along a plane parallel to the axis of the cylinder.

Analysis

Let us consider a solid circular cylinder with radius R, and choose in its cross section sets of nondimensional rectangular and polar coordinate systems ξ, η, and ρ, θ as shown in Fig. 1. Here

$$\xi = \frac{X}{R}, \quad \eta = \frac{Y}{R}, \quad \rho = \frac{r}{R}. \tag{1}$$

It is assumed that there is no dependence of the properties of the material in the Z direction, and that the surface of the cylinder is kept at zero temperature. Since the heat conduction is two-dimensional, from this point we focus our attention only to the circular cross-sectional area. The governing differential equation for the temperature field T in the aforementioned cylinder of homogeneous isotropic material is given by

$$\nabla^2 T = p^*, \quad p^* = -\frac{R^2}{\kappa} q^* \tag{2}$$

in which κ is thermal conductivity, and ∇^2 is the two-dimensional Laplace operator.

Case I. Uniform Heat Generation on one Side of a Plane Parallel to the Axis of the Cylinder. For this case p^* can be written as

$$p^* = \bar{p} U(\xi - \xi_0), \tag{3}$$

in which $\bar{p}$ is a constant, ξ_0 is shown in Fig. 1, and

$$\left.\begin{aligned} U(\xi - \xi_0) &= 1 \quad \text{for } \xi \geq \xi_0, \\ U(\xi - \xi_0) &= 0 \quad \text{for } \xi < \xi_0. \end{aligned}\right\} \tag{4}$$

Let us substitute (3) in (2) and choose T_p as an η-independent particular integral of the differential equation to get

$$\frac{d^2 T_p}{d\xi^2} = \bar{p} U(\xi - \xi_0). \tag{5}$$

Integrating both sides of equation (5) twice, and considering that T_p and $\partial T_p/\partial \xi$ must be continuous at $\xi = \xi_0$, we obtain:

$$\left.\begin{aligned} T_p &= \frac{\bar{p}}{2}(\xi - \xi_0)^2 \quad \text{for } \xi \geq \xi_0, \\ T_p &= 0 \quad \text{for } \xi < \xi_0. \end{aligned}\right\} \tag{6}$$

In polar coordinate form, one can write relation (6) as

$$\left.\begin{aligned} T_p &= \frac{\bar{p}}{2}(\rho \cos\theta - \cos\theta_0)^2 \quad \text{for } \rho \cos\theta \geq \cos\theta_0 \\ T_p &= 0 \quad \text{for } \rho \cos\theta < \cos\theta_0 \end{aligned}\right\} \tag{7}$$

in which θ_0 is shown in Fig. 1.

Due to the symmetry with respect to the ξ axis, one can write the complementary solution T_c of equation (2) in the following polar coordinate form:

$$T_c = A_0 + A_1 \rho \cos\theta + \ldots + A_n \rho^n \cos n\theta + \ldots. \tag{8}$$

Here $A_0, A_1, \ldots A_n$ are the unknown constants to be determined from the boundary condition:

$$T = T_p + T_c = 0 \quad \text{at } \rho = 1. \tag{9}$$

Let us expand $T_p|_{\rho=1}$ in Fourier series with respect to θ and employ (9) to get

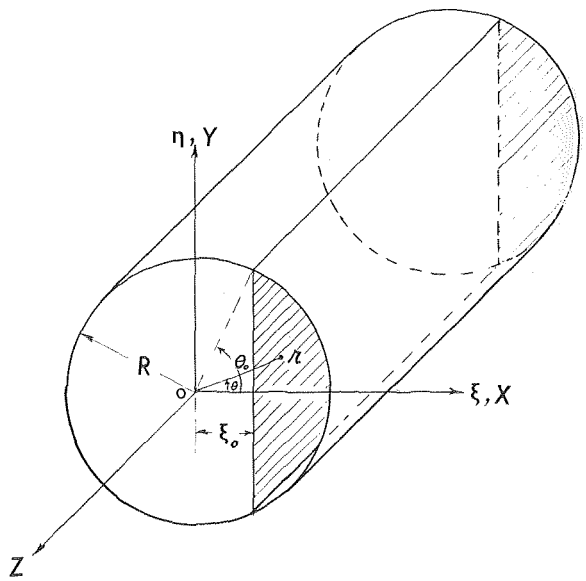

Fig. 1 Circular cylinder subjected to a heat source on one side of a plane parallel to the axis of the cylinder.

[1] Professor of Aeronautical-Astronautical Engineering and Mathematical Sciences, Indiana-Purdue University, Indianapolis, Ind. 46205

Contributed by the Heat Transfer Division for publication in the JOURNAL OF HEAT TRANSFER. Manuscript received by the Heat Transfer Division, October 17, 1977.

$$A_n = -a_n, \tag{10}$$

in which

$$\left.\begin{aligned}
a_0 &= \frac{\bar{p}}{2\pi}\left[\left(\frac{1}{2}+b^2\right)\theta_0 - 2b\sin\theta_0 + \frac{1}{4}\sin 2\theta_0\right],\\
a_1 &= \frac{\bar{p}}{\pi}\left[\left(\frac{1}{2}+b^2\right)\sin\theta_0 - b\left(\theta_0+\frac{1}{2}\sin 2\theta_0\right)\right.\\
&\qquad \left.+\frac{1}{4}\left(\frac{1}{3}\sin 3\theta_0+\sin\theta_0\right)\right],\\
a_2 &= \frac{\bar{p}}{\pi}\left[\frac{1}{2}\left(\frac{1}{2}+b^2\right)\sin 2\theta_0 - b\left(\frac{1}{3}\sin 3\theta_0+\sin\theta_0\right)\right.\\
&\qquad \left.+\frac{1}{4}\left(\theta_0+\frac{1}{4}\sin 4\theta_0\right)\right],\\
a_n &= \frac{\bar{p}}{\pi}\left\{\left(\frac{1}{2}+b^2\right)\frac{1}{n}\sin n\theta_0\right.\\
&\qquad -b\left[\frac{1}{n+1}\sin(n+1)\theta_0+\frac{1}{n-1}\sin(n-1)\theta_0\right]\\
&\qquad \left.+\frac{1}{4}\left[\frac{1}{n+2}\sin(n+2)\theta_0+\frac{1}{n-2}\sin(n-2)\theta_0\right]\right\},\\
&\qquad b=\cos\theta_0, \quad n\geq 3.
\end{aligned}\right\} \tag{11}$$

It is seen from (11), that the general term in T_c has elements in the form

$$\frac{\rho^n}{n+n_0}\sin[(n+n_0)\theta_0]\cos n\theta, \tag{12}$$

where $n_0 = 0, \pm 1, \pm 2$, and is independent of n. Combining $\sin n\theta_0$ or $\cos n\theta_0$ with $\cos n\theta$ in (12) and letting $N = n + n_0$ one finds

$$\left.\begin{aligned}
&\sum_{n=3}^{\infty}\frac{\rho^n}{n+n_0}\sin[(n+n_0)\theta_0]\cos n\theta\\
&\quad=\frac{1}{2\rho^{n_0}}\cos n_0\theta\left[\sum_{N=3+n_0}^{\infty}\frac{\rho^N}{N}\sin N\phi_1+\sum_{N=3+n_0}^{\infty}\frac{\rho^N}{N}\sin N\phi_2\right]\\
&\quad+\frac{1}{2\rho^{n_0}}\sin n_0\theta\left[\sum_{N=3+n_0}^{\infty}\frac{\rho^N}{N}\cos N\phi_2-\sum_{N=3+n_0}^{\infty}\frac{\rho^N}{N}\cos N\phi_1\right],\\
&\qquad \phi_1=\theta_0+\theta, \quad \phi_2=\theta_0-\theta.
\end{aligned}\right\} \tag{13}$$

The reason that the series on the left-hand side of equation (13) starts with $n = 3$ is that the expressions for a_0, a_1, a_2 do not follow that of the general term a_n for $n \geq 3$.

It has been shown in the previous works [1, 2, 3] that series similar to those on the right-hand side of (13) have closed form sums:

$$\left.\begin{aligned}
&\sum_{m=1}^{\infty}\frac{\bar{e}^{m\lambda}}{m}\cos m\phi \equiv \frac{1}{2}\ln\frac{\cosh\lambda-1}{\cosh\lambda-\cos\phi} - \ln(1-\bar{e}^{\lambda}), \quad \lambda>0,\\
&\sum_{m=1}^{\infty}\frac{\bar{e}^{m\lambda}}{m}\sin m\phi \equiv -\frac{\phi}{2}+\operatorname{Arc\,tan}\left[\frac{(1+\cosh\lambda)\tan\frac{\phi}{2}}{\sinh\lambda}\right],\\
&\qquad \lambda>0, \quad \pi>\phi>-\pi.
\end{aligned}\right\} \tag{14}$$

It is obvious that for $\rho < 1$, one can transform the series on the right-hand side of (13) to the form given by relation (14). As an example for $n_0 = 1$ we write

$$\left.\begin{aligned}
\sum_{N=4}^{\infty}\frac{\rho^N}{N}\sin N\phi_1 &= \left[\sum_{N=1}^{\infty}\frac{e^{-\lambda N}}{N}\sin N\phi_1\right]-\rho\sin\phi_1\\
&\quad -\frac{\rho^2}{2}\sin 2\phi_1-\frac{\rho^3}{3}\sin 3\phi_1-\frac{\rho^4}{4}\sin 4\phi_1,
\end{aligned}\right\} \tag{15}$$

where $\lambda = -\ln\rho$ is a positive number. Therefore, the desired closed-form solution for the temperature distribution in this case is written in the following form:

$$\left.\begin{aligned}
T &= T_c+\frac{\bar{p}}{2}(\rho\cos\theta-\cos\theta_0)^2 \quad \text{for } \rho\cos\theta\geq\cos\theta_0,\\
T &= T_c \quad \text{for } \rho\cos\theta<\cos\theta_0,
\end{aligned}\right\} \tag{16}$$

in which

$$\left.\begin{aligned}
T_c &= -a_0-a_1\rho\cos\theta-a_2\rho^2\cos 2\theta-\frac{\bar{p}}{\pi}\left\{\left[\frac{1}{2}\left(\frac{1}{2}+b^2\right)\right.\right.\\
&\quad \left.-\frac{b}{2}\left(\frac{1}{\rho}+\rho\right)\cos\theta+\frac{1}{8}\left(\frac{1}{\rho^2}+\rho^2\right)\cos 2\theta\right][F_1(\rho,\theta)+F_2(\rho,\theta)]\\
&\quad +\left[\frac{b}{2}\left(\frac{1}{\rho}-\rho\right)\sin\theta-\frac{1}{8}\left(\frac{1}{\rho^2}-\rho^2\right)\sin 2\theta\right][G_1(\rho,\theta)-G_2(\rho,\theta)]\\
&\quad -\frac{1}{2}\left(\frac{1}{2}+b^2\right)\left[\sum_{N=1}^{2}\frac{\rho^N}{N}(\sin N\phi_1+\sin N\phi_2)\right]\\
&\quad +\frac{b}{2\rho}\cos\theta\left[\sum_{N=1}^{3}\frac{\rho^N}{N}(\sin N\phi_1+\sin N\phi_2)\right]\\
&\quad +\frac{b}{2\rho}\sin\theta\left[\sum_{N=1}^{3}\frac{\rho^N}{N}(\cos N\phi_2-\cos N\phi_1)\right]\\
&\quad +\frac{b}{2}\rho^2\cos\theta(\sin\phi_1+\sin\phi_2)-\frac{b}{2}\rho^2\sin\theta(\cos\phi_2-\cos\phi_1)\\
&\quad -\frac{1}{8\rho^2}\cos 2\theta\left[\sum_{N=1}^{4}\frac{\rho^N}{N}(\sin N\phi_1+\sin N\phi_2)\right]\\
&\quad \left.-\frac{1}{8\rho^2}\sin 2\theta\left[\sum_{N=1}^{4}\frac{\rho^N}{N}(\cos N\phi_2-\cos N\phi_1)\right]\right\},
\end{aligned}\right\} \tag{17}$$

$$\left.\begin{aligned}
F_1(\rho,\theta) &= \begin{cases}F(\rho,\phi_1) & \text{for } \pi>\phi_1>-\pi,\\ -F(\rho,[2\pi-\phi_1]) & \text{for } 2\pi>\phi_1>\pi,\end{cases}\\
F_2(\rho,\theta) &= F(\rho,\phi_2) \quad \text{for } \pi>\phi_2>-\pi,\\
F(\rho,\phi) &= -\frac{\phi}{2}+\operatorname{Arctan}\left\{\frac{\left[1+\cosh\left(\ln\frac{1}{\rho}\right)\right]\tan\frac{\phi}{2}}{\sinh\left(\ln\frac{1}{\rho}\right)}\right\},\\
&\qquad \text{For } \rho<1, \quad \pi>\phi>-\pi,\\
G_1(\rho,\theta) &= G(\rho,\phi_1),\\
G_2(\rho,\theta) &= G(\rho,\phi_2),\\
G(\rho,\phi) &= \frac{1}{2}\ln\left[\frac{\cosh\left(\ln\frac{1}{\rho}\right)-1}{\cosh\left(\ln\frac{1}{\rho}\right)-\cos\phi}\right]+\ln(1-\rho),\\
&\qquad \text{For } \rho<1.
\end{aligned}\right\} \tag{18}$$

Note that the expression for the function $F(\rho, \phi) = \Sigma_{N=1}^{\infty}\rho^N/N\sin N\phi$ does not include the cases for $\phi = \pm\pi$. However, it is obvious that the values of the series for those angles are zero.

Case II. Cylinder subject to a concentrated heat source uniformly distributed along a plane parallel to the axis of the cylinder. In this case p^* can be written as

$$p^* = \bar{p}_s\delta(\xi-\xi_0), \tag{19}$$

in which $\bar{p}_s$ is a constant, and $\delta(\xi - \xi_0)$ is the unit impulse function. The procedure for the determination of the solution in this case is identical to that of Case I. Thus, for the sake of brevity we shall only list the results:

$$\left.\begin{aligned}
T_s &= T_{cs}+\bar{p}_s(\rho\cos\theta-\cos\theta_0) \quad \text{for } \rho\cos\theta\geq\cos\theta_0,\\
T_s &= T_{cs} \quad \text{for } \rho\cos\theta<\cos\theta_0,
\end{aligned}\right\} \tag{20}$$

in which

$$T_{cs} = -a_{0s}-a_{1s}\rho\cos\theta$$

$$
\left.
\begin{aligned}
-\frac{\bar{p}_s}{\pi}\Bigg\{\Bigg[\frac{1}{2}\left(\frac{1}{\rho}+\rho\right)\cos\theta - b\Bigg]\,[F_1(\rho,\theta)+F_2(\rho,\theta)] \\
-\frac{1}{2}\left(\frac{1}{\rho}-\rho\right)\sin\theta\,[G_1(\rho,\theta)-G_2(\rho,\theta)] \\
-\frac{1}{2\rho}\cos\theta\left[\sum_{N=1}^{2}\frac{\rho^N}{N}(\sin N\phi_1+\sin N\phi_2)\right] \\
-\frac{1}{2\rho}\sin\theta\left[\sum_{N=1}^{2}\frac{\rho^N}{N}(\cos N\phi_2-\cos N\phi_1)\right] \\
+b\rho\,(\sin\phi_1+\sin\phi_2)\Bigg\}, \\
a_{0s}=\frac{\bar{p}_s}{\pi}\,(\sin\theta_0-b\theta_0), \\
a_{1s}=\frac{2\bar{p}_s}{\pi}\left(\frac{1}{2}\theta_0+\frac{1}{4}\sin 2\theta_0-b\sin\theta_0\right).
\end{aligned}
\right\} \quad (21)
$$

It is obvious that in this case $\partial T/\partial\xi$ is not continuous across the plane $\xi = \xi_0$.

The closed form solutions to the problems of temperature field for the cases such as linear or parabolic or other polynomial distributions of q^* on one side of the plane $\xi = \xi_0$ can be obtained similarly.

Discussion

Most of the heat conduction problems that are routinely solved fall in the category of those in which the boundary of the object and the heat source coincide with the employed coordinate lines. Many problems of this type have been solved in the past and published in text books such as Carslaw and Jaeger [4]. Unfortunately simple techniques of solution which solve the aforementioned problems cannot easily be applied to the cases considered in this article. This is because one of the boundaries of the heat source does not coincide with a coordinate line in the polar system ρ and θ. The contribution of this paper can be summarized as follows. The particular integral of the governing equation is obtained in closed-form. This process, which removes the term representing the singular heat source from the differential equation, results in a better convergence of the complementary series solution even if the series terms are not summed.

References

1 Kantorovich, L. V., and Krylov, V. I., *Approximate Methods of Higher Analysis*, Interscience Publishers, Inc., New York and The Netherlands, 1964.

2 Naghdi, A. K., and Gersting, J. M., Jr., "The Effect of a Transverse Shear Acting on the Edge of a Circular Cutout in a Simply Supported Circular Cylindrical Shell," *Ingenieur-Archiv*, Vol. 42, No. 2, Jan. 1973.

3 Naghdi, A. K., "On the Convergence of Series Solutions for a Short Beam," Trans. of ASME, Vol. 96, *Journal of Applied Mechanics*, Vol. 41, No. 2.

4 Carslaw, H. S., and Jaeger, J. C., *Conduction of Heat in Solids*, Second ed., Oxford, 1959.

journal of heat transfer

discussion

The Heat Balance Integral in Steady-State Conduction[1]

B. T. F. Chung.[2] The application of heat balance integral method to two-dimensional steady heat conduction problems is of interest because of its simplicity. Although the problems can be solved exactly, the evaluation of temperature profile often requires a digital computer, due to the infinite series and eigen-values involved in the solutions. As demonstrated by the author, the approximate analysis shows a significant improvement over the one-dimensional analysis of heat transfer in extended surfaces. However, we do not agree with the author in the following aspects:

1 There appear to be obvious typographical errors in author's equation (13) which should be

$$\frac{t_s}{t_0} = \frac{\cos h\, M(\ell - x) + H \sin h\, M(\ell - x)}{\cos h\, M\ell + H \sin h\, M\ell}$$

2 We obtained an expression for b which is quite different from that given by equation (17). Our formulation for D is symmetrical with respect to B_1 and B_2 and is given by

$$D = \frac{1}{b}\left[\frac{6(B_1 + B_2 + 2B_1B_2}{2B_1 + 2B_2 + B_1B_2 + 3}\right]^{1/2}$$

I am puzzled by the statement, "Note that although the expression for D is not symmetric with respect to B_1 and B_2, the solution itself is actually symmetric." The solution of heat transfer rate, q/kt_{01} is a function of Db and λ/b only. How can it be symmetric with respect to B_1 and B_2 if Db is not symmetric?

3 We agree with the author on equation (19) only when H is defined by $h_e/(kD)$. The definition for H given below equation (19) is inconsistent with the one defined earlier for the case of straight fin with identical fin coefficient on lower and upper surfaces.

4 Equation (25) should be corrected to

$$\frac{d^2t_s}{dr^2} + \frac{1}{r}\frac{dt_s}{dr} - \frac{2ht_s}{kbC} = 0$$

An equal sign and zero are missing in equation (31).

5 In Figs. 2 and 3, the independent variable $2\ell/b$ is chosen to range from 0.1 to 10.0 and the ratio of transfer coefficient between the lower and the upper surfaces B_1/B_2 ranges from 1 to 100 (the subscript 1 implies lower surface as can be seen from equation 15). In practice, the values of $2\ell/b$ for a straight fin are very unlikely to be less than unity; on the other hand, the values of B_1/B_2 are always less than unity in the case of heat dissipation by free convection.

[1] By A. A. Sfeir, published in the JOURNAL OF HEAT TRANSFER Vol. 98, No. 3, pp. 466–470.

[2] Associate Professor, Department of Mechanical Engineering, The University of Akron, Akron, Ohio.

Author's Closure

The Author wishes to thank Professor Chung for presenting a discussion on the subject paper.

Due to circumstances beyond the control of the author and the Journal, this paper was printed with incomplete correction of the galley proofs. This resulted in the typographical errors pointed out by Professor Chung.

However, there seems to be a more serious error in the original paper in the expression for D. The new expression given by Professor Chung is correct and so are his comments in this regard. Also, in the definition of H (following equation (19)), H must be multiplied by $b/2$.

As for the last point raised, and as far as the heat conduction problem is concerned, it makes no difference which of the two surfaces, the upper or the lower, has a higher h. In any case, Fig. 3 is given only to illustrate the analysis and should not be used as a design chart in view of the fact that we have assumed $h_e = \frac{1}{2}(h_1 + h_2)$. In practice, h_e will be larger than both h_1 and h_2 and this would make a big difference, particularly for short fins.

The Numerical Prediction of the Turbulent Flow and Heat Transfer in the Entrance Region of a Parallel Plate Duct[1]

M. R. Malik[2] and **R. H. Pletcher.**[3] The recent calculations of entry flow in a plane duct [1][4] have been of interest to us, since such a duct is a limiting case of an annular channel, a geometry which we are currently studying. The discussions of this paper have become a forum for comparing the predictions of various turbulence models for this flow. In this spirit, the present communication compares the predictions of a recently developed turbulence model with some of these earlier calculations [1, 2].

In the model to be described in the present communication, we have assumed that the eddy viscosity is given by

$$\epsilon = \ell^2 \left|\frac{\partial u}{\partial y}\right| \tag{1}$$

[1] By A. F. Emery and F. B. Gessner, published in the November 1976 issue of the JOURNAL OF HEAT TRANSFER, Vol. 98, No. 4, pp. 594–600.

[2] Research Assistant, Department of Mechanical Engineering, Iowa State University, Ames, Iowa.

[3] Professor, Department of Mechanical Engineering, Iowa State University, Ames, Iowa.

[4] Numbers in brackets designate additional References at end of discussion.

